# Anionic redox for high-energy batteries. Fundamental understanding, practical challenges, and future outlook

Gaurav Assat

Sorbonne Université

*Ecole Doctorale – ED 397 · Physique et Chimie des Matériaux*

Collège de France

*Laboratoire – Chaire de Chimie du Solide et de l'Energie*


# Anionic redox for high-energy batteries – Fundamental understanding, practical challenges, and future outlook


Gaurav Assat


Doctoral thesis in Materials Science / Chemistry

Directed by Charles Delacourt and Jean-Marie Tarascon

Presented and defended in public on December 14th 2018 in front of the jury :

| | | |
|---|---|---|
| Dr. Marnix Wagemaker | Associate Professor · TU Delft · The Netherlands | Referee |
| Prof. Lorenzo Stievano | Professor · Université de Montpellier | Referee |
| Prof. Petr Novák | Section Head · PSI Villigen · Switzerland | Examiner |
| Prof. Renaud Bouchet | Professor · Institut Polytechnique de Grenoble | Examiner |
| Prof. Christel Laberty-Robert | Professor · UMPC - Sorbonne Université · Paris | Examiner |
| Dr. Bruno Delobel | Team Leader · Battery R&D · Renault Group | Examiner |
| | | |
| Dr. Charles Delacourt | Research Leader · CNRS · UPJV · Amiens | Co-director |
| Prof. Jean-Marie Tarascon | Professor · Collège de France · Paris | Director |

*“ Don’t accept that what’s happening*
*is just a case of others’ suffering,*
*or you’ll find that you’re joining in*
*the turning away ”*

*– David Gilmour and Anthony Moore, 1987*

*dedicated to my parents · dédié à mes parents*

*Pushpa Soni et Rajendra Prasad Assat*

# Acknowledgements

I learnt tremendously while working under the direction of Prof. Jean-Marie Tarascon at Collège de France. His passion for chemistry, his broad vision, his 100 % availability for us, and his energy at work are simply unmatchable. I wonder whether there are some hidden batteries of high energy, high power, and long-life inside of him! *Merci* Jean-Marie for constantly pushing me beyond my comfort zone, trusting me with challenging tasks (like the Review paper we wrote), allowing me to freely explore my own research paths, and hence bringing the best out of me. Keeping up with your levels of energy and exigence was not at all easy. Sometimes it even felt unnecessary and unfair. But looking back, I can see how the past three years not only transformed me into a competent researcher, but also shaped me for the bigger challenges to come in my professional future.

I could not have done this PhD without the guidance of Dr. Charles Delacourt. *Maaaan*…thanks a lot! You are a great mentor and an exceptionally kind person. I was always impressed with your knowledge about batteries and electrochemistry, but more importantly your ability to transmit this knowledge, while staying completely humble at the same time. Your outstanding scientific rigour was always something I tried to emulate. Thanks for bringing a cheerful aspect to my PhD with tonnes of positive feedback that helped me stay confident in this cutting-edge research world. I will cherish the fruitful long discussions we had, both scientific ones as well as general ones, regarding the society and the environment. *Merci beaucoup* Charles, I will always miss the visits to Amiens!

A substantial amount of data in this thesis was acquired at the SOLEIL synchrotron, where the help of Dr. Antonella Iadecola was always indispensable. *Grazie mille* Antonella for bearing me during (at least) 7 separate beam-time experiments that we performed together. It was thanks to your ability to organize the teamwork throughout these stressful 24-hour experiments that I was able to acquire high quality data, which led to strong publications. Thanks also for patiently teaching me how to do my own data analysis, rather than simply doing it yourself for the sake of rapid publication. I really appreciated such a student-centred philosophy of carrying out research. Lastly, thanks also for your warm yet dynamic attitude as well as your self-proclaimed “psychotherapy” sessions free of cost throughout the past three years!

I consider myself very fortunate to have had the chance of working in the Solid-State Chemistry & Energy lab at Collège de France. It's a terrific building, a spotless lab, with all the state-of-the-art equipment. Added to that, working alongside students and researchers from various countries and backgrounds made it a richer experience. I am especially thankful to Dr. Daniel Alves Dalla Corte for helping me settle down during the initial months of my PhD, to Paul Pearce for the collaboration on iridates and for surviving 2 beam-times with me (including a "lost" laptop in Barcelona), and to Sujoy Saha for the rich collaboration on sulfides. I simply cannot list here the numerous lab members that I met over my three years here, but I am really grateful for having known all of you! Thanks especially to Florent Lepoivre for his never-ending dynamism, to Robin Beer and Qing Wang for the invigorating discussions, to Yin Yang for sharing his knowledge, and to Jessica Duvoisin for the smooth (and cheerful) functioning of the administrative processes.

This thesis also benefitted strongly from external collaborations. The HAXPES studies could not have been successful without the long and fruitful collaboration with Prof. Rémi Dedryvère, with complementary XPS experiments done by Dr. Dominique Foix. Thank you both! Another fruitful collaboration resulted from the willingness of Dr. Stephen Glazier (from Jeff Dahn's group in Canada) to share the expertise on isothermal calorimetry. Thanks Stephen for acquiring the data and for the fruitful discussions around this topic.

I am grateful to the RS2E research network in France for funding this thesis. I sincerely thank those who work hard to keep the network running as well as all its academic and industrial members for their enthusiastic participation.

Lastly, on a more personal note, I cannot imagine having survived these past three years and the tough life in Paris without the unconditional support of Ava, who kept me afloat in the worst of times. Thanks for acting like a giant sponge made out of kindness.

# Table of Contents

# Broader context and thesis outline

Driven primarily by economic growth in the developing world (non-OECD countries), the global energy demand is forecasted to increase by 37% by 2040, with Asia accounting for 60% of the total increase. To meet this rising demand, we cannot simply rely on the energy production methods prevalent today, which are based on fossil fuel combustion, as they represent two-thirds of global emissions of $CO_2$ – a gas that accounts for 75% of global greenhouse gas (GHG) emissions. Because anthropogenic (related to humans) GHG emissions are considered to be a highly likely cause of global temperature rise and subsequent environmental changes since the mid-20$^{th}$ century, there is a strong need to (*i*) transition towards renewables in the energy supply, (*ii*) reduce energy consumption and improve the efficiency of our energy systems, (*iii*) electrify the transportation sector, as well as (*iv*) innovate on carbon capture/sequestration (CCS) technologies in order to curtail global $CO_2$ emissions (**Figure 1**).[1,2]

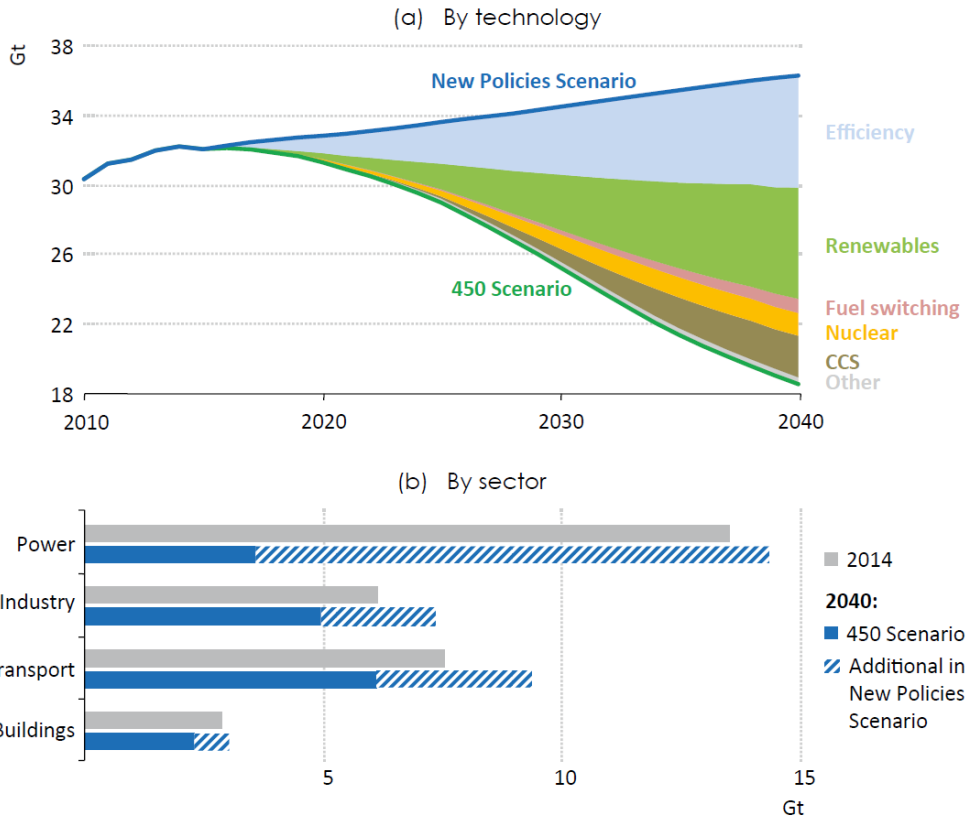


**Figure 1 | Global $CO_2$ emissions (gigatonne per year) under two different policy scenarios‡‡.** Adapted from: *IEA World Energy Outlook 2016*.[1]

‡‡ The 'New Policies Scenario' is designed to show where existing policies as well as announced policy intentions (such as the Paris Climate Deal) might lead the energy sector. The '450 Scenario' is an even more stringent policy-mix (but hypothetical as of today) to limit the global temperature rise to 2 °C in 2100 by limiting atmospheric $CO_2$ to below 450 ppm.

Towards these goals, energy-storage technologies (ESTs) play a crucial role. The deployment of renewables in the energy supply, such as solar and wind that are intermittent in nature and difficult to accurately predict, is impossible without parallel innovation in ESTs. Moreover, ESTs can provide flexibility to energy systems, hence allowing for better optimization and efficiency gains. Lastly, electrification of the transportation sector cannot accelerate without cost-competitiveness of ESTs.

> *"Energy storage technologies are essential to bridge temporal and geographical gaps between energy demand and supply. They represent considerable economic potential with far-reaching business opportunities*."[2]

ESTs can be divided into electrical, electrochemical, thermal, and mechanical, having varying degrees of scale and decentralization. Among these, electrochemical technologies, such as batteries, fuel-cells, and supercapacitors, have experienced major research and innovation acceleration in the recent years. Of note is the progress made by lithium-based batteries that, after having ousted their predecessors – namely lead-acid and nickel metal-hydride batteries, already dominate the portable electronics sector and are well on-route towards massive commercialization for electrified transportation. These batteries are even being deployed for larger-scale grid applications (**Figure 2**).

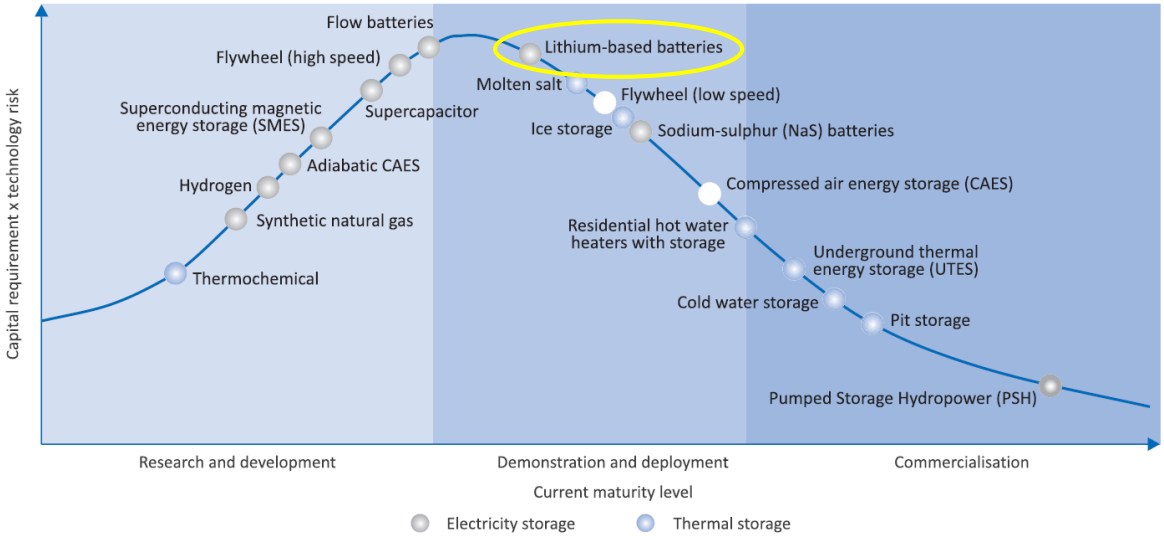


**Figure 2 | Maturity of energy storage technologies.** Adapted from: *OECD Science, Technology, and Innovation Outlook 2016*.[2]

To understand the rise of lithium-based batteries to this juncture, we can look at the trends of their cost ($ kWh$^{-1}$) and energy density (Wh L$^{-1}$) in the recent years (**Figure 3**). Batteries have become about four-times cheaper over the last decade and can now store up to three-times more energy within the same size (volume). The key factors that have contributed to these advancements are: (*i*) innovations in battery chemistry, (*ii*) cell engineering and optimization, (*iii*) growth of manufacturing volume (mass production), and (*iv*) transfer of know-how from the portable electronics sector to the sectors of transportation and stationary storage. At this pace, battery prices are projected to drop below €100 per kWh by 2020, a price range that is believed to render batteries fully competitive against internal combustion engines in the automotive sector.[3,4] In the power sector on the other hand, there is much higher uncertainty in the predicted timespan for coupled solar photovoltaic plus lithium-ion battery systems to become cost-competitive against today's electricity supply.[4] Therefore, the near-future success of lithium-ion batteries in the automotive sector will partly determine whether these will persist as the batteries of choice for grid applications or whether other emerging battery concepts will become more attractive in the meantime. In either case, thanks to ongoing research and engineering efforts, the favourable trends for cost and performance of batteries are expected to continue, with the near-future belonging to 'advanced lithium-ion'‡‡ technologies and 'beyond lithium-ion'§§ technologies becoming practical in the long run.

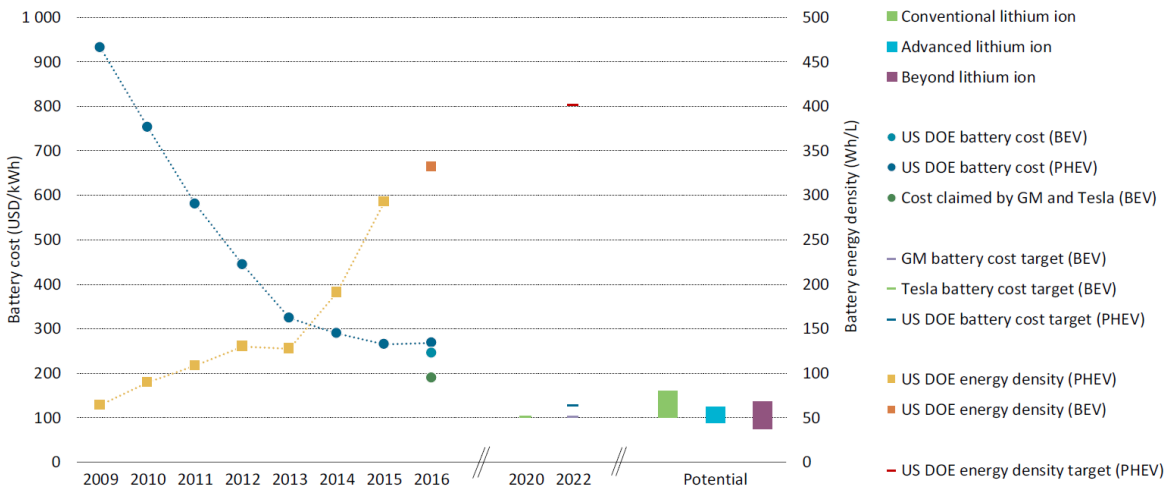


**Figure 3 | Evolution of battery energy density and cost at the pack level.** Adapted from: *Global EV Outlook 2017*.[5]

‡‡ 'Advanced lithium-ion' technologies are based on innovation in cathode, anode, and electrolyte chemistry, particle design and electrode construction, as well as cell component design and cell format optimizations.

§§ 'Beyond lithium-ion' technologies refer to sodium-ion, lithium-sulfur, and metal-air chemistries.

## ○ Outline of thesis

This thesis aims to contribute to the development of 'advanced lithium-ion batteries', and more specifically of their positive electrode materials, by using the knowledge from the fields of solid-state chemistry, electrochemistry, X-ray spectroscopy, and thermochemistry.

It is structured into the following six Chapters:

Chapter I begins with a brief introduction of lithium-ion batteries and intercalation electrodes, before shifting focus to the central topic of this thesis, i.e. high energy Li-rich cathodes based on **anionic redox chemistry**, for which this Chapter provides a comprehensive historical perspective, a theoretical background, some materials' design rules, and a survey of characterization techniques specific to anionic redox.

Chapter II explores the role of anionic redox concerning **practical limitations of Li-rich electrodes** for real-world battery applications. To this end, a 'model' Li-rich layered oxide $Li_2Ru_{0.75}Sn_{0.25}O_3$ (LRSO) is used as a fertile test-bed for scrutinizing independently the effects of cationic and anionic redox in triggering voltage hysteresis, poor electrochemical kinetics, and voltage fade.

Chapter III presents a detailed ***operando* XAS[‡] spectroscopy investigation** of the 'model' LRSO cathode to track its redox processes as well as the electrochemically-driven changes in its local structure, such as the anionic-oxidation-driven distortion of oxygen network. Through a chemometric approach for spectra analysis, the cationic–anionic redox processes are neatly decoupled to explain the origins of voltage hysteresis and sluggish kinetics.

Leveraging the learnings about the 'model' LRSO from the previous two Chapters, Chapter IV explores the fundamental role of anionic redox in the practically important cathode $Li_{1.2}Ni_{0.13}Mn_{0.54}Co_{0.13}O_2$ (Li-rich NMC). The first part of this Chapter combines **HAXPES[§] spectroscopy and electroanalytical methods** to elucidate the relationship of charge-compensation mechanism with voltage hysteresis, slow kinetics, and voltage decay

[‡] X-ray absorption spectroscopy (XAS)
[§] Hard X-ray photoemission spectroscopy (HAXPES)

in Li-rich NMC. The second part of this Chapter provides a direct spectroscopic quantification of capacity from anionic redox over **long cycling of Li-rich NMC**.

Chapter V clarifies the enigmatic issue of voltage hysteresis in Li-rich cathodes via a detailed **isothermal calorimetry investigation** of the 'model' LRSO material. By directly measuring the heat generation and showing how it relates to the loss of electrical work due to voltage hysteresis, this Chapter is able to reveal the thermodynamic mechanism behind the hysteretic anionic redox reaction.

The concluding Chapter VI summarizes the main fundamental and practical achievements of this thesis along with the remaining questions. This is immediately followed by the opening of **two future directions** for further expanding the materials design-space via Li-rich layered sulfides and for advancing the underlying mechanism via phenomenological modelling. I then close the thesis with my optimistic **personal opinion on the viability of anionic redox**.

# ○ List of publications related to this thesis

This thesis is based on the following articles.

*— in chronological order —*

**(1)** Practical assessment of anionic redox in Li-rich layered oxide cathodes : A mixed blessing for high energy Li-ion batteries
**Assat G** · Delacourt C · Dalla Corte D A · Tarascon J M
***Journal of The Electrochemical Society***,163(14), A2965–A2976 (**2016**)
https://doi.org/10.1149/2.0531614jes

**(2)** Decoupling cationic–anionic redox processes in a model Li-rich cathode via *operando* X-ray absorption spectroscopy
**Assat G** · Iadecola A · Delacourt C · Dedryvère R · Tarascon J M
***Chemistry of Materials***, 29(22), 9714–9724 (**2017**)
https://doi.org/10.1021/acs.chemmater.7b03434

**(3)** Fundamental interplay between anionic/cationic redox governing the kinetics and thermodynamics of lithium-rich cathodes
**Assat G** · Foix D · Delacourt C · Iadecola A · Dedryvère R · Tarascon J M
***Nature Communications***, 8, Article number 2219 (**2017**)
https://doi.org/10.1038/s41467-017-02291-9

**(4)** Fundamental understanding and practical challenges of anionic redox activity in Li-ion batteries (*Review Article*)
**Assat G** · Tarascon J M
***Nature Energy***, 3, 373–386 (**2018**)
https://doi.org/10.1038/s41560-018-0097-0

**(5)** Direct quantification of anionic redox over long cycling of Li-rich NMC via hard X-ray photoemission spectroscopy
**Assat G** · Iadecola A · Foix D · Dedryvère R · Tarascon J M
***ACS Energy Letters***, 3 (11), 2721–2728 (**2018**)
https://doi.org/10.1021/acsenergylett.8b01798

**(6)** Mechanism and thermal effects of voltage hysteresis in lithium-rich layered oxide electrodes – An isothermal calorimetry study
**Assat G** · Glazier S L · Delacourt C · Tarascon J M
*submitted* (**2018**)

# Chapter I – Today's battery materials and the advent of anionic redox

Several properties are desired in a good rechargeable battery. These include: low cost, long cycle and calendar life, high energy density, high power density (or rate capability), high energy efficiency, wide temperature tolerance, high safety, and low environmental impact. Among these, energy density has arguably been the main driver of technological progress in batteries starting from the early lead-acid batteries (invented in the 1850s) and nickel–cadmium cells (invented in the 1890s) to nickel–metal-hydride cells (invented in the 1960s) and ultimately leading to lithium-based batteries (invented in the 1970s).[6,7] Critics may argue that the improvement in energy density of electrochemical batteries has not been as spectacular as the advances made in other fields (e.g. computer processors, telecommunications)[6], but close observers of the battery market would recall key achievements. These range from the widespread adoption of portable electronics in the 1990s to that of electric vehicles in 2010s – all made possible because of the growing energy density of commercial lithium-ion (Li-ion) batteries[8,9], i.e. more than 3 times‡‡ in 25 years (see **Figure I.1**).

Electrochemical batteries are assembled from electrochemical cells that consist of a positive (cathode) and a negative (anode) electrode separated by an ion-containing electrolyte solution (see later **Figure I.2** for Li-based cells). The external circuit allows for the flow of electrons only, while the internal electrolyte solution allows for the flow of ions only. Simultaneous electrochemical reactions at the two electrodes lead to energy storage or liberation (charge or discharge), depending on the direction of flow of electrons. The reversibility and kinetics of the electrochemical reactions determine, respectively, the cyclability and rate capability of such batteries. The difference in electrochemical potentials of the two electrodes determines the cell voltage, whereas the extent of the reactions determines the charge storage capacity. The energy stored is simply a product of the cell voltage and the cell capacity. Therefore, the energy density (Wh $L^{-1}$) and specific energy (Wh $kg^{-1}$) of a rechargeable electrochemical battery depend mainly on the specific capacities (mAh $kg^{-1}$) and the operating potentials (V) of the two electrodes. Selecting the right electrochemical reactions and tuning the properties of the electrode materials are thus the most effective ways to increase the energy density as well as other desired properties of batteries.

‡‡ Energy density and specific energy (cell level) of the Li-ion technology has increased from 190 Wh $L^{-1}$ and 80 Wh $kg^{-1}$ in 1991 (Sony) to 683 Wh $L^{-1}$ and 260 Wh $kg^{-1}$ in 2017 (Tesla/Panasonic).

Today's most popular electrochemical cells for energy storage, i.e. Li-ion batteries, are based on lithium-intercalation materials as the electrodes, which will be introduced in detail in the next section. With ongoing research on advanced cathode and anode materials, the energy density of Li-ion batteries is expected to continue rising (**Figure I.1**).[9] Batteries based on other electrochemical reactions, such as Na-ion, K-ion, Mg-ion, Li(Na)-sulfur, Li(Na)-$O_2$, and redox-flow are also being researched.[7,10] However, engineering estimates reveal that none of these are expected to outperform future Li-ion in terms of energy density.[11–14] For example, contrary to what is often quoted in papers, Li-$O_2$ becomes too bulky from a full-system perspective and Li-sulfur electrodes are not dense and have significant dead mass/volume (carbon).[11,13,15–17] The Li-ion technology will therefore prevail in the near future for electric vehicle applications, where size is a key design condition.[9] On the other hand, elemental abundance and low cost may turn out as the driving forces towards the commercialization of Na-ion, Li-S, and redox-flow batteries for applications where size is less crucial, e.g. stationary storage.[12,18,19]

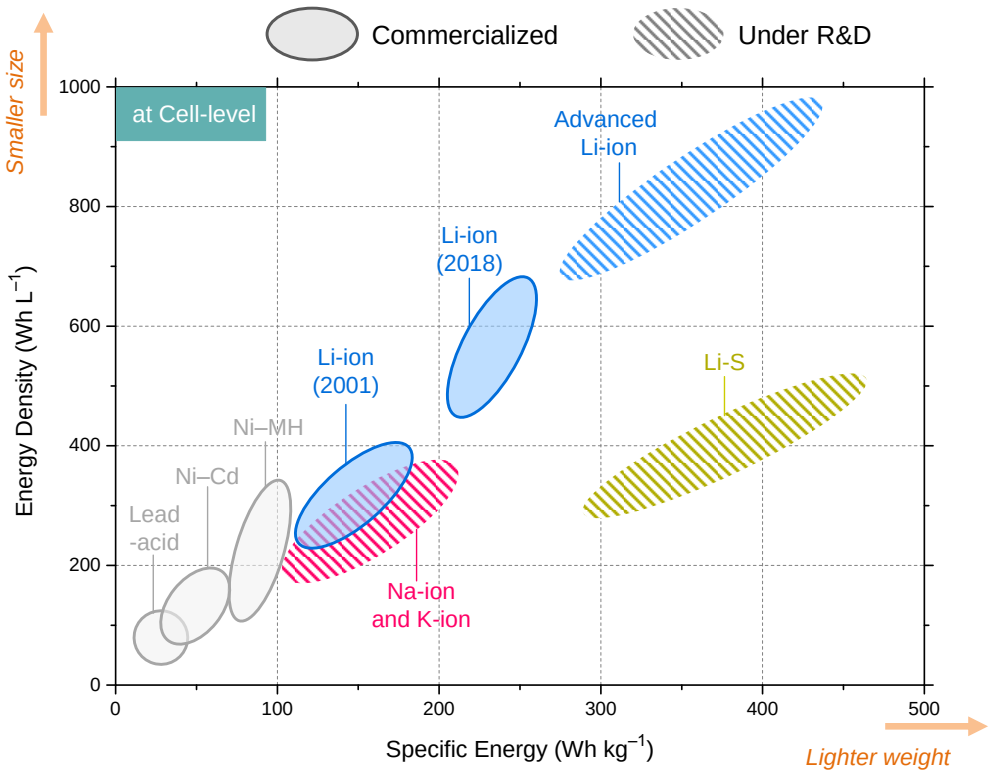


**Figure I.1 | Roadmap of different battery technologies in terms of energy density and specific energy.** Such trends, originally reported in 2001 by *Tarascon and Armand*[6], have been extended here to show today's status and future likelihoods based on a survey of literature.[9,11,12,16,17,20–23] Among future technologies, only those with fully demonstrated prototype cells have been included.

This thesis concerns with advanced Li-ion batteries, in particular the electrochemical properties of their next-generation cathode materials. The working principle of today's Li-ion batteries and a brief overview of the important classes of known cathode materials are presented next, followed by an in-depth introduction of the materials of primary interest for this thesis, i.e. the ones based on anionic redox chemistry.

# I.1 – From intercalation chemistry to Li-ion batteries

Intercalation (or insertion) chemistry can be defined as the ability to insert a guest chemical species into a host structure via an external chemical or electrochemical stimulus. Intercalation chemistry became popular with the discovery that certain organic and inorganic species could be penetrated between the crystalline layers of a number of transition-metal di-chalcogenides, e.g. $TaS_2$, leading to changes in interesting properties such as superconductivity.[24] In the 1970s, lithium-free 3*d*/4*d* transition-metal chalcogenides ($TiS_2$, $MoS_2$, $NbSe_3$,…) were first identified as lithium insertion hosts for developing energy storage batteries with a Li-metal negative electrode (Li-metal battery, **Figure I.2a**).[25–27] The Li/$TiS_2$ system among these, pioneered at Exxon, was the most promising because of its low weight and the excellent reversibility of the $Li_xTiS_2$ ($0 < x < 1$) guest–host solid-solution. Similarly, the Li/$MoS_2$ battery, developed at Moli Energy, was considered very promising initially.

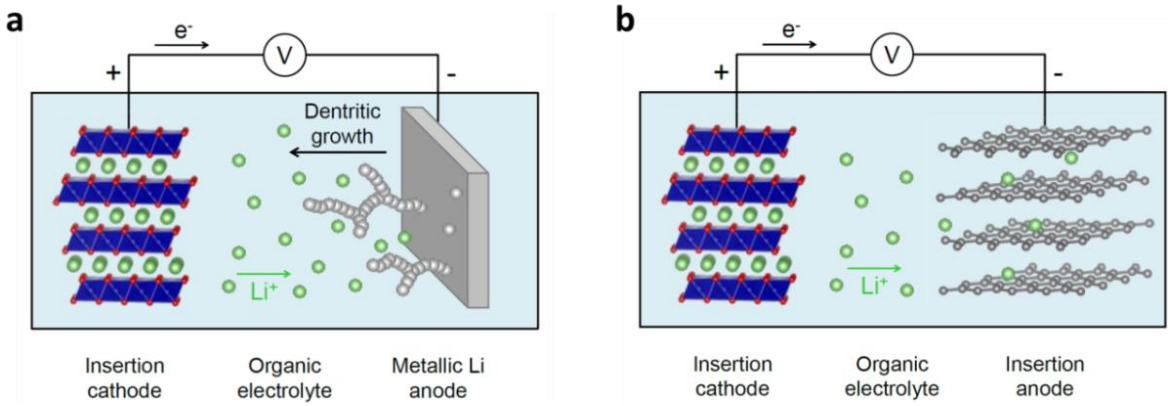


**Figure I.2 | Two configurations of electrochemical lithium batteries.** The Li-metal battery (**a**) showing the safety problem of dendritic Li growth as it can cause short-circuiting, and the Li-ion battery (**b**) having two insertion electrodes. The electron/ion flow directions are during the charge. Adapted from: *PhD thesis of Arnaud Perez, 2017.*

Unfortunately, because of the poor cyclability of the Li-metal anode, and more importantly because of the safety risks concerning dendritic lithium growth at the metallic-lithium anode, Exxon's battery could never be commercialized and Moli's batteries had to be recalled from the market after fire accidents.[8] To circumvent these issues, the concept of Li-ion technology (or 'rocking-chair' battery, **Figure I.2b**) was proposed in the 1980[28] with its commercialization occurring in 1991[29]. This breakthrough involved the simultaneous replacement of lithium metal by carbonaceous materials at the negative electrode, and of lithium-free insertion hosts by lithium-based oxide insertion compounds at the positive electrode. These oxide electrodes offered an increased cell potential due to higher electronegativity of oxygen than sulfur. Sony's first commercial batteries employed layered $LiCoO_2$ as the positive electrode, owing to the excellent electrochemical reversibility of the $Li_{1-x}CoO_2$ ($0 < x < 0.5$) guest–host phase that was first reported from Goodenough's lab in 1980.[30] **Figure I.3** compares the electrochemical curves and the layered crystal structures of the two seminal insertion cathodes : $Li_xTiS_2$ and $Li_{1-x}CoO_2$.

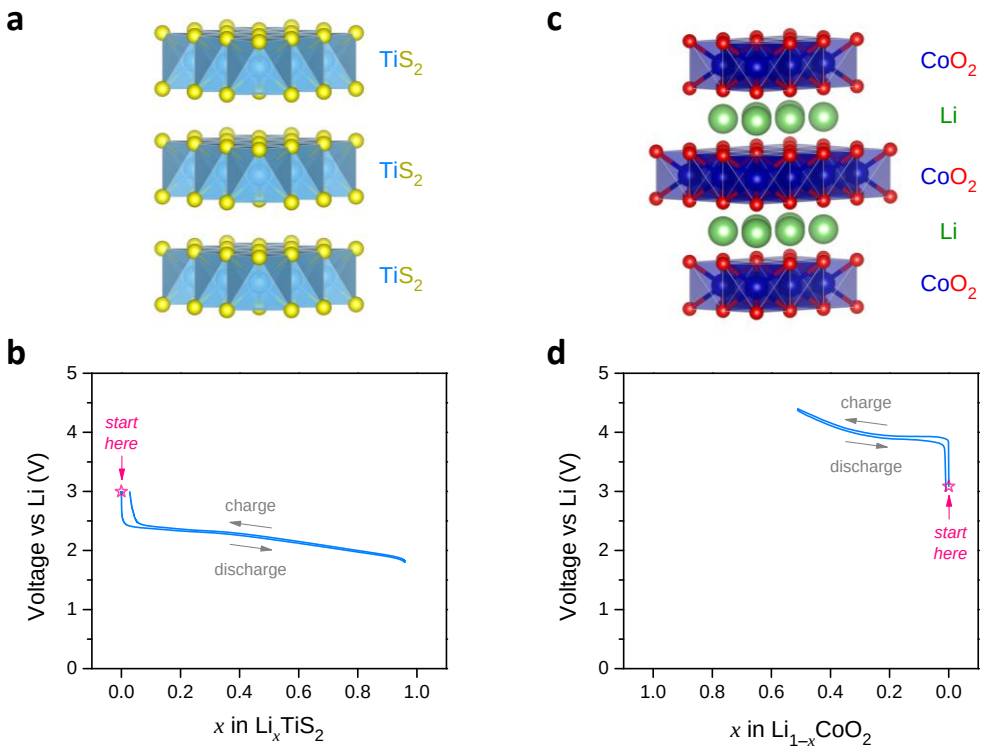


**Figure I.3 | The crystal structures and voltage profiles of $TiS_2$ and $LiCoO_2$.** Li-free layered $TiS_2$ (**a**) can insert 1 Li per formula unit at an average 2.2 V (**b**), while Li-containing layered $LiCoO_2$ (**c**) can release 0.5 Li per formula unit at an average 3.9 V (**d**). Further Li removal beyond $Li_{0.5}CoO_2$ is possible but leads to poor reversibility. Voltage profile of $TiS_2$ : courtesy of *Sujoy Saha.*

The success of Li-ion batteries with $LiCoO_2$ opened the floodgates for solid-state chemists to test/screen many known crystalline compounds as well as to design/discover new cathode materials for reversible Li intercalation. The most interesting ones among these are briefly discussed below.

## ○ Important classes of intercalation cathodes

An ideal high energy cathode material needs to satisfy many criteria[31]: it should possess an open-framework structure with many interstitial sites available for reversible Li (de)intercalation at a high potential, have high electronic conductivity and fast Li diffusion, be composed of inexpensive and environmentally benign elements, be easy to synthesize with large particles for minimizing surface side-reactions, and have high thermal and chemical stability of its delithiated form. In the early years of oxide exploration, only three compounds could meet this long list of requirements, namely layered $LiCoO_2$[30] and $LiNiO_2$[32], and spinel $LiMn_2O_4$[33]. Later on, the discovery of electrochemical activity in $LiFePO_4$[34] triggered a massive exploration of many families of 'polyanionic' frameworks[35], e.g. phosphates, silicates, borates, sulphates, fluorophosphates, fluorosulphates, oxyphosphates, oxysulphates, etc., leading to some promising materials.

Among the layered oxides, $LiCoO_2$ is still used in the majority of commercial Li-ion batteries today.[8,36,37] However, its usage is levelling off because of the high cost of Co and the ethical issues[38] associated with Co mining. On the other hand, $LiNiO_2$-based layered electrodes, such as $Li[Ni_xCo_yAl_{1-x-y}]O_2$ (NCA) and $Li[Ni_xMn_yCo_{1-x-y}]O_2$ (NMC), are witnessing a widespread adoption. The voltage profiles over complete delithiation of these layered oxides are shown in **Figure I.4**. $LiNiO_2$, although initially overlooked by battery manufacturers due the poor thermal stability of its delithiated form, could show much better performances after chemical substitutions of Ni with other cations. In NCA, Ni provides the capacity, Co the structural stability, and Al the thermal stability. Similarly in NMC, Ni governs the capacity, Mn the thermal stability, and Co the capacity retention.[39,40] Many of the popular electric cars today use NMC and NCA as cathodes.[8,9,20] Moreover, the requirement for high energy density in electric cars is catalysing the development of high nickel-content NMC ($x > 0.6$) that can reach up to 850 Wh $kg^{-1}$ (material level). Materials chemists are nowadays attempting to master the

cyclability and thermal stability of these compositions by chemical substitution (doping), protective surface coatings, microstructure design (core-shell or concentration-gradient particles, large crystallite size), and electrolyte additives.[21,41–44] **Figure I.5** summarizes some recent performances obtained with optimized Ni-rich layered oxides.[45] There are also a few renewed efforts to enable the high potential cycling of $LiCoO_2$ via doping.[46] Another promising type of layered oxide cathodes, called Li-rich, has the general formula : $Li_{1+y}M_{1-y}O_2$ with M being a combination of mainly Mn, Ni, and Co. These materials are core to this thesis and will be introduced in depth separately in **Figure I.9** and Section I.2.

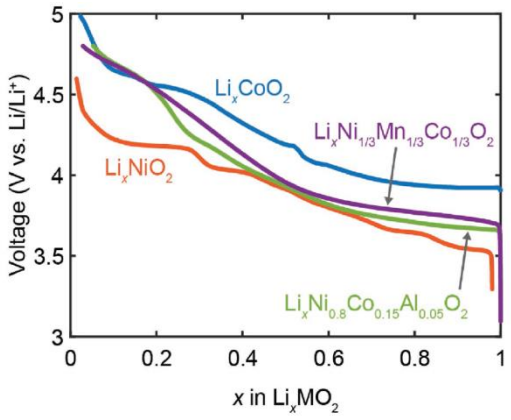


**Figure I.4 | Voltage curves upon first charging of different layered oxides.** Note that such complete delithiation is not utilized in real batteries because of instability of the delithiated layered structure, leading to poor cyclability. Adapted from *Radin et al.*[43]

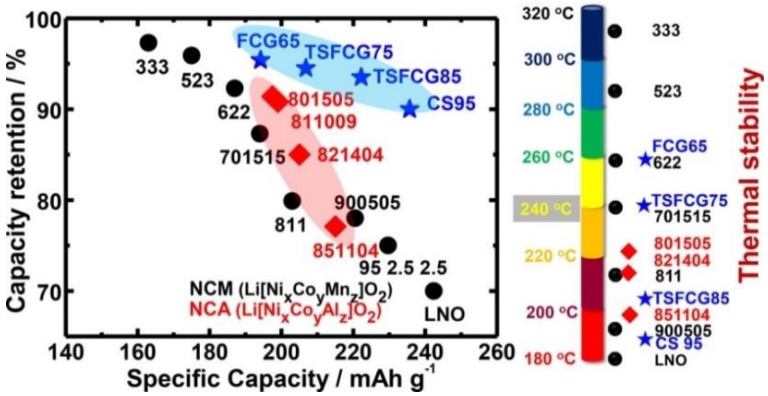


**Figure I.5 | Specific capacity, cycling stability, and thermal stability of state-of-the-art Ni-rich layered oxide cathodes.** The NCA series (red diamonds), the NMC series (black circles), and composition partitioned Ni-rich materials (blue stars) are compared. The nomenclature is based on elemental composition, e.g. NMC 622 ≡ $Li[Ni_{0.60}Mn_{0.20}Co_{0.20}]O_2$. Cyclability and thermal stability are improved with particles with composition partitioning, such as full concentration gradient (FCG), two-sloped full concentration gradient (TSFCG), and core-shell (CS). Adapted from *Yoon et al.*[45]

In the spinel family of oxide cathodes, $LiMn_2O_4$ was the first viable candidate. It is capable of both Li removal, i.e. $Li_{1-x}Mn_2O_4$ at 4.0 V, as well as Li insertion, i.e. $Li_{1+x}Mn_2O_4$ at 2.9 V.[47] For various practical reasons, only the higher voltage process is utilized in real cells. Contrary to layered $LiCoO_2$, the implementation of spinel $LiMn_2O_4$ in full cells required 15 years of tedious research, especially to master the surface Mn dissolution problem that affects cycle life.[31] Apart from Mn being inexpensive and environmentally benign, $Li_{1-x}Mn_2O_4$ shows a very good thermal stability and power capability owing to its three-dimensional crystal structure (**Figure I.6a**). $LiMn_2O_4$, blended with layered oxides, was used in some early electric cars, but it cannot compete anymore with the Ni-rich layered cathodes in terms of energy density.[8] The only way to increase the energy density of the spinel phase is by chemical substitutions, e.g. by partially replacing Mn with Ni to make $LiMn_{1.5}Ni_{0.5}O_4$.[48–50] This compound crystallizes, depending on the synthesis conditions, with Mn/Ni being either ordered or disordered, thus leading to different electrochemical performances. Compared to $Li_{1-x}Mn_2O_4$ that operates at around 4.0 V with the $Mn^{3.5+/4+}$ redox process, the electrochemical reaction of $Li_{1-x}Mn_{1.5}Ni_{0.5}O_4$ proceeds predominantly around 4.7 V through $Ni^{2+/3+/4+}$, owing to the different cationic band positions as schematized by a classical band diagram in **Figure I.6b**.[51] The high-voltage Mn/Ni spinel is promising for high energy and power applications, but mastering its cyclability, especially in full cells, still remains a challenge.[48–50]

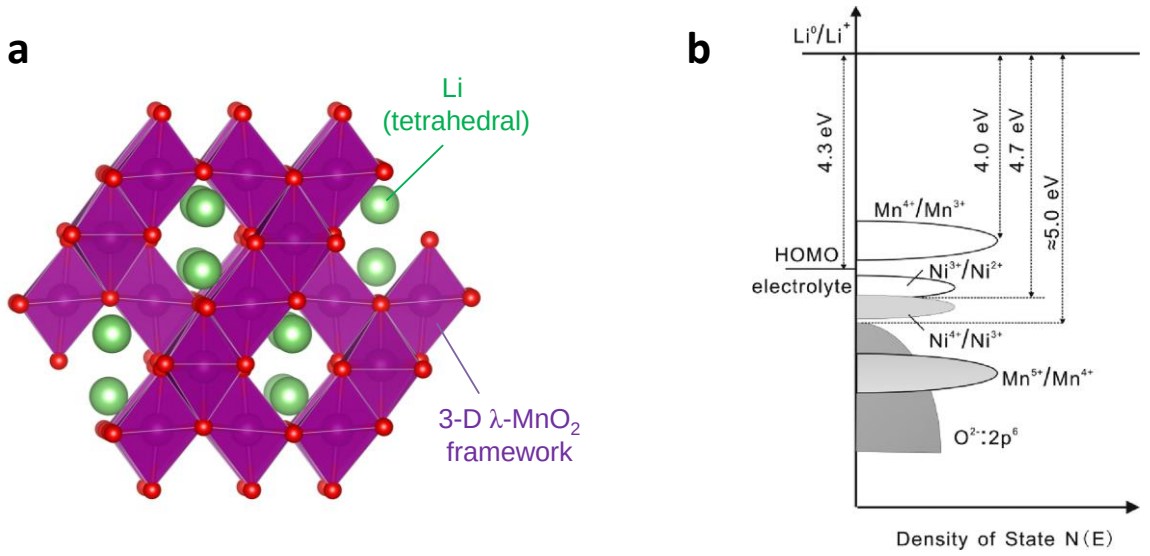


**Figure I.6 | Crystal structure of spinel $LiMn_2O_4$ and its schematic band diagram.** Panel (**b**) adapted from *Song et al.*[51]

Turning now to the polyanionic cathodes[35], these compounds derive their name from the 'polyanionic' groups that make the structural backbone, e.g. $(PO_4)^{3-}$ in $LiFePO_4$ and $(SO_4F)^{3-}$ in $LiFeSO_4F$. Their advantages are: (*i*) higher thermal stability due to the strong covalently bonded oxygen atoms in the polyanionic group, (*ii*) higher redox potentials than oxides for a given $M^{n+}/M^{(n+1)+}$ redox couple due to the so-called 'inductive effect'[52] exerted by the polyanionic group (**Figure I.7**), and (*iii*) vast structural and compositional diversity. On the other hand, their main drawbacks are: (*i*) limited specific capacities because of the heavy polyanionic groups, (*ii*) low crystallographic density, and (*iii*) poor intrinsic electronic conductivities due to the isolation of the metal polyhedrons.

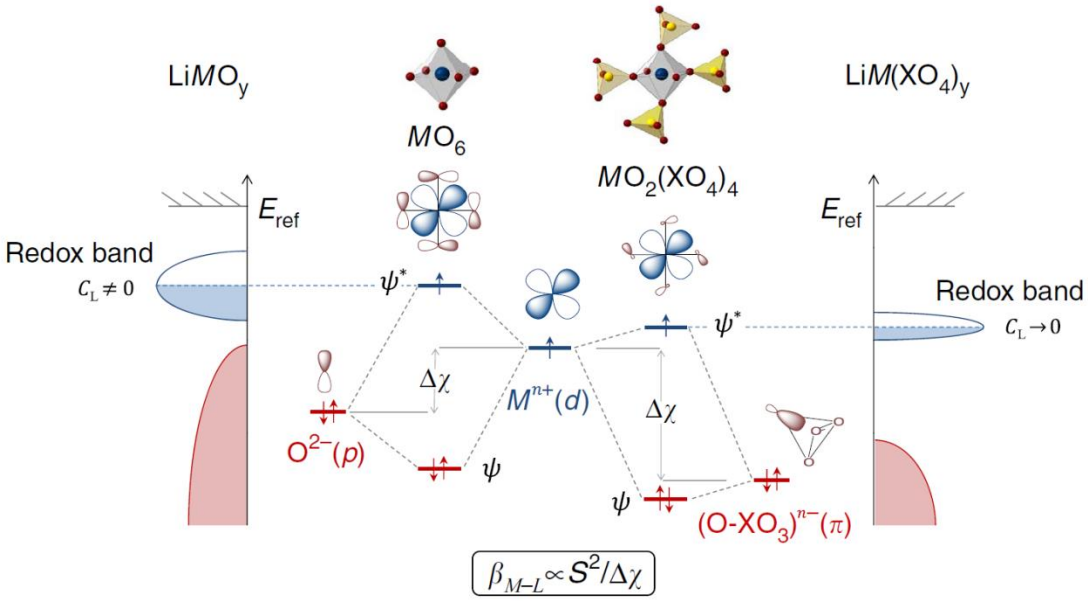


**Figure I.7 | Schematic density of states of transition metal oxides and transition metal polyanionic systems as deduced from local orbital interactions.** $\beta_{M-L}$, the local interaction between the metallic (M) *d*-orbitals and the ligands (L) *p*-orbitals, is as a function of the orbital overlap *S* and the electronegative character of the ligand with respect to the transition metal ($\Delta\chi$). $\psi$ and $\psi^*$ are respectively the bonding and antibonding molecular orbitals of the $ML_n$ redox entity. $C_L$, the weight of the ligands *p*-orbitals in the redox band $\psi^*$ of the material, is dependent on $\beta_{M-L}$. For sake of clarity, only one M-*d* orbital is represented without showing the Mott gap that exists in strongly correlated systems. Adapted from *Saubanère et al.*[53]

Following to the demonstration electrochemical activity in *olivine*-$Li_{1-x}FePO_4$ at 3.4 V[34], several polyanionic cathode families have been investigated in the past 20 years. Such diversity has offered enriching scientific experience to all kinds of solid-state

chemists: crystallographers have enjoyed deciphering new structures and polymorphs, synthetic chemists have relished the feasibility of employing uncommon/exotic/'green' methods to prepare such materials, and theoreticians have enjoyed decrypting the electrochemical properties.[54] I too am indebted to the polyanionic family for my first battery materials research experience in Prof. Manthiram's group (University of Texas at Austin), where I had the opportunity to explore polymorphism[55,56] and elemental substitution[57] via microwave synthesis of the $LiMPO_4$ family (M = Mn, Fe, Co, and Ni).

Despite being a scientific 'goldmine', polyanionic cathodes have been less stellar in terms of market penetration. Carbon-coated, nano-sized $LiFePO_4$ (3.4 V) and $LiFe_{1-y}Mn_yPO_4$ (3.4–4.0 V) were commercialized in some electric cars[††], the motivation being their high safety, long cycle life, elemental abundance, and environmental friendliness. However, the market-share of $LiFePO_4$ is now levelling off[8], as it cannot compete with Ni-rich NMC and NCA in terms of energy density. Other polyanionic cathodes operating at higher potentials do exist, e.g. *olivine*-$LiCoPO_4$ (4.8 V) and $LiVPO_4F$ (4.2 V), but they remain, as of today, far from mass-implementation. Similarly, higher capacity multi-electron-redox-based vanadium-containing phosphates[14,35,58] suffer from large voltage gaps between successive redox processes.

Cation-disordered oxides/oxyfluorides form another emerging class of intercalation cathodes, starting with the earliest report on $Li_2VO_2F$ that could cross 750 Wh $kg^{-1}$.[59] Beyond intercalation, some conversion-based electrochemical reactions that occur at an adequately high potential can also serve as the positive electrode.[60] Some examples include: $Li_2S \leftrightarrow S$[61], $Li_2O \leftrightarrow Li_2O_2$[62], and $FeF_3$[20,63]. However, their practicability is still debated, owing to large volume changes, poor conductivity, low density, and large voltage hysteresis. These materials are beyond the scope of this thesis.

## ○ What are the cathode energy limits ? Can they be pushed ?

The extent of electrochemical Li (de)intercalation, and hence the energy storage limit, in all of the above-mentioned cathode materials is mainly governed by how much the

[††] $LiFePO_4$ by A123 in Chevrolet Spark (2012) and $LiFe_{1-y}Mn_yPO_4$ in Autolib-Paris by Bolloré. $LiFePO_4$ continues to be deployed in electric cars in China.

oxidation state of their transition metal (TM) cations can change[52], i.e. $Co^{3+/4+}$ in $Li_{1-x}CoO_2$, $Ni^{3+/4+}$ in $Li_{1-x}NiO_2$, $Mn^{3+/4+}$ in $Li_{1-x}Mn_2O_4$, $Ni^{2+/3+/4+}$ in $Li_{1-x}Mn_{1.5}Ni_{0.5}O_4$, $Fe^{2+/3+}$ in $Li_{1-x}FePO_4$, and $Mn^{2+/3+}$ in $Li_{1-x}MnPO_4$. This is called 'cationic redox' in order to differentiate from what is nowadays known as 'anionic redox', wherein the ligand is redox-active ($O^{2-} \leftrightarrow O^{n-}$ in oxides, $n < 2$). Such reversible anionic redox chemistry can enable high capacity/energy cathodes, as demonstrated in **Figure I.8** below, wherein the existing and some prospective classes of cathode materials are compared.

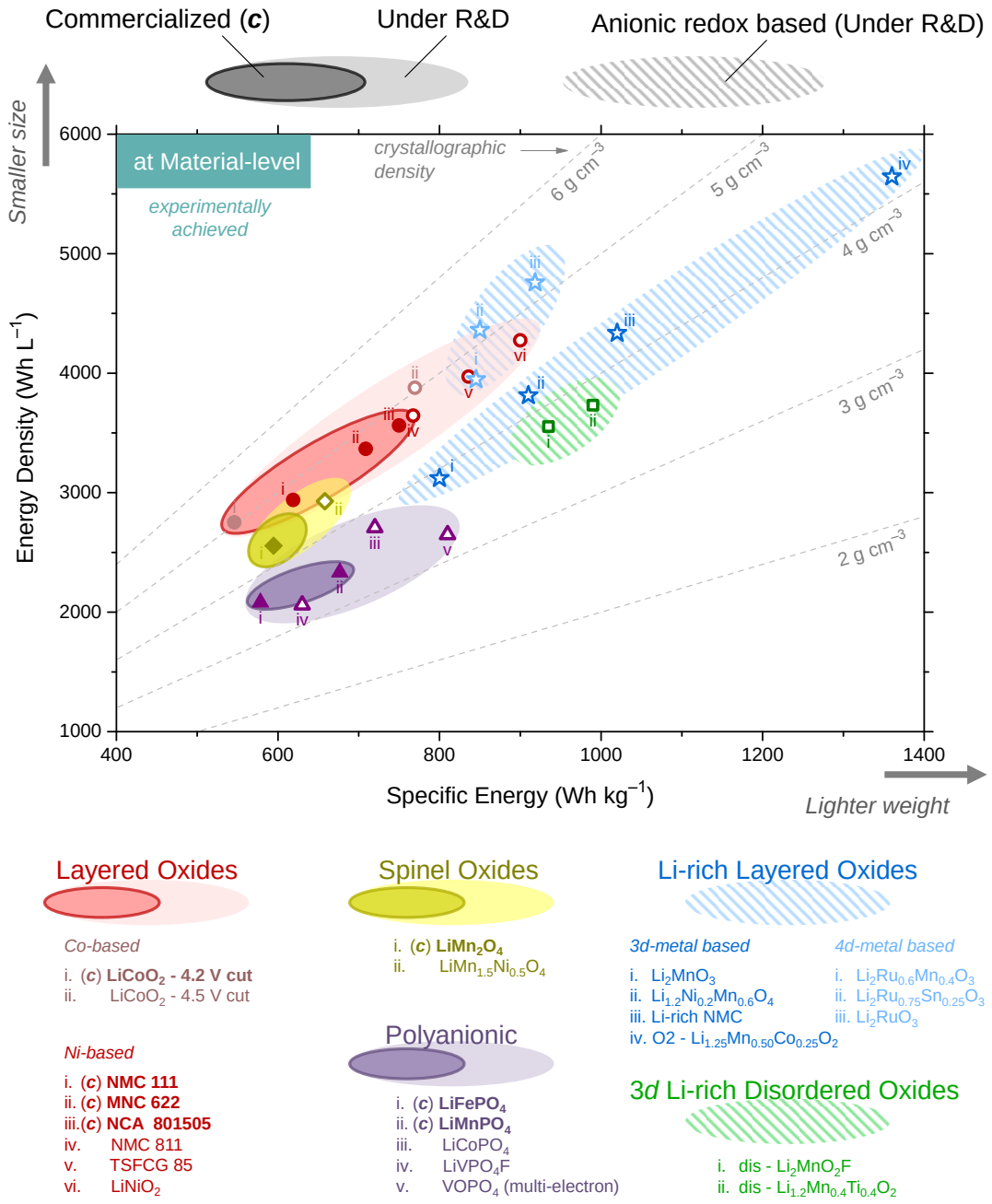


**Figure I.8 | Energy comparison of cathode material families for Li-ion batteries.** Only intercalation cathodes are included.

Energy-wise, as it stands today, the superiority of layered oxides over spinel oxides and polyanionic cathodes is evident from the above graph. This superiority is expected to continue in the near-future since layered oxides still have a decent scope for improvement (pale-red zone in **Figure I.8**), especially with the ongoing efforts to enable high energy Ni-rich layered cathodes. Beyond that, the only cathodes that can push the energy limits are those based on combined cationic/anionic redox. Among these, Li-rich Mn-based layered oxides such as $Li_{1.2}Ni_{0.13}Mn_{0.54}Co_{0.13}O_2$ (Li-rich NMC) (**Figure I.9**) that are derived from $Li_2MnO_3$ (also expressed as $Li[Li_{1/3}Mn_{2/3}]O_2$) are known since 2001[64–66]. However, mastering their electrochemistry has been challenging, partly because their underlying reaction mechanism was not fully understood. The demonstration of reversible anionic redox by our group just before this thesis commenced, notably via $Li_2RuO_3$-based[67–69] and $Li_2IrO_3$-based[70] model materials, rejuvenated worldwide interest in Li-rich layered oxides (blue zones in **Figure I.8**). This led not only to their better understanding and the discovery of new 3*d*-metal-based Li-rich layered oxides[71], but also to the emergence of a new class of cathodes called Li-rich disordered oxides (green zone in **Figure I.8**).[72–76]

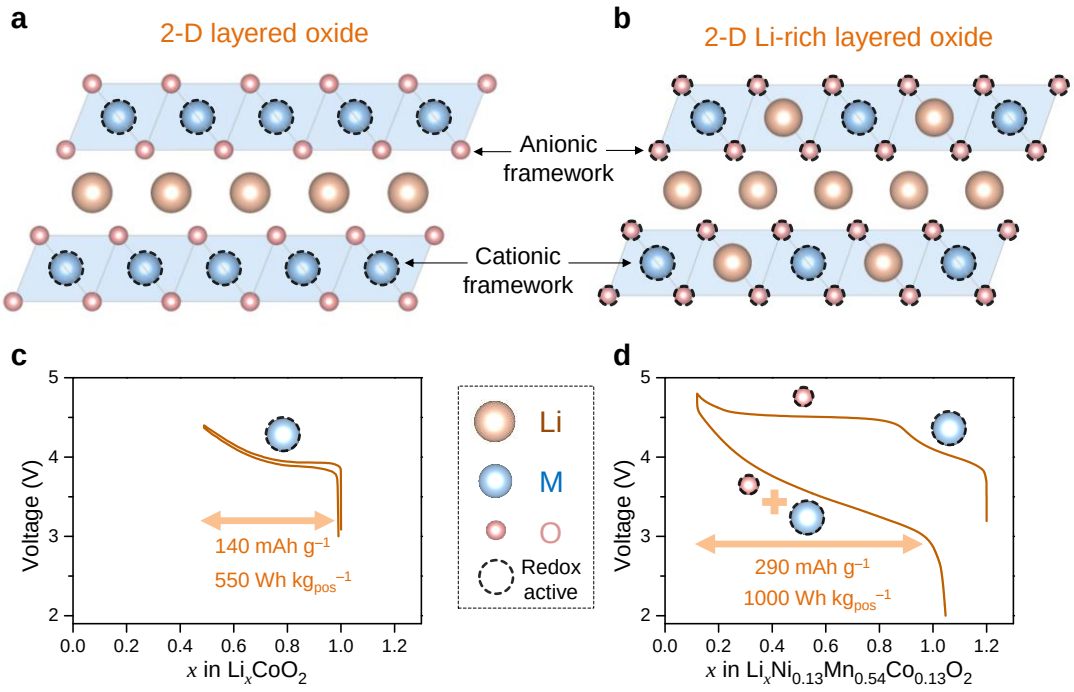


**Figure I.9 | Comparing Li-stoichiometric and Li-rich layered oxides.** The schematic structure of layered oxides, such as $LiCoO_2$ (**a**), is compared with that of Li-rich layered oxides, such as Li-rich NMC (**b**). The latter contains excess Li within the metal layers. Their voltage profiles (**c** and **d**) indicate nearly a doubling of capacity and specific energy for the Li-rich phase due to cumulative cationic and anionic redox processes, which occur as indicated on the voltage curves by the nature of ions involved in the redox processes.

# I.2 – In-depth review of anionic redox in electrodes[§§]

Reversible anionic redox chemistry is now considered as a transformational approach for pushing the energy limits of intercalation cathodes. In this section, the history of anionic redox will first be revisited, followed by a comprehensive pedagogical description of the underlying science. Then after addressing the chemical and structural principles to design new materials, some developments in characterization techniques specific to anionic redox will be highlighted.

## ○ A historical account of the journey of anionic redox

The key steps that led to anionic redox in batteries are listed in **Table I.1** and **Figure I.10** at the end of this sub-section, whereas a detailed account is provided below.

Due to the success of Li-ion technology employing layered oxide cathodes, the original sulfide electrodes mentioned in Section I.1 fell into oblivion, despite notable scientific advances extremely relevant to this Chapter, especially in laying out the history of anionic redox. Among them are the early pioneering works by Rouxel et al.[77,78] on ligand-hole chemistry in sulfides, e.g. $TiS_3$ or $Ti^{4+}S^{2-}(S_2)^{2-}$, $FeS_2$ or $Fe^{2+}(S_2)^{2-}$, etc.. These materials show the possibility of sulfur ligands to exist in a more oxidized state than $S^{2-}$ by virtue of the relative positioning of metal *d* and ligand *sp* bands (**Figure I.10a**). Besides chalcogenides, the exacerbated capacity shown by highly covalent transition-metal pnictide negative electrodes ($Li_xMPn_4$, M = Ti, V, Mn etc. and Pn = N, P, As, etc.) was also explained via anionic redox activity of the $(Pn_4)^{n-}$ units.[79]

Since oxides are less covalent than sulfides, anionic redox in oxides was not envisioned initially. The successful preparation of fully delithiated '$Li_0CoO_2$', back in 1996[80], was therefore quite puzzling as Co was not fully oxidized to 4+, as deduced by magnetic measurements.[81] Furthermore, based on the slight shortening of O–O interplanar distances deduced by synchrotron diffraction, the participation of oxygen at high potential

[§§] This Section is based on the following review article that I co-authored :

**Assat, G.** & Tarascon, J.-M. Fundamental understanding and practical challenges of anionic redox activity in Li-ion batteries. ***Nature Energy***, 3, 373–386 (**2018**). (https://doi.org/10.1038/s41560-018-0097-0)

in the redox reaction of $Li_xCoO_2$ was proposed back in 1999.[82] This suggestion was supported by early theoretical papers[83,84] that predicted the feasibility to design $LiAl_{1-y}Co_yO_2$ wherein oxygen, rather than transition-metals, functions as the electron donor upon Li removal at high potential (**Figure I.10b**). Moreover a crude extrapolation of such calculations to the insulating $LiAlO_2$ phase shows, as expected for a chemist, that the extracted electron will have to come from the oxygen 2*p* orbitals since $Al^{3+}$ cannot be oxidized.

For whatever reasons, such an illicit redox participation of oxygen in $Li_xCoO_2$ at high potential remained overlooked by the battery community for the next decade, despite being supported by additional experimental papers probing the oxygen electronic state using X-ray absorption spectroscopy (XAS) and X-ray photoelectron spectroscopy (XPS).[85,86] This neglect was surprising, since ligand-hole chemistry was well-accepted for high-temperature superconducting cuprates[87] and continues to be studied in the rare-earth nickelates[88,89], also called "negative charge-transfer" materials. The next example, as intriguing as the electrochemical preparation of $Li_0CoO_2$, came a few years later with the detection of electrochemical activity in $Li_2MnO_3$ allegedly involving anionic redox since the oxidation of octahedral $Mn^{4+}$ ions in oxides is believed to be impossible.[90,91] $Li_2MnO_3$, also expressed as $Li[Li_{1/3}Mn_{2/3}]O_2$, is made of Li layers sandwiched between $MO_2$ (M = $Li_{1/3}Mn_{2/3}$) layers wherein one-third of Mn is replaced by Li in a specific honeycomb-like arrangement[67], hence leading to compounds with excess Li that are termed as Li-rich layered oxides. Identifying the reaction mechanism of $Li_2MnO_3$ was complicated by the need to go to high potential (> 4.5 V) to trigger electrochemical activity, therefore favouring electrolyte decomposition which was shown to occur in parallel with some irreversible loss of lattice oxygen.[91,92]

Despite a limited performance and a complicated mechanism, $Li_2MnO_3$ had the merit to allow various chemical substitutions aiming towards enhancing its performance. This saga, which began with $Ni^{2+}$ substitution leading to $Li[Li_{(1/3-2x/3)}Ni_xMn_{(2/3-x/3)}]O_2$ phases that demonstrated reversible capacities over 230 mAh $g^{-1}$ when cycled to 4.8 V[66], later bloomed with the synthesis of numerous phases described as $x\ LiMO_2 \cdot (1-x)\ Li[Li_{1/3}Mn_{2/3}]O_2$ having M = Ni, Mn, Co, Cr, Fe, etc. Standing out among these were the high capacity (over 250 mAh $g^{-1}$) Li-rich NMCs having compositions similar to $Li[Li_{0.2}Ni_{0.13}Mn_{0.54}Co_{0.13}]O_2$ layered oxides cathodes.[93] These materials show a peculiar

two-step charge profile followed by a sloped S-shaped discharge curve (**Figure I.9d**) in which the cationic redox activity could only account for around half of the measured discharge capacity. Researchers thus debated upon several possibilities – such as transition-metal over-oxidation[90], irreversible oxygen loss with surface densification[92,94,95], $Li^+/H^+$ exchange[91,96], $Li_2O$ removal with '$MnO_2$-like' activation[93,97], oxygen release/re-accommodation[98], oxygen redox at the interphase[99], and finally, reversible redox of bulk lattice oxygen[67,100–102]. All controversies have converged and it is now well accepted, based on complementary experimental[103–107] and theoretical[108–110] works, that the extraordinary capacity offered by Li-rich NMC is due to the cumulative contribution of both cationic and anionic reversible redox processes in the bulk.

Such a unified view was made possible by first designing model Li-rich compounds, namely lithium ruthenates ($Li_2Ru_{1-y}Sn_yO_3$)[68] that are structurally and electrochemically similar to the Li-rich NMC phases, while having a simpler redox chemistry since Ru is the only redox-active cation in comparison to Li-rich NMCs that contain three different redox-active cations (Ni, Co and Mn). For these model electrodes, electron paramagnetic resonance (EPR)[111], which detects single-spin or radical species, was used to unambiguously detect "peroxo-like" species in the charged materials which was further confirmed using O 1*s* XPS[105]. This finding was firmly established with the visualization of O–O "peroxo-like" dimers in the model Li-rich $Li_2IrO_3$ phases via transmission electron microscopy (TEM) and neutron diffraction.[70] These experimental proofs were further complemented by density functional theory (DFT) calculations[108–110,112], and using theoretical tools such as the projected density of states (PDOS) for identifying the cation/anion band positions, the Fukui function to identify redox centres[70], and the crystal orbital overlap population (COOP) plots to show O–O bond formation[109].

The demonstration of anionic redox in 4*d* and 5*d* based model Li-rich cathodes served as a platform to assess whether this scenario could be naturally extended to explain the complicated charge compensation mechanism in Li-rich NMC. Providing a straight answer was not easy as direct TEM visualization of the oxygen network, like neatly done in $Li_2IrO_3$ to spot O–O dimers, has not been possible in Li-rich NMC due to the absence of a clear structure projection. On the other hand, EPR could not be used due to signal interferences between the TMs and oxygen. Lastly, XPS on charged samples of Li-rich

NMC could show the appearance of oxidized lattice oxygen, but doubts still remained because of the limited probe-depth of in-house XPS.[105] This is no longer the case, thanks to recent measurements with hard-XPS (or HAXPES)[106] having higher probe-depths, and bulk-sensitive O K-edge XAS measurements[103,104,107], which showed that the anionic redox activity in Li-rich NMC is truly a bulk process. The HAXPES work on Li-rich NMC was carried out as a part of this thesis (Chapter IV).

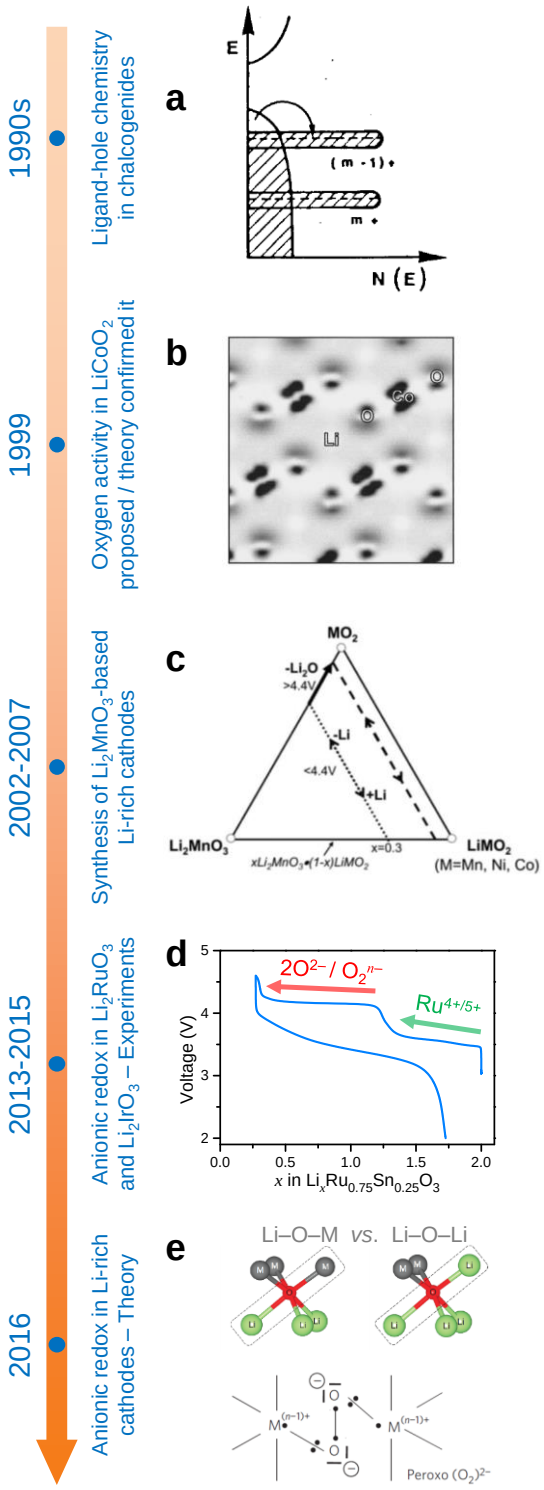


**Figure I.10 | Key steps in the emergence of anionic redox chemistry.** Panels reproduced or adapted from: (**a**) *Rouxel*[77], (**b**) *Aydinol et al.*[83], (**c**) *Thackeray et al.*[93]. (**d**, **e**) *Sathiya et al.*[68], (**e**) *Seo et al.*[108].

**Table I.1 | Key steps in the emergence of anionic redox chemistry.**

| | |
|---|---|
| **1990s** | It was explained using schematic band diagrams shown in **Figure I.10a** that in highly covalent chalcogenides, the transition-metal *d* band penetrates into the ligand *sp* band so that part of the *sp* electrons are poured into the *d* band – leaving behind holes – hence the terminology ligand-hole chemistry.[77,78] |
| **1999** | The onset of oxygen redox was proposed at high potential in $Li_xCoO_2$ based on the observation of slightly shortened O–O distances as deduced by synchrotron diffraction[82] together with magnetic studies[81]. Such an oxygen activity was simultaneously endorsed by theorists via first-principle calculation of electron-density maps shown in **Figure I.10b**.[83,84] |
| **2002 – 2008** | Direct spectroscopic measurements of the ligand electronic state confirmed oxygen redox-activity in $Li_xCoO_2$ (through O K-edge XAS[85] and O 1*s* XPS[86]) and sulfur redox in $Li_xTiO_yS_z$ (through S 2*p* XPS[113]). |
| **2002 – 2007** | Early reports of electrochemical activity in $Li_2MnO_3$[91] were followed by the works of several prominent research groups leading to the discovery of high capacity Li-rich NMCs[66,93], which can be visualized on a ternary phase diagram (**Figure I.10c**) as combinations of $Li_2MnO_3$ and $LiMO_2$ end-members. |
| **2013 – 2015** | The reversible activity of lattice oxygen was proposed in Li-rich NMC based on a series of characterizations[100–102], notably *operando* XAS measurement of transition-metal K-edges which indirectly showed that solely cationic redox was insufficient to account for the overall charge compensation. |
| **2013 – 2015** | Model Li-rich phases ($Li_2MO_3$ with M being Ru and Ir), which are isostructural with Li-rich NMC and likewise show the typical staircase-like charge and sloped discharge (**Figure I.10d**), were designed.[68,70] Using XPS and EPR, the appearance of $(O_2)^{n-}$ species on charging was first proven, prior to directly visualizing O–O dimers using TEM and neutron diffraction. |
| **2016** | Reversible oxygen activity was experimentally proven in Li-rich NMC through an arsenal of characterization techniques, with notably the use of $^{18}O$-labelled *operando* mass spectrometry to quantify the amount of lattice oxygen released as $O_2$ and $CO_2$ during first charge.[103] |
| **2016** | The anionic redox mechanism was theoretically rationalized in different types of 3*d*, 4*d*, and 5*d* metal-based cathodes. Such calculations revealed the importance of O 2*p* non-bonding states (or Li–O–Li configurations in **Figure I.10e**, top), the conditions for O–O shortening, and the reductive coupling mechanism (**Figure I.10e**, bottom) to achieve reversible anionic redox.[108–110] |

Altogether the aforementioned contributions have commenced a new era in battery research which views anionic redox as a transformational change for creating advanced electrode materials, and several novel ones have already been found. Before proceeding further in the thesis, there is a need for returning to fundamentals and understand the theoretical rationale for the underlying science, as addressed next.

## ○ Science underlying the anionic redox chemistry

In the band structure of insertion compounds, the Fermi level ($E_F$) can be related to their electrochemical redox potential such that holes above $E_F$ and electrons below $E_F$ form a redox couple.[52] The band structure of lithium-based transition-metal oxides simply considers orbital-overlaps between the transition-metal *d* orbitals and the oxygen *p* orbitals resulting in bonding (M–O) and antibonding (M–O)* bands having, respectively, strong ligand and metal characters (**Figure I.11a–c**). The energy difference between (M–O) and (M–O)*, also called the charge transfer term Δ, depends on the electronegativity difference $\Delta\chi$ between M and O. Δ reflects the iono-covalent character of the M–O bonds, e.g. Δ decreases (lower ionicity) by replacing O with less electronegative S, and this trend continues from S towards Te. For classical cathodes, their redox process involves solely the (M–O)* band (often called the '*d* band' for simplicity's sake) having strong metal character (**Figure I.11c**), hence the term cationic redox.

Recently theorists recognized the occurrence of non-bonding oxygen states in the band structure of Li-rich materials through simple Lewis descriptions.[109] The Lewis configuration of $O^{2-}$ enlists one 2*s* and three 2*p* doublets, the former being redox-inactive by lying deep in energy. In contrast, the higher energy O 2*p* doublets participate in M–O bond formation with the degree of involvement being structure dependent. All three 2*p* orbitals engage in M–O bond formation in classical layered $LiMO_2$ (O/M = 2, **Figure I.11d**), unlike in structures having higher O/M ratios, e.g. lithium-rich $Li_2MO_3$ (**Figure I.11e**). Indeed, in $Li_2MnO_3$-type structures, one of the O 2*p* orbitals (the one pointing towards Li in the $Li_{1/3}M_{2/3}O_2$ layer) is weakly bonded because of its relatively small overlap with the Li 2*s* orbital. Hence, it behaves like an O non-bonding state and is located above the stabilized (M–O) bonding band (**Figure I.11c**). Note that it is also sometimes

called 'orphaned' or 'unhybridized' O 2*p* state, or 'O lone-pair', or 'Li–O–Li' configuration', or the '$b_1$* state in $C_{2v}$ point-group symmetry of O in $OM_2Li_4$ – leading to unnecessary confusion arising from semantics.[103,108,110,114]

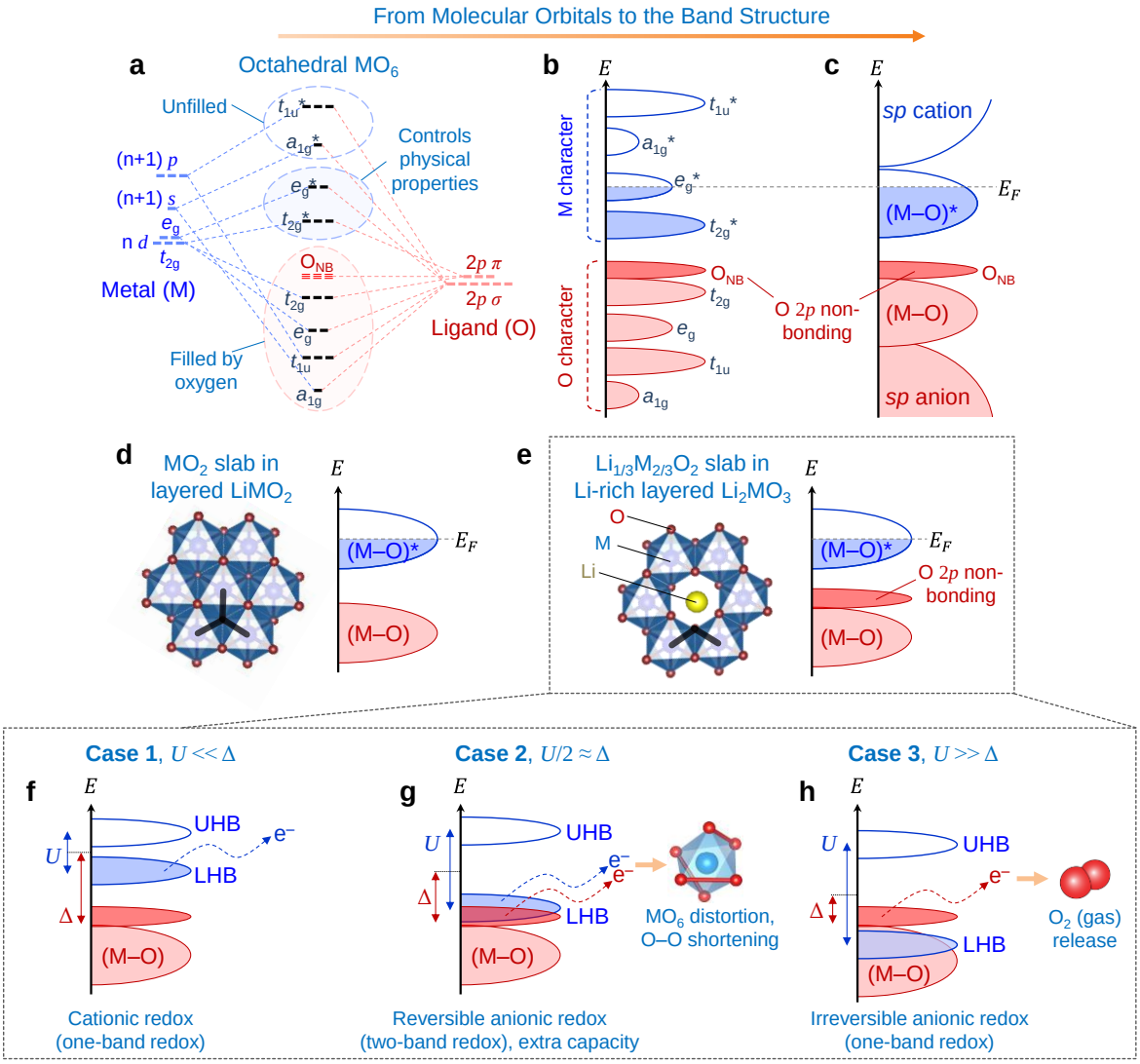


**Figure I.11 | Band structure of oxides and the anionic redox mechanism.** As depicted from (**a**) to (**b**) to (**c**), the schematic band structure of transition-metal oxides (**c**) can be built by extrapolating the molecular orbital energy diagram for octahedral $MO_6$ (**a**). $O_{NB}$ denotes the O 2*p* non-bonding states located below the antibonding (M–O)* band and just above the bonding (M–O) band. A comparison of $LiMO_2$ (**d**) and Li-rich $Li_2MO_3$ (**e**), in terms of their crystal structures (focusing on slabs of $MO_2$ or $Li_{1/3}M_{2/3}O_2$) and the relevant parts of their band structures, reveals how the two structures differ in oxygen coordination. Thick black lines highlight three M neighbours for each O in $LiMO_2$ (**d**), compared to only two in the honeycomb-arranged $Li_2MO_3$ (**e**), thus giving rise to O 2*p* non-bonding states in the latter. Note that these are schematic band structures without taking into account electron-electron correlations. Taking Mott-Hubbard splitting into account, (…*cont*…)

(…*cont*…) the $Li_2MO_3$ band structure is further classified under three cases (**f**–**h**), depending on the interplay between the *d-d* Coulomb repulsion term *U* and the charge transfer term Δ. UHB and LHB denote the upper and lower Hubbard bands respectively. *U* typically ranges from 0 to 6 eV. In Case 2 (**g**), the overlap of LHB and non-bonding O 2*p* states leads to adequately positioned bands for triggering reversible anionic redox. Electron removal from this scenario results in a two-band redox process giving extra capacity and is usually followed by $MO_6$ octahedral distortion leading to short O–O distances. In contrast, this is not possible in Case 3 (**h**) that shows irreversible anionic redox, leading to $O_2$ gas release upon electron removal.

Why is this O non-bonding state electrochemically so interesting? Simply because it offers, besides the usual (M–O)* band, a second band for removing extra electrons and gaining capacity without the risk of structural destabilization, unlike in classical systems where extra electrons can only come from the stabilized (M–O) bonding bands once (M–O)* is emptied. Triggering such a two-band redox process depends on the respective positions of (M–O)* antibonding and O 2*p* non-bonding bands.

To better assess the band positioning, we need to first introduce herein the *d-d* Coulomb interaction term *U*, usually not explicitly sketched by battery chemists but frequently used by solid-state physicists to characterize the on-site electron repulsion within the *d* orbitals.[115] This term, which tends to favour on-site localized electrons as opposed to the kinetic energy, splits the partially filled (M–O)* band, called Mott-Hubbard splitting, resulting in empty upper- and filled lower-Hubbard bands (UHB and LHB respectively, **Figure I.11f**). More quantitatively, *U* is inversely proportional to the orbital volume and hence strongly depends on the *d* metal involved. Therefore, it increases from left to right of the periodic table ($Ti^{n+} \rightarrow Ni^{n+}$) due to orbital contraction, and it decreases from 3*d* to 5*d* transition-metals due to orbital expansion.

The position of LHB with respect to O 2*p* non-bonding band thus depends on the relative values of *U* vs. Δ, giving rise of three different scenarios (**Figure I.11f–h**).[110] First for $U << \Delta$, a situation that widely applies to oxides and fluorides having highly ionic (large Δ) M–L bonds (L being the ligand), electrons are exchanged from the filled LHB (**Figure I.11f**) alike the classical one-band cationic redox scenario. Turning to the opposite situation of highly correlated systems with $U >> \Delta$ (**Figure I.11h**), the one-band redox process still persists however with the electrons now directly removed from the non-bonding O 2*p* band sitting above the filled LHB. This situation creates, owing to the high

chemical hardness of localized non-bonding O 2*p* states, highly reactive $O^{n-}$ species that may de-coordinate from the metallic network via reductive elimination or by attacking the electrolyte. This leads to partially irreversible processes as observed for $Li_2MnO_3$[91,92] and related Li-rich NMCs[94,103,116], or $Li_4FeTeO_6$[117] and $Li_4FeSbO_6$[118] cathodes.

For Li-rich NMCs, to what extent the surrounding $Mn^{4+}$ cations stabilize, as recently proposed[103], the $O^{n-}$ species? Certainly not fully, since oxygen loss is always evidenced when these materials undergo the first charge plateau. Note that this simultaneous oxygen and Li removal obviously modifies Li-rich NMCs' initial band structure, which may afterwards become more favourable for reversible anionic redox and/or the formation of O–O dimers. Capturing such dynamic changes of the band structure requires further DFT development.

Lastly, the middle situation of $U/2 \approx \Delta$ (**Figure I.11g**) results in overlapping LHB and O 2*p* non-bonding bands, which are simultaneously available for electrochemical activity that can occur either sequentially (as in $Li_{2-x}RuO_3$)[119] or simultaneously (as in $Li_{2-x}IrO_3$)[70,120] resulting in a doubled capacity. In this case, removal of electrons leads to a degenerated Fermi level which is unstable. To circumvent this instability, the degeneracy is lifted via either Jahn-Teller or Peierls distortions that consist of oxygen network reorganization and lowering of symmetry to shorten some O–O distances and to enable the emergence of stabilizing $M–(O_2)^{n-}$ interactions.[110] Such stabilization of the "peroxo-like" O–O dimers through covalent interactions from the transition-metal was previously termed as reductive coupling[68,109], drawing an analogy with coordination chemistry. The above description explains the experimentally observed distortion of $MO_6$ octahedra in $Li_2IrO_3$[70,120] and $Li_2RuO_3$[112,119] as well as their analogous Na-phases $Na_2IrO_3$[121] and $Na_2RuO_3$[122]. The characterization of local structural changes in a $Li_2RuO_3$-based material was carried out as a part of this thesis (Chapter III).

We thus have a unique situation in which the electrons are partially removed from the anion's non-bonding band, hence the term anionic redox. This is totally different from highly delithiated $Li_xCoO_2$ where O appears redox-active, as deduced by Bader charge calculations[83], XAS[85], or XPS[86] analyses, simply because of high covalence that imparts a significant O character to the redox-active (M–O)* band. We therefore caution against calling this situation as anionic redox since it basically remains just a one-band process offering no extra capacity.

Overall in light of these band diagrams, the situation of interest for extra capacity requires $U/2 \approx \Delta$, thus opening the door for materials designers to play with the delicate balance between $\Delta$ and $U$ by properly choosing metal–ligand combinations. In contrast, the situation to definitely avoid is the one corresponding to irreversible $O_2$ loss. Theorists have thoroughly explored this frontier by calculating the enthalpy of the oxygen loss reaction ($Li_xMO_3 \rightarrow Li_xMO_{3-\delta} + \delta/2\ O_2$) as a function of Li content for all 3*d*, 4*d*, and 5*d* metals. Their calculations highlight and have highlighted that the difficulty to avoid this prohibited situation is greater with 3*d* metals than with 4*d* or 5*d* ones.[110,123] Although such a theoretical conclusion is pessimistic considering raw material costs, we should not give up with 3*d* metals and various engineering strategies to slow down the oxygen loss in Li-rich NMC are already being pursued.[124,125]

For sake of completeness, we emphasize that neither high covalence nor the presence of ligand non-bonding *p* bands are individually sufficient conditions to ensure reversible anionic redox. For example concerning covalence, although early XAS measurements on $TiS_2$ showed a strong redox involvement of S[126], it was simply due to the high ligand character of antibonding (M–S)* states because of high covalence and it does not give extra capacity via what we herein call the anionic redox process. Likewise for non-bonding O 2*p* states, they also exist in polyanionic compounds, such as $LiFePO_4$ or $LiFeSO_4F$, which solely show cationic redox because such states are too deep in energy (too far from $E_F$) to be redox-active in these ionic structures.

Although the abovementioned picture is built around oxides, it also fully rationalizes the early works on chalcogenides. For instance in the tri-sulfide $TiS_3$, electrochemical Li uptake first accompanies the disappearance of S–S dimers via anionic reduction of $(S_2)^{2-} + 2e^- \leftrightarrow 2S^{2-}$, followed by $Ti^{4+/3+}$ reduction, as neatly evidenced by *ex situ* XPS measurements.[113] Put simply, $Ti^{4+}$ in $TiS_3$ cannot satisfy the $S^{2-}$ state ($Ti^{6+}$ is not possible), thus triggering a structural distortion to remix the empty S 3*p* non-bonding levels and to form $(S_2)^{2-}$ dimers which eventually stabilize the $TiS^{2-}(S_2)^{2-}$ structure in which $(S_2)^{2-}$ can be electrochemically reduced as shown above. Let's recall that such anion–anion interactions can go far beyond just dimers in a highly covalent lattice such as $IrTe_2$ (or $Ir^{3+}(Te^{3/2-})_2$), which demonstrates a Te–Te sub-lattice polymerization to form a 'polymerized $CdI_2$-type' structure.[77,78,127]

Although satisfactorily describing Li-rich oxides and chalcogenides, the overall explanation relying on filled non-bonding ligand states will be continually challenged with the discovery of new materials showing unexpected features. Note in this regard that, reports of anionic redox in Na-poor $Na_{2/3}[Mg_{0.28}Mn_{0.72}]O_2$, also having non-bonding O 2*p* states (those pointing towards Mg), neatly fall into the framework discussed above.[128,129] Similarly, anionic redox activity in Na-poor $Na_{4/7-x}[\square_{1/7}Mn_{6/7}]O_2$ (□ being Mn vacancy)[130] and P3-type $Na_{0.6}[Li_{0.2}Mn_{0.8}]O_2$[131] also arises from non-bonding O 2*p* states (those pointing towards □ or Li, respectively). However, recent claims of oxygen activity in similar structures containing neither alkali ($Li^+$, $Na^+$) nor vacancy (□) nor alkaline-earth ($Mg^{2+}$) cations in the $MO_2$ layers, and thus having apparently no non-bonding O 2*p* states, are intriguing and demand further scrutiny.[132,133] Besides pinning down the anionic redox mechanism, theory has also provided guidance in the search for novel high capacity materials that are discussed next.

## ○ Widening the spectrum of Li-rich oxide electrodes

In light of the anionic redox mechanism established above, the ability to tune the relative position of cationic vs. anionic levels is sorely needed for solid-state chemists to uncover novel anionic-redox materials. The preferred approach of chemical substitutions, which has already marked the successful 25 year-long journey of layered oxide cathodes from the simple $LiCoO_2$ towards $LiNi_xMn_yCo_{1-x-y}O_2$ (NMC) and $Li[Li_{1-x-y-z}Ni_xMn_yCo_z]O_2$ (Li-rich NMCs), as discussed in Section I.1, could again be fruitful here. Li-rich NMCs were subjected to intense chemical manipulations aiming for performance enhancement, which enlisted partial substitutions of 3*d* metals for Cr, Al, Ti, Mo etc., alkali Li for Na and K, and even of O for F, as comprehensively listed in some review papers.[49,124,134,135] Another promising direction, reported only recently, has been the design of Li-rich layered oxides with O2 stacking instead of the conventional O3 stacking. The resulting so-called O2-type $Li_{1.25}Mn_{0.50}Co_{0.25}O_2$ cathode could reversibly deliver up to 400 mAh $g^{-1}$, although at a very low C-rate.[71] The quest for novel anionic redox cathodes beyond Li-rich NMC went naturally in the direction of increasing the Li-rich character (**Figure I.12**), resulting in a wide variety of new materials with versatile compositions, crystal-structure dimensionality, and structural order/disorder, the most interesting of which are discussed

herein whereas a complete listing can be found in other papers reviewing anionic redox.[74,114,136–138]

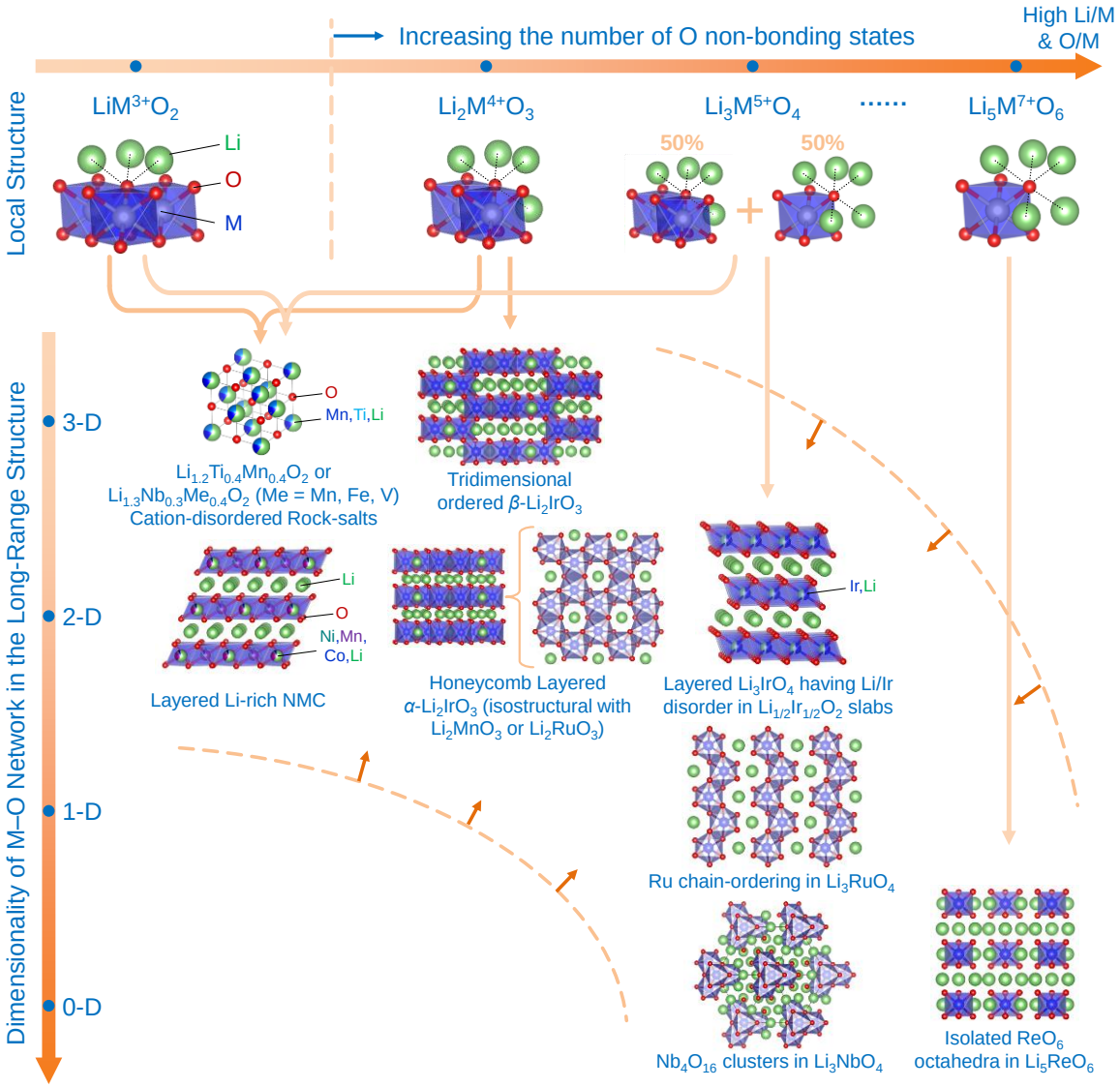


**Figure I.12 | Materials exploration pathway for Li-rich oxides.** Cathode materials having anionic redox activity are shown as a function of their O/M ratio (top horizontal axis, increasing from left to right). The local structure around oxygen is displayed in the top row to highlight the increasing amount of O 2*p* non-bonding states when going from $LiMO_2$ to Li-rich compositions of $Li_2MO_3$, $Li_3MO_4$, and so on. The vertical axis on the left simultaneously monitors the dimensionality of the M–O network in the long-range structure (decreasing from top to bottom). The best candidates known today can be found within the quadrant delimited by $2.5 \leq O/M \leq 4$ and a dimensionality ranging from 2-D to 3-D. Curved dashed lines demarcate the composition–dimensionality boundaries beyond which finding Li-rich materials seems unfeasible. Lastly, the bottom right corner of this plot is rich in known compositions, with most of them unfortunately being unstable against $O_2$ release, besides the fact that their structure consists of isolated $MO_y$ units.

Owing to the richness of the layered rock-salt $Li_2MO_3$ family, great effort was initially placed in exploring elements other than 3*d* metals such as Mn. This led to the work on 4*d* and 5*d* metals giving rise to ruthenates ($Li_2RuO_3$) and iridates ($Li_2IrO_3$) that show capacities exceeding 230 mAh $g^{-1}$.[68,70] The $Li_2MO_3$ family was further explored by designing phases of the general formula $Li_4MM'O_6$, within which M and M' can be selected either from di-, tri-, tetra-, penta-, or hexa-valent cations as long as their valence sum equals eight. Examples include $Li_4Fe^{2+}Te^{6+}O_6$[117] and $Li_4Fe^{3+}Sb^{5+}O_6$[118] that copiously release gas, and $Li_4Ni^{2+}Te^{6+}O_6$[139] that doesn't show anionic participation, hence revealing the delicate balance between anionic redox and $O_2$ release.

Exploring further in the $Li_2MO_3$ family, a particular attention was dedicated to the model $Li_2(Ru,M)O_3$ system containing either ($Mn^{4+}$)[67] or $d^0$ ($Ti^{4+}$, $Zr^{4+}$)[69,140] and $d^{10}$ ($Sn^{4+}$)[68] metals as substituents. Of special significance was the fundamental insight that these materials provided about a practical issue that afflicts Li-rich cathodes, i.e. gradual voltage fading over cycling. By comparing the Sn- and Ti-substituted phases, it could be deduced that voltage fade was exacerbated in the latter and mainly rooted in the migration of small-sized (hence more mobile) Ti ions from octahedral sites, together with their capturing in tetrahedral sites[69]. These works therefore led to a chemical clue for mitigating voltage fade, i.e. the incorporation of large-sized cations such as Sn, which unfortunately has been difficult so far to implement in the synthesis of Li-rich NMC.

Another interesting chemical direction, driven by the willingness to probe the effect of modifying the crystal structure on the anionic redox reactivity, involved the testing of various disordered rock-salt structures having an excess amount of Li.[74] Such compounds with Li/M ratio > 1 are derived from either $Li_2TiO_3$[73,141], $Li_3NbO_4$[72,73], $Li_4MoO_5$ [142,143,75], or $Li_5ReO_6$[142], by partially substituting the $d^0$ metal cations with 3*d* metal-ions having a non-$d^0$ configuration for both weight minimization and electronic conductivity enhancement as the unsubstituted phases are highly insulating. Within this context, numerous Li-rich $Li_{2-x-y}Nb_xM_yO_2$ (M= V, Mn, Fe, Co, and Ni) systems were tested with the most interesting results obtained with the disordered rock-salt composition of $Li_{1.3}Nb_{0.3}Mn_{0.4}O_2$ that reaches capacities of 300 mAh $g^{-1}$ at 50°C.[72,73,144] The authors explained their choice of $Nb^{5+}$ ($d^0$) by recalling that peroxides easily form with $d^0$ ions, e.g. $CaO_2$. Although demonstrating a high capacity, application-wise, such disordered rock-salt phases show sluggish kinetics with moderate capacity retention, likely due to the total

intermixing of Li, Nb, and 3*d*-metal cations, which prevents well-defined 3-D Li diffusion pathways. Similar limitations are also present for the so-called '$Li_4Mn_2O_5$' disordered rock-salt phase.[145] Interestingly, theoretical predictions had been more optimistic about Li diffusion in Li-excess disordered phases[146], hence further work could lead to better performances. Recent advances in this class of materials have led to some high capacity compositions based solely on 3*d*-metals, such as $Li_{1.2}Mn_{0.4}Ti_{0.4}O_2$ (300 mAh $g^{-1}$)[73] and $Li_2MnO_2F$ (275 mAh $g^{-1}$)[76], hence attractive in terms of cost.

The effect of two-dimensional (2-D) vs. three-dimensional (3-D) structures on the anionic redox systems was elucidated by further exploring polymorphism in $Li_2IrO_3$, which exhibits a layered 2-D $\alpha$-$Li_2IrO_3$ polymorph and a 3-D $\beta$-$Li_2IrO_3$ polymorph. This 3-D compound was shown to reversibly exchange 2 Li per transition-metal atom via insertion mechanism with good capacity retention and high rate capability at room temperature.[120] Moreover, such a large activity was shown to result from joint reversible cationic and anionic redox processes as deduced via complementary XPS, TEM, and neutron diffraction experiments supported by DFT calculations. This discovery ended the long-held belief that anionic redox process could solely exist in layered (2-D) materials. Unlocking this dimensionality constraint has widened the design space for high-energy-density electrodes based on anionic redox, since 3-D oxides form a large class of existing materials.

Driven by the rationale that increasing the number of O 2*p* non-bonding states should increase the capacity of Li-rich materials, another recently developed direction has consisted in designing materials with Li/M or O/M ratios greater than 2 and 3 respectively, i.e. departing from $Li_2MO_3$ and moving towards $Li_3MO_4$, $Li_4MO_5$, and so on. Note that all such compositions can be expressed as $Li_{1+y}M_{1-y}O_2$ (e.g. $y$ = 1/3 for $Li_2MO_3$ and $y$ = 1/2 for $Li_3MO_4$) where $y$ also represents the fraction of non-bonding O 2*p* states (e.g. 1 out of 3 in $Li_2MO_3$). Along this strategy, the most interesting behaviour was obtained via the design of a novel layered $Li_{3-x}IrO_4$ compound[147] from which 2 Li can be removed through a charge compensation process solely involving anionic oxidation to produce a $LiIrO_4$ phase which, upon further delithiation, irreversibly releases $O_2$. However by limiting the charge process to $x$ = 2, such a phase could reversibly exchange 3.5 $e^-$ per transition-metal atom via intercalation mechanism. The resulting cumulative activity of anionic ($LiIr^{5+}O_4$ ↔ $Li_3Ir^{5+}O_4$) and cationic ($Li_3Ir^{5+}O_4$ ↔ $Li_{4.5}Ir^{4+/3+}O_4$) redox processes led to a nearly stable reversible capacity of 356 mAh $g^{-1}$ for at least 25 cycles, with a part of it coming at low

potential. This new approach is appealing but it must be realized that pushing oxygen redox brings about complications since highly oxidized $MO_y$ materials become increasingly unstable towards $O_2$ release or even decomposition, as reported for $Li_3RuO_4$. This is because the poorly connected 1-D chain structure of $Li_3RuO_4$ is unable to hold together after Li extraction.[148] Similarly, the recently reported $Li_{5-x}FeO_4$ phase also releases $O_2$, leading to poor cyclability.[149] In this regard, **Figure I.12** demonstrates a clear trend towards lower dimensional structures when Li/M and O/M ratios are pushed up to increase the amount of O 2*p* non-bonding states, ultimately leading to 0-D structures like $Li_3NbO_4$ or $Li_4MoO_5$ that have isolated $Nb_4O_{16}$ clusters or isolated $Mo_2O_{10}$ units respectively, while the extreme cases of $Li_5ReO_6$ and $Li_7RuO_6$ show isolated $MO_6$ octahedra. Because such 0-D structures are not good candidates for conductive and stable cathodes for lithium (de)insertion, the O/M ratio cannot be arbitrarily pushed and there is a need to find a trade-off between extra-capacity and structural stability against $O_2$ release. This is a difficult task, as we want to use light and practical 3*d* metals, but their stability is not supported by theoretical predictions.[110,123] Alternatively, the O/M ratio's upper limits may be breached by moving beyond insertion hosts to instead design fundamentally different conversion-type electrodes having small TM amounts. Along that line, worth mentioning is the emergence of nanocomposite electrodes, named 'Co-doped $Li_2O$'[62,150]. They function mainly via solid-phase anionic redox, i.e. $Li_2O$ (s) ↔ $Li_2O_2$ (s) ↔ $LiO_2$ (s), while avoiding $O_2$ (g) release thanks to an overcharge-preventing shuttle. Although attractive in terms of specific energy (1000 Wh $kg^{-1}$ at the material level), further studies are awaited to evaluate their real-world potential. Similarly, this use of $Li_2S$ as a conversion cathode based on sulfur anionic redox needs further development.[61]

The discovery of anionic redox in such a wide variety of materials also led to the simultaneous development of characterization techniques specific to anionic redox. These are discussed next.

## ○ New paradigms in characterization tools for anionic redox

Characterizing anionic redox calls for specific structural (**Figure I.13**) and spectroscopic (**Figure I.14**) techniques that often require access to large instruments.[151]

**Structural characterization.** Neutron diffraction is very sensitive to light elements and can accurately assess the atomic positions within a structure, hence allowing the quantification of interatomic distances to spot the O–O dimers, provided that such species exhibit long-range ordering and that stacking faults are at a minimum. **Figure I.13a** shows the refined crystal-structure of $\alpha$-$Li_{2-x}IrO_3$ for $x$ = 1.5 and **Figure I.13b** shows the distorted $IrO_6$ octahedra in $Na_{2-x}IrO_3$ for $x$ = 1.5.[70,121] Electron diffraction and annular bright field scanning transmission electron microscopy (ABF-STEM) are advanced tools to directly visualize the O–O shortening, as shown for $\alpha$-$Li_{2-x}IrO_3$, $x$ = 1.5 in **Figure I.13c**.[70] ABF-STEM imaging requires high sample-stability against electron-beam irradiation, unlike electron diffraction that can be applied to more fragile structures that are typically obtained after charging. An ultimate goal would be to combine STEM with electron energy loss spectroscopy (EELS), in order to map the electronic states of individual oxygen and TM atoms. Note that the above techniques are suitable only for crystalline materials, whereas O–O distance determination is still awaited in less-ordered materials via local structural techniques, such as pair distribution function (PDF) analysis[131] of diffraction data.

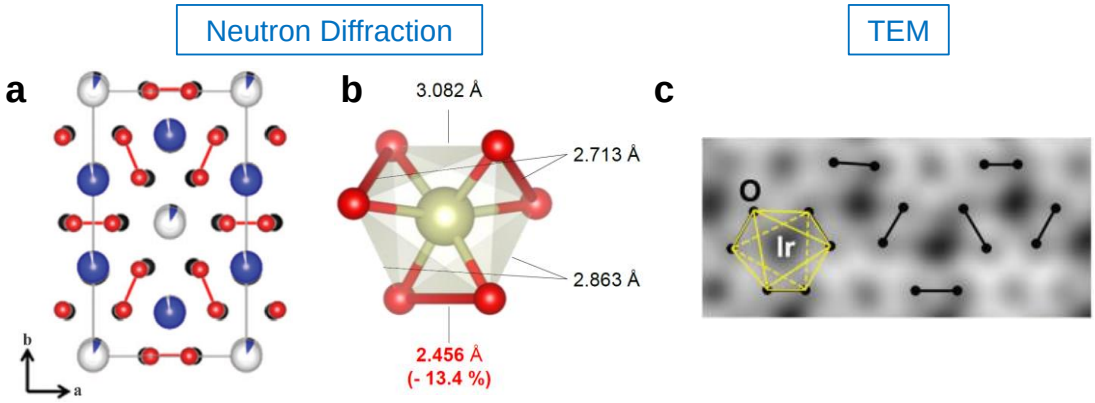


**Figure I.13 | Structural characterization techniques for anionic redox.** Reproduced from: (**a**) and (**c**) *McCalla et al.*[70], (**b**) *Perez et al.*[121].

**Characterizing the charge compensation mechanism.** A powerful technique for measuring changes in the ligand's electronic state for a variety of battery materials is X-ray photoelectron spectroscopy (XPS).[86,105,113] However, it remains surface-sensitive. This drawback can partially be overcome with hard-XPS (HAXPES), through which higher energy synchrotron X-rays can reveal bulk information (**Figure I.14c** shows $O^{n-}$ species in fully-charged Li-rich NMC, obtained as part of this thesis and described in detail with

Chapter IV).[106] Note that HAXPES can only detect the $O^{n-}$ species, without the possibility to further reveal its nature. Moreover, *operando* HAXPES remains tricky to develop. On the other hand, electron paramagnetic resonance (EPR) spectroscopy, which detects radical or unpaired-spin species, is bulk-sensitive with *operando* capability for semi-quantitatively probing the $(O_2)^{n-}$ species as well as for visualizing their nucleation via EPR imaging whose spatial resolution needs further improvement (**Figure I.14a** shows the 1st discharge process of $Li_2Ru_{0.75}Sn_{0.25}O_3$)[111]. EPR requires that the sample is not exceedingly metallic, that the interfering signals from transition metals are absent, and that the $(O_2)^{n-}$ species are EPR-active. Therefore, complementary characterizations may be needed.

Soft X-ray absorption spectroscopy (soft-XAS) at the O K-edge is also being used frequently.[73,103,104] However, a common pitfall is encountered when correlating the intensity changes in O K-edge XAS spectra with the holes on oxygen, because of O-2*p*/TM-n*d* hybridization.[151] Moreover, the choice of detection mode is crucial for obtaining true bulk information, for which soft-XAS-based scanning transmission X-ray microscopy (STXM) has emerged as a more suitable method for revealing the redox mechanisms along with particle-level inhomogeneities. **Figure I.14d** shows the bulk sensitivity of STXM unlike other detection-modes (such as total electron yield (TEY), total fluorescence yield (TFY) or fluorescence yield X-ray microscopy (FY-XRM)), and its ability to clearly spot the signature of anionic redox in Li-rich NMC, as marked by red arrow.[107] Further theoretical developments are awaited to fully interpret the O K-edge XAS spectra. In contrast, soft-XAS measurements of TM L-edges provide unambiguously their oxidation states[152], which can then indirectly be used to discuss the anionic redox activity[72,73]. Resonant inelastic X-ray scattering (RIXS) can also characterize oxygen holes, as neatly done in rare-earth nickelates[89]. In O K-edge resonant inelastic X-ray scattering (RIXS) maps obtained for Li-rich NMC-type cathodes, a unique and sharp absorption–emission feature appeared on charge and disappeared on discharge (marked by white arrow in top panel of **Figure I.14e**).[103,107,153,154] This feature is now believed to be a signature of oxidized lattice oxygen[155], especially since the same has also been reported for disordered $Li_2MnO_2F$[76] as well as a Na-based cathode[129]. Band structure based explanations of this interesting RIXS feature are still awaited. On the other hand, *operando* measurement of TM K-edges with hard-XAS is technically simpler.[102,112] Moreover, when performed in transmission mode encompassing an ensemble of particles, it can provide an accurate quantification of charge compensation (**Figure I.14b** shows the

deconvoluted 5th cycle of $Li_2Ru_{0.75}Sn_{0.25}O_3$, obtained as part of this thesis and further elaborated upon in Chapter III).[119]

Lastly, one can experimentally reconstruct the density of states of Li-rich cathodes near $E_F$, as recently achieved for perovskite-oxides and 3*d*-metal fluorides, by combining XAS, X-ray emission spectroscopy (XES), and valence-band XPS.[151] The *U* and Δ terms can thus be quantified, leading to a harmonization of the theoretical framework governing the anionic redox chemistry that was presented in **Figure I.11**.

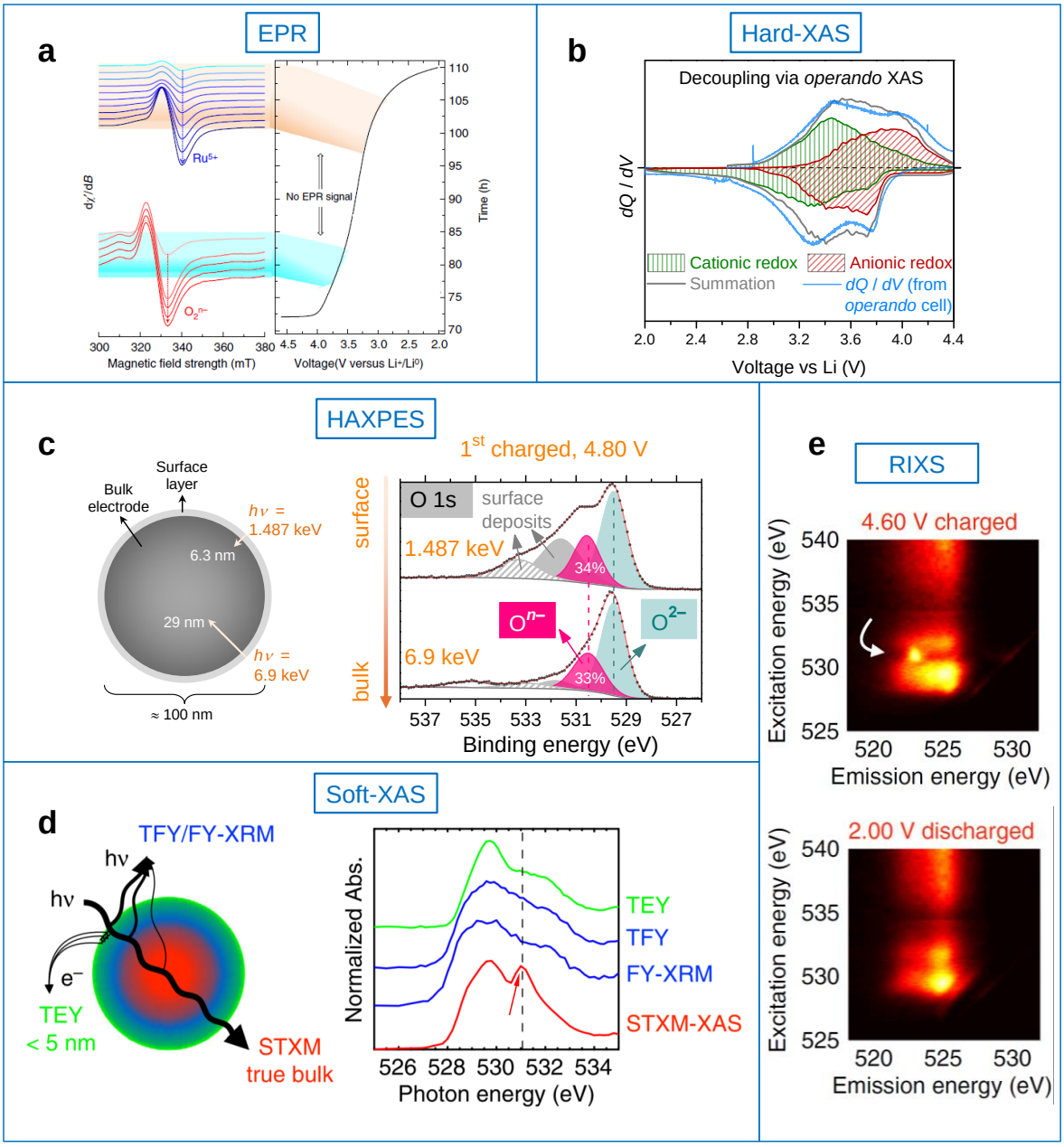


**Figure I.14 | Spectroscopic techniques for characterizing anionic redox activity.** (**a**) *Sathiya et al.*[111], (**b**) *Assat et al.*[119], (**c**) *Assat et al.*[106], (**d**, **e**) *Gent et al.*[107].

# I.3 – Chapter Conclusions

The first part of this Chapter provided a brief overview of today's state-of-the-art cathode materials, and showed that anionic-redox-based electrodes are, energy-wise, the most promising candidates for future batteries (**Figure I.8**).

The second part of this Chapter provided a comprehensive review of this relatively nascent concept of anionic redox chemistry for battery applications. It covered the theoretical understanding of anionic redox (**Figure I.11**), the materials discovery/design pathway (**Figure I.12**), and specific characterization techniques (**Figure I.13** and **Figure I.14**) developed for detecting oxygen redox activity. The embracement of these new directions by the battery community has enabled the exploration of many facets that govern the anionic redox process – such as disorder, dimensionality, O/M ratio, and stability against $O_2$ release, amongst others.

This prolific research has resulted in, besides practical compounds based on 3*d* metals, some 'model' materials based on 4*d* and 5*d* metals for fundamental studies. These model compounds have not only enabled the establishment of a sound scientific platform for rationalizing the design of future anionic-redox-based cathodes, but they also have helped unravelling the origins of practical roadblocks in Li-rich cathodes. This is exactly what the next Chapter addresses via detailed electrochemical studies of a 'model' Li-rich layered oxide $Li_2Ru_{0.75}Sn_{0.25}O_3$ (LRSO).

# Chapter II – Practical assessment of anionic redox via a 'model' oxide

# II.1 – Background and Motivation‡‡

Despite the promise of large capacity, unfortunately, a decade-long research effort in commercializing Li-rich NMC cathodes, e.g. $Li_{1.2}Ni_{0.13}Mn_{0.54}Co_{0.13}O_2$, has remained unsuccessful. This is because the extra capacity comes with undesirable practical drawbacks, such as voltage fade, voltage hysteresis, and poor rate capability[41,134,135]. These issues will be introduced in detail in this Chapter and discussed throughout the thesis. Firstly, irreversible and gradual voltage fading over cycling diminishes the energy output and would make state-of-charge (SoC) management difficult. Secondly, voltage hysteresis, i.e. large gap between charge and discharge voltage profiles, also complicates SoC management. In addition, it penalizes the round trip energy efficiency[156], just like in conversion materials which unfortunately failed to commercialize, despite decades of research, due to the unsolved hysteresis problem.[157–160] Thirdly, poor rate capability reduces power density and energy efficiency to generate irreversible heat.

Strategies for mitigation of these issues must target their fundamental origins, which are difficult to determine using Li-rich NMC since it is complicated by interweaved electrochemical activity of three transition metals (TMs) and oxygen. It is widely believed that the anionic redox in Li-rich NMC, as well as its deficiencies listed above, mainly originate from its Li and Mn-rich nature, leaning towards $Li_2MnO_3$, which can also be expressed as $Li[Li_{1/3}Mn_{2/3}]O_2$, a notation that elucidates the layered structure having excess Li in the Mn layers. Direct experimental evidence for oxygen redox participation in $Li_2MnO_3$ came recently with soft XAS.[161,162] Further spectroscopic evidence of sluggish de-lithiation kinetics of the Mn sites[163] in Li-rich NMC corroborates the electrochemically observed kinetic limitations[164] at potentials where its $Li_2MnO_3$ component is believed to be active. Besides, according research at Argonne, the issues of hysteresis and voltage fade are correlated and have also been attributed to arise from the $Li_2MnO_3$ 'domains'.[165]

Aware of the aforementioned complexity of Li-rich NMC and the key role of its $Li_2MnO_3$ component, our group designed simplified (or 'model') Li-rich layered oxides based on solid solutions of $Li_2M^{4+}O_3$ (M = Mn, Ru, Sn, and Ti) crystalizing within the

‡‡ This Chapter is based on the following research article that I co-authored :

**Assat, G.**, Delacourt, C., Dalla Corte, D. A., & Tarascon, J.-M. Practical assessment of anionic redox in Li-rich layered oxide cathodes : A mixed blessing for high energy Li-ion batteries. ***Journal of The Electrochemical Society***, 163(14), A2965–A2976 (**2016**). (https://doi.org/10.1149/2.0531614jes)

same structure. The electrochemical parallel between Li-rich NMC and our 'model' oxides is embodied in a characteristic two-step first charge followed by an 'S-shaped'-sloped discharge. This resemblance has roots in the structural and chemical similarities between them. By partially substituting Mn with Ru in $Li_2MnO_3$, clear evidence was obtained for both cationic redox (from $Ru^{4+/5+}$) and anionic redox (from $(O_2)^{4-/n-}$).[67] Later, by switching from $Mn^{4+}$ to electrochemically inactive $Sn^{4+}$ ($d^{10}$), the undesirable $Mn^{3+/4+}$ redox was also eliminated, leaving behind a simplified system with just two main redox active elements, i.e. Ru and O.[68] By leveraging this simplified system, we can now investigate the role of anionic redox in triggering practical issues such as voltage fade, hysteresis, and poor kinetics. This is important because anionic redox is the key physico-chemical phenomenon in these materials such that once the electrons are removed from the O-2*p* levels, it can subsequently lead to further structural reorganizations [69,70,109], such as O–O shortening, TM migration, or $O_2$ release that were mentioned in Chapter I. For the sake of clarity, we use the term 'anionic redox' in this Chapter to discuss the effects of the complete process of Li-transfer with electron exchange from the O bands that may consequently also lead to such structural reorganizations.

In this Chapter, the optimized composition of $Li_2Ru_{0.75}Sn_{0.25}O_3$ (LRSO) serves as a 'model' material. It reversibly delivers a high capacity in excess of 240 mAh $g^{-1}$, thanks to a combination of cationic and anionic redox that are neatly separated at low and high potentials respectively, thus enabling their individual scrutiny.[68] Furthermore, large-sized spectator cations of $Sn^{4+}$ preserve structural integrity upon cycling and hence reduce cycling-induced voltage fade.[69] Although the higher cost of Ru might confine LRSO to niche applications such as space or defence, our main objective with this material is to develop fundamental understandings for the class of Li-rich layered oxides in general. We thus embarked into a detailed electrochemical study of LRSO to explore its thermodynamic, kinetic and transport properties in a step by step manner, starting from the first charge 'activation' process, then continuing with 'activated' LRSO which is application-wise important, and finally ending with the cycling induced voltage fade and impedance build-up. In the next sections, the results on LRSO are first presented, followed by a detailed discussion comparing the two Li-rich layered oxides – LRSO (the 'model' system with *4d* TM) and Li-rich NMC (the 'practical' system with *3d* TMs). Many striking similarities are revealed between the two, despite moving from *3d* to *4d* TMs, providing fundamental insights towards practical challenges that affect Li-rich layered oxides.

# II.2 – Results

$Li_2Ru_{0.75}Sn_{0.25}O_3$ (LRSO) powders were synthesized by a solid-state route† as described previously[68], and then cast into Bellcore-type electrodes[166] with high-porosity and low-loading for electrochemical testing in the Li half-cell configuration. Such Bellcore electrode design is essential for safely ignoring porous-electrode effects and ensuring that the electrode's electrochemical response is dominated by the sought-after properties of the positive electrode material. Details of the experimental procedures and electroanalytical techniques can be found in the Methods section of the Supporting Information for this Chapter in Appendix A1. The typical voltage vs. composition trace of a Li half-cell, having either Li-rich NMC or LRSO as the positive electrode, shows a stair-case voltage profile on oxidation that modifies into an 'S-shaped' one on reduction (**Figure II.1a**). The superimposition of the voltage profiles for four consecutively assembled LRSO cells indicates the robustness of our experiments.

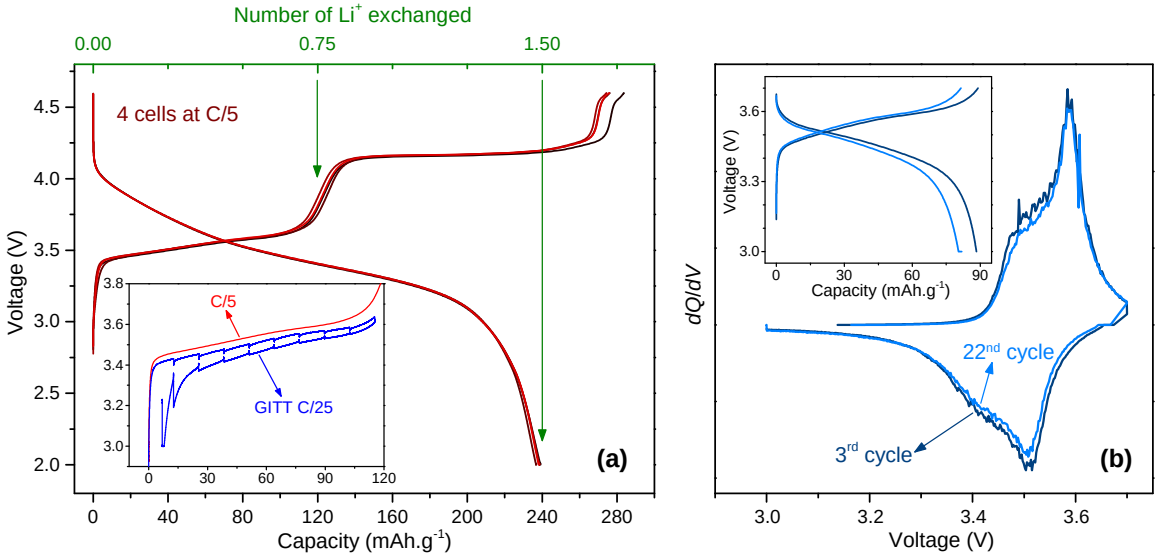


**Figure II.1 | Electrochemical characterization of the 1st cycle and the 3.5 V step.** (**a**) Typical voltage profile during LRSO's first cycle (CC protocol at C/5) changes from 'staircase' charge to S-shaped' discharge. Four identical cells show excellent repeatability. Inset shows GITT voltage profiles (2 hr. C/25 pulse, 4 hr. rest) that match closely in terms of OCV between charge and discharge. (**b**) *dQ*/*dV* curves for restricted cycling only over the 3.5 V redox step with their corresponding voltage profiles in the inset.

† I thank K. Ramesha (CECRI Chennai) for synthesizing and providing the LRSO powders for this thesis.

## ○ Initial step at 3.5 V in the staircase-like 1st charge

The first 3.5 V redox process corresponding to the de-insertion of 0.75 Li per formula unit (theoretical as well as practical capacity of 120 mAh $g^{-1}$), is known to be purely associated to the oxidation of 0.75 $Ru^{4+}$ to $Ru^{5+}$.[68,111] We evaluate the reversibility of this process vs. Li / $Li^+$ with galvanostatic intermittent titration technique (GITT). **Figure II.1a** (inset) shows a good matching of open-circuit voltages (OCVs) between charge and discharge along with almost complete recovery of capacity that indicates excellent reversibility. Furthermore, cycling over the first redox step is fairly stable (**Figure II.1b**). This is evidenced by the derivative capacity ($dQ/dV$) graph showing a double peak that is mirrored between charge and discharge and that neatly superimposes between the 3rd and 22nd cycles with a small capacity loss, thus indicating the absence of any irreversible voltage fade. Overall, the abovementioned results demonstrate that LRSO behaves alike a classical intercalation mechanism when cycling in this limited range of Li stoichiometry.

To interrogate LRSO's kinetic and transport properties during the first redox step, i.e. respectively, the charge-transfer resistance and diffusion coefficient, we use complementary electrochemical techniques, namely potentiostatic intermittent titration technique (PITT) and electrochemical impedance spectroscopy (EIS) in addition to the aforementioned GITT. The variation of Li diffusion coefficient with SoC, measured using GITT, is presented in **Figure A1.4a** in the Appendix. A linear variation of $V$ vs. $t^{0.5}$, as theoretically expected at short time after switching on the current pulse, is exemplified in **Figure A1.4b**. Note that $D/R^2$ [$s^{-1}$] ($D$ being the diffusion coefficient and $R$ the particle radius), which refers to the time constant associated with diffusion of Li in the bulk, varies from 8 x $10^{-6}$ to 2 x $10^{-5}$ $s^{-1}$ throughout most of the 3.5 V step.

EIS measurements were performed in a three-electrode cell (see Methods in the Appendix for cell details) at varying SoCs over charge and discharge that correspond to the OCVs in the EIS-GITT curve (**Figure II.2a**). As an example, the Nyquist plot for Point 1 on charge is shown in **Figure II.2b** and it can be subdivided broadly into three frequency domains. The depressed semicircle at high frequencies (HF) in the 1000–100 Hz range is ascribed to a combination of fast electrochemical processes, such as interface contact with the current collector, electronic conductivity, inter-particle contact or thin solid electrolyte

interface (SEI) layer. Next, the charge-transfer resistance ($R_{ct}$) at the electrode / electrolyte interface and the double layer charging / discharging are responsible for a semi-circular feature at medium frequencies (MF) in the range of 10–0.1 Hz. Finally, at low frequencies (LF) < 0.1 Hz, a 45° straight line in the Nyquist plot denotes the Warburg impedance related to solid-state diffusion of Li in the bulk.[167–169] Based on this description, an equivalent circuit model (**Figure II.2b**-top) excellently fits of the experimental data.

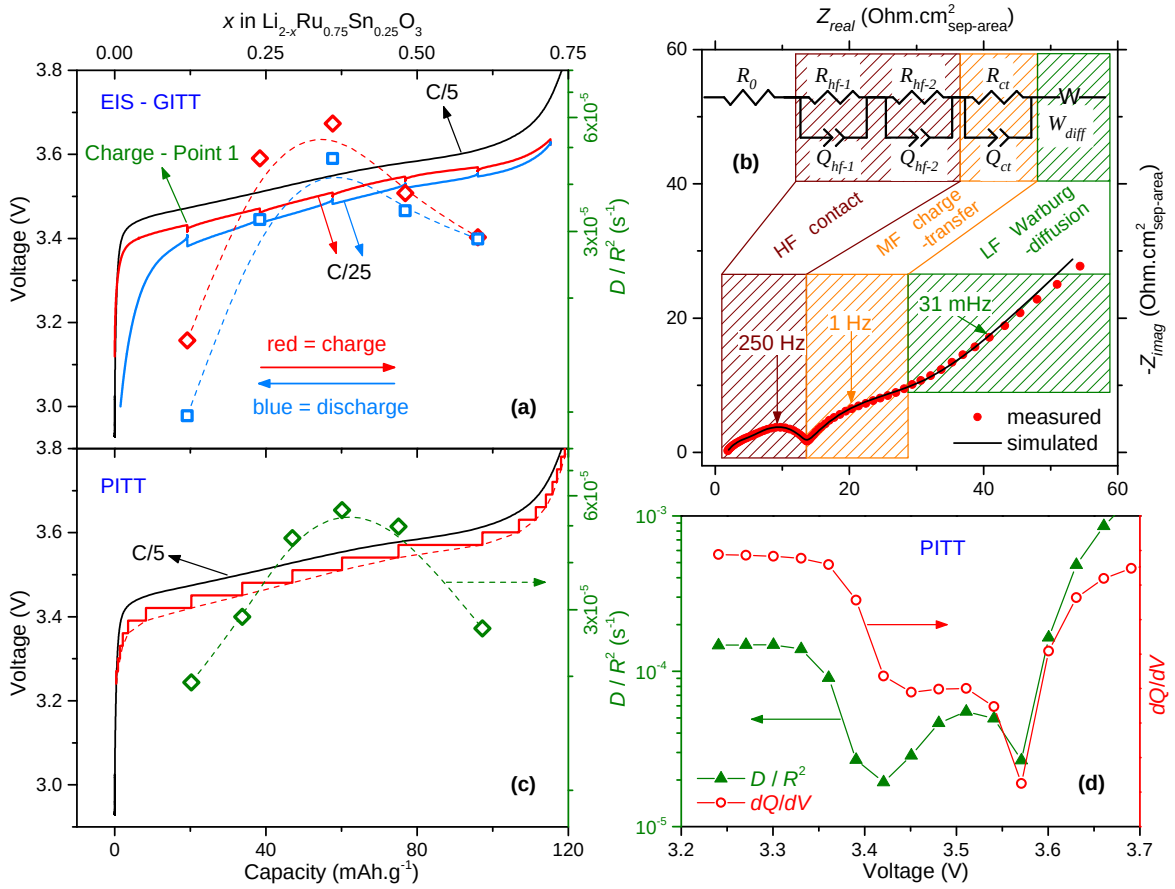


**Figure II.2 | Kinetics of the 3.5 V step.** (**a**) EIS-GITT voltage profiles (left axis) (3 hr. C/25 pulse, 4 hr. rest) and corresponding diffusion time constants, $D/R^2$ (right axis). (**b**) Example EIS Nyquist spectrum measured at point 1 on charge along with the simulated spectrum based on the equivalent circuit model shown at the top. (**c**) PITT voltage profile (30 mV step, C/500 cutoff) and corresponding values for $D/R^2$. (**d**) Variation of $D/R^2$ vs. potential measured with PITT, showing its correlation with the $dQ/dV$ profile (right axis).

The evolution of EIS spectra over the first redox step can be followed in **Figure A1.5** where it is evident that the HF arc does not change much with SoC. Secondly, the MF feature related to $R_{ct}$ remains small throughout the process, barely discernible from the Warburg tail. On the other hand, the most noticeable changes occur in the LF domain,

related to Li diffusion. Fitting the EIS spectra with the equivalent circuit model (**Figure II.2b**–top) provides parameters for calculation of $D/R^2$. As seen in **Figure II.2a**, $D/R^2$ varies from 2 x $10^{-5}$ to 5 x $10^{-5}$ $s^{-1}$, similar to the results from GITT (**Figure A1.4a**). Lastly, the $D/R^2$ and interfacial resistance terms are also deduced from PITT by fitting the experimental data (**Figure A1.6**) using the two-parameter single-particle model having spherical geometry, as described in the Methods (Appendix) PITT confirms (**Figure II.2c**) the trends deduced from both EIS and GITT measurements. Moreover, PITT also enables us to deduce the diffusion coefficients at this step's very beginning / end, where voltage changes steeply with Li content. **Figure II.2d** shows the complete variation of $D/R^2$ vs. $V$, having two minima that neatly correspond with the two $dQ/dV$ (right axis) peaks. Such a correlation between $D/R^2$ and $dQ/dV$ again characterizes a typical intercalation mechanism, also known for example for graphite[170,171] and spinel-$LiMn_2O_4$[172], that has theoretical origins in non-idealities expressed by a thermodynamic factor for activity correction.[173,174]

## ○ Second step (4.15 V plateau) in the staircase-like 1st charge

We now turn to the exploration of the thermodynamic and kinetic properties at LRSO's high voltage plateau (4.15 V). The GITT voltage profile, collected through the whole first charge (**Figure II.3a**), reveals a striking difference between the two staircase steps, namely in terms of the time to reach OCV, which is only of a few hours for the first 3.5 V step (**Figure II.3a**–inset), in agreement with the above-mentioned results. In contrast, the OCV vs. time curves (**Figure II.3a**–inset) at the 4.15 V plateau show a seemingly never-ending voltage relaxation even for rest periods close to 2 days, hence indicating a process having a large time constant. Remarkably, **Figure II.3b** shows that upon very slow charging (i.e. CC at C/100 and PITT with C/500 cutoff), the under-current potential traces cling to the 4.15 V plateau instead of the significantly lower potentials seen during open-circuit conditions. Also, only a weak increase of polarization, despite increasing the current by a factor of 20 (C/100 to C/5), implies that the plateau has fast charge-transfer kinetics. However, the fundamental origin of slow relaxation under open-circuit condition is unclear and it may be related to the sluggish equilibration and hence mixed potential[175] between pristine and 'activated' LRSO, resembling conversion-type materials in this regard. In summary, the removal of Li from LRSO at the 4.15 V plateau,

that accompanies anionic redox, triggers an irreversible, electrochemically-driven phase transformation (or 'activation'), which turns out to have fast charge-transfer kinetics but slow equilibration dynamics. Transformed or 'activated' LRSO exhibits a permanently modified electrochemistry, expressed in subsequent cycling as 'S-shaped'-sloped charge and discharge profiles.

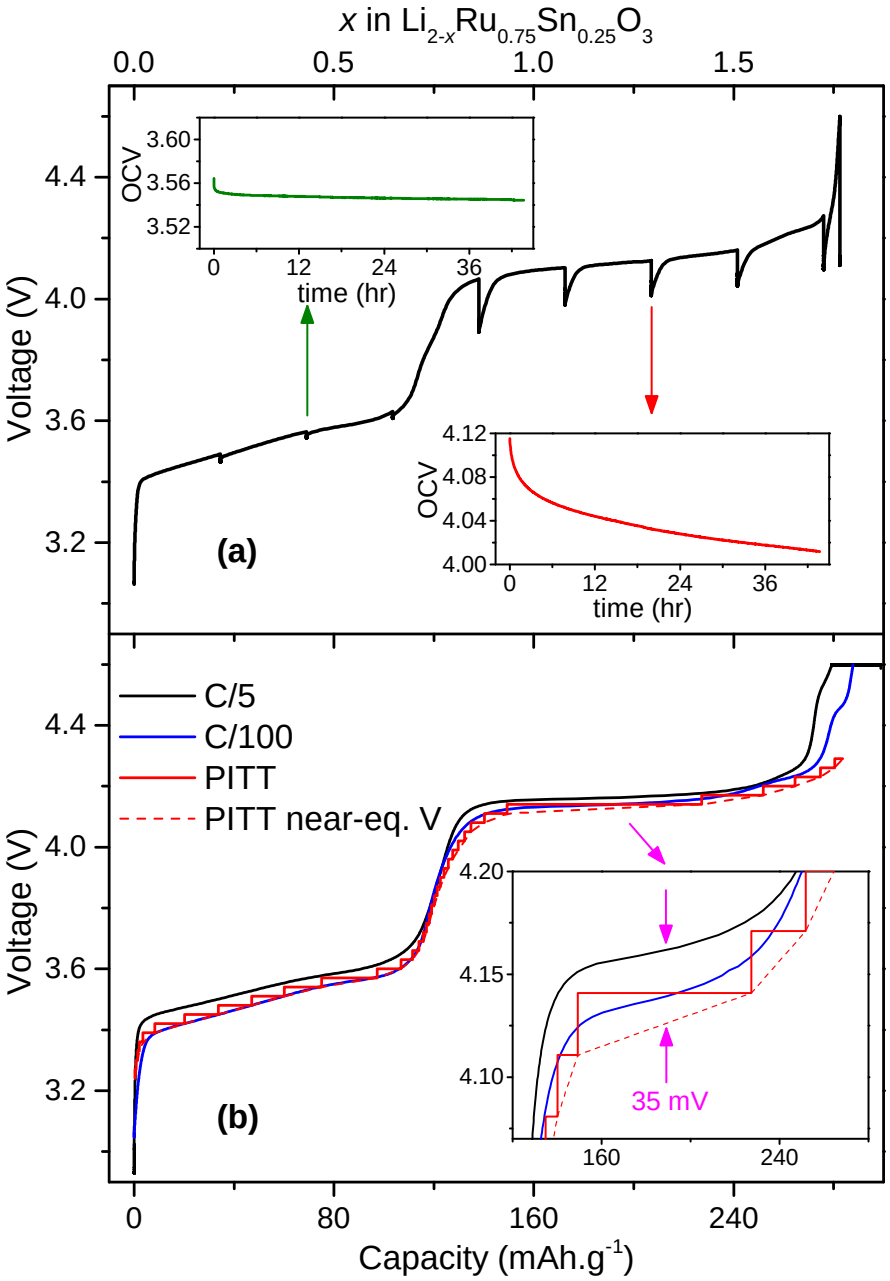


**Figure II.3 | Electrochemical characterization of the 4.15 V plateau.** (**a**) Long-rest GITT voltage profile (4 hr. C/20 pulse, 44 hr. rest) over the whole first-charge with the insets tracing OCV vs. time to highlight contrasting behaviour of the two staircase steps. (**b**) Comparison of first-charge voltage profiles at C/5, C/100, and PITT (30mV step, C/500 cut-off) with the inset showing a small polarization overpotential at the 4.15 V plateau.

## ○ Post activation – Hysteresis and path-dependence

The above fundamental exploration of the first cycle was essential, but when considering real-world applications, it is important to know how the cell behaves after reaching its transformed (or 'activated') state. It takes around five cycles with a CCCV protocol (at C/5 with C/100 cut-off) or ten cycles with a CC protocol (at C/5) within 2–4.6 V for LRSO to achieve a fairly stable voltage profile on charge and discharge. Post activation, GITT findings in **Figure II.4a** show a significant voltage gap (~100 mV) between OCVs at charge vs. discharge despite very long rest periods of 24 hours. In classical intercalation materials, the OCVs match at a particular SoC between charge and discharge, however in our case, very slow equilibration dynamics (beyond 24 hrs.) prevail. Therefore, GITT indicates thermodynamic hysteresis in activated LRSO and this is further confirmed with complementary experiments at a small C-rate of C/50 (**Figure A1.7**) to minimize kinetic effects. Again, a 150–250 mV voltage gap remains despite small currents indicating that it is not arising from kinetic limitations but is rather related to hysteresis, such that the path followed during de-lithiation is different from the one on lithiation.

Next, we explore what causes the onset of this hysteresis through electrochemical techniques and particularly, we identify the role of anionic redox. 'Activated'-LRSO is cycled by charging alternatively with CC or CCCV protocols, switching back and forth between them with increasing number of cycles. The resulting discharge voltage profiles and *dQ*/*dV* traces are shown in **Figure II.4b**. A total capacity of nearly 240 mAh $g^{-1}$ is delivered, out of which about half accounts theoretically for the oxidation of 0.75 $Ru^{4+}$. This indicates almost equal capacity contributions from the cationic redox of $Ru^{4+/5+}$ and the anionic redox of $(O_2)^{4-/n-}$. These two processes on discharge can respectively be assigned to the *dQ*/*dV* peaks centred around 3.3 V and 3.7 V.[111] In short, the first half of the 'S-shaped'-sloped profile at lower voltages primarily involves cationic redox and after crossing the mid-point (or 50% SOC), oxygen is the major redox species at higher voltages. A deeper charge with CCCV (implying more oxygen oxidation) leads to an expected additional discharge capacity (more intense 3.7 V *dQ*/*dV* peak) that is however shifted down to a slightly lower discharge voltage, which is counterintuitive (**Figure II.4b**). This unanticipated drop in the entire voltage profile upon full activation of anionic redox with CCCV is not permanent because the voltage jumps back up if the next cycle is charged with CC only. Therefore, it cannot be assigned to irreversible formation of a

passivation SEI layer during the hold at 4.6 V and we hypothesize that anionic redox either leads to poorer kinetics / transport properties and / or it causes a reversible thermodynamic hysteresis. To test this claim, voltage window experiments were next conducted and the results are shown in **Figure II.5**.

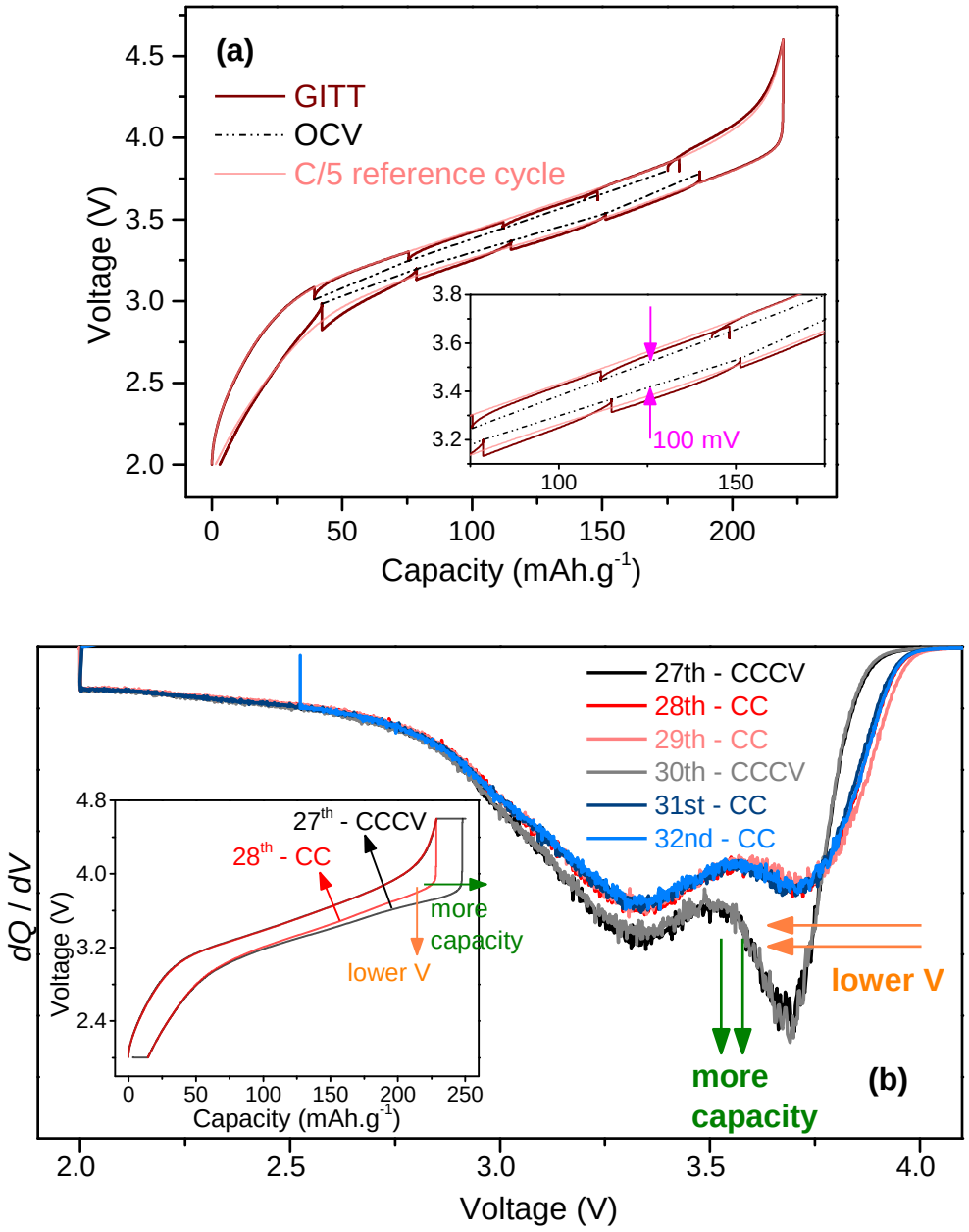


**Figure II.4 | Onset of hysteresis in activated LRSO.** (**a**) GITT voltage profile (C/5, 24 hr. rest) with magnification in the inset showing significant thermodynamic hysteresis (~100 mV) despite very long OCV periods. (**b**) Discharge *dQ*/*dV* profiles and corresponding voltage traces (inset) for cycling at C/5 alternatively with CC or CCCV charge protocols. CCCV charge at 4.6 V fully oxidizes anions to produce extra discharge capacity (green arrow) however at slightly lower potentials (orange arrow).

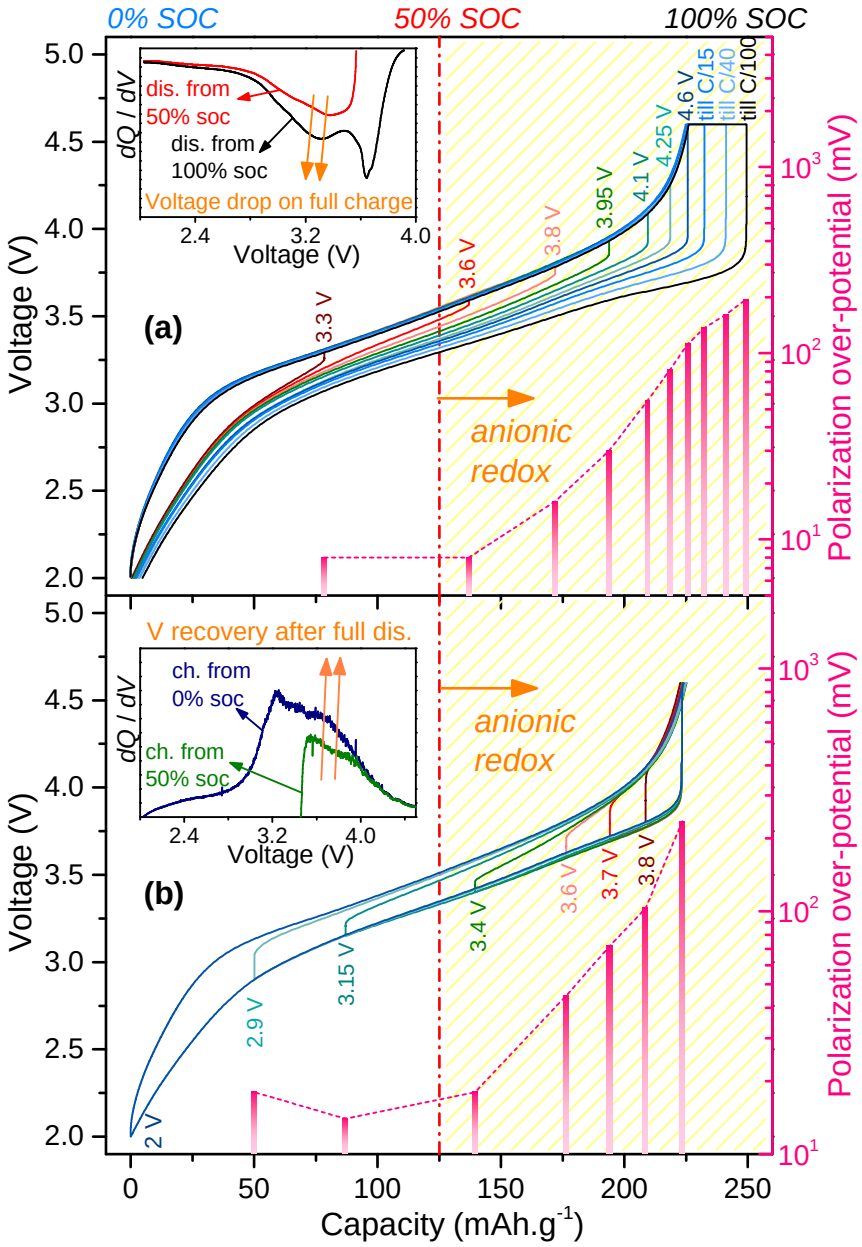


**Figure II.5 | Voltage window experiments to understand hysteresis in 'activated'-LRSO.** (**a**) The charge window is progressively opened with each cycle by increasing the upper cut-off voltage. Charge profiles are identical but discharge profiles drop gradually upon activating anionic redox after 50% SoC with simultaneous rapid growth of the overpotential (right axis). The inset compares discharge *dQ*/*dV* profiles of 50% and 100% charged LRSO with the latter displaying more capacity but at a dropped potential. (**b**) A complementary experiment of opening the discharge window with each cycle such that all discharges are identical but the charge profiles start to regain higher potentials only after complete anionic reduction (inset). Overpotentials (right axis) also decrease back with anionic reduction. The inset shows charge voltage recovery after full discharge. All profiles are taken at C/5 and polarization overpotentials (right axis) are measured during the first 10 s of the current pulse after a 2 hr OCV period when switching between charge and discharge at a particular cut-off voltage.

**Figure II.5a** shows the effect of cycling 'activated'-LRSO by progressively increasing the charge cut-off voltage with each cycle but always followed by a discharge to 2 V after a 2 hour OCV period in between. In each cycle, starting from the fully discharged state, LRSO follows the same charge profile as one would expect. However, discharge voltage profiles steadily fall along with a simultaneous growth of polarization overpotential (right axis), after the de-lithiation level crosses the half way mark, i.e. 50 % SoC. These effects are particularly severe after passing 3.6 V, above which is primarily the anionic redox region. The discharge profile of 50 % charged LRSO is compared against 100 % charged LRSO and the latter shows a larger overall polarization (about 200 mV at 50 % SOC), which can alternatively be visualized in the *dQ*/*dV* curves (**Figure II.5a**–inset) as a voltage profile collapse, thereby pointing to a hysteresis that is triggered upon full charging.

In a complementary experiment, shown in **Figure II.5b**, LRSO is cycled with a similar protocol but this time by gradually opening the discharge voltage window. It can be inferred that a discharge of at least more than 50 % SoC is necessary to begin the recovery of dropped voltage profiles (**Figure II.5b**–inset). This shows that charge paths are dependent on discharge histories (also vice-versa), and not just SoC, therefore this path dependence has thermodynamic origins. Lastly, polarization overpotentials (right axis), which represent electrochemical resistance, are found to recuperate in a reverse fashion during the first half of discharge. In summary, this pair of experiments confirms our hypothesis that activating anionic redox not only causes a reversible thermodynamic hysteresis (or path-dependence) but also triggers kinetic limitations (overpotentials), which are investigated next in greater detail.

## ○ Post activation – Kinetics and transport properties

A part of the voltage polarization seen above, is attributable to slow interfacial kinetics and / or bulk Li diffusion, and when operating at practical current values, these limitations can impact energy efficiency and also limit the attainable charge / discharge capacity. We thus begin to explore the kinetic and transport properties of 'activated'-LRSO with the help of various electroanalytical techniques such as EIS, GITT, and PITT, applied

to well-designed electrodes that permit the use of simplified models for reliable quantification of the desired properties. Qualified electrodes must have low active-material loading and high porosity (specifications in Methods and **Figure A1.2** in the Appendix) to minimize undesired porous-electrode effects and counter electrode polarization and thus ensure that the intrinsic properties of LRSO govern the results.

**Rate capability.** Once the Li / LRSO cells are activated, they are tested with a CCCV charge and discharge protocol involving step-by-step increments in current (or C-rate) with each cycle, scanning from a very slow C/50 to a more practical value of 1C. **Figure II.6a** shows the resulting voltage profiles and **Figure II.6b** shows the corresponding *dQ*/*dV* curves. During charge, polarizations do not show up until the last stages of de-lithiation, demonstrating excellent rate capability for charging of LRSO throughout the cationic redox regime but suggests limitations at higher potential, where at higher currents, we see an earlier termination of capacity with correspondingly diminishing *dQ*/*dV* profiles above 3.7 V. This contrasts with the discharge voltage profiles that are more polarized in the beginning at the higher potential peak. Most evidently, the *dQ*/*dV* profiles (**Figure II.6b**) show a striking movement of the oxygen reduction peaks upon increasing the current from C/50 to 1C in comparison to the $Ru^{4+/5+}$ peaks that are virtually anchored at 3.3 V at all C-rates. Because the cell in this experiment ages with every cycle, we performed two consecutive cycles each at C/2.5 and 1C, which virtually superimpose to validate that ageing-related voltage fade and impedance build-up cause a much smaller voltage drop ($\Delta V_{ageing}$) compared to the kinetic polarization induced by current increment ($iR_{kinetic}$), i.e. $\Delta V_{ageing} << iR_{kinetic}$ (**Figure II.6a**–inset).

In an analogous supporting test, we scanned the discharge response to increasing currents for 'activated'-LRSO, which is this time charged only to 3.9 V at C/5 (just cationic redox therefore) for every discharge C-rate. The *dQ*/*dV* peak is anchored again at 3.3 V in **Figure A1.8**, hence reinforcing faster discharge kinetics of cationic redox while the higher potential peak related to oxygen redox is not triggered.

The above experiments clearly point to kinetic and transport resistances for anionic redox in comparison to the much faster cationic redox. These two properties are now quantified individually in the following section using EIS, GITT and PITT.

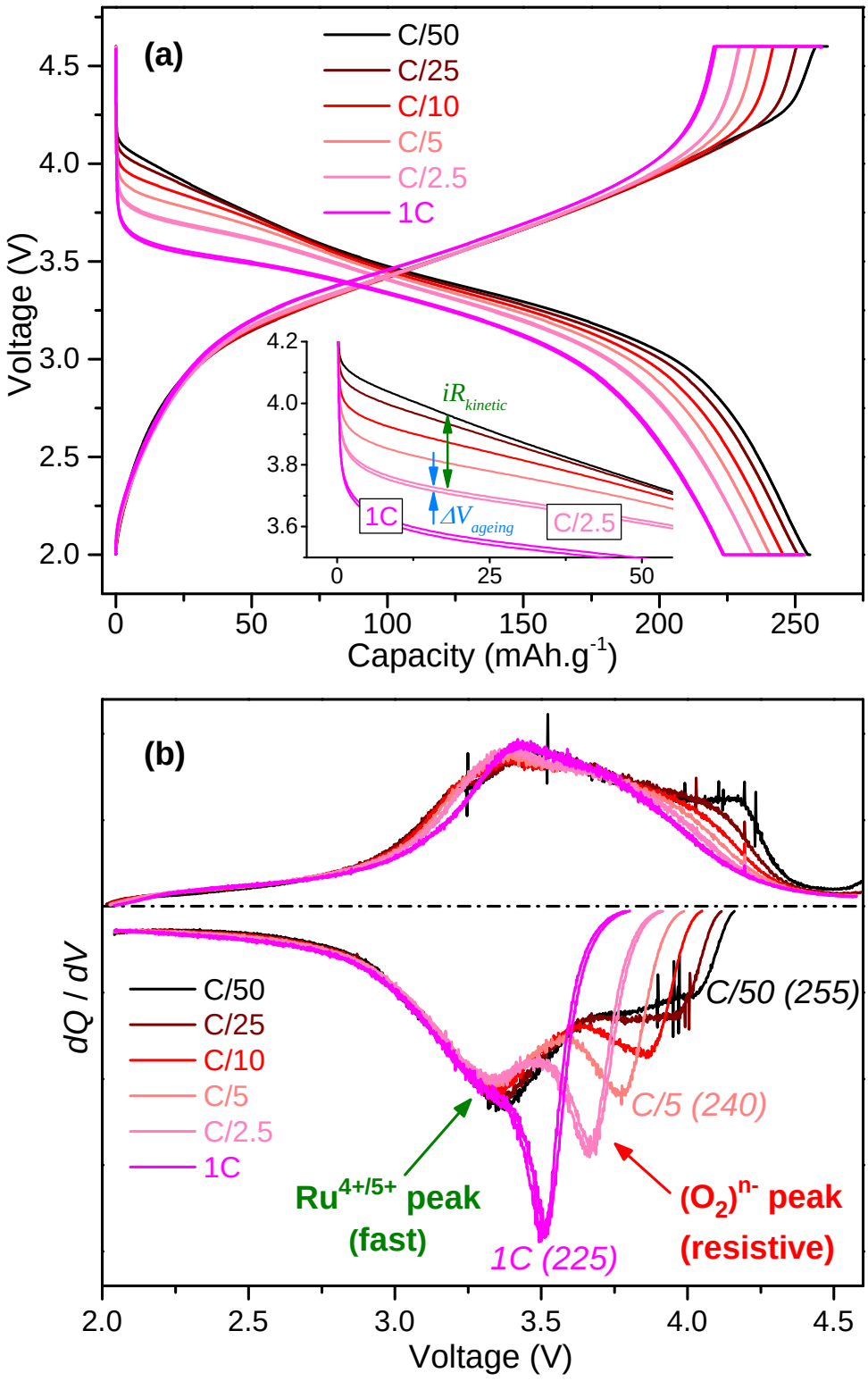


**Figure II.6 | Rate capability of 'activated'-LRSO from C/50 to 1C**. CCCV protocol ensures identical starting and ending states for each C-rate measurement, i.e. between fully charged to 4.6 V and fully discharged to 2.0 V. (**a**) Voltage profiles that are also magnified in the inset to show negligible effect of ageing, $\Delta V_{ageing} << iR_{kinetic}$. (**b**) Corresponding *dQ*/*dV* profiles showing large polarizations for the oxygen reduction peak. The parentheses show total discharge capacity in mAh $g^{-1}$ before reaching 2.0 V.

**Electrochemical Impedance Spectroscopy (EIS).** For this experiment, a Li / LRSO coin cell is first activated by carrying out five CCCV cycles, then the cycled electrode is recovered in the discharged state and transferred to a fresh three-electrode Swagelok cell having Li metal at both the counter and reference electrodes. By using two different cells, EIS spectra are measured separately on the charge and discharge paths with varying levels of SoC. More specifically, a GITT procedure with OCV periods of 4 hours (**Figure II.7a,e**) is used to reach the desired SOCs before measuring EIS spectra. Features of the spectra are interpreted and modelled similar to first section of Results and for sake of conciseness, only three representative spectra, covering the low, middle, and high SOCs, each for charge and discharge paths, are reported and discussed next. The complete set of spectra can be found in **Figure A1.9**.

In the beginning of charge (**Figure II.7b**), the EIS Nyquist plots show a small HF arc related to fast electrochemical processes, which in fact stays relatively constant in size throughout the whole charging process (**Figure A1.9**). Moreover, there is the onset of a very small arc in the MF region related to interfacial charge-transfer resistance that can be seen but very faintly since it is severely overshadowed by the LF Warburg-like feature representing Li diffusion. Next, at mid-SOC (**Figure II.7c**), the $R_{ct}$ arc in MF becomes large enough to be clearly distinguishable visually although its magnitude is still quite small (comparable to the HF resistance), which indicates fast charge-transfer kinetics overall. However, from then onwards, charging further causes a rapid enlargement of the semicircle related to $R_{ct}$. Near the end of charge (**Figure II.7d**), the MF arc becomes very large, thus marking a clear evidence of poor interfacial kinetics for anionic redox. The trends for variations of $R_{ct}$ and $D/R^2$ vs. SOC (**Figure II.7a**) are deduced by fitting using the aforementioned equivalent circuit model (**Figure II.2b**-top). $R_{ct}$ (right axis) stays small for the first half of charging but afterwards it grows exponentially by 2 orders of magnitude from mid charge to full charge and towards the end, the spectra move closer to a fully blocking capacitor. In comparison to pristine LRSO (discussed in the beginning of Results), Li diffusion is much faster after the activation cycles with $D/R^2$ reaching a higher value of 2 x $10^{-4}$ $s^{-1}$. $D/R^2$ hovers around this value for the first half of charging and then exponentially deteriorates by two orders of magnitude while crossing through the anionic redox regime. We do not however observe a correlation between $D/R^2$ and $dQ/dV$ trends, unlike for the pristine material (**Figure II.2d**), highlighting that 'activated'-LRSO deviates from a purely intercalation-type mechanism.

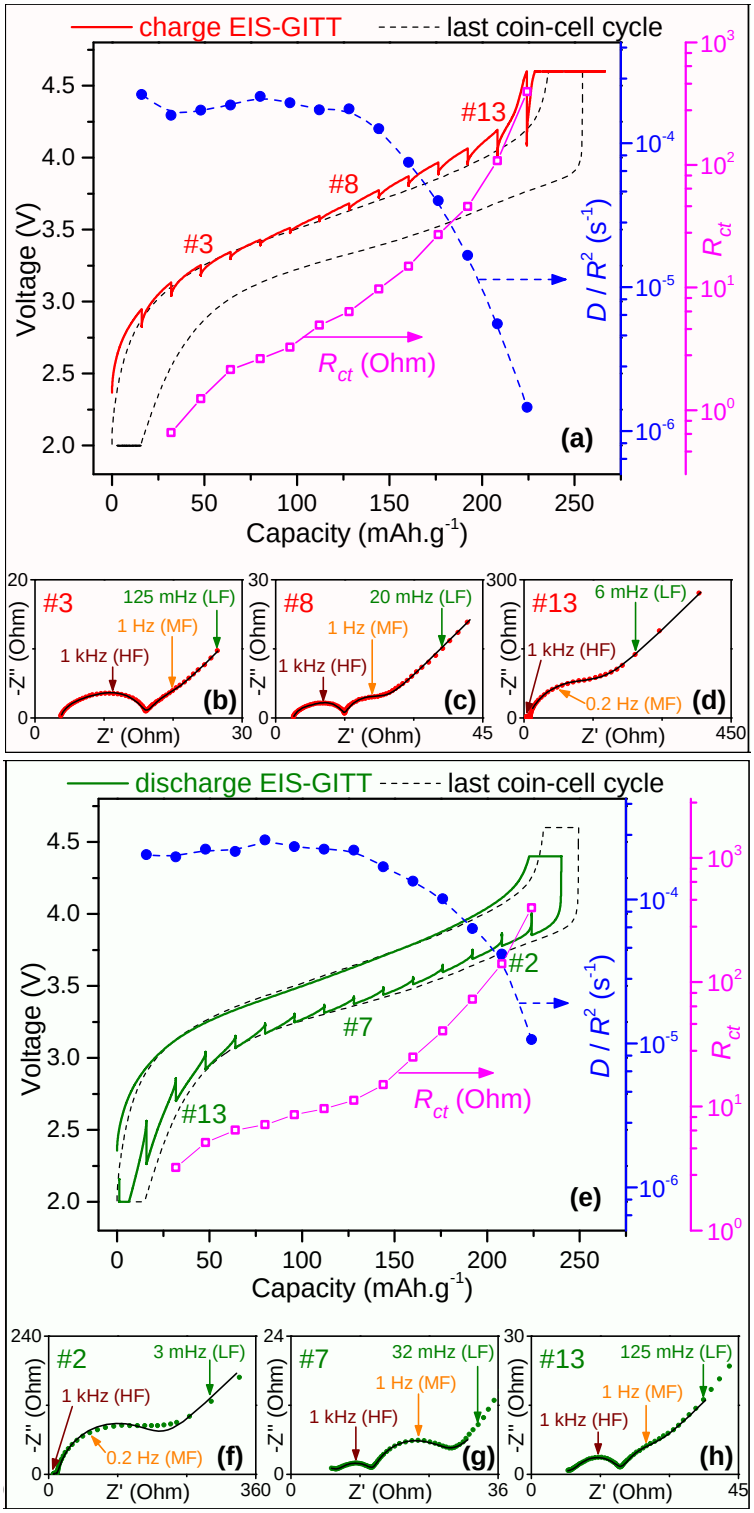


**Figure II.7 | Impedance results for 'activated'-LRSO.** EIS - GITT profiles (30 min pulse at C/5, 4 hr. rest) for (**a**) charge and (**e**) discharge in three-electrode cells match well with last formation cycles in respective coin-cells. Variation of $D/R^2$ and $R_{ct}$ is shown with the right side axes. Measured and simulated Nyquist spectra on charge are shown for points #3–slightly-charged in (**b**), #8–mid-charged in (**c**), and #13–nearly-charged in (**d**). Similarly, for discharge points #2–slightly-discharged in (**f**), #7–mid-discharged in (**g**), and #13–nearly-discharged in (**h**). Note the different scales in the Nyquist plots.

An identical EIS experiment performed during discharge on a different cell yields similar results which are shown in **Figure II.7e**. Again, three representative EIS Nyquist spectra are shown in **Figure II.7f,g,h**, respectively, for slightly-discharged, mid-discharged, and deeply-discharged states, which are fitted satisfactory according to the equivalent circuit model. Reverse trends are seen for $R_{ct}$ and $D/R^2$ on discharge such that both of these properties improve significantly as the anionic redox is discharged, while remaining essentially constant afterwards during cationic discharge. The variations in the HF arc (**Figure A1.9**) are nowhere as drastic as the MF arc and it remains at a fairly constant and small value, thereby not governing the kinetic properties.

The values of $R_{ct}$ and $D/R^2$ obtained from EIS were further used in a simple single-particle continuum model[176] having variable (SoC dependent) Li diffusion coefficient as well as variable interfacial resistance. The resulting simulations could reproduce (qualitatively only, not shown in the thesis) the trends in voltage profiles and d$Q$/d$V$ profiles that were shown in **Figure II.6**, thus confirming further the EIS results. Note that separate charge vs. discharge OCV profiles had to be assumed for such simulations, as the voltage hysteresis is quite large in LRSO and the averaging method sometimes used, e.g for $LiFePO_4$[177] or graphite[178], is therefore not applicable here.

**GITT and PITT.** To confirm the limitations spotted by EIS, we tested 'activated'-LRSO electrodes with two additional electrochemical titration techniques, namely GITT and PITT. **Figure II.8a** shows the GITT voltage profiles on charge and discharge and a clear hysteresis is again fully confirmed despite rather long OCV periods of 10 hours (Continuous drifting of OCV is again observed, as shown in **Figure A1.10**). $D/R^2$ values, as deduced by following earlier protocol, hardly vary in the first half of charge before encountering anionic redox that initiates a sharp fall in $D/R^2$ by two orders of magnitude from around $10^{-4}$ to $10^{-6}$ $s^{-1}$. The diffusion coefficient recovers back during the initial half of discharge to become flat again in the cationic redox region.

PITT profiles (**Figure II.8b**) also show hysteresis even after allowing the currents to decay to an extremely small value of C/500 before launching the next voltage steps. Current responses at short times after the voltage steps are fitted satisfactorily (**Figure A1.11**) with a simplified spherical single-particle model described by two parameters, namely interfacial charge-transfer and bulk diffusion. From **Figure II.8b**, both $D/R^2$ and $R_{ct}$ can be again seen to deteriorate at higher SoCs that are linked with anionic redox.

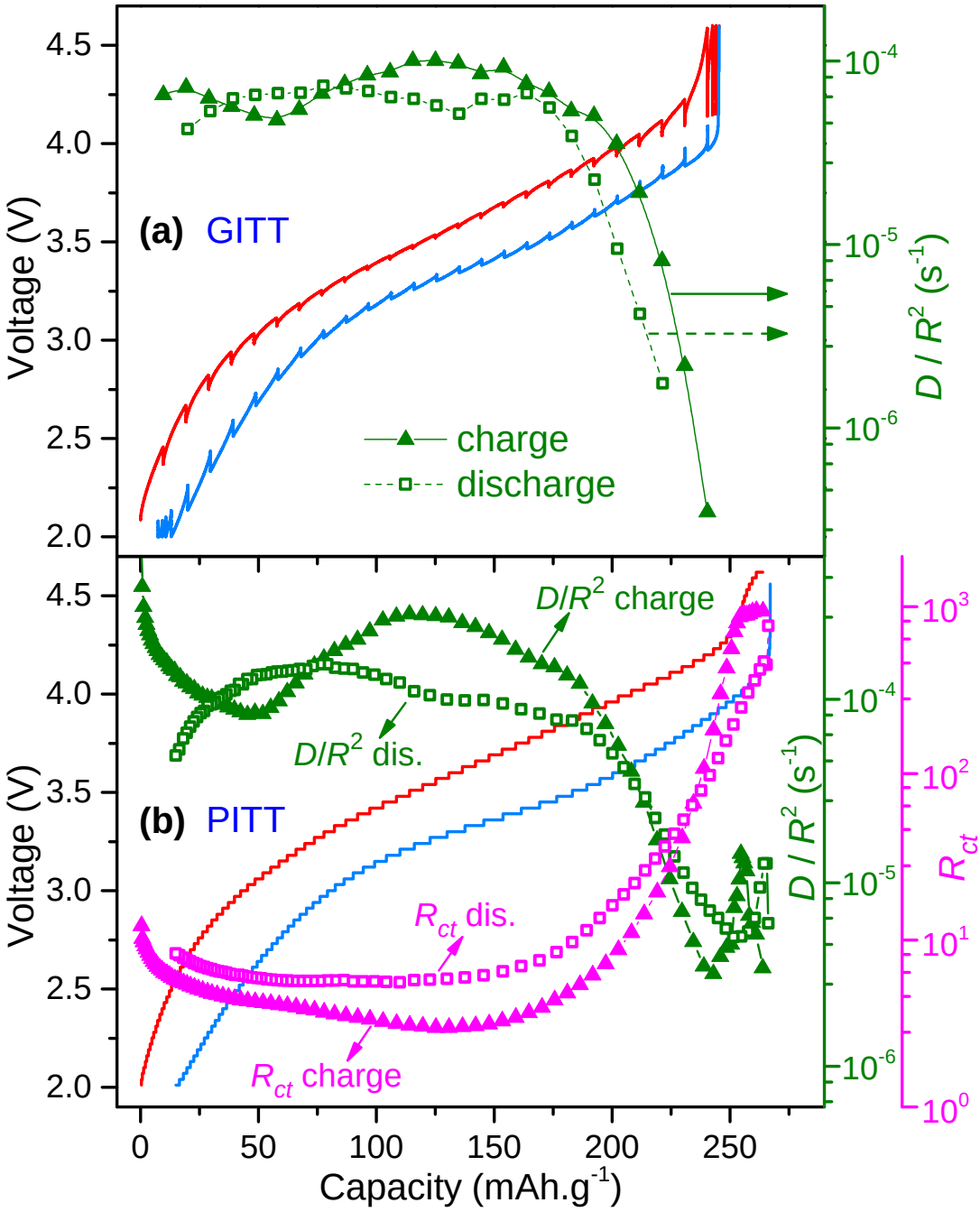


**Figure II.8 | GITT and PITT results for 'activated'-LRSO.** (**a**) Voltage profiles with GITT (C/25 90 min pulse, 10 hr. rest, 25°C) and diffusion time constants (right axis). (**b**) PITT voltage profile (30 mV step, C/500 cutoff, 25°C) with $D/R^2$ and $R_{ct}$ (right axes). Both PITT and GITT show voltage hysteresis.

In summary, using complementary electroanalytical techniques, we have identified a robust correlation of anionic redox with poor interface kinetics and bulk transport properties.

## ○ Cycling – Voltage fade and impedance build-up

It was shown in the preceding work[69] that the incorporation of large $Sn^{4+}$ ions in LRSO considerably mitigated voltage fade but it could not be fully eliminated, motivating us to pursue it further in this thesis. In this section, we investigate the ageing of LRSO upon long-term cycling, focusing particularly on irreversible voltage fade and impedance build-up. Cycling data for LRSO in two cells over 100 cycles shows how the energy density gradually fades due to a combination of capacity loss (**Figure II.9a,c**) as well as decaying average voltage (**Figure II.9b,d**), which are plotted as a function of the cycle number. The coulombic efficiency is close to 100 %, which proves that side reactions are at minimum, and therefore the low energy efficiency of 86 - 88 % is a direct consequence of voltage polarization resulting significantly from hysteresis. We note however that the overall performance is not bad given that the material and electrode design was not at all optimized for long-term cycling. A continuous evolution of *dQ*/*dV* profiles (**Figure II.9a,c**–insets) reveals the trends of shrinking capacities at higher potentials with a simultaneous growth in capacity at lower potentials, explaining the net decay of average charge and discharge voltages. The very broad *dQ*/*dV* peak at lower potentials of 2 - 2.8 V keeps growing upon ageing for both charge and discharge and additionally, a sharp peak is also seen to appear at 3.1 V. This irreversible growth of a sharp charge-discharge peak at 3.1 V is much clearer from the *dQ*/*dV* profiles taken at 3$^{rd}$, 11$^{th}$ and 27$^{th}$ cycles in three cells operated at a very low current of C/50 (**Figure II.9e**) in order to eliminate kinetic effects. Later on, after 50 cycles (**Figure II.9a,c**–insets), another sharp peak at 3.5 V can also be seen on charge.

Overall, the growth of sharp and broad *dQ*/*dV* peaks at different potentials highlights the complicated nature of voltage fade in LRSO since it may be related to different types of irreversible mechanisms such as permanent TM migrations or local crystallization of new phases, the exploration of which is beyond the scope of this work. Apart from voltage fade, impedance also builds up upon cycling due to worsening kinetics as evident from the *dQ*/*dV* profiles that show a continuous drop in voltage at the very onset of discharge (**Figure II.9a,c**–insets).

Despite the cyclability issues discussed above, the high specific energy of LRSO makes it promising for real applications, although only for niche sectors such as space or

defence where cost is less important. In this regard, coin-type full cells were tested and they offer good capacity retention over 1000 cycles, high Coulombic efficiency, and low self-discharge (**Figure A1.12**).

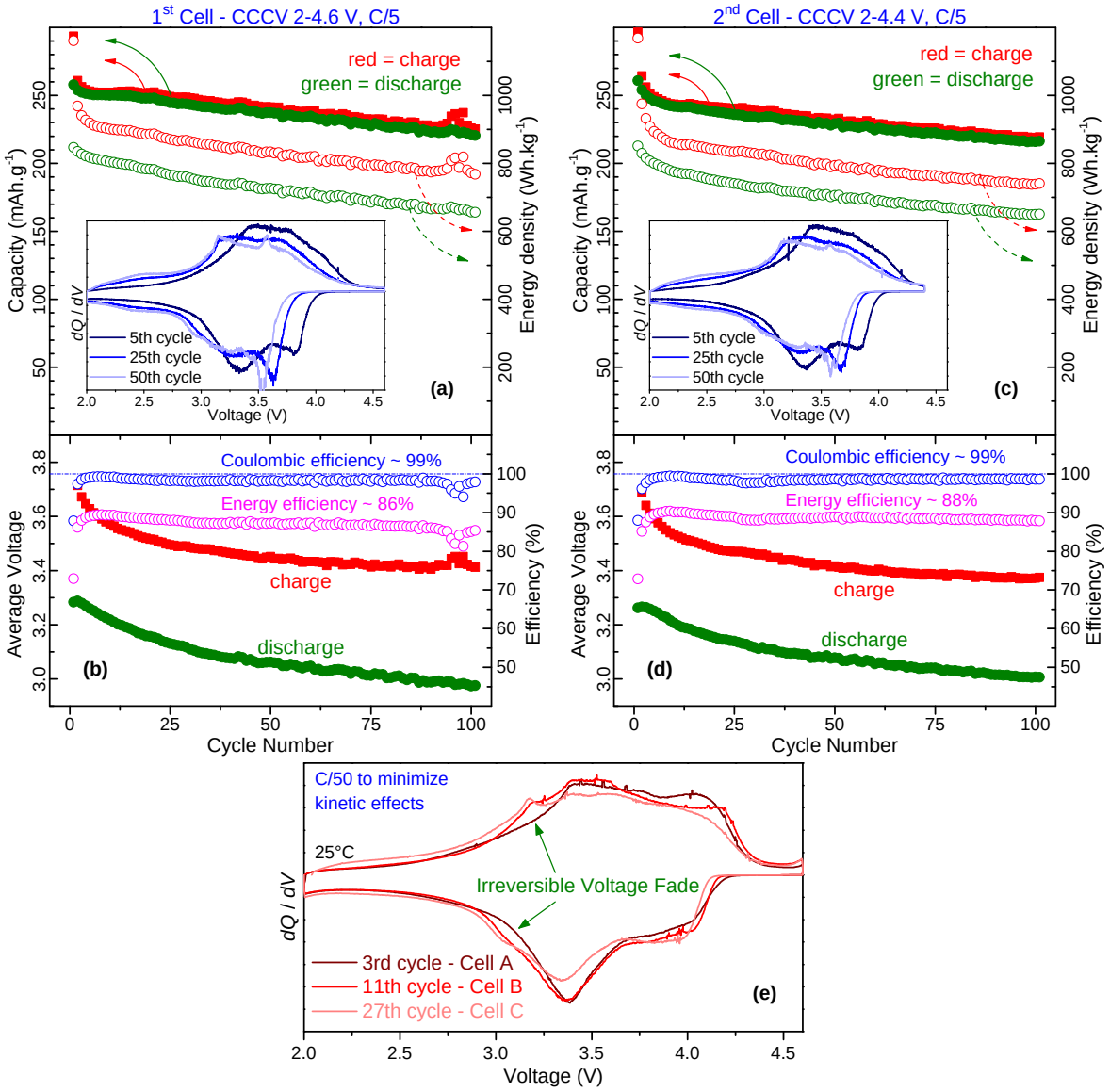


**Figure II.9 | Long-cycling properties of 'activated'-LRSO.** Key performance parameters vs. cycle number over 100 cycles with CCCV protocols within 2 - 4.6 V (panels **a**, **b**) and a slightly less harsh 2 - 4.4 V (panels **c**, **d**). Insets show the evolution of the corresponding *dQ*/*dV* profiles. Average voltages are calculated by dividing the energy density by specific capacity. (**e**) *dQ*/*dV* profiles at low current (CCCV C/50) for three cells having different ages show new broad redox peaks at ~3.1 V that appear upon ageing.

Next, voltage fade and impedance growth in LRSO are examined through a controlled ageing and check-up experiment, the exact protocol details of which are provided with **Figure A1.13**. In short, three identical 'activated'-LRSO half cells were aged simultaneously by galvanostatic cycling (CCCV at C/5, 2.0 - 4.6 V, 2 cycles) accompanied with an intermediate storage (or 24 hr. OCV period) at distinct SoCs for the three cells, i.e. respectively, fully-discharged (0 % SoC), half-charged (50 % SoC), and fully-charged (100 % SoC). EIS spectra are acquired during discharge one by one at 3.4 V (**Figure II.10a**) and 3.7 V (**Figure II.10b**), corresponding respectively to cationic and anionic redox processes. In all spectra, there is a small HF depressed semicircle, a larger MF arc, and a LF Warburg tail, which make these two-electrode cell spectra very similar to three-electrode measurements described previously, highlighting minor impedance contributions from the Li counter electrode. Also, we can again see a much larger MF arc at 3.7 V compared to 3.4 V confirming poorer interfacial kinetics for anionic redox. Initially before ageing, EIS spectra neatly superimpose for the three cells at both potentials to demonstrate excellent reproducibility. As the cells age with cycling, the MF arc progressively grows at both potentials, however with a much faster rate at 3.7 V (**Figure II.10b**) becoming severely blocking towards the end of the experiment. Thus, impedance builds up much more aggressively at anionic redox explaining the aforementioned increasingly larger overpotentials in the beginning of discharge (**Figure II.9a,c**–insets).

Because the three cells age in a similar fashion, it shows that impedance growth in LRSO is essentially because of cycling and the SoC at which the cells are rested does not play a significant role in impedance. From **Figure II.10c**, we can also compare the $dQ/dV$ profiles on charge for the three cells such that they perfectly superimpose in the beginning when the three cells are identical. After ageing however, voltage fades ($dQ/dV$ growth around 2.5V as deduced by a zoom of the data in **Figure II.10c**–inset) slightly more for the cell that is rested intermittently at 100% SOC while the cell rested at 0% SOC fades the least in voltage. A weak correlation is hence concluded between storage SoC and irreversible voltage fade, i.e. spending more time at higher potentials with oxygen in the oxidized state makes LRSO more susceptible to larger irreversible changes and thereby permanent voltage fade. Conversely, when activated LRSO is cycled only till 3.9 V (**Figure A1.14**), thereby without triggering anionic redox, voltage does not fade at all and the discharge capacity and energy density are also very stable (**Figure A1.14**). These results agree with that of Li-rich NMC which is known to show a faster voltage fade only

when cycled at higher potentials.[179–181] In summary, anionic redox to a certain extent promotes voltage fade and suffers from rapid impedance build-up upon cycling.

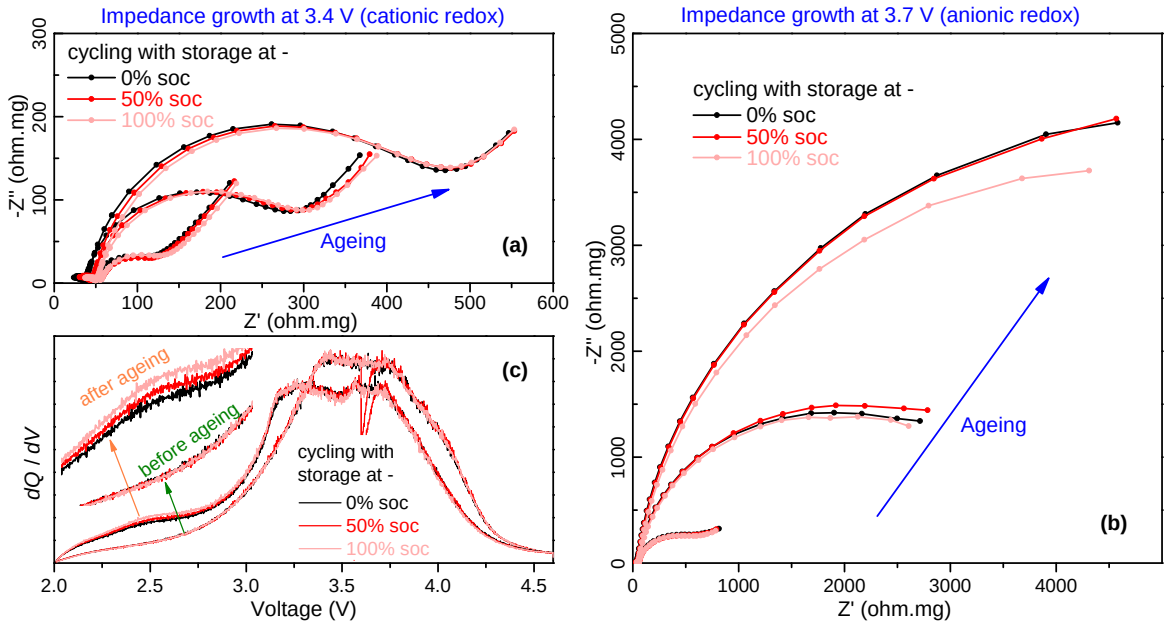


**Figure II.10 | Impedance build-up and voltage fade in a controlled ageing experiment.** Three 'activated'-LRSO cells were cycled with intermediate 24 hr. storage periods, respectively at 0 %, 50 %, and 100 % SoC. (**a**) EIS spectra at 3.4 V (cationic redox) and (**b**) 3.7 V (anionic redox) show growth in $R_{ct}$ (MF arc) but at a much faster rate for the latter. Active material loading is ~5 mg cm$^{-2}$. There is no clear trend in terms of impedance among the three cells and minor variations between them are most likely because of uncertainty in AC measurements, especially for large impedance values at 3.7 V. Therefore, their subtle differences are better distinguished with a more precise DC measurement, i.e. *dQ*/*dV* in panel (**c**). Voltage fade around the broad 2.5 V hump (inset-zoom) is the most severe for the cell with storage at full charge.

## II.3 – Discussion

By applying detailed electroanalytical techniques to LRSO, which is a 'model' Li-rich layered oxide owing to its structural and electrochemical similarities with Li-rich NMC, the roles of cationic and anionic redox processes are clarified. LRSO, just like Li-rich NMC, undergoes a first-cycle activation during which the staircase oxidation profile converts to an 'S-shaped' reduction curve. When oxidation is limited only to the first

staircase step (cationic redox), LRSO shows complete reversibility without hysteresis or voltage fade, identical to the previously reported GITT and cycling results on Li-rich NMC prior to its 4.5 V plateau, indicating a classical intercalation reaction for both materials.[181–183] Further oxidation beyond this triggers an anionic redox plateau associated to the generation of $(O_2)^{n-}$ species that can reduce back on discharge; however, it is at the expense of a thermodynamic irreversibility because the path taken on discharge ('S'-shaped) is different from that on charge (staircase). Thus, LRSO's 4.15 V plateau can be viewed as an electrochemically induced, irreversible transformation (or 'activation') at a constant potential in agreement with previous measurements (XRD and TEM, also supported by DFT) that suggested the nucleation of a disordered phase having permanent local structural changes due to oxygen network distortion and/or TM migration, so that a full discharge can never reset the pristine state.[68,69] On the other hand, these previous works could only spot a few local structural differences between pristine vs. 1$^{st}$ discharged samples, primarily because these two appear very similar and the characterization techniques that were implemented could not pinpoint the subtle structural motions of either O or Li atoms. We will address some of these knowledge-gaps via Chapter III that deals with a detailed study of the local structural evolution of LRSO.

Another specific aspect of LRSO is highlighted from the difficulty to measure the OCV at its flat 4.15 V 'activation' plateau, as we observe a seemingly never-ending equilibration even though the kinetic overpotential is quite small. This observation points to an analogy with conversion-type battery materials that display a similar initial flat plateau with low kinetic overpotential and for which the OCV also drifts for long periods (days to weeks) and departs substantially from the quasi-static potential traces at low currents or under PITT.[159,184,185] 'Activation' in conversion materials is explained by an irreversible transformation of micro-sized starting particles into a nano-composite which interestingly afterwards cycles according to a rather sloped potential profile.[157,159] Conversion materials typically show stable voltage profiles once the 'micro to nano activation' is finished, in contrast with Li-rich materials which show continuous voltage fade with cycling. The key difference in Li-rich materials is that their activation plateau is associated with anionic redox and in fact, such a plateau may be an early indication of structural instability of oxidized oxygen because it leads to reorganization. Whether fortuitous or not, the similarity between Li-rich LRSO and conversion materials deserves greater attention on a fundamental basis.

Once the Li-rich layered oxide is activated, we have spotted another practical issue, i.e. voltage hysteresis that ranges from 150–250 mV in LRSO, which makes SoC management cumbersome. Also, such a potential hysteresis, which is nearly zero in conventional intercalation materials, such as NMC and NCA, contributes to lowering the round trip energy efficiency of LRSO to around 86 to 88% (**Figure II.9**) and likewise for Li-rich NMC (**Figure A1.15** and **Figure A1.16**). Although quasi-static, this hysteresis leads to heat generation during operation, which will be reported in Chapter V. A consequence is that thermal management would be more complicated with these Li-rich materials than with regular materials. We agree with previous hypotheses that such a voltage hysteresis has structural origins since it is supported by Nuclear Magnetic Resonance (NMR) experiments from which different pathways between charge and discharge were identified on the second cycle for LRSO[186] as well as for 'activated'-Li-rich NMC[187]. Moving beyond this initial understanding, we have now fundamentally answered whether such a structural hysteresis originates from anionic redox, a question that was legitimized by previous studies that blamed oxidation at high potentials around 4.5 V (and hence oxygen redox) for hysteresis in Li-rich NMC.[182,183,188,189] This was achieved by simply probing the effect of cut-off voltages. Hysteresis begins only after triggering anionic redox and afterwards, it grows gradually as more $O^{2-}$ anions in LRSO are oxidized at higher potential. On the other hand, cycling only till 3.9 V and hence not triggering the anionic redox-driven hysteresis, leads to much higher energy efficiencies of 95 % (**Figure A1.14**). We recall that the above understanding of hysteresis is based purely on electrochemistry, and therefore spectroscopic evidences will be reported in Chapter III.

Concerning hysteresis, one must recall that the triggering of anionic redox is possibly accompanied by the migration of TMs that partially reverts back on discharge when the anionic species are reduced, as deduced from TEM studies[69]. Fortunately, DFT fully supported this mechanism even though TEM could not directly monitor the formation of O–O species owing to structural symmetry incompatibilities associated to LRSO's O3-type arrangement. Regardless, oxidation / reduction causes formation / dissociation of O–O dimers leading to structural changes, a process that would require a threshold energy and therefore causing voltage hysteresis, quite similar again to conversion reactions where there is also a repeated breaking and creating of bonds. In this regards, a more detailed thermodynamic mechanism understanding will be presented in Chapter V. Although the magnitude of hysteresis in LRSO (~150–250 mV at C/50) is much lesser compared to Li-

rich NMC's ~400–500 mV at C/300[190] and ~500 mV at C/5 (**Figure A1.15** and **Figure A1.16**), it appears to be an inherent feature of such Li-rich layered oxides with varying degrees of severity depending on the chemical composition.

Kinetics is also another important figure of merit regarding practical applications as it is necessary for high power density and low joule heating. The connection of anionic redox with poor kinetics was first speculated in LRSO with Electron Paramagnetic Resonance Imaging (EPRI)[111] and now we are confident that this connection is robust as deduced by complementary EIS, GITT, and PITT, which show that that $D/R^2$ and $R_{ct}$ for 'activated'-LRSO deteriorate by two orders of magnitude leading to severe impedance rise when triggering anionic redox. Such a negative effect of anionic redox on kinetics can also be spotted in other Li-rich layered oxides, for example in $Li_2RuO_3$'s non-explored GITT data[112] and from Li-rich NMC's rate-capability data[164], both showing larger overpotentials in the beginning of discharge.

The last major practical issue in Li-rich NMC, and undoubtedly the most studied, is voltage fade because it gradually diminishes the cell's energy output (**Figure A1.15**) and the continuously evolving voltage profiles make it hard from a battery management perspective. Herein, we unambiguously showed that anionic redox is at the heart of the voltage fade and impedance build-up, but the exact mechanisms by which this takes place remain unexplored. It could either arise from the capturing of some TM ions in tetrahedral sites during the back-and-forth cationic migrations upon cycling as previously reported[69] or via some irreversible modification of the oxygen lattice. Overall, cycling induced voltage fade and resistance build-up, respectively, are thermodynamic and kinetic phenomena that take place together in LRSO and quantifying their individual contributions to performance decay calls for the development of electrochemical and phenomenological models, similar to those recently implemented for Li-rich NMC.[190,191]

Lastly, our data suggests that voltage fade and hysteresis are correlated (because both are aggravated by anionic redox at higher potentials), as previously also suggested for Li-rich NMC[192]. An attempt to model successfully the large hysteresis in Li-rich MNC with an electrochemical model, assuming back-and-forth conversions of $Li_2MnO_3$ 'domains' during charge and discharge, was previously published.[190] Likewise, the better understanding gained from this study about the different roles of cationic and anionic redox will help me in proposing a phenomenological model for LRSO in Chapter V.

# II.4 – Chapter Conclusions

The commercialization of high energy anionic-redox-based Li-rich layered oxide cathodes, e.g. $Li[Li_{0.20}Ni_{0.13}Mn_{0.54}Co_{0.13}]O_2$ (Li-rich NMC), has been stalled by practical issues (i.e. voltage hysteresis, poor rate capability, and voltage fade). Hence it was necessary to investigate whether these problems are intrinsically inherent to anionic redox and its structural consequences. To this end, the 'model' Li-rich layered oxide $Li_2Ru_{0.75}Sn_{0.25}O_3$ (LRSO) was here used as a fertile test-bed for scrutinizing the effects of cationic and anionic redox independently since they are neatly isolated at low and high potentials, respectively.

Through an arsenal of electrochemical techniques, we were able to reveal that anionic redox is indeed linked to the initiation of these key practical problems. The staggering increase in capacity brought by anionic redox in Li-rich layered materials comes at a price, i.e. it simultaneously triggers hysteresis, promotes voltage fade and impedance build-up upon cycling. It also has become clear that kinetics-wise anionic redox process is more sluggish than the cationic one. Concerning future work, we lengthily pointed out in the Discussion section remarkable similarities between the two Li-rich layered oxides – Li-rich NMC (a practical cathode) and LRSO (a model cathode). Such similarities naturally steered us to later extend the methodology developed in this Chapter to the practically-important Li-rich NMC, the results of which will be presented in Chapter IV.

As for the next Chapter, we move beyond pure electrochemical tools used herein towards more sophisticated X-ray spectroscopy techniques, in order to further understand the underlying mechanisms in LRSO.

# Chapter III – *Operando* XAS for fundamental insights on anionic redox

# III.1 – Background and Motivation‡‡

As discussed through the historical account in Chapter I, the demonstration of reversible redox activity of oxygen (anionic redox), initially in 'model' Li-rich layered cathodes such as $Li_2RuO_3$[68,112,193] and $Li_2IrO_3$[70], paved the way for directly evidencing the same in Li-rich NMC.[40,100,102,103,108] Anionic redox has thus rejuvenated the search for novel high energy cathodes by unlocking the possibility for capacity enhancement beyond what one expects solely from transition metals' (TM) redox.[136] However, fundamental understanding of anionic redox is still nascent since isolating its effects is not straightforward in Li-rich NMC cathodes, owing to their complicated charge compensation mechanism from TMs (Ni, Mn, and Co) as well as O.

$Li_2Ru_{0.75}Sn_{0.25}O_3$ (LRSO) on the other hand, offers this possibility since its redox activity stems from just two species, namely Ru (cationic) and O (anionic) whereas Sn is just a spectator.[68] Moreover, as thoroughly investigated in Chapter II, this cathode emulates the electrochemical signature of Li-rich NMC, i.e. a staircase-like 1$^{st}$ charge followed by an S-shaped-sloped profile, and is structurally analogous to the $Li_2MnO_3$ component in Li-rich NMC (also expressed as $Li[Li_{1/3}Mn_{2/3}]O_2$). These peculiarities, plus a large reversible capacity (~250 mAh $g^{-1}$) with long cyclability[68,69,194], make LRSO a powerful model for the Li-rich layered oxide class of cathodes. The previous Chapter relied solely on electrochemical techniques, whereas interpretations about redox processes and structural changes were based on previous[68,105,111] knowledge. Therefore, we attempt in this Chapter to further advance the fundamental knowledge about the cationic–anionic charge compensation and local-structure evolutions in LRSO by using *operando* (and complementary *ex situ*) X-ray absorption spectroscopy (XAS).

Concerning charge compensation, previous X-ray photoemission spectroscopy (XPS) studies (in *ex situ* conditions) proved the redox activity of Ru and lattice oxygen,[105] but doubts regarding quantification still remained because of the limited probe depth of in-house XPS. On the other hand, electron paramagnetic resonance (EPR) provided bulk-sensitivity along with *operando* capability. However, a part of the electrochemical cycle

‡‡ This Chapter is based on the following research article that I co-authored :

**Assat, G.**, Iadecola, A., Delacourt, C., Dedryvère, R., & Tarascon, J.-M. Decoupling cationic–anionic redox processes in a model Li-rich cathode via *operando* X-ray absorption spectroscopy. ***Chemistry of Materials***, 29(22), 9714–9724 (**2017**). (https://doi.org/10.1021/acs.chemmater.7b03434)

yielded no paramagnetic signal, hence eluding an exhaustive quantification of cationic–anionic redox.[111]

Crystal-structure-wise, *operando* X-ray diffraction (XRD) for LRSO simply evidenced the anionic-redox-driven nucleation of a disordered phase (XRD peak broadening).[68] The short-range local structure, inaccessible from XRD, thus still remains obscure and deserves greater attention since local effects, e.g. oxygen network distortion to form "peroxo-like" species, are expected to majorly influence the electrochemical properties, such as voltage hysteresis (or path dependence), kinetics, and voltage fade, which were reported previously in Chapter II.[194] A technique more suitable for atomic-scale investigation is transmission electron microscopy (TEM), as successfully applied to visualize cationic migrations (in *ex situ* conditions) over long cycling in order to explain voltage fade.[69] However, atomically resolved TEM visualization of the oxygen network, like neatly done in $Li_2IrO_3$ to spot O–O dimers[70], has not been possible in LRSO due to symmetry incompatibilities.[68] Lastly, LRSO's investigation with *operando* $^7$Li nuclear magnetic resonance (NMR), a technique sensitive to local environments, also left open-questions about path dependence and cationic ordering.[186]

Aware of the abovementioned shortcomings and knowledge gaps, we present herein a detailed *operando* XAS investigation to track the electrochemically-driven evolutions in LRSO's electronic structure as well as its local structure. We reveal changes in the Ru oxidation state, and visualize, among other local effects, the anionic-redox-driven distortion in the oxygen network around Ru atoms that leads to short O–O distances, a result that was as of yet only theoretically envisaged for LRSO.[109] Through a chemometric methodology for XAS data analysis[195–198], which has recently been introduced to the field of Li (and Na) batteries[199–202], we neatly decouple the cationic–anionic redox reactions to explain each feature in LRSO's differential capacity ($dQ/dV$) curves. Moreover, we show how these findings can underscore the crucial role of anionic redox towards application-wise important properties (i.e. hysteresis and kinetics,) for this model Li-rich cathode.

# III.2 – Results

$Li_2Ru_{0.75}Sn_{0.25}O_3$ (LRSO) powders were synthesized by a solid-state route as described previously[68], and then cast into Bellcore-type electrodes[166] for electrochemical testing, as described in the Methods section of the Supporting Information for this Chapter in Appendix A2. The Ru K-edge X-ray absorption near edge structure (XANES) spectrum of the pristine electrode, recorded *ex situ* in transmission mode, is shown in **Figure III.1a**. The rising edge is followed by two peaks, the first of which can be ascribed to the dipole allowed transition from 1*s* to 5*p* levels while the second one is dominated by single-scattering events involving the absorber and its Ru/Sn neighbours.[203] The rising edge for pristine LRSO superimposes neatly with that of two references, $Ru^{4+}O_2$ and $Li_2Ru^{4+}O_3$, thus establishing its $Ru^{4+}$ oxidation state. Besides, the absence of a pre-edge feature indicates centrosymmetric Ru coordination.[204–206]

Structure-wise, the $Li_2MO_3$ (M = Ru, Sn, Mn) family is made from layers of Li alternating with $LiM_2$ layers, the latter having edge-shared $MO_6$ octahedra in a honeycomb-like arrangement around the $LiO_6$ octahedra.[68] For $Li_2RuO_3$, the $LiRu_2$ honeycomb layer, illustrated in **Figure III.1b**, shows an interesting asymmetry in the Ru hexagons such that one-third of the Ru–Ru distances are short (Ru–Ru dimers) - an arrangement only recently identified in literature using the $P2_1/m$ space group.[207,208] Ru K-edge extended X-ray absorption fine structure (EXAFS) oscillations contain information about the neighbouring atoms around Ru absorbers located in the honeycomb layer. For pristine LRSO, the magnitude of Fourier Transform of EXAFS oscillations, $|\chi(R)|$, shows three peaks (**Figure III.1c**) of which the first one corresponds to $RuO_6$ octahedron (first shell), while the next two peaks come from the abovementioned asymmetric $RuM_3$ (M = Ru, Sn) honeycomb arrangement (second shell) involving one short and two long Ru–M distances. This local structural arrangement is fully established by modelling the EXAFS oscillations using six Ru–O (2.03 Å) distances, one short Ru–M (2.60 Å) distance and two long Ru–M (3.08 Å) distances (detailed fitting results in **Table III.1**).

Such a clear characterization of the asymmetric $RuM_3$ distances (one short and two long) using EXAFS analysis asserts this technique's superiority in determining structures at the local scale, compared to long-range techniques like XRD that missed this effect for many years. Note that our EXAFS model ignores Li owing to its light-weight, and neither

do we differentiate between Ru and Sn (our model considers M = Ru), which is justified because LRSO and $Li_2RuO_3$ show nearly identical Fourier Transforms (see comparison in **Figure A2.3**). Nevertheless, the quality of fits is excellent and the distances match with literature.[207–209] Building up from this initial XAS characterization of pristine LRSO, we next study the effect of delithiation (oxidation).

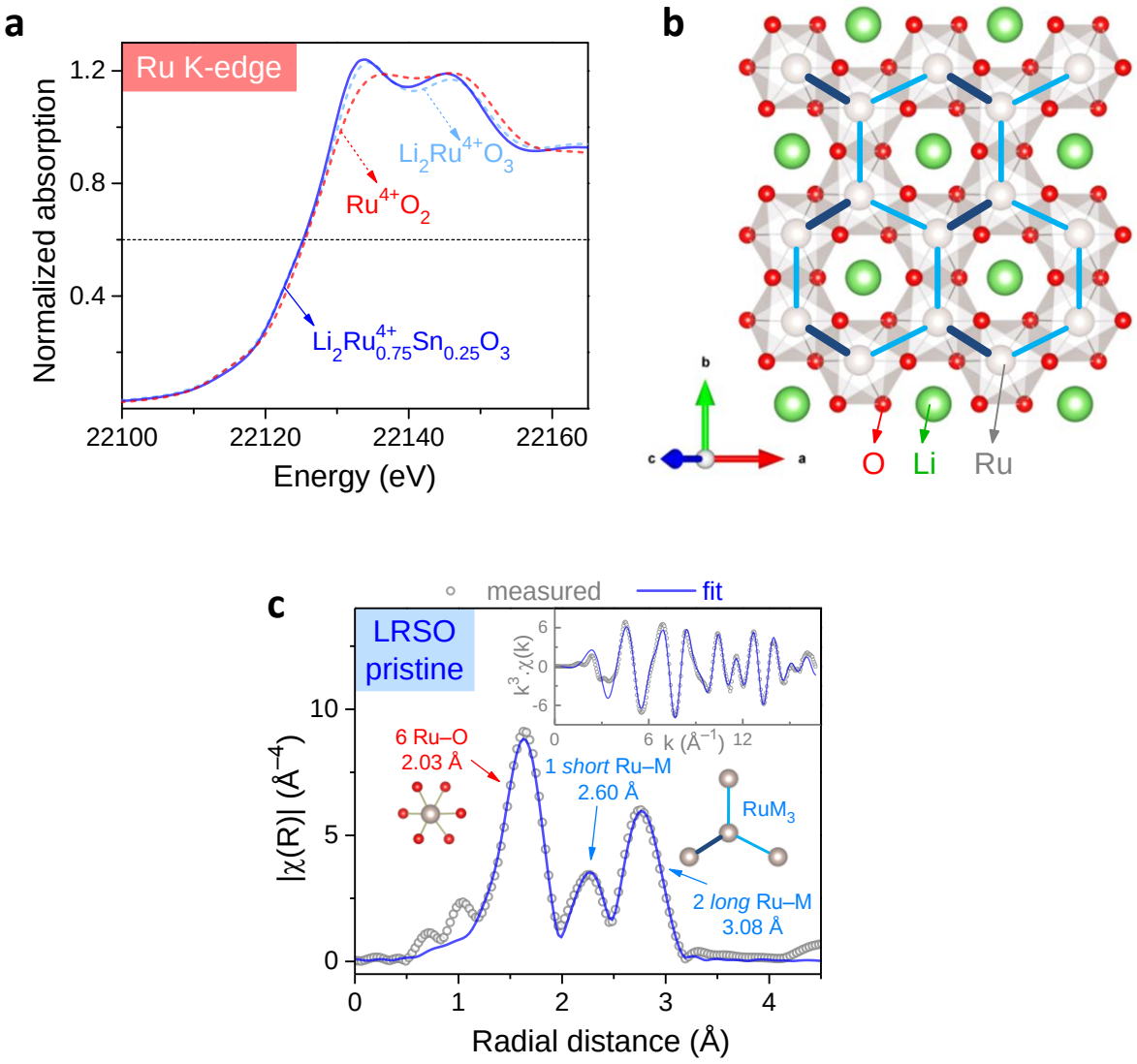


**Figure III.1 | XAS characterization of $Li_2Ru_{0.75}Sn_{0.25}O_3$ (LRSO).** (**a**) Ru K-edge XANES spectra recorded for LRSO and compared with two $Ru^{4+}$ references. The three samples show the same edge positions (defined at jump of 0.6). (**b**) $LiRu_2$ honeycomb layer in $Li_2RuO_3$'s crystal structure[207] showing asymmetric Ru hexagons. Short Ru–Ru dimers are represented by thinker dark blue lines. (**c**) Magnitude of Fourier Transform of $k^3$-weighted EXAFS oscillations for pristine LRSO along with fitting results. The $|\chi(R)|$ plot is not corrected for phase shifts. Inset shows the fit quality in $k$-space.

**Table III.1 | Detailed results of fitting of EXAFS oscillations for pristine $Li_2Ru_{0.75}Sn_{0.25}O_3$ (LRSO).**[†]

| Sample | $RuO_6$ (first shell) | | | $RuM_3$ (second shell) M = Ru/Sn | | |
|---|---|---|---|---|---|---|
| | *CN* | *R* (Å) | $\sigma^2$ (Å$^2$) | *CN* | *R* (Å) | $\sigma^2$ (Å$^2$) |
| **A) Pristine LRSO** | 6 | 2.025 (2) | 0.0042 (2) | 1 | 2.604 (3) | 0.0045 (2) |
| | | | | 2 | 3.081 (2) | 0.0040 (2) |
| | | | | | *R-factor* = 0.0047 | |

## ○ Staircase-like 1st charge – *Operando* XAS

An *in situ* electrochemical cell[210], equipped with two Be windows (one on either side) that allow transmission of the X-ray beam (**Figure A2.1** and **Figure A2.2** in the Appendix), was used for studying LRSO positive electrodes in a Li half-cell configuration. The voltage profile measured during oxidation in such a cell features a staircase-like charging process (**Figure III.2**, top), replicating neatly the profile obtained with conventional coin or Swagelok cells.[68,194] Ru K-edge XAS spectra were collected in *operando* conditions without any current interruption, as shown in **Figure III.3**. Each spectrum shown herein consists of data averaged over 250 seconds (500 raw scans) and the time interval between two spectra was ~20 minutes.

It can be observed that the spectra evolve differently during the two voltage steps. Delithiation near 3.6 V accompanies a shift of the rising edge to higher energy by ~2 eV (**Figure III.3a**) and an inversion of intensities of the two peaks (situated about 22,135 and 22,147 eV), thereby demonstrating the $Ru^{4+/5+}$ cationic redox associated with the removal of 0.75 $Li^+$ per formula unit of LRSO. In contrast, further oxidation at the 4.2 V plateau does not lead to an additional shift of the Ru K-edge (**Figure III.3b**), hence signifying that the $Ru^{5+}$ state remains unchanged and further implying the occurrence of $2O^{2-} \rightarrow (O_2)^{n-}$

[†] $E_0$ was determined from the energy value where jump is 0.6. The difference in threshold energy ($\Delta E_0$) and the amplitude reduction factor ($S_0^2$) were fixed at 0 and 1, respectively. The coordination numbers (*CN*) were kept constant and only the radial distances (*R*) and the Debye-Waller factors ($\sigma^2$) were allowed to vary. The fits are performed with M = Ru at the second shell.

($n$ < 4) anionic redox process as expected for charge compensation.[68] Note therefore the gradual growth of a pre-edge peak during the 4.2 V plateau. Such a pre-edge is due to the dipole-mediated 1*s* → 4*d* transition that reflects the non-centrosymmetric environment of $RuO_6$ in the fully charged state. In fact, as already reported for 4*d* transition-metal oxides and complexes[204–206], the hybridization between the Ru 5*p* and 4*d* states becomes enhanced in a distorted octahedral coordination, leading to an increase of the pre-edge peak. In our case, the distortion of $RuO_6$ is triggered as a consequence of anionic oxidation, and similar behaviour of the pre-edge was also reported for highly delithiated $Li_2RuO_3$.[112]

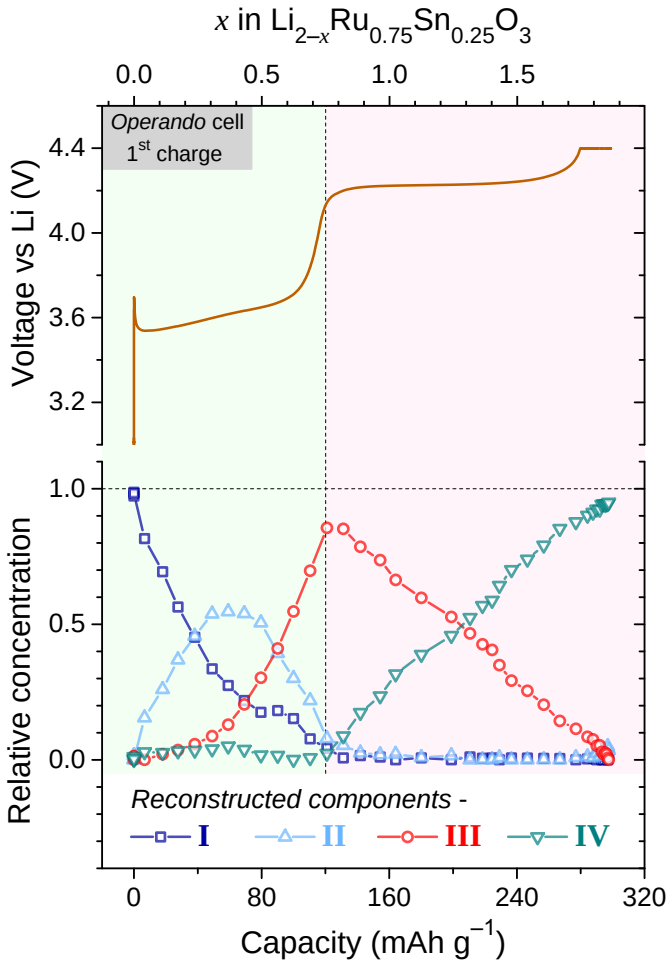


**Figure III.2 | *Operando* XAS characterization of LRSO's 1st charge process.** The voltage profile (top) measured in the *operando* cell shows two steps, respectively around 3.6 V (cationic redox, green background) and 4.2 V (anionic redox, red background). Current density is 32 mA $g^{-1}$ (C/5 for 1.0 $Li^+$ exchanged per formula unit). A potentiostatic hold at 4.4 V is applied till current decays to 1.6 mA $g^{-1}$ (C/100) for achieving a full charge. The bottom of the figure tracks relative concentrations of the four components reconstructed using the MCR-ALS method, explaining nearly 100 % of the variance in the experimental data with the lack of fit being 0.039 %. Summation of concentrations is unity.

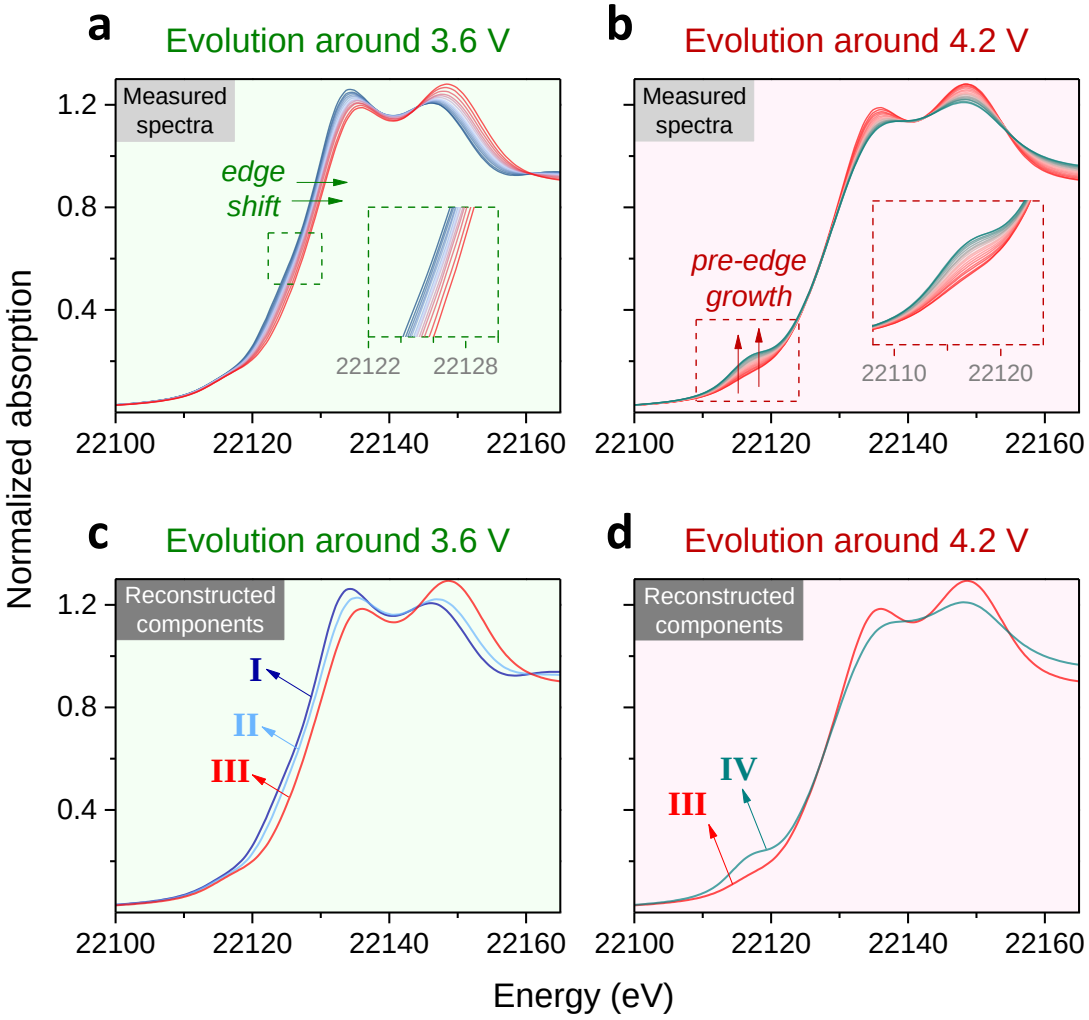


**Figure III.3 | Evolution of *operando* XAS spectra during LRSO's 1st charge process.** The evolution of Ru K-edge XANES spectra during the redox steps around (**a**) 3.6 V (cationic redox, green background) and (**b**) 4.2 V (anionic redox, red background). Insets show enlarged views of interesting regions identified by dashed boxes. Reconstructed XANES spectra for the (**c**) first three and the (**d**) last two components.

Principal component analysis (PCA)[195,199–202] results, as shown in **Figure A2.4**, revealed that four orthogonal principal components are needed to capture all variations in the dataset of XAS spectra measured on 1st charge. Therefore, four components were reconstructed with the multivariate curve resolution - alternating least squares (MCR-ALS)[196–202] method such that their linear combinations attempt to simultaneously fit each complete spectrum (covering both XANES and EXAFS regions). The resulting Li-driven evolution of relative concentrations of the four components (**Figure III.2**, bottom) shows two separate regimes during the two voltage steps. Cationic redox (3.6 V step) involves the first three components (**I** to **II** to **III**), whereas the anionic plateau around 4.2 V involves

the last two (**III** to **IV**). The XANES region of the reconstructed components shows an edge-shift from **I** to **II** to **III** (**Figure III.3c**) and a pre-edge growth from **III** to **IV** (**Figure III.3d**), agreeing with the cationic–anionic charge compensation discussed above.

Since XAS is a local technique, these reconstructed components reflect the changes in short-range structure and not the long-range symmetry. EXAFS analysis of the reconstructed components was consequently carried out to track the Li-driven modifications at the local scale. For the four components, **Figure III.4a–d** respectively show the magnitudes of Fourier Transforms of the EXAFS oscillations, $|\chi(R)|$, with their fits (fitting results in **Table III.2**).

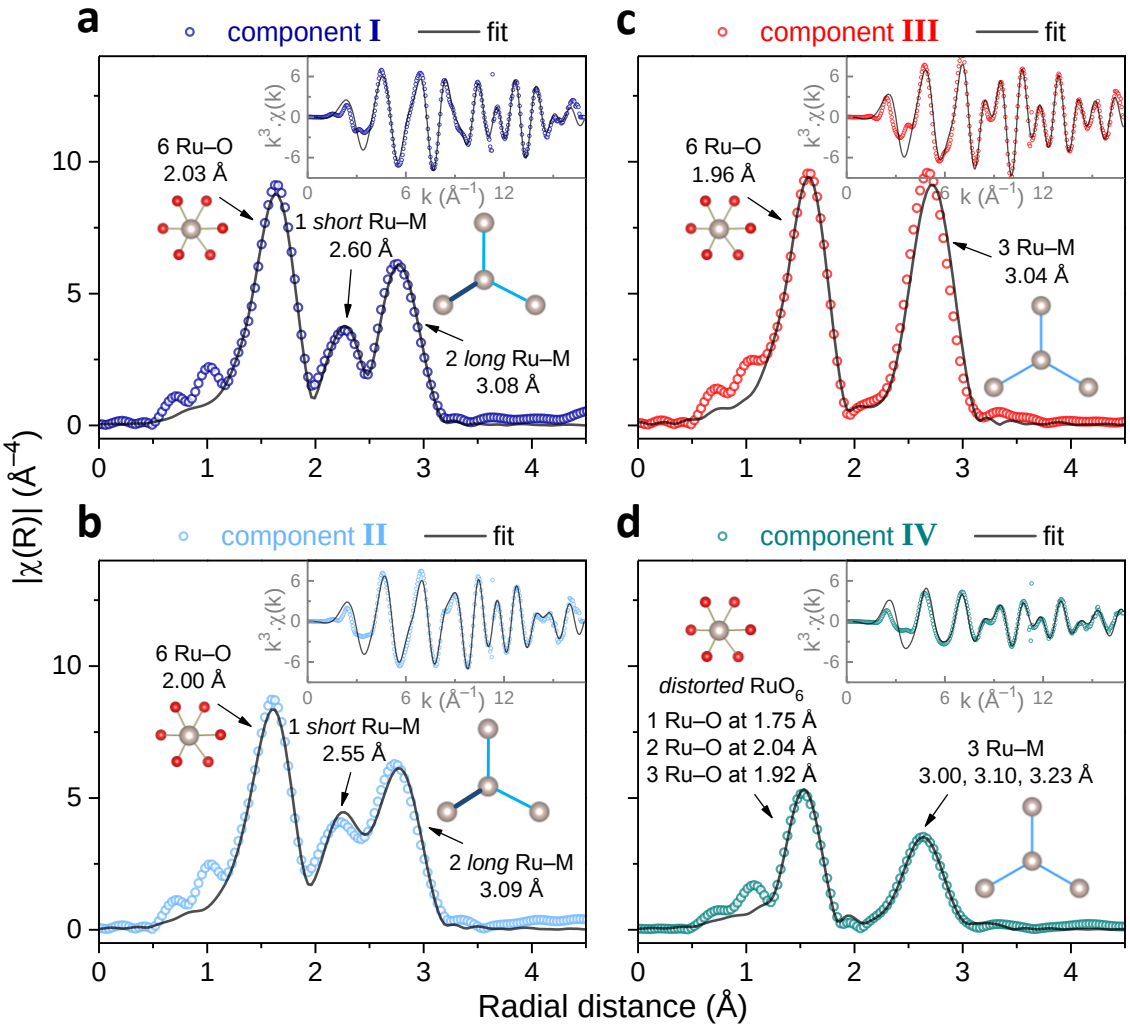


**Figure III.4 | EXAFS analysis of reconstructed components for LRSO's 1st cycle.** Magnitude of Fourier Transforms of $k^3$-weighted EXAFS oscillations for the four components (**a** to **d**) along with fitting results. The $|\chi(R)|$ plots are not corrected for phase shifts. Insets show the quality of fits in $k$-space.

**Table III.2 | Detailed results of fitting of EXAFS oscillations for the four reconstructed components obtained on 1st charge.**[†]

| Reconstructed Component (during 1st charge) | $RuO_6$ (first shell) | | | $RuM_3$ (second shell) M = Ru/Sn | | |
|---|---|---|---|---|---|---|
| | *CN* | *R* (Å) | $\sigma^2$ (Å$^2$) | *CN* | *R* (Å) | $\sigma^2$ (Å$^2$) |
| **I** | 6 | 2.026 (2) | 0.0042 (2) | 1 | 2.604 (3) | 0.0043 (2) |
| | | | | 2 | 3.085 (2) | 0.0040 (2) |
| | | | | | | *R-factor* = 0.0054 |
| **II** | 6 | 1.996 (2) | 0.0047 (2) | 1 | 2.549 (3) | 0.0041 (3) |
| | | | | 2 | 3.092 (2) | 0.0039 (2) |
| | | | | | | *R-factor* = 0.0079 |
| **III** | 6 | 1.962 (2) | 0.0041 (2) | 3 | 3.037 (2) | 0.0041 (2) |
| | | | | | | *R-factor* = 0.0115 |
| **IV** | 1 | 1.751 (35) | 0.0063 (29) | 1 | 2.997 (15) | 0.0019 (17) |
| | 2 | 2.037 (18) | 0.0041 (23) | 1 | 3.226 (49) | 0.0065 (59) |
| | 3 | 1.919 (10) | 0.0024 (10) | 1 | 3.102 (28) | 0.0025 (36) |
| | | | | | | *R-factor* = 0.0146 |

Component **I** (**Figure III.4a**) is identical to the pristine LRSO electrode measured *ex situ* (recall **Figure III.1c**), displaying three peaks in $|\chi(R)|$ as discussed before. Initial Li removal leads to the consumption of component **I** to produce **II** (recall **Figure III.2**, bottom). The $|\chi(R)|$ of component **II** is quite similar to that of **I**, such that the three peaks are still present (**Figure III.4b**), which correspond respectively to six Ru–O (2.00 Å) distances, one short Ru–M (2.55 Å) distance and two long Ru–M (3.09 Å) distances. The very initial Li removal therefore does not alter the overall local arrangement, whereas the Ru–O shrinking supports partial $Ru^{4+/5+}$ oxidation. Further oxidation leads to the production of component **III** as **I** and **II** get consumed (again, recall **Figure III.2**, bottom).

[†] $E_0$ was determined from the energy value where jump is 0.6. The difference in threshold energy ($\Delta E_0$) and the amplitude reduction factor ($S_0^2$) were fixed at 0 and 1, respectively. The coordination numbers (*CN*) were kept constant and only the radial distances (*R*) and the Debye-Waller factors ($\sigma^2$) were allowed to vary. The fits are performed with M = Ru at the second shell.

The local geometry of **III** is different from **I** and **II** since only two peaks feature in its $|\chi(R)|$ (**Figure III.4c**), the first one representing six Ru–O (1.96 Å) distances and the second peak coming from three Ru–M (3.04 Å) distances. Again the shrinking of Ru–O comes as an effect of $Ru^{4+/5+}$ oxidation, whereas the merging of initially unequal Ru–M distances into a single stronger peak indicates a Li-driven rearrangement of the second shell ($RuM_3$), such that the irregular hexagons described in **Figure III.1b** become regular. This justifies the symmetry change in $Li_{2-x}RuO_3$ from monoclinic ($x$ = 0) to rhombohedral ($x$ = 1.1) when Li is removed.[209] Moreover from the EXAFS fitting results, the shortest O–O distance in component **III** can also be estimated to be 2.48 Å since it is located at the shared edge between two $RuO_6$ octahedra, as schematized in **Figure III.5**. Similar cooperative O–O distance shortening was also reported for $Na_{2-x}RuO_3$ (from $x$ = 0 to 1)[122] and it is simply a consequence of Ru–O shrinkage due to $Ru^{4+/5+}$ (cationic) oxidation.

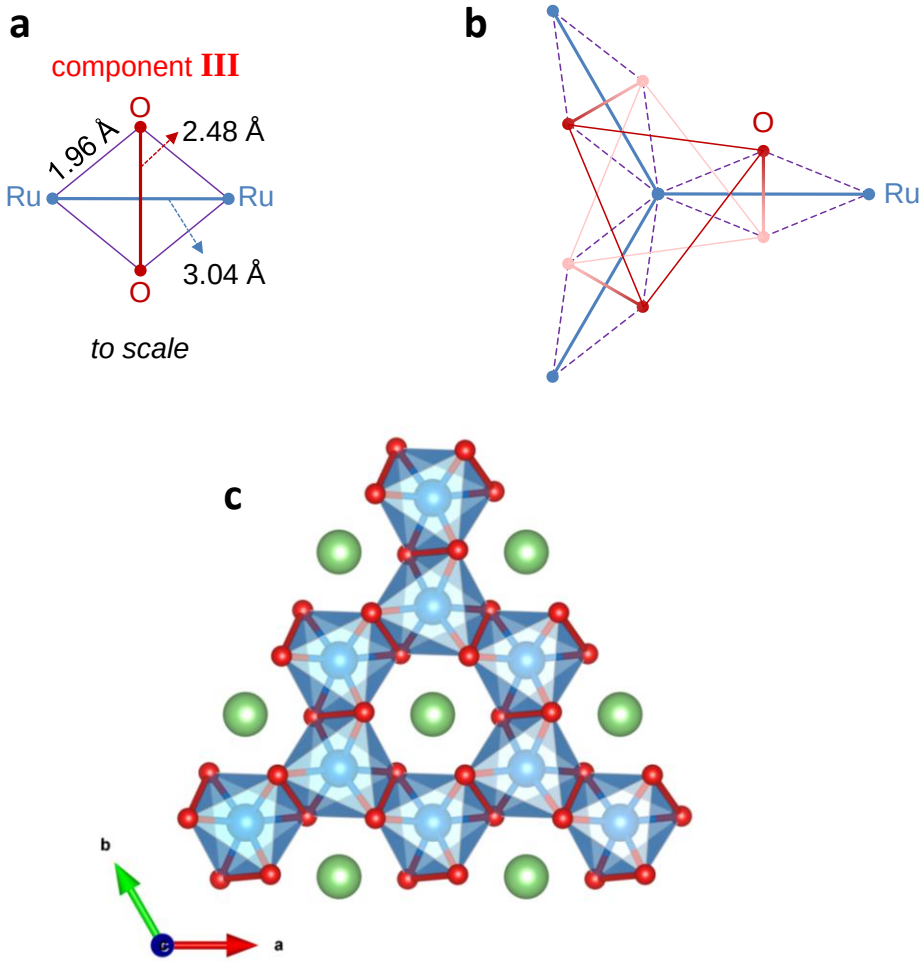


**Figure III.5 | Local structure of 1st cycle's component III as deduced from EXAFS.** Component **III** is after cationic but before anionic oxidation. (**a**) Determination of O–O distance at the shared edge between two $RuO_6$ octahedra. (**b**) Schematically extending this local unit in all three directions. (**c**) Resulting structure of the honeycomb TM / Li layer.

In summary, the 3.6 V cationic redox process on LRSO's 1st charge is composed of two steps, i.e. (*a*) from **I** to **II** where the overall local arrangement having a short Ru–M distance remains intact and then (*b*) from **II** to **III** that involves equalization of the three Ru–M distances (second shell of neighbours). Note that this mechanism is fully reproducible, as demonstrated with complementary *ex situ* XAS measurements (**Figure A2.5**). Such a two-step mechanism bears a full meaning when looking at the experimental differential capacity (*dQ*/*dV*) profile, which also shows a double peak even at very low currents (**Figure III.6**). A comparison of the two-step mechanism (revealed from EXAFS analysis) with the double peak in *dQ*/*dV* therefore implies that the first peak corresponds to the reaction from **I** to **II** while the second one is due to the reaction from **II** to **III**.

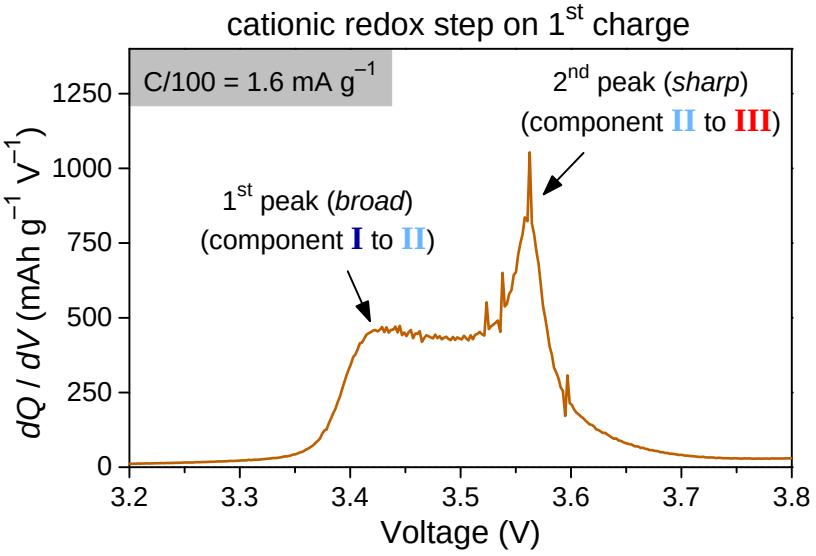


**Figure III.6 | *dQ*/*dV* profile of LRSO's 1st charge recorded at a very low current of C/100 (T = 25 °C).** The two peaks can be assigned to the two-step reaction mechanism revealed from PCA and MCR-ALS analyses. The C/100 profile shown here displays the same features as the profile measured with a PITT protocol in the previous Chapter (**Figure II.2c,d**) and represents the near-equilibrium potential profile.

Furthermore, for components **I**, **II**, and **III**, the amplitude of EXAFS oscillations (insets in **Figure III.4a–c**) and consequently the intensity of $|\chi(R)|$ peaks as wells as the Debye-Waller factors (**Table III.2**) remain nearly unchanged, thus implying the preservation of structural order upon Li removal. This sheds light on the previous Chapter's electrochemical evidence that indicated a full reversibility of the 3.6 V cationic redox step (**Figure II.1**), thereby demonstrating a classical Li-intercalation mechanism within a 'breathing' host structure.

Concerning the anionic oxidation plateau at 4.2 V, it leads to the consumption of component **III** to produce **IV**, such that both vary linearly vs. capacity which indicates the robustness of the results (recall **Figure III.2**, bottom). The $|\chi(R)|$ of **IV** (**Figure III.4d**) shows two peaks located at similar positions as in **III**, however with a much lower intensity (thereby damped oscillations in *k*-space also, inset of **Figure III.4d**). This indicates that the fully charged phase becomes disordered, which is also reproducibly observed with *ex situ* measurements (**Figure A2.6**). This finding is in agreement with previous XRD data showing a broadening of peaks with no shifting, and supports the interpretation that a disordered phase nucleates with anionic oxidation[68], hence producing the electrochemical signature of a conversion-like mechanism that was observed in the previous Chapter (recall **Figure II.3**). Another possible explanation for such disordering, proposed only recently for Li-rich NMC via Bragg coherent diffractive imaging[211], could be the nucleation of dislocation defects upon anionic oxidation.

EXAFS fitting of component **IV** (**Figure III.4d**) is best achieved using a distorted $RuO_6$ coordination to fit the first peak, the most appropriate model having three types of Ru–O distances (1+2+3, see **Table A2.1** comparing different models considered). The second peak is fitted using three slightly dissimilar Ru–M distances. Moreover, the same model remains equally valid for the *ex situ* measured 1$^{st}$ charged sample (**Figure A2.6d**), thus strengthening its validity. The experimental observation of distorted $RuO_6$ octahedral coordination via EXAFS modelling is a unique finding as it was so far only a theoretical prediction[112]. Moreover, it justifies the growth of the XANES pre-edge peak (**Figure III.3b**). On the other hand, the Ru–M geometry cannot be further interpreted since the structural model is not simple, partly because of the non-quantifiable TM migration as was previously observed with TEM.[69]

Nevertheless, one of the six Ru–O distances in component **IV** is significantly shorter (1.75 Å) than the rest, which indicates an off-centring type of octahedral $RuO_6$ distortion. This contrasts with cationic redox that accompanies uniform octahedral shrinkage / expansion, as evidenced for the 3.6 V process and illustrated above in **Figure III.5**. With such a distortion in component **IV**, we can envisage that the "peroxo-like" oxidized-oxygen $(O–O)^{n–}$ could be stabilized between two such short Ru–O distances, as illustrated in **Figure III.7a**, consequently forming a $Ru^{5+}$—$(O_2)^{n–}$—$Ru^{5+}$ entity. Experimentally evidencing this mechanism reinforces previous theoretical calculations that

predicted similar effects.[109,110,112] Although exact estimation of the O–O distance is not trivial since several combinations are possible, but we can expect that O–O < 2.33 Å, which is significantly shorter than the 2.48 Å distance seen in component **III** before anionic oxidation (**Figure III.5a**), and signifies the "peroxo-like" nature of oxidized oxygen. Extending this local distorted structure to the longer range is not evident. One possibility, consistent with the observation of unequal Ru–M distances in EXAFS fits, is illustrated in **Figure III.7b**. Hoverer, precise structural identification of the charged phase remains a challenge for theorists (DFT) as well as experimentalists, and both directions are being pursued in our lab.

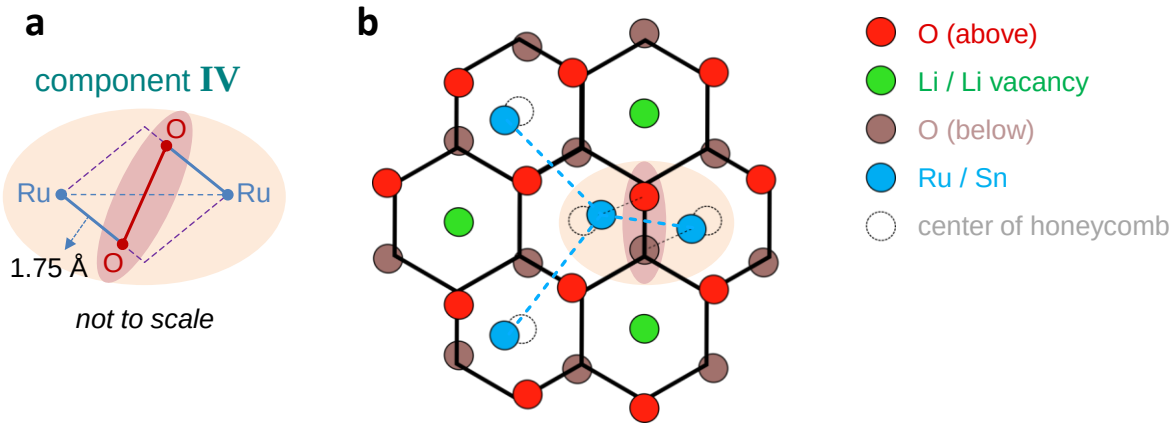


**Figure III.7 | Local structure of 1st cycle's component IV as deduced from EXAFS.** Note that the illustration in (**a**) is not drawn to scale. (**b**) An off-centring-driven possible structure of the honeycomb layer. Although regular hexagons are drawn, the O atoms lie away from the vertices due to $RuO_6$ distortion. Panel (**b**) : courtesy of *Jean Vergnet.*

## ○ Staircase-like 1st charge – *Ex situ* HAXPES and soft-XAS

Although a signature of oxygen oxidation can be seen on the Ru K-edge XANES via the pre-edge peak's growth, we also measured the O 1*s* photoemission spectra with bulk-sensitive hard-X-ray photoemission spectroscopy†† (HAXPES) for directly probing the anionic redox process (**Figure III.8**). The probe depth with HAXPES is significantly higher compared to classical in-house XPS due to the higher excitation photon energy (set

†† **HAXPES** was performed in collaboration with Rémi Dedryvère (IPREM, Pau). Rémi, Antonella Iadecola (RS2E, CNRS), and myself performed the HAXPES experiments. Rémi carried out the fitting of the obtained spectra.

to 6.9 keV in present work). For the O 1*s* core peak measured herein, the probe depth (defined as three times the photoelectron inelastic mean free path (IMFP) that was estimated according to the TPP-2M model[212]) is 26 nm at 6.9 keV, compared to 5.6 nm at 1.487 keV for in-house XPS. The pristine sample shows a peak at 529.5 eV that is associated with lattice oxygen $O^{2-}$, whereas the peaks at higher binding energy are due to oxygen-containing surface species.

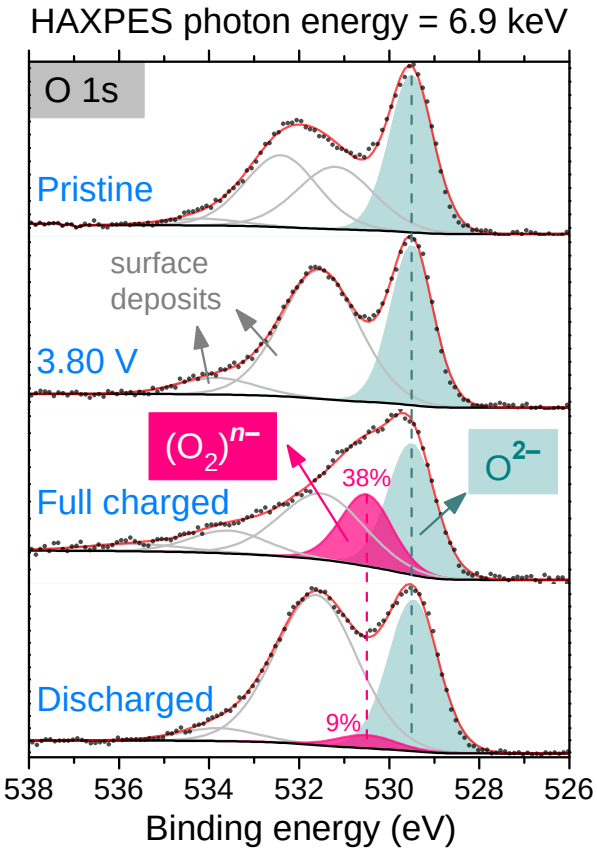


**Figure III.8 | The evolution of HAXPES O 1*s* spectra of LRSO during the first cycle.**

When LRSO is charged to 3.80 V (i.e. traversing the Ru oxidation step), no signature of anionic oxidation is observed. In contrast, fully charging to 4.4 V leads to a new oxygen environment at 530.5 eV (pink), which is ascribed to oxidized lattice oxygen $(O_2)^{n-}$. This assignment is justified because the oxygenated surface species in the solid-electrolyte interface (SEI) layer, coming from the decomposition of electrolyte solvents and salt, are known to lie at higher binding energies.[213–215] For instance, decomposition of carbonate solvents may lead to a plenty of organic oxygenated species, but the binding energies of all such groups are observed between 531.5 and 534 eV. Similarly, inorganic

species resulting from the decomposition of $LiPF_6$, e.g. phosphates, fluorophosphates $Li_xPO_yF_z$, or LiOH, are also observed at a higher binding energy than that of $(O_2)^{n-}$. Therefore the binding energy range of the oxygenated compounds found in the SEI does not overlap with $O^{2-}$ and $(O_2)^{n-}$ peaks of the material. Moreover, a comparison of different photon energies (6.9 vs. 1.487 keV, see **Figure A2.7**) shows that when probe depth is increased, the relative intensity of O 1*s* signals from the surface species decreases by a factor more than two (about 2.3) with respect to the $O^{2-}$ component. On the contrary, the $(O_2)^{n-}/O^{2-}$ intensity ratio is not modified. The higher probe depth with HAXPES thus demonstrates the presence of $(O_2)^{n-}$ in the bulk. Since the polluting signal from surface deposits is lowered at higher photon energy, the quantification of % $(O_2)^{n-}$ is much easier with HAXPES than with in-house XPS, however the obtained % $(O_2)^{n-}$ (38 %) is similar for the two energies.[105] HAXPES will be extensively used in Chapter IV for Li-rich NMC. We also measured the O K-edge XAS spectra[§§] for $Li_{2-x}RuO_3$ (i.e. without Sn) in bulk-sensitive fluorescence mode (**Figure A2.8**), however only qualitative interpretation was possible since supporting theoretical calculations are needed owing to the Ru–O hybridization and the particular role of oxygen non-bonding states in these materials.[109,110]

## ○ Sloped S-shaped 1st discharge after anionic activation

On discharge, the $(O_2)^{n-}$ HAXPES peak diminishes (**Figure III.8**), demonstrating the reversibility of anionic redox. The discharge voltage profile shows a sloped S-shape (**Figure III.9a**) during which the capacity arises from combined cationic and anionic reductions, which are respectively located at low and high potentials, as indicated by *operando* Ru K-edge XANES spectra. The spectra on the high potential regime (**Figure III.9b**) show a reduction of the pre-edge peak as well as a shift of edge-position to lower energy (marked by arrows). In contrast, the low potential discharge only accompanies an edge shift whereas no changes are seen in the pre-edge region (**Figure III.9c**). Therefore, it can be concluded that anionic reduction takes place at a higher potential compared to cationic reduction, which is further confirmed by *ex situ* XAS measurements (**Figure A2.9**).

[§§] **O K-edge soft-XAS** measurements were performed by Rémi Dedryvère (IPREM, Pau) and Antonella Iadecola (RS2E, CNRS). Antonella normalized the spectra.

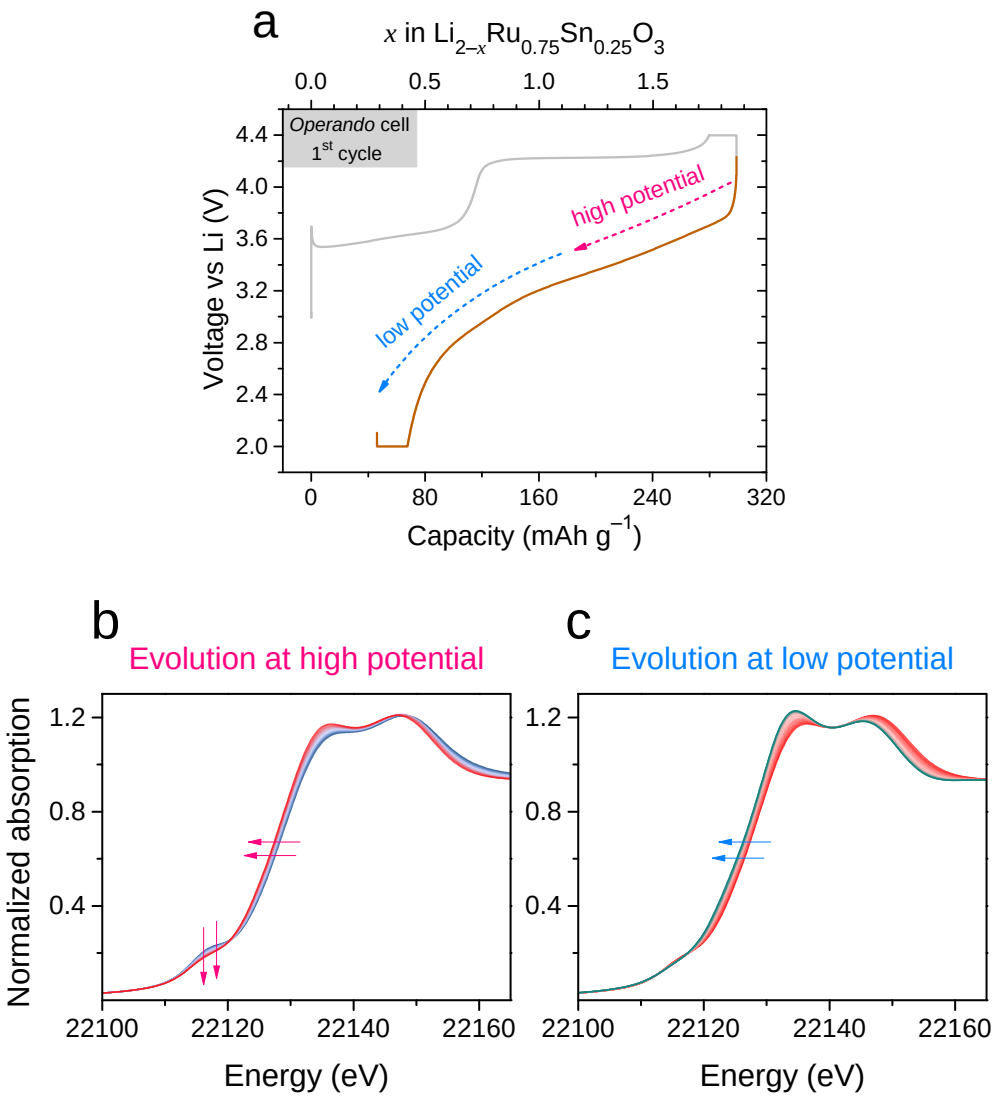


**Figure III.9 | *Operando* XAS results on 1st discharge.** (**a**) The 1st cycle voltage profile measured in the *operando* cell. The spectra over the sloped S-shaped discharge curve are divided into two regimes, located at (**b**) high and (**c**) low potentials, respectively.

Ru K-edge XANES of the fully discharged sample shows a slight back-shift of the edge position towards lower energy with respect to the pristine spectrum, as marked by arrows near the jump of 0.6 in **Figure III.10a**. This means that Ru is reduced slightly below the pristine material's $Ru^{4+}$ oxidation state due to reduction at a low potential of 2.0 V. Additionally, a small pre-edge feature can still be seen in the sample after one cycle (marked by arrows), which may indicate a small amount of unreduced $(O_2)^{n-}$, as also seen above with HAXPES (**Figure III.8**, bottom) and as well as previous in-house XPS[105]. This remaining $(O_2)^{n-}$ in the discharged state may partially contribute to the first cycle irreversibility. Over long cycling, the edge is expected to continue shifting further to lower

energies because of the voltage fade effect that would result in the gradual reduction of Ru.[69] Such unreduced oxidized oxygen and gradual TM reduction with cycling will also be seen later in Chapter IV for Li-rich NMC.

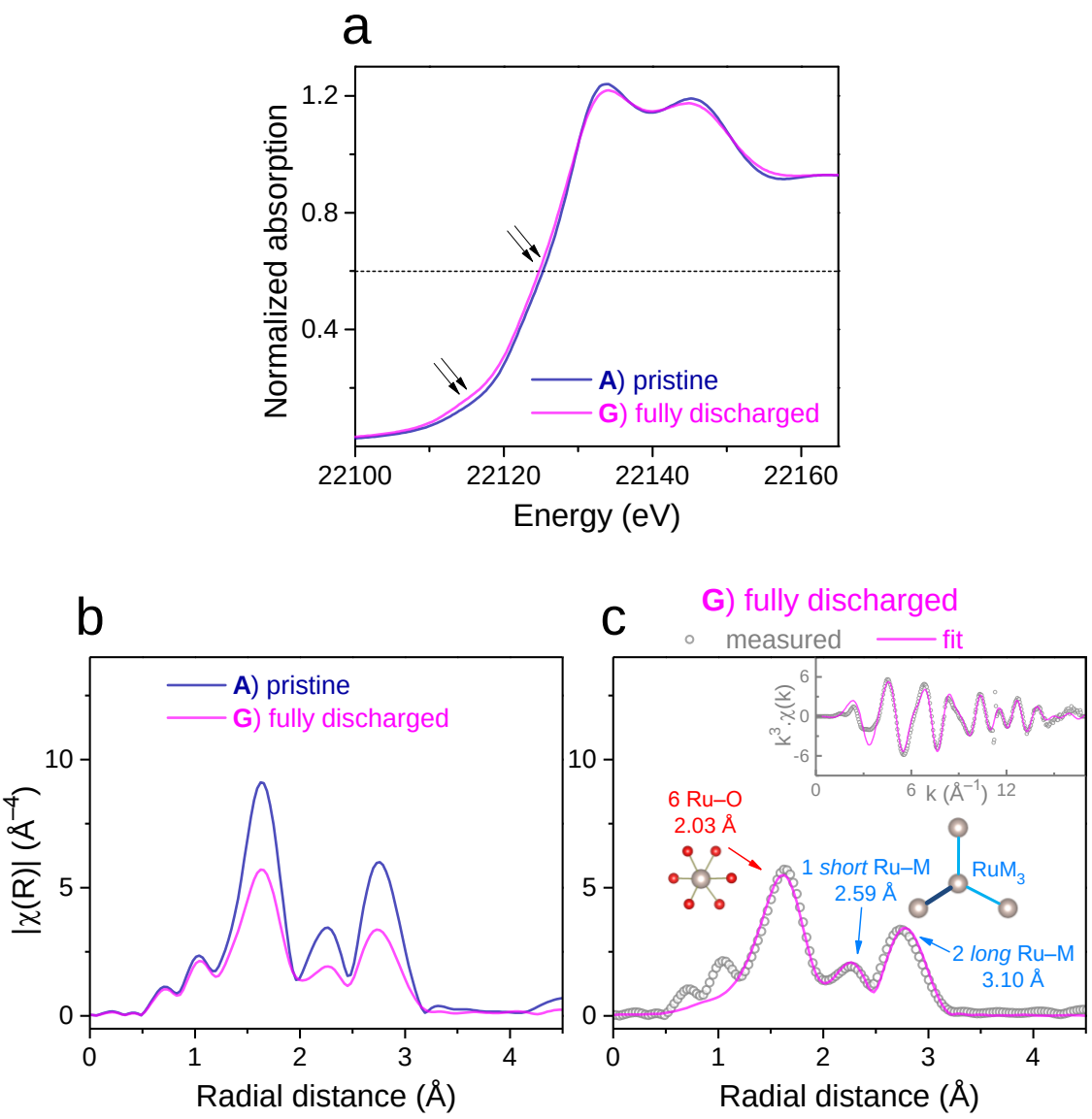


**Figure III.10 | XAS characterization after 1st discharge compared with pristine LRSO.** (**a**) Ru K-edge XANES spectra comparing pristine LRSO with the sample after one complete cycle. (**b**) $|\chi(R)|$ of the discharged sample compared with the pristine one. (**c**) EXAFS fit for the discharged sample. The $|\chi(R)|$ plots are not corrected for phase shifts.

EXAFS analysis shows that the local structure after 1st discharge becomes similar to the pristine material, i.e. the three peaks reappear at original local distances. Despite this

recovery, the disordering that was triggered by anionic oxidation is not reversed, as evidenced by the lower intensity of $|\chi(R)|$ peaks in **Figure III.10b** as well as the higher Debye-Waller factors in **Table III.3** compared to the pristine materials. This irreversible disordering explains the permanent change of voltage profile from a staircase-like to a sloped S-shape that is characteristic of anionic-redox materials, notably Li-rich NMC. We next explore the cationic–anionic charge compensation mechanism once this sloped electrochemistry is stabilized during the 5$^{th}$ cycle.

**Table III.3 | Detailed results of fitting of EXAFS oscillations for fully discharged LRSO after one cycle.**[††]

| Sample | $RuO_6$ (first shell) | | | $RuM_3$ (second shell) M = Ru/Sn | | |
|---|---|---|---|---|---|---|
| | *CN* | *R* (Å) | $\sigma^2$ (Å$^2$) | *CN* | *R* (Å) | $\sigma^2$ (Å$^2$) |
| **G) fully discharged LRSO** (after one cycle) | 6 | 2.031 (3) | 0.0071 (3) | 1 | 2.593 (5) | 0.0068 (4) |
| | | | | 2 | 3.095 (3) | 0.0063 (3) |
| | | | | | *R-factor* = 0.0119 | |

## ○ Sloped S-shaped 5$^{th}$ cycle – Decoupling the redox processes

LRSO was first activated in a regular coin cell by performing four formation cycles. The cell was then disassembled to harvest the activated electrode, which was immediately transferred into the *operando* XAS cell for studying the 5$^{th}$ cycle. The electrochemical profile obtained in the *operando* cell (**Figure III.11**, top) is characterized by a sloped S-shape having a notable hysteresis between charge vs. discharge potentials, quite similar to that observed in coin cells in previous Chapter II. The as-recorded Ru K-edge XAS spectra (measured without current interruption; time interval between two spectra was ~27 minutes) during one complete cycle are shown in **Figure III.11**.

[††] $E_0$ was determined from the energy value where jump is 0.6. The difference in threshold energy ($\Delta E_0$) and the amplitude reduction factor ($S_0^2$) were fixed at 0 and 1, respectively. The coordination numbers (*CN*) were kept constant and only the radial distances (*R*) and the Debye-Waller factors ($\sigma^2$) were allowed to vary. The fits are performed with M = Ru at the second shell.

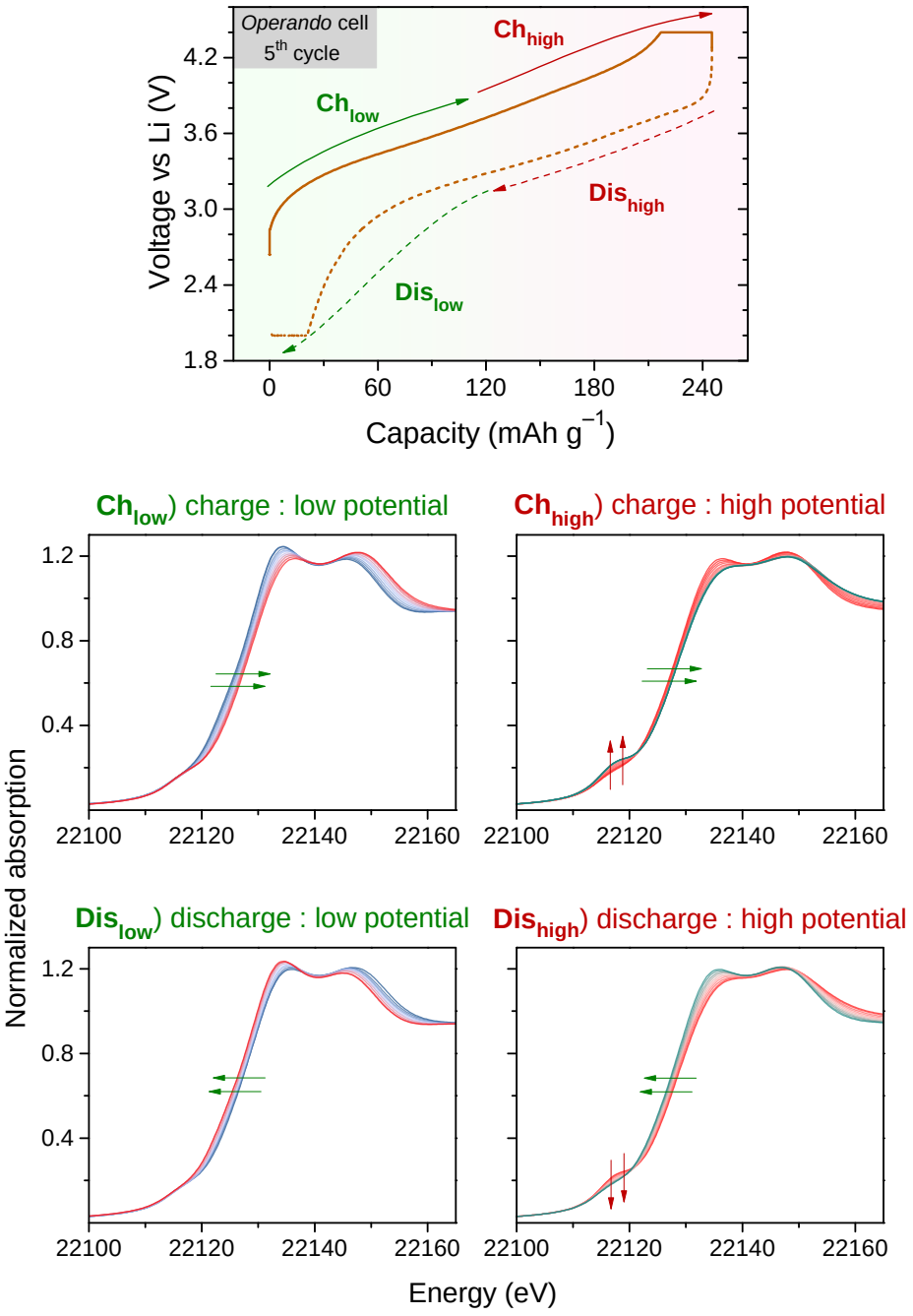


**Figure III.11 | *Operando* XAS Ru K-edge spectra recorded during the 5th cycle**. The voltage profile (top) measured in the *operando* cell with a CCCV protocol (constant current constant voltage) using a current density of 32 mA $g^{-1}$ (C/5 for 1.0 $Li^+$ exchanged per formula unit). Potentiostatic holds at 4.4 V and 2.0 V are applied till current decays to 1.6 mA $g^{-1}$ (C/100) for achieving a full charge and discharge. The electrode used was previously activated in a coin cell and recovered in the discharged state after four CCCV cycles. The spectra are divided into four segments, as marked on the voltage profile.

The beginning of charge (segment **$Ch_{low}$**) at lower potential mainly involves a shift of the rising edge towards higher energy, meaning primarily the cationic oxidation of Ru.

Further charging at higher potential (segment **Ch$_{high}$**) leads to some edge shifting and also the growth of pre-edge peak which also indicates anionic oxidation. A reverse behaviour is seen on discharge (segments **Dis$_{high}$** and **Dis$_{low}$**). Overall, it can be concluded that the cationic (edge shift) and anionic redox (changes in the pre-edge peak) processes are located at low and high potentials respectively, but they have a considerable overlap. Their decoupling thus calls for a PCA followed by MCR-ALS analysis, as performed next.

PCA revealed the presence of three principal components (detailed PCA results in **Figure A2.10**). Three components were thus reconstructed using the MCR-ALS method attempting to simultaneously fit all spectra measured during the 5$^{th}$ charge-discharge cycle. The resulting evolutions of relative concentrations of the three reconstructed components as a function of capacity are shown in **Figure III.12a**. The charging process starts with the consumption of component **I**$_{5th}$ (*discharged*) to produce **II**$_{5th}$ (*intermediate*). Further oxidation leads to the appearance of **III**$_{5th}$ (*charged*) at the expense of **I**$_{5th}$ and **II**$_{5th}$. A reverse behavior is seen on the discharge path. Overall, the 5$^{th}$ cycle can hence be characterized by a sequential reaction mechanism (**I**$_{5th}$ to **II**$_{5th}$ to **III**$_{5th}$ on charge and vice-versa on discharge). Note however that the profiles of relative concentrations as a function of capacity do not superimpose when compared on the charge vs. discharge paths (**Figure III.12a**, bottom), hence demonstrating a path dependence. This explains the presence of a voltage hysteresis reported in previous Chapter II, because slightly different concentration ratios of the three reacting components would lead to slightly different electrochemical potentials.

The isolation of component **II**$_{5th}$ (the *intermediate* species) was not trivial here as it stays far from achieving a pure relative concentration during the entire cycle, thereby underscoring the importance of PCA and MCR-ALS analyses in extracting the reaction mechanism. Further analysis of the reconstructed spectra reveals the nature of the three components. The reaction step between components **I**$_{5th}$ and **II**$_{5th}$ involves primarily a shift of the rising edge in the XANES part (**Figure III.12b**), therefore meaning a change in Ru oxidation state (cationic redox). On the other hand, the main change between components **II**$_{5th}$ and **III**$_{5th}$ (**Figure III.12c**) is at the pre-edge peak that arises from the distortion of oxygen network (distorted $RuO_6$ coordination) as a consequence of anionic oxidation, a result similar to the 1$^{st}$ cycle.

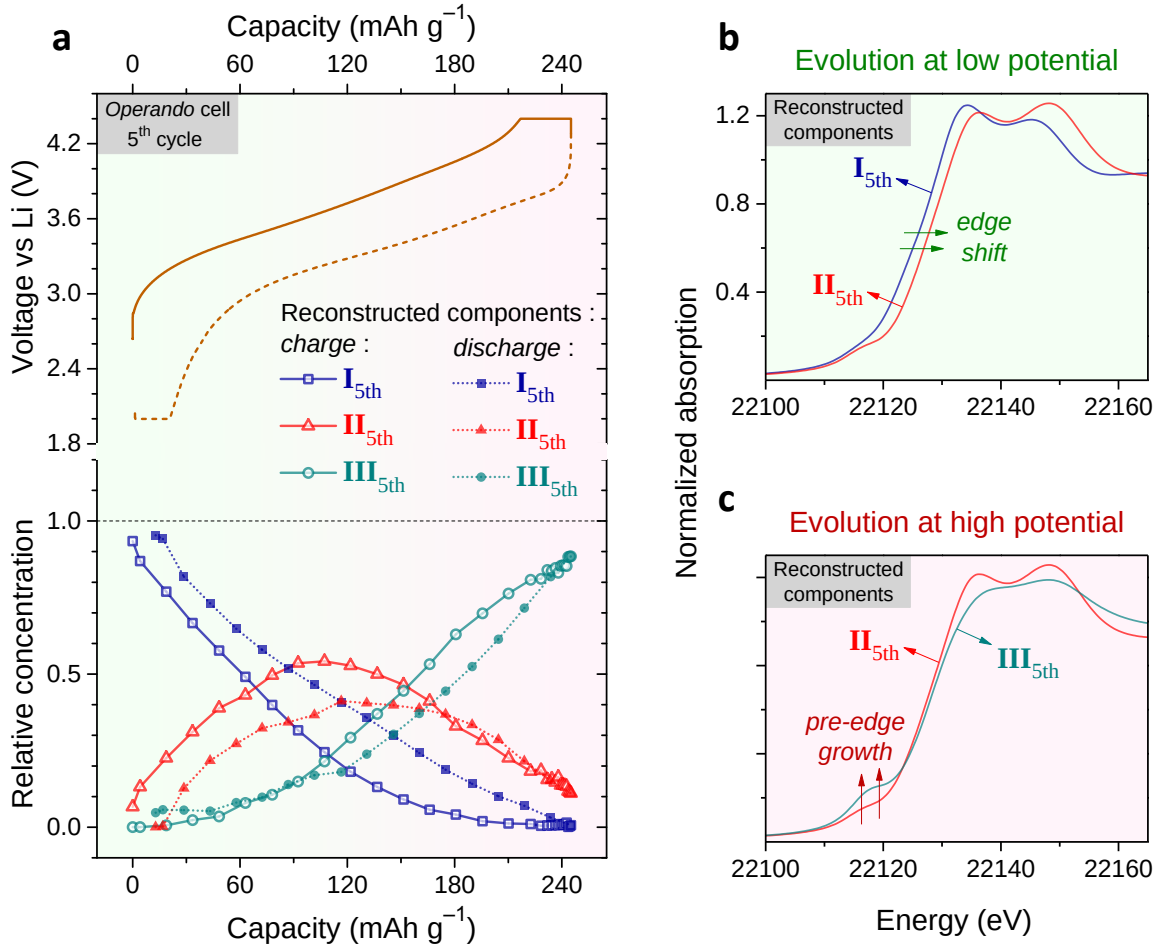


**Figure III.12 | *Operando* XAS characterization of LRSO's 5th cycle.** (**a**) The top part shows the voltage profile, whereas the bottom part shows the variation of relative concentrations of the three reconstructed components as a function of capacity over the charge and discharge paths. These components, reconstructed using MCR-ALS method, explain 99.9999 % of the variance in the experimental data with the lack of fit being 0.093 %. (**b**) XANES region of the reconstructed Ru K-edge spectra comparing components $\mathbf{I}_{5th}$ and $\mathbf{II}_{5th}$. (**c**) Comparison of components $\mathbf{II}_{5th}$ and $\mathbf{III}_{5th}$.

PCA followed by MCR-ALS analysis is thus successful in decoupling the overlapping cationic–anionic redox reactions, which can in turn be individually tracked on the *dQ*/*dV* curve using a methodology schematized in **Figure III.13** (top). In short, charge compensation from the cationic redox process ($dQ_{cationic}$) is proportional to the change in concentration of component $\mathbf{I}_{5th}$ ( $d[\mathbf{I}_{5th}]$ ) and charge compensation from the anionic redox process is proportional to the change in concentration of component $\mathbf{III}_{5th}$ ( $d[\mathbf{III}_{5th}]$ ). The hence decoupled *dQ*/*dV* profiles (**Figure III.13**, bottom) clearly show how the cationic and anionic processes are separated at low and high potentials respectively, however with a

considerable overlap. Moreover, summation of the two profiles can generate the overall *dQ*/*dV* profile (gray trace in **Figure III.13**, bottom), which matches well with the as-measured *dQ*/*dV* in the *operando* cell (blue trace) and also resembles the profile observed in regular coin cells (**Figure A2.11**). Such an agreement of the deconvoluted profiles with the one measured experimentally further shows the robustness of our approach.

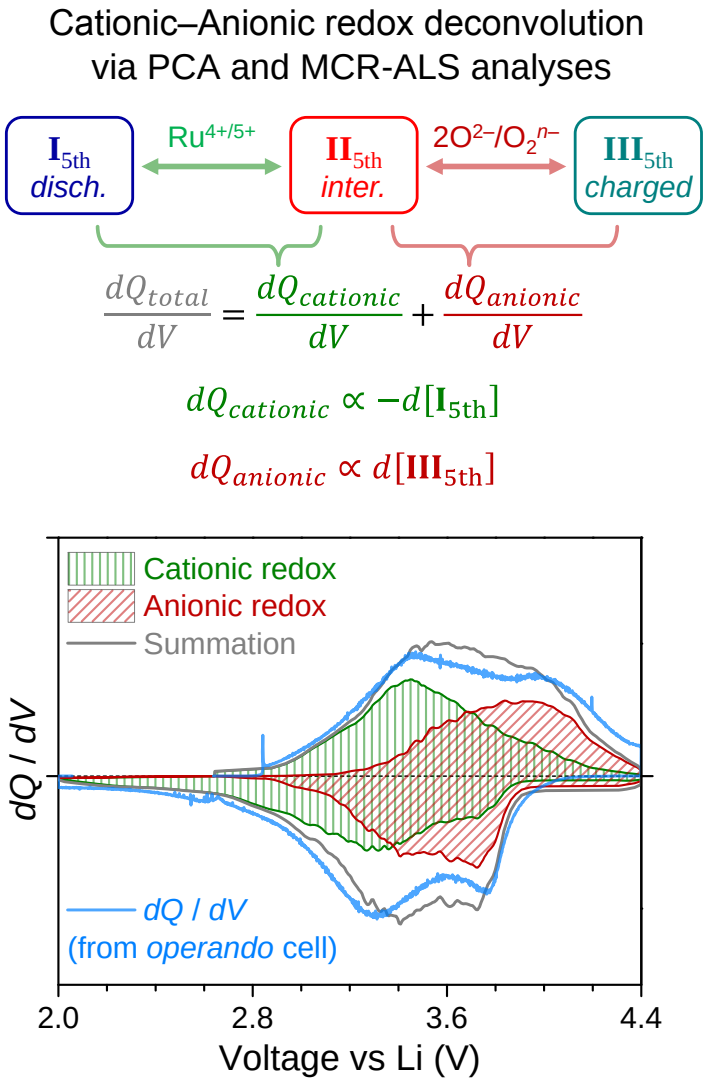


**Figure III.13 | Decoupling cationic–anionic *dQ*/*dV* profiles.** The top part shows the reaction scheme deduced from PCA followed by MCR-ALS analysis and the methodology to decouple the *dQ*/*dV* contributions of the cationic and anionic processes. The bottom part shows the decoupled *dQ*/*dV* profiles and their resulting summation (gray trace) which resembles the overall as-measured *dQ*/*dV* profile from the *operando* cell (blue trace).

Moreover, *ex situ* measurements over the 5$^{th}$ cycle fully support the above identified cationic–anionic redox potentials (**Figure A2.12**). Overall, our detailed XAS

analysis unambiguously proves that the high potential *dQ*/*dV* peak is due to anionic redox, strengthening what was previously proposed based on EPR[111] and electrochemical measurements in Chapter II. Furthermore, it can also be noted in **Figure III.13** (bottom) that the cationic redox *dQ*/*dV* peaks (centred around ~3.4 V) mirror between charge vs. discharge, unlike the anionic redox peaks (centred around ~3.8 V) that are highly asymmetric. It is this asymmetry in the anionic redox process that is responsible for voltage hysteresis. Even for *ex situ* samples (relaxed over several days) on the 5$^{th}$ cycle, a similar hysteresis mechanism is reproduced such that the cationic–anionic reaction extent (identified from XANES part) as well as the local structure (from EXAFS analysis) differs slightly for samples prepared at the same state of charge (SoC), i.e. with equal Li content, but via different paths - namely mid-charged vs. mid-discharged (**Figure A2.12**).

The local structure of the discharged state in the 5$^{th}$ cycle is revealed from EXAFS fitting of component $\mathbf{I}_{5th}$ (**Figure III.14a**). It is comparable to the 1$^{st}$ discharged sample (recall **Figure III.10c**), showing a similar arrangement as the pristine material but with increased disorder (thereby increased Debye-Waller factor also, see detailed fitting results in **Table III.4**). The three peaks in $|\chi(R)|$ correspond respectively to six Ru–O (2.04 Å) distances, one short Ru–M (2.60 Å) distance and two long Ru–M (3.09 Å) distances. Component $\mathbf{II}_{5th}$ (**Figure III.14b**) appears similar to $\mathbf{I}_{5th}$ in terms of peak intensities and peak positions. The first peak can be modelled with a $RuO_6$ octahedron having minor distortion (five Ru–O distances at 1.98 Å and one at 1.85 Å, see **Table A2.2** justifying the use of such a model). The shrinking of Ru–O when going from $\mathbf{I}_{5th}$ to $\mathbf{II}_{5th}$ comes from the cationic oxidation of Ru. One short Ru–M (2.57 Å) distance and two long Ru–M (2.75 and 3.12 Å) distances are still present in $\mathbf{II}_{5th}$. Component $\mathbf{III}_{5th}$ represents the charged state and it is more disordered than $\mathbf{I}_{5th}$ and $\mathbf{II}_{5th}$, as indicated by the reduced intensity of $|\chi(R)|$ peaks in **Figure III.14c** as well as damped oscillations in the *k*-space (see inset). Its first peak in $|\chi(R)|$ can be modelled with a distorted $RuO_6$ octahedron (again using a 1+2+3 model that is appropriate for the charged material, recall **Table A2.1** for justification) and its second peak with three slightly dissimilar Ru–M distances. This local structural model is comparable to the 1$^{st}$ charged sample (recall **Figure III.4d**), but with somewhat higher disorder.

When comparing the Fourier Transforms, note the larger structural change during the anionic redox step between components $\mathbf{II}_{5th}$ and $\mathbf{III}_{5th}$ (**Figure III.14 b vs. c**) that

involves a distortion of $RuO_6$ coordination plus a loss of order upon oxidation, compared to the less severe changes during the cationic redox step between components $\mathbf{I}_{5th}$ and $\mathbf{II}_{5th}$ (**Figure III.14 a vs. b**). A higher kinetic barrier can thus be envisaged for the anionic redox process, bringing a structural explanation to the previously reported sluggish electrochemical kinetics (**Chapter II**) at high potentials where anionic redox is located.[194]

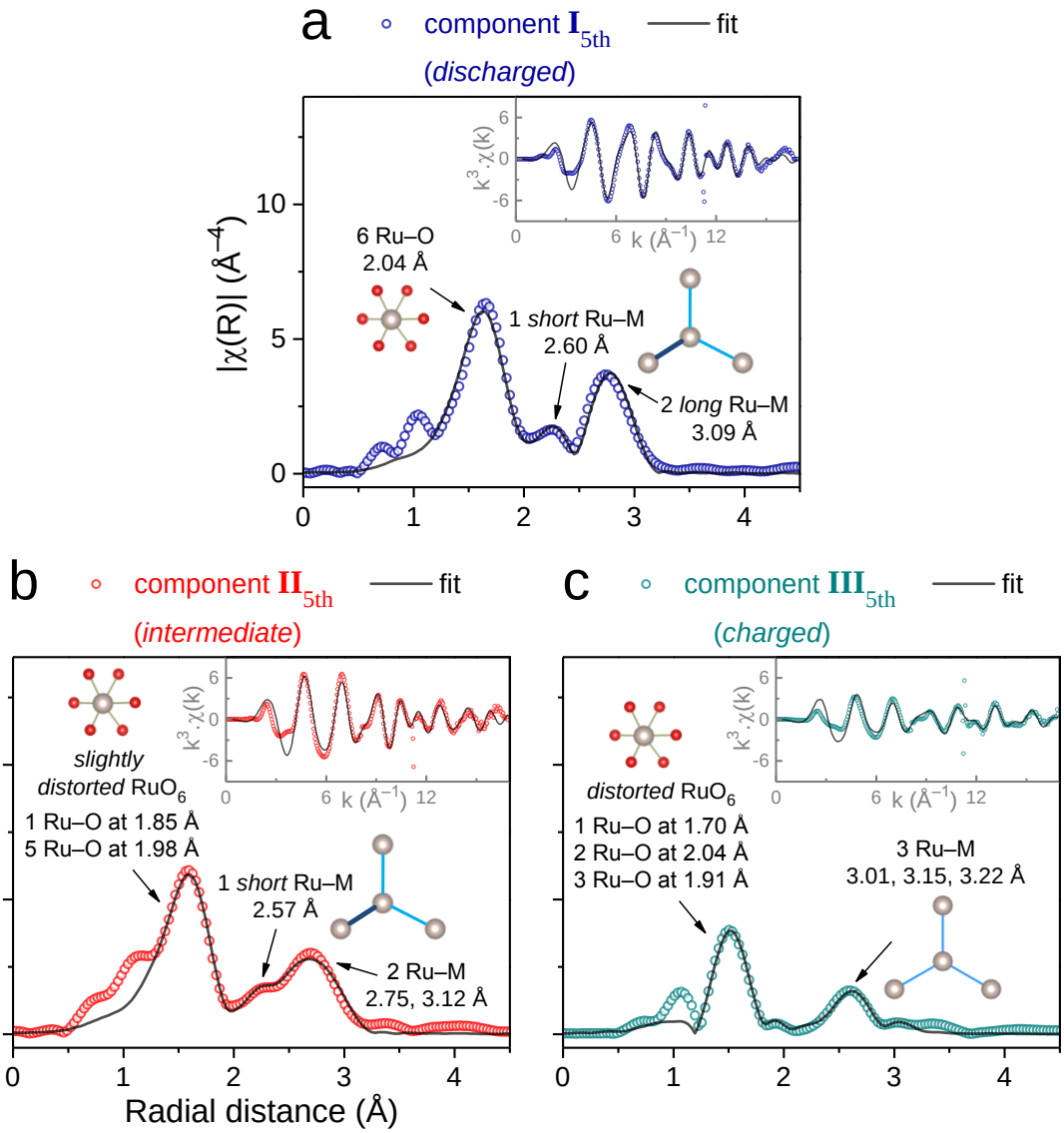


**Figure III.14 | EXAFS analysis of reconstructed components on the 5th cycle of LRSO.** Magnitude of Fourier Transforms of $k^3$-weighted EXAFS oscillations for the three components (**a** to **c**) along with fitting results. The $|\chi(R)|$ plots are not corrected for phase shifts. Insets show the quality of fits in the $k$-space.

**Table III.4 | Detailed results of fitting of EXAFS oscillations for the three reconstructed components obtained on 5th cycle.**[†]

| Reconstructed component (during 5th cycle) | $RuO_6$ (first shell) | | | $RuM_3$ (second shell) M = Ru/Sn | | |
|---|---|---|---|---|---|---|
| | *CN* | *R* (Å) | $\sigma^2$ (Å$^2$) | *CN* | *R* (Å) | $\sigma^2$ (Å$^2$) |
| **$I_{5th}$** (*discharged*) | 6 | 2.040 (3) | 0.0064 (3) | 1 | 2.598 (7) | 0.0073 (6) |
| | | | | 2 | 3.094 (4) | 0.0059 (3) |
| | | | | | | *R-factor* = 0.0159 |
| **$II_{5th}$** (*intermediate*) | 1 | 1.851 (21) | 0.0050 (28) | 1 | 2.570 (10) | 0.0059 (8) |
| | 5 | 1.983 (5) | 0.0050 (7) | 1 | 2.753 (12) | 0.0055 (10) |
| | | | | 1 | 3.118 (7) | 0.0046 (7) |
| | | | | | | *R-factor* = 0.0044 |
| **$III_{5th}$** (*charged*) | 1 | 1.703 (11) | 0.0039 (8) | 1 | 3.014 (15) | 0.0049 (13) |
| | 2 | 2.038 (11) | 0.0061 (14) | 1 | 3.225 (93) | 0.0119 (244) |
| | 3 | 1.909 (6) | 0.0044 (8) | 1 | 3.148 (116) | 0.0077 (63) |
| | | | | | | *R-factor* = 0.0042 |

# III.3 – Discussion

Using *operando* XAS, we have studied in detail the charge compensation mechanism and local structural evolution in a model Li-rich layered oxide, $Li_2Ru_{0.75}Sn_{0.25}O_3$ (LRSO), in order to advance the fundamental understanding of cationic–anionic redox processes that govern these high capacity battery cathodes.

Starting with the analysis of pristine LRSO, we were able to neatly capture the asymmetric $RuM_3$ arrangement (one short and two long distances) at the local scale, an effect that is difficult to observe with long-range techniques such as XRD.[68,207,208]

[†] $E_0$ was determined from the energy value where jump is 0.6. The difference in threshold energy ($\Delta E_0$) and the amplitude reduction factor ($S_0^2$) were fixed at 0 and 1, respectively. The coordination numbers (*CN*) were kept constant and only the radial distances (*R*) and the Debye-Waller factors ($\sigma^2$) were allowed to vary. The fits are performed with M = Ru at the second shell.

LRSO's staircase-like 1st charge profile, which is characteristic of Li-rich layered oxides in general[40], starts with $Ru^{4+/5+}$ cationic oxidation around 3.6 V, as characterized by the edge shift on Ru K-edge XANES spectra. Furthermore, via PCA and MCR-ALS analyses, we have shown how the cationic de-intercalation process is in fact characterized by a three-component reaction mechanism (**I** to **II** to **III**), where initial Li removal (**I** to **II**) does not alter the asymmetric $RuM_3$ units, whereas the completion of cationic oxidation (**II** to **III**) equalizes the $RuM_3$ distances, as demonstrated by EXAFS modelling of the three reconstructed components. Note that these subtle evolutions of the local structure could not previously be detected with XRD[68], EPR[111], or NMR[186]. On the other hand, the high sensitivity of purely electrochemical methods deserves acknowledgement here since a double-peak around 3.6 V in the *dQ*/*dV* and diffusion coefficient profiles (recall **Figure II.2d**)[194] had indicated the possibility of a two-step mechanism, which has now been established via *operando* XAS.

On further charging across the 4.2 V plateau, Ru does not oxidize anymore, as also confirmed by comparing with $Li_3RuO_4$ having a formal $Ru^{5+}$ state (**Figure A2.6b**). Instead, a pre-edge peak grows in the Ru K-edge XANES, which signifies the distortion of $RuO_6$ coordination as a consequence of anionic oxidation. Quantification of this oxygen network distortion around Ru atoms via EXAFS modelling has in turn revealed the crucial role of short Ru–O distances in stabilizing the "peroxo-like" oxidized-oxygen $(O–O)^{n–}$ and preventing oxygen loss. Moreover, we have also directly proven the presence of oxidized lattice oxygen in fully charged LRSO using bulk-sensitive HAXPES. Structure-wise, as the anionic oxidation process triggers severe disordering, long-range techniques like XRD cannot provide further information[68] and hence the local-scale sensitivity of XAS was valuable herein for visualizing the oxygen network distortion. The EXAFS modelling methodology developed in our work was later adopted for Li-rich $Li_{1.2}Ni_{0.2}Mn_{0.6}O_2$ to show similar $NiO_6$ distortion in the charged state.[216] This structural distortion permanently impacts the electrochemical curve on discharge, which is no longer staircase-like with disconnected cationic–anionic processes, but rather sloped S-shaped involving overlapping cationic–anionic reductions. Moreover, a full discharge cannot reinstate the pristine ordering, although the asymmetric $RuM_3$ arrangement reappears at the local scale.

Application-wise, it was important to study the sloped S-shaped voltage profile as it will govern the electrochemical properties of a battery with Li-rich cathodes. Via PCA and

MCR-ALS analyses of the 5$^{th}$ cycle *operando* XAS data, we established a three-component reaction mechanism (**I**$_{5th}$ to **II**$_{5th}$ to **III**$_{5th}$). Through this spectroscopy-driven analysis, the overlapping cationic (at lower potential) and anionic (at higher potential) redox processes were neatly decoupled from each other by tracing their individual *dQ*/*dV* contributions. Apart from being one of the first spectroscopic demonstrations of reversibility of anionic activity in Li-rich cathodes beyond just the first couple of cycles (that are usually characterized in literature[102,111,136,163,186,217]), this work has also revealed fundamental insights about the issues of voltage hysteresis and kinetics that were found in the preceding electrochemical investigations of Chapter II.

Concerning hysteresis in the 5$^{th}$ cycle, we demonstrate how the relative concentration profiles for the three components do not superimpose when compared on charge vs. discharge paths, thereby demonstrating a path-dependence. The same can alternatively be visualized from the decoupled cationic–anionic *dQ*/*dV* contributions, in which the anionic redox process displays a higher asymmetry. In light of these XAS-based results, the detrimental effect of anionic redox in triggering hysteresis when LRSO is charged to higher potentials is now fully established.[194] Note that this hysteresis mechanism appears different from that of $LiFePO_4$ (non-monotonic equilibrium potential[218,219]) or conversion materials (core-shell mechanism[160] or different thermodynamic reaction paths[220]), and will further be explored in Chapter V. Furthermore, subtle XAS differences were observed even for the *ex situ* samples (relaxed over several days) prepared at the same SoC (or Li content) via either charge or discharge paths, which indicates the thermodynamic-like nature of hysteresis (independent of current). Overall, it can be concluded from *operando* XAS that hysteresis in LRSO results from the interplay between cationic–anionic redox processes which compete to compensate for the overall charge, resulting in the differences between oxidation vs. reduction paths. Whether a similar charge compensation mechanism holds true for Li-rich NMC is addressed in the next Chapter IV. Concerning kinetics, the cationic reaction (**I**$_{5th}$ to **II**$_{5th}$) causes less severe changes to the local structure compared to the anionic one (**II**$_{5th}$ to **III**$_{5th}$), with the latter leading to disordering and oxygen network distortion around Ru atoms which is an energy consuming process. EXAFS analysis has therefore provided a local structural explanation behind the previously reported sluggish kinetics of the anionic redox reaction in Chapter II.[194]

# III.4 – Chapter Conclusions

Chapter I in the beginning of this thesis summarized how reversible anionic redox in Li-rich layered oxides has revitalized the search for higher energy battery cathodes. To advance the fundamentals of this promising mechanism, we investigated herein the cationic–anionic redox processes in $Li_2Ru_{0.75}Sn_{0.25}O_3$ (LRSO) – a model cathode in which Ru (cationic) and O (anionic) are the only redox-active elements. We revealed its charge compensation mechanism and local structural evolutions by applying *operando* XAS. Among other local effects, the anionic-oxidation-driven distortion of $RuO_6$ octahedra was thereby visualized. Oxidation of lattice oxygen was also directly proven via HAXPES.

A key highlight of this Chapter was the chemometric approach to XAS data analysis that is based on PCA and MCR-ALS methods. Thanks to this approach, we now fully understand not just LRSO's staircase-like 1$^{st}$ charge, but also it's more convoluted S-shaped sloped 5$^{th}$ cycle. This approach led to a spectroscopy-driven visualization of electrochemical reaction paths, enabling us to neatly decouple the individual cationic–anionic *dQ*/*dV* contributions. We could hence establish the redox and local-structural origins of the *dQ*/*dV* features and demonstrate the vital role of anionic redox concerning hysteresis and kinetics, thereby bridging the electrochemical results of Chapter II with spectroscopic results of this Chapter. Overall, this study reveals the potential of *operando* XAS, when complemented with chemometric methods, in revealing reaction intermediates, decoupling overlapped reactions, and tracking the local structure in a non-invasive manner, making it an indispensable technique for electrochemical systems such as batteries. The *dQ*/*dV* deconvolution method developed herein is already being adopted by others.[221]

Having hitherto relied in this thesis solely on a model material (LRSO) for fundamental understanding, it is now time to move on to the practical material (Li-rich NMC) and explore the similarities and differences, as addressed in the next Chapter.

# Chapter IV – Bridging the fundamental & practical aspects in Li-rich NMC

# Part - IV*a* - ‡‡

This Part addresses diverse issues in Li-rich NMC, with particular emphasis on the role of anionic redox, and forms the main chunk of this Chapter.

The next Part, on the other hand, is a focused investigation of long cycling.

## IV*a*.1 – Background and Motivation

In line with what we have already seen in Chapter I, Li-rich layered oxide cathodes, e.g. $Li_{1.2}Ni_{0.13}Mn_{0.54}Co_{0.13}O_2$ (Li-rich NMC) that is an archetypical composition, have been demonstrated to hold the highest promise regarding practical energy density at the cell-level.[4,11,12,20] Moreover, they also have a cost advantage[4,11,12] by being mainly based on abundant Mn, instead of Co or Ni. For these reasons, Li-rich NMC is termed as the 'practical' cathode in this thesis. It can deliver capacities reaching 300 mAh $g^{-1}$, which had only recently been shown, at the time this work was carried out, to arise from combined anionic and cationic redox processes.[100,103,108]

In Chapter II, we pointed out the poor electrochemical kinetics of anionic redox and its detrimental role in triggering voltage fade and hysteresis using a 'model' Li-rich layered oxide, $Li_2Ru_{0.75}Sn_{0.25}O_3$ (LRSO).[194] In light of these findings, it is imperative to ask whether the same is true for Li-rich NMC. This calls for revisiting Li-rich NMC with a fresh perspective by including anionic redox in order to understand the fundamental origins of some practical roadblocks (i.e. voltage fade, poor kinetics, and voltage hysteresis). These issues jeopardize cycle life, power rate, energy efficiency, and state of charge (SoC) management, and hence have plagued the commercialization of Li-rich NMCs despite several years of academic and industrial interest.[124,222]

‡‡ Part - IV*a* - of this Chapter is based on the following research article that I co-authored :
**Assat, G.**, Foix, D., Delacourt, C., Iadecola, A., Dedryvère, R. & Tarascon, J.-M. Fundamental interplay between anionic/cationic redox governing the kinetics and thermodynamics of lithium-rich cathodes. ***Nature Communications***, 8, Article number: 2219 (**2017**). (https://doi.org/10.1038/s41467-017-02291-9)

This task is not straightforward because Li-rich NMC is complicated by the redox activity of Ni, Mn, Co, and O, whose redox potentials must first be identified to establish the charge-compensation mechanism, like we did in Chapter III for the simplified 'model' LRSO. Starting with oxygen, it was believed for quite a few years that Li-rich NMC's anomalous 1st charge capacity is compensated by irreversible oxygen loss from the electrode's surface resulting in densification.[66,94,96,99] However, recent measurements suggest that such oxygen loss is largely insufficient to account for the extra 1st charge capacity.[103,116,223] Thus the early models of surface oxygen loss were only partially complete and it is now believed that most of the oxidized oxygen remains in the lattice and participates in redox[101,100], as directly observed via *ex situ* X-ray absorption spectroscopy (XAS)[103,104,153], X-ray photoelectron spectroscopy (XPS)[105] and hard-X-ray photoelectron spectroscopy (HAXPES)[224]. The remaining task now is to look beyond the 1st charge and identify the electrochemical potentials with corresponding states of charge (SoC) where anionic redox occurs.

As for charge compensation from the TMs, *operando* XAS[102,163,217] as well as *ex situ* XAS[98,103,153,182,225] at TM K-edges have clearly shown how the $Ni^{2+/3+/4+}$ redox process proceeds but there are still discrepancies in literature concerning the extent of $Mn^{3+/4+}$ contribution because the complicated shape of Mn K-edge led to ambiguities. Finally for Co, the XAS data in literature is insufficient to precisely conclude the redox potential of $Co^{3+/4+}$, which is often wrongly assumed when interpreting the differential capacity ($dQ/dV$) plots. We note that soft-XAS at Mn and Co L-edges can provide a clear signature of oxidation states, but these data are scarce in literature.[104,226,227]

Filling the abovementioned charge-compensation knowledge gaps is necessary to explore the role of anionic redox on battery performance issues, i.e. voltage hysteresis, poor kinetics, and voltage fade. So far, the Mn-rich nature of Li-rich NMC leaning towards $Li_2MnO_3$ was blamed for these issues. A phenomenological model involving irreversible and reversible TM migrations was proposed to explain voltage fade and hysteresis, respectively.[165] However, it is highly likely that such migration is in fact a consequence of anionic redox. Concerning kinetics, there is XAS-based evidence for sluggish reaction of the $Li_2MnO_3$-type component[163] and also evidences of a mysterious impedance rise at low SoCs[164,228,229] that encourage us to examine whether this is actually because of anionic redox.

Towards these goals, we report here the complete charge-compensation mechanism in Li-rich NMC as deduced by bulk-sensitive synchrotron-based spectroscopic techniques, namely HAXPES and soft-XAS. The ability of HAXPES to systematically increase probe depths[230] allowed us to distinguish between surface and bulk effects. We consequently correlate these findings with detailed electrochemical measurements to reveal the interplay between anionic/cationic redox and electrochemical kinetics/thermodynamics of these electrodes. We provide direct evidence of bulk anionic redox activity, which compensates for a substantial capacity not just at high but quite surprisingly at low potentials also. Moreover, we confirm, as previously reported for $Li_2Ru_{0.75}Sn_{0.25}O_3$,[194] that the cationic redox from $Ni^{2+/3+/4+}$ and $Co^{3+/4+}$ exhibits fast kinetics and diffusion in comparison to the sluggish anions. On the other hand, Mn is found to be essentially redox-inactive with only a small contribution from $Mn^{3+/4+}$ at the lowest potentials. To effectively convey these findings, the results will be structured in two subparts, dealing first with the charge-compensation mechanism, followed by a detailed electrochemical investigation.

## IV*a*.2 – Results

$Li_{1.2}Ni_{0.13}Mn_{0.54}Co_{0.13}O_2$ (Li-rich NMC) powders† were prepared by carbonate co-precipitation followed by annealing at 850 °C (detailed Methods for the Chapter in Appendix A3). The obtained single-phase powders were hand-mixed with 10 % conductive carbon (without binders) and used as positive electrodes in Li half-cells. They exhibit, as widely known, a staircase-like 1st charge profile that changes to a sloped S-shape on 1st discharge and this S-shape is maintained from 2nd cycle onwards (**Figure IV.1a,b**).

During the first two cycles, a series of *ex situ* samples at different SoCs was prepared by taking apart the cells, then electrode powders being recovered and thoroughly mixed to average-out any concentration gradients. These samples' SoCs were chosen based on *dQ*/*dV* plots that show several peaks corresponding presumably to different redox couples (**Figure IV.1c,d**).

† I thank Yin Yang for synthesizing and providing the pristine Li-rich NMC powders.

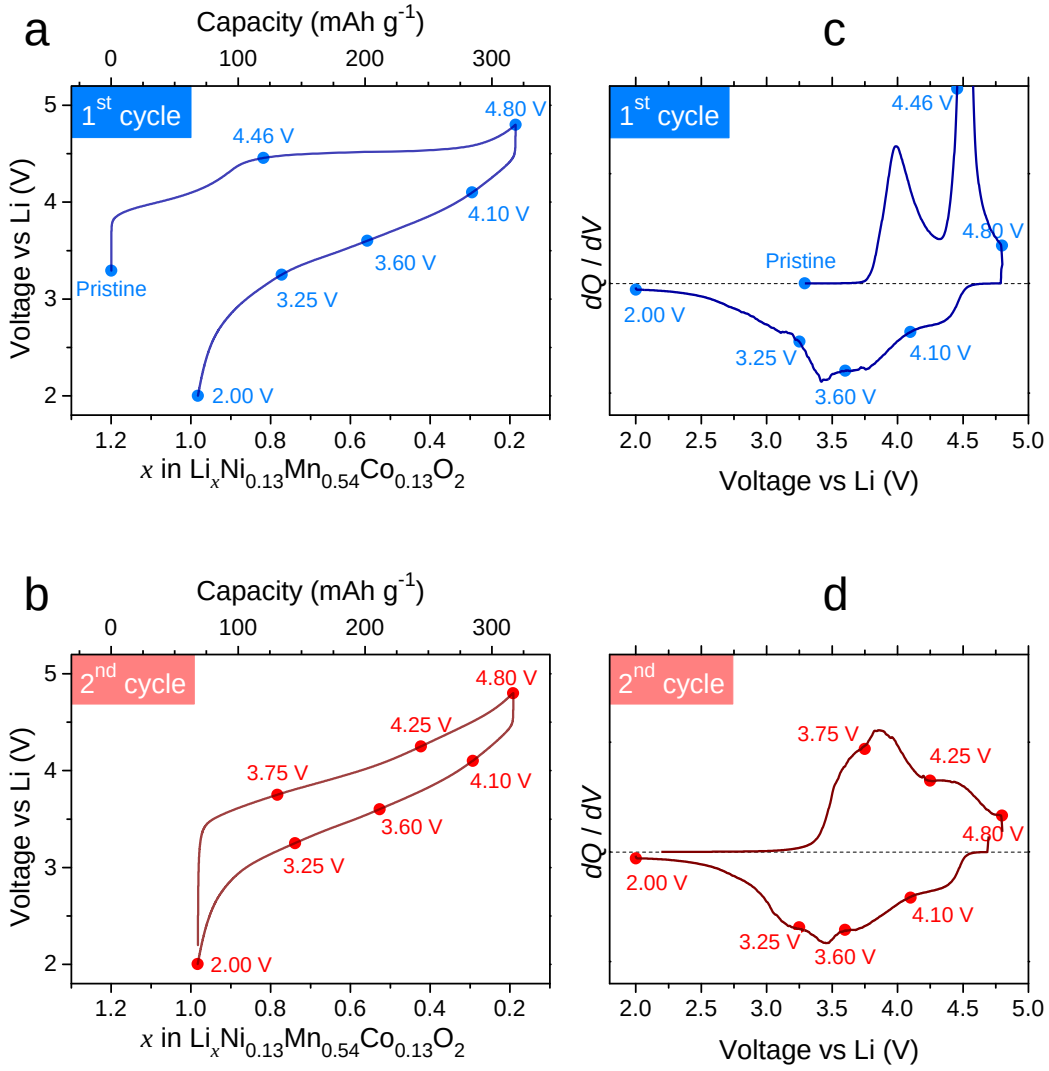


**Figure IV.1 | Electrochemical curves with sample positions.** Voltage profiles of $Li_{1.2}Ni_{0.13}Mn_{0.54}Co_{0.13}O_2$ (Li-rich NMC) in Li half-cells as a function of Li content for the 1st (**a**, **c**) and 2nd (**b**, **d**) cycles with corresponding *dQ*/*dV* curves. Current density is 20 mA $g^{-1}$. Circles mark the sample positions on the curves.

## ○ Charge-compensation mechanism via HAXPES

Charge compensation from cationic and anionic redox processes was examined with XPS[††] performed at increasing probe depths achieved by increasing the photon energy from $h\upsilon$ = 1.487 keV (in-house XPS) to $h\upsilon$ = 3.0 and 6.9 keV (HAXPES), thus elucidating surface vs. bulk effects. The resulting probe depths are tabulated in **Table IV.1**. Since the

[††] **HAXPES** was performed in collaboration with Rémi Dedryvère (IPREM, Pau). Rémi, Antonella Iadecola (RS2E, CNRS), and myself performed the HAXPES experiments. Rémi carried out the fitting of the spectra. Dominique Foix (IPREM, Pau) recorded the **in-house XPS** spectra and performed the fits.

Li-rich NMC primary particles are relatively small (~100 nm, **Figure IV.2**), the highest photon energy of 6.9 keV can thus access their bulk, as illustrated for O 1*s* in **Figure IV.3**.

**Table IV.1 | XPS and HAXPES probe depths.**[‡] The probe depths are defined as three times the photoelectron inelastic mean free path (IMFP) that corresponds to 95% of the signal coming from the sample, and were estimated from the TPP-2M model[§] in ref.[212]

| **Photon energy (keV)** | **Probe depth (nm)** | | | |
|---|---|---|---|---|
| | O 1*s* | Mn 2*p* | Co 2*p* | Ni 2*p* |
| **1.487** | 6.3 | 5.7 | 5.0 | 4.6 |
| **3.0** | 13 | 13 | 12 | 12 |
| **6.9** | 29 | 28 | 28 | 28 |
| **10.0** [*] | 40 | 40 | 39 | 39 |

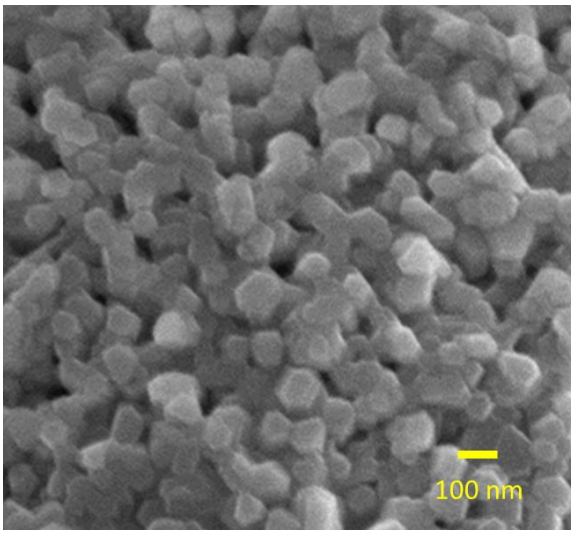


**Figure IV.2 | Scanning electron microscopy (SEM) image of the pristine material showing the primary particle size.**

[‡] The probe depth calculations were carried out by Rémi Dedryvère.

[§] This model uses four parameters: (*i*) the formula molecular weight, (*ii*) the density, (*iii*) the number of valence electrons per formula, and (*iv*) the band gap. Given the composition of the material $Li_{1.2}Ni_{0.13}Mn_{0.54}Co_{0.13}O_2$, its molecular weight is 85.29 g mol$^{-1}$ and the number of valence electrons is 19.45 per formula unit. The density is 4.18 g cm$^{-3}$. The band gap is unknown, but this parameter has only little influence on the final result (for example, the calculated probe depth for $h\nu$ = 6900 eV is 29 nm using band gap = 0 eV and 30 nm using band gap = 5 eV). The band gap was fixed to 2 eV for the calculations.

[*] The 10.0 keV photon energy is only used in Part - IV*b* -.

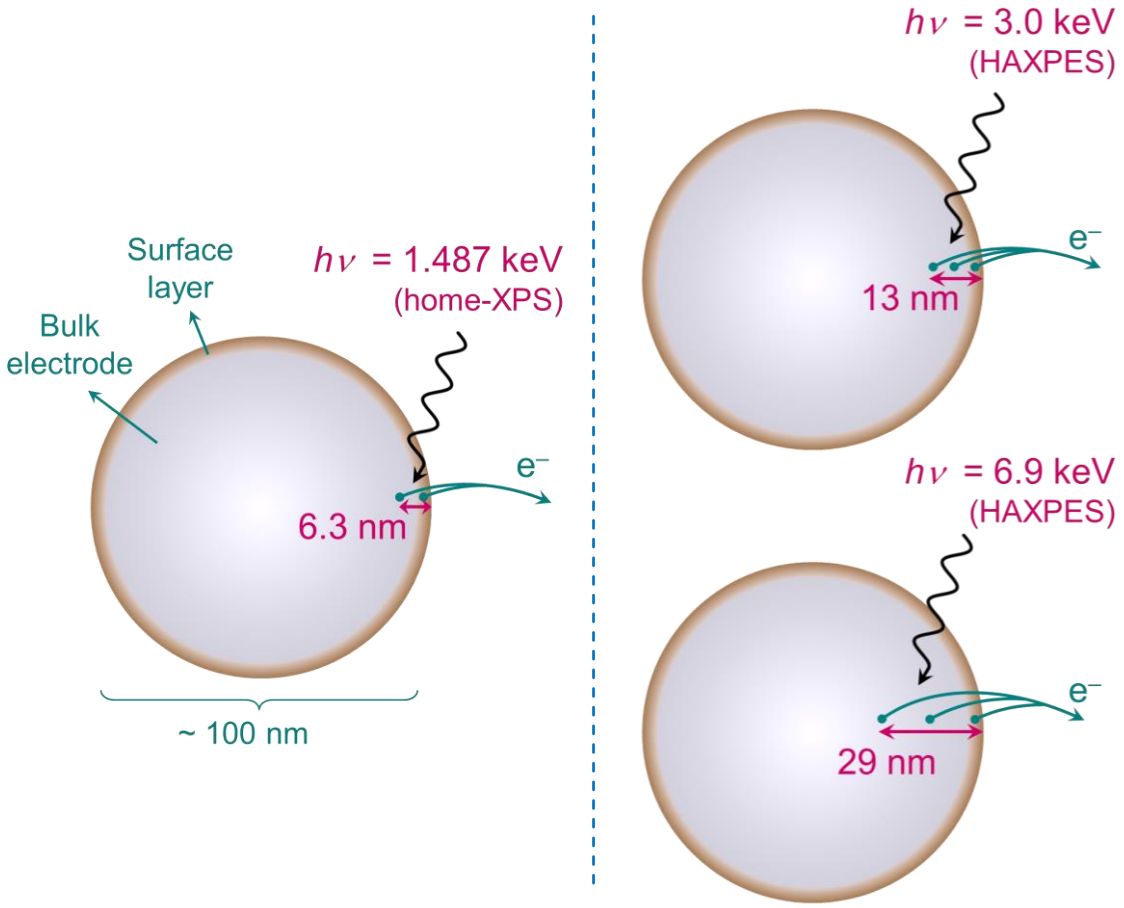


**Figure IV.3 | Schematic view of XPS probe depths estimated for the O 1*s* core peak**. Higher energy photons allow for probing much beyond the surface layer to provide bulk information from the ~100 nm sized primary particles. Note that the probe depths are related to the escape depth of photoelectrons and not to the penetration depth of photons, and that the photoelectron intensity exponentially decreases as a function of the distance from the surface.

Before discussing the spectra, it is worth noting that all precautions have been taken to prevent any contact of the samples with air by maintaining them in dry argon atmosphere or in high vacuum at all steps (details in Methods in Appendix A3).

## —— Anionic redox characterization

Starting with oxygen, **Figure IV.4** shows the O 1*s* HAXPES spectra as they evolve during the 1st and 2nd cycles. For the sake of conciseness, results with only $h\upsilon$ = 6.9 keV

having the highest probe depth (~29 nm, or 120 times the interlayer distance) are shown here (see **Figure A3.2** for 3.0 keV and **Figure A3.3** 1.487 keV in the Appendix). The pristine sample is characterized by a strong peak at binding energy (BE) ≈ 529.5 eV due to lattice $O^{2-}$ whereas the smaller peaks at higher BEs come from surface deposits.

On charging to 4.8V, a shoulder grows on the higher BE side of lattice $O^{2-}$ at ~530.5 eV that can be clearly distinguished thanks to the low contribution of surface species and to the very good monochromator energy resolution at 6.9 keV (see fitting procedure details in Methods). The ~530.5 eV BE for this new O 1*s* component is much lower than the values reported for oxygenated species in the surface film. For instance, degradation of carbonate solvents may lead to various organic oxygenated species, but their BEs are observed between 531.5 and 534 eV.[213–215] Similarly, the inorganic species resulting from degradation of the electrolyte salt $LiPF_6$, such as phosphates, fluorophosphates $Li_xPO_yF_z$ or LiOH, are also observed at higher BEs. Therefore the ~530.5 eV component can be ascribed to anionic oxygen bound to the TMs. Note however the BE increase of +1 eV with respect to classical lattice $O^{2-}$. This can be explained (in light of Extended Hückel Theory-Tight Binding (EHT-TB) and other calculations that have shown a correlation of the BE of oxygen in an oxide with the net charge on the oxygen anion[231–234]) by a significant decrease of the negative charge on oxygen due to its participation in the electrochemical oxidation. The new component at BE ≈ 530.5 eV is thus oxidized lattice oxygen, $O^{n-}$ ($n < 2$), which was also seen in Chapter III for LRSO and is in complete agreement with our lab's previous report on a series of Li-rich materials ($Li_2RuO_3$, $Li_2IrO_3$ and Li-rich NMC)[105] as well as on highly-delithiated $Li_xCoO_2$ ($x < 0.4$)[86]. Note that we avoid using the "peroxo-like" $(O_2)^{n-}$ notation for Li-rich NMC, unlike for LRSO in the previous Chapter, because this nuance is still being debated as of today. Bulk-sensitive HAXPES enables us to unambiguously observe $O^{n-}$ on charge and its gradual reduction when discharge proceeds to 2.0 V (**Figure IV.4a**). On further cycling (**Figure IV.4b**), $O^{n-}$ regrows at the expense of $O^{2-}$ on 2$^{nd}$ charge and then decreases again on 2$^{nd}$ discharge, thereby confirming the sustained and reversible anionic reactivity.

An interesting satellite at BE ≈ 535–536 eV is also observed, especially with $h\upsilon$ = 6.9 keV. Although the satellite's origin is still unclear, its gradual energy-shift and intensity variation on charge/discharge suggest its correlation with anionic redox, which should be addressed in future work.

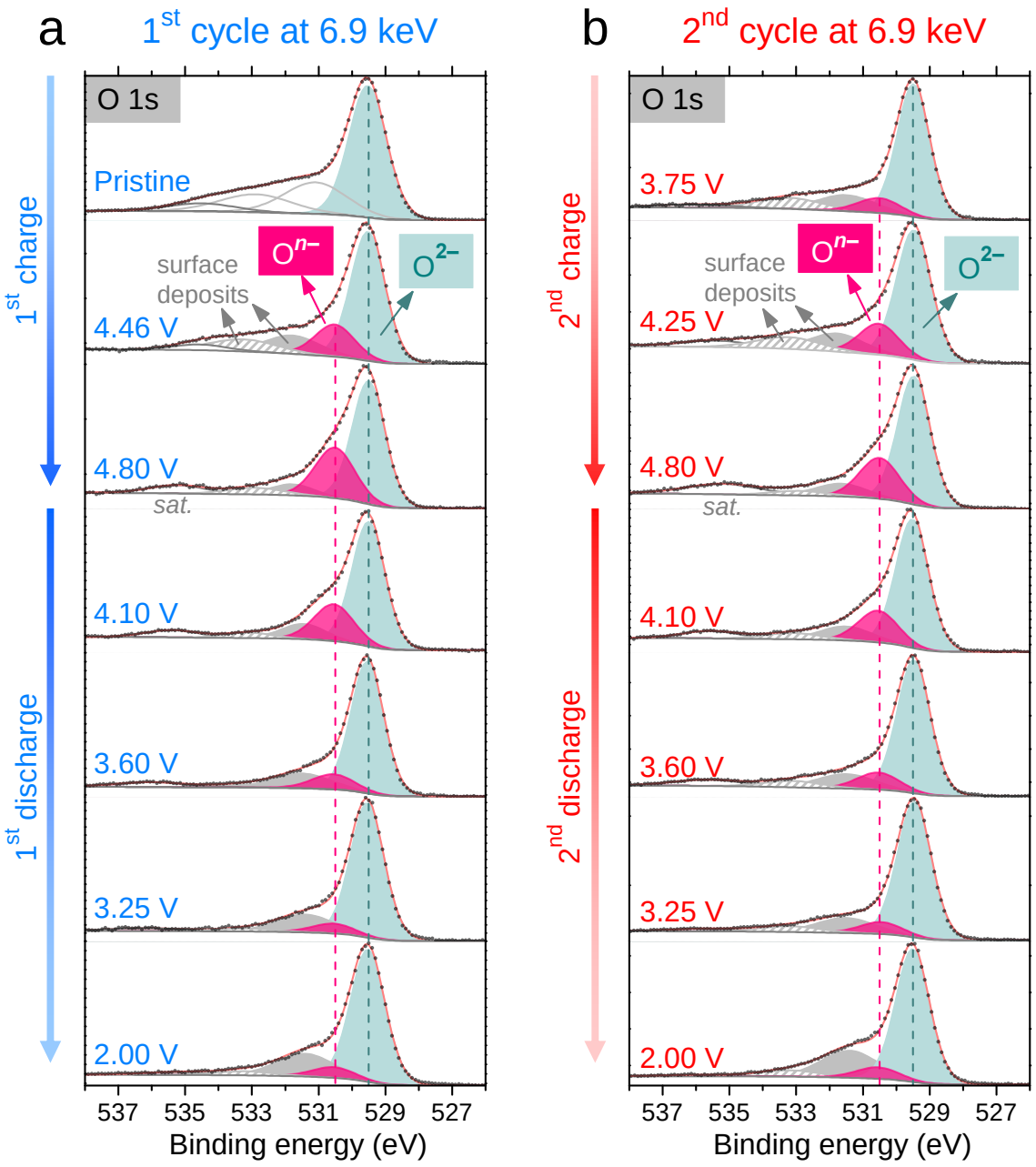


**Figure IV.4 | Evolution of O 1*s* HAXPES spectra at 6.9 keV (highest probe depth).** (**a**) 1st cycle and (**b**) 2nd cycle. Black dots are experimental data and red curves are fits. Lattice $O^{2-}$ peak is at binding energy (BE) ≈ 529.5 eV. On charge, oxidized lattice oxygen, $O^{n-}$ grows at BE ≈ 530.5 eV (pink component) followed by its reduction on discharge. Surface deposits appear at higher BEs (grey components). Each O 1*s* panel has been normalized to keep the same intensity of the $O^{2-}$ component (green component) for all spectra. Note that the pristine sample was never in contact with the electrolyte and that its oxygenated surface species are those commonly observed at the surface of oxides. The other samples are electrochemically prepared and hence show new surface oxygenated species compared to the pristine, which come from electrolyte decomposition and passivating surface-film formation. An extra satellite peak at BE ≈ 535-536 eV is seen with 6.9 keV (and also weakly with 3.0 keV).

To answer the important question about bulk vs. surface anionic redox, we compare the effect of different probe depths as shown here for two samples, i.e. 1st charged (**Figure IV.5a**) and 1st discharged (**Figure IV.5b**). While gradually probing deeper into the two samples, the intensity of $O^{n-}$ component is not dependent on the photon energy and we do not observe much variation in % $O^{n-}$ (percentage of oxidized lattice oxygen), defined as $O^{n-}$ / ($O^{n-}$ + $O^{2-}$) by considering the integrated areas. In contrast, the contribution from surface deposits neatly decreases as *hυ* increases, becoming quite small at 6.9 keV. Thus, we can unambiguously conclude that $O^{n-}$ is present in the bulk. Additionally, the quantification of % $O^{n-}$ with HAXPES is more reliable than with surface-sensitive in-house XPS because the polluting O 1*s* signal from surface deposits is diminished at high *hυ* and hence the $O^{n-}$ peak is not overshadowed.

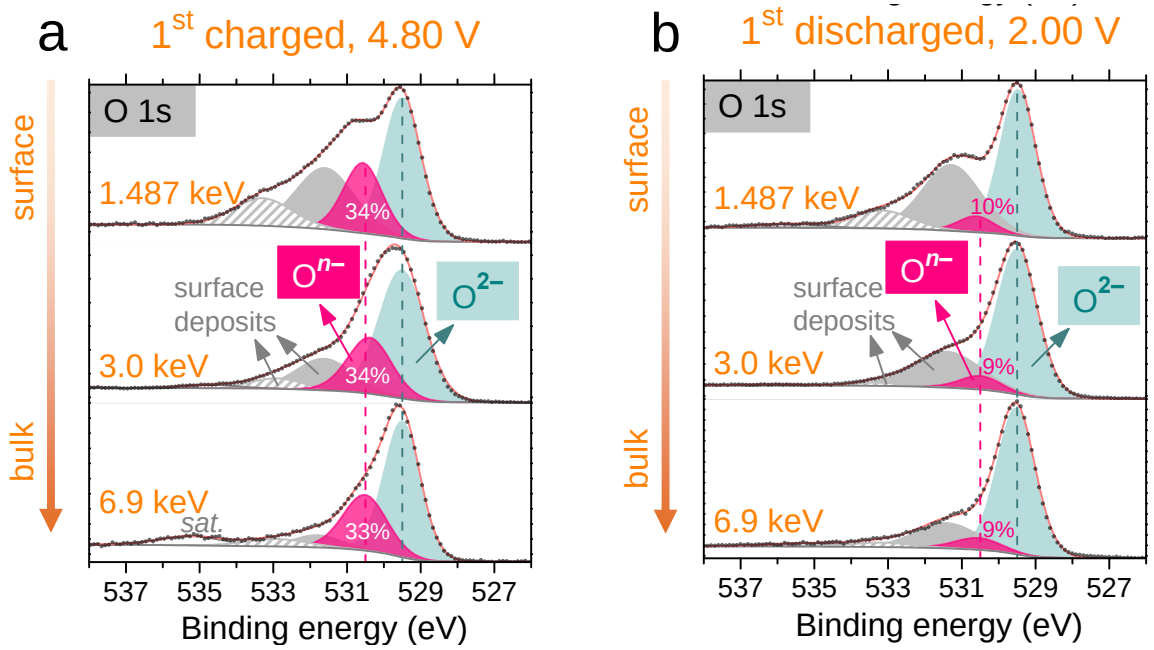


**Figure IV.5 | The effect of probe depth on the O 1*s* photoelectron spectra.** Two samples are shown, i.e. (**c**) 1st charged at 4.80 V and (**d**) 1st discharged at 2.00 V. Surface deposits diminish at high photon energies in contrast to the steady $O^{n-}$. Changes in the monochromator energy resolution at different photon energies affect the shape of spectra (the worst energy resolution was obtained for 3.0 keV).

The overall charge-compensation mechanism from anionic redox can be understood from the changes in % $O^{n-}$ as a function of Li insertion/removal. During the 1st charge (**Figure IV.6a**), % $O^{n-}$ grows to 33 ± 3% and then steadily reduces to 9 ± 3% on discharge. $O^{n-}$ gradually grows back to 28 ± 3% on 2nd charge (**Figure IV.6b**) followed by its

reduction on discharge that is quite similar to the 1st discharge, hence showing the excellent repeatability of the samples.

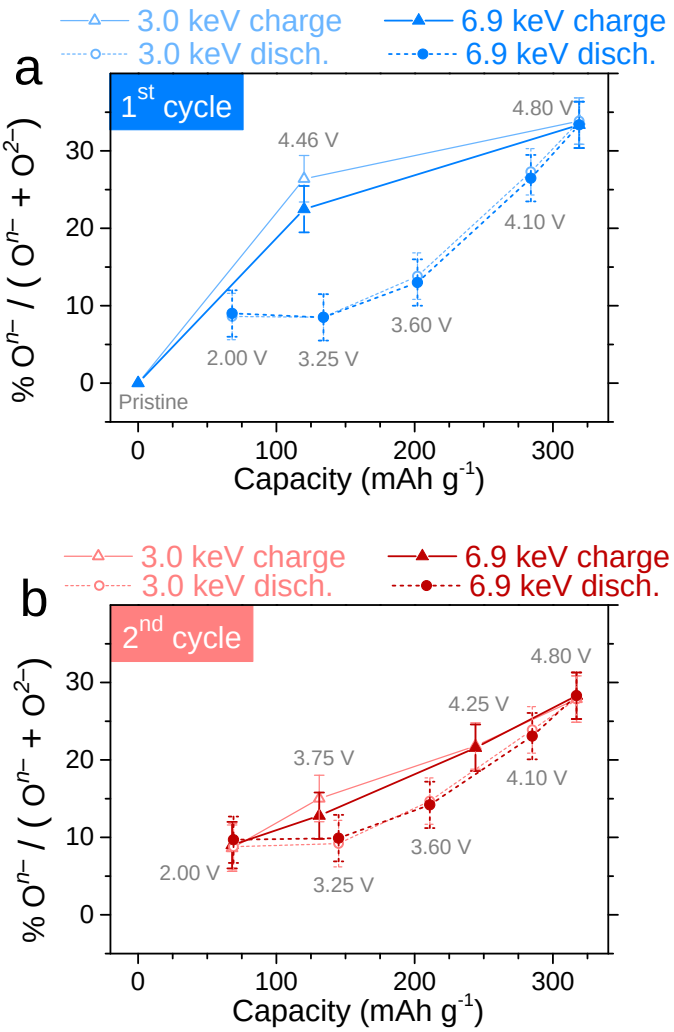


**Figure IV.6 | Quantitatively tracking anionic redox.** The estimated % $O^{n-}$ is plotted as a function of capacity to understand the anionic charge-compensation during the (**e**) 1st and (**f**) 2nd cycles. Results from 3.0 and 6.9 keV are overlaid. The ± 3% absolute error bars represent the uncertainty in the fitting procedure, which was determined by comparing the effect of different initial conditions on the resulting fits.

The ± 3% absolute error in % $O^{n-}$ quantification (error bars in **Figure IV.6**) arises from the fitting procedure's uncertainty, which was determined by comparing the effect of different initial conditions on the resulting fits. To this aim, the two surface components were allowed to vary between 531.5–532.0 eV and 533.0–533.5 eV, respectively. These values fall within the range of BEs commonly observed at the surface of various cathode

materials cycled with the electrolyte used herein, and are in good agreement with the 1.487 keV spectra (**Figure A3.3**) that have higher relative intensities of surface components. Our fitting procedure (details in Methods) aims to prevent over-interpretations, but the ± 3% absolute error is not insignificant as it leads to rather high relative errors (r. e.) when % $O^{n-}$ is low (33% r. e. for % $O^{n-}$ = 9 ± 3% vs. 10% r. e. for % $O^{n-}$ = 33 ± 3%) and further work should try on overcome this uncertainty via improved energy resolution and/or via surface cleaning. The % $O^{n-}$ profiles at 3.0 keV and 6.9 keV neatly superimpose in **Figure IV.6**. However, $O^{n-}$ quantification at 1.487 keV is less reliable as stated above, resulting in a slight over-prediction of % $O^{n-}$ (**Figure A3.4**). This underscores the importance of HAXPES in accurately probing bulk anionic redox.

The incomplete reduction of oxygen on discharge to 2.0 V suggests its sluggish kinetics and this would also partly contribute to the 1$^{st}$ cycle irreversibility. A potentiostatic hold at 2.0 V (till current decays to 1 mA $g^{-1}$) is in turn necessary to fully reduce $O^{n-}$ (**Figure A3.5**), which further strengthens this hypothesis. In light of this result, a detailed study of electrochemical kinetics is presented later. The gradual variation of $O^{n-}$ in the 2$^{nd}$ cycle from 2.0 to 4.8 V shows that anionic redox takes place at high as well as at low potentials. This is an interesting result which distinguishes Li-rich NMC from 'model' $Li_2Ru_{0.75}Sn_{0.25}O_3$ systems in which cationic and anionic redox are well separated at low and high potentials, respectively, as seen in the previous two Chapters.[111,119,194]

## —— Cationic redox characterization

Turning now to TMs, their formal oxidation states in pristine Li-rich NMC are expected as follows: $Li_{1.2}Ni^{2+}_{0.13}Mn^{4+}_{0.54}Co^{3+}_{0.13}O_2$. Starting with Ni, its 2$p_{3/2}$ HAXPES spectra recorded at 3.0 keV during 1$^{st}$ cycle are shown in **Figure IV.7a** (2$^{nd}$ cycle is very similar, see **Figure A3.6**). The Ni 2$p_{3/2}$ main peak and its shake-up satellite shift to higher binding energies on oxidation and then come back on reduction. Note that due to the relatively large width of this core peak recorded at 3.0 keV (full width half maximum (FWHM) being ~3 eV), it is not possible to resolve the underlying $Ni^{2+}$, $Ni^{3+}$, and $Ni^{4+}$ components and only a gradual shift of the whole peak is observed. The average Ni oxidation state can be estimated from the main peak's maximum position and is plotted in

**Figure IV.7b** vs. capacity. The 1st charge starts with complete Ni oxidation to 4+ before 4.46 V with no further Ni redox during the anionic activation plateau. After 1st cycle activation, the $Ni^{2+/3+/4+}$ redox process occurs reversibly, but with a noticeable hysteresis loop (red trace in **Figure IV.7b**) wherein Ni oxidizes (charge) at lower SoCs compared to Ni reduction (discharge), with the above results in complete agreement with the literature on bulk-sensitive Ni K-edge XAS.[102,163,217,225] This loop is important for voltage hysteresis as we will discuss in detail later. From the variation of Ni oxidation state vs. potential, $Ni^{2+/3+/4+}$ from 2nd cycle onwards can be assigned to the same *dQ*/*dV* peak on both charge and discharge, i.e. the middle one around 3.8 V.

Concerning Mn, its $2p_{3/2}$ photoelectron spectra recorded at 3.0 keV during the 1st cycle are shown in **Figure IV.7c** (2nd cycle is very similar, **Figure A3.7**). The Mn $2p_{3/2}$ peak can be assigned to $Mn^{4+}$ and the fine structure at this peak's maximum undergoes changes on charge/discharge. Note that the presence of such a fine structure does not indicate two different Mn oxidation states. Other materials containing solely $Mn^{4+}$ are known to show the same kind of Mn $2p_{3/2}$ main peak fine structure, for example $Li_2MnO_3$, $MnO_2$, or $Li_{2/3}Co_{2/3}Mn_{1/3}O_2$ (shown in **Figure A3.8**). The origin of this particular shape can instead be explained by final state effects in the 2*p* photoemission process involving the first and second neighbouring atoms.[235] Therefore, the evolutions of fine structure in **Figure IV.7c** are not due to changes in Mn oxidation state, but can be attributed to the redox activity of neighbouring Ni, Co and to crystal structure changes. Moreover, the $2p_{3/2}$ fine structure evolves identically when comparing the 1st and 2nd discharges, thus again demonstrating the sample reproducibility. A slight change in Mn oxidation state occurs at the end of discharge (from 3.25 to 2.00 V), i.e. the appearance of a small shoulder at BE ≈ 641 keV (marked by arrow) denoting partial reduction to $Mn^{3+}$. $Mn^{3+}$ is limited to merely ~10% at the end of 1st discharge as estimated in **Figure IV.7d** (and ~11% after 2nd discharge, **Figure A3.9**). Moreover, $Mn^{3+}$ content is quite similar when characterized with surface-sensitive in-house XPS (**Figure A3.10** and previous study[105]). Therefore, $Mn^{3+}$ reduction is not just a surface effect as widely believed. A potentiostatic hold at 2.0 V (till current decays to 1 mA $g^{-1}$) further increases $Mn^{3+}$ to 18% (**Figure A3.11**) confirming the low potential for partial $Mn^{3+/4+}$ activity. Furthermore, this $Mn^{3+}$ is rechargeable, since the $Mn^{3+}$ shoulder disappears in the early stage of 2nd charge (**Figure A3.7**). To conclude, the $Mn^{4+}$ state stays mostly unchanged except for a relatively small contribution from reversible $Mn^{3+/4+}$ at low potentials.

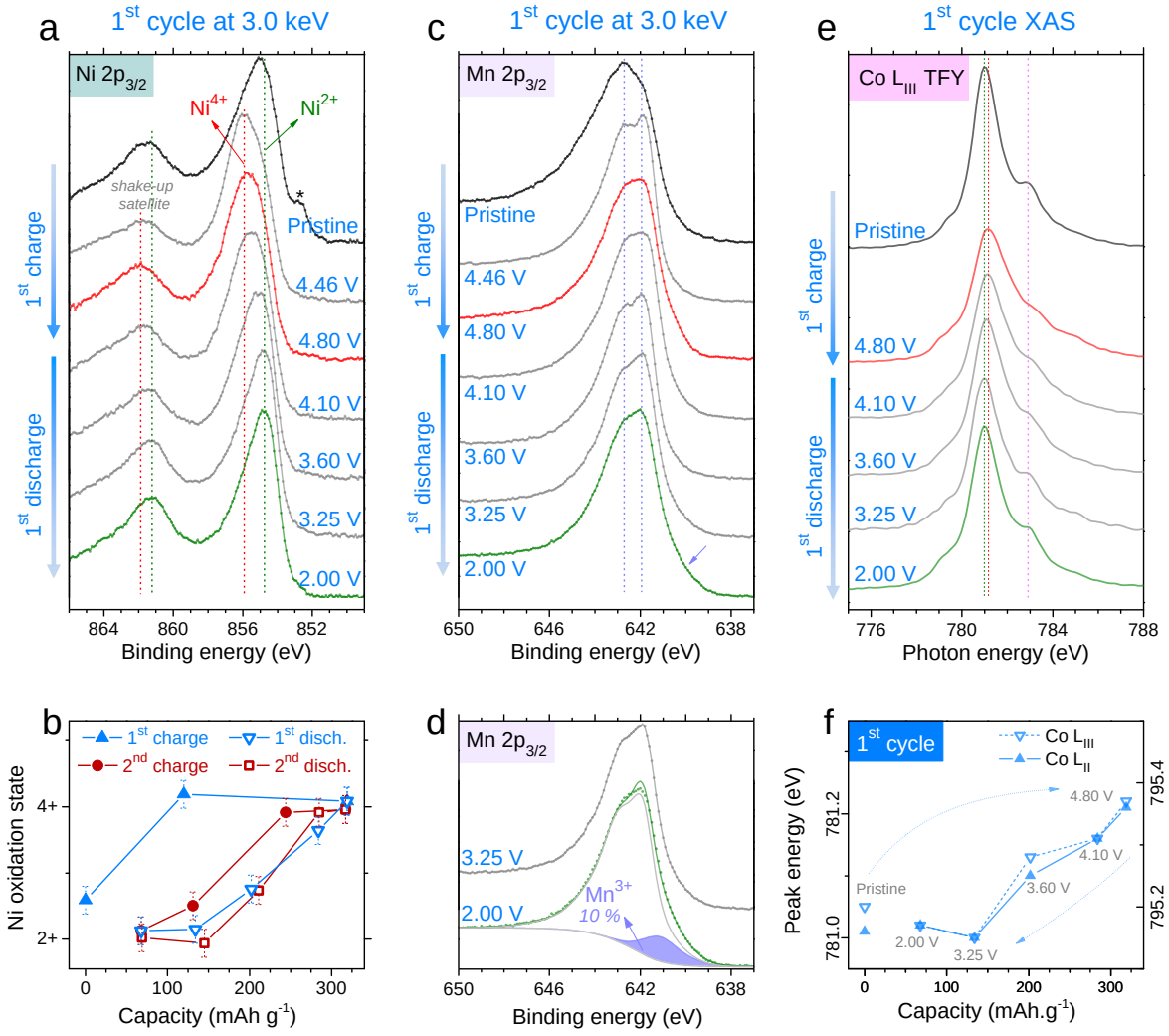


**Figure IV.7 | Charge compensation from transition metals (cationic redox), as deduced by HAXPES and XAS.** (**a**) Evolution of Ni $2p_{3/2}$ photoelectron spectra during the 1st cycle at 3.0 keV (probe depth ≈ 12 nm). The main peak at 855 eV shifts to higher BEs on charge (oxidation from $Ni^{2+}$ to $Ni^{3+}$ to $Ni^{4+}$) and vice-versa. A small degradation of the pristine sample under X-ray beam is marked by *. (**b**) From the BE shift of the main peak, the average Ni oxidation state is estimated as a function of capacity over two cycles. The error bars are determined from the 0.1 eV error in the estimation of the main peak's maximum. (**c**) Evolution of Mn $2p_{3/2}$ photoelectron spectra during the 1st cycle at 3.0 keV (probe depth ≈ 13 nm). The fine structure of the main peak maximum evolves along the two dashed lines. A small shoulder on discharge to 2.00 V (marked by arrow) indicates minor $Mn^{3+}$. (**d**) The $Mn^{3+}$ amount is estimated by fitting the 2.00 V spectrum with two components, namely the spectrum envelope at 3.25 V (which contains only $Mn^{4+}$) and an additional component (purple, ~641 keV) attributed to $Mn^{3+}$. (**e**) soft-XAS spectra for Co $L_{III}$-edge (dipole allowed transition from $2p_{3/2}$ core level to unoccupied 3*d* states) recorded in TFY mode (probe depth ~100 nm) during the 1st cycle. The peak slightly shifts to higher photon energy indicating Co oxidation on charge and vice-versa. (**f**) As a function of 1st cycle capacity, the evolution of Co $L_{III}$ (left axis) and $L_{II}$ (right axis) peak energies is shown.

Lastly for Co, it is known from previous XPS measurements on layered $Li_xCoO_2$ that the oxidation of $Co^{3+}$ does not result in a shift of the Co $2p_{3/2}$ main peak's position and instead leads to a subtle change in the ratio of the main peak to its shake-up satellite.[86] As this parameter was not exploitable in our Co $2p_{3/2}$ HAXPES spectra (**Figure A3.12**), we performed soft-XAS‡‡ at Co L-edges (**Figure IV.7e**) in bulk-sensitive Total Fluorescence Yield (TFY) mode. On 1st charge to 4.80 V, the Co-$L_{III}$ peak shifts to higher energies with a loss of intensity followed by a reverse behaviour on discharge to 2.0 V. Likewise, there is also a back-and-forth evolution of the peak shape, especially around 783 eV where the shoulder is more pronounced for Co in reduced state (pristine and discharged samples). Similar shifts and shape changes are also observed in the Co-$L_{II}$ peak (**Figure A3.13**). Such evolutions in the Co L-edges over charge/discharge are analogous to $Li_xCoO_2$,[85,152] thus confirming some $Co^{3+/4+}$ activity. Complete oxidation of Co to 4+ in these layered oxides is unlikely as it is now well-admitted, based on an early speculation of oxidized oxygen in $Li_0CoO_2$[81] that was later confirmed via several spectroscopic studies (listed in a review article[136]), that O competes with Co for charge compensation at stages of high delithiation. Nevertheless, our spectra show Co redox activity and to identify its redox potential, the Co-$L_{III}$ and $L_{II}$ peak positions are plotted vs. capacity in **Figure IV.7f**, which indicates a continuous Co reduction till 3.25 V. This trend neatly overlays with that of $Ni^{2+/3+/4+}$ from **Figure IV.7b**, and thus $Co^{3+/4+}$ and $Ni^{2+/3+/4+}$ take place at similar potentials, i.e. as stated above for Ni, around the 3.8 V $dQ/dV$ peak on both charge and discharge.

Altogether, these abovementioned results clarify the charge-compensation mechanism. The 1st charge starts with cationic oxidation of Ni and Co ($dQ/dV$ peak around 4.0 V). Afterwards, bulk anionic oxidation, which already begins before 4.46 V, compensates for charge during the activation plateau ($dQ/dV$ peak around 4.5 V). After 1st charge, the electrochemistry permanently changes to a sloped S-shape in which $Ni^{2+/3+/4+}$ and $Co^{3+/4+}$ are the main cationic redox processes (maximum 122 mAh $g^{-1}$ assuming the extreme case of complete oxidation to 4+) whereas $Mn^{4+}$ stays essentially inactive except for the minor activity at the lowest potentials. The small amount of $Mn^{3+}$ found at 2.0 V (~11%, compensating for just 19 mAh $g^{-1}$) results from the reversible $Mn^{3+/4+}$ couple, which is known to get activated following the small amount of irreversible oxygen loss on 1st charge[116]. Reversible bulk anionic redox therefore accounts for a substantial capacity,

‡‡ José Avila and and Maria-Carmen Asensio (ANTARES beamline of SOLEIL synchrotron) recorded the **Co soft-XAS** spectra. Antonella Iadecola (RS2E, CNRS) normalized the spectra.

i.e. at least 109 mAh $g^{-1}$ in 2.0–4.8 V (deduced by subtracting 122 and 19 mAh $g^{-1}$ cationic contributions from 250 mAh $g^{-1}$ total), which is delivered at not just high but quite importantly at low potentials as well.

## ○ Anionic/cationic redox interplay vis-à-vis practical aspects

A full understanding of charge compensation was necessary to initiate a detailed electrochemical investigation of Li-rich NMC like we have done for $Li_2Ru_{0.75}Sn_{0.25}O_3$ in Chapter II.[194] Towards this, we focus on the S-shaped-sloped electrochemistry after 1st cycle activation, as this is what real-world batteries with Li-rich cathodes will be based on. Activated Li-rich NMC is afflicted by several performance-limiting issues – namely voltage hysteresis, sluggish kinetics and voltage fade – and therefore we investigate whether they depend on the anionic/cationic redox interplay.

### —— Voltage hysteresis

The S-shaped-sloped electrochemistry of Li-rich NMC is stabilized after a few formation cycles in the voltage range 2.0–4.8 V. Charge-discharge profiles in this wide potential range display a large hysteresis (or path dependence), which is quasi-static, i.e. it does not vanish at near-zero currents and is therefore not due to kinetic polarization.[182,183,188,190,225,236] How this hysteresis depends upon the potential cut-offs was tested by progressive opening of voltage windows.

First, the charge voltage window is opened gradually (**Figure IV.8a**) starting each scan from 2.0 V. Charging beyond 4.1 V (red curves) leads to a noticeable hysteresis that lowers the discharge potential around mid-SoCs. The corresponding *dQ*/*dV* curves reveal that the oxidative capacity above 4.1 V (**Figure IV.8b**, area in red) is only partially recovered on reduction at high potential (till 4.0 V) whereas its remaining reduction happens at a significantly lower potential (below 3.6 V), as pointed by arrows. Since cationic oxidation nearly completes before 4.1 V on charge, the *dQ*/*dV* oxidation peak above 4.1 V is mainly charge-compensated by anionic oxidation. Because the reduction of

thus formed $O^{n-}$ is split between high (till 4.0 V) and low potentials (below 3.6 V), this causes voltage hysteresis. Moreover, such a change in the sequence of anionic redox also justifies the hysteresis loop seen with HAXPES for Ni's oxidation state vs. capacity (recall **Figure IV.7b**).

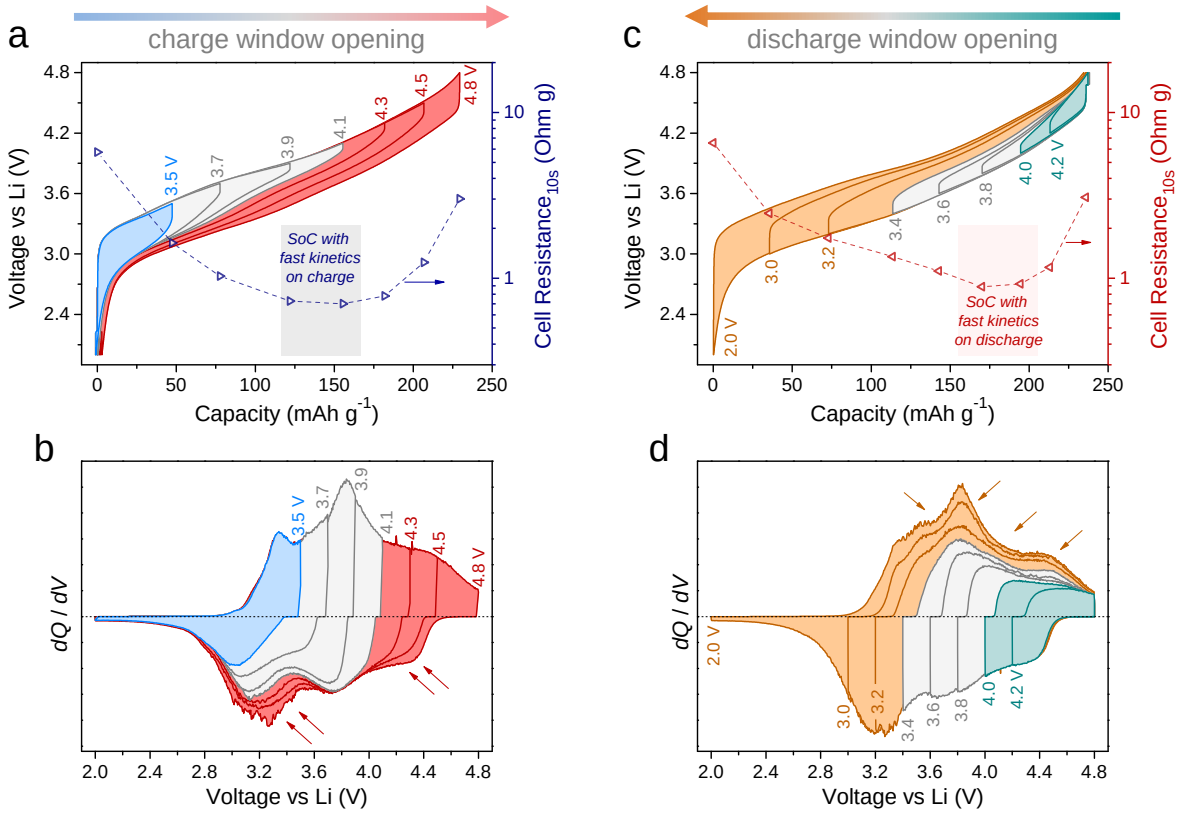


**Figure IV.8 | Hysteresis and path dependence in activated Li-rich NMC studied by voltage window opening.** (**a**) Voltage profiles and (**b**) corresponding *dQ*/*dV* curves as the charge window is opened stepwise from 2.0 to 4.8 V. Li-rich NMC is first activated by a few formation cycles in 2.0 to 4.8 V. All curves in **a** and **b** start on the charge direction from 2.0 V (at 0 mAh $g^{-1}$) and trace identical charging paths, whereas the discharges vary with cut-off voltages. Different regimes are highlighted with different colours. Hysteresis is triggered above 4.1 V as the capacity expected from high-potential charge (4.1 to 4.8 V, red) is split on discharge between high and low potentials, as marked by arrows in **b**. At each cut-off, the cell's resistance (right axis in **a**) is also estimated by Ohm's law applied to the voltage relaxation during 10 s of rest when switching from charge to discharge. The SoC is highlighted where resistance minimizes during charge. (**c**) Voltage profiles and (**d**) corresponding *dQ*/*dV* curves as the discharge window is opened stepwise from 4.8 to 2.0 V, in a fashion opposite the first experiment. All curves in **c** and **d** start on the discharge direction from 4.8 V (fully charged initially). The capacity expected from low potential discharge (3.4 to 2.0 V, orange) is spread from low to high potentials on charge, as marked by arrows. The SoC with cell-resistance (right axis in **c**) minimum on discharge path is shaded. Current density in these experiments was 40 mA $g^{-1}$.

Next, the discharge voltage window is sequentially opened starting each scan from 4.8 V (**Figure IV.8c**). It is necessary to discharge below 3.4 V (orange curves) for regaining the higher voltage on charge, as seen in the form of a large hysteresis around mid-SoCs. The corresponding *dQ*/*dV* curves show that the capacity reduced below 3.4 V (**Figure IV.8d**, area in orange) is oxidized throughout charging at low as well as at high potentials (marked by arrows). This *dQ*/*dV* reduction peak below 3.4 V is mainly due to anionic reduction, as also supported by the HAXPES-based finding that $Mn^{3+/4+}$ contribution remains minor. Moreover, as the subsequent oxidation of the discharge capacity below 3.4 V is spread across all potentials from 2.0 to 4.8 V, it agrees with the continuous trend of % $O^{n-}$ seen with HAXPES in **Figure IV.6b**.

Overall, since cationic redox has the same *dQ*/*dV* peak on either charge or discharge, i.e. the middle one around 3.8 V, it can be concluded that voltage hysteresis is associated with anionic redox which takes place asymmetrically between charge and discharge, with this asymmetry being much severer than what was observed in LRSO (recall **Figure III.13**)

## —— Electrochemical kinetics

As function of capacity, cell resistance (deduced from the first 10 seconds of relaxation) displays different trends on charge vs. discharge paths (**Figure IV.8a** and **Figure IV.8c** respectively), thus again emphasizing a path dependence. Resistance is quite large at low and high SoCs (notice the log scale) and undergoes minima in the middle that are situated at lower SoCs during oxidation in comparison to reduction. Interestingly, the SoCs with minimum resistance correspond to cationic redox around 3.8 V during both charge and discharge.

Next, the kinetics of different *dQ*/*dV* peaks was studied by recording the discharge profiles at various current densities (**Figure IV.9a**). On discharging from 4.8 V, the first *dQ*/*dV* peak (above 4.0 V) and the last one (below 3.6 V) are clearly sensitive to changes in current (**Figure IV.9b**), indicating the poor kinetics of anionic redox that takes place at these peaks. Furthermore, note that when discharging from 4.2 V instead of 4.8 V (**Figure A3.14**), the cationic redox peak around 3.8 V is not affected by current (meaning fast

kinetics), unlike the anionic peak below 3.6 V. To further investigate the role of positive-electrode in these results, three-electrode EIS was performed at different SoCs.

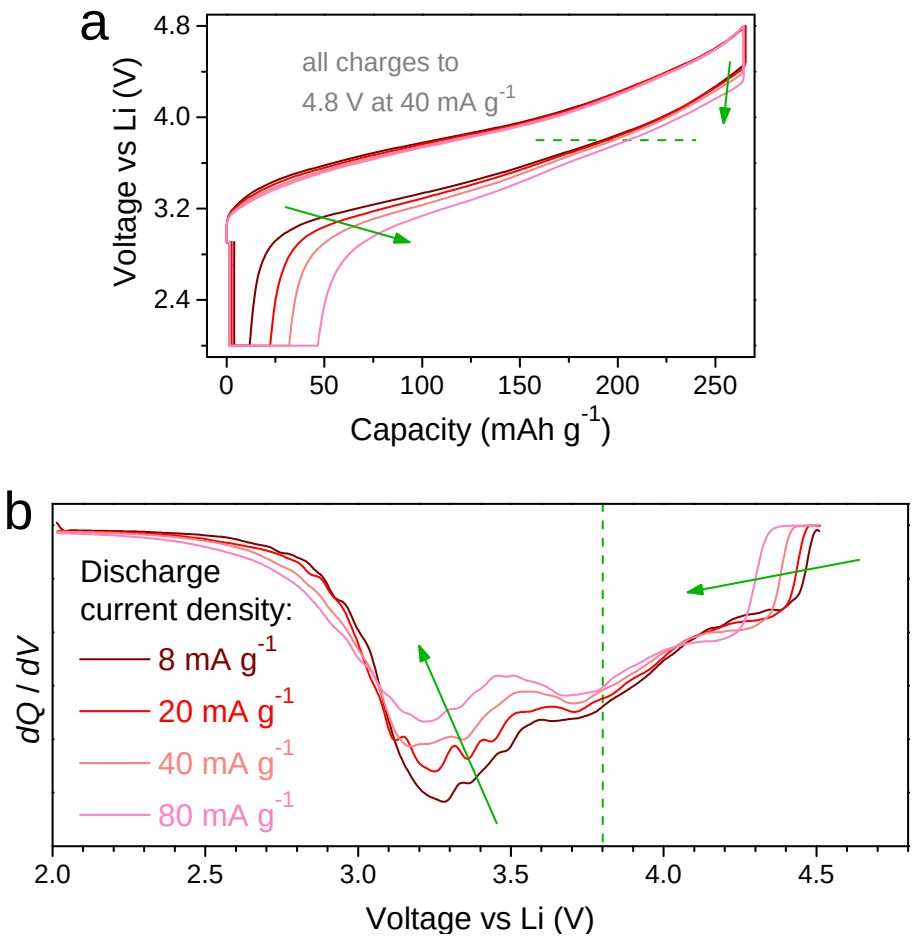


**Figure IV.9 | Sensitivity of voltage profiles as discharge current is increased.** The resulting (**a**) half-cell voltage profiles and (**b**) corresponding *dQ*/*dV* curves. Li-rich NMC is first activated by a few formation cycles in 2.0–4.8 V. Discharges end with a potentiostatic hold at 2.0 V, till the current decays to 2 mA $g^{-1}$, ensuring identical Li stoichiometry at the beginning of each scan. Arrows show the shift of profiles as current increases.

**Figure IV.10a** shows the voltage profile obtained via a GITT protocol which sets different SoCs where EIS was performed. To conveniently present the EIS Nyquist plots, they are separated into three groups each on charge ("ch-I", "ch-II", and "ch-III") and discharge ("dis-I", "dis-II", and "dis-III"), as demarcated in **Figure IV.10a**. An example of EIS fitting is given in **Figure IV.11**, with the changes in impedance during charge (black) and discharge (red) shown respectively in **Figure IV.12a** and **Figure IV.12b**.

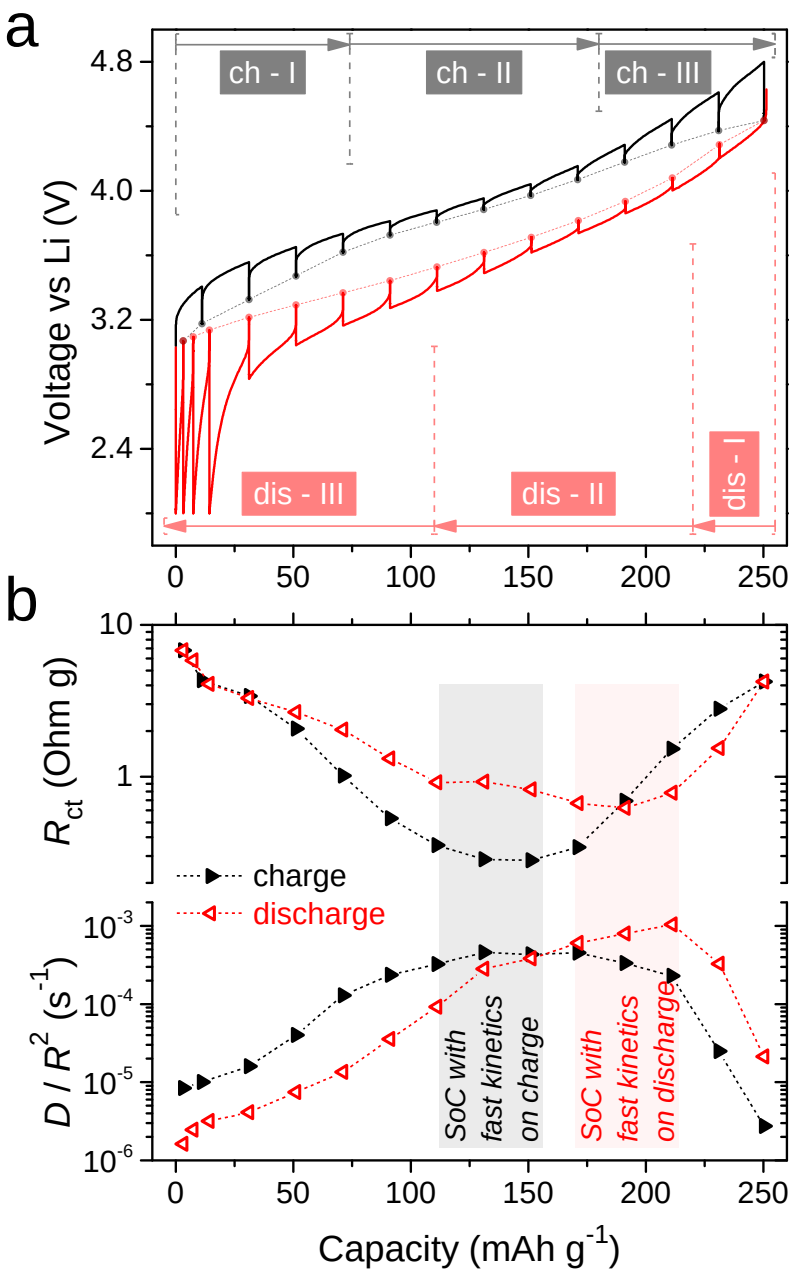


**Figure IV.10 | Electrochemical kinetics as a function of SoC for activated Li-rich NMC**. (**a**) The positive electrode's voltage profile in a three-electrode cell, recorded with a GITT protocol (40 mA $g^{-1}$ pulses with 4 hour rests for equilibration). Circles denoting OCVs are connected with dashed lines to trace a voltage hysteresis loop. Impedance is measured at each step after the 4 hour rest. For convenience, charge (black) and discharge (red) are divided into three segments each and the spectra are shown in **Figure IV.12**. (**b**) The variation of charge-transfer resistance and diffusion coefficient as a function of SoC on charge and discharge paths. $R_{ct}$ is the charge-transfer resistance and $D/R^2$ is the reciprocal of time constant associated with the Li diffusion process, where $D$ is the Li diffusion coefficient and $R$ is the particle radius. The SoCs with fastest kinetics (minimum $R_{ct}$ and maximum $D/R^2$) are different on charge and discharge paths, as shaded in **b** with black (charge) and red (discharge), respectively.

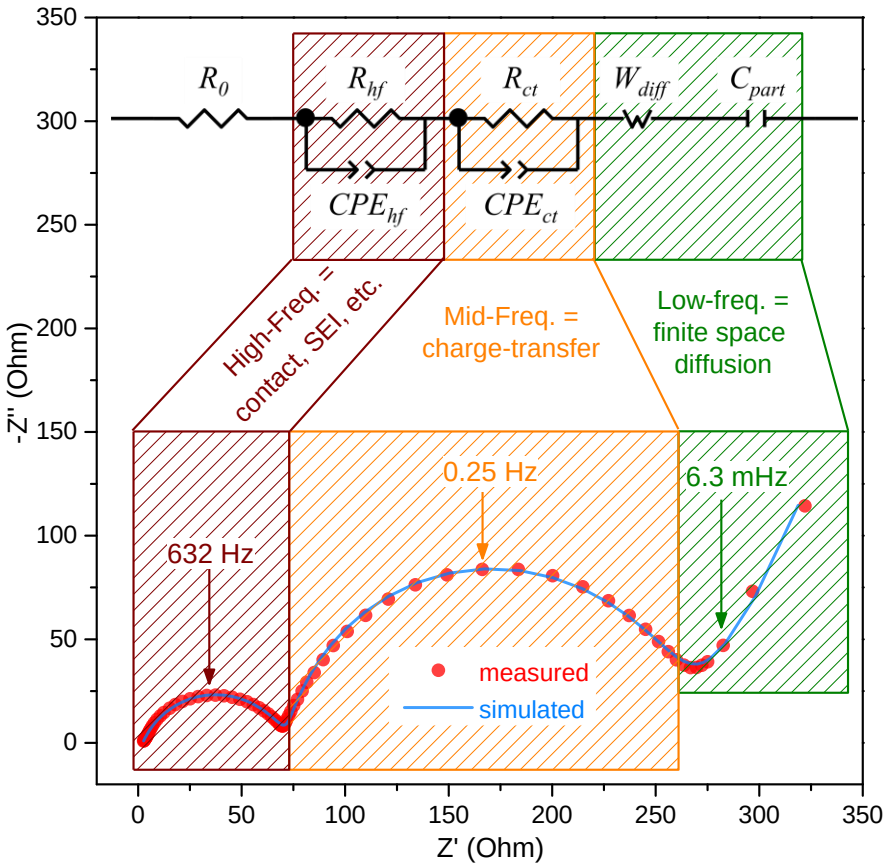


**Figure IV.11 | The fitting procedure of a typical EIS Nyquist curve.** The spectrum starts with a high-frequency arc representing interphase contacts and surface film etc., followed by a mid-frequency arc signifying interfacial charge-transfer, before ending with a Warburg tail typical of restricted solid-phase Li diffusion.[168,169,237] A good agreement is observed between measurements and simulations based on an equivalent circuit model that is shown on the top part. Features corresponding to different electrochemical phenomena are demarcated and some characteristic frequencies marked. The Fickian diffusion coefficient is calculated by applying a spherical single-particle model using the Warburg resistance obtained at low frequencies, where the imaginary and real parts of impedance show linearity with $f^{-0.5}$, where $f$ is the frequency.[237,238]

From the variation of spectra in **Figure IV.12,** it can be seen that the high-frequency arc (interphase contacts, surface film, etc.) stays constant and relatively small throughout, whereas significant changes take place in the mid-frequency arc (interfacial charge transfer) and the low-frequency Warburg tail (restricted solid-phase Li diffusion).[167–169] Impedance decreases in the beginning of charge path (‘ch-I’) and remains small in the middle SoCs (‘ch-II’), before increasing again at high SoCs (‘ch-III’).

A similar trend is seen on discharge. In fact, the large impedance rise at the end of discharge explains why $O^{n-}$ is not fully reduced at 2.0 V (recall **Figure IV.4**) thereby needing a potentiostatic hold to recover anionic capacity (recall **Figure A3.5**).

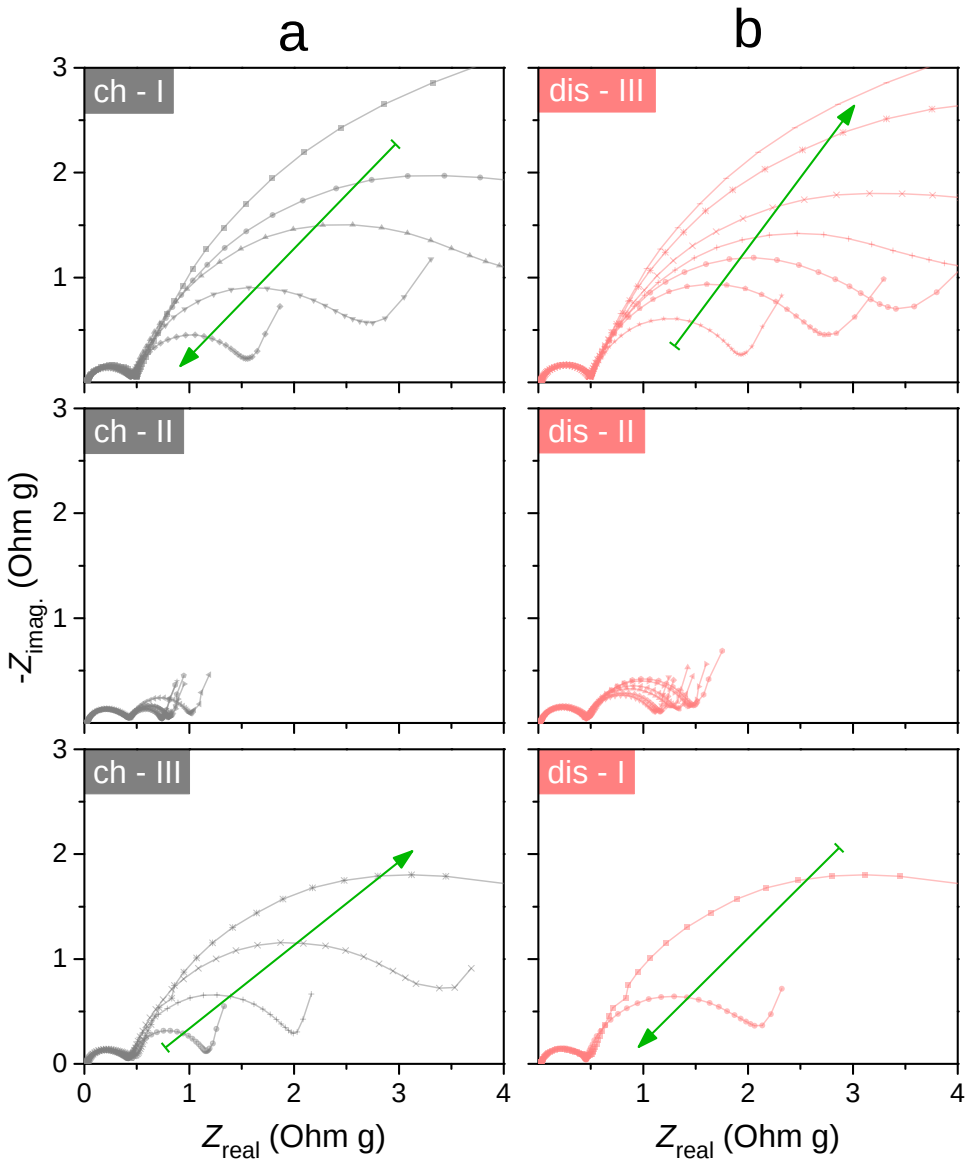


**Figure IV.12 | The evolutions of the positive electrode's EIS Nyquist plots.** For each segment demarcated in the previous **Figure IV.10**, the EIS plots are shown for (**a**) charge (black) and (**b**) discharge (red). The equivalent circuit model used to fit these spectra along with some characteristic frequencies is shown in the previous **Figure IV.11**.

An equivalent-circuit model (**Figure IV.11**) was used to quantify the charge-transfer resistance, $R_{ct}$ and the diffusion coefficient, $D/R^2$ (**Figure IV.10b**).[237,238] In

agreement with the trend seen earlier for simple cell resistance (**Figure IV.8a** and **Figure IV.8c**), electrochemical kinetics is the fastest in the middle (low $R_{ct}$ and high $D/R^2$), however this occurs at lower SoCs on charge and higher SoCs on discharge, a trend which follows the Ni oxidation state hysteresis loop (recall **Figure IV.7b**). Alternatively, when $R_{ct}$ and $D/R^2$ are plotted vs. potential (**Figure A3.15**), fast kinetics corresponds to the same OCVs (around 3.8 V) on both charge and discharge, which falls over the cationic redox potential range.

Overall, in light of this detailed electrochemical analysis, it can be concluded that cationic redox has faster kinetics than anionic redox, such that moving away from cationic redox into the anionic redox regime towards higher and lower SoCs (or potentials) causes $R_{ct}$ to rise by more than one order of magnitude and $D/R^2$ reduces by more than two orders.

## —— Voltage fade

To study the effects of long-term cycling on voltage fade, a controlled ageing experiment was performed, similar to the one in Chapter II for LRSO. Three identical half-cells, after a few initial formation cycles, were charged and discharged between 2.0 to 4.8 V, but with long storage periods in every alternate cycle (24 hours under open-circuit). Everything else being constant, the only difference between the three cells was the SoC at which this storage step was repeatedly performed, i.e. the three cells were cycled with 24 hour storage either at 0%, 50% or 100% SoC respectively. Not surprisingly, all three cells show a fade in average cell voltage, defined as the mean of average charge and discharge voltages (**Figure IV.13a**). However, voltage fade is the most severe for the cell that spends its storage periods while being fully charged, i.e. with fully oxidized oxygen. Consequently, the $dQ/dV$ profiles (**Figure IV.13b**) that are initially identical (cycle #1), start deviating as cycling proceeds. The growth of low potential redox peaks around 3.0 V can be seen in the mid of ageing (#36) and quite prominently at the end of the experiment after several cycles (#72) for the cell with storage at 100% SoC. We also monitored the impedance growth with ageing that takes place in all cells. However, there is no detrimental effect of storage at 100% SoC, unlike what is shown above for voltage fade. Overall, this ageing experiment concludes that spending more time in fully charged state,

i.e. with highly oxidized oxygen, promotes voltage fade in Li-rich NMC but does not particularly affect impedance growth, which rather seems to be a function of cycle number.

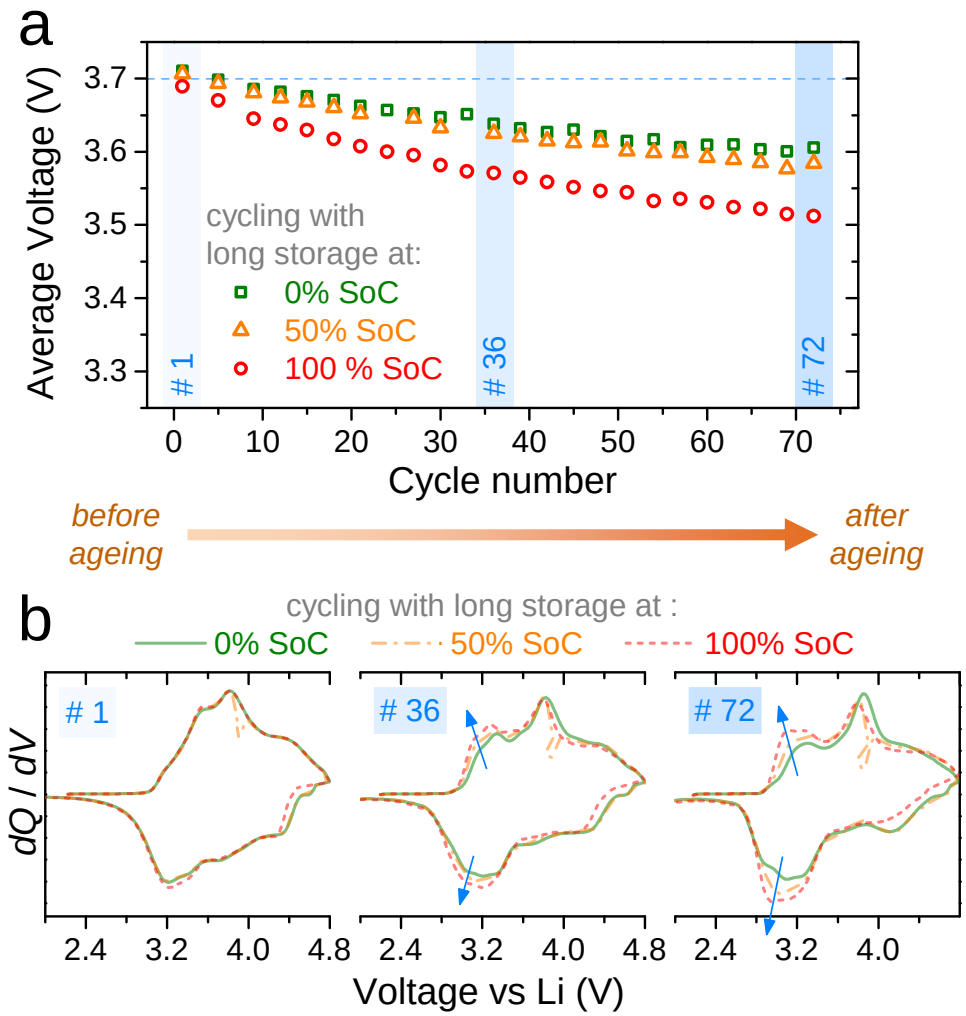


**Figure IV.13 | Role of anionic redox on voltage fade over long-term ageing.** (**a**) Effect of storage SoC on voltage fade in a controlled ageing experiment of three Li-rich NMC half-cells. The cells are identically assembled and activated, after which the same cycling conditions are imposed on the three with only one variable differing, which is the SoC where each cell rests during cycling. 'Average voltage' is defined as the mean of average charge and discharge voltages. Cycling window is 2.0–4.8 V at 40 mA $g^{-1}$ with long (24 hour storage) rest periods in every alternate cycle. (**b**) The corresponding *dQ*/*dV* profiles of the above test in the beginning (cycle #1), middle (#36) and end (#72) of ageing. Arrows show the ageing-related growth of low potential *dQ*/*dV* peaks. One set of curves has small distortions on charge because of this cell's resting step at 3.9 V (50% SoC).

# IV*a*.3 – Discussion

Via detailed spectroscopic and electrochemical analyses of $Li_{1.2}Ni_{0.13}Mn_{0.54}Co_{0.13}O_2$ (Li-rich NMC) cathodes, we have revealed (*i*) their charge-compensation mechanism from anionic/cationic redox, and (*ii*) how the interplay between these two processes governs application-wise important challenges, such as kinetics, hysteresis, and voltage fade. Next, we connect our results with published knowledge in this area.

The two-stepped 1$^{st}$ charge voltage profile, typical for Li-rich cathodes, starts with a classical cationic redox step till 4.4 V, which is fully reversible[181–183,225,239], followed by the 4.5 V activation plateau where lattice $O^{2-}$ oxidizes to $O^{n-}$ ($n$ < 2). We have unambiguously spotted $O^{n-}$ in the bulk thanks to the high probe depth of HAXPES (~29 nm, 120 layers). HAXPES characterization of anionic redox is repeatable, quantitative and tuneable from surface to bulk, which makes this technique indispensable for studying charge-compensation mechanisms, especially if *operando* mode is developed in future.[230]

A simple charge balance suggests that $n$ = 1.24 ± 0.07 in the charged sample for 33 ± 3% $O^{n-}$ to compensate for the capacity of 0.5 $e^-$ per formula unit (157 mAh $g^{-1}$) that was proposed by Luo *et al*.[103] This value of $n$ appears to be insufficient to make true peroxide $(O–O)^{2-}$, contrasting a new Raman spectroscopy-based study[240], although relying on controversial bond-distance estimation, that came out after our work got published. The physico-chemical nature of $O^{n-}$ still needs to be investigated on a fundamental basis. On further cycling, HAXPES demonstrated the reversibility of anionic reactivity spread in a wide voltage range from 2.0 to 4.8 V. Although such reactivity is beneficial for capacity enhancement, the preceding anionic activation plateau unavoidably causes (*i*) some irreversible oxygen loss[103,116,223,241] and (*ii*) permanently modifies the electrochemical profile, likely due to oxygen network distortion and rearrangement that is challenging to experimentally visualize. Designing cathodes that can avoid these irreversible changes and can show complete reversibility and stability of anionic redox from the very beginning has theoretically been shown to be a difficult task with 3*d* TM-based layered oxides.[110,123]

Li-rich NMC's S-shaped-sloped electrochemistry after 1$^{st}$ cycle activation consists of several $dQ/dV$ peaks, which we have now properly assigned by combining spectroscopic and electrochemical evidences, as summarized in **Figure IV.14**.

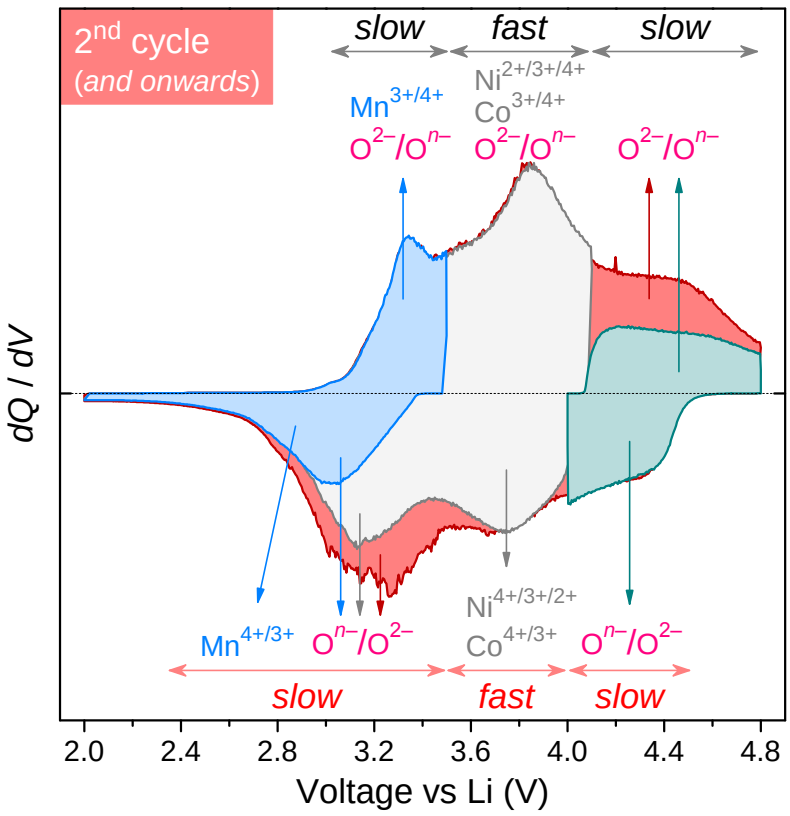


**Figure IV.14 | Summary of activated Li-rich NMC's charge-compensation mechanism and electrochemical kinetics.** Key voltage window opening experiments in **Figure IV.8** are superimposed on each other, keeping the same colours as before. Electrochemical kinetics is classified as either 'slow' or 'fast' based on impedance analysis in **Figure IV.10**. The small $Mn^{3+/4+}$ contribution is restricted to low potentials (shaded blue) with some concomitant anionic activity. Charging to 4.1 V (shaded grey) leads to the peak at 3.8 V mainly from cationic oxidation ($Ni^{2+/3+/4+}$ and $Co^{3+/4+}$) along with some anionic contribution. If charging is limited to 4.1 V, the discharge curve (shaded grey) shows two peaks, respectively due to cationic (3.8 V peak) and anionic (3.2 V peak) reductions. If further charging is continued to 4.8 V (shaded red and green), it is mainly charge-compensated by anions and then the corresponding discharge capacity is split at high potential (shaded green) and low potential (3.2 V reduction peak, shaded red), thus causing the large voltage hysteresis. Note that fast kinetics accompanies cationic redox on both charge and discharge.

Cationic redox occurs at nearly the same potentials during either charge or discharge, such that the middle *dQ*/*dV* peak around 3.8 V shows $Ni^{2+/3+/4+}$ and $Co^{3+/4+}$ activity and the lowest potentials have a minor $Mn^{3+/4+}$ capacity. In contrast, anionic redox proceeds asymmetrically between charge and discharge. On oxidation, anionic redox is spread from 2.0 to 4.8 V with a large contribution above 4.1V. While on discharge, anionic

reduction at high potential is small and the remaining reduction occurs at much lower potentials (peak below 3.6 V). This resolves several charge-compensation-related discrepancies in literature, some of which were called for by preceding investigations[242,243] and reviews[49,222]. For example, the first *dQ*/*dV* discharge peak (4.8 to 4.1 V) is not from Co reduction as many studies assumed, but rather due to anionic redox. Moreover, this peak is also exhibited by Co-free Li-rich compositions[164,188,239,243,244], which further confirms our assignment. More important is the *dQ*/*dV* reduction peak below 3.6 V, which is mainly charge-compensated by anionic redox and not by $Mn^{3+/4+}$, whose contribution is very small. Note that our claims got further strengthened by a new soft-XAS-based study[107] that appeared online in the same week this work got published. Interestingly, some cation-disordered materials also appear to display anionic redox activity at low potential on discharge.[75,118] Concerning Mn, we later carried out a follow-up study on quantifying the evolution of $Mn^{3+/4+}$ contribution over long cycling, as presented in the Part - IV*b* -.

After the 1st cycle, a large quasi-static hysteresis of ~ 500 mV has been reported even at C/300[190], which negatively affects energy efficiency and complicates SoC management. It is now clear, as stated above, that the anionic/cationic redox sequence differs on charge vs. discharge, resulting in path-dependence and hysteresis. Consistent with the anionic/cationic sequence hypothesis, our Ni $2p_{3/2}$ HAXPES results show a hysteresis loop in Ni oxidation state vs. capacity (**Figure IV.7b**). However, we could not observe a complementary hysteresis loop for % $O^{n-}$ (**Figure IV.6b**) in a sense opposite to that of Ni, as one would expect for charge balancing. Besides, it also remains unanswered why anionic redox occurs in a wide potential range but differently on charge vs. discharge. One possible explanation could be nested in changes of *n* with SoC, implying different types of $O^{n-}$ that can only be unambiguously distinguished with very sharp energy resolutions, thus calling for technical improvements on HAXPES. Previous works suggested a structural origin for hysteresis, i.e. a back-and-forth cationic migration resulting in different thermodynamic potentials during Li removal vs. insertion.[165,187,190,191] Although this hypothesis is valid, as further confirmed by a new study[107], it must be recalled that structural distortion / rearrangements are in fact a consequence of instability induced by anionic oxidation. Nevertheless, the hysteresis mechanism poses a fundamental challenge that could greatly benefit from *operando* (hence dynamic) experiments as well as phenomenological models. Recently, *operando* EPR[245]

and *operando* NMR[246] were indeed attempted for Li-rich NMC, but these studies had poor electrochemical profiles under *operando* conditions. Mastering *operando* cells to replicate regular coin/Swagelok cells, like we did in Chapter III, is therefore a pre-requisite for being able to use such methods for understanding voltage hysteresis.

The larger hysteresis in anionic redox d*Q*/d*V* peaks compared to the symmetric cationic redox for Li-rich NMC (**Figure IV.14**) is reminiscent of the decoupled d*Q*/d*V* profiles of LRSO (recall **Figure III.13**), with in fact such hysteresis being more severe for Li-rich NMC. This similarity between the 'model' and the 'practical' materials is very important and suggests that the underlying mechanism of anionic redox could be fundamentally different from cationic redox and responsible for the large voltage hysteresis. This is exactly what Chapter V will later reveal.

Apart from hysteresis, poor rate-capability has been another barrier in the success of Li-rich NMC, as the large impedance growth at high and low SoCs is disadvantageous, respectively, for applications requiring fast charging and discharging.[164,228,229,247]. Moreover, our results highlight the contrasting electrochemical kinetics of cationic and anionic redox, wherein the latter displays sluggish charge-transfer and diffusion; a situation alike the one previously reported for the 'model' $Li_2Ru_{0.75}Sn_{0.25}O_3$ in Chapter II.[119,194] At this stage, the fundamental atomic-scale reasons why oxygen redox is sluggish is still up for debate and the possible correlation between voltage hysteresis and sluggish kinetics cannot be ruled out either.

Lastly for voltage fade, we have systematically revealed the detrimental role of time spent with highly oxidized oxygen. Thus, the stability of $O^{n-}$ is very important for preventing permanent reorganizations, such as irreversible cationic migrations, oxygen loss by recombination or nucleophilic (electrolyte) attack, and oxygen lattice modification. Low potential anionic redox is exciting by being more robust against voltage fade[179], and hence could be a new focus for materials design.

# IV*a*.4 – Conclusions from this Part

Real-world success of anionic redox necessitates the complete mastering of this electrochemistry's kinetics, thermodynamics, and stability. Herein, we proved oxygen redox reactivity in the archetypical Li- and Mn-rich layered cathode (Li-rich NMC) through bulk-sensitive synchrotron-based HAXPES spectroscopy, and elucidated its complete anionic/cationic charge-compensation mechanism to provide a full understanding of its *dQ*/*dV* curve. Furthermore, via various electroanalytical methods, we answered how the anionic/cationic interplay governs application-wise important issues – namely sluggish kinetics, large hysteresis, and voltage fade – that afflict these promising cathodes despite widespread industrial and academic efforts aimed towards commercialization. We found that cationic redox is kinetically fast and without hysteresis, unlike sluggish anions which furthermore show hysteretic oxidation vs. reduction potentials. Additionally, more time spent with fully oxidized oxygen promotes voltage fade.

Quite remarkably, the detailed electrochemical investigation of the 'model' Li-rich cathode $Li_2Ru_{0.75}Sn_{0.25}O_3$ (LRSO) in Chapter II had already warned about these side effects. Such a convergence of findings across different members of the Li-rich family underscores the importance of bridging the learnings between 'model' and 'practical' systems. This approach is crucial, since practical solutions to mitigate the above-mentioned issues can only come from fundamental global insights.

A key highlight of this study was the clear spectroscopic demonstration of anionic redox activity in Li-rich NMC. However, doubts still remained about the sustained activity of anionic redox over long cycling. We therefore extended the HAXPES characterization developed herein to long-cycled samples, as summarized in the next Part of this Chapter.

# Part - IV*b* - ‡‡

This Part is a focused HAXPES investigation of the evolution of redox processes in Li-rich NMC over long cycling.

## IV*b*.1 – Background and Motivation

High specific energy, along with the limited use of scarce cobalt and nickel, make the Li-rich NMC family a strong competitor against today's Ni-based layered oxides[21] (NMCs) that are derived from $LiNiO_2$. However, for Li-rich cathodes to stay relevant in this duel[248], several obstacles need to be eliminated – namely insufficient electrode density[124], large voltage hysteresis[106,182], sluggish kinetics[106,194], and voltage decay upon ageing[165]. The previous part explored the role of cationic/anionic redox interplay concerning several of the above issues. This part focuses mainly on the ageing behaviour of Li-rich NMC, particularly on how the anionic/cationic redox activities evolve over cycling, which is essential for the fundamental understanding of degradation mechanisms.

Most reports on anionic redox in these materials were limited to the investigation of charge-compensation in the first couple of cycles.[102–107,153,217] Although a recent study reported redox evolutions over long cycling, it relied on transition metals' spectra since the direct quantification of oxygen spectra was not possible.[249] Among the spectroscopic methods that have been adopted by the battery community specifically for the direct characterization of oxygen redox (listed in previous **Figure I.14**)[248], two particular classes of techniques, based respectively on soft X-ray absorption spectroscopy (soft-XAS) and X-ray photoemission spectroscopy (XPS), have been particularly successful in demonstrating oxygen redox activity in Li-rich NMC, as summarized below.

‡‡ Part - IV*b* - of this Chapter is based on the following research article that I co-authored :

**Assat, G.**, Iadecola, A., Foix, D., Dedryvère, R. & Tarascon, J.-M. Direct quantification of anionic redox over long cycling of Li-rich NMC via hard X-ray photoemission spectroscopy. ***ACS Energy Letters***, 3 (11), 2721–2728 (**2018**). (https://doi.org/10.1021/acsenergylett.8b01798)

To recall briefly, initial soft-XAS measurements at the O K-edge[103,104,153] showed changes in the pre-edge intensity that were assigned to changes in the electronic state of bulk oxygen. This assignment was further strengthened by switching later to transmission mode as well as by obtaining O K-edge RIXS maps.[107,153,155]. RIXS was also used to show that oxygen remains active after long cycling, but further quantification could not be performed.[107] Concerning XPS-based results on the other hand, we overcame this surface-sensitivity shortcoming of regular XPS by moving to synchrotron-based hard X-ray photoemission spectroscopy (HAXPES) for accessing bulk information and systematically explored in Part - IV*a* - the complete anionic/cationic charge compensation mechanism of Li-rich NMC in the first two cycles.[106]

The results from both types of direct oxygen spectroscopies have converged[106,107] – an important mutual conclusion being, apart from the reversibility of oxygen redox, the correct assignment of the differential capacity (d*Q*/d*V*) discharge peak at low potential to anionic redox (recall **Figure IV.14**). The remaining task now is to investigate the effect of ageing, for which we extend herein our investigation of Li-rich NMC using HAXPES over long cycling. Taking advantage of this technique's bulk-sensitivity and quantitative nature[230], we investigate the reversibility of oxygen redox during ageing and also quantify the evolution of cationic redox processes, especially $Mn^{3+/4+}$. Our results present optimistic insights on the cyclability of anionic redox, and further elucidate the ageing mechanism of these practically important materials.

## IV*b*.2 – Results

Similar to the previous Part, $Li_{1.2}Ni_{0.13}Mn_{0.54}Co_{0.13}O_2$ (Li-rich NMC) powders, mixed with 10 % conductive carbon, were used as positive electrodes in Swagelok-type Li half-cells. No polymeric binders were used in order to avoid decreasing the intensity of XPS signals from the active material. The electrodes exhibit, as per the 1$^{st}$ cycle voltage vs. composition curve recorded at 20 mA $g^{-1}$ (**Figure IV.15a**), a staircase-like charging process followed by a sloped discharge in which the capacity is 270 mAh $g^{-1}$. Such an electrochemistry is typical for a good batch of Li-rich NMC.

## ○ Effect of long cycling on anionic/cationic redox processes

A series of identical cells was prepared and after the first activation cycle mentioned above, they were continued at 40 mA $g^{-1}$ (circa C/6) for making long-cycled samples with gradually increasing levels of ageing. Such a relatively low C-rate is expected to uniformly utilize the particles and was chosen to simulate realistic ageing conditions, in contrast to fast cycling (e.g. at 1C) that may lead to non-uniform ageing besides inflating the total cycle number[107] and lowering the overall run-time which is known to be an important variable concerning the degradation of Li-rich NMC[106,179]. Fully charged and discharged samples in cycles 2, 13, 57, and 72 were thus obtained for *ex situ* HAXPES analysis, extending our previous study in Part - IV*a* - on only the first two cycles.[106] Note that a lower current of 20 mA $g^{-1}$ was used in the final cycle for maximizing the electrode utilization (see Methods in Appendix A3 for further sample preparation details). **Figure IV.15b** shows the capacity retention for the longest cycled cell (at 40 mA $g^{-1}$, circles) along with the decay of average voltage (triangles). The same graph also shows the respective capacities obtained during the final sample preparation cycles (at 20 mA $g^{-1}$, stars).

It is clear from **Figure IV.15b** that the main issue concerning the cyclability of this class of materials is the gradual fading of voltage rather than capacity retention. The voltage instability can also be visualized via the evolution of voltage profiles and their respective d*Q*/d*V* plots in **Figure IV.15c–e**. These panels also highlight the adequate repeatability of Swagelok-type cells having powder electrodes over the cycling durations studied herein.

To study the evolution of cationic and anionic redox processes over cycling, the samples were characterized with HAXPES[††]. As schematized in **Figure IV.16** for O 1*s* photoelectrons, the use of high energy synchrotron radiation leads to probe depths of up to 29 nm at 6.9 keV and an even higher 40 nm at 10.0 keV, making HAXPES a bulk-sensitive technique. The estimation of probe depths was already explained with **Table IV.1**.

[††] **HAXPES** was performed in collaboration with Rémi Dedryvère (IPREM, Pau). Rémi, Antonella Iadecola (RS2E, CNRS), and myself performed the HAXPES experiments. Rémi carried out the spectra fitting. Dominique Foix (IPREM, Pau) recorded the complementary **in-house XPS** spectra and performed the fits.

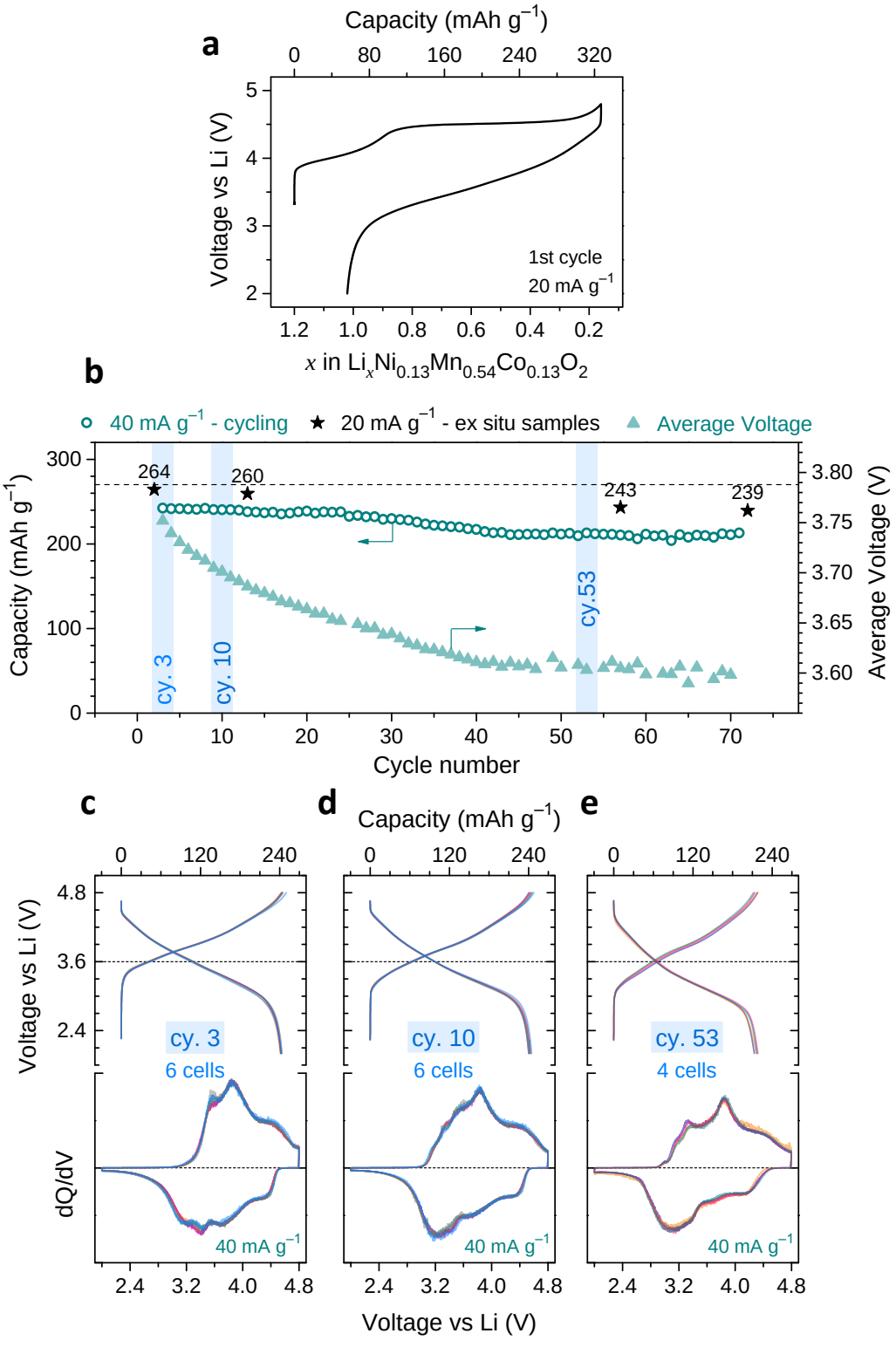


**Figure IV.15 | Electrochemical performance of Li-rich NMC.** (**a**) Voltage vs. composition profile in the first cycle. (**b**) Capacity retention (left axis) and average voltage (right axis) over long cycling. 'Average voltage' is defined as the mean of the average charge and discharge voltages. The stars with corresponding values denote the capacities obtained during the *ex situ* sample preparation cycles. Voltage profiles and d*Q*/d*V* plots are shown for the six cells in cycle 3 (**c**) and 10 (**d**), and for the four cells in cycle 53 (**e**).

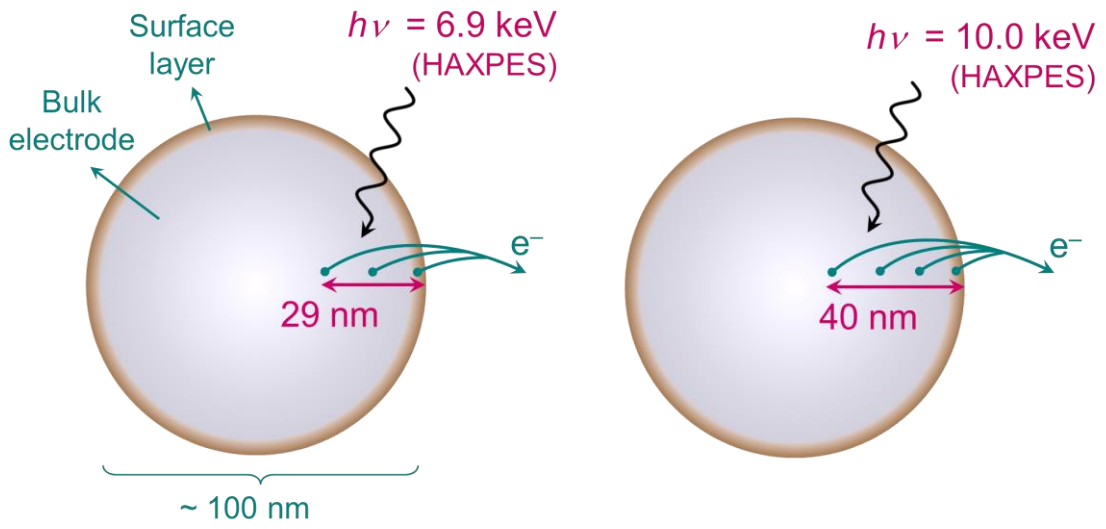


**Figure IV.16 | Schematic illustration of probe depths for O 1*s* (based on the escaping of photoelectrons) using bulk-sensitive HAXPES.**

## —— Anionic redox evolution

The O 1*s* HAXPES spectra are shown in **Figure IV.17a** for samples charged to 4.8 V and **Figure IV.17b** for samples discharged to 2.0 V as the cycle number increases, allowing us to directly monitor the changes in electronic state of lattice oxygen. We have previously shown in Part - IV*a* - that the O 1*s* spectrum after the first charge (**Figure IV.17a**, top) is characterized by an asymmetric main peak, which can be modelled by two types of lattice oxygen environments[106]. These are, respectively, classical lattice $O^{2-}$ at a binding energy (BE) of 529.5 eV and oxidized lattice oxygen $O^{n-}$ ($n < 2$, pink component at BE of 530.5). Furthermore, their ratio can be reliably quantified (% $O^{n-}$ = 33 %, **Figure IV.18**) thanks to HAXPES since it leads to a diminution of polluting signals from oxygen-containing surface deposits. These surface species, which arise from electrolyte and salt decomposition at the cathode electrolyte interface, are usually observed at BEs from 531.5 to 534 eV[213–215] and are represented by the low intensity grey peaks in **Figure IV.17**. An additional satellite peak corresponding to the active material is also overserved (yellow) at BE = 535 eV. The main peak becomes symmetric upon discharge (**Figure IV.17b**, top), thus signifying the electrochemical reduction of $O^{n-}$ to give back $O^{2-}$. Additionally, the satellite peak also disappears. For comparison, the O 1*s* spectra of the same samples were recorded in standard laboratory conditions (in-house XPS with $h\upsilon$ = 1.487 keV, **Figure**

**A3.16** in the Appendix). These spectra display, as expected at lower photon energy, much higher contributions of surface species relative to the lattice $O^{2-}$ and $O^{n-}$ components.

The 6.9 keV HAXPES spectrum of the charged sample after cycle 2 is very similar to cycle 1, but with slightly less amount of oxidized oxygen (% $O^{n-}$ = 28 %, **Figure IV.18**). $O^{n-}$ reduces back to $O^{2-}$ after the second discharge. This back-and-forth appearance of $O^{n-}$ on charge and its disappearance on discharge demonstrates the reversibility of the anionic redox process. Note that the results obtained on cycle 2 in this study are nearly identical to our previous report in Part - IV*a* -, thus underscoring the high reproducibility in sample preparation and analysis. By increasing the photon energy from 6.9 keV to 10.0 keV herein, a further suppression of the signal from surface species is achieved for both the charged and discharged samples. Although the $O^{n-}$ shoulder at BE 530.5 eV is visually less evident in the charged state due to the slightly lower energy resolution at 10.0 keV, the value of % $O^{n-}$ remains unchanged.

Over long cycling, $O^{n-}$ continues to be observed in the charged samples (**Figure IV.17a**), without any drastic decline in the value of % $O^{n-}$ that stays at 25, 23, and 23 % in cycles 13, 57, and 72 respectively (**Figure IV.18**). $O^{2-}$ reappears on the respective discharges (**Figure IV.17b**), with % $O^{n-}$ always reducing to 9 % (**Figure IV.18**). Note that the contribution of surface species tends to increase after long cycling, especially on the discharged samples, which was further confirmed by in-house XPS that offers higher surface sensitivity (O 1*s*, C 1*s*, and F 1*s* spectra in **Figure A3.16**, **Figure A3.17**, and **Figure A3.18**). The increase of such electrolyte / salt decomposition products upon cycling is expected to cause impedance rise and hence capacity fade under fixed current cycling. However, the exact quantification of these surface effects is not the main aim of the present study. Interestingly, the 535 eV satellite also continues to appear on charge and disappear on discharge in all pairs of long-cycled samples characterized with HAXPES. Although the fundamental origin of this satellite is yet to be understood, we believe that it might be concomitant with the $O^{n-}$ species, especially because the same phenomenon is observed in $Li_{2-x}Ru_{0.75}Sn_{0.25}O_3$ (recall **Figure IV.4**).[119] Further research is therefore needed to conclude whether the satellite can be ascribed as a general spectroscopic signature of oxidized oxygen.

On the basis of the above results that are summarized in **Figure IV.18**, it can be concluded that reversible oxygen redox activity stabilizes after a few cycles and continues

to persist over long cycling in Li-rich NMC. This is an optimistic finding considering real-world application of anionic redox.

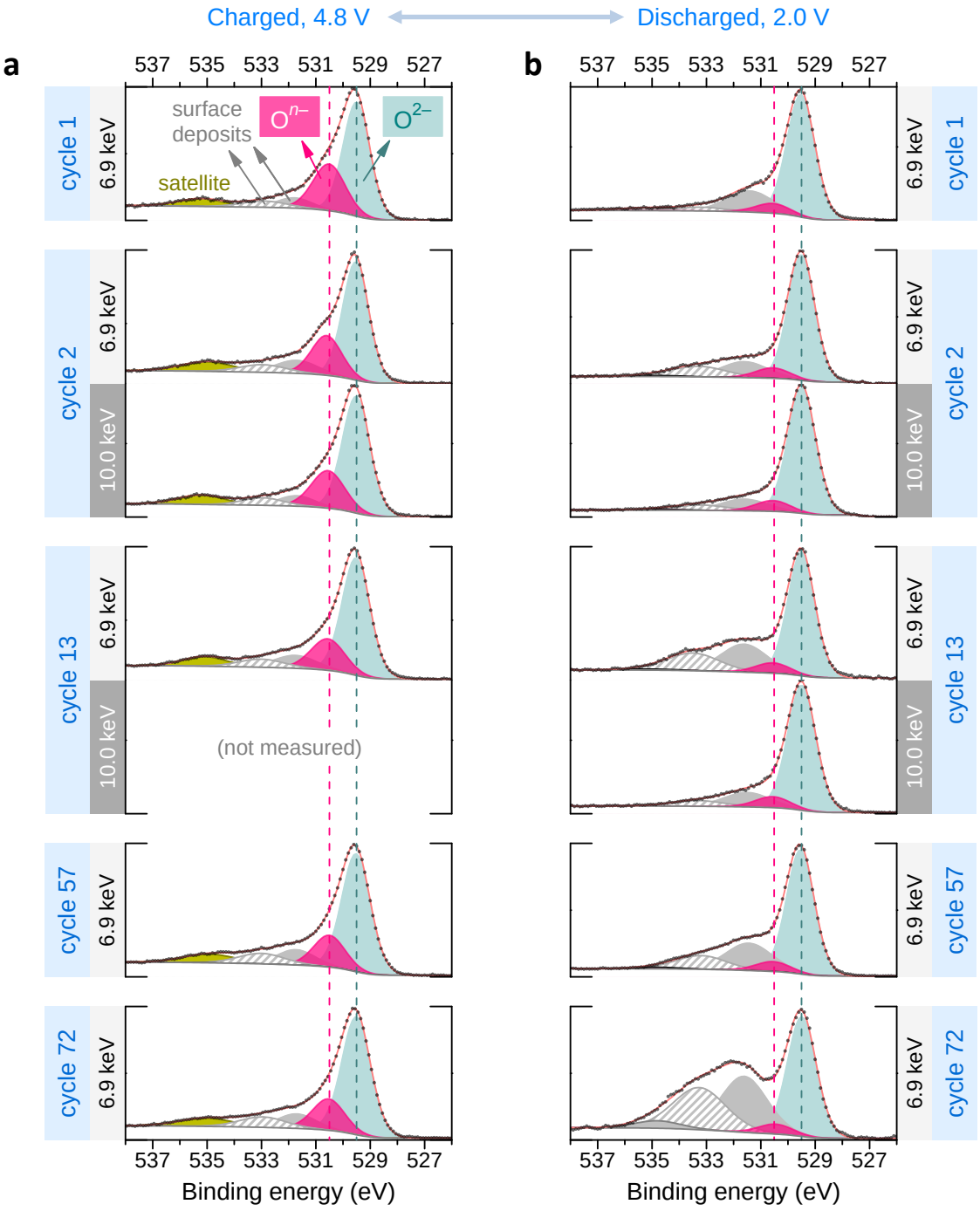


**Figure IV.17 | Evolution of the O 1*s* HAXPES spectra over long cycling.** Spectra recorded at 6.9 keV and 10.0 keV photon energies along with their respective fits for (**a**) the samples charged to 4.8 V and (**b**) discharged to 2.0 V with gradually increasing cycle numbers. The spectra for cycle 1 are the same as **Figure IV.4a**.

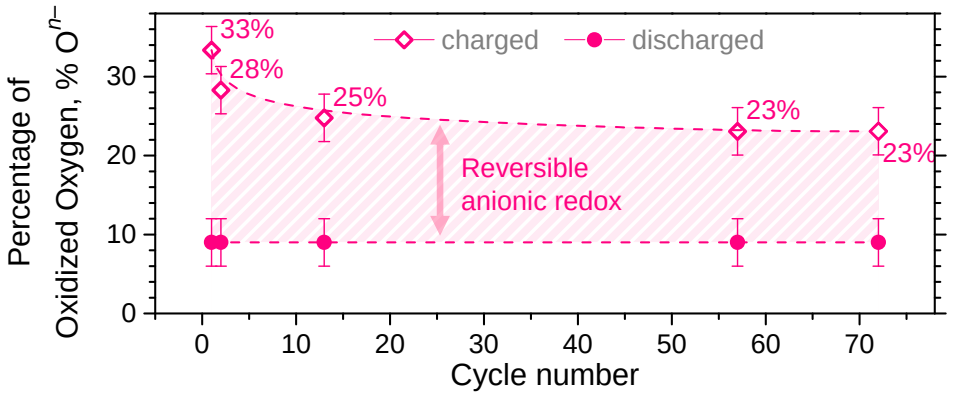


**Figure IV.18 | Quantification of the reversible anionic redox process.** The percentage of oxidized oxygen, or % $O^{n-}$ ($n < 2$), is plotted as a function of cycle number. It is based on the ratio of the amounts of $O^{n-}$ with respect to ($O^{2-}$ + $O^{n-}$) that are estimated from the fits using integrated peak areas. % $O^{n-}$ is 9 % for all discharged samples. The absolute error bars of ± 3 % arise from the uncertainty in the fitting procedure that is described in detail in the preceding Part - IV*a* -.

## —— Cationic redox evolution

Turning now to the transition metals for understanding cationic redox, the Mn $2p_{3/2}$ HAXPES spectra recorded at 6.9 keV are shown in **Figure IV.19a** for the charged and **Figure IV.19b** for the discharged samples. The as-synthesized material is in $Mn^{4+}$ state, which cannot be further oxidized on charge. We have previously shown with 3.0 keV HAXPES that on the subsequent discharge to 2.0 V, only a partial reduction of $Mn^{4+}$ takes place giving only 10 % $Mn^{3+}$ after the first discharge (recall **Figure IV.7d**).[106] Herein, the use of 6.9 keV provides a higher probing depth as well as a better energy resolution (due to the change of monochromator). The spectrum after charging in cycle 2 (**Figure IV.19a**, top) is again characteristic of $Mn^{4+}$. On the second discharge (**Figure IV.19b**, top), a clear shoulder appears on the lower BE-side of the main peak, which can be ascribed to 11 % $Mn^{3+}$ (purple component).[250] The spectra of the charged samples do no evolve much over long cycling, except for a broadening of the fine doublet structure of the main peak that may be because of gradually increasing disorder. Therefore, all spectra of charged samples are characteristic of $Mn^{4+}$. On the other hand for the discharged samples, the $Mn^{3+}$ shoulder gradually becomes more apparent with cycling, albeit the signal from $Mn^{4+}$ is still predominant. It can thus be concluded that $Mn^{3+/4+}$ redox activity gradually augments over cycling, with $Mn^{3+}$ amount on discharge reaching 14, 21, and 22 % in cycles 13, 57, and 72

respectively, as summarized in **Figure IV.19c**. This systematic quantification is utilized later in this work for determining the capacity contributions from each redox process.

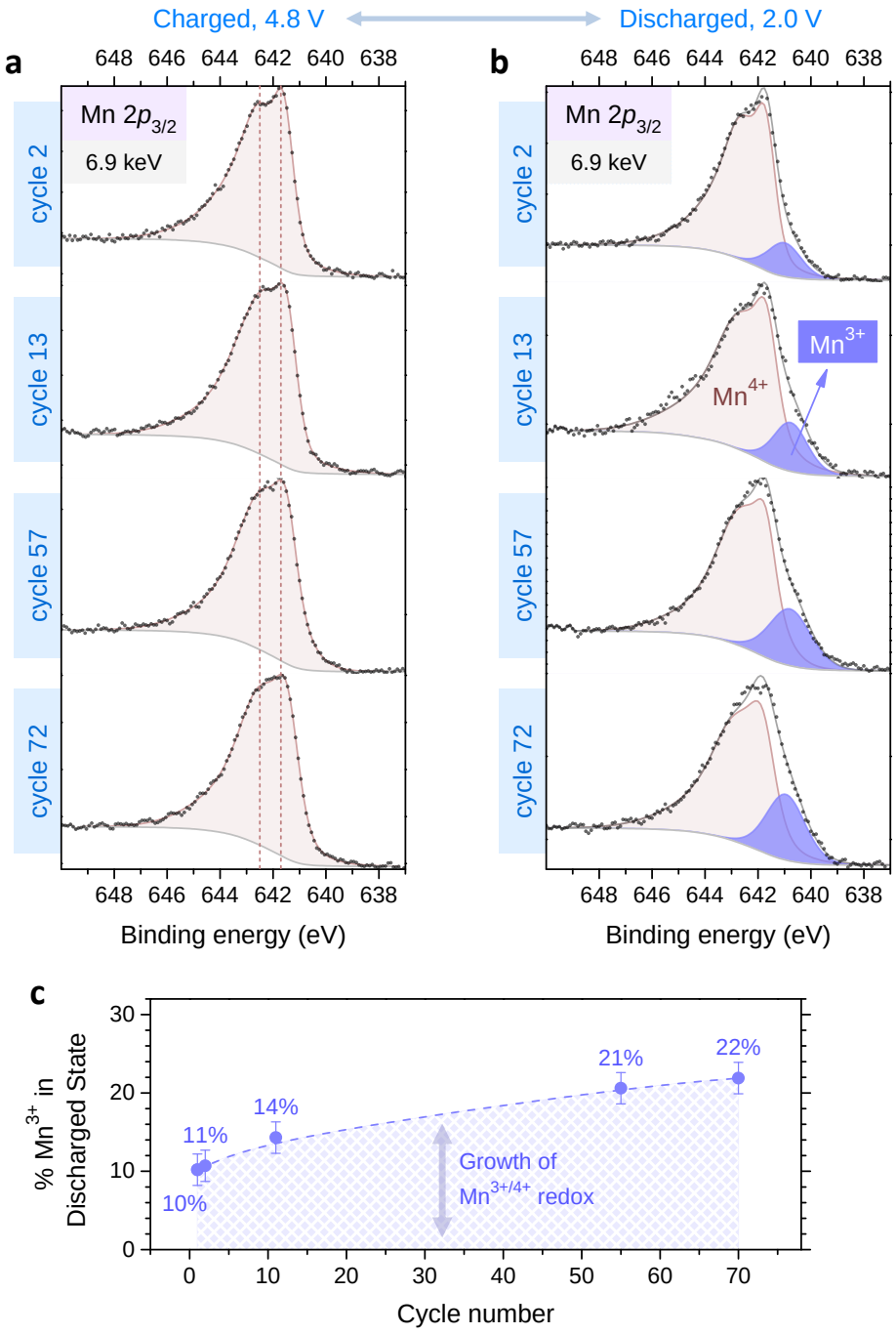


**Figure IV.19 | Evolution of the Mn HAXPES spectra over cycling.** The Mn $2p_{3/2}$ spectra for (**a**) the samples charged to 4.8 V and (**b**) the samples discharged to 2.0 V. Each spectrum on discharge has been fitted with two components, the first one being the spectrum of the corresponding charged sample as a reference for the $Mn^{4+}$ shape and the second one accounting for the presence of $Mn^{3+}$ at low binding energy (purple component around 641 eV). (**c**) The estimated amount of $Mn^{3+}$ in the discharged state is plotted as a function of cycle number. All spectra in this Figure are recorded at 6.9 keV photon energy.

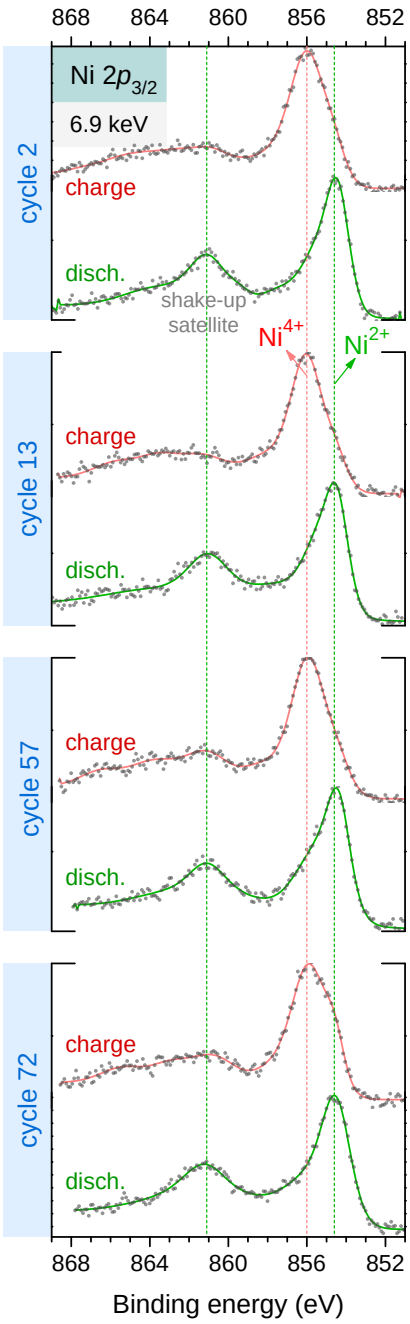


**Figure IV.20 | Evolution of the Ni HAXPES spectra over cycling.** Ni $2p_{3/2}$ spectra are shown as charged-discharged pairs with increasing cycle number. All spectra in this Figure are recorded at 6.9 keV photon energy.

Concerning nickel, which is the main redox-active cation in Li-rich NMC, it starts as $Ni^{2+}$ in the pristine material and is known to undergo the multi-electron $Ni^{2+/3+/4+}$ redox process over charge and discharge (recall **Figure IV.7b**). Ni $2p_{3/2}$ HAXPES at 6.9 keV was performed, as shown in **Figure IV.20**, to characterize the evolution of this process. In

cycle 2, a clear shift in the main peak's position can be observed between the charged to the discharged states. Moreover, the intensity and shape of the shake-up satellite can additionally be used, along with the main peak's shift, as a signature to follow the $Ni^{2+/3+/4+}$ process.[251] The charged-discharged pairs of spectra continue to display these signatures over long cycling, indicating the repeated occurrence of the $Ni^{2+/3+/4+}$ process. However, the charged samples for cycles 57 and 72 show slight signs of reduced nickel on the main peak as well as on the satellite feature, suggesting a small under-completion of the cationic redox process after ageing of the electrodes. We exclude the possibility of significant signal contribution from reduced Ni at the surface as such reduction is limited to the first couple of nanometres[252,253], which is much lower than the HAXPES probe depth. Although the signal to noise ratio is not good enough for precise quantification, qualitative capacity estimation is presented later in the work.

Lastly for cobalt, the Co $2p_{3/2}$ HAXPES spectra were recorded at 6.9 keV (**Figure A3.19**) but the main peak position remains unchanged, since it is known to be independent of $Co^{3+/4+}$ redox as previously shown for $Li_{1-x}CoO_2$.[86] Therefore, we rely on our previous finding based on soft-XAS[106] that $Co^{3+/4+}$ occurs concomitantly with $Ni^{2+/3+/4+}$ in Li-rich NMC (recall **Figure IV.7**), and assume the same herein.

## IV*b*.3 – Discussion

We now discuss the implication of our HAXPES results on the cyclability in Li-rich NMC, further dividing this issue in two parts – namely capacity retention (**Figure IV.21a**) and voltage fade (**Figure IV.21b**). Capacity-wise, out of the 264 mAh $g^{-1}$ delivered in the second cycle, transition metals can account for a maximum possible capacity of 141 mAh $g^{-1}$, with 123 mAh $g^{-1}$ from the main cationic processes of $Ni^{2+/3+/4+}$ and $Co^{3+/4+}$ (complete oxidation assumed) along with 18 mAh $g^{-1}$ from the 10 % activity measured for $Mn^{3+/4+}$. Therefore, reversible redox of bulk lattice oxygen ($O^{2-} \leftrightarrow O^{n-}$), which we have unambiguously demonstrated at probe depths of up to 40 nm (corresponding to 10.0 keV incident energy), compensates for 123 mAh $g^{-1}$, i.e. nearly half of the measured capacity. We also provide direct spectroscopic proof that reversible anionic redox remains active over long cycling. Although lesser % $O^{n-}$ is detected in the

charged state after 72 cycles, the capacity associated with it is still circa 90 mAh $g^{-1}$ and therefore well above one-third of the total capacity (conversion ratio to get capacity from the net change in % $O^{n-}$ is assumed same as that in cycle 2, further details in Methods). At the same time, the growth of $Mn^{3+/4+}$ to 22 % corresponds to only 37 mAh $g^{-1}$ and the remaining capacity from nickel and cobalt (112 mAh $g^{-1}$) turns out to be lower than their contribution in the initial cycles. This last observation is in agreement with the HAXPES evidence of incomplete nickel oxidation after long cycling (recall **Figure IV.20**).

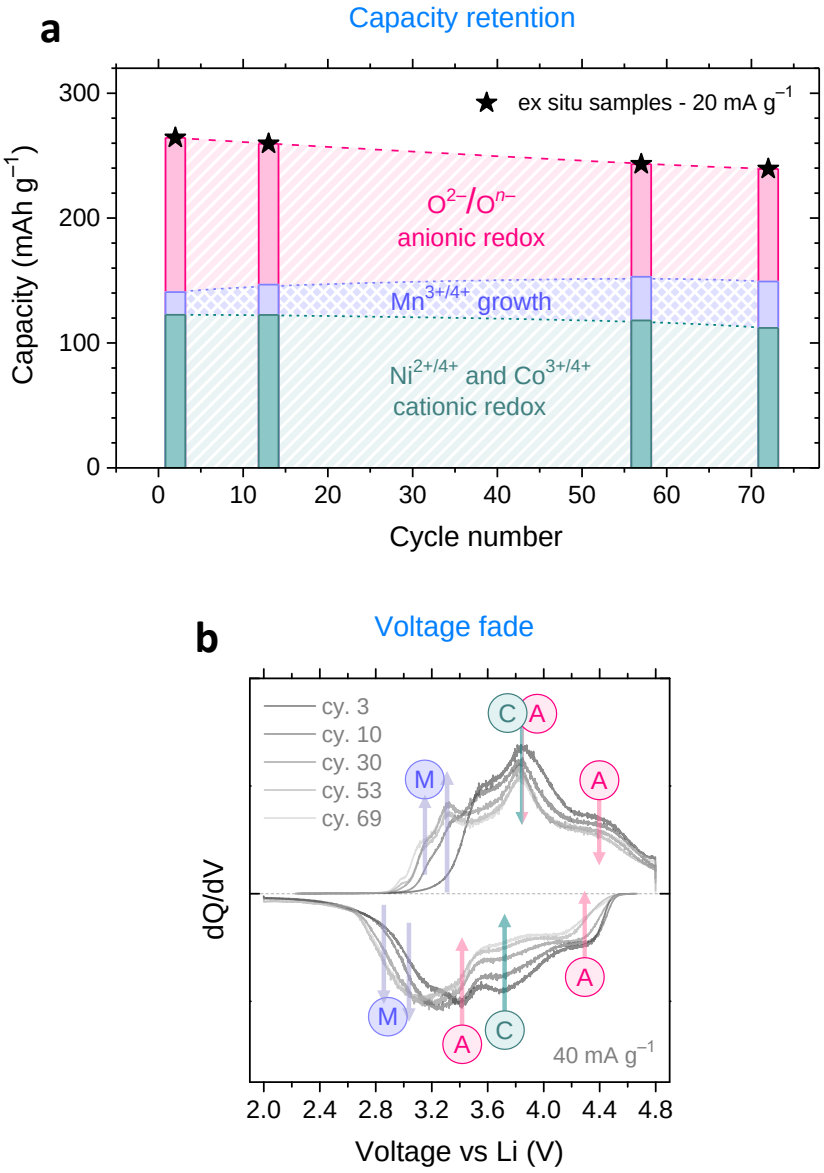


**Figure IV.21 | Evolution of capacity and voltage of cationic and anionic redox processes over long cycling.** (**a**) The capacity from different redox couples is estimated from the qualitative and quantitative analysis of HAXPES spectra. (**b**) The evolution of different features in the d*Q*/d*V* curves is assigned to cationic "**C**", or anionic "**A**", or $Mn^{3+/4+}$ "**M**" redox processes.

Our quantification of the long-cycling reversibility of anionic redox directly from oxygen spectroscopy is consistent with a fresh study[249] relying on transition-metal K-edge XAS to quantify long cycling evolutions of cationic redox. The quantitative differences between the two studies likely arise from differences in the studied materials (composition and/or morphology), with our material showing lesser voltage fading. Nevertheless, the different techniques employed in the two works, and hence the different quantification approaches used (HAXPES on oxygen herein vs. XAS on transition metals in ref.[249]), make them complementary to each other. These new works provide a systematic evolution of redox processes in Li-rich NMC materials, which was only partially understood in previous literature dealing with the analysis of cycled samples using techniques mainly focused on transition metal redox.[135,181,227,252,254–256] In **Figure IV.21a**, the diminution in oxygen redox capacity appears to be counterbalanced by the build-up of $Mn^{3+/4+}$. This is consistent with the gradual irreversible loss of lattice oxygen, either directly as $O_2$ or via chemically attacking the electrolyte, which leads to material densification as the local stoichiometry partially changes from $Li_2Mn^{4+}O_3$-like (O/Mn = 3) to $LiMn^{3+}O_2$- and $LiMn^{3.5+}{}_2O_4$-like (O/Mn = 2) wherein $Mn^{3+/4+}$ is possible.[103,116,135,153,241,257] This also has implications on voltage fade, as discussed next.

**Figure IV.21b** shows the evolution of d*Q*/d*V* profiles with ageing. In general, the redox features at higher potential become less intense over cycling with the simultaneous appearance and growth of low potential processes, explaining the gradual fade in average voltage. In light of the correct redox assignments of these d*Q*/d*V* features that were performed in the previous Part (recall **Figure IV.14**)[106,107], we can observe the growth of low potential $Mn^{3+/4+}$ (denoted by "**M**") as well as a degradation in the voltage of both cationic (denoted by "**C**") and anionic (denoted by "**A**") redox process. Voltage fade can thus be envisaged to be a consequence of irreversible changes in the material's overall bulk, and not simply due to surface reconstruction, which is also supported by model-based d*Q*/d*V* analyses of up to 500 cycles[191] as well as long-term *in situ* diffraction data[258]. Eliminating voltage fade therefore calls for a paradigm-shift in designing mitigation strategies, especially since conventional strategies of surface-coating and cation-doping have only been partially effective in Li-rich NMC.[124] In this regard, an interesting recent experiment demonstrated the recovery of faded voltage by heat treating the cycled material to 150 °C.[211] However, it remains to be seen if such a finding will lead to real implementable solutions to voltage fade.

# IV*a*.4 – Conclusions from this Part

Cumulative anionic/cationic bulk redox processes are responsible for the outstanding specific energy (1000 Wh $kg^{-1}$) of Li-rich Mn-based layered oxides as positive electrodes for lithium-ion batteries. Previous attempts to quantify redox processes in these materials were either limited to initial cycles or relied solely on the transition metals' redox. It thus remained unclear to what extent does oxygen redox persist over cycling. This study provided the answer via synchrotron-based bulk-sensitive hard X-ray photoemission spectroscopy (HAXPES) by directly following the changes in electronic state of lattice oxygen over gradually increasing cycles.

By quantifying the reversibility of oxygen redox, we found that its contribution stabilizes after initial cycles in $Li_{1.2}Ni_{0.13}Mn_{0.54}Co_{0.13}O_2$ (Li-rich NMC) such that even after 70 cycles, it accounts for more than one-third of the overall capacity for the batch of material studied herein. Consequently, from the systematic quantification of Mn spectra, we observed a gradual but limited growth of $Mn^{3+/4+}$ redox, and not its complete activation. Partial degradation of the $Ni^{2+/3+/4+}$ redox was also observed.

This fundamental study generates optimism for the relatively nascent concept of anionic redox, which can now without scepticism be envisaged for long-cycling high-energy batteries. On the other hand, the issue of voltage fade still plagues Li-rich NMC and appears to be bulk-related. Unconventional materials' strategies are therefore needed for fully eliminating voltage fade.

The two works presented in the two Parts of this Chapter highlight the capability of HAXPES in distinguishing bulk vs. surface effects, especially for oxygen, in these Li-rich oxide cathodes. Among the various practical aspects of Li-rich NMC that were discussed throughout this Chapter, the issue of voltage hysteresis remains the most enigmatic. Through parallel studies on Li-rich NMC (this Chapter) and LRSO (Chapter II and Chapter III), we have unambiguously demonstrated that anionic redox is associated with voltage hysteresis. However, we still do not understand "Why?" and whether/how such voltage hysteresis leads to heat generation. These open questions led us to initiate an isothermal calorimetry study that is presented in the next Chapter.

# Chapter V – Mechanism and thermal effects of voltage hysteresis

# V.1 – Background and Motivation‡‡

The previous three Chapters revealed how the issue of voltage hysteresis in 'practical' Li-rich NMC as well as in 'model' LRSO is correlated with anionic redox activity – the very same mechanism that enhances their capacity as cathodes. Aiming towards fundamental understanding of this correlation, the present Chapter attempts to scrutinize voltage hysteresis in a different manner, i.e. by measuring its thermal effects.

Voltage hysteresis is undesirable in rechargeable batteries for several reasons. It leads to energy inefficiency, presumably dissipated as heat, that consequently imposes an additional energy cost on the end-users.[156] Voltage hysteresis would also complicate the state of charge (SoC) management as well as the thermal management and safety of real battery-packs employing such materials. Li-rich NMCs show a relatively large difference (~400–500 mV after the first cycle, ~87% energy efficiency) between their charge and discharge voltage profiles, as discussed in the first Part of Chapter IV. This gap does not diminish with cycling and it persists even at extremely low rates (C/300)[190], at high temperatures (55 and 85 °C)[239], and after long relaxation periods (up to 100 hours)[190]. Such a hysteresis therefore cannot be explained by simple electrochemical kinetics and it points towards complicated reaction mechanisms that lead to the observed path dependence and quasi-static hysteresis. Interestingly and similar to Li-rich NMCs, many other newly-discovered Li- and Na-based materials with reversible anionic redox activity also suffer from voltage hysteresis.[248] These include layered $Li_2Ru_{1-y}M_yO_3$ (M = Mn, Sn, Ti)[67,69,194], O2-type $Li_{1.25}Mn_{0.50}Co_{0.25}O_2$[71] , $Na_{2/3}[Mn_{1-x}Mg_x]O_2$[128,129], and $Na_2RuO_3$[122]; as well as disordered $Li_{1.3}Mn_{0.4}Nb_{0.3}O_2$[72,144], $Li_{1.2}Mn_{0.4}Ti_{0.4}O_2$[73] and $Li_2MnO_2F$[76].

Only a few studies, mostly focused on Li-rich NMCs, have attempted to understand the origin of voltage hysteresis in this class of cathodes. These include detailed electrochemical measurements in different voltage windows to identify correlated differential capacity ($dQ/dV$) peaks[106,165,165,182,259], $^6$Li nuclear magnetic resonance (NMR) spectroscopy to observe path-dependence in lithium site occupation[187], X-ray diffraction (XRD) to claim the occurrence of back-and-forth (reversible) transition metal

‡‡ This Chapter is based on the following research article that I co-authored :

**Assat, G.**, Glazier, S. L., Delacourt, C. & Tarascon, J.-M. Mechanism and thermal effects of voltage hysteresis in lithium-rich layered oxide electrodes – An isothermal calorimetry study. ***submitted*** (**2018**).

migration[258], and X-ray absorption (XAS)[102,119,163,189,217] and hard X-ray photoemission (HAXPES)[106] spectroscopies to demonstrate the absence of hysteresis in the redox potential of transition metals in contrast to the hysteretic oxygen redox process. A couple of phenomenological models assuming either a Li-driven phase change[190] or an asymmetry in transition-metal migration[191] were also conceived to understand voltage hysteresis in Li-rich NMC. These studies do provide microscopic and macroscopic insights about these materials; however the general thermodynamic mechanistic behind voltage hysteresis and its thermal effects remain unclear. Two questions need answering: (*i*) how exactly is the lost energy dissipated as heat and how can it be better managed/predicted? and (*ii*) what is the underlying mechanism and the corresponding thermochemical conditions that lead to hysteresis?

To answer these questions, we adopt a different approach herein and perform isothermal calorimetry measurements during the cycling of a 'model' Li-rich layered cathode – $Li_2Ru_{0.75}Sn_{0.25}O_3$ (LRSO) that can also be written as $Li[Li_{0.33}Ru_{0.5}Sn_{0.17}]O_2$. This high-performance material[68,194], although only suitable for niche applications wherein cost is not a barrier (e.g. space, defence), shows remarkable similarities with the practically important Li-rich NMCs (recall Discussion section of Chapter II).[194] For instance LRSO also exhibits, apart from the same crystal structure-type as Li-rich NMC, a two-stepped voltage profile on first charge followed by a sloped hysteretic profile on further cycling, as shown in **Figure V.1**. Further "head-to-head" comparison of the two materials in **Figure A4.2**). Therefore LRSO serves as a simplified 'model' compound to understand the general properties of Li-rich layered electrodes. The magnitude of voltage hysteresis in LRSO (~200–300 mV) is lower than Li-rich NMCs but the role of anionic redox activity is particularly similar, such that high potential charging triggers the onset of hysteresis.[119,194]

Using isothermal calorimetry in this work, we report the heat generation during different electrochemical stages of LRSO, starting with the classical cationic redox step in first charge followed by the anionic activation plateau and finally the hysteretic voltage profiles that stabilize after a few cycles. These measurements allow us to discuss the thermodynamics in terms of enthalpy change, entropy change, and entropy production. We highlight the thermal asymmetry in the charge vs. discharge paths as well as the difficulties in locating the true equilibrium properties of such hysteretic materials. A multi-step reaction scheme for solid-state oxygen redox is finally proposed to comprehend the results.

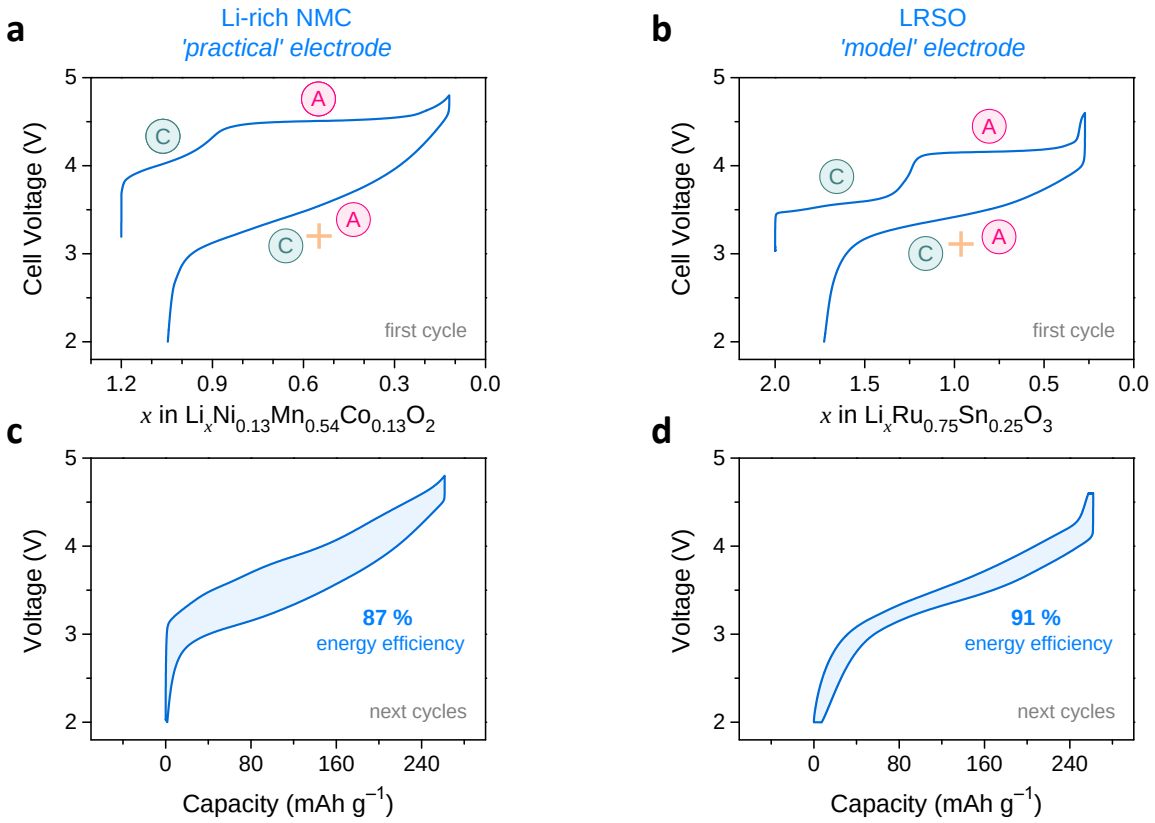


**Figure V.1 | Comparison of voltage profiles of Li-rich NMC and LRSO.** The first cycle (**a** and **b**) displays a two-stepped charge followed by a sloped discharge. The labels "**C**" and "**A**" denote respectively the cationic and anionic redox processes. The later cycles (**c** and **d**) display a quasi-static voltage hysteresis, leading to energy inefficiency.

# V.2 – Thermodynamic Considerations

The general energy balance for an electrochemical system was derived by Newman and co-workers.[260,261] For a thermally thin electrochemical cell in isothermal (constant temperature) and isobaric (constant pressure) conditions, the heat generation rate $\dot{q}|_{T,P}$ (if heats of mixing are neglected[262,263]) is given by

$$\dot{q}|_{T,P} = I\,(V - U) + I\,T\,\frac{\partial U}{\partial T} + \sum_i \Delta H_i\, r_i$$

**Equation [1]**

where $\dot{q}|_{T,P}$ is positive if heat is released by the cell, $I$ is the current (positive for charging), $V$ is the cell voltage, $U$ is the equilibrium potential, $T$ is the temperature, $P$ is the surrounding pressure, and $\Delta H_i$ is the enthalpy of reaction of a chemical reaction $i$ (other than the main electrochemical reaction) occurring at a rate $r_i$. Recognizing the first term as irreversible heat generation due to overpotential, the second term as reversible entropic heat, and the last term as parasitic heat due to side reactions, **Equation [1]** can also be equivalently formulated as[264]

$$\dot{q}|_{T,P} = I\,\eta + \frac{I\,T}{F}\left(\frac{ds_+}{dx} - \tilde{s}_{Li}\right) + \dot{q}_p$$

**Equation [2]**

where $\eta$ is the cell's overpotential (the product $I\,\eta$ is always positive), $F$ is the Faraday's constant, $x$ is the stoichiometric content of Li in the positive electrode material, $s_+$ is the total entropy of the positive electrode material at a given $x$, $\tilde{s}_{Li}$ is the molar entropy of Li metal negative electrode, and $\dot{q}_p$ is the parasitic heat flow due to chemical reactions. These formulations have extensively been used for investigating the entropic heat of intercalation materials[265] and more recently the parasitic heat in Li-ion cells[266–269]. For quantifying the entropy change, one possibility (potentiometric method) is to perform temperature-dependent equilibrium potential measurements for directly determining $\frac{\partial U}{\partial T}$ in **Equation [1]**.[263,270–274] The other (calorimetric method) is to measure $V$, $I$, and $\dot{q}|_{T,P}$ over a charge–discharge cycle and obtain the terms in **Equation [2]** while considering these terms to be path independent (same on charge vs. discharge), which is a reasonable assumption for classical intercalation materials.[264,268,269] To understand the effect of quasi-static voltage hysteresis, the irreversible heat term can be empirically modelled, when $I$ is relatively low, as[268]

$$I\,\eta = I^2\,R_{int} + |I|\,V_{hyst}$$

**Equation [3]**

where $R_{int}$ is the cell's internal resistance and $V_{hyst}$ the inherent quasi-static (extrapolated to zero-current) voltage hysteresis. This equation was successfully applied to empirically model the heat flow in $LiNi_{0.4}Mn_{0.4}Co_{0.2}O_2$/graphite cells by including a small (± ~4 mV) voltage hysteresis equally on charge and discharge and by considering $R_{int}$ as a function of SoC only.[268] However for the Li-rich electrodes, this approach is not suitable because (*i*) they show a much larger hysteresis (both Li-rich NMC and LRSO that are of interest in this thesis) and (*ii*) their $R_{int}$ is known to vary differently on charge vs. discharge with SoC.[106,194] Likewise, $V_{hyst}$ can be expected to differ on charge vs. discharge in these highly path-dependent materials. In other words, the position of $U$ in hysteretic Li-rich electrodes cannot simply be assumed in the middle of the charge and discharge profiles, unlike classical intercalation materials.

We therefore need a different approach. Neglecting parasitic heat flow for the rest of this work, the energy balance in **Equation [1]** can be recast as

$$V - \frac{\dot{q}|_{T,P}}{I} = U - T\frac{\partial U}{\partial T} = U_H$$

**Equation [4]**

where $U_H$ is the so-called "enthalpy potential".[262] Just as $U$ is directly related to the partial change in Gibbs free energy of the cell as its SoC is varied, $U_H$ is directly related to the partial change in the enthalpy of the cell. In other words, $U_H$ captures the energy change while $U$ includes the entropy change as well. $U_H$ can simply be obtained by measuring $V$, $I$, and $\dot{q}|_{T,P}$ without any further assumption. Knowing $U_H$ can help in predicting the heat generation under real operating conditions, which is of principal interest for thermal management of batteries. Integrating the energy balance in **Equation [4]** over a closed path, such as a charge–discharge cycle after which the material returns to its original state, gives

$$\oint_{cycle} I\,V\,dt = \oint_{cycle} \dot{q}|_{T,P}\,dt$$

**Equation [5]**

because enthalpy is a state variable and cancels out over a stable cycle as follows:

$$\oint_{cycle} U_H \, dx = 0$$

**Equation [6]**

**Equation [5]** demonstrates that the net electrical work due to hysteretic charge–discharge voltage profiles is dissipated as waste heat. Note that the $U_H$ measured via **Equation [4]** (under applied current) can be path dependent, i.e. different on charge vs. discharge for the same SoC, if the materials inside the cell remain as metastable phases under dynamic conditions far from the true equilibrium. Nevertheless even in that case, $U_H$ over a stable cycle is constrained by **Equation [6]** and therefore cannot form a hysteretic loop (although the total enthalpy would form a hysteretic loop), as schematized in **Figure A4.3** of the Appendix.

In addition to energy balance, the entropy change, while recalling the Second Law of Thermodynamics, is related to the heat exchange as[275]

$$\frac{\dot{q}|_{T,P}}{T} = -\dot{s} + \dot{\sigma}_{prod} \, ,$$

$$\dot{\sigma}_{prod} \geq 0$$

**Equation [7]**

where $\dot{s}$ is the rate of entropy change of the cell, and $\dot{\sigma}_{prod}$ is the rate of entropy production due to the irreversible processes inside the cell. $\dot{\sigma}_{prod}$ is zero only over a thermodynamically reversible path. Since entropy is a state variable, its integration over a closed path (e.g. a stable charge–discharge cycle) becomes

$$\oint_{cycle} \dot{s} \, dt = \oint_{cycle} \frac{ds}{dx} \, dx = 0$$

**Equation [8]**

Consequently, the integration of **Equation [7]** over a closed path, when combined with **Equation [5]**, gives

$$\oint_{cycle} I\,V\,dt = \oint_{cycle} \dot{q}|_{T,P}\,dt = \oint_{cycle} T\,\dot{\sigma}_{prod}\,dt \geq 0$$

**Equation [9]**

The overall voltage hysteresis (both resistive and quasi-static in nature) is therefore a measure of entropy production that is dissipated as heat. In the realm of chemical reactions, $\dot{\sigma}_{prod}$ for a closed system, wherein several reactions could be simultaneously taking place, can be given as[275]

$$\dot{\sigma}_{prod} = \sum_{k} \frac{A_k}{T} \frac{d\xi_k}{dt} \geq 0$$

**Equation [10]**

where $A_k$ is the affinity of reaction $k$ and $\xi_k$ is its degree of advancement. Affinity relates to the driving force for chemical reactions and is zero only at the equilibrium, as schematized in **Figure A4.4**. Therefore, the presence of entropy production in chemical/electrochemical systems, which for batteries is related to the overall voltage hysteresis as demonstrated by **Equation [9]**, is a sign of non-equilibrium of the underlying chemical steps. If all reactions are elementary steps whose reaction rates are specified by the stoichiometry, **Equation [10]** can further be simplified as[275]

$$\dot{\sigma}_{prod} = R \sum_{k} \left(R_{f,k} - R_{b,k}\right) ln\left(\frac{R_{f,k}}{R_{b,k}}\right) \geq 0$$

**Equation [11]**

where $R$ is the gas constant while $R_{f,k}$ and $R_{b,k}$ are respectively the forward and backward reaction rates of an elementary chemical step $k$. For the simplest case of an

elementary electrochemical reaction that follows the Butler-Volmer kinetics[175] with an overpotential $\eta$, it can be shown from **Equation [11]** that

$$T\,\dot{\sigma}_{prod} = I\,\eta \geq 0$$

**Equation [12]**

which is simply the first term (irreversible heat) of the energy balance in **Equation [2]**. However for more complicated systems, as we will show later to be the case for Li-rich LRSO electrodes, the precise thermodynamic and kinetic knowledge of the underlying reaction mechanism, which may be composed of a set of $k$ chemical/electrochemical steps, is necessary to obtain the true mathematical form of entropy production and move beyond the empirical models such as **Equation [3]**. This unfortunately is not a trivial task.

# V.3 – Results

## ○ Initial cationic redox step before activation

Electrochemical removal of lithium from $Li_2Ru_{0.75}Sn_{0.25}O_3$ (LRSO) initially takes place around 3.5 V with the oxidation of $Ru^{4+}$ to $Ru^{5+}$ (recall **Figure III.3a**) as 0.75 Li per formula unit is de-intercalated. This cationic redox step is completely reversible (recall **Figure II.1**).[119,194] Isothermal calorimetry[§§] measurements at 40 °C were performed over this step in coin-type Li half-cells at different C-rates[††], ranging from C/20 to C/5 (see experimental details in the Methods section of the Supporting Information for this Chapter in Appendix A4).

**Figure V.2a** shows the resulting voltage profiles, wherein the polarization gradually increases as expected when the C-rate is increased. These voltage profiles along

[§§] **Isothermal calorimetry** was carried out in collaboration with Stephen L. Glazier from Jeff Dahn's group (Dalhousie University, Canada). Using the cells that I made, Stephen acquired the calorimetry data, on which I performed the analysis.

[††] The C-rate in this work is defined such that 1C corresponds to the removal of 1.0 Li per formula unit of LRSO in one hour (i.e. 1C = 160.13 mA $g^{-1}$).

with the simultaneously measured heat flow rates $\dot{q}|_{T,P}$ were used to obtain the profiles of enthalpy potential $U_H$ using **Equation [4]**, as shown for example in **Figure V.2b** for the slowest rate of C/20. The symmetric shape of the heat flow profiles (orange traces) arises because of reversible entropic heat (second term in **Equation [2]**) that is equal and opposite in sign on charge vs. discharge, whereas the net positive shift is due to irreversible heat from overpotential (first term in **Equation [2]**). The calculated $U_H$ profiles (pink traces) superimpose neatly on charge and discharge, indicating that the enthalpy change is path independent and is only a function of the Li stoichiometry (or SoC). Such a symmetric behaviour is typical for classical electrochemical intercalation reactions.[264,269]

It can also be observed from **Figure V.2b** that $U_H$ lies at values higher than the equilibrium potential $U$ located somewhere between the charge and discharge voltage profiles (blue curves). Therefore the entropic term is such that the cell's entropy increases on charge (causing heat absorption) and decreases on discharge (causing heat release). In other words, the temperature coefficient $\frac{\partial U}{\partial T}$ is negative. Understanding the exact shape of entropic heat flow is beyond the scope of this study, as it may be related to diverse aspects of the cathode material such as the changes in Ru–Ru bond distance ordering (recall EXAFS results in **Figure III.4**)[119], charge ordering, Li vacancy ordering, or the shape of the $dQ/dV$ profile (**Figure A4.5**).

The deviation (early drop, marked by green arrows in **Figure V.2b**) of the discharge $U_H$ profile compared to the one on charge is likely because of concentration gradients and can be understood better by looking at the effect of C-rates. The $U_H$ profiles obtained at different rates are compared in **Figure V.2c** (see **Figure A4.6** for the raw heat flow profiles). They converge over a broad range of SoCs for both charge and discharge, however with some rate-dependent discrepancies at the extremities as highlighted with pink backgrounds in **Figure V.2c**. As the C-rate increases, the charge $U_H$ profiles develop a small distortion at the onset of charge and show an early rise towards the end of charge. Similarly, the discharge $U_H$ profiles show an early drop towards the end of discharge that gradually intensifies at faster rates. These kinetic effects arise from the formation and relaxation of concentration gradients, mostly in the solid phase due to lithium diffusion since the electrode is designed with a high porosity, and the associated heat of mixing effects[262,263,272] that were neglected in **Equation [1]** and **Equation [4]**. Nevertheless, the

$U_H$ profiles at the slowest rate superimpose adequately and reflect the enthalpy change of the electrochemical reaction.

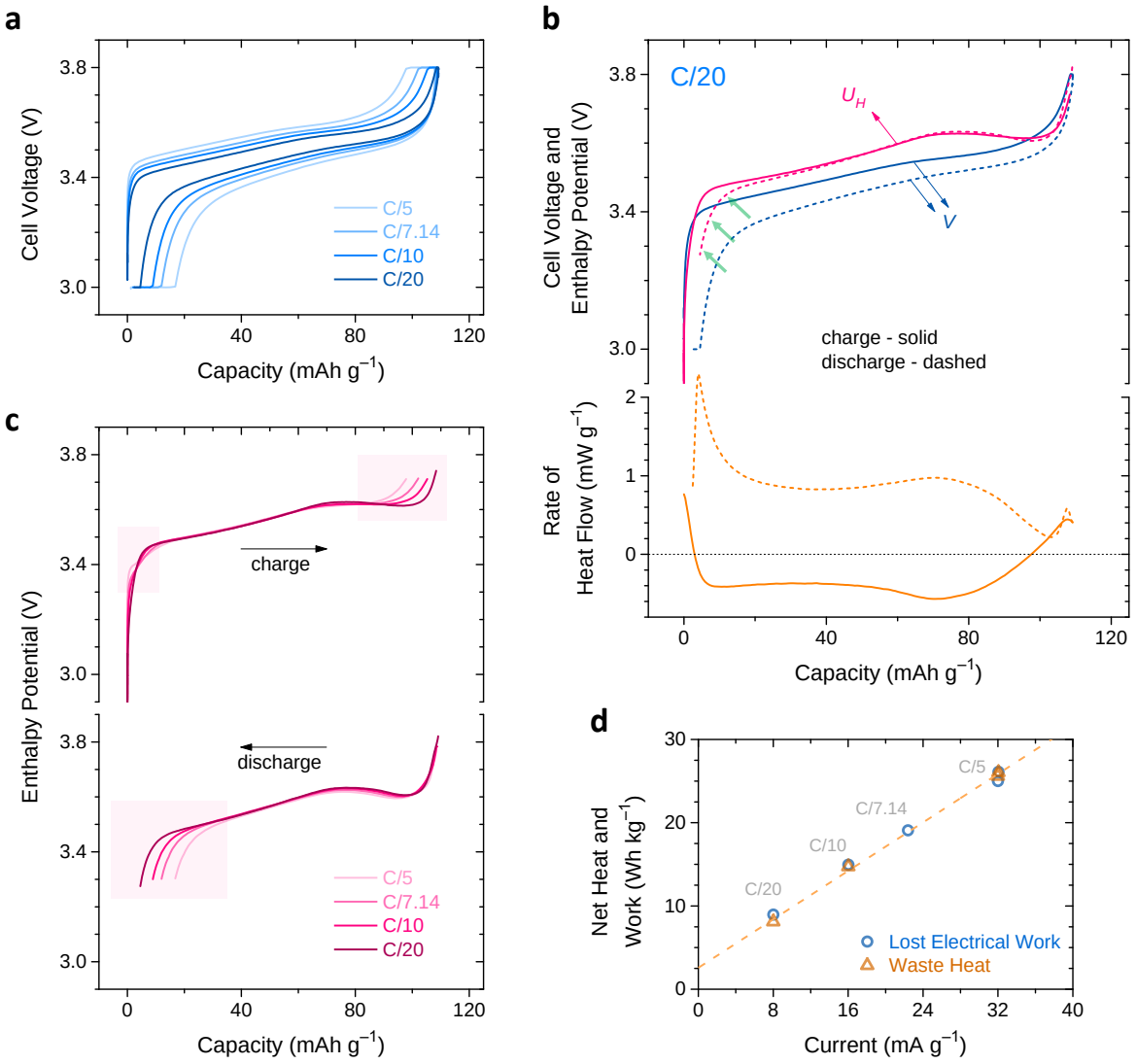


**Figure V.2 | Isothermal calorimetry characterization of the 3.5 V cationic redox step.** The voltage profiles (**a**) obtained with LRSO cycled inside the calorimeter using CCCV protocol (current cut-off of C/100 for ending the potentiostatic holds). The experiments were carried out after a few formation cycles. For C/20 (**b**), the measured profiles of cell voltage (blue) and heat flow rate (orange) that were used to obtain the enthalpy potential profiles (pink). (**c**) Convergence of enthalpy potential profiles obtained at different rates, with pink backgrounds highlighting the deviations possibly due to heat of mixing. (**d**) As a function of C-rate, a comparison of lost electrical work with waste heat over a complete charge–discharge cycle obtained by integrating respectively the cell voltage and the heat flow rate. One of the integrations could not be performed (missing data point for C/7.14) because of an unintended cycler interrupt.

Lastly, **Figure V.2d** compares the net electrical work and the net heat generated from the cell over a complete charge–discharge cycle at different rates. The heat and work are positive and match with each other, in agreement with **Equation [9]**. Moreover, they exhibit a linear relationship with current that approaches close to zero as the current diminishes. The slope and intercept are respectively related to the average values of $R_{int}$ and $V_{hyst}$ in **Equation [3]**. Overall, the calorimetric analysis of the 3.5 V cationic redox step demonstrates its classical nature, i.e. it is path independent, it shows a very small quasi-static voltage hysteresis, and can be thermodynamically treated as a single-step electrochemical reaction.

## ○ Anionic oxidation (activation) plateau

Further extraction of Li from LRSO takes place around 4.2 V and a flat voltage plateau is observed (**Figure V.3a**, top). This plateau, which is charge-compensated by the oxidation of bulk lattice oxygen, as demonstrated in Chapter III[119], is termed as the so-called 'activation process' in Li-rich layered electrodes. **Figure V.3a** (bottom) shows that the outflow of heat from the cell during this process is significantly larger than the preceding cationic redox step. Such a large heat release cannot be simply explained by electrochemical resistance, since we have previously shown in Chapter II that this value remains small for the voltage plateau.[194] We had additionally reported very slow equilibration dynamics, such that the open-circuit voltage (OCV) slowly relaxes and keeps drifting away for long periods of time from the under-current voltage (recall **Figure II.3**). Note in this case that the direct determination of the entropic term $\frac{\partial U}{\partial T}$ based on temperature-dependent equilibrium potential measurements as attempted for Li-rich NMC[276], is questionable. Moreover, the subsequent discharge does not display the same plateau but instead results in a sloped S-shaped voltage profile (**Figure V.3b**). All these observations indicate that 4.2 V plateau is an electrochemically-driven irreversible phase transformation (or 'activation') that cannot be treated as a single-step electrochemical reaction. We therefore propose a two-step mechanism to explain the anomalous heat generation. Following the electrochemical step of anionic oxidation that governs the plateau's voltage, a chemical rearrangement step occurs to stabilize the structure, e.g. the distortion of $RuO_6$ octahedra and the possible shortening of O–O distances (recall **Figure**

**III.7**).[119,248] This stabilizing chemical step explains the large heat generation over the plateau that could ideally be computed using the third term in **Equation [1]** if its kinetics is precisely known.

The $U_H$ profiles obtained from **Equation [4]** are also shown in **Figure V.3b**. Note that these represent the overall changes in enthalpy of the cell (without any distinction of the underlying steps). Since the $U_H$ profile on discharge is well separated from the one on charge, the condition in **Equation [6]** cannot be fulfilled over the first cycle. Hence, there is a net change in enthalpy of the cell. In other words, the material does not return to the pristine state after a full charge–discharge cycle, as also observed with other characterizations, including EXAFS (recall **Figure III.10**).[119,186]

In summary, the large heat release during the voltage plateau may be due to the underlying rearrangement step that accompanies anionic oxidation. The subsequent discharge follows a thermodynamically different path. For application purposes, the observation of large heat flow must be kept in mind when designing protocols to safely activate Li-rich electrodes.

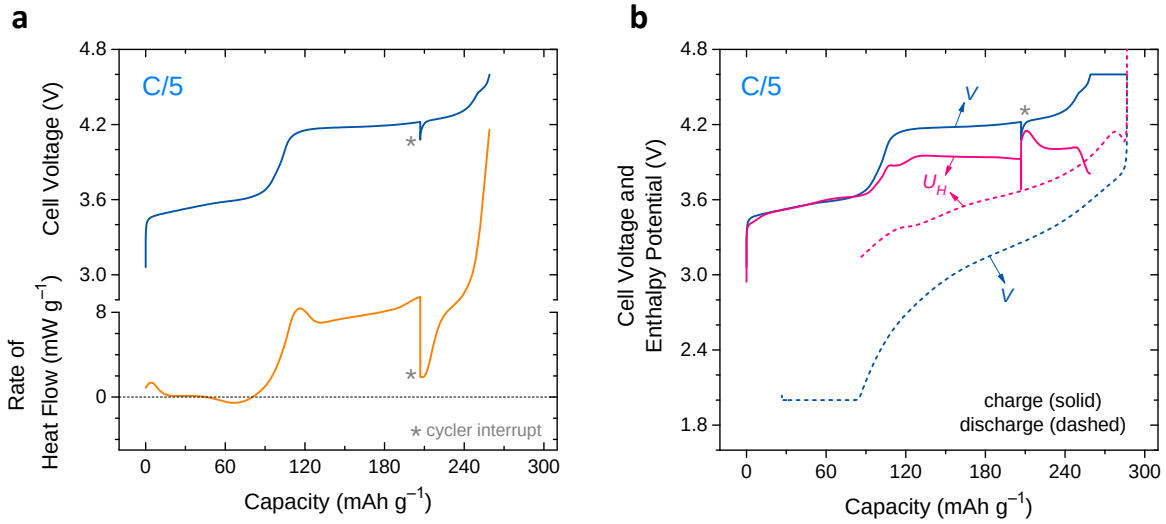


**Figure V.3 | Isothermal calorimetry characterization of the first cycle.** (**a**) Voltage profile (blue) and heat flow profile (orange) for the staircase-like first charge. An unintended interrupt of 104.4 mins (marked by *) occurred during the anionic oxidation plateau. The steep rise in heat release at the end of the plateau could be due to partial oxygen release and/or side reactions. The cell used was the same as the one in **Figure V.2**. (**b**) The calculated enthalpy potential profiles (pink) are shown along with the cell voltage profile over the complete first cycle.

## ○ Voltage hysteresis after activation

After some formation cycles, LRSO's sloped S-shaped voltage profiles stabilize, with nearly equal capacity contributions from the cationic and anionic redox processes that take place at low and high potentials respectively, as deduced from *operando* XAS (recall **Figure III.13**).[119,194] To understand the electrochemical properties of this 'activated' phase, isothermal calorimetry was performed at different rates ranging from C/50 to C/5. The voltage profiles, shown in **Figure V.4a** ($dQ/dV$ curves in **Figure A4.7**), exhibit a significant voltage hysteresis that does not diminish by lowering the current. This quasi-static hysteresis appears to be larger in the higher potential range where anionic redox takes place. The heat flow for the slowest rate of C/50 (orange trace in **Figure V.4b**, bottom) is not symmetric and remains largely above zero for the entire cycle, unlike the classical situation that was discussed for the initial cationic redox step in **Figure V.2**. Notice that the discharge leads to larger heat generation compared to the charge.

Again, the $U_H$ profiles were calculated from **Equation [4]** using the measured values of $V$, $I$, and $\dot{q}|_{T,P}$, as shown in **Figure V.4b** for C/50 (other rates in **Figure A4.8**). Interestingly, the $U_H$ profiles on charge vs. discharge are much closer in comparison to the hysteretic voltage profiles. A larger heat generation on discharge indicates that the reaction's enthalpy potential is located further away from the discharge voltage than the charge voltage. Note that, despite at a low rate of C/50, the $U_H$ profiles on charge and discharge do not fully superimpose, especially in the second half of SoCs (anionic redox region), thus reflecting a slight path dependence in the cell's enthalpy, as also schematically explained in **Figure A4.3**. This effect was consistently observed for several cells (**Figure A4.9**). Whether this slight mismatch is due to kinetic or thermodynamic reasons can be understood by comparing the $U_H$ profiles at different rates, as shown in **Figure V.4c**. On either charge or discharge, the $U_H$ profiles obtained at different rates converge over almost the entire SoC range, except possible heat of mixing effects of at the end of charge and the beginning of discharge (highlighted with pink backgrounds). Therefore, enthalpy-wise, the charge and discharge paths, which are slightly different from each other, as they do not converge to a single unique curve, are rate independent over the range of rates studied herein (from C/50 to C/5). This means that the material inside the cell follows metastable paths that have slightly different enthalpies on charge vs. discharge

for the same SoC. Therefore, reaction coordinates other than the overall Li content are necessary to fully describe the system, as discussed later in the Chapter.

Nevertheless, since 'activated' LRSO is fairly stable with negligible voltage fade in one charge–discharge cycle, the $U_H$ profiles should satisfy **Equation [6],** despite being slightly different on charge vs. discharge. This can be verified by comparing the net electrical work to the net heat dissipation over a cycle for different rates. As shown in **Figure V.4d**, the net heat and work are positive and indeed match with each other. The extra work needed to charge the cell (compared to the work recovered on discharge) due to voltage hysteresis is therefore dissipated has heat. These integrals scale linearly with current, with the slope and intercept respectively related to the average values of $R_{int}$ and $V_{hyst}$ in **Equation [3]**. The zero-current intercept in **Figure V.4d** is large, unlike in **Figure V.2d**, because of the large quasi-static hysteresis for the C-rates being considered. It is key here to note that this significant dissipation due to voltage hysteresis can be viewed, according to **Equation [9]**, as entropy production and implies that the underlying steps are far away from equilibrium (**Equation [10]** and **Figure A4.4**) even at the lowest rates. Entropy production (the value of the integrals in **Figure V.4d**) should ideally vanish to zero at infinitesimally small rates at which all the underlying steps would be near equilibrium. However, demonstrating this is not trivial simply due to prohibitively long experiments as well as the interfering side-reactions at extremely low C-rates.

Such non-equilibrium arguments also explain the continuous voltage relaxation observed for LRSO under open circuit conditions despite long time periods (10 to 24 hours, recall **Figure A1.10**)[194] because some of the underlying steps have slow equilibration dynamics with very large time constants. Similarly for Li-rich NMC, the long equilibration durations could only be reproduced in a phenomenological-model-based study by slowing down the dynamics.[190] Moreover, with such drifting OCVs, the direct measurement of entropic term $\frac{\partial U}{\partial T}$ is definitely questionable, which explains why such values reported for Li-rich NMC[276] violate **Equation [8]** during the sloped cycles.

Overall, it is clear that voltage hysteresis is linked to non-equilibrium entropy production, which can be quantified over a complete cycle as the net dissipated heat or lost work. However, further deconvolution of the heat flow rate (at each instant of the cycle) into entropy change and entropy production rates, as per **Equation [7]**, is not possible at

this stage without precise knowledge of the underlying mechanism. Therefore, a multi-step mechanism consistent with experimental observations is presented later in the Chapter.

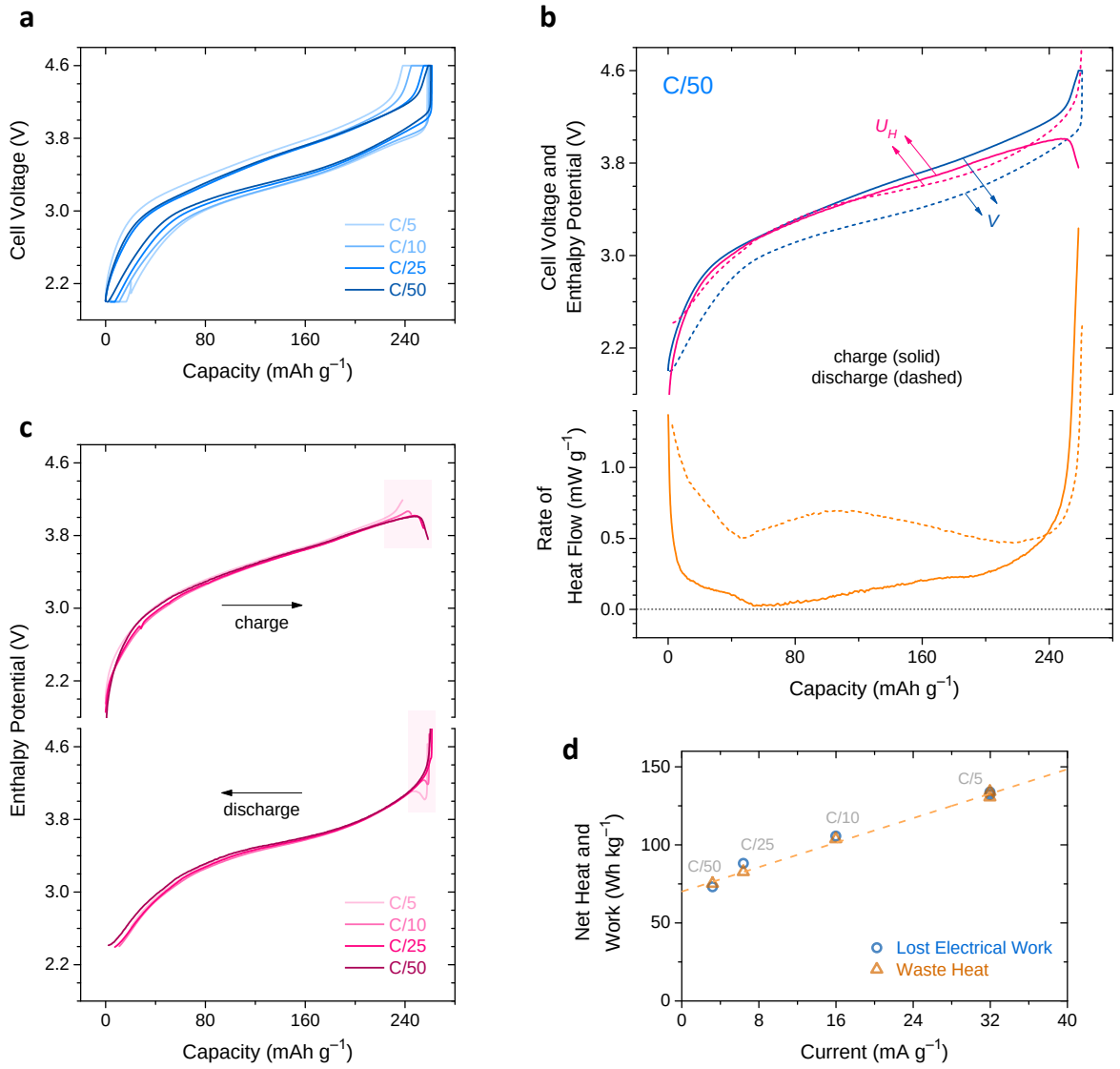


**Figure V.4 | Isothermal calorimetry characterization of 'activated' LRSO.** The hysteretic voltage profiles (**a**) obtained with LRSO cycled inside the calorimeter using CCCV protocol (current cut-off of C/100 for ending the potentiostatic holds). The experiments were carried out after a few formation cycles in the full potential range leading to complete activation. For C/50 (**b**), the measured profiles of cell voltage (blue) and heat flow rate (orange) that were used to obtain the enthalpy potential profiles (pink). (**c**) Convergence of enthalpy potential profiles obtained at different rates for charge (top) and on discharge (bottom), with pink backgrounds highlighting the deviations possibly due to heat of mixing. (**d**) As a function of C-rate, the comparison of lost electrical work with waste heat over a complete charge–discharge cycle obtained by integrating respectively the cell voltage and the heat flow rate.

To further understand the onset of voltage hysteresis, isothermal calorimetry was performed on 'activated' LRSO while gradually opening the charging voltage window. The resulting voltage profiles, shown in **Figure V.5a** ($dQ/dV$ curves in **Figure A4.10**), reveal that charging to high potentials, particularly beyond 50 % SoC, gradually triggers voltage hysteresis. Akin to the discharge voltage profiles that are path dependent, i.e. they depend on the extent of charging, the discharge heat flow profiles, shown in **Figure V.5b**, also exhibit similar path dependence (complete heat profiles in **Figure** A4.11). Discharging from the fully charged state results in a larger heat generation over a broad range of SoCs (denoted by arrows) compared to discharge from partially charged states.

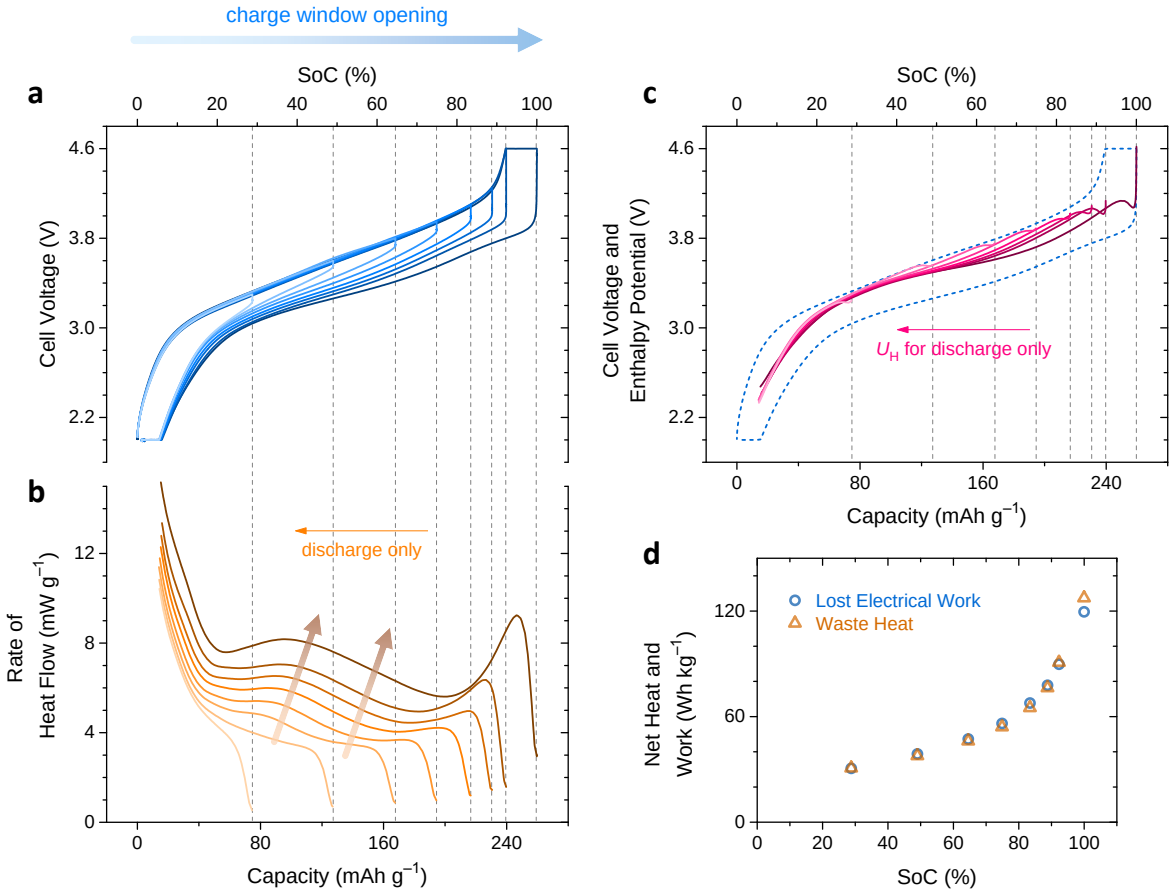


**Figure V.5 | Isothermal calorimetry for charge voltage window opening of 'activated' LRSO.** (**a**) Voltages profiles (blue). C/100 current cut-off was used for the CCCV steps. (**b**) Heat flow profiles (orange) on discharge only. (**c**) The calculated $\boldsymbol{U_H}$ profiles (pink, for discharge only). Background (dashed curve) shows the full range charge–discharge voltage profile. The initial kinks in the $\boldsymbol{U_H}$ profiles at the onset of discharges is likely due to heat of mixing, as also observed in **Figure V.4c**. (**d**) As a function of SoC to which the cell is charged, a comparison of lost electrical work with waste heat over a complete charge–discharge cycle obtained by integrating respectively the cell voltage and the heat flow rate.

The $U_H$ profiles obtained over the different discharges are shown in **Figure V.5c** ($U_H$ profiles on charge are identical as expected, see **Figure A4.12**). In the lower half of SoCs (predominantly cationic redox), all discharge $U_H$ curves converge independently of the charging history. In contrast, for the upper half of SoCs (predominantly anionic redox), the discharge $U_H$ curves gradually evolve as a function of the extent of charge, thus highlighting the distinctive role of anionic redox in causing voltage hysteresis. Lastly, the net heat and work over complete cycles are compared in **Figure V.5d** as a function of the charging SoC. They again match with each other, as expected from **Equation [9]**. Instead of a linear trend with current that is expected for path reversible intercalation materials, a non-linear rise is observed in **Figure V.5d** because of gradually worsening voltage hysteresis as the voltage window is opened. Such a non-linear trend was verified with another cell (**Figure A4.13**). In light of these unusual observations upon high potential charging, a multi-step mechanism for anionic redox is proposed next.

## V.4 – Proposed Mechanism / Discussion

Our previous work with *operando* X-ray absorption spectroscopy in Chapter III led to the decoupling of cationic/anionic $dQ/dV$ contributions in the sloped voltage profiles of 'activated' LRSO, revealing a higher symmetry in cationic redox, unlike the hysteretic anionic redox process (recall **Figure III.13**).[119] The mechanism behind such hysteresis in anionic redox can now fundamentally be understood with the calorimetry results of this Chapter.

From the point of view of local structure, cationic redox (occurring at low potentials) can be treated as a single electrochemical step having the thermodynamic potential $U^C$, therefore free from quasi-static voltage hysteresis (**Figure V.6a**). On the other hand, anionic redox (occurring at high potentials) is a multi-step process, consisting of sequential redox (electrochemical) and rearrangement (chemical) steps, which form a "square-scheme"[277–280] (**Figure V.6b**). On charge, the electrochemical oxidation of anions is followed by a stabilizing rearrangement. This rearrangement could either be the distortion of octahedral symmetry leading to O–O shortening as revealed via EXAFS in Chapter III[109,119,248], the migration of cations[107,165,182,187,258], or (for some Na-based

materials) a change in the stacking of layers[122,129]. Among these, we believe that octahedral distortion is a key step, since it is the most local effect and common for all anionic redox materials, while the other effects are not universal (they are material dependent) and may actually be a consequence of octahedral distortion. Owing to this structural modification, a different redox step is needed on discharge, which is again followed by a stabilizing rearrangement to the original state. Interestingly, these features are analogous to the "square-scheme" mechanism that causes voltage hysteresis in certain molecular machines.[278–280] Note that the four elementary steps are thermodynamically constrained as they form a closed cycle.

Such a multi-step mechanism allows for non-equilibrium to exist if the kinetics of some of the elementary steps is slow enough (much slower than the C-rates at which the cells are cycled). Li content is not the only reaction coordinate in that case and metastable paths can thus persist, independent of current, such that charging predominantly occurs via the upper path in **Figure V.6b** and discharging via the lower one. Therefore in non-equilibrium conditions, the cell potentials during charge and discharge are respectively closer to the thermodynamic potentials $U_{\mathrm{ch}}^{\mathrm{A}}$ and $U_{\mathrm{dis}}^{\mathrm{A}}$ of the two redox steps, with the latter being lower in value, hence giving rise to voltage hysteresis. Voltage hysteresis due to such non-equilibrium leads, by definition, to dissipative entropy production[275], whose value on charge and discharge is related to the Gibbs free energy of reaction of the respective rearrangement step. If the large heat generation observed on discharge is assumed mostly due to entropy production (i.e. if reversible entropy terms are considered small), then $\Delta G_{\mathrm{dis}}^{\mathrm{r}}$ is expected to be larger than $\Delta G_{\mathrm{ch}}^{\mathrm{r}}$. This would imply that the O–O dissociation is energy-wise costlier than its formation. Nevertheless, the exact mathematical form of entropy production, obtainable from **Equation [10]**, depends on the underlying thermodynamics and kinetics of the elementary steps that are, unfortunately, not easy to parametrize for LRSO. A different, more 'ideal' electrode material with lesser parameters will therefore be used in a model-based follow-up study to compute entropy production. Novel experimental methods also need to be developed for determining the entropy change for such path-dependent materials that show continuous OCV drift.

Note that true equilibrium theoretically does exist in the scheme of **Figure V.6b**, i.e. when the four steps occur in unison, but this situation is never achieved at practical C-rates, thus leading to metastability. This is the key difference versus cationic redox, which

also involves local-structural changes such as octahedral expansion/contraction, but these are kinetically fast and therefore always in equilibrium with the redox step.

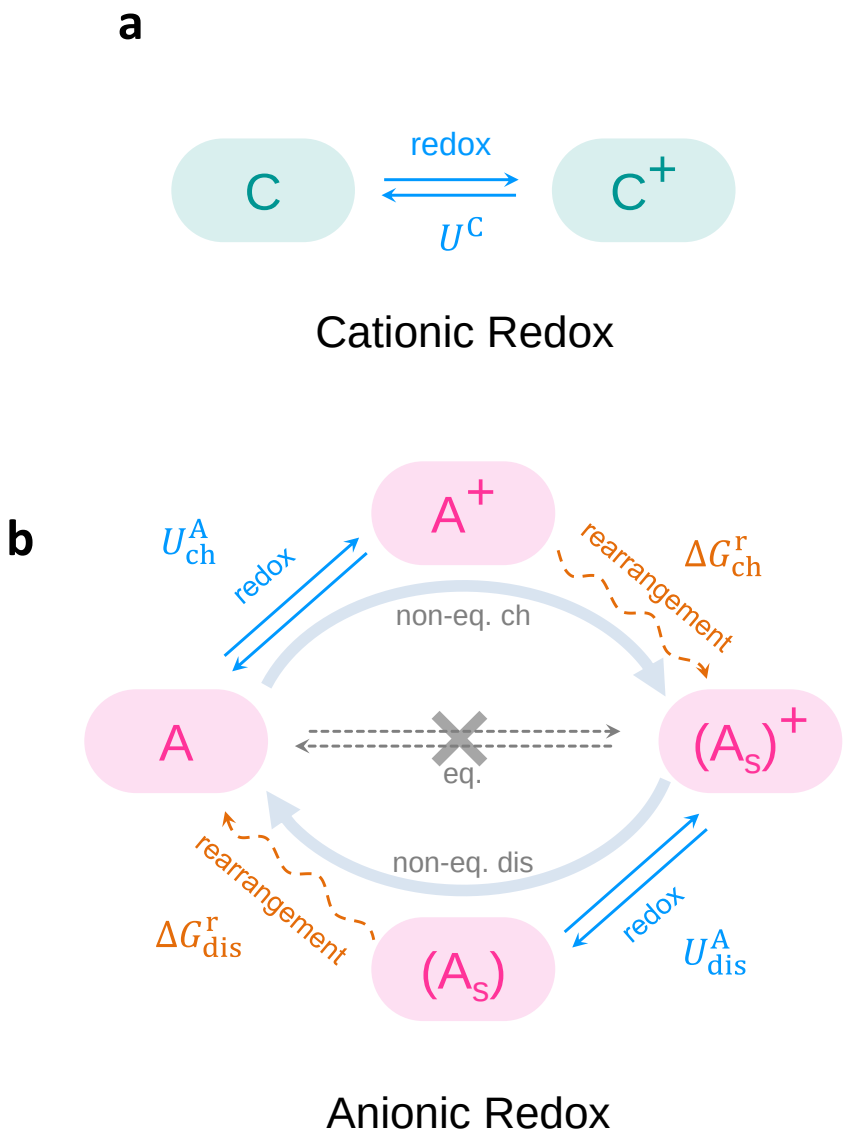


**Figure V.6 | Simplest possible mechanism for anionic redox to account for voltage hysteresis.** (**a**) Cationic redox can be described as a single step electrochemical reaction. **C** and **C**$^{+}$ are respectively the reduced and oxidized cationic species (e.g. $Ru^{4+}$ and $Ru^{5+}$). (**b**) Anionic redox is described by a multi-step "square-scheme" mechanism. The upper and lower paths denote respectively the far-from-equilibrium charging and discharging paths. **A** denotes the anionic species in reduced state (e.g. $O^{2-}$) that upon oxidation forms unstable **A**$^{+}$ (e.g. $O^{n-}$ with $n < 2$). Structural reorganization thus spontaneously takes place to form stabilized **(A$_S$)**$^{+}$ (e.g. $(O–O)^{2n-}$ with $n < 2$). Reduction on discharge goes though the unstable **A$_S$** state (e.g. $(O–O)^{4-}$) that spontaneously rearranges back to the original state. Electrons and Li are not explicitly shown in these reaction schemes but are obviously needed for charge/material balancing. The cationic and anionic reactions may occur in an overlapped fashion depending of the values of kinetic and thermodynamic parameters.

The above mechanism for anionic redox bears a similarity with the previously proposed 'activated bonding change' model to explain voltage hysteresis in hydrogen-containing carbons[281,282] as well as the phase-change-based model to explain voltage hysteresis in Li-rich NMC[190,191]. All these models lead to a non-equilibrium situation under operating conditions, thus making it necessary to consider the heat associated with bonding change or with phase change. Consistent with our explanations, a large heat generation was also observed in the plateau regions for hysteretic carbons[283] and assigned to the exothermic chemical step related to bonding change.

Concerning practical applications, the obstacle of quasi-static voltage hysteresis in Li-rich electrodes can only be overcome by addressing directly the anionic redox process. One possibility is to eliminate the occurrence of metastable reaction pathways by designing/discovering electrodes with fast kinetics of the rearrangement steps. The other is to design/discover electrodes with low energy penalties in the rearrangement steps. Towards these goals, revisiting anionic redox chemistry in chalcogenides[77], owing to their low chemical hardness, may prove beneficial for fundamental understanding. Preliminary results with layered sulfides already look promising and are presented in Chapter VI. Another way to lower the energy penalty of rearrangements could be the use of 5*d* transition metals, e.g. $Na_{2-x}IrO_3$[121] and $Li_{2-x}IrO_3$[70,120] appear to be hysteresis-free, but this option is cost-wise impractical.

Lastly, apart from providing mechanistic insights about the anionic redox reaction in Li-rich electrodes, this work provides a new direction in the characterization of batteries with isothermal calorimetry. A particular highlight is the importance of $U_H$, the enthalpy potential. Concerning thermal management, the knowledge of $U_H$ can greatly help in predicting the total heat generation. Therefore, we recommend its measurement, especially for battery materials that either show large entropy changes or a quasi-static voltage hysteresis (silicon, graphite, $LiFePO_4$, Li–S, Li–$O_2$, and conversion electrodes). The non-equilibrium thermodynamics approach developed in the present work may also help in understanding the underlying mechanisms of other electrochemical systems beyond batteries, such as water-splitting catalysts that also show a large overpotential or perovskite solar cells that display an anomalous current-voltage hysteresis.

# V.5 – Chapter Conclusions

In summary, isothermal calorimetry has elucidated the general thermodynamic mechanism governing the 'model' LRSO cathode's electrochemistry, especially concerning its hysteretic anionic redox reaction.

We proved that before anionic activation, LRSO exhibits a classical and fully reversible intercalation mechanism for the $Ru^{4+/5+}$ cationic redox process. Further charging leads to the anionic oxidation plateau that accompanies a permanent change of the material, such that it displays sloped and hysteretic voltage profiles with reversible oxygen redox chemistry in the subsequent cycles. In a thermodynamically consistent manner, we demonstrated that the electrical work lost due to such voltage hysteresis is dissipated as waste heat. This heat release is higher on discharge and indicates larger energy penalties in reversing the structural rearrangements that are caused by anionic oxidation. It is now clear that voltage hysteresis is a direct consequence of non-equilibrium entropy production, and not simply due to large differences in the enthalpy of paths. Far-from-equilibrium is therefore an essential condition for quasi-static voltage hysteresis, which renders it difficult to obtain the true equilibrium properties.

The extension of this work to the 'practical' Li-rich NMC among other anionic redox cathodes is immediately imminent, along with the implementation of model-based simulations that are preliminarily presented in the next Chapter VI. This could help in generalizing the multi-step "square-scheme" model proposed herein, which is a necessary step to inspire mitigation approaches for the eventual elimination of voltage hysteresis. In the broader context, we hope that this new direction for battery characterization using isothermal calorimetry would inspire the electrochemistry community to further exploit this tool as well as to adopt the concepts of enthalpy potential and entropy production.

# Chapter VI – Final outcome, pending issues, and future guidelines

This thesis dealt with lithium-rich layered oxides – a class of materials that are being studied extensively as positive electrodes for lithium-ion batteries due to their very high capacities stemming from combined cationic and anionic redox activities, which our group directly demonstrated in 2013. Throughout my PhD, we witnessed many researchers worldwide jumping into the wagon for exploring the fundamental science or for creating advanced high-capacity electrode materials. This burgeoning activity was enough to keep me excited for three years, during which I could actively engage not just in fundamental mechanism exploration, but equally in highlighting the practical issues with the novel anionic redox phenomenon. So, in the first part of this concluding Chapter[‡‡], I will summarize how my findings have contributed to the field, further bearing in mind that much remains to be done. Then, guided by the pending questions, I will open two imminent pathways for fundamental research, before ending this Chapter with perspective strategies that would help in catapulting anionic redox into a new era.

## VI.1 – Thesis achievements and remaining questions

The electrochemical fingerprint of anionic redox, as evidenced in either Li-rich NMC or LRSO, is arguably the presence of staircase-like charging followed by sloped S-shaped discharging, with the S-type behaviour maintained from second cycle onwards. Through this thesis, we clearly demonstrated that such a specific shape modification is associated with the irreversible local structural disordering triggered by the anionic oxidation plateau. Interestingly, some newly discovered materials, such as cation-disordered $Li_{1.2}Mn_{0.4}Ti_{0.4}O_2$[73] and layered $Na_{2/3}[Mn_{1-x}Mg_x]O_2$[128,129], do not lose their staircase-like charging after the first cycle. Therefore, a remaining task is to reconcile these differences across materials for eventually being able to control the voltage profiles. State-of-the-art local-scale characterization tools should be pursued for valuable insights in this regard. Equally, the recent demonstration of voltage recovery, via mild temperature (150 °C) annealing that leads to reordering of cycled Li-rich NMC samples, is another exciting direction to further scrutinize, perhaps *in situ* within a solid-state battery.[211]

‡‡ Parts of this Chapter are based on the following review article that I co-authored :

**Assat, G.** & Tarascon, J.-M. Fundamental understanding and practical challenges of anionic redox activity in Li-ion batteries. ***Nature Energy***, 3, 373–386 (**2018**). (https://doi.org/10.1038/s41560-018-0097-0)

Continuing further with local structure, another debated issue was the shortening of O–O distances through octahedral distortion that our group reported earlier for $Li_2IrO_3$.[70] Through this thesis, we not only provided a significant advancement of *operando* XAS beyond existing literature by combining it with chemometric analyses to neatly decouple the redox processes, but also were able to identify an off-centring type of octahedral $RuO_6$ distortion in LRSO based on the pre-edge peak along with EXAFS modelling. Following our footsteps, a new EXAFS modelling study could show similar octahedral distortion in charged Li-rich NMC[216], with a more controversial Raman study[240] even claiming the formation of peroxo-like $(O–O)^{2–}$. Clearly, there is further scope for understanding such distortion, besides the even more obscure local effect of cation migration, across several anionic redox materials.

A burning task after the successes with 'model' LRSO was to come back to 3*d* metals and understand anionic redox in Li-rich NMC. With this thesis, we clarified for the first time the complete charge compensation mechanism of this promising electrode material. Not only that, this thesis also opened a new characterization direction by implementing the HAXPES technique for directly quantifying anionic redox in the bulk and over long cycling. As HAXPES is becoming our go-to technique for oxygen redox while also gaining popularity amongst other groups, the chances to resolve some remaining technical issues are quite high. These ambiguities include the observation of $O^{n–}$ component in charged $Li_{1–x}CoO_2$[86], despite the absence of non-bonding oxygen 2*p* states, and the possible dependence of $O^{n–}$ binding energy on the value of *n*. We will henceforth continue to push the limits of HAXPES, with new data already acquired for $\beta$-$Li_{2–x}IrO_3$, while hunting for more direct spectroscopies. In this regard, the emergence of RIXS[155] for anionic redox, over the same time-frame as our HAXPES, has been a pleasant development. With these new tools now in the hands of the community, time has also come to move beyond merely identifying the "signature" of oxidized oxygen and pursue the characterization of the subsequent valence band rearrangement.[284] Here, solid-state physicists have to be brought on-board, both theorists with correct DFT implementation and experimentalists with advanced spectroscopies. A couple of sophisticated experimental possibilities include: (*i*) playing with the incident photon energy (*hv*) and hence the element/orbital cross-section in HAXPES to highlight different cationic/anionic states in the valence band[285,286], and (*ii*) resonant photoemission spectroscopy (RPES) to selectively resonate certain states after the valence bands get reshuffled.[287]

Such a bringing of new techniques into the battery field, although intimidating at the debut, can be immensely fruitful later, as already witnessed in this thesis that widened the horizons of isothermal micro-calorimetry beyond its traditional usage (intercalation entropy or parasitic side-reactions), by instead using it for revealing the thermochemical mechanism of anionic redox. The lesser known concepts of enthalpy potential and entropy production emerged as central ideas, which I believe will greatly benefit electrochemists, not just with battery SoC/thermal management, but also with fundamental science. As with every technique, isothermal micro-calorimetry showed its own limitations, which should motivate us to further design out-of-the-box electro-thermal experiments.

Science aside, we were also one of the few groups who dared questioning via this thesis the practicality of anionic redox. When I started, voltage fade was undoubtedly the most discussed practical issue with Li-rich NMC, but over the past three years, we have also brought voltage hysteresis and sluggish kinetics into the spotlight, as summarized in **Figure VI.1**. Worth listing are the updated electrochemical testing protocols developed within this thesis (see Appendix A5) that pertain to the unique electrochemical properties differentiating anionic redox compounds from classical cathodes.

Starting with voltage hysteresis, it was the 'model' LRSO phase that first led us to distinguish the detrimental role of high potential anionic oxidation in opening the voltage gap, with *operando* XAS spectroscopically confirming this finding. This was an important stepping stone in generalizing this relationship to the 'practical' Li-rich NMC cathode. Since voltage hysteresis leads to energy inefficiency that is dissipated as waste heat that we directly confirmed with isothermal calorimetry, the onus now is to find a solution, perhaps by taking inspiration from emerging materials. Among the newly discovered Li-based anionic redox materials made of 3*d* metals, cation-disordered $Li_{1.2}Mn_{0.4}Ti_{0.4}O_2$[73] and $Li_2MnO_2F$[76] show severe hysteresis, and so does layered O2-type $Li_{1.25}Mn_{0.50}Co_{0.25}O_2$[71]. In contrast, the two $Li_2IrO_3$ polymorphs[70,120] exhibit superimposing charge-discharge voltage curves. At the beginning, it was facile to proclaim the high covalence of 5*d* iridates in explaining this improvement. But now the vital role of other parameters is evident from the emerging Na-based anionic redox materials that show, while all of them being based on 3*d* metals, varying degrees of hysteresis. $Na_{2/3}[Mn_{1-x}Mg_x]O_2$[128,129] shows a large hysteresis, while it is less severe in $Na_{4/7-x}[\square_{1/7}Mn_{6/7}]O_2$ (□ being Mn vacancy)[130] and P3-type $Na_{0.6}[Li_{0.2}Mn_{0.8}]O_2$[131]. These mixed results highlight the complexity of the

underlying science, unifying which will be a large leap towards mastering this issue. We have already spurred this direction by proposing a multi-step "square-scheme" model for anionic redox, which now needs to be complemented by atomic-scale characterization of the formation/breaking of O–O dimers and/or the reversible migration of TM ions. Overall, I can safely conclude that voltage hysteresis, which became my personal obsession over the past three years, exhibits a complex science…therefore the solution will have to be unorthodox.

Turning now to the poor rate performance of Li-rich cathodes, this thesis pioneered in providing evidence of sluggish anionic redox kinetics, once again via parallel studies on LRSO and Li-rich NMC. These results implore the battery community to carefully characterize and report the kinetics, especially for emerging materials. Among these, unfortunately, the rate performance of the new O2-type layered $Li_{1.25}Mn_{0.50}Co_{0.25}O_2$ falls from 400 mAh $g^{-1}$ at 5 mA $g^{-1}$ to just 225 mAh $g^{-1}$ at 80 mA $g^{-1}$.[71] Similarly, the need for high temperature (50 °C) to cycle the cation-disordered materials is reminiscent of poor kinetics[74], which further puts into question the theoretical prediction of improved diffusion in Li-excess disordered materials as a result of the creation of local 3-D channels within the disordered network[146]. All hope is not lost as some optimistic examples do exist, including the 3-D $\beta$-$Li_2IrO_3$ polymorph that is significantly quicker than the 2-D layered $\alpha$-$Li_2IrO_3$.[120]. However, we can no longer rely on such trial-and-error and the route towards a meaningful solution has to pass by the scientific detour, which is where the proposed multi-step mechanism for anionic redox will come into the spotlight. With this mechanism in mind, we need to question the apparent correlation observed between $R_{ct}$ and $D/R^2$, and whether the diffusion-like limitations are actually a manifestation of a very slow rearrangement step. It may even turn out that voltage hysteresis and sluggish kinetics are two facets of the same coin. If we can develop and parametrize a thermodynamically-consistent phenomenological model for anionic redox that unifies all experimental observations, including the long-time GITT or PITT relaxations, the fundamental questions above can be answered, leading to the pushing of limits of classical battery electrochemistry that we know today.

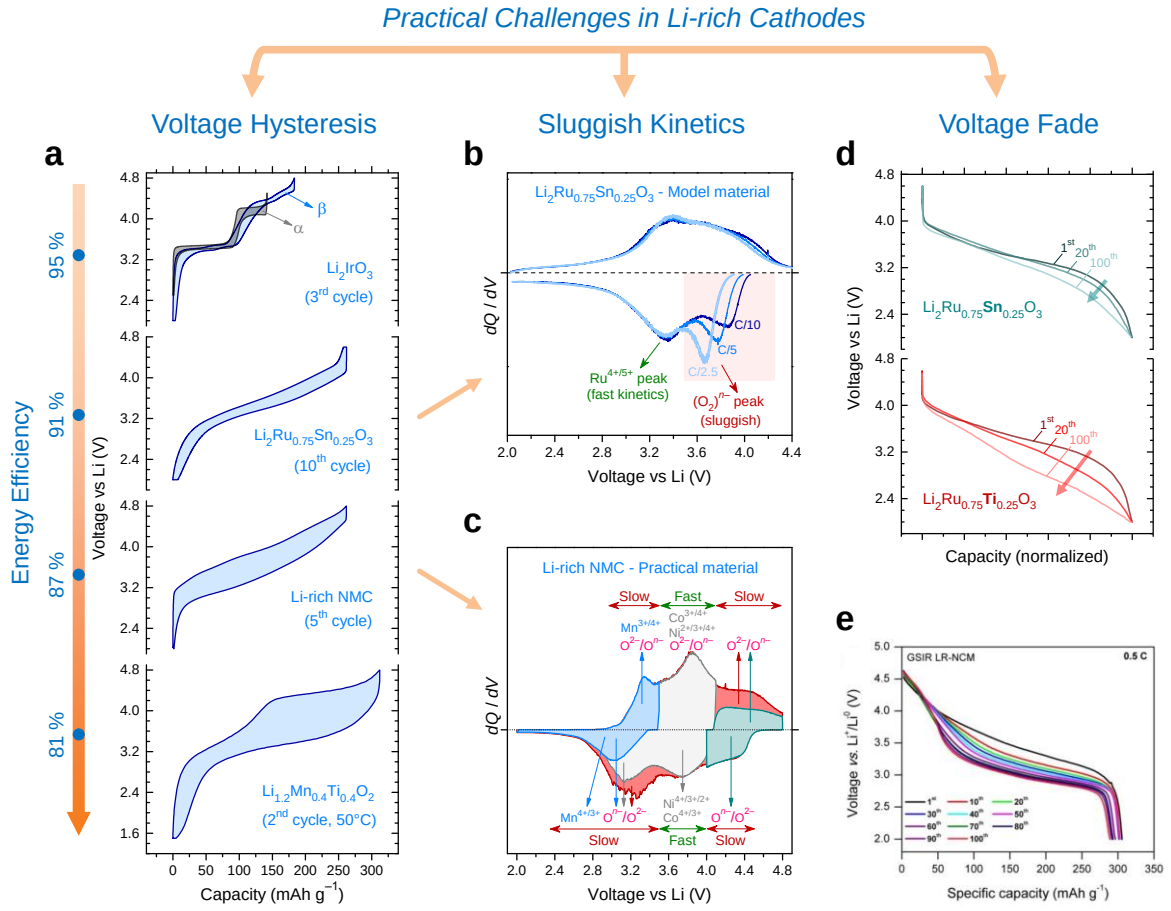


**Figure VI.1 | Practical challenges facing Li-rich cathodes.** Voltage hysteresis (**a**) which lowers the energy efficiency, sluggish kinetics (**b** and **c**) which reduces power density, and voltage fade (**d** and **e**) which complicates the BMS. Note that voltage hysteresis is lower for model compounds based on heavy 4*d*/5*d* metals (upper two panels in **a**) and increases noticeably as we move to Li-rich NMC, then becoming huge for the cation-disordered phases, such as $Li_{1.2}Mn_{0.4}Ti_{0.4}O_2$[73] (lowest panel in **a**). Using the model $Li_2Ru_{0.75}Sn_{0.25}O_3$ cathode, the sluggish kinetics of anionic redox is revealed (as shown in **b**) by recording the voltage profiles at increasing C-rates. A large polarization is seen for the anionic reduction peak[194] that is located at high potential[119]. The cationic/anionic charge compensation is more complicated in Li-rich NMC (**c**), but the same trend of slow kinetics is observed at potentials where anionic redox activity is found.[106] Concerning voltage fade, the stabilized voltage profiles in the model $Li_2Ru_{0.75}Sn_{0.25}O_3$ system is compared against $Li_2Ru_{0.75}Ti_{0.25}O_3$ (**d**) that shows an aggravated voltage fade (marked by thick arrows).[69] In contrast, significant voltage fade persists even in a state-of-the-art surface-modified Li-rich NMC (**e**).[125] $Li_{1.2}Mn_{0.4}Ti_{0.4}O_2$ data in (**a**) from *Yabuuchi et al.*[73]. Panels adapted from: (**d**) *Sathiya et al.*[69] and (**e**) *Qiu et al.*[125].

Turning now to voltage fade, this thesis revealed that the overall time spent with oxidized oxygen (not just the charging voltage) plays a key role in voltage decay. We also

contributed to the growing evidence that voltage fade results from bulk degradation, and not merely from surface reconstruction. The exact irreversible transitions leading to voltage fade may vary across materials, ranging from the permanent trapping of TM ions in tetrahedral sites to a change from "layered to spinel-like" structure. However, this issue seems unavoidable in all Li-based materials, including the cation-disordered cathodes[76,144] or even the 5*d* iridates $Li_2IrO_3$[70,120] that gradually lose their original voltage profiles over long cycling. Since existing literature casts doubts whether "perfect" voltage retention can ever be achieved with reversible oxygen redox in Li-ion cathodes, time has now come to invest in learning how to better manage this issue, besides trying to eliminate it.

The last important issue with Li-rich electrodes, which was not investigated within this thesis but deserves mentioning, pertains to their poor stability when charged to high potentials for gaining extra anionic capacity that eventually triggers oxygen release. Such a correlation between high activity and poor stability is not astonishing, as the same is witnessed in other electrochemical systems, e.g. water-splitting catalysts.[288] Since gas release promotes parasitic side-reactions and causes 1$^{st}$ cycle irreversible capacity loss, understanding it in Li-rich NMC led to intense recent debates.[103,116,223,241,257,289,290] Starting from the early speculation of copious oxygen release in 2006[94], which was reinvestigated in 2016[103] and found to be much lesser, research has now moved into identifying the precise electrochemical versus chemical pathways mechanisms for lattice oxygen loss. Other than Li-rich NMC, gas release also affects the cation-disordered cathodes[76,144,291] but not the Na-based $Na_{2/3}[Mn_{1-x}Mg_x]O_2$[129], which may simply be due to the lower extent of overall oxidation in the latter. Once again, the 'model' $\beta$-$Li_2IrO_3$ phase stands out by allowing complete Li removal without losing oxygen.[120] There is a clear need for further understanding this issue's multifaceted relationship with bulk structure, band positioning, surface chemistry, and electrode–electrolyte interface.

To summarize, this thesis has clarified that, depending on the material composition, covalence, and structure, the fundamental interplay between cationic–anionic redox processes governs the practically important properties of Li-rich materials. The above-mentioned pending questions are complex and highlight that although the anionic redox concept has matured, it still remains a rich playground for further science, ranging from designing new materials to understanding the mechanism. Towards these goals, two future directions, one experimental and one theoretical, are introduced next.

# VI.2 – Two future directions for fundamental science

From a materials perspective, besides continuing the pursuit to chemically improve the promising Li-rich NMC layered oxides, efforts are still required to widen the number of M–L couples (with L beyond oxygen) as well as to widen the range of host structures showing reversible anionic redox chemistry. This calls for selecting M–L couples with suitable band positions (recall **Figure I.11**), a task towards which theory can be of great predictive help whereas inorganic chemistry imminently offers at least two options. As already initiated, one consists in increasing the energy of the TM *d* states by moving down within the periodic table (Mn → Ru → Ir) and reducing the *U* term so that they approach the O 2*p* non-bonding states to enhance the chances of triggering anionic redox while lowering $O_2$ release, but at the expense of raw material costs. Another option relies on replacing oxygen with less electronegative ligands, such as L = S, Se, or Te, so as to raise the energy of the L *np* non-bonding levels (*n* = 3 for L = S) which now will approach/penetrate the TM *d* band, hence the making of various transition metal sulfides (or selenides, tellurides). By returning to the sulfur chemistry, we will of course minimize the chances of releasing $S_2$, as the chemical hardness of sulfur is lower than that of oxygen, but at the expense of a lower operating voltage. On the optimistic side, the larger size of the ligand may offer a higher structural flexibility of the oxidized ligand network that seems to be a possible way to overcome the kinetics and hysteresis issues. To test these hypotheses, we designed some new sulfide electrodes that are briefly introduced below, with detailed investigations to follow in the PhD work of Sujoy Saha.

## ○ Design of 'model' Li-rich layered sulfides

The most attractive Li-based anionic redox cathode, i.e. Li-rich NMC, is derived from the honeycomb layered $Li_2MnO_3$, also written as $Li[Li_{1/3}Mn_{2/3}]O_2$. Driven by the motivation to design an analogous layered sulfide $Li_2MS_3$, we first need to select the right transition metal M by revisiting the literature. Two such honeycomb layered sulfides, namely $Li_2SnS_3$[292,293] and $Li_2US_3$[294], were known to exist but more recently (this year) the first report on 3*d* metal based $Li_2TiS_3$[295] came out. Note that this phase has no structural relation to the well-known $TiS_3$.[113] We therefore synthesized this new material

for testing it as a positive electrode in Li-ion batteries. Although the electrochemical activity of $Li_{2-x}TiS_3$ turned out to be poor (not shown here), it does not come as a total surprise, especially in light of its schematic band structure shown in **Figure VI.2**. Owing to the $d^0$ electronic configuration of $Ti^{4+}$ in $Li_2TiS_3$, Li removal from it cannot be charge compensated by Ti and thus directly attempts to extract electrons from the S 3*p* states. This situation is unfavourable and analogous to $Li_2Mn^{4+}O_3$, in which the filled $Mn^{4+/5+}$ band is too deep in energy such that Li removal also directly leads to oxygen oxidation (**Figure VI.2**), which turns out to be unstable against $O_2$ release since the relative cationic/anionic band positioning is not suitable for reversible anionic redox (recall **Figure I.11**).

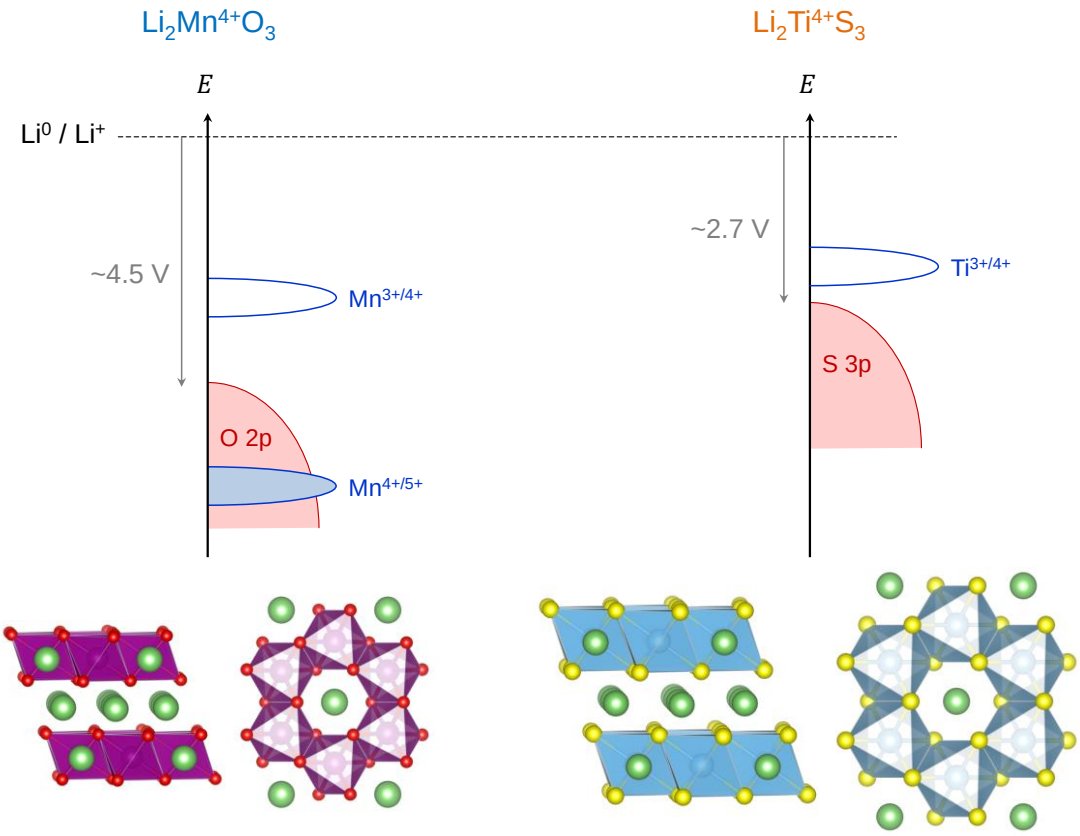


**Figure VI.2 | Schematic band diagrams of honeycomb layered $Li_2MnO_3$ (left) and $Li_2TiS_3$ (right).** The band positions are deduced from the works of *Goodenough et al.*[52,296] The higher band positioning of S 3*p* compared to O 2*p* is due to the lower electronegativity of S. Note that the non-bonding ligand states and Hubbard splitting are not explicitly shown. Note also the bulkier crystal structure of sulfides compared to oxides.

Chemical substitutions to overcome such an unfavourable band positioning in $Li_2TiS_3$ can again be inspired from the way Li-rich NMC phases were designed on the

basis of $Li_2MnO_3$. One of the earliest successful attempts to make Li-rich NMC type of cathodes came with the partial chemical substitution of $Ni^{2+}$ into $Li_2Mn^{4+}O_3$, leading to compounds of the general formula – $Li[Li_{1/3-2y/3}Ni_yMn_{2/3-y/3}]O_2$.[64–66] For $y$ = 0.2, this series gives the well-studied $Li[Li_{0.2}Ni_{0.2}Mn_{0.6}]O_2$ Li-rich layered cathode. The introduction of electron-containing $Ni^{2+/3+/4+}$ bands just above the O 2*p* band in these materials leads to a band positioning that is favourable for reversible anionic redox activity (**Figure VI.3a**). The electrochemical response of this material as a cathode in Li-ion batteries is shown in **Figure VI.3b**. On first charge, initial cationic redox activity of $Ni^{2+/3+/4+}$ is followed by the anionic oxidation plateau, whereas the subsequent sloped discharge involves the combined cationic/anionic redox activities.[153]

Applying a similar chemical substitution strategy to $Li_2Ti^{4+}S_3$ first necessitates the identification of a suitable $M^{2+}$ substituent, such that the electron-containing $M^{2+/3+}$ band would be placed above the S 3*p* bands. Previous work indicates that the $Co^{2+/3+}$ band lies too deep in energy[295], but the $Fe^{2+/3+}$ band could be suitable by being pinned at the top of the S 3*p* band (**Figure VI.3c**), as revealed from previous investigations of the Li-stoichiometric $Li[Ti_{1-y}Fe_y]S_2$ layered sulfides.[296,297] We thus prepared the series of Li-rich layered sulfide cathode materials – $Li[Li_{1/3-2y/3}Fe_yTi_{2/3-y/3}]S_2$, that are structurally and electronically analogous to the abovementioned Li-rich layered oxide family. For example at $y$ = 0.2, the $Li[Li_{0.2}Fe^{2+}_{0.2}Ti^{4+}_{0.6}]S_2$ sulfide corresponds to the $Li[Li_{0.2}Ni^{2+}_{0.2}Mn^{4+}_{0.6}]O_2$ oxide. Moreover, the electrochemical properties of the two families are comparable as well. **Figure VI.3d** shows the voltage profile of the Li-rich $Li_{1.13-x}Fe_{0.3}Ti_{0.57}S_2$ that begins upon charge with partial $Fe^{2+/3+}$ oxidation at the slope followed by a plateau for the $2S^{2-}$ / $(S_2)^{n-}$ ($n$ < 4) anionic redox process. The subsequent discharge also highlights the reversibility of these cationic/anionic redox processes.

The possibility of creating more such newly discovered Li-rich layered sulfides is not just limited to the Fe-substituted series and we are currently working to expand the material design-space to other combinations. For example, suitable $M^{3+}$ substitution, that leads to electron-containing $M^{3+/4+}$ bands placed above the S 3*p* band, can also provide a favourable band positioning to trigger the reversible anionic redox process. In oxides, this is achieved by introducing the $Co^{3+/4+}$ bands, leading to the formation of Li-rich NMC.[135] For pursuing this direction in layered sulfides, it is not adequate to introduce the $Cr^{3+/4+}$ band that lies too deep in energy.[298] On the other hand, $Ti^{3+}$ self-substitution in $Li_2Ti^{4+}S_3$

is possible such that the Li-rich layered $Li[Li_{0.2}Ti^{3+}_{0.4}Ti^{4+}_{0.4}]S_2$ phase can be prepared and it shows quite interesting electrochemical properties as a cathode material (**Figure VI.4**).[299]

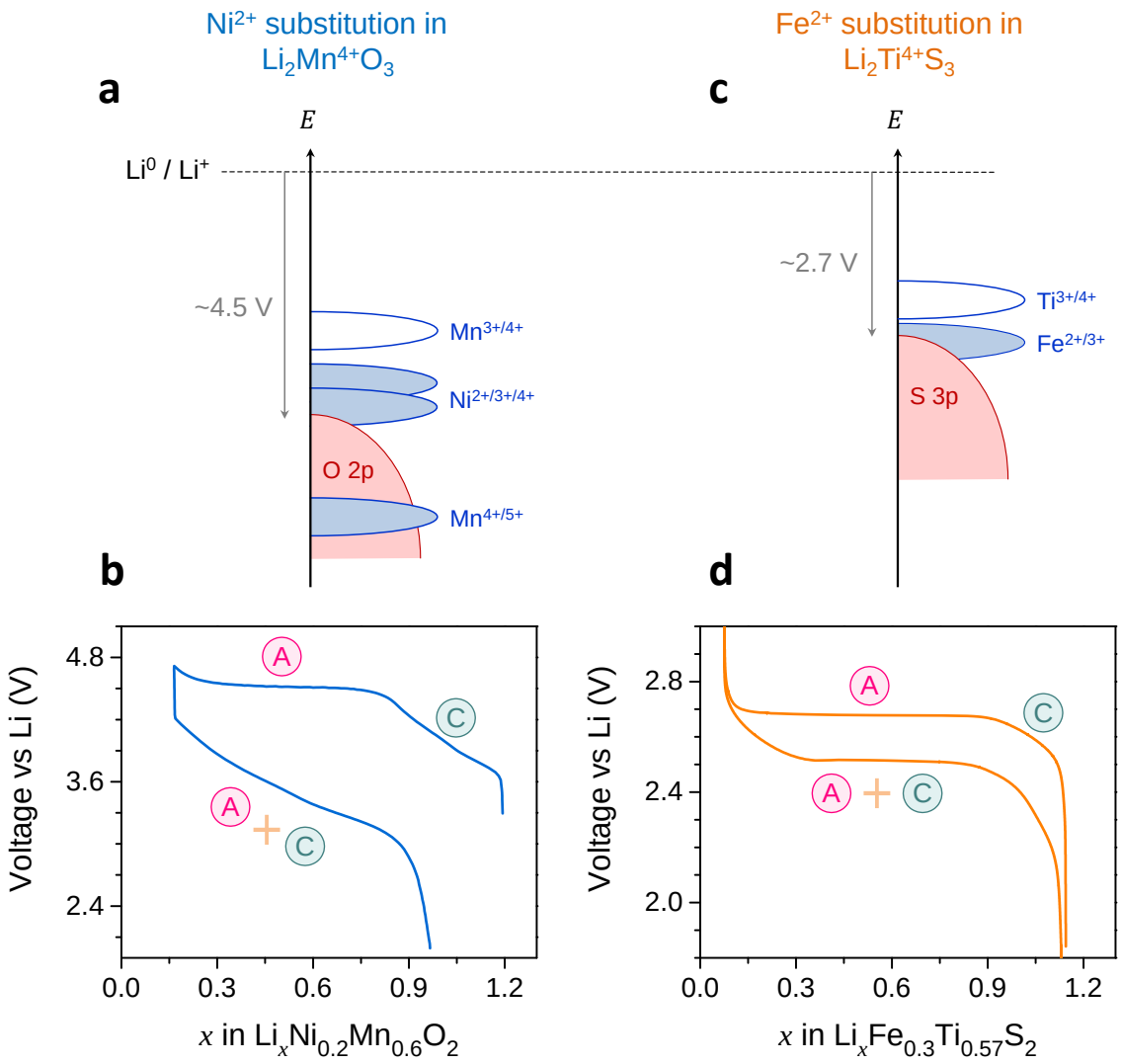


**Figure VI.3 | Design of Li-rich layered sulfides inspired from Li-rich NMC.** The band positions (**a**) and voltage profile (**b**) for the Li-rich oxide are adapted from *Luo et al.*[153] Band positions for the Li-rich sulfide (**c**) were deduced from the works of *Goodenough et al.*[296] and *Tarascon et al.*[297]. "**A**" and "**C**" denote respectively the anionic ($O^{2-}$ / $O^{n-}$ in **b**, $2S^{2-}$ / $(S_2)^{n-}$ in **d**) and cationic ($Ni^{2+/3+/4+}$ in **b**, $Fe^{2+/3+}$ in **d**) redox processes. Voltage profile in (**d**) is at C/20 : courtesy of *Sujoy Saha*.

Although these newly designed Li-rich layered sulfide class of positive electrodes lead to a specific capacity in the range of 250 mAh $g^{-1}$ (reaching 600 Wh $kg^{-1}$) at the material-level while being composed of earth-abundant elements (3*d* metals only), they may not offer any real-world competitiveness against oxide electrodes due to their low

operating potential as well as the practical issues with sulfur-handling. Nevertheless, we believe that this new class of materials will serve as excellent 'model' electrodes to study the general properties of anionic redox chemistry. Since the concept of oxidized sulfide anions is well-accepted in solid-state chemistry (e.g. the famous pyrites $Fe^{2+}(S_2)^{2-}$, $Co^{2+}(S_2)^{2-}$, etc.), proving the reactivity of anionic sulfur redox will be easier in front of the battery community, unlike the tough case of oxides. Therefore, these sulfides can potentially open the wide playground for solid-state electrochemists to tune the cationic/anionic band positions (and hence the redox potentials) for obtaining the desired properties. Moreover, these materials can also provide answers to some of the remaining fundamental questions that were listed in the previous Section VI.1.

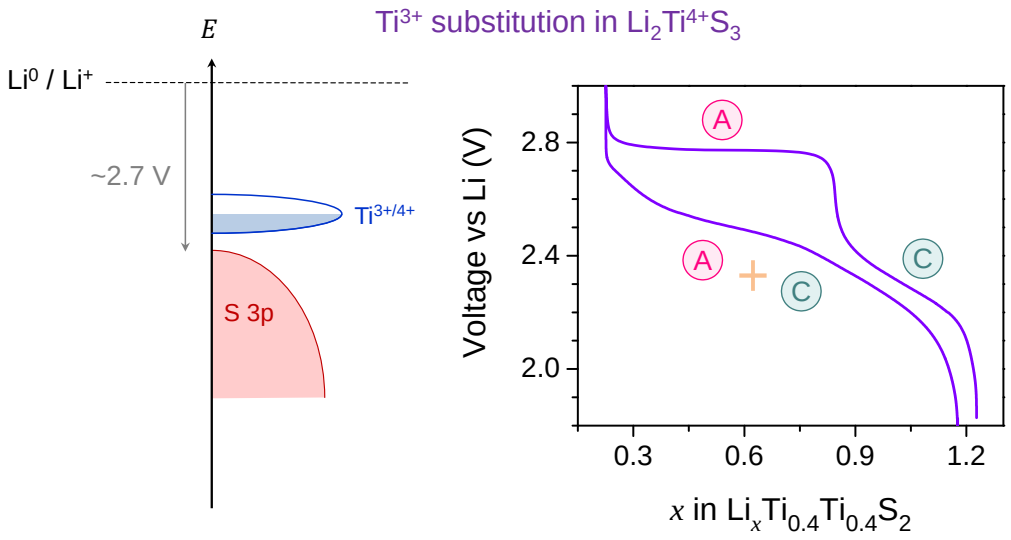


**Figure VI.4 | Schematic band positions and voltage profiles of a Li-rich layered sulfide made only from Ti.** Voltage profile is at C/20 : courtesy of *Sujoy Saha*.

For example, the staircase-like charge followed by sloped discharge can again be observed in **Figure VI.4**, even though no gas release is expected in sulfides, which highlights the importance of local structural changes ($MS_6$ distortion and/or metal ion migration) in possibly explaining this phenomenon. But more importantly, these sulfides can help in fundamentally understanding the kinetics and hysteresis issues that this thesis was able to reveal for the oxygen anionic redox. A first glance at the voltage profiles from second cycle onwards (**Figure VI.5**) shows very low overall polarizations (less than 160 mV), which are in fact lower than any Li-based oxygen redox cathode composed of 3*d*

metals or even of 4*d* metals (e.g. polarization in Li-rich NMC is ~400–500 mV and in LRSO is ~200–300 mV).

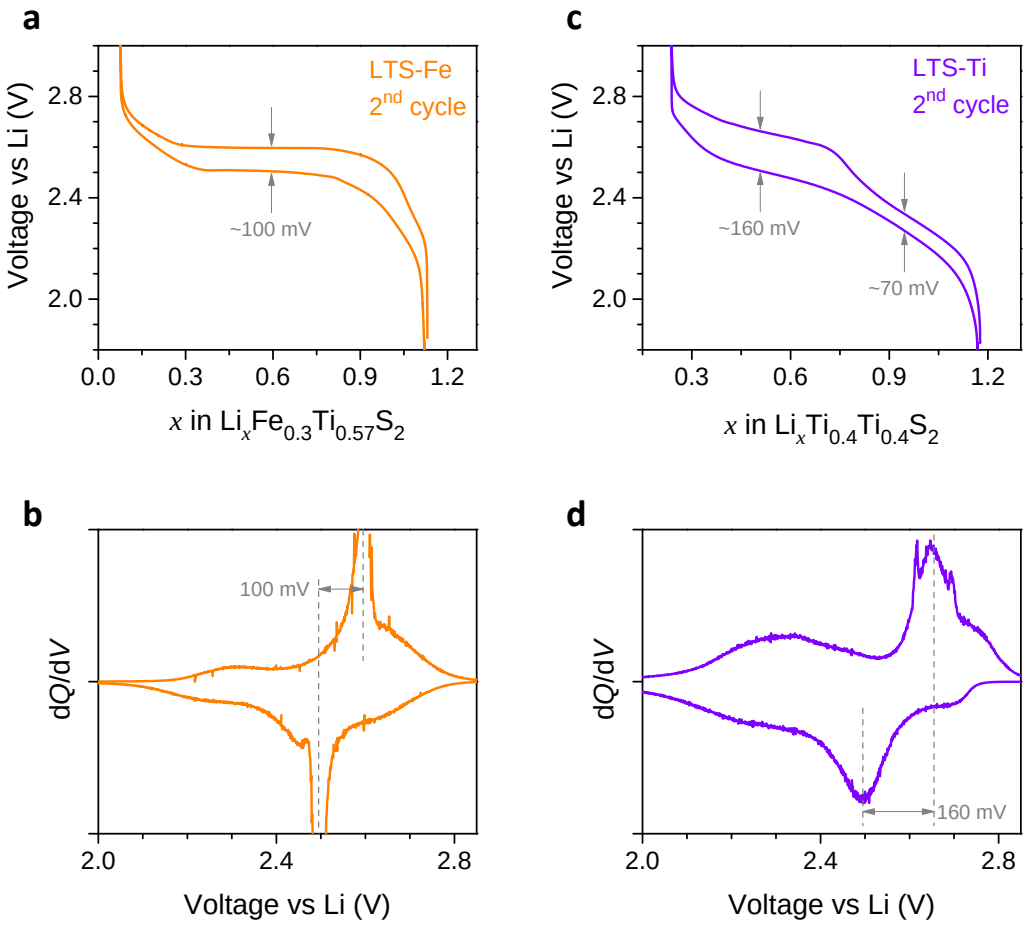


**Figure VI.5 | Electrochemical polarization in Li-rich layered sulfides.** The second cycle is compared for two of the newly designed cathodes. $Fe^{2+}$ substituted $Li_2TiS_3$ (LTS-Fe) in (**a**) and (**b**); and $Ti^{3+}$ substituted $Li_2TiS_3$ (LTS-Ti) in (**c**) and (**d**). The two peaks marked by dashed lines in each d*Q*/d*V* plot are presumably assigned to the sulfur anionic redox. All voltage profiles are at C/20 : courtesy of *Sujoy Saha*.

In summary, besides expanding the chemical space for designing novel anionic redox based cathodes with tuneable electrochemical properties, these sulfide materials will help in understanding the extent to which the limitations observed with oxygen redox in this thesis can be overcome by moving to a softer ligand. This future direction is currently being pursued in our lab by Sujoy Saha. Within the same context, the exploration of anionic redox in nitrides, although more audacious because of the lack of any known and promising nitride battery materials, could provide significant insights if successful. Lastly, recalling that chalcogenides are more ideal materials than oxides and therefore were more

easily able to satisfy the early thermodynamic models, e.g. the lattice-gas model (mean field theory)[264,300–302], some of the sulfides designed herein can serve as 'model' materials to quantitatively validate / parametrize the phenomenological model proposed for anionic redox in this thesis (recall **Figure V.6**). A preliminary investigation towards this future direction is shown next.

## ○ Towards a generalized model for anionic redox

Several of the remaining questions listed in the previous Section VI.1 were concerning the unique electrochemical properties associated with anionic redox. Answering them is impossible without the development of a generalized electrochemical model that would be able to capture the main experimental observations across a variety of materials. This is not a straightforward task, as I realized throughout the three years of my PhD. One has to first correctly measure / understand the experimental facts, which was the focus of a large chunk of this thesis, and then conceive a top → down model that would reproduce those facts, first in imagination and then in a computer.

> *"It doesn't make any difference how beautiful your guess (theory) is, it doesn't matter how smart you are who made the guess, or what its name is,…if it disagrees with experiment, it's wrong."* **– *Richard P. Feynman***

Keeping the above words in mind, I present here some preliminary simulations obtained with a chemical kinetics model based on the "multi-step" reaction scheme that was deduced in Chapter V for the anionic redox process (recall **Figure V.6**).

The first example is that of a Li-rich layered sulfide introduced just previously – $Li[Li_{0.2}Ti^{3+}_{0.4}Ti^{4+}_{0.4}]S_2$. Even after the first cycle, its voltage profiles continue to show two clear regimes at low and high potentials that are respectively charge compensated by $Ti^{3+/4+}$ (cationic redox) and $2S^{2-}$ / $(S_2)^{n-}$ (anionic redox). This simplified situation is a good starting point to validate the model that consists of parallel (simultaneous) cationic and anionic redox reactions. The thermodynamic parameters used for the simulations are listed in **Figure VI.6**, along with the resulting galvanostatic voltage profiles at C/20 that show excellent semi-quantitative agreement with the experiments.

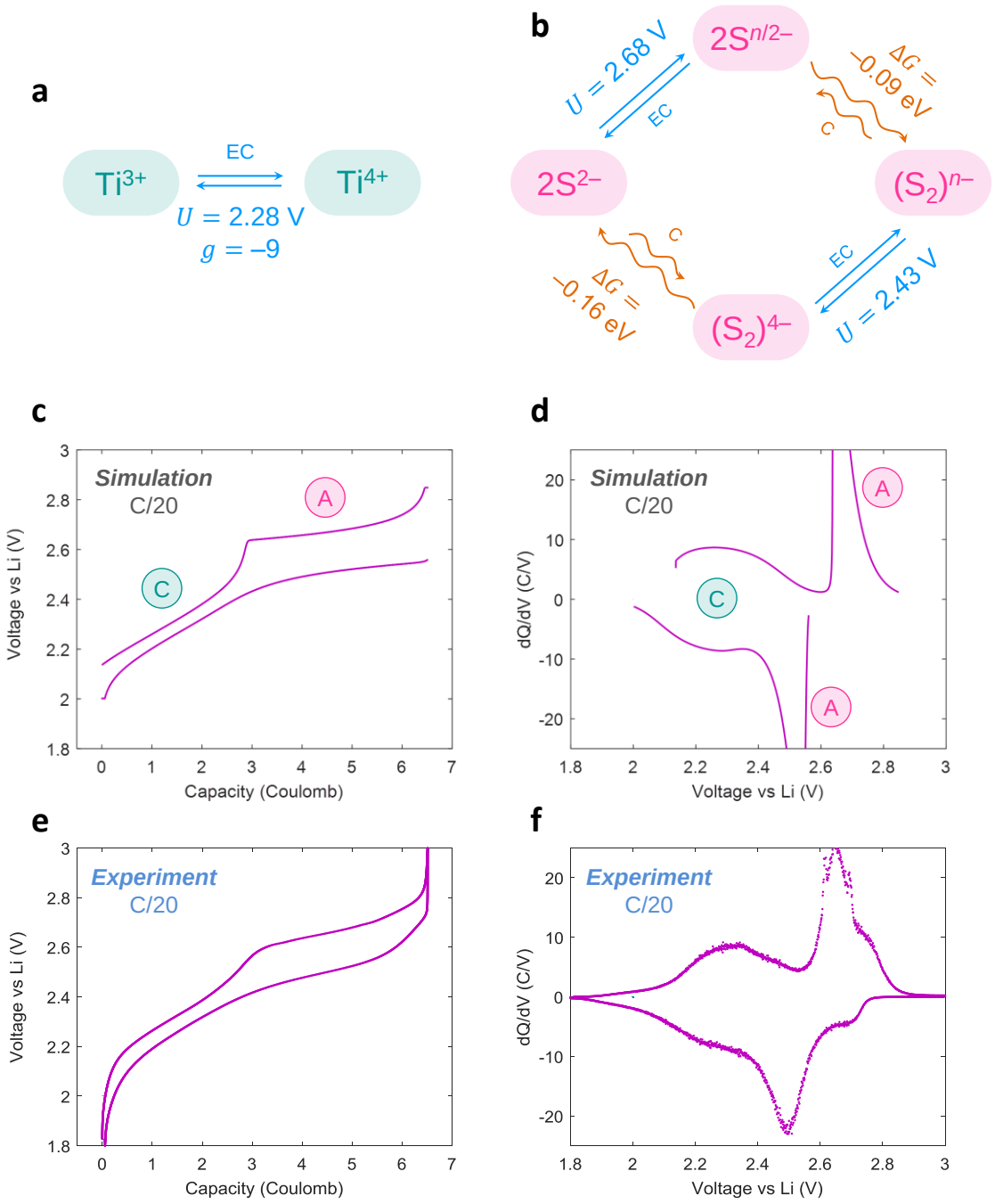


**Figure VI.6 | Simulations of the 2nd cycle voltage profile of $Li_{1.2}Ti^{3+}_{0.4}Ti^{4+}_{0.4}S_2$.** The thermodynamic parameters used for (**a**) cationic redox "**C**" and (**b**) anionic redox "**A**". Simulated galvanostatic voltage profiles (**c** and **d**) at 96.4 µA (C/20) along with the experimental profiles (**e** and **f**). Finite (and equal) electrochemical kinetics parameters were used for all electrochemical steps. The kinetics parameters for the chemical steps were chosen arbitrarily and not further optimized. Experimental data : courtesy of *Sujoy Saha*.

The cationic redox reaction was modelled as a single-step electrochemical reaction obeying the one-parameter Margules activity-coefficient model[219] having repulsive

interaction of the like neighbours ($g$ = –9) to take into account the sloped voltage profile in the low potential region. The electrochemical steps in the anionic redox EC / C / EC / C square-scheme were modelled by the Nernst equation and the thermodynamic parameters were constrained to form a closed cycle. Bulter-Volmer kinetics was used for all electrochemical steps (either cationic or anionic) and simple chemical equilibrium kinetics for all chemical steps. All mass and charge balance / conservation conditions were implemented. The simulated profiles in **Figure VI.6** display a larger voltage hysteresis over the anionic redox regime, despite the use of equal kinetic constants for all electrochemical steps (whether cationic or anionic). This underscores the thermodynamic aspect of voltage hysteresis, which is by design implemented in the multi-step model.

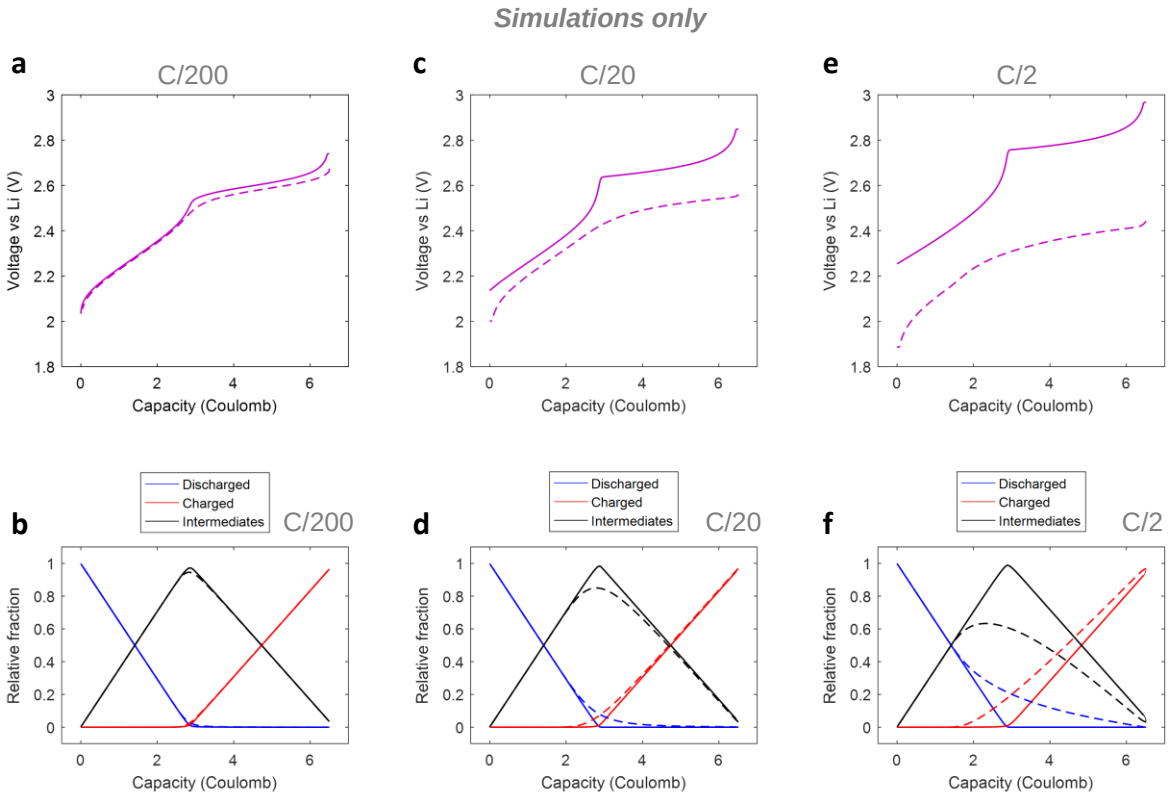


**Figure VI.7 | Effect of changing the C-rate on the 2nd cycle of $Li_{1.2}Ti^{3+}_{0.4}Ti^{4+}_{0.4}S_2$.** Same parameters are used as in the previous Figure. $Ti^{3+}$ represents the 'Discharged' phase (blue), $(S_2)^{n-}$ represents the 'Charged' phase (red), and the remaining species are clubbed into the 'Intermediates' (black). Charging = Solid lines, Discharging = Dashed lines.

The effect of changing the C-rate can also be understood on the basis of such simulations, especially how the underlying phase fractions evolve. **Figure VI.7** shows the

simulation results as the C-rate is varied by two orders of magnitude (from C/200 to C/20 to C/2). Larger polarization (even at C/200) and higher rate-sensitivity can be observed in the voltage profiles over the anionic redox regime, which is qualitatively consistent with experimental observations throughout this thesis using LRSO and Li-rich NMC. Path dependence (departure from equilibrium), particularly at higher rates, can also be observed from the evolution of relative phase fractions in **Figure VI.7**, which is again qualitatively consistent with experiments (recall *operando* XAS results of **Figure III.12**).

In the above simulations focused on a sulfide, the equilibrium potentials of the two electrochemical steps in the anionic redox scheme were set to be less separated (2.68 and 2.43 V, i.e. 250 mV apart) than what would be expected for oxides. For simulating some cases that would resemble oxides, the thermodynamic parameters of the oxygen redox scheme were set, as shown in **Figure VI.8a**, with a larger difference between the equilibrium potentials of the two anionic electrochemical steps (4.23 and 3.68 V, i.e. 550 mV apart). Using these parameters, two hypothetical cases are discussed next that were obtained by varying the cationic redox potential relative to the anionic scheme.

In the first case (**Figure VI.8b**), the cationic redox potential (3.60 V) is placed below 3.68 V, leading to well-separated cationic/anionic redox regimes – a situation qualitatively representative of layered $Na_{2/3}[Mn_{1-x}Mg_x]O_2$[128,129] and $Na_2RuO_3$[122]; as well as of disordered $Li_{1.3}Mn_{0.4}Nb_{0.3}O_2$[72,144], $Li_{1.2}Mn_{0.4}Ti_{0.4}O_2$[73] and $Li_2MnO_2F$[76]. In the second case (**Figure VI.8c**), the cationic redox potential (4.15 V) is set much above 3.68 V, leading to a situation where charging involves concomitant cationic and anionic oxidations followed by a reversal of the redox sequence usually observed on discharge (usually anions reduce before cations on discharge). In the case herein, cationic reduction occurs before anionic reduction and this situation is qualitatively representative of Li-rich NMC (recall **Figure IV.14**), layered $Li_4FeSbO_6$[118], and possibly some Ni-based cation-disordered[72,75] cathodes. Note also that, in both the simulated hypothetical cases, quasi-static voltage hysteresis could be reproduced at rates as low as C/200 by setting the kinetic parameters of the chemical steps to be slower than in the above case of a sulfide.

With these preliminary simulations, the validity of the model proposed for anionic redox is further strengthened, especially with regards to the thermodynamic nature of quasi-static voltage hysteresis. The simulations also point that the issues of voltage hysteresis and sluggish kinetics may be interconnected, which was a remaining question

listed in Section VI.1. Another feature of this model is the feasibility to calculate heat generation, both reversible (entropy change) and irreversible (entropy production), by inputting the simulated voltages and phase evolutions into the thermodynamic balances developed in Chapter V. However, this calls for additional thermodynamic parameters, such as the reaction entropy of each step, that remain elusive as of yet. Nevertheless, preliminary calculations with assumed parameters (not shown here) appear to support the calorimetry results of Chapter V.

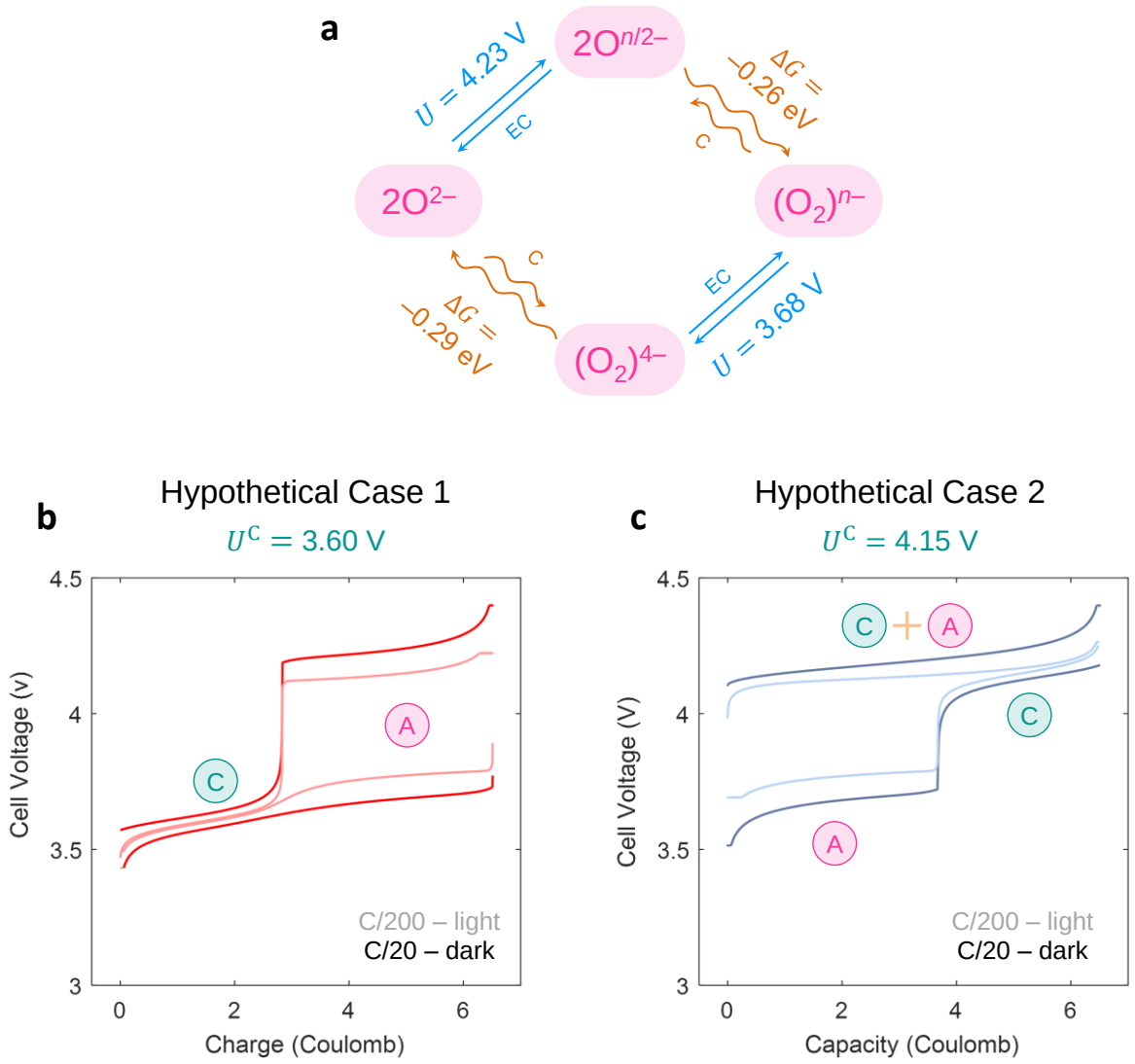


**Figure VI.8 | Two hypothetical cases simulated as representatives for oxides.** (**a**) The thermodynamic parameters were set with a larger voltage hysteresis than in the previous case of a sulfide. Simulated voltage profiles for two hypothetical cases demonstrating (**b**) well-separated cationic/anionic redox regimes or (**c**) a reversal of redox sequences. "**A**" and "**C**" denote respectively the anionic and cationic redox processes.

The biggest inconvenience with the such a top → down modelling approach is the need for guessing the appropriate physics and obtaining the correct parameters. This task seems easier with the more "ideal" sulfides, whereas further work will be needed for achieving quantitative agreement in case of oxides. To this end, it may even be necessary to improve the model construction, e.g. by implementing more sophisticated kinetics models for the chemical rearrangement steps (for instance the Avrami phase-change model[190,236]). Quantitative matching with long-time relaxation experiments would also help in obtaining the kinetic constants. Overall, these preliminary results have provided a promising direction towards the development of a generalized and thermodynamically-consistent electrochemical / phenomenological model for anionic redox electrodes.

## VI.3 – Final verdict on the viability of anionic redox

Thanks to theoretical and experimental advances, the novel concept of anionic redox has matured but not enough to yet reach the marketplace. Taking into account the fundamental and practical learnings from this thesis, I devote this final Section towards providing my verdict on the viability and future of Li-rich cathodes that are based on anionic redox. For achieving this task, Li-rich NMC is first compared with regular NMCs.

### ○ Evaluating Li-rich NMC versus stoichiometric NMCs

Since several roadblocks have been found to affect the real-world performance of Li-rich NMCs, it is necessary to evaluate their positioning with respect to the evolving NMC cathodes (111 → 622 → 811) in terms of different figures of merit (**Figure VI.9**). Apart from specific energy (gravimetric) and energy density (volumetric), cost (elemental abundance), energy efficiency, rate performance, and cycle life are also of varying degrees of importance, depending on the targeted applications. For the sake of comparison, two promising anionic redox cathodes other than Li-rich NMC, i.e. layered $Li_2Ru_{0.75}Sn_{0.25}O_3$ (LRSO) and cation-disordered $Li_{1.2}Mn_{0.4}Ti_{0.4}O_2$ (Li-Mn-Ti-O)[73], are also included in **Figure VI.9b–e**.

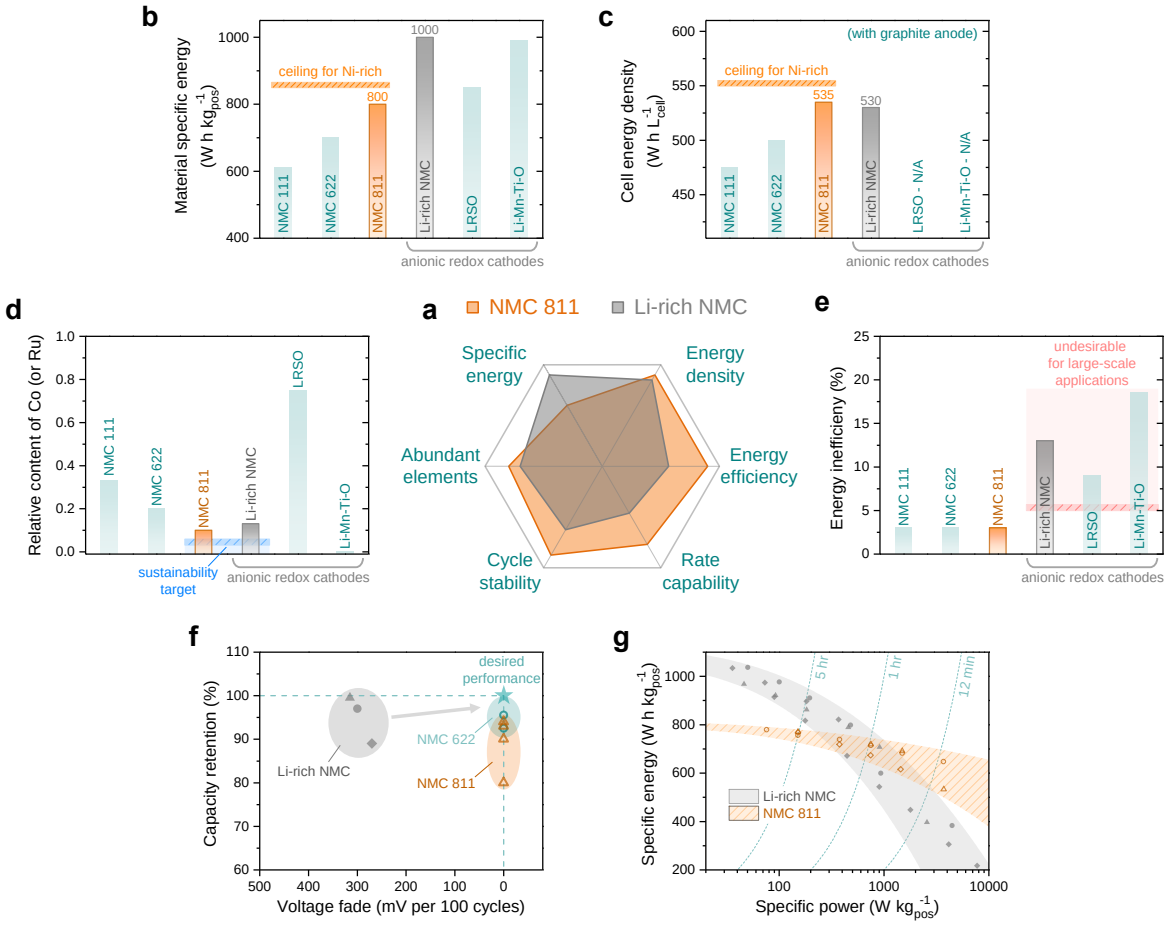


**Figure VI.9 | Benchmarking Li-rich NMC against stoichiometric NMCs.** The spider-chart (**a**) in the centre of this Figure compares electrode materials in terms of six key figures of merit (**b**–**g**) that are important for practical applications. Material-level specific energy (**b**) and cell-level energy density considering graphite anode (**c**) are compared in detail. While both NMC 811 and Li-rich NMC are similar in terms of Co content (**d**), note the poorer energy efficiency of the latter (**e**). Also the Li-rich NMC presently falls short in terms of cyclability (**f**) and power density (**g**), the former being based on capacity retention as well as voltage fade (over 100 cycles in Li half-cells). The Ragone plot in (**g**) reports material-level values on discharge and is drawn with a logarithmic scale for specific power. Panels (**b**–**e**) are based on literature survey, where only high performance materials are included.[21,45,124,303] The data in (**f**) for Li-rich NMC (filled symbols) are based on: ref.[125] (circle); ref.[304] (diamond); ref.[305] (triangle); and for NMC 622 (unfilled circles) and NMC 811 (unfilled triangles) on ref.[45]. The data in (**g**) for Li-rich NMC (filled symbols) are based on: ref.[305] (circles); ref.[164] (diamonds), ref.[244] (triangles); and for NMC 811 (unfilled symbols) on: ref.[39] (circles), ref.[306] (diamonds), ref.[307] (triangles).

Parallel to today's activities on Li-rich NMCs, there is an as intense push on NMC materials to increase their Ni contents, with the NMC 622 composition already gaining popularity for electric vehicles. These compositions can enable high energy-density

batteries (>250 Wh $kg^{-1}$ at cell-level), while showing excellent cycle/calendar life and preserving safety.[21,45,49,303] Further increasing the Ni content and minimizing the problematic Co results in the even higher energy NMC 811 composition that is foreseen to be commercialized by 2021, once the capacity fade problem is solved. At that stage, Li-rich NMC will no longer be advantageous concerning low Co content (**Figure VI.9d**), unless Co-free Li-rich materials are mastered. Nevertheless, being Mn-based, Li-rich NMC will still remain cost-wise advantageous vs. Ni-based NMC 811.[9,303] Since Li-rich NMCs are intrinsically penalized by their slightly lower crystallographic density in addition to the lower electrode tap-density usually achieved in practice as compared to the denser NMCs[124], this weakens their volumetric energy density at the cell-level – a critical metric for electric vehicles but not for stationary storage (**Figure VI.9c**, note that NMC 811 fares equally to Li-rich NMC). Overall, more work is still needed to fully exploit the energy advantages of Li-rich cathodes, whereas the cost benefit of using Mn is quite evident.

Besides energy density and elemental composition, voltage hysteresis, sluggish kinetics, and voltage fade have emerged as other major concerns with Li-rich NMCs, since these issues deteriorate respectively the energy efficiency, cyclability, and power density (**Figure VI.9e–g**). The poorer energy efficiency of Li-rich NMC is undesirable for large batteries (e.g. electric cars, stationary storage) where the cost of wasted energy as well as the associated heat generation would become important, but this issue may be less important in smaller batteries (e.g. portable electronics, power tools). A survey of relevant literature in **Figure VI.9f** compares the cyclability issues in these materials. It is evident that the main concern with Li-rich NMC is the fading of voltage and not of capacity, as opposed to NMC 811. Earlier market implementation will therefore depend on which issue is solved first. A comparison of rate performance of reported materials on a Ragone plot in **Figure VI.9g** demonstrates that Li-rich NMC retains its superiority for high energy applications (e.g. low P/E electric cars, portable electronics). However, NMCs are more advantageous for applications requiring faster than 1C discharge rates (e.g. high P/E hybrid electric vehicles, stationary storage for grid fluctuations, power tools).

In summary, the central spider-chart in **Figure VI.9** indicates that the enthusiastic expectations generated by the Li-rich NMC phases due to their outstanding specify energy and elemental abundance may need to be reconsidered, as further work is needed on other frontiers. Failing to solve/manage the identified issues in due time could delay the market

implementation of Li-rich NMC vs. NMC 622 and NMC 811 for applications that require high power, low energy wastage, and long cycle life.

## ○ Perspective recommendations to move forward

Based on the learnings from this thesis, one may be tempted to ask the following question, with my answer given just below.

> ***Question*** *– So…should we give up with anionic redox and Li-rich cathodes?*
> ***Answer*** *– My answer is a clear NO…we should continue!*

The rationale is simple. Among the known chemistries of today, energy-wise, the only options beyond Ni-rich NMCs are the Li-rich cathodes that are based on anionic redox. They offer anywhere from 10 to 40 % higher energy at the cathode-level than the maximum possible 850 Wh $kg^{-1}$ with Ni-rich layered oxides. Li-rich cathodes can enable cells with higher than 700 Wh $L^{-1}$ of energy density. The other emerging technologies of Na-ion and Li-S will never be able to offer this possibility, respectively because of lower achievable capacity and lower density. Likewise, Li-air is too immature currently, in addition to being bulky at the system-level. Therefore, Li-rich cathodes are the viable alternative and with this optimism in mind, I propose strategies in three directions in order to move forward with anionic redox.

Firstly, as already initiated in the previous section with the opening of two future research directions, we need to continue striving forward in understanding the fundamental origins of the practical roadblocks. In other words, (*i*) what parameters control voltage hysteresis, sluggish kinetics, and voltage fade, and (*ii*) why exactly do certain materials show better performances (e.g. ruthenates, iridates, sulfides, and some Na-based materials). I believe that revealing the underlying science via ‘model’ materials will continue to guide the way in designing effective mitigation strategies.

On the chemistry/materials side, since it is now clear that the practical viability of Li-rich cathodes is closely tied to the anionic redox process, mitigation strategies must directly target it. Concerning voltage fade, chemists are endeavouring with well-selected

chemical substitutions, surface treatments, core-shell and concentration-gradient particles, as well as "magic cocktail" electrolytes. A couple of new and promising strategies include (*i*) increasing the Ni : Mn ratio to avoid the activation of low potential $Mn^{3+/4+}$ redox[308–310], and (*ii*) increasing the disorder in TM/Li layer of the as-synthesized materials to prevent voltage fade[311]. On the other hand, solving the issue of voltage hysteresis would be more challenging, because no known Li-ion anionic redox cathode based only on 3*d*-metals is hysteresis-free. Concerning kinetics, one idea could be the design of materials within which cationic and anionic redox processes are not separated but occur at the same potential, so that cationic redox with fast kinetics can serve as a "redox-mediator" for the sluggish anions – a situation offered by the $Li_2IrO_3$.[70,120] Unfortunately, achieving such a specific situation with 3*d* metals is not trivial, but with growing family of 3*d* metal-based Na-ion anionic redox cathodes, which although are energy-wise less stellar owing to their limited amount of Na, chances to find the good combination are increasing.

The third approach, and perhaps a wiser one, would be the engineer's approach of simply adapting to the drawbacks and striking a compromise by matching the right cathode to the right application, with further investment in developing better battery management systems (BMS). For instance, battery engineers are already optimistic that voltage fade can be tackled via a sophisticated BMS and some models[191] also exist to predict voltage fade over long cycling. Similarly, voltage hysteresis, path-dependence, and the resulting heat generation may be handled with sophisticated SoC / thermal management methods. On the materials engineering side, a trade-off strategy could be the limited utilization of Li-rich character (i.e. 5–10 %, instead of the usual 20 %), as practical issues are known to aggravate with higher Li in the TM/Li layers. Likewise, cell engineers can also envisage electrode blends to optimize the overall performance, especially the power density. Such electrode blends are not new to the automotive sector, wherein high-rate $LiMn_2O_4$ was blended with NCA in the early days partly for the rate performance.[312]

In summary, although practical issues have discouraged certain researchers, who are now trying to design anionic-redox-free materials[313], I remain optimistic that anionic redox is still a viable future direction for high energy batteries, especially if the clearly highlighted issues can be tackled, as discussed above, through balanced efforts from fundamental chemists, applied materials scientists, and cell engineers. Such a synergy will play a crucial role in the eventual market implementation of this new technology.

# VI.4 – Chapter Conclusions

In the first part of this concluding Chapter, I recalled the main achievements (ranging from fundamental to practical) of this thesis along with remaining questions. In light of the remaining questions, the second part opened two fundamental directions for further expanding the materials design-space and for advancing the underlying mechanism. Lastly, I provided my personal opinion on the viability of Li-rich cathodes and anionic redox, which turns out to be optimistic despite the remaining bottlenecks.

In the future context, the fundamental insights about anionic redox in insertion materials gained through this thesis will be indispensable for improving lithium-rich cathodes. Moreover, the methodology developed herein provides guidelines for assessing the merits of existing and future anionic-redox-based high-energy cathodes, which are being discovered rapidly. With this thesis, we have learned the added value of model systems in not just revealing fundamental insights but also in inspiring mitigation strategies. We have also demonstrated how the concepts of theoretical chemistry and thermodynamics can rationalize a new mechanism and guide in the design of new materials.

Our future direction should therefore be to master holistically the underlying thermodynamics and kinetics of anionic redox by bridging the learnings between model and practical materials, aided by theory. Such an approach, followed by more complex considerations such as mesoscale inhomogeneities during electrochemical reactions, is essential for taking high-capacity anionic redox cathodes beyond the labs and into the market and the chance of succeeding is high provided we solve the identified limitations in due time. This time constraint is dictated by the rapidly shrinking window of opportunity that was expected early-on for Li-rich NMCs because of steady progresses realized with NMCs. However, hope must prevail since the issues are well-identified and finding solutions will be catalysed by the ever improving synergy between theorists and experimentalists.

# References

(1) International Energy Agency / OECD. *World Energy Outlook 2016*. **(2016).**

(2) OECD Publishing, Paris. *OECD Science, Technology and Innovation Outlook 2016*. **(2016).**

(3) Nykvist, B. & Nilsson, M. Rapidly falling costs of battery packs for electric vehicles. *Nat. Clim. Change 5*, 329–332 **(2015).** https://doi.org/10.1038/nclimate2564

(4) Schmidt, O., Hawkes, A., Gambhir, A. & Staffell, I. The future cost of electrical energy storage based on experience rates. *Nat. Energy 6*, 17110 **(2017).** https://doi.org/10.1038/nenergy.2017.110

(5) International Energy Agency / OECD. *Global EV Outlook 2017*. **(2017).**

(6) Tarascon, J.-M. & Armand, M. Issues and challenges facing rechargeable lithium batteries. *Nature 414*, 359–367 **(2001).** https://doi.org/10.1038/35104644

(7) Choi, J. W. & Aurbach, D. Promise and reality of post-lithium-ion batteries with high energy densities. *Nat. Rev. Mater. 1*, 16013 **(2016).** https://doi.org/10.1038/natrevmats.2016.13

(8) Blomgren, G. E. The Development and Future of Lithium Ion Batteries. *J. Electrochem. Soc. 164*, A5019–A5025 **(2017).** https://doi.org/10.1149/2.0251701jes

(9) Schmuch, R., Wagner, R., Hörpel, G., Placke, T. & Winter, M. Performance and cost of materials for lithium-based rechargeable automotive batteries. *Nat. Energy 3*, 267–278 **(2018).** https://doi.org/10.1038/s41560-018-0107-2

(10) Dunn, B., Kamath, H. & Tarascon, J.-M. Electrical Energy Storage for the Grid: A Battery of Choices. *Science 334*, 928–935 **(2011).** https://doi.org/10.1126/science.1212741

(11) Gallagher, K. G. *et al.* Quantifying the promise of lithium–air batteries for electric vehicles. *Energy Environ. Sci. 7*, 1555–1563 **(2014).** https://doi.org/10.1039/C3EE43870H

(12) Berg, E. J., Villevieille, C., Streich, D., Trabesinger, S. & Novák, P. Rechargeable Batteries: Grasping for the Limits of Chemistry. *J. Electrochem. Soc. 162*, A2468–A2475 **(2015).**

(13) Gröger, O., Gasteiger, H. A. & Suchsland, J.-P. Review—Electromobility: Batteries or Fuel Cells? *J. Electrochem. Soc. 162*, A2605–A2622 **(2015).** https://doi.org/10.1149/2.0211514jes

(14) Whittingham, M. S., Siu, C. & Ding, J. Can Multielectron Intercalation Reactions Be the Basis of Next Generation Batteries? *Acc. Chem. Res. 51*, 258–264 **(2018).** https://doi.org/10.1021/acs.accounts.7b00527

(15) Freunberger, S. A. True performance metrics in beyond-intercalation batteries. *Nat. Energy 2*, 17091 **(2017).** https://doi.org/10.1038/nenergy.2017.91

(16) Pope, M. A. & Aksay, I. A. Structural Design of Cathodes for Li-S Batteries. *Adv. Energy Mater. 5*, 1500124 **(2015).** https://doi.org/10.1002/aenm.201500124

(17) McCloskey, B. D. Attainable Gravimetric and Volumetric Energy Density of Li–S and Li Ion Battery Cells with Solid Separator-Protected Li Metal Anodes. *J. Phys. Chem. Lett. 6*, 4581–4588 **(2015).** https://doi.org/10.1021/acs.jpclett.5b01814

(18) Vaalma, C., Buchholz, D., Weil, M. & Passerini, S. A cost and resource analysis of sodium-ion batteries. *Nat. Rev. Mater. 3,* 18013 **(2018).** https://doi.org/10.1038/natrevmats.2018.13

(19) M. Darling, R., G. Gallagher, K., A. Kowalski, J., Ha, S. & R. Brushett, F. Pathways to low-cost electrochemical energy storage: a comparison of aqueous and nonaqueous flow batteries. *Energy Environ. Sci. 7,* 3459–3477 **(2014).** https://doi.org/10.1039/C4EE02158D

(20) Andre, D. *et al.* Future generations of cathode materials: an automotive industry perspective. *J Mater Chem A 3,* 6709–6732 **(2015).** https://doi.org/10.1039/C5TA00361J

(21) Myung, S.-T. *et al.* Nickel-rich Layered Cathode Materials for Automotive Lithium-ion Batteries: Achievements and Perspectives. *ACS Energy Lett.* **(2016).** https://doi.org/10.1021/acsenergylett.6b00594

(22) Kubota, K., Dahbi, M., Hosaka, T., Kumakura, S. & Komaba, S. Towards K-Ion and Na-Ion Batteries as 'Beyond Li-Ion'. *Chem. Rec. 18,* 459–479 **(2018).** https://doi.org/10.1002/tcr.201700057

(23) Placke, T., Kloepsch, R., Dühnen, S. & Winter, M. Lithium ion, lithium metal, and alternative rechargeable battery technologies: the odyssey for high energy density. *J. Solid State Electrochem. 21,* 1939–1964 **(2017).** https://doi.org/10.1007/s10008-017-3610-7

(24) Gamble, F. R., Osiecki, J. H., Cais, M., Pisharody, R., DiSalvo, F. J. & Geballe, T. H. Intercalation Complexes of Lewis Bases and Layered Sulfides: A Large Class of New Superconductors. *Science 174,* 493–497 **(1971).** https://doi.org/10.1126/science.174.4008.493

(25) Whittingham, M. S. Electrical Energy Storage and Intercalation Chemistry. *Science 192,* 1126–1127 **(1976).** https://doi.org/10.1126/science.192.4244.1126

(26) Whittingham, M. S. Chemistry of intercalation compounds: Metal guests in chalcogenide hosts. *Prog. Solid State Chem. 12,* 41–99 **(1978).** https://doi.org/10.1016/0079-6786(78)90003-1

(27) Whittingham, M. S. Lithium Batteries and Cathode Materials. *Chem. Rev. 104,* 4271–4302 **(2004).** https://doi.org/10.1021/cr020731c

(28) Lazzari, M. & Scrosati, B. A Cyclable Lithium Organic Electrolyte Cell Based on Two Intercalation Electrodes. *J. Electrochem. Soc. 127,* 773–774 **(1980).** https://doi.org/10.1149/1.2129753

(29) Ozawa, K. Lithium-ion rechargeable batteries with $LiCoO_2$ and carbon electrodes: the $LiCoO_2$/C system. *Solid State Ion. 69,* 212–221 **(1994).** https://doi.org/10.1016/0167-2738(94)90411-1

(30) Mizushima, K., Jones, P. C., Wiseman, P. J. & Goodenough, J. B. $Li_xCoO_2$ ($0<x<1$): A new cathode material for batteries of high energy density. *Mater. Res. Bull. 15,* 783–789 **(1980).** https://doi.org/10.1016/0025-5408(80)90012-4

(31) Tarascon, J. M. The Li-Ion Battery: 25 Years of Exciting and Enriching Experiences. *Electrochem. Soc. Interface 25,* 79–83 **(2016).** https://doi.org/10.1149/2.F08163if

(32) Dahn, J. R., von Sacken, U. & Michal, C. A. Structure and electrochemistry of $Li_{1\pm y}NiO_2$ and a new $Li_2NiO_2$ phase with the $Ni(OH)_2$ structure. *Solid State Ion. 44,* 87–97 **(1990).** https://doi.org/10.1016/0167-2738(90)90049-W

(33) Thackeray, M. M., David, W. I. F., Bruce, P. G. & Goodenough, J. B. Lithium insertion into manganese spinels. *Mater. Res. Bull. 18,* 461–472 **(1983).** https://doi.org/10.1016/0025-5408(83)90138-1

(34) Padhi, A. K., Nanjundaswamy, K. S. & Goodenough, J. B. Phospho-olivines as Positive-Electrode Materials for Rechargeable Lithium Batteries. *J. Electrochem. Soc. 144,* 1188–1194 **(1997).** https://doi.org/10.1149/1.1837571

(35) Masquelier, C. & Croguennec, L. Polyanionic (Phosphates, Silicates, Sulfates) Frameworks as Electrode Materials for Rechargeable Li (or Na) Batteries. *Chem. Rev. 113,* 6552–6591 **(2013).** https://doi.org/10.1021/cr3001862

(36) Julien, C. *et al.* Comparative Issues of Cathode Materials for Li-Ion Batteries. *Inorganics 2,* 132–154 **(2014).** https://doi.org/10.3390/inorganics2010132

(37) Nitta, N., Wu, F., Lee, J. T. & Yushin, G. Li-ion battery materials: present and future. *Mater. Today 18,* 252–264 **(2015).** https://doi.org/10.1016/j.mattod.2014.10.040

(38) Amnesty International, Index: AFR 62/3183/2016. *'This is what we die for': human rights abuses in the Democratic Republic of the Congo power the global trade in cobalt*. **(2016).**

(39) Noh, H.-J., Youn, S., Yoon, C. S. & Sun, Y.-K. Comparison of the structural and electrochemical properties of layered $Li[Ni_xCo_yMn_z]O_2$ (x = 1/3, 0.5, 0.6, 0.7, 0.8 and 0.85) cathode material for lithium-ion batteries. *J. Power Sources 233,* 121–130 **(2013).** https://doi.org/10.1016/j.jpowsour.2013.01.063

(40) Rozier, P. & Tarascon, J. M. Review—Li-Rich Layered Oxide Cathodes for Next-Generation Li-Ion Batteries: Chances and Challenges. *J. Electrochem. Soc. 162,* A2490–A2499 **(2015).** https://doi.org/10.1149/2.0111514jes

(41) Manthiram, A., Knight, J. C., Myung, S.-T., Oh, S.-M. & Sun, Y.-K. Nickel-Rich and Lithium-Rich Layered Oxide Cathodes: Progress and Perspectives. *Adv. Energy Mater. 6,* 1501010 **(2016).** https://doi.org/10.1002/aenm.201501010

(42) Kim, J., Lee, H., Cha, H., Yoon, M., Park, M. & Cho, J. Prospect and Reality of Ni-Rich Cathode for Commercialization. *Adv. Energy Mater. 8,* 1702028 **(2018).** https://doi.org/10.1002/aenm.201702028

(43) Radin, M. D. *et al.* Narrowing the Gap between Theoretical and Practical Capacities in Li-Ion Layered Oxide Cathode Materials. *Adv. Energy Mater.* 1602888 **(2017).** https://doi.org/10.1002/aenm.201602888

(44) Konarov, A., Myung, S.-T. & Sun, Y.-K. Cathode Materials for Future Electric Vehicles and Energy Storage Systems. *ACS Energy Lett. 2,* 703–708 **(2017).** https://doi.org/10.1021/acsenergylett.7b00130

(45) Yoon, C. S., Park, K.-J., Kim, U.-H., Kang, K. H., Ryu, H.-H. & Sun, Y.-K. High-Energy Ni-Rich $Li[Ni_xCo_yMn_{1-x-y}]O_2$ Cathodes via Compositional Partitioning for Next-Generation Electric Vehicles. *Chem. Mater. 29,* 10436–10445 **(2017).** https://doi.org/10.1021/acs.chemmater.7b04047

(46) Liu, Q. *et al.* Approaching the capacity limit of lithium cobalt oxide in lithium ion batteries via lanthanum and aluminium doping. *Nat. Energy* 1 **(2018).** https://doi.org/10.1038/s41560-018-0180-6

(47) Tarascon, J. M., Wang, E., Shokoohi, F. K., McKinnon, W. R. & Colson, S. The Spinel Phase of $LiMn_2O_4$ as a Cathode in Secondary Lithium Cells. *J. Electrochem. Soc. 138,* 2859–2864 **(1991).** https://doi.org/10.1149/1.2085330

(48) Manthiram, A., Chemelewski, K. & Lee, E.-S. A perspective on the high-voltage $LiMn_{1.5}Ni_{0.5}O_4$ spinel cathode for lithium-ion batteries. *Energy Environ. Sci. 7,* 1339–1350 **(2014).** https://doi.org/10.1039/C3EE42981D

(49) Li, W., Song, B. & Manthiram, A. High-voltage positive electrode materials for lithium-ion batteries. *Chem Soc Rev* **(2017).** https://doi.org/10.1039/C6CS00875E

(50) Liu, D. *et al.* Spinel materials for high-voltage cathodes in Li-ion batteries. *RSC Adv. 4,* 154–167 **(2013).** https://doi.org/10.1039/C3RA45706K

(51) Song, J., Shin, D. W., Lu, Y., Amos, C. D., Manthiram, A. & Goodenough, J. B. Role of Oxygen Vacancies on the Performance of $Li[Ni_{0.5-x}Mn_{1.5+x}]O_4$ (x = 0, 0.05, and 0.08) Spinel Cathodes for Lithium-Ion Batteries. *Chem. Mater. 24,* 3101–3109 **(2012).** https://doi.org/10.1021/cm301825h

(52) Goodenough, J. B. & Kim, Y. Challenges for Rechargeable Li Batteries. *Chem. Mater. 22,* 587–603 **(2010).** https://doi.org/10.1021/cm901452z

(53) Saubanère, M., Yahia, M. B., Lebègue, S. & Doublet, M.-L. An intuitive and efficient method for cell voltage prediction of lithium and sodium-ion batteries. *Nat. Commun. 5,* Article number: 5559 **(2014).** https://doi.org/10.1038/ncomms6559

(54) Melot, B. C. & Tarascon, J.-M. Design and Preparation of Materials for Advanced Electrochemical Storage. *Acc. Chem. Res. 46,* 1226–1238 **(2013).** https://doi.org/10.1021/ar300088q

(55) Assat, G. & Manthiram, A. Rapid Microwave-Assisted Solvothermal Synthesis of Non-Olivine *Cmcm* Polymorphs of $LiMPO_4$ (M = Mn, Fe, Co, and Ni) at Low Temperature and Pressure. *Inorg. Chem. 54,* 10015–10022 **(2015).** https://doi.org/10.1021/acs.inorgchem.5b01787

(56) Kreder, K. J., Assat, G. & Manthiram, A. Microwave-Assisted Solvothermal Synthesis of Three Polymorphs of $LiCoPO_4$ and Their Electrochemical Properties. *Chem. Mater. 27,* 5543–5549 **(2015).** https://doi.org/10.1021/acs.chemmater.5b01670

(57) Kreder, K. J., Assat, G. & Manthiram, A. Aliovalent Substitution of $V^{3+}$ for $Co^{2+}$ in $LiCoPO_4$ by a Low-Temperature Microwave-Assisted Solvothermal Process. *Chem. Mater. 28,* 1847–1853 **(2016).** https://doi.org/10.1021/acs.chemmater.5b05042

(58) Whittingham, M. S. Ultimate Limits to Intercalation Reactions for Lithium Batteries. *Chem. Rev. 114,* 11414–11443 **(2014).** https://doi.org/10.1021/cr5003003

(59) Chen, R. *et al.* Disordered Lithium-Rich Oxyfluoride as a Stable Host for Enhanced $Li^+$ Intercalation Storage. *Adv. Energy Mater. 5,* 1401814 **(2015).** https://doi.org/10.1002/aenm.201401814

(60) Wu, F. & Yushin, G. Conversion cathodes for rechargeable lithium and lithium-ion batteries. *Energy Env. Sci 10,* 435–459 **(2017).** https://doi.org/10.1039/C6EE02326F

(61) Su, D., Zhou, D., Wang, C. & Wang, G. Toward High Performance Lithium-Sulfur Batteries Based on $Li_2S$ Cathodes and Beyond: Status, Challenges, and Perspectives. *Adv. Funct. Mater.* 1800154 **(2018).** https://doi.org/10.1002/adfm.201800154

(62) Zhu, Z. *et al.* Anion-redox nanolithia cathodes for Li-ion batteries. *Nat. Energy 1,* 16111 **(2016).** https://doi.org/10.1038/nenergy.2016.111

(63) Fan, X. *et al.* High energy-density and reversibility of iron fluoride cathode enabled via an intercalation-extrusion reaction. *Nat. Commun. 9,* 2324 **(2018).** https://doi.org/10.1038/s41467-018-04476-2

(64) Lu, Z., MacNeil, D. D. & Dahn, J. R. Layered Cathode Materials $Li[Ni_xLi_{(1/3-2x/3)}Mn_{(2/3-x/3)}]O_2$ for Lithium-Ion Batteries. *Electrochem. Solid-State Lett. 4,* A191 **(2001).** https://doi.org/10.1149/1.1407994

(65) Lu, Z., Beaulieu, L. Y., Donaberger, R. A., Thomas, C. L. & Dahn, J. R. Synthesis, Structure, and Electrochemical Behavior of $Li[Ni_xLi_{(1/3-2x/3)}Mn_{(2/3-x/3)}]O_2$. *J. Electrochem. Soc. 149,* A778–A791 **(2002).** https://doi.org/10.1149/1.1471541

(66) Lu, Z. & Dahn, J. R. Understanding the Anomalous Capacity of $Li/Li[Ni_xLi_{(1/3-2x/3)}Mn_{(2/3-x/3)}]O_2$ Cells Using In Situ X-Ray Diffraction and Electrochemical Studies. *J. Electrochem. Soc. 149,* A815 **(2002).** https://doi.org/10.1149/1.1480014

(67) Sathiya, M. *et al.* High Performance $Li_2Ru_{1-y}Mn_yO_3$ ($0.2 \leq y \leq 0.8$) Cathode Materials for Rechargeable Lithium-Ion Batteries: Their Understanding. *Chem. Mater. 25,* 1121–1131 **(2013).** https://doi.org/10.1021/cm400193m

(68) Sathiya, M. *et al.* Reversible anionic redox chemistry in high-capacity layered-oxide electrodes. *Nat. Mater. 12,* 827–835 **(2013).** https://doi.org/10.1038/nmat3699

(69) Sathiya, M. *et al.* Origin of voltage decay in high-capacity layered oxide electrodes. *Nat. Mater. 14,* 230–238 **(2014).** https://doi.org/10.1038/nmat4137

(70) McCalla, E. *et al.* Visualization of O-O peroxo-like dimers in high-capacity layered oxides for Li-ion batteries. *Science 350,* 1516–1521 **(2015).** https://doi.org/10.1126/science.aac8260

(71) Zuo, Y. *et al.* A High-Capacity O2-Type Li-Rich Cathode Material with a Single-Layer $Li_2MnO_3$ Superstructure. *Adv. Mater.* **(2018).** https://doi.org/10.1002/adma.201707255

(72) Yabuuchi, N. *et al.* High-capacity electrode materials for rechargeable lithium batteries: $Li_3NbO_4$ -based system with cation-disordered rocksalt structure. *Proc. Natl. Acad. Sci. 112,* 7650–7655 **(2015).** https://doi.org/10.1073/pnas.1504901112

(73) Yabuuchi, N. *et al.* Origin of stabilization and destabilization in solid-state redox reaction of oxide ions for lithium-ion batteries. *Nat. Commun. 7,* 13814 **(2016).** https://doi.org/10.1038/ncomms13814

(74) Yabuuchi, N. Solid-state Redox Reaction of Oxide Ions for Rechargeable Batteries. *Chem. Lett. 46,* 412–422 **(2017).** https://doi.org/10.1246/cl.161044

(75) Lee, J., Seo, D.-H., Balasubramanian, M., Twu, N., Li, X. & Ceder, G. A new class of high capacity cation-disordered oxides for rechargeable lithium batteries: Li–Ni–Ti–Mo oxides. *Energy Environ. Sci. 8,* 3255–3265 **(2015).** https://doi.org/10.1039/C5EE02329G

(76) A. House, R. *et al.* Lithium manganese oxyfluoride as a new cathode material exhibiting oxygen redox. *Energy Environ. Sci.* **(2018).** https://doi.org/10.1039/C7EE03195E

(77) Rouxel, J. Anion–Cation Redox Competition and the Formation of New Compounds in Highly Covalent Systems. *Chem. – Eur. J. 2,* 1053–1059 **(1996).** https://doi.org/10.1002/chem.19960020904

(78) Rouxel, J. Some solid state chemistry with holes: Anion–cation redox competition in solids. *Curr. Sci. 73,* 31–39 **(1997).**

(79) Bichat, M.-P. *et al.* Redox-Induced Structural Change in Anode Materials Based on Tetrahedral $(MPn_4)^{x-}$ Transition Metal Pnictides. *Chem. Mater. 16,* 1002–1013 **(2004).** https://doi.org/10.1021/cm035101l

(80) Amatucci, G. G., Tarascon, J. M. & Klein, L. C. $CoO_2$, The End Member of the $Li_xCoO_2$ Solid Solution. *J. Electrochem. Soc. 143,* 1114–1123 **(1996).** https://doi.org/10.1149/1.1836594

(81) Amatucci, G. G. PhD dissertation (Rutgers University). **(1995).**

(82) Tarascon, J. M. *et al.* In Situ Structural and Electrochemical Study of $Ni_{1-x}Co_xO_2$ Metastable Oxides Prepared by Soft Chemistry. *J. Solid State Chem. 147,* 410–420 **(1999).** https://doi.org/10.1006/jssc.1999.8465

(83) Aydinol, M. K., Kohan, A. F., Ceder, G., Cho, K. & Joannopoulos, J. Ab initio study of lithium intercalation in metal oxides and metal dichalcogenides. *Phys. Rev. B 56,* 1354 **(1997).**

(84) Ceder, G., Chiang, Y. M., Sadoway, D. R., Aydinol, M. K. & others. Identification of cathode materials for lithium batteries guided by first-principles calculations. *Nature 392,* 694 **(1998).**

(85) Yoon, W.-S. *et al.* Oxygen Contribution on Li-Ion Intercalation−Deintercalation in $LiCoO_2$ Investigated by O K-Edge and Co L-Edge X-ray Absorption Spectroscopy. *J. Phys. Chem. B 106,* 2526–2532 **(2002).** https://doi.org/10.1021/jp013735e

(86) Dahéron, L. *et al.* Electron Transfer Mechanisms upon Lithium Deintercalation from $LiCoO_2$ to $CoO_2$ Investigated by XPS. *Chem. Mater. 20,* 583–590 **(2008).** https://doi.org/10.1021/cm702546s

(87) Sarma, D. D., Sreedhar, K., Ganguly, P. & Rao, C. N. R. Photoemission study of $YBa_2Cu_3O_7$ through the superconducting transition: Evidence for oxygen dimerization. *Phys. Rev. B 36,* 2371–2373 **(1987).** https://doi.org/10.1103/PhysRevB.36.2371

(88) Demourgues, A. *et al.* Additional Oxygen Ordering in '$La_2NiO_{4.25}$' ($La_8Ni_4O_{17}$): II. Structural Features. *J. Solid State Chem. 106,* 330–338 **(1993).** https://doi.org/10.1006/jssc.1993.1293

(89) Bisogni, V. *et al.* Ground-state oxygen holes and the metal–insulator transition in the negative charge-transfer rare-earth nickelates. *Nat. Commun. 7,* ncomms13017 **(2016).** https://doi.org/10.1038/ncomms13017

(90) Kalyani, P., Chitra, S., Mohan, T. & Gopukumar, S. Lithium metal rechargeable cells using $Li_2MnO_3$ as the positive electrode. *J. Power Sources 80,* 103–106 **(1999).** https://doi.org/10.1016/S0378-7753(99)00066-X

(91) Robertson, A. D. & Bruce, P. G. Mechanism of Electrochemical Activity in $Li_2MnO_3$. *Chem. Mater. 15*, 1984–1992 **(2003).** https://doi.org/10.1021/cm030047u

(92) Yu, D. Y. W., Yanagida, K., Kato, Y. & Nakamura, H. Electrochemical Activities in $Li_2MnO_3$. *J. Electrochem. Soc. 156*, A417–A424 **(2009).** https://doi.org/10.1149/1.3110803

(93) M. Thackeray, M., Kang, S.-H., S. Johnson, C., T. Vaughey, J., Benedek, R. & A. Hackney, S. $Li_2MnO_3$-stabilized $LiMO_2$ (M = Mn, Ni, Co) electrodes for lithium-ion batteries. *J. Mater. Chem. 17*, 3112–3125 **(2007).** https://doi.org/10.1039/B702425H

(94) Armstrong, A. R. *et al.* Demonstrating Oxygen Loss and Associated Structural Reorganization in the Lithium Battery Cathode $Li[Ni_{0.2}Li_{0.2}Mn_{0.6}]O_2$. *J. Am. Chem. Soc. 128*, 8694–8698 **(2006).** https://doi.org/10.1021/ja062027+

(95) Boulineau, A., Simonin, L., Colin, J.-F., Bourbon, C. & Patoux, S. First Evidence of Manganese–Nickel Segregation and Densification upon Cycling in Li-Rich Layered Oxides for Lithium Batteries. *Nano Lett. 13*, 3857–3863 **(2013).** https://doi.org/10.1021/nl4019275

(96) Tran, N. *et al.* Mechanisms Associated with the 'Plateau' Observed at High Voltage for the Overlithiated $Li_{0.12}(Ni_{0.425}Mn_{0.425}Co_{0.15})_{0.88}O_2$ System. *Chem. Mater. 20*, 4815–4825 **(2008).** https://doi.org/10.1021/cm070435m

(97) Hy, S., Felix, F., Rick, J., Su, W.-N. & Hwang, B. J. Direct In situ Observation of $Li_2O$ Evolution on Li-Rich High-Capacity Cathode Material, $Li[Ni_xLi_{(1-2x)/3}Mn_{(2-x)/3}]O_2$ $(0 \leq x \leq 0.5)$. *J. Am. Chem. Soc. 136*, 999–1007 **(2014).** https://doi.org/10.1021/ja410137s

(98) Muhammad, S. *et al.* Evidence of reversible oxygen participation in anomalously high capacity Li- and Mn-rich cathodes for Li-ion batteries. *Nano Energy 21*, 172–184 **(2016).** https://doi.org/10.1016/j.nanoen.2015.12.027

(99) Yabuuchi, N., Yoshii, K., Myung, S.-T., Nakai, I. & Komaba, S. Detailed Studies of a High-Capacity Electrode Material for Rechargeable Batteries, $Li_2MnO_3 - LiCo_{1/3}Ni_{1/3}Mn_{1/3}O_2$. *J. Am. Chem. Soc. 133*, 4404–4419 **(2011).** https://doi.org/10.1021/ja108588y

(100) Koga, H. *et al.* Reversible oxygen participation to the redox processes revealed for $Li_{1.20}Mn_{0.54}Co_{0.13}Ni_{0.13}O_2$. *J. Electrochem. Soc. 160*, A786–A792 **(2013).**

(101) Koga, H., Croguennec, L., Ménétrier, M., Mannessiez, P., Weill, F. & Delmas, C. Different oxygen redox participation for bulk and surface: A possible global explanation for the cycling mechanism of $Li_{1.20}Mn_{0.54}Co_{0.13}Ni_{0.13}O_2$. *J. Power Sources 236*, 250–258 **(2013).** https://doi.org/10.1016/j.jpowsour.2013.02.075

(102) Koga, H. *et al.* Operando X-ray Absorption Study of the Redox Processes Involved upon Cycling of the Li-Rich Layered Oxide $Li_{1.20}Mn_{0.54}Co_{0.13}Ni_{0.13}O_2$ in Li Ion Batteries. *J. Phys. Chem. C 118*, 5700–5709 **(2014).** https://doi.org/10.1021/jp412197z

(103) Luo, K. *et al.* Charge-compensation in 3d-transition-metal-oxide intercalation cathodes through the generation of localized electron holes on oxygen. *Nat. Chem. 8*, 684–691 **(2016).** https://doi.org/10.1038/nchem.2471

(104) Oishi, M. *et al.* Direct observation of reversible charge compensation by oxygen ion in Li-rich manganese layered oxide positive electrode material, $Li_{1.16}Ni_{0.15}Co_{0.19}Mn_{0.50}O_2$. *J. Power Sources 276,* 89–94 **(2015).** https://doi.org/10.1016/j.jpowsour.2014.11.104

(105) Foix, D., Sathiya, M., McCalla, E., Tarascon, J.-M. & Gonbeau, D. X-ray Photoemission Spectroscopy Study of Cationic and Anionic Redox Processes in High-Capacity Li-Ion Battery Layered-Oxide Electrodes. *J. Phys. Chem. C 120,* 862–874 **(2016).** https://doi.org/10.1021/acs.jpcc.5b10475

(106) Assat, G., Foix, D., Delacourt, C., Iadecola, A., Dedryvère, R. & Tarascon, J.-M. Fundamental interplay between anionic/cationic redox governing the kinetics and thermodynamics of lithium-rich cathodes. *Nat. Commun. 8,* Article number: 2219 **(2017).** https://doi.org/10.1038/s41467-017-02291-9

(107) Gent, W. E. *et al.* Coupling between oxygen redox and cation migration explains unusual electrochemistry in lithium-rich layered oxides. *Nat. Commun. 8,* **(2017).** https://doi.org/10.1038/s41467-017-02041-x

(108) Seo, D.-H., Lee, J., Urban, A., Malik, R., Kang, S. & Ceder, G. The structural and chemical origin of the oxygen redox activity in layered and cation-disordered Li-excess cathode materials. *Nat. Chem. 8,* 692–697 **(2016).** https://doi.org/10.1038/nchem.2524

(109) Saubanère, M., McCalla, E., Tarascon, J.-M. & Doublet, M.-L. The intriguing question of anionic redox in high-energy density cathodes for Li-ion batteries. *Energy Env. Sci 9,* 984–991 **(2016).** https://doi.org/10.1039/C5EE03048J

(110) Xie, Y., Saubanère, M. & Doublet, M.-L. Requirements for reversible extra-capacity in Li-rich layered oxides for Li-ion batteries. *Energy Env. Sci 10,* 266–274 **(2017).** https://doi.org/10.1039/C6EE02328B

(111) Sathiya, M., Leriche, J.-B., Salager, E., Gourier, D., Tarascon, J.-M. & Vezin, H. Electron paramagnetic resonance imaging for real-time monitoring of Li-ion batteries. *Nat. Commun. 6,* 6276 **(2015).** https://doi.org/10.1038/ncomms7276

(112) Li, B. *et al.* Understanding the Stability for Li-Rich Layered Oxide $Li_2RuO_3$ Cathode. *Adv. Funct. Mater. 26,* 1330–1337 **(2016).** https://doi.org/10.1002/adfm.201504836

(113) Lindic, M. H. *et al.* XPS investigations of $TiO_yS_z$ amorphous thin films used as positive electrode in lithium microbatteries. *Solid State Ion. 176,* 1529–1537 **(2005).** https://doi.org/10.1016/j.ssi.2005.04.007

(114) Okubo, M. & Yamada, A. Molecular Orbital Principles of Oxygen-Redox Battery Electrodes. *ACS Appl. Mater. Interfaces* **(2017).** https://doi.org/10.1021/acsami.7b09835

(115) Zaanen, J., Sawatzky, G. A. & Allen, J. W. Band gaps and electronic structure of transition-metal compounds. *Phys. Rev. Lett. 55,* 418–421 **(1985).** https://doi.org/10.1103/PhysRevLett.55.418

(116) Strehle, B. *et al.* The Role of Oxygen Release from Li-and Mn-Rich Layered Oxides during the First Cycles Investigated by On-Line Electrochemical Mass Spectrometry. *J. Electrochem. Soc. 164,* A400–A406 **(2017).**

(117) McCalla, E. *et al.* Reversible Li-Intercalation through Oxygen Reactivity in Li-Rich Li-Fe-Te Oxide Materials. *J. Electrochem. Soc. 162,* A1341–A1351 **(2015).**

(118) McCalla, E. *et al.* Understanding the Roles of Anionic Redox and Oxygen Release during Electrochemical Cycling of Lithium-Rich Layered $Li_4FeSbO_6$. *J. Am. Chem. Soc. 137,* 4804–4814 **(2015).** https://doi.org/10.1021/jacs.5b01424

(119) Assat, G., Iadecola, A., Delacourt, C., Dedryvère, R. & Tarascon, J.-M. Decoupling Cationic–Anionic Redox Processes in a Model Li-rich Cathode via Operando X-ray Absorption Spectroscopy. *Chem. Mater.* **(2017).** https://doi.org/10.1021/acs.chemmater.7b03434

(120) Pearce, P. E. *et al.* Evidence for anionic redox activity in a tridimensional-ordered Li-rich positive electrode β-$Li_2IrO_3$. *Nat. Mater. 16,* 580–586 **(2017).** https://doi.org/10.1038/nmat4864

(121) Perez, A. J. *et al.* Strong Oxygen Participation in the Redox Governing the Structural and Electrochemical Properties of Na-Rich Layered Oxide $Na_2IrO_3$. *Chem. Mater. 28,* 8278–8288 **(2016).** https://doi.org/10.1021/acs.chemmater.6b03338

(122) Mortemard de Boisse, B. *et al.* Intermediate honeycomb ordering to trigger oxygen redox chemistry in layered battery electrode. *Nat. Commun. 7,* 11397 **(2016).** https://doi.org/10.1038/ncomms11397

(123) Kim, S. *et al.* Material design of high-capacity Li-rich layered-oxide electrodes: $Li_2MnO_3$ and beyond. *Energy Environ. Sci.* **(2017).** https://doi.org/10.1039/C7EE01782K

(124) Zheng, J. *et al.* Li- and Mn-Rich Cathode Materials: Challenges to Commercialization. *Adv. Energy Mater.* 1601284 **(2016).** https://doi.org/10.1002/aenm.201601284

(125) Qiu, B. *et al.* Gas-solid interfacial modification of oxygen activity in layered oxide cathodes for lithium-ion batteries. *Nat. Commun. 7,* 12108 **(2016).** https://doi.org/10.1038/ncomms12108

(126) Wu, Z. Y. *et al.* Sulfur K-Edge X-Ray-Absorption Study of the Charge Transfer upon Lithium Intercalation into Titanium Disulfide. *Phys. Rev. Lett. 77,* 2101–2104 **(1996).** https://doi.org/10.1103/PhysRevLett.77.2101

(127) Jobic, S., Deniard, P., Brec, R., Rouxel, J., Jouanneaux, A. & Fitch, A. N. Crystal and electronic band structure of $IrTe_2$: Evidence of anionic bonds in a $CdI_2$-like arrangement. *Z. Für Anorg. Allg. Chem. 598,* 199–215 **(1991).** https://doi.org/10.1002/zaac.19915980119

(128) Yabuuchi, N., Hara, R., Kubota, K., Paulsen, J., Kumakura, S. & Komaba, S. A new electrode material for rechargeable sodium batteries: P2-type $Na_{2/3}[Mg_{0.28}Mn_{0.72}]O_2$ with anomalously high reversible capacity. *J. Mater. Chem. A 2,* 16851–16855 **(2014).** https://doi.org/10.1039/C4TA04351K

(129) Maitra, U. *et al.* Oxygen redox chemistry without excess alkali-metal ions in $Na_{2/3}[Mg_{0.28}Mn_{0.72}]O_2$. *Nat. Chem.* **(2018).** https://doi.org/10.1038/nchem.2923

(130) Boisse, B. M. de *et al.* Highly Reversible Oxygen-Redox Chemistry at 4.1 V in $Na_{4/7-x}[□_{1/7}Mn_{6/7}]O_2$ (□: Mn Vacancy). *Adv. Energy Mater. 0,* 1800409 https://doi.org/10.1002/aenm.201800409

(131) Rong, X. *et al.* Structure-Induced Reversible Anionic Redox Activity in Na Layered Oxide Cathode. *Joule* **(2017).** https://doi.org/10.1016/j.joule.2017.10.008

(132) Talaie, E., Kim, S. Y., Chen, N. & Nazar, L. F. Structural Evolution and Redox Processes Involved in the Electrochemical Cycling of P2–$Na_{0.67}[Mn_{0.66}Fe_{0.20}Cu_{0.14}]O_2$. *Chem. Mater. 29,* 6684–6697 **(2017).** https://doi.org/10.1021/acs.chemmater.7b01146

(133) Li, Q. *et al.* Both Cationic and Anionic Co-(de)intercalation into a Metal-Oxide Material. *Joule* **(2018).** https://doi.org/10.1016/j.joule.2018.03.010

(134) Hy, S., Liu, H., Zhang, M., Qian, D., Hwang, B.-J. & Meng, Y. S. Performance and design considerations for lithium excess layered oxide positive electrode materials for lithium ion batteries. *Energy Environ. Sci. 9,* 1931–1954 **(2016).** https://doi.org/10.1039/C5EE03573B

(135) Hong, J., Gwon, H., Jung, S.-K., Ku, K. & Kang, K. Review—Lithium-Excess Layered Cathodes for Lithium Rechargeable Batteries. *J. Electrochem. Soc. 162,* A2447–A2467 **(2015).**

(136) Li, B. & Xia, D. Anionic Redox in Rechargeable Lithium Batteries. *Adv. Mater.* 1701054 **(2017).** https://doi.org/10.1002/adma.201701054

(137) Zhao, C., Wang, Q., Lu, Y., Hu, Y.-S., Li, B. & Chen, L. Review on anionic redox for high-capacity lithium- and sodium-ion batteries. *J. Phys. Appl. Phys. 50,* 183001 **(2017).** https://doi.org/10.1088/1361-6463/aa646d

(138) Qiu, B., Zhang, M., Xia, Y., Liu, Z. & Meng, Y. S. Understanding and Controlling Anionic Electrochemical Activity in High-Capacity Oxides for Next Generation Li-Ion Batteries. *Chem. Mater. 29,* 908–915 **(2017).** https://doi.org/10.1021/acs.chemmater.6b04815

(139) Sathiya, M. *et al.* $Li_4NiTeO_6$ as a positive electrode for Li-ion batteries. *Chem. Commun. 49,* 11376–11378 **(2013).** https://doi.org/10.1039/C3CC46842A

(140) Moore, G. J., Johnson, C. S. & Thackeray, M. M. The electrochemical behavior of x $LiNiO_2 \cdot (1-x)\ Li_2RuO_3$ and $Li_2Ru_{1-y}Zr_yO_3$ electrodes in lithium cells. *J. Power Sources 119,* 216–220 **(2003).** https://doi.org/10.1016/S0378-7753(03)00184-8

(141) Glazier, S. L., Li, J., Zhou, J., Bond, T. & Dahn, J. R. Characterization of Disordered $Li_{(1+x)}Ti_{2x}Fe_{(1-3x)}O_2$ as Positive Electrode Materials in Li-Ion Batteries Using Percolation Theory. *Chem. Mater. 27,* 7751–7756 **(2015).** https://doi.org/10.1021/acs.chemmater.5b03530

(142) Yabuuchi, N., Tahara, Y., Komaba, S., Kitada, S. & Kajiya, Y. Synthesis and Electrochemical Properties of $Li_4MoO_5$–NiO Binary System as Positive Electrode Materials for Rechargeable Lithium Batteries. *Chem. Mater. 28,* 416–419 **(2016).** https://doi.org/10.1021/acs.chemmater.5b04092

(143) Matsuhara, T., Tsuchiya, Y., Yamanaka, K., Mitsuhara, K., Ohta, T. & Yabuuchi, N. Synthesis and Electrode Performance of $Li_4MoO_5$-$LiFeO_2$ Binary System as Positive Electrode Materials for Rechargeable Lithium Batteries. *Electrochemistry 84,* 797–801 **(2016).** https://doi.org/10.5796/electrochemistry.84.797

(144) Kan, W. H. *et al.* Unravelling Solid-State Redox Chemistry in $Li_{1.3}Nb_{0.3}Mn_{0.4}O_2$ Single-Crystal Cathode Material. *Chem. Mater. 30,* 1655–1666 **(2018).** https://doi.org/10.1021/acs.chemmater.7b05036

(145) Freire, M. *et al.* A new active Li-Mn-O compound for high energy density Li-ion batteries. *Nat. Mater. 15,* 173–177 **(2016).** https://doi.org/10.1038/nmat4479

(146) Lee, J., Urban, A., Li, X., Su, D., Hautier, G. & Ceder, G. Unlocking the Potential of Cation-Disordered Oxides for Rechargeable Lithium Batteries. *Science 343,* 519–522 **(2014).** https://doi.org/10.1126/science.1246432

(147) Perez, A. J. *et al.* Approaching the limits of cationic and anionic electrochemical activity with the Li-rich layered rocksalt $Li_3IrO_4$. *Nat. Energy 2,* 954–962 **(2017).** https://doi.org/10.1038/s41560-017-0042-7

(148) Jacquet, Q., Perez, A., Batuk, D., Van Tendeloo, G., Rousse, G. & Tarascon, J.-M. The $Li_3Ru_yNb_{1-y}O_4$ ($0 \leq y \leq 1$) System: Structural Diversity and Li Insertion and Extraction Capabilities. *Chem. Mater. 29,* 5331–5343 **(2017).** https://doi.org/10.1021/acs.chemmater.7b01511

(149) Zhan, C. *et al.* Enabling the high capacity of lithium-rich anti-fluorite lithium iron oxide by simultaneous anionic and cationic redox. *Nat. Energy 2,* 963–971 **(2017).** https://doi.org/10.1038/s41560-017-0043-6

(150) Yamada, A. *et al.* A New Sealed Lithium-Peroxide Battery with a Co-Doped $Li_2O$ Cathode in a Superconcentrated Lithium Bis(fluorosulfonyl)amide Electrolyte. *Sci. Rep. 4,* 5684 **(2014).** https://doi.org/10.1038/srep05684

(151) Lin, F. *et al.* Synchrotron X-ray Analytical Techniques for Studying Materials Electrochemistry in Rechargeable Batteries. *Chem. Rev.* **(2017).** https://doi.org/10.1021/acs.chemrev.7b00007

(152) Li, Q. *et al.* Quantitative probe of the transition metal redox in battery electrodes through soft x-ray absorption spectroscopy. *J. Phys. Appl. Phys. 49,* 413003 **(2016).** https://doi.org/10.1088/0022-3727/49/41/413003

(153) Luo, K. *et al.* Anion Redox Chemistry in the Cobalt Free 3d Transition Metal Oxide Intercalation Electrode $Li[Li_{0.2}Ni_{0.2}Mn_{0.6}]O_2$. *J. Am. Chem. Soc. 138,* 11211–11218 **(2016).** https://doi.org/10.1021/jacs.6b05111

(154) Xu, J. *et al.* Elucidating anionic oxygen activity in lithium-rich layered oxides. *Nat. Commun. 9,* 947 **(2018).** https://doi.org/10.1038/s41467-018-03403-9

(155) Yang, W. & Devereaux, T. P. Anionic and cationic redox and interfaces in batteries: Advances from soft X-ray absorption spectroscopy to resonant inelastic scattering. *J. Power Sources 389,* 188–197 **(2018).** https://doi.org/10.1016/j.jpowsour.2018.04.018

(156) Meister, P., Jia, H., Li, J., Klöpsch, R., Winter, M. & Placke, T. Best Practice: Performance and Cost Evaluation of Lithium Ion Battery Active Materials with Special Emphasis on Energy Efficiency. *Chem. Mater. 28,* 7203–7217 **(2016).** https://doi.org/10.1021/acs.chemmater.6b02895

(157) Khatib, R., Dalverny, A.-L., Saubanère, M., Gaberscek, M. & Doublet, M.-L. Origin of the Voltage Hysteresis in the CoP Conversion Material for Li-Ion Batteries. *J. Phys. Chem. C 117,* 837–849 **(2013).** https://doi.org/10.1021/jp310366a

(158) Yu, H.-C., Ling, C., Bhattacharya, J., Thomas, J. C., Thornton, K. & Van der Ven, A. Designing the next generation high capacity battery electrodes. *Energy Environ. Sci. 7,* 1760 **(2014).** https://doi.org/10.1039/c3ee43154a

(159) Ponrouch, A., Cabana, J., Dugas, R., Slack, J. L. & Palacín, M. R. Electroanalytical study of the viability of conversion reactions as energy storage mechanisms. *RSC Adv. 4,* 35988 **(2014).** https://doi.org/10.1039/C4RA05189K

(160) Li, L. *et al.* Origins of Large Voltage Hysteresis in High-Energy-Density Metal Fluoride Lithium-Ion Battery Conversion Electrodes. *J. Am. Chem. Soc. 138,* 2838–2848 **(2016).** https://doi.org/10.1021/jacs.6b00061

(161) Oishi, M. *et al.* Direct observation of reversible oxygen anion redox reaction in Li-rich manganese oxide, $Li_2MnO_3$, studied by soft X-ray absorption spectroscopy. *J Mater Chem A 4,* 9293–9302 **(2016).** https://doi.org/10.1039/C6TA00174B

(162) Yuge, R. *et al.* Charge Compensation Mechanism during Cycles in Fe-Containing $Li_2MnO_3$ Cathode for High Energy Density and Low-Cost Lithium-Ion Batteries. *Electrochimica Acta 189,* 166–174 **(2016).** https://doi.org/10.1016/j.electacta.2015.12.041

(163) Yu, X. *et al.* Understanding the Rate Capability of High-Energy-Density Li-Rich Layered $Li_{1.2}Ni_{0.15}Co_{0.1}Mn_{0.55}O_2$ Cathode Materials. *Adv. Energy Mater. 4,* 1300950 **(2014).** https://doi.org/10.1002/aenm.201300950

(164) Zheng, J. *et al.* Electrochemical Kinetics and Performance of Layered Composite Cathode Material $Li[Li_{0.2}Ni_{0.2}Mn_{0.6}]O_2$. *J. Electrochem. Soc. 160,* A2212–A2219 **(2013).**

(165) Croy, J. R., Balasubramanian, M., Gallagher, K. G. & Burrell, A. K. Review of the U.S. Department of Energy's 'Deep Dive' Effort to Understand Voltage Fade in Li- and Mn-Rich Cathodes. *Acc. Chem. Res. 48,* 2813–2821 **(2015).** https://doi.org/10.1021/acs.accounts.5b00277

(166) Tarascon, J.-M., Gozdz, A. S., Schmutz, C., Shokoohi, F. & Warren, P. C. Performance of Bellcore's plastic rechargeable Li-ion batteries. *Solid State Ion. 86,* 49–54 **(1996).**

(167) Gaberscek, M., Moskon, J., Erjavec, B., Dominko, R. & Jamnik, J. The Importance of Interphase Contacts in Li Ion Electrodes: The Meaning of the High-Frequency Impedance Arc. *Electrochem. Solid-State Lett. 11,* A170 **(2008).** https://doi.org/10.1149/1.2964220

(168) Atebamba, J.-M., Moskon, J., Pejovnik, S. & Gaberscek, M. On the Interpretation of Measured Impedance Spectra of Insertion Cathodes for Lithium-Ion Batteries. *J. Electrochem. Soc. 157,* A1218 **(2010).** https://doi.org/10.1149/1.3489353

(169) Levi, M. D. & Aurbach, D. Simultaneous Measurements and Modeling of the Electrochemical Impedance and the Cyclic Voltammetric Characteristics of Graphite Electrodes Doped with Lithium. *J. Phys. Chem. B 101,* 4630–4640 **(1997).** https://doi.org/10.1021/jp9701909

(170) Levi, M. D. & Aurbach, D. Diffusion coefficients of lithium ions during intercalation into graphite derived from the simultaneous measurements and modeling of electrochemical impedance and potentiostatic intermittent titration characteristics of thin graphite electrodes. *J. Phys. Chem. B 101,* 4641–4647 **(1997).**

(171) Baker, D. R. & Verbrugge, M. W. Intercalate Diffusion in Multiphase Electrode Materials and Application to Lithiated Graphite. *J. Electrochem. Soc. 159,* A1341–A1350 **(2012).** https://doi.org/10.1149/2.002208jes

(172) Xiao, L., Guo, Y., Qu, D., Deng, B., Liu, H. & Tang, D. Influence of particle sizes and morphologies on the electrochemical performances of spinel $LiMn_2O_4$ cathode materials. *J. Power Sources 225,* 286–292 **(2013).** https://doi.org/10.1016/j.jpowsour.2012.10.070

(173) Bernardi, D. M., Chandrasekaran, R. & Go, J. Y. Solid-State Transport of Lithium in Lithium-Ion-Battery Positive Electrodes. *J. Electrochem. Soc. 160,* A1430–A1441 **(2013).** https://doi.org/10.1149/2.042309jes

(174) Farkhondeh, M. & Delacourt, C. Mathematical Modeling of Commercial $LiFePO_4$ Electrodes Based on Variable Solid-State Diffusivity. *J. Electrochem. Soc. 159,* A177 **(2012).** https://doi.org/10.1149/2.073202jes

(175) Newman, J. S. & Thomas-Alyea, K. E. *Electrochemical systems*. **(J. Wiley, 2004).**

(176) Delacourt, C. & Safari, M. Analysis of lithium deinsertion/insertion in $Li_yFePO_4$ with a simple mathematical model. *Electrochimica Acta 56,* 5222–5229 **(2011).** https://doi.org/10.1016/j.electacta.2011.03.030

(177) Safari, M. & Delacourt, C. Mathematical Modeling of Lithium Iron Phosphate Electrode: Galvanostatic Charge/Discharge and Path Dependence. *J. Electrochem. Soc. 158,* A63 **(2011).** https://doi.org/10.1149/1.3515902

(178) Malifarge, S., Delobel, B. & Delacourt, C. Experimental and Modeling Analysis of Graphite Electrodes with Various Thicknesses and Porosities for High-Energy-Density Li-Ion Batteries. *J. Electrochem. Soc. 165,* A1275–A1287 **(2018).** https://doi.org/10.1149/2.0301807jes

(179) Bettge, M. *et al.* Voltage Fade of Layered Oxides: Its Measurement and Impact on Energy Density. *J. Electrochem. Soc. 160,* A2046–A2055 **(2013).** https://doi.org/10.1149/2.034311jes

(180) Yang, J. *et al.* Understanding Voltage Decay in Lithium-Rich Manganese-Based Layered Cathode Materials by Limiting Cutoff Voltage. *ACS Appl. Mater. Interfaces 8,* 18867–18877 **(2016).** https://doi.org/10.1021/acsami.6b04849

(181) Wu, Y. *et al.* Probing the initiation of voltage decay in Li-rich layered cathode materials at the atomic scale. *J. Mater. Chem. A 3,* 5385–5391 **(2015).** https://doi.org/10.1039/C4TA06856D

(182) Croy, J. R. *et al.* Examining Hysteresis in Composite $x\ Li_2MnO_3 \cdot (1–x)\ LiMO_2$ Cathode Structures. *J. Phys. Chem. C 117,* 6525–6536 **(2013).** https://doi.org/10.1021/jp312658q

(183) Kasai, M. *et al.* Electrochemical study on x $Li_2MnO_3$ - (1-x) $LiNi_{1/3}Co_{1/3}Mn_{1/3}O_2$ (x=0.5) layered complex cathode showing voltage hysteresis. *Electrochimica Acta 146,* 79–88 **(2014).** https://doi.org/10.1016/j.electacta.2014.08.073

(184) Taberna, P. L., Mitra, S., Poizot, P., Simon, P. & Tarascon, J.-M. High rate capabilities $Fe_3O_4$-based Cu nano-architectured electrodes for lithium-ion battery applications. *Nat. Mater. 5,* 567–573 **(2006).** https://doi.org/10.1038/nmat1672

(185) Ko, J. K. *et al.* Transport, Phase Reactions, and Hysteresis of Iron Fluoride and Oxyfluoride Conversion Electrode Materials for Lithium Batteries. *ACS Appl. Mater. Interfaces 6,* 10858–10869 **(2014).** https://doi.org/10.1021/am500538b

(186) Salager, E. *et al.* Solid-State NMR of the Family of Positive Electrode Materials $Li_2Ru_{1-y}Sn_yO_3$ for Lithium-Ion Batteries. *Chem. Mater. 26,* 7009–7019 **(2014).** https://doi.org/10.1021/cm503280s

(187) Dogan, F. *et al.* Re-entrant Lithium Local Environments and Defect Driven Electrochemistry of Li- and Mn-Rich Li-Ion Battery Cathodes. *J. Am. Chem. Soc. 137,* 2328–2335 **(2015).** https://doi.org/10.1021/ja511299y

(188) Croy, J. R., Gallagher, K. G., Balasubramanian, M., Long, B. R. & Thackeray, M. M. Quantifying Hysteresis and Voltage Fade in x $Li_2MnO_3$ ● (1-x) $LiMn_{0.5}Ni_{0.5}O_2$ Electrodes as a Function of $Li_2MnO_3$ Content. *J. Electrochem. Soc. 161,* A318–A325 **(2014).**

(189) Konishi, H., Hirano, T., Takamatsu, D., Gunji, A., Feng, X. & Furutsuki, S. Origin of hysteresis between charge and discharge processes in lithium-rich layer-structured cathode material for lithium-ion battery. *J. Power Sources 298,* 144–149 **(2015).** https://doi.org/10.1016/j.jpowsour.2015.08.056

(190) Dees, D. W., Abraham, D. P., Lu, W., Gallagher, K. G., Bettge, M. & Jansen, A. N. Electrochemical Modeling and Performance of a Lithium- and Manganese-Rich Layered Transition-Metal Oxide Positive Electrode. *J. Electrochem. Soc. 162,* A559–A572 **(2015).** https://doi.org/10.1149/2.0231504jes

(191) Rinaldo, S. G. *et al.* Physical Theory of Voltage Fade in Lithium- and Manganese-Rich Transition Metal Oxides. *J. Electrochem. Soc. 162,* A897–A904 **(2015).** https://doi.org/10.1149/2.0181506jes

(192) Gallagher, K. G. *et al.* Correlating hysteresis and voltage fade in lithium- and manganese-rich layered transition-metal oxide electrodes. *Electrochem. Commun. 33,* 96–98 **(2013).** https://doi.org/10.1016/j.elecom.2013.04.022

(193) Mori, D., Kobayashi, H., Okumura, T., Nitani, H., Ogawa, M. & Inaguma, Y. XRD and XAFS study on structure and cation valence state of layered ruthenium oxide electrodes, $Li_2RuO_3$ and $Li_2Mn_{0.4}Ru_{0.6}O_3$, upon electrochemical cycling. *Solid State Ion. 285,* 66–74 **(2016).** https://doi.org/10.1016/j.ssi.2015.09.025

(194) Assat, G., Delacourt, C., Corte, D. A. D. & Tarascon, J.-M. Editors' Choice—Practical Assessment of Anionic Redox in Li-Rich Layered Oxide Cathodes: A Mixed Blessing for High Energy Li-Ion Batteries. *J. Electrochem. Soc. 163,* A2965–A2976 **(2016).** https://doi.org/10.1149/2.0531614jes

(195) Massart, D. L., Vandeginste, B. G., Buydens, L. M. C., Lewi, P. J., Smeyers-Verbeke, J. & Jong, S. D. *Handbook of Chemometrics and Qualimetrics: Part A.* **(Elsevier Science Inc., 1997).**

(196) de Juan, A. & Tauler, R. Chemometrics applied to unravel multicomponent processes and mixtures: Revisiting latest trends in multivariate resolution. *Anal. Chim. Acta 500,* 195–210 **(2003).** https://doi.org/10.1016/S0003-2670(03)00724-4

(197) Juan, A. de, Jaumot, J. & Tauler, R. Multivariate Curve Resolution (MCR). Solving the mixture analysis problem. *Anal. Methods 6,* 4964–4976 **(2014).** https://doi.org/10.1039/C4AY00571F

(198) Jaumot, J., de Juan, A. & Tauler, R. MCR-ALS GUI 2.0: New features and applications. *Chemom. Intell. Lab. Syst. 140,* 1–12 **(2015).** https://doi.org/10.1016/j.chemolab.2014.10.003

(199) Broux, T. *et al.* VIV Disproportionation Upon Sodium Extraction From $Na_3V_2(PO_4)_2F_3$ Observed by Operando X-ray Absorption Spectroscopy and Solid-State NMR. *J. Phys. Chem. C 121,* 4103–4111 **(2017).** https://doi.org/10.1021/acs.jpcc.6b11413

(200) C. Loaiza, L. *et al.* Understanding the lithiation/delithiation mechanism of $Si_{1-x}Ge_x$ alloys. *J. Mater. Chem. A 5,* 12462–12473 **(2017).** https://doi.org/10.1039/C7TA02100C

(201) Landa-Medrano, I. *et al.* Architecture of Na-$O_2$ battery deposits revealed by transmission X-ray microscopy. *Nano Energy 37,* 224–231 **(2017).** https://doi.org/10.1016/j.nanoen.2017.05.021

(202) Iadecola, A., Perea, A., Aldon, L., Aquilanti, G. & Stievano, L. Li deinsertion mechanism and Jahn–Teller distortion in $LiFe_{0.75}Mn_{0.25}PO_4$ : an *operando* x-ray absorption spectroscopy investigation. *J. Phys. Appl. Phys. 50,* 144004 **(2017).** https://doi.org/10.1088/1361-6463/aa605c

(203) Wu, Z. *et al.* Ru K-edge absorption study on the $La_{1-x}Ce_xRu_2$ system. *J. Phys. Condens. Matter 12,* 6971 **(2000).**

(204) Getty, K., Delgado-Jaime, M. U. & Kennepohl, P. Assignment of pre-edge features in the Ru K-edge X-ray absorption spectra of organometallic ruthenium complexes. *Inorganica Chim. Acta 361,* 1059–1065 **(2008).** https://doi.org/10.1016/j.ica.2007.07.029

(205) Yamamoto, T. Assignment of pre-edge peaks in K-edge x-ray absorption spectra of 3d transition metal compounds: electric dipole or quadrupole? *X-Ray Spectrom. 37,* 572–584 **(2008).** https://doi.org/10.1002/xrs.1103

(206) Aritani, H., Tanaka, T., Funabiki, T., Yoshida, S., Kudo, M. & Hasegawa, S. Structure of Mo−Mg Binary Oxides in Oxidized/Reduced States Studied by X-ray Absorption Spectroscopy at the Mo K Edge and Mg K Edge. *J. Phys. Chem. 100,* 5440–5446 **(1996).** https://doi.org/10.1021/jp9525245

(207) Miura, Y., Yasui, Y., Sato, M., Igawa, N. & Kakurai, K. New-Type Phase Transition of $Li_2RuO_3$ with Honeycomb Structure. *J. Phys. Soc. Jpn. 76,* 33705 **(2007).** https://doi.org/10.1143/JPSJ.76.033705

(208) Kimber, S. A. J. *et al.* Valence bond liquid phase in the honeycomb lattice material $Li_2RuO_3$. *Phys. Rev. B 89,* **(2014).** https://doi.org/10.1103/PhysRevB.89.081408

(209) Kobayashi, H., Kanno, R., Kawamoto, Y., Tabuchi, M., Nakamura, O. & Takano, M. Structure and lithium deintercalation of $Li_{2-x}RuO_3$. *Solid State Ion. 82,* 25–31 **(1995).** https://doi.org/10.1016/0167-2738(95)00135-S

(210) Leriche, J. B. *et al.* An Electrochemical Cell for Operando Study of Lithium Batteries Using Synchrotron Radiation. *J. Electrochem. Soc. 157,* A606 **(2010).** https://doi.org/10.1149/1.3355977

(211) Singer, A. *et al.* Nucleation of dislocations and their dynamics in layered oxide cathode materials during battery charging. *Nat. Energy* 1 **(2018).** https://doi.org/10.1038/s41560-018-0184-2

(212) Tanuma, S., Powell, C. J. & Penn, D. R. Calculations of electron inelastic mean free paths. IX. Data for 41 elemental solids over the 50 eV to 30 keV range. *Surf. Interface Anal. 43,* 689–713 **(2011).** https://doi.org/10.1002/sia.3522

(213) Dedryvère, R., Laruelle, S., Grugeon, S., Gireaud, L., Tarascon, J.-M. & Gonbeau, D. XPS Identification of the Organic and Inorganic Components of the Electrode/Electrolyte Interface Formed on a Metallic Cathode. *J. Electrochem. Soc. 152,* A689 **(2005).** https://doi.org/10.1149/1.1861994

(214) Edström, K., Gustafsson, T. & Thomas, J. O. The cathode–electrolyte interface in the Li-ion battery. *Electrochimica Acta 50,* 397–403 **(2004).** https://doi.org/10.1016/j.electacta.2004.03.049

(215) Ouatani, L. E. *et al.* The Effect of Vinylene Carbonate Additive on Surface Film Formation on Both Electrodes in Li-Ion Batteries. *J. Electrochem. Soc. 156,* A103–A113 **(2009).** https://doi.org/10.1149/1.3029674

(216) Kawaguchi, T. *et al.* Strain-Induced Stabilization of Charged State in Li-Rich Layered Transition-Metal Oxide for Lithium-Ion Batteries. *J. Phys. Chem. C 122,* 19298–19308 **(2018).** https://doi.org/10.1021/acs.jpcc.8b03205

(217) Ito, A., Sato, Y., Sanada, T., Hatano, M., Horie, H. & Ohsawa, Y. In situ X-ray absorption spectroscopic study of Li-rich layered cathode material $Li[Ni_{0.17}Li_{0.2}Co_{0.07}Mn_{0.56}]O_2$. *J. Power Sources 196,* 6828–6834 **(2011).** https://doi.org/10.1016/j.jpowsour.2010.09.105

(218) Dreyer, W., Jamnik, J., Guhlke, C., Huth, R., Moškon, J. & Gaberšček, M. The thermodynamic origin of hysteresis in insertion batteries. *Nat. Mater. 9,* 448–453 **(2010).** https://doi.org/10.1038/nmat2730

(219) Farkhondeh, M., Pritzker, M., Fowler, M., Safari, M. & Delacourt, C. Mesoscopic modeling of Li insertion in phase-separating electrode materials: application to lithium iron phosphate. *Phys Chem Chem Phys 16,* 22555–22565 **(2014).** https://doi.org/10.1039/C4CP03530E

(220) Kim, H. *et al.* Understanding Origin of Voltage Hysteresis in Conversion Reaction for Na Rechargeable Batteries: The Case of Cobalt Oxides. *Adv. Funct. Mater. 26,* 5042–5050 **(2016).** https://doi.org/10.1002/adfm.201601357

(221) Fehse, M. *et al.* In-Depth Analysis of the Conversion Mechanism of TiSnSb vs Li by Operando Triple-Edge X-ray Absorption Spectroscopy: a Chemometric Approach. *Chem. Mater. 29,* 10446–10454 **(2017).** https://doi.org/10.1021/acs.chemmater.7b04088

(222) Erickson, E. M. *et al.* Review—Recent Advances and Remaining Challenges for Lithium Ion Battery Cathodes II. Lithium-Rich, x $Li_2MnO_3$ · (1-x) $LiNi_aCo_bMn_cO_2$. *J. Electrochem. Soc. 164,* A6341–A6348 **(2017).**

(223) Streich, D., Guéguen, A., Mendez, M., Chesneau, F., Novák, P. & Berg, E. J. Online Electrochemical Mass Spectrometry of High Energy Lithium Nickel Cobalt Manganese Oxide/Graphite Half-and Full-Cells with Ethylene Carbonate and Fluoroethylene Carbonate Based Electrolytes. *J. Electrochem. Soc. 163,* A964–A970 **(2016).**

(224) Shimoda, K. *et al.* Oxidation behaviour of lattice oxygen in Li-rich manganese-based layered oxide studied by hard X-ray photoelectron spectroscopy. *J Mater Chem A 4,* 5909–5916 **(2016).** https://doi.org/10.1039/C6TA01152G

(225) Konishi, H. *et al.* Potential hysteresis between charge and discharge reactions in $Li_{1.2}Ni_{0.13}Mn_{0.54}Co_{0.13}O_2$ for lithium ion batteries. *Solid State Ion. 300,* 120–127 **(2017).** https://doi.org/10.1016/j.ssi.2016.11.016

(226) Oishi, M. *et al.* Charge compensation mechanisms in $Li_{1.16}Ni_{0.15}Co_{0.19}Mn_{0.50}O_2$ positive electrode material for Li-ion batteries analyzed by a combination of hard and soft X-ray absorption near edge structure. *J. Power Sources 222,* 45–51 **(2013).** https://doi.org/10.1016/j.jpowsour.2012.08.023

(227) Hy, S. *et al.* Understanding the Role of Ni in Stabilizing the Lithium-Rich High-Capacity Cathode Material $Li[Ni_xLi_{(1-2x)/3}Mn_{(2-x)/3}]O_2$ $(0 \leq x \leq 0.5)$. *Chem. Mater. 26,* 6919–6927 **(2014).** https://doi.org/10.1021/cm501664y

(228) Mao, W. *et al.* Nature of the Impedance at Low States of Charge for High-Capacity, Lithium and Manganese-Rich Cathode Materials. *J. Electrochem. Soc. 163,* A3091–A3098 **(2016).**

(229) Gowda, S. R., Dees, D. W., Jansen, A. N. & Gallagher, K. G. Examining the electrochemical impedance at low states of charge in lithium-and manganese-rich layered transition-metal oxide electrodes. *J. Electrochem. Soc. 162,* A1374–A1381 **(2015).**

(230) Philippe, B., Hahlin, M., Edström, K., Gustafsson, T., Siegbahn, H. & Rensmo, H. akan. Photoelectron spectroscopy for lithium battery interface studies. *J. Electrochem. Soc. 163,* A178–A191 **(2016).**

(231) Dupin, J.-C., Gonbeau, D., Vinatier, P. & Levasseur, A. Systematic XPS studies of metal oxides , hydroxides and peroxides. *Phys. Chem. Chem. Phys. 2,* 1319–1324 **(2000).** https://doi.org/10.1039/A908800H

(232) Silvi, B., Fourati, N., Nada, R. & Catlow, C. R. A. Pseudopotential periodic hartree-fock study of rutile $TiO_2$. *J. Phys. Chem. Solids 52,* 1005–1009 **(1991).** https://doi.org/10.1016/0022-3697(91)90029-Y

(233) Hjelm, A., Granqvist, C. G. & Wills, J. M. Electronic structure and optical properties of $WO_3$, $LiWO_3$, $NaWO_3$, and $HWO_3$. *Phys. Rev. B 54,* 2436–2445 **(1996).** https://doi.org/10.1103/PhysRevB.54.2436

(234) Corà, F., Patel, A., Harrison, N. M., Dovesi, R. & Catlow, C. R. A. An ab Initio Hartree−Fock Study of the Cubic and Tetragonal Phases of Bulk Tungsten Trioxide. *J. Am. Chem. Soc. 118,* 12174–12182 **(1996).** https://doi.org/10.1021/ja961514u

(235) Van Veenendaal, M. A. & Sawatzky, G. A. Nonlocal screening effects in 2p x-ray photoemission spectroscopy core-level line shapes of transition metal compounds. *Phys. Rev. Lett. 70,* 2459 **(1993).**

(236) Gallagher, K. G., Dees, D. W., Jansen, A. N., Abraham, D. P. & Kang, S.-H. A Volume Averaged Approach to the Numerical Modeling of Phase-Transition Intercalation Electrodes Presented for $Li_xC_6$. *J. Electrochem. Soc. 159,* A2029–A2037 **(2012).** https://doi.org/10.1149/2.015301jes

(237) Ho, C., Raistrick, I. D. & Huggins, R. A. Application of A-C Techniques to the Study of Lithium Diffusion in Tungsten Trioxide Thin Films. *J. Electrochem. Soc. 127,* 343–350 **(1980).** https://doi.org/10.1149/1.2129668

(238) Doyle, M., Meyers, J. P. & Newman, J. Computer simulations of the impedance response of lithium rechargeable batteries. *J. Electrochem. Soc. 147,* 99–110 **(2000).**

(239) Ohzuku, T., Nagayama, M., Tsuji, K. & Ariyoshi, K. High-capacity lithium insertion materials of lithium nickel manganese oxides for advanced lithium-ion

batteries: toward rechargeable capacity more than 300 mA h $g^{-1}$. *J. Mater. Chem. 21,* 10179 **(2011).** https://doi.org/10.1039/c0jm04325g

(240) Li Xiang *et al.* Direct Visualization of the Reversible $O^{2-}/O^{-}$ Redox Process in Li-Rich Cathode Materials. *Adv. Mater. 30,* 1705197 **(2018).** https://doi.org/10.1002/adma.201705197

(241) Teufl, T., Strehle, B., Müller, P., Gasteiger, H. A. & Mendez, M. A. Oxygen Release and Surface Degradation of Li- and Mn-Rich Layered Oxides in Variation of the $Li_2MnO_3$ Content. *J. Electrochem. Soc. 165,* A2718–A2731 **(2018).** https://doi.org/10.1149/2.0691811jes

(242) Riekehr, L. *et al.* Fatigue in 0.5 $Li_2MnO_3$ : 0.5 $Li(Ni_{1/3}Co_{1/3}Mn_{1/3})O_2$ positive electrodes for lithium ion batteries. *J. Power Sources 325,* 391–403 **(2016).** https://doi.org/10.1016/j.jpowsour.2016.06.014

(243) Peralta, D. *et al.* Role of the composition of lithium-rich layered oxide materials on the voltage decay. *J. Power Sources 280,* 687–694 **(2015).** https://doi.org/10.1016/j.jpowsour.2015.01.146

(244) Konishi, H., Gunji, A., Feng, X. & Furutsuki, S. Effect of transition metal composition on electrochemical performance of nickel-manganese-based lithium-rich layer-structured cathode materials in lithium-ion batteries. *J. Solid State Chem. 249,* 80–86 **(2017).** https://doi.org/10.1016/j.jssc.2017.02.022

(245) Tang, M. *et al.* Operando EPR for Simultaneous Monitoring of Anionic and Cationic Redox Processes in Li-Rich Metal Oxide Cathodes. *J. Phys. Chem. Lett. 8,* 4009–4016 **(2017).** https://doi.org/10.1021/acs.jpclett.7b01425

(246) Li, X. *et al.* Lithiation and Delithiation Dynamics of Different Li Sites in Li-Rich Battery Cathodes Studied by Operando Nuclear Magnetic Resonance. *Chem. Mater. 29,* 8282–8291 **(2017).** https://doi.org/10.1021/acs.chemmater.7b02589

(247) Yu, H., Wang, Y., Asakura, D., Hosono, E., Zhang, T. & Zhou, H. Electrochemical kinetics of the 0.5 $Li_2MnO_3 \cdot 0.5\ LiMn_{0.42}Ni_{0.42}Co_{0.16}O_2$ 'composite' layered cathode material for lithium-ion batteries. *RSC Adv. 2,* 8797 **(2012).** https://doi.org/10.1039/c2ra20772a

(248) Assat, G. & Tarascon, J.-M. Fundamental understanding and practical challenges of anionic redox activity in Li-ion batteries. *Nat. Energy* 1 **(2018).** https://doi.org/10.1038/s41560-018-0097-0

(249) Hu, E. *et al.* Evolution of redox couples in Li- and Mn-rich cathode materials and mitigation of voltage fade by reducing oxygen release. *Nat. Energy* 1 **(2018).** https://doi.org/10.1038/s41560-018-0207-z

(250) Azmi, R., Trouillet, V., Strafela, M., Ulrich, S., Ehrenberg, H. & Bruns, M. Surface analytical approaches to reliably characterize lithium ion battery electrodes. *Surf. Interface Anal. 50,* 43–51 **(2018).** https://doi.org/10.1002/sia.6330

(251) Doubaji, S. *et al.* Passivation Layer and Cathodic Redox Reactions in Sodium-Ion Batteries Probed by HAXPES. *ChemSusChem 9,* 97–108 **(2016).** https://doi.org/10.1002/cssc.201501282

(252) Zheng, J. *et al.* Structural and Chemical Evolution of Li- and Mn-Rich Layered Cathode Material. *Chem. Mater. 27,* 1381–1390 **(2015).** https://doi.org/10.1021/cm5045978

(253) Lin, F. *et al.* Surface reconstruction and chemical evolution of stoichiometric layered cathode materials for lithium-ion batteries. *Nat. Commun. 5,* 3529 **(2014).** https://doi.org/10.1038/ncomms4529

(254) Yang, F. *et al.* Nanoscale Morphological and Chemical Changes of High Voltage Lithium–Manganese Rich NMC Composite Cathodes with Cycling. *Nano Lett. 14,* 4334–4341 **(2014).** https://doi.org/10.1021/nl502090z

(255) Yabuuchi, N., Kubota, K., Aoki, Y. & Komaba, S. Understanding Particle-Size-Dependent Electrochemical Properties of $Li_2MnO_3$ -Based Positive Electrode Materials for Rechargeable Lithium Batteries. *J. Phys. Chem. C 120,* 875–885 **(2016).** https://doi.org/10.1021/acs.jpcc.5b10517

(256) Hy, S., Su, W.-N., Chen, J.-M. & Hwang, B.-J. Soft X-ray Absorption Spectroscopic and Raman Studies on $Li_{1.2}Ni_{0.2}Mn_{0.6}O_2$ for Lithium-Ion Batteries. *J. Phys. Chem. C 116,* 25242–25247 **(2012).** https://doi.org/10.1021/jp309313m

(257) Wandt, J., Freiberg, A. T. S., Ogrodnik, A. & Gasteiger, H. A. Singlet oxygen evolution from layered transition metal oxide cathode materials and its implications for lithium-ion batteries. *Mater. Today* **(2018).** https://doi.org/10.1016/j.mattod.2018.03.037

(258) Kleiner, K. *et al.* Origin of High Capacity and Poor Cycling Stability of Li-Rich Layered Oxides: A Long-Duration in Situ Synchrotron Powder Diffraction Study. *Chem. Mater. 30,* 3656–3667 **(2018).** https://doi.org/10.1021/acs.chemmater.8b00163

(259) Konishi, H. *et al.* Electrochemical reaction mechanisms under various charge-discharge operating conditions for $Li_{1.2}Ni_{0.13}Mn_{0.54}Co_{0.13}O_2$ in a lithium-ion battery. *J. Solid State Chem. 262,* 294–300 **(2018).** https://doi.org/10.1016/j.jssc.2018.03.028

(260) Bernardi, D., Pawlikowski, E. & Newman, J. A general energy balance for battery systems. *J. Electrochem. Soc. 132,* 5–12 **(1985).**

(261) Rao, L. & Newman, J. Heat-generation rate and general energy balance for insertion battery systems. *J. Electrochem. Soc. 144,* 2697–2704 **(1997).**

(262) Thomas, K. E. & Newman, J. Thermal Modeling of Porous Insertion Electrodes. *J. Electrochem. Soc. 150,* A176 **(2003).** https://doi.org/10.1149/1.1531194

(263) Thomas, K. E. & Newman, J. Heats of mixing and of entropy in porous insertion electrodes. *J. Power Sources 119–121,* 844–849 **(2003).** https://doi.org/10.1016/S0378-7753(03)00283-0

(264) Dahn, J. R., McKinnon, W. R., Murray, J. J., Haering, R. R., McMillan, R. S. & Rivers-Bowerman, A. H. Entropy of the intercalation compound $Li_xMo_6Se_8$ from calorimetry of electrochemical cells. *Phys. Rev. B 32,* 3316–3318 **(1985).** https://doi.org/10.1103/PhysRevB.32.3316

(265) Bandhauer, T. M., Garimella, S. & Fuller, T. F. A Critical Review of Thermal Issues in Lithium-Ion Batteries. *J. Electrochem. Soc. 158,* R1 **(2011).** https://doi.org/10.1149/1.3515880

(266) Downie, L. E. & Dahn, J. R. Determination of the Voltage Dependence of Parasitic Heat Flow in Lithium Ion Cells Using Isothermal Microcalorimetry. *J. Electrochem. Soc. 161,* A1782–A1787 **(2014).** https://doi.org/10.1149/2.0301412jes

(267) Downie, L. E., Hyatt, S. R., Wright, A. T. B. & Dahn, J. R. Determination of the Time Dependent Parasitic Heat Flow in Lithium Ion Cells Using Isothermal Microcalorimetry. *J. Phys. Chem. C 118,* 29533–29541 **(2014).** https://doi.org/10.1021/jp508912z

(268) Downie, L. E., Hyatt, S. R. & Dahn, J. R. The Impact of Electrolyte Composition on Parasitic Reactions in Lithium Ion Cells Charged to 4.7 V Determined Using Isothermal Microcalorimetry. *J. Electrochem. Soc. 163,* A35–A42 **(2016).** https://doi.org/10.1149/2.0081602jes

(269) Glazier, S. L., Nelson, K. J., Allen, J. P., Li, J. & Dahn, J. R. The Effect of Different $Li(Ni_{1-x-y}Mn_xCo_y)O_2$ Positive Electrode Materials and Coatings on Parasitic Heat Flow as Measured by Isothermal Microcalorimetry, Ultra-High Precision Coulometry and Long Term Cycling. *J. Electrochem. Soc. 164,* A1203–A1212 **(2017).**

(270) Wen, C. J. & Huggins, R. A. Thermodynamic Study of the Lithium-Tin System. *J. Electrochem. Soc. 128,* 1181–1187 **(1981).** https://doi.org/10.1149/1.2127590

(271) Dahn, J. R. & Haering, R. R. Entropy measurements on $Li_xTiS_2$. *Can. J. Phys. 61,* 1093–1098 **(1983).**

(272) Thomas, K. E., Bogatu, C. & Newman, J. Measurement of the Entropy of Reaction as a Function of State of Charge in Doped and Undoped Lithium Manganese Oxide. *J. Electrochem. Soc. 148,* A570 **(2001).** https://doi.org/10.1149/1.1369365

(273) Reynier, Y., Yazami, R. & Fultz, B. The entropy and enthalpy of lithium intercalation into graphite. *J. Power Sources 119–121,* 850–855 **(2003).** https://doi.org/10.1016/S0378-7753(03)00285-4

(274) Forgez, C., Vinh Do, D., Friedrich, G., Morcrette, M. & Delacourt, C. Thermal modeling of a cylindrical $LiFePO_4$/graphite lithium-ion battery. *J. Power Sources 195,* 2961–2968 **(2010).** https://doi.org/10.1016/j.jpowsour.2009.10.105

(275) Kondepudi, D. & Prigogine, I. *Modern thermodynamics: from heat engines to dissipative structures*. **(Wiley & Sons, 2015).**

(276) Shi, W., Zheng, J., Xiao, J., Chen, X., Polzin, B. J. & Zhang, J.-G. The Effect of Entropy and Enthalpy Changes on the Thermal Behavior of Li-Mn-Rich Layered Composite Cathode Materials. *J. Electrochem. Soc. 163,* A571–A577 **(2016).**

(277) Bard, A. J. & Faulkner, L. R. *Electrochemical methods: fundamentals and applications*. **(Wiley, 2001).**

(278) Sauvage, J.-P. Transition Metal-Containing Rotaxanes and Catenanes in Motion: Toward Molecular Machines and Motors. *Acc. Chem. Res. 31,* 611–619 **(1998).** https://doi.org/10.1021/ar960263r

(279) Sano, M. Mechanism of the molecular hysteresis. *Polym. Adv. Technol. 6,* 178–184 **(1995).** https://doi.org/10.1002/pat.1995.220060312

(280) Sano, M. & Taube, H. 'Molecular hysteresis' in an electrochemical system revisited. *Inorg. Chem. 33,* 705–709 **(1994).** https://doi.org/10.1021/ic00082a014

(281) Zheng, T. & Dahn, J. R. Hysteresis observed in quasi open-circuit voltage measurements of lithium insertion in hydrogen-containing carbons. *J. Power Sources 68,* 201–203 **(1997).**

(282) Zheng, T., McKinnon, W. R. & Dahn, J. R. Hysteresis during Lithium Insertion in Hydrogen-Containing Carbons. *J. Electrochem. Soc. 143,* 2137–2145 **(1996).** https://doi.org/10.1149/1.1836972

(283) Inaba, M., Fujikawa, M., Abe, T. & Ogumi, Z. Calorimetric Study on the Hysteresis in the Charge-Discharge Profiles of Mesocarbon Microbeads Heat-Treated at Low Temperatures. *J. Electrochem. Soc. 147,* 4008–4012 **(2000).**

(284) Zhuo, Z. *et al.* Spectroscopic Signature of Oxidized Oxygen States in Peroxides. *J. Phys. Chem. Lett.* **(2018).** https://doi.org/10.1021/acs.jpclett.8b02757

(285) Kahk, J. M. *et al.* Understanding the Electronic Structure of $IrO_2$ Using Hard-X-ray Photoelectron Spectroscopy and Density-Functional Theory. *Phys. Rev. Lett. 112,* 117601 **(2014).** https://doi.org/10.1103/PhysRevLett.112.117601

(286) Körber, C. *et al.* Electronic structure of $In_2O_3$ and Sn-doped $In_2O_3$ by hard x-ray photoemission spectroscopy. *Phys. Rev. B 81,* 165207 **(2010).** https://doi.org/10.1103/PhysRevB.81.165207

(287) Lee, E. *et al.* The 7 × 1 Fermi Surface Reconstruction in a Two-dimensional *f* -electron Charge Density Wave System: $PrTe_3$. *Sci. Rep. 6,* 30318 **(2016).** https://doi.org/10.1038/srep30318

(288) Stamenkovic, V. R., Strmcnik, D., Lopes, P. P. & Markovic, N. M. Energy and fuels from electrochemical interfaces. *Nat. Mater. 16,* 57–69 **(2016).** https://doi.org/10.1038/nmat4738

(289) Castel, E., Berg, E. J., El Kazzi, M., Novák, P. & Villevieille, C. Differential Electrochemical Mass Spectrometry Study of the Interface of $x\ Li_2MnO_3 \cdot (1–x)\ LiMO_2$ (M = Ni, Co, and Mn) Material as a Positive Electrode in Li-Ion Batteries. *Chem. Mater. 26,* 5051–5057 **(2014).** https://doi.org/10.1021/cm502201z

(290) Renfrew, S. E. & McCloskey, B. D. Residual Lithium Carbonate Predominantly Accounts for First Cycle $CO_2$ and CO Outgassing of Li-Stoichiometric and Li-Rich Layered Transition-Metal Oxides. *J. Am. Chem. Soc. 139,* 17853–17860 **(2017).** https://doi.org/10.1021/jacs.7b08461

(291) Lee, J. *et al.* Mitigating oxygen loss to improve the cycling performance of high capacity cation-disordered cathode materials. *Nat. Commun. 8,* **(2017).** https://doi.org/10.1038/s41467-017-01115-0

(292) Brant, J. A. *et al.* Fast Lithium Ion Conduction in $Li_2SnS_3$: Synthesis, Physicochemical Characterization, and Electronic Structure. *Chem. Mater. 27,* 189–196 **(2015).** https://doi.org/10.1021/cm5037524

(293) Kuhn, A., Holzmann, T., Nuss, J. & V. Lotsch, B. A facile wet chemistry approach towards unilamellar tin sulfide nanosheets from $Li_{4x}Sn_{1-x}S_2$ solid solutions. *J. Mater. Chem. A 2,* 6100–6106 **(2014).** https://doi.org/10.1039/C3TA14190J

(294) Masuda, H., Fujino, T., Sato, N., Yamada, K. & Wakeshima, M. Synthesis and crystal structure of alkali metal uranium sulfides, $Li_2US_3$ and $Na_2US_3$. *J. Alloys Compd. 284,* 117–123 **(1999).** https://doi.org/10.1016/S0925-8388(98)00920-7

(295) Li, B., Jiang, N., Huang, W., Yan, H., Zuo, Y. & Xia, D. Thermodynamic Activation of Charge Transfer in Anionic Redox Process for Li-Ion Batteries. *Adv. Funct. Mater. 28,* **(2018).** https://doi.org/10.1002/adfm.201704864

(296) Goodenough, J. B. & Kim, Y. Locating redox couples in the layered sulfides with application to $Cu[Cr_2]S_4$. *J. Solid State Chem. 182,* 2904–2911 **(2009).** https://doi.org/10.1016/j.jssc.2009.08.005

(297) Tarascon, J. M., DiSalvo, F. J., Eibschutz, M., Murphy, D. W. & Waszczak, J. V. Preparation and chemical and physical properties of the new layered phases $Li_xTi_{1-y}M_yS_2$ with M = V, Cr, or Fe. *Phys. Rev. B 28,* 6397–6406 **(1983).** https://doi.org/10.1103/PhysRevB.28.6397

(298) Shadike, Z. *et al.* Antisite occupation induced single anionic redox chemistry and structural stabilization of layered sodium chromium sulfide. *Nat. Commun. 8,* 566 **(2017).** https://doi.org/10.1038/s41467-017-00677-3

(299) Flamary-Mespoulie, F. Synthèse et caractérisation de sulfures de métaux de transition comme matériaux d'électrode positive à forte capacité pour microbatteries au lithium (Thèse de doctorat, Université de Bordeaux). **(2016).**

(300) McKinnon, W. R., Dahn, J. R., Murray, J. J., Haering, R. R., McMillan, R. S. & Rivers-Bowerman, A. H. Entropy of intercalation compounds. II. Calorimetry of electrochemical cells of the Chevrel compound $Li_xMo_6Se_8$ for $0 \leqslant x \leqslant 4$. *J. Phys. C Solid State Phys. 19,* 5135 **(1986).**

(301) Zheng, T. & Dahn, J. R. Lattice-gas model to understand voltage profiles of $LiNi_xMn_{2-x}O_4$ / Li electrochemical cells. *Phys. Rev. B 56,* 3800 **(1997).**

(302) McKinnon, W. R. & Haering, R. R. in *Modern Aspects of Electrochemistry: No. 15* (eds. White, R. E., Bockris, J. O. & Conway, B. E.) 235–304 **(Springer US, 1983).**

(303) Ahmed, S. *et al.* Cost of automotive lithium-ion batteries operating at high upper cutoff voltages. *J. Power Sources 403,* 56–65 **(2018).** https://doi.org/10.1016/j.jpowsour.2018.09.037

(304) Kim, S., Cho, W., Zhang, X., Oshima, Y. & Choi, J. W. A stable lithium-rich surface structure for lithium-rich layered cathode materials. *Nat. Commun. 7,* 13598 **(2016).** https://doi.org/10.1038/ncomms13598

(305) Martha, S. K., Nanda, J., Veith, G. M. & Dudney, N. J. Electrochemical and rate performance study of high-voltage lithium-rich composition: $Li_{1.2}Mn_{0.525}Ni_{0.175}Co_{0.1}O_2$. *J. Power Sources 199,* 220–226 **(2012).** https://doi.org/10.1016/j.jpowsour.2011.10.019

(306) Zheng, J., Kan, W. H. & Manthiram, A. Role of Mn Content on the Electrochemical Properties of Nickel-Rich Layered $LiNi_{0.8-x}Co_{0.1}Mn_{0.1+x}O_2$ ($0.0 \leq x \leq 0.08$) Cathodes for Lithium-Ion Batteries. *ACS Appl. Mater. Interfaces 7,* 6926–6934 **(2015).** https://doi.org/10.1021/acsami.5b00788

(307) Woo, S.-U., Yoon, C. S., Amine, K., Belharouak, I. & Sun, Y.-K. Significant Improvement of Electrochemical Performance of $AlF_3$-Coated $Li[Ni_{0.8}Co_{0.1}Mn_{0.1}]O_2$ Cathode Materials. *J. Electrochem. Soc. 154,* A1005–A1009 **(2007).** https://doi.org/10.1149/1.2776160

(308) Shi, J.-L. *et al.* Mitigating Voltage Decay of Li-Rich Cathode Material via Increasing Ni Content for Lithium-Ion Batteries. *ACS Appl. Mater. Interfaces 8,* 20138–20146 **(2016).** https://doi.org/10.1021/acsami.6b06733

(309) Ku, K. *et al.* Suppression of Voltage Decay through Manganese Deactivation and Nickel Redox Buffering in High-Energy Layered Lithium-Rich Electrodes. *Adv. Energy Mater. 0,* 1800606 **(2018).** https://doi.org/10.1002/aenm.201800606

(310) Shi Ji-Lei *et al.* High-Capacity Cathode Material with High Voltage for Li-Ion Batteries. *Adv. Mater. 30,* 1705575 **(2018).** https://doi.org/10.1002/adma.201705575

(311) Myeong, S. *et al.* Understanding voltage decay in lithium-excess layered cathode materials through oxygen-centred structural arrangement. *Nat. Commun. 9,* 3285 **(2018).** https://doi.org/10.1038/s41467-018-05802-4

(312) Chikkannanavar, S. B., Bernardi, D. M. & Liu, L. A review of blended cathode materials for use in Li-ion batteries. *J. Power Sources 248,* 91–100 **(2014).** https://doi.org/10.1016/j.jpowsour.2013.09.052

(313) Lee, J. *et al.* Reversible $Mn^{2+}/Mn^{4+}$ double redox in lithium-excess cathode materials. *Nature 556,* 185–190 **(2018).** https://doi.org/10.1038/s41586-018-0015-4

(314) Wen, C. J., Boukamp, B. A., Huggins, R. A. & Weppner, W. Thermodynamic and Mass Transport Properties of ' LiAl '. *J. Electrochem. Soc. 126,* 2258–2266 **(1979).** https://doi.org/10.1149/1.2128939

(315) Guo, M. & White, R. E. An approximate solution for solid-phase diffusion in a spherical particle in physics-based Li-ion cell models. *J. Power Sources 198,* 322–328 **(2012).** https://doi.org/10.1016/j.jpowsour.2011.08.096

(316) Li, J., Xiao, X., Yang, F., Verbrugge, M. W. & Cheng, Y.-T. Potentiostatic Intermittent Titration Technique for Electrodes Governed by Diffusion and Interfacial Reaction. *J. Phys. Chem. C 116,* 1472–1478 **(2012).** https://doi.org/10.1021/jp207919q

(317) Li, J., Yang, F., Xiao, X., Verbrugge, M. W. & Cheng, Y.-T. Potentiostatic intermittent titration technique (PITT) for spherical particles with finite interfacial kinetics. *Electrochimica Acta 75,* 56–61 **(2012).** https://doi.org/10.1016/j.electacta.2012.04.050

(318) Briois, V. *et al.* ROCK: the new Quick-EXAFS beamline at SOLEIL. *J. Phys. Conf. Ser. 712,* 12149 **(2016).** https://doi.org/10.1088/1742-6596/712/1/012149

(319) Ravel, B. & Newville, M. ATHENA, ARTEMIS, HEPHAESTUS: data analysis for X-ray absorption spectroscopy using IFEFFIT. *J. Synchrotron Radiat. 12,* 537–541 **(2005).** https://doi.org/10.1107/S0909049505012719

(320) Rueff, J.-P. *et al.* The GALAXIES beamline at the SOLEIL synchrotron: inelastic X-ray scattering and photoelectron spectroscopy in the hard X-ray range. *J. Synchrotron Radiat. 22,* 175–179 **(2015).** https://doi.org/10.1107/S160057751402102X

(321) Rueff, J.-P., Rault, J. E., Ablett, J. M., Utsumi, Y. & Céolin, D. HAXPES for Materials Science at the GALAXIES Beamline. *Synchrotron Radiat. News 31,* 4–9 **(2018).** https://doi.org/10.1080/08940886.2018.1483648

(322) Bianchini, M. *et al.* Comprehensive Investigation of the $Na_3V_2(PO_4)_2F_3$–$NaV_2(PO_4)_2F_3$ System by Operando High Resolution Synchrotron X-ray Diffraction. *Chem. Mater. 27,* 3009–3020 **(2015).** https://doi.org/10.1021/acs.chemmater.5b00361

(323) Ouvrard, G. *et al.* Heterogeneous behaviour of the lithium battery composite electrode $LiFePO_4$. *J. Power Sources 229*, 16–21 **(2013).** https://doi.org/10.1016/j.jpowsour.2012.11.057

(324) Pimenta, V. *et al.* Synthesis of Li-Rich NMC: A Comprehensive Study. *Chem. Mater. 29*, 9923–9936 **(2017).** https://doi.org/10.1021/acs.chemmater.7b03230

# Appendix

# A1 – Supporting Information for Chapter II

## ○ Methods

**Material synthesis and electrode fabrication.** Single-phase $Li_2Ru_{0.75}Sn_{0.25}O_3$ (LRSO) samples, as determined by X-ray powder diffraction (XRD) (BRUKER D8 Advance diffractometer with Cu Kα radiation, $\lambda_{K\alpha1}$=1.54056 Å, $\lambda_{K\alpha2}$=1.54439 Å), were prepared by solid-state synthesis, as reported previously.[68] The powders consist of 'potato-shaped' particles having an average size ranging from 1 to 3 µm, as deduced by Scanning Electron Microscopy (SEM) (Hitachi S-3400N) (**Figure A1.1**).

Electrochemical testing was performed with electrodes made by Bellcore's plastic method.[166] A blend of active material and Carbon Super P (CSP), mixed first in a SPEX 8000M ball-miller for 15 minutes, was stirred overnight in dry acetone with a binder - Poly(vinylidene fluoride-co-hexafluoropropylene) (PVDF-HFP), and a plasticizer - dibutylphthalate (DBP). After casting this slurry on a smooth surface, a self-standing electrode could be peeled off once the acetone evaporates. DBP was then extracted by rinsing the film thoroughly with diethyl ether, which leaves behind a large porosity. The final electrode film was composed of 73% (by weight) active material, 9% CSP, and 18% binder with an active material loading of ~5 $mg.cm^{-2}$, ~50 µm film-thickness, and ~60% porosity. Such an electrode design is essential for safely ignoring porous-electrode effects; low loading and high porosity ensure that the electrode's electrochemical response is dominated by the sought-after properties of the active material. **Figure A1.2** shows a photograph of such an electrode. Circular disks of ~1 $cm^2$ geometric area were used in each cell.

**Electrochemical measurement protocols.** Two-electrode electrochemical measurements were carried out in coin-type cells with Li metal foil as the counter electrode, whereas three-electrode measurements were performed with Swagelok-type cells also having Li metal foil as the counter electrode and a small piece of Li metal as the reference electrode, fixed at the exposed tip of an otherwise enamelled thin copper wire (180 µm diameter) (**Figure A1.3**). The cells were assembled in an argon-filled glove-box with a Whatman GF/D borosilicate glass fibre sheet as the separator soaked with an electrolyte - LP100 (Merck) having 1M $LiPF_6$ in ethylene carbonate : propylene carbonate

: dimethyl carbonate in a 1 : 1 : 3 weight ratio. All cells were rested overnight before testing. Depending on the experiment, measurements were either performed with a constant current (CC) or a constant current constant voltage (CCCV) protocol. The CCCV protocol holds the voltage at the end of the CC step until the current decays to a predefined small value, such as C/100 (unless otherwise specified). In Chapter II, 1C corresponds to 160 mA $g^{-1}$ based on 1 Li exchanged from LRSO in one hour. Activation of LRSO requires five formation cycles with a CCCV protocol within 2–4.6 V vs. Li / $Li^+$.

**Electroanalytical techniques and their description.** Galvanostatic intermittent titration technique (GITT), Potentiostatic intermittent titration technique (PITT), and Electrochemical Impedance Spectroscopy (EIS) were used to quantify the near-equilibrium voltage profiles, the interfacial charge-transfer resistance, and the bulk diffusion coefficient by using a simplified model assuming spherical particles.

At short time after switching on the current pulse, the GITT solution of the Fick's diffusion equation predicts a linear relationship between the cell potential and the square root of time[314,315] from which the diffusion coefficient can be determined.

In Chapter II, we used the short time PITT solutions of Fick's diffusion equation in a spherical geometry that also incorporate the boundary condition of finite interfacial kinetics[316,317] , which therefore are more accurate compared to the original solution for planar geometry[314], where infinitely fast surface reaction is assumed. This PITT model is based on two parameters that quantify, respectively, the surface reaction resistance and the bulk diffusion coefficient.

For EIS, a GITT type of protocol was followed to allow the material to rest and equilibrate at a desired SoC before measuring impedance with a 10 mV wave having frequencies varying from 200 kHz to 1.4 mHz. With EIS, the Fickian diffusion coefficient was calculated from the Warburg resistance at low frequencies where the imaginary and real parts of impedance show linearity with $f^{0.5}$, where $f$ is the frequency.[237,238] Throughout Chapter II, we report the values of $D/R^2$ [$s^{-1}$] as deduced directly from the experiments, where $D$ is the diffusion coefficient and $R$ is the particle radius. $D/R^2$ represents the reciprocal of the time constant associated with the Li diffusion process and hence it is a physically meaningful quantity. We do not calculate $D$ by multiplying with $R^2$, in order to avoid the error associated with estimating $R$ from SEM images.

## ○ Supporting Figures

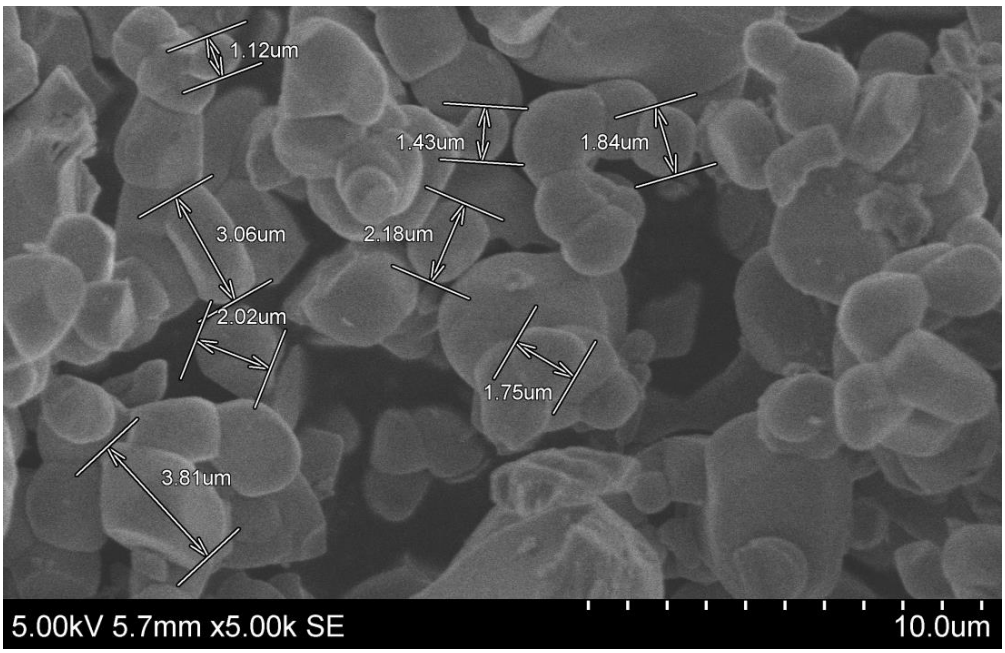


**Figure A1.1 |** SEM image of the as-synthesized LRSO powders.

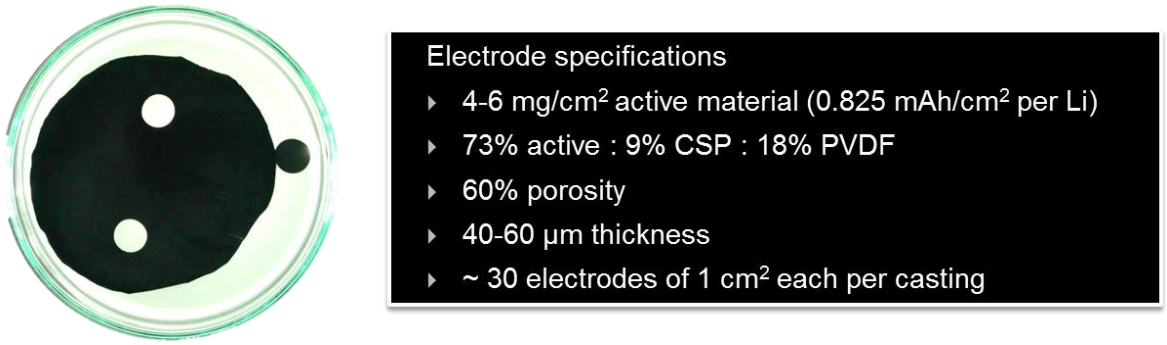


**Figure A1.2 |** Photograph of the Bellcore electrode casted in a Petri dish with its technical specifications.

**Figure A1.3 |** Photograph of the Li metal reference electrode at the tip of an enamelled copper wire placed inside the three-electrode Swagelok cell.

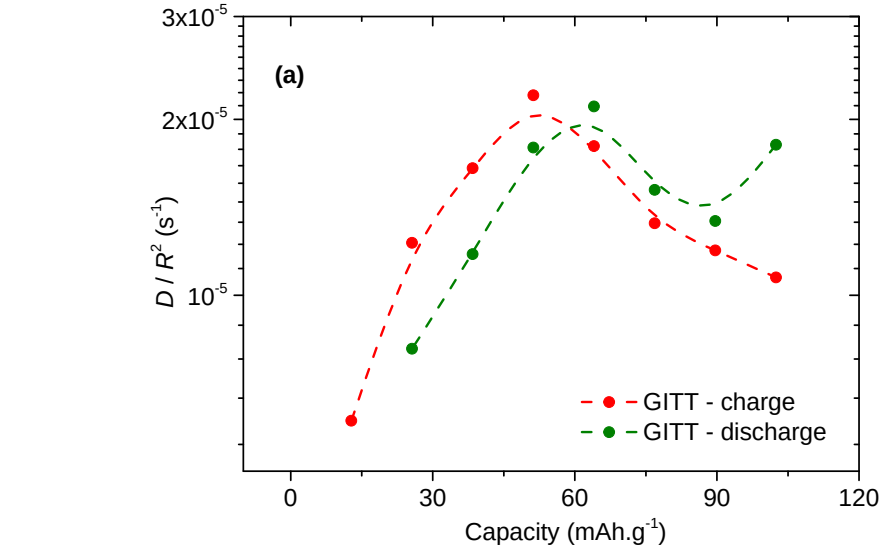


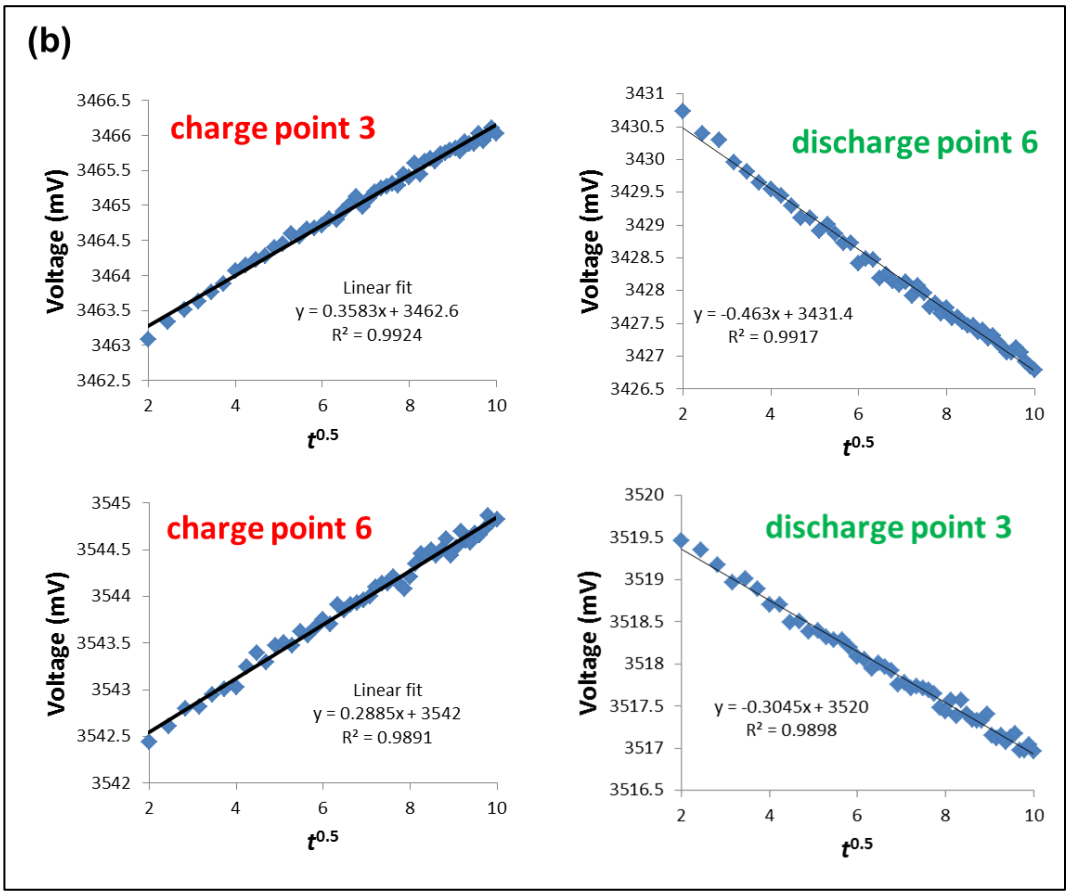


**Figure A1.4 |** GITT results at the first staircase step of 3.5 V during 1st charge. (**a**) Variation of $D / R^2$. (**b**) Example fits showing the linear variation of $V$ vs. $t^{0.5}$ at short time after switching on the current pulse.

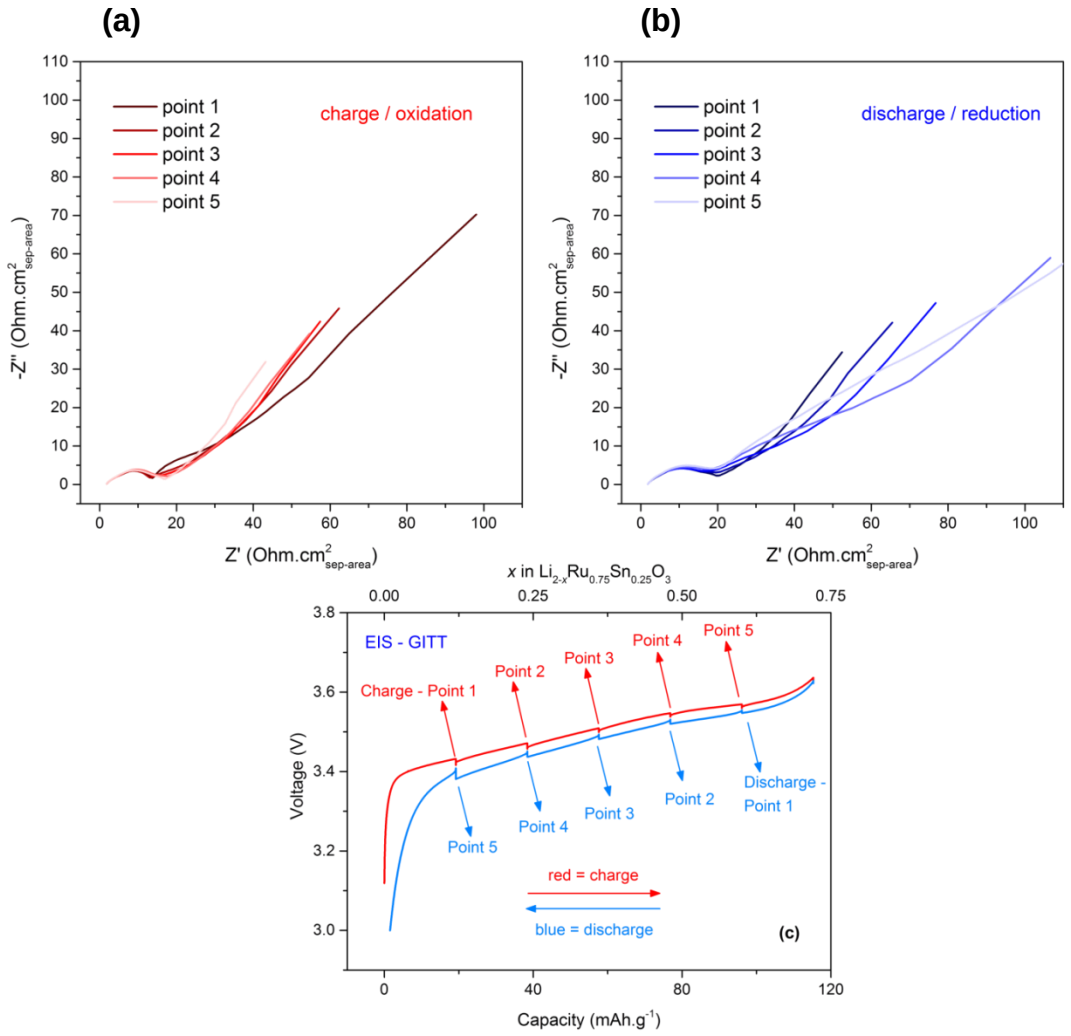


**Figure A1.5 |** Variation of the EIS spectra over the first staircase step of 3.5 V during 1st charge under (**a**) oxidation and (**b**) reduction. (**c**) Corresponding GITT-EIS voltage profiles showing the points where EIS is measured.

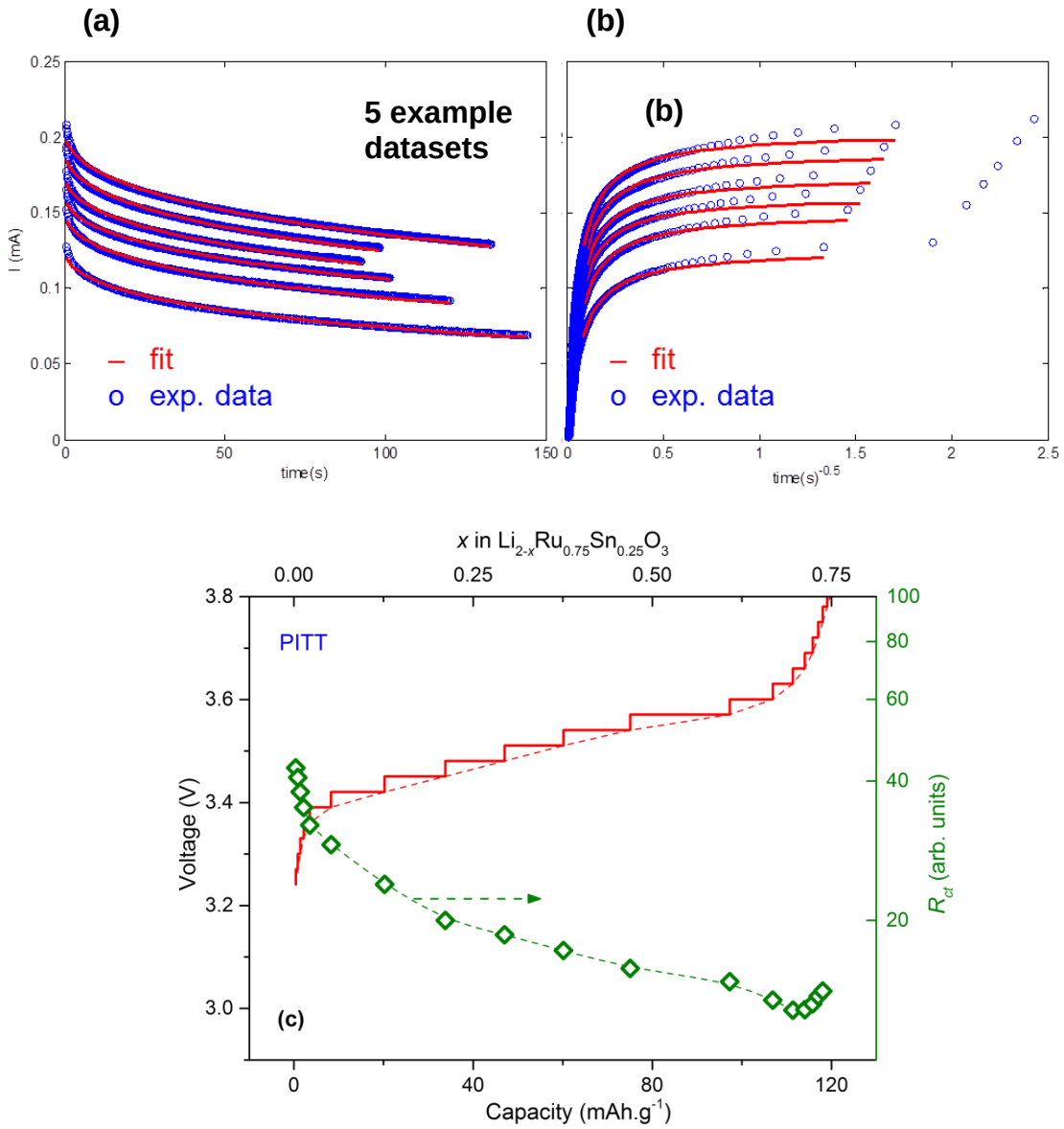


**Figure A1.6 |** PITT results at the 3.5 V redox step modelled with a spherical particle model having surface reaction resistance and bulk diffusion (ref.[317]). Excellent agreement between measured and simulated current decays at short times (first 90 to 140 s) after the application of voltage steps is shown in (**a**) $I$ vs. $t$ and (**b**) $I$ vs $t^{-0.5}$ plots. (**c**) Interfacial resistance $R_{ct}$, modeled with PITT (herein, we define $R_{ct} = (D.B.Q)^{-1}$, where $D$ is diffusion coefficient, $B$ is Biot number, and $Q$ is the net charge transferred over a PITT step, as per the model developed in (ref.[317]). $R_{ct}$ remains small throughout the first 0.75 Li extraction.

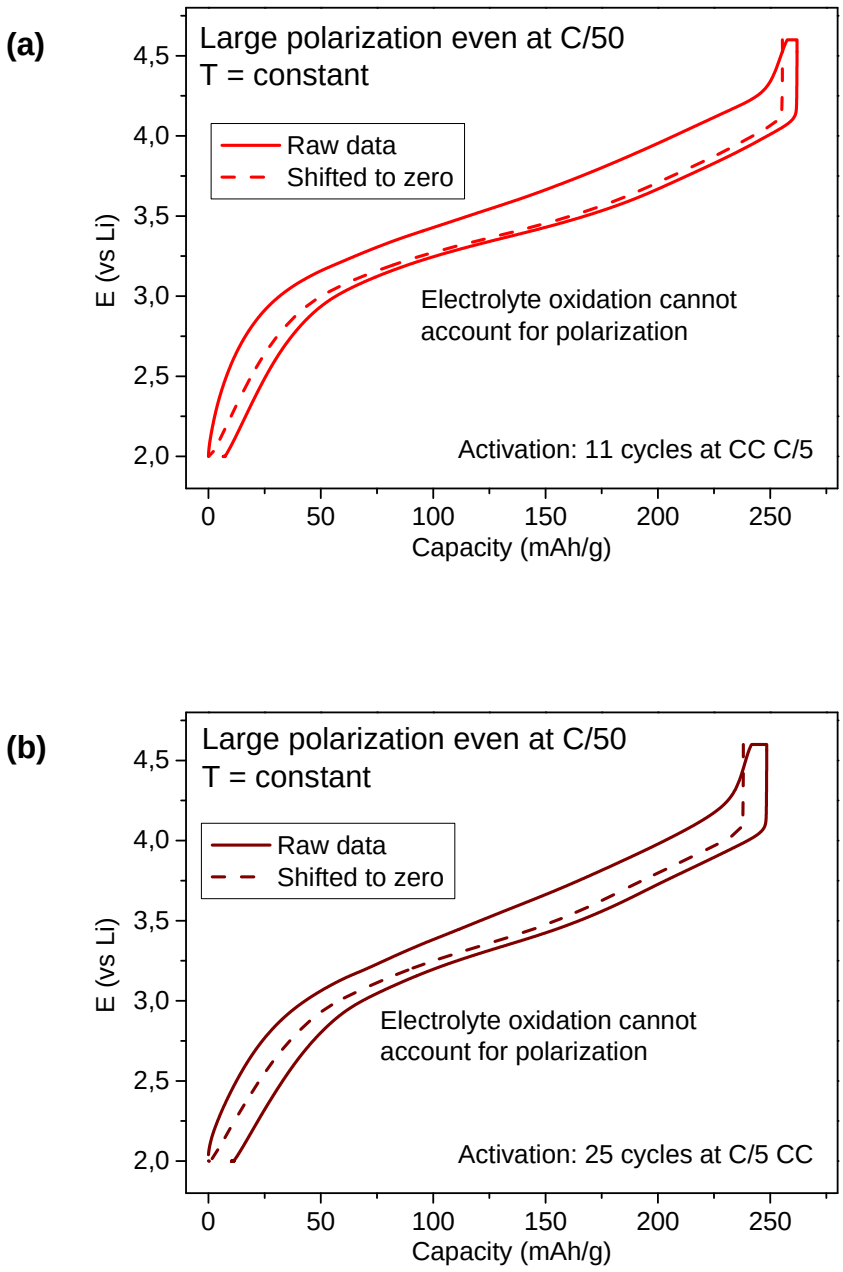


**Figure A1.7 |** CCCV cycling results at a low current of C/50 within 2 - 4.6 V for LRSO after (**a**) 11 and (**b**) 25 activation cycles. The charge and discharge profiles do not superimpose leaving a voltage gap of ~150 - 250 mV attributable to quasi-static hysteresis. Although side reactions are magnified at slow cycling but they cannot explain the remaining voltage gap even after correcting for coulombic inefficiency (dashed lines). T = 25°C.

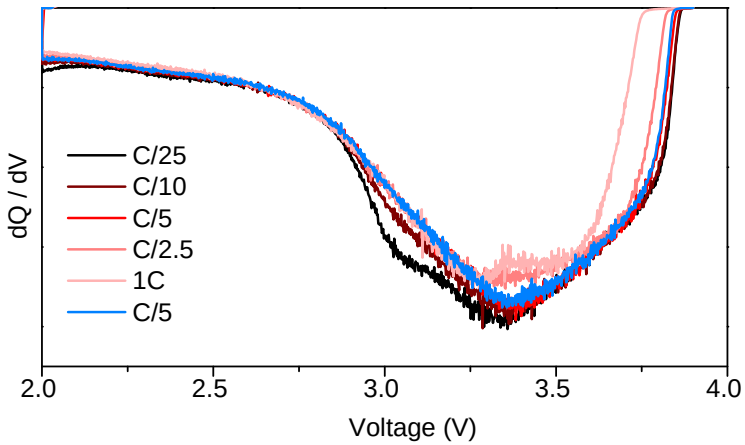


**Figure A1.8 |** Discharge *dQ*/*dV* profiles of 'activated'-LRSO with increasing C rates. All curves begin from the same SOC, which is reached by charging only to 3.9 V at C/5 each time. The 3.3 V discharge peak (cationic redox) does not move much with changing currents, hence indicating low resistance for the case when anionic redox is not involved.

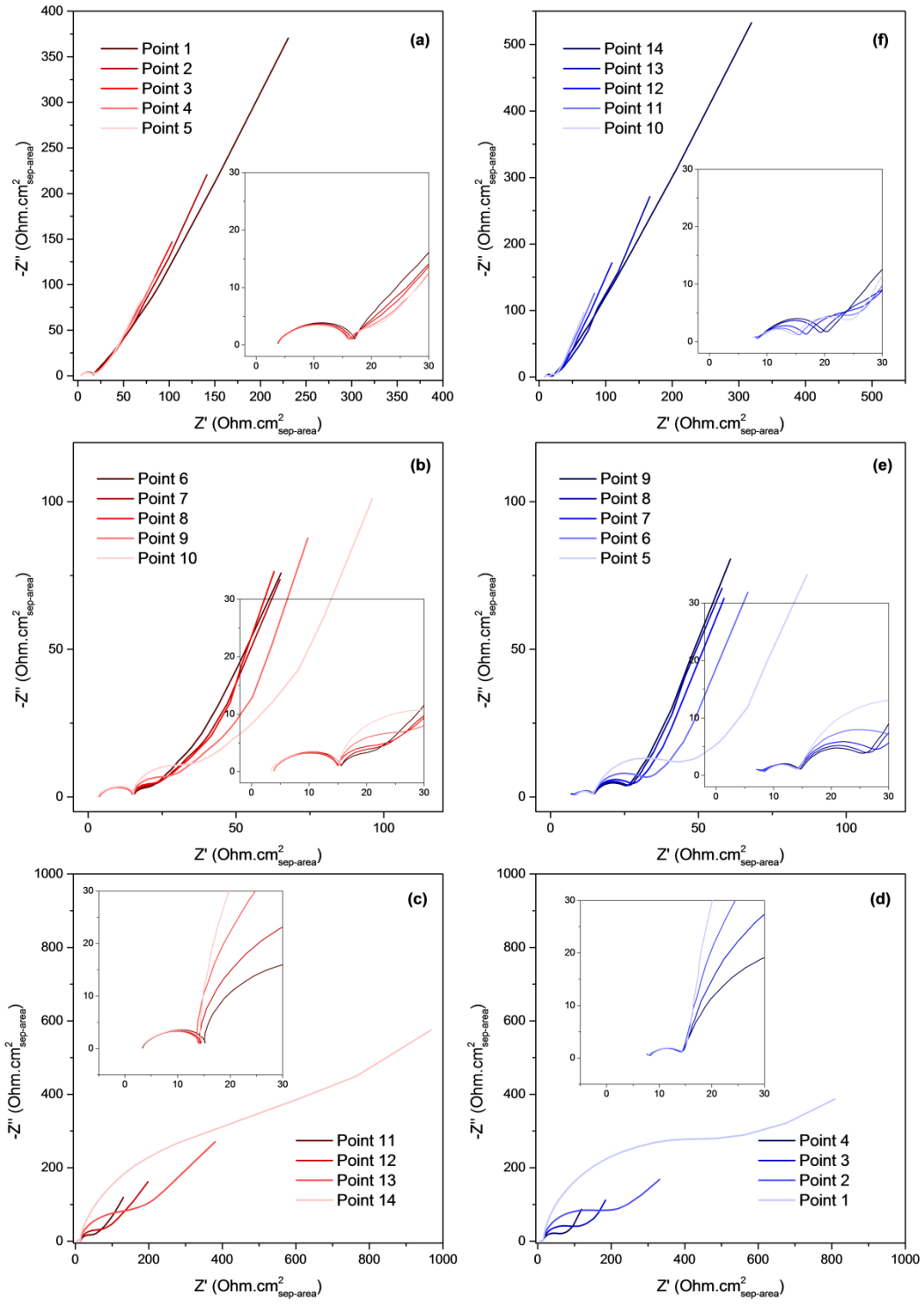


**Figure A1.9** | EIS spectra for 'activated'-LRSO during charge (panels **a**, **b**, **c**) and discharge (panels **d**, **e**, **f**) with insets magnifying the HF regions. The HF arc (related to contact resistance) stays fairly constant throughout either charge or discharge.

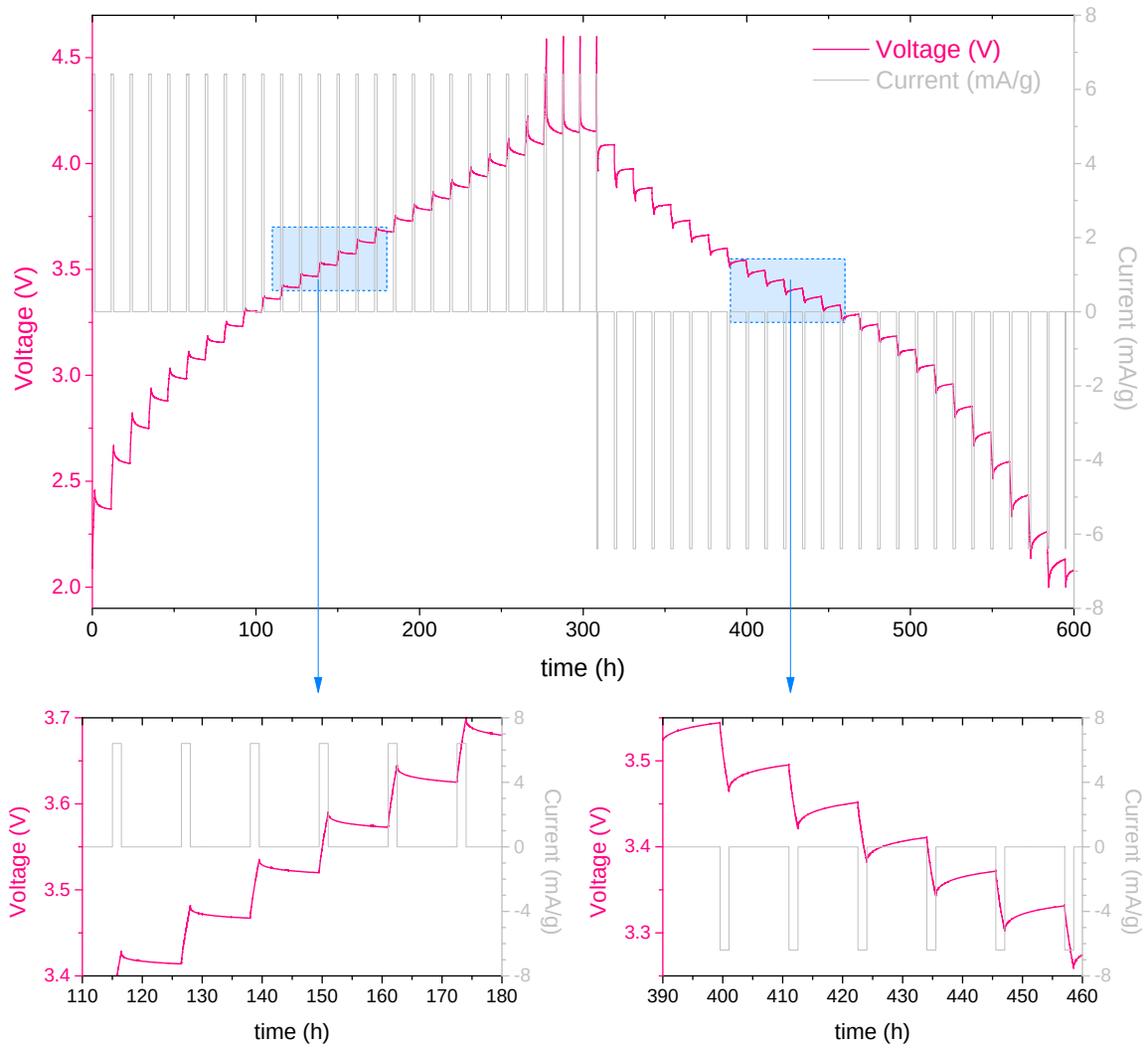


**Figure A1.10 |** Voltage and current as a function of time during the GITT (C/25 90 min pulse, 10 hr. rest, 25°C) experiment that is analysed in **Figure II.8a**. A closer look at the OCV relaxation profiles in the bottom panels reveals the long and continuous OCV drifting, such that true equilibrium does not seem to be achieved even after 10 hours of relaxation, thus indicating the presence of long time-constants for the underlying processes.

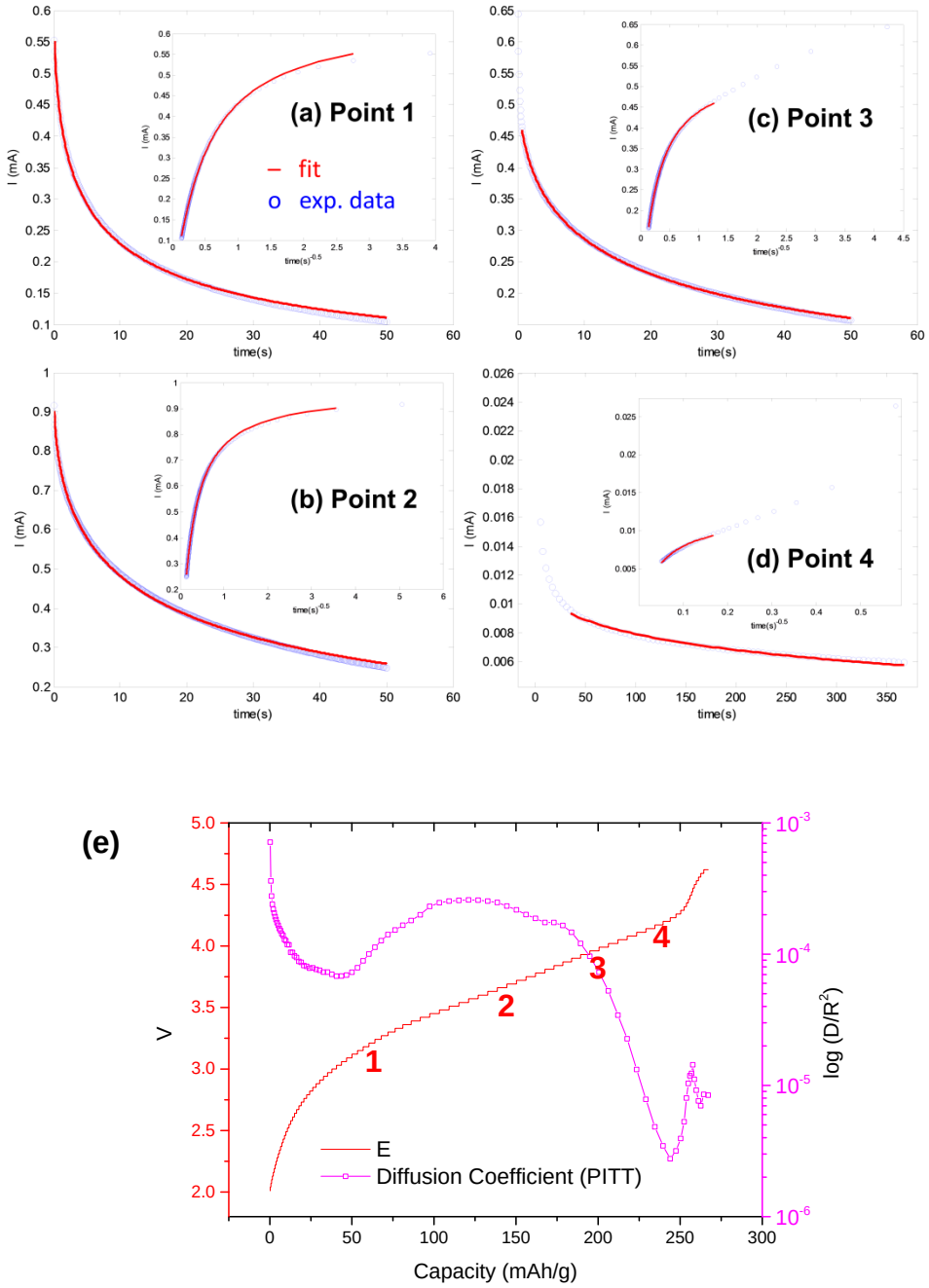


**Figure A1.11 |** For 'activated'-LRSO, four example PITT measurements and their respective fits (panels **a** to **d**) showing $I$ vs. $t$ and $I$ vs. $t^{-0.5}$ (insets) with short time approximation. The charge voltages corresponding to the four examples are marked in (**e**). The experimental data has been fitted to equation (7) of ref.[317].

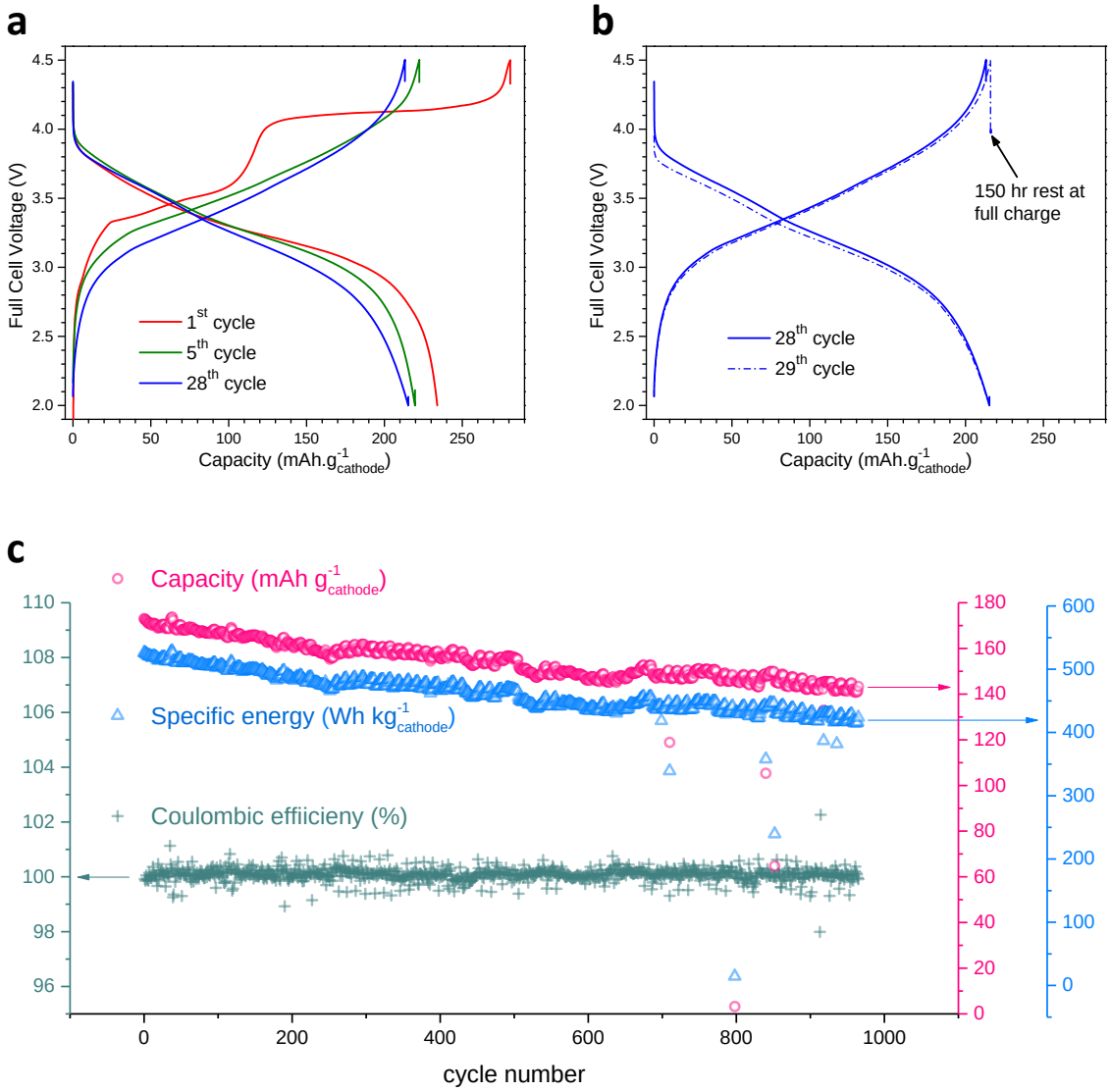


**Figure A1.12 |** Cycling properties of a LRSO full cell having a commercial graphite negative electrode and LP30 electrolyte. The cell was balanced by putting 5 % excess of negative electrode capacity compared to the positive electrode's first charge capacity. (**a**) Voltage profiles are shown for the 1st, 5th, and 28th cycles at 32 mA $g^{-1}$. The specific energy in 5th discharge is 714 Wh $kg^{-1}$ (positive electrode basis). (**b**) In a self-discharge test, no capacity loss was observed after a 150 hr rest period in fully charged condition. (**c**) Capacity retention, energy retention, and Coulombic efficiency during 1000 cycles performed at 160 mA $g^{-1}$ (1C). Minor fluctuations are due to temperature changes in the laboratory.

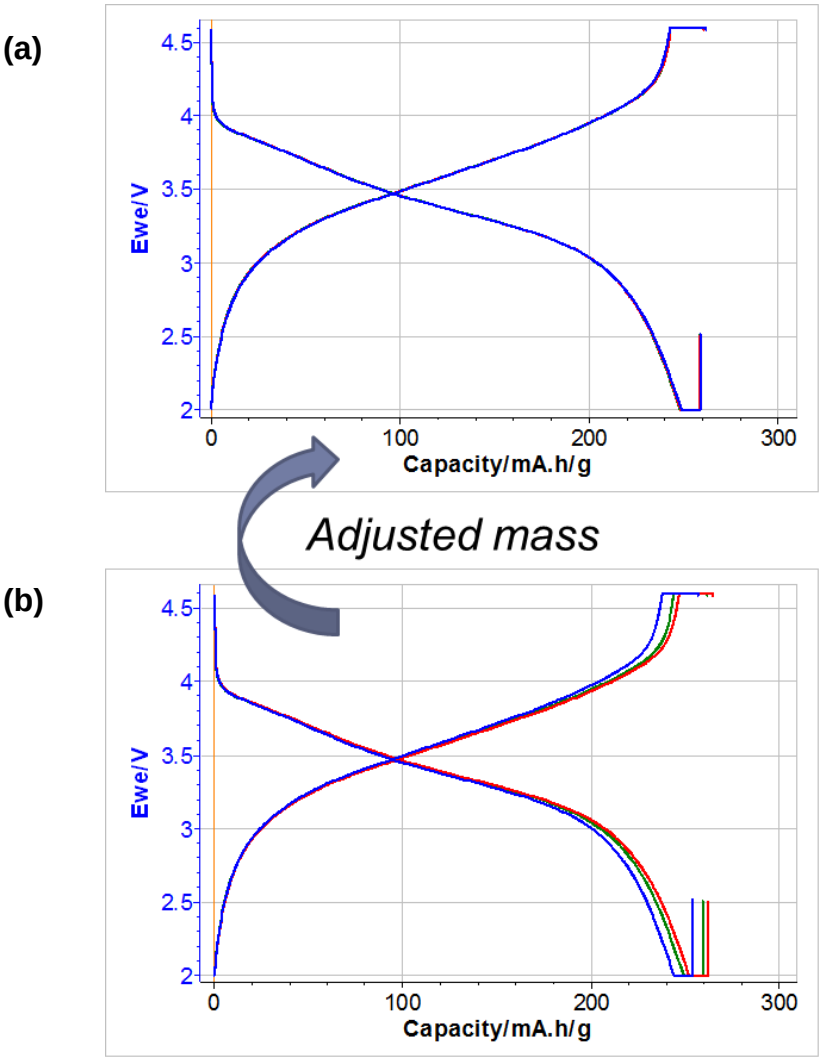


**Figure A1.13 | Protocol for the controlled ageing experiment**. Three simultaneously assembled LRSO coin-cells are first activated by 5 formation cycles (CCCV at C/5 within 2 - 4.6 V). The fifth cycle for the three cells is shown in (**b**). The minor variation in capacity among the three is then normalized by adjusting the mass of the active material in each cell such that they become identical to each other, as demonstrated by the perfect superimposition of voltage profiles in (**a**). Starting from this initial identical state before ageing, the cells are cycled simultaneously at C/5 CCCV within 2 - 4.6 V with a 24 hour OCV period (storage) at either 0 %, 50 %, or 100 % SOC for the three cells respectively. After every 2 cycles, a check-up cycle is performed in which there is no 24 hour OCV period. Also, the cell impedance is measured during the check-up cycle's discharge at 3.7 V and 3.4 V (after a 3 hour equilibration OCV period) that represent, respectively, the anionic and cationic redox potentials. The check-up cycle is followed again by 2 ageing cycles with a 24 hour rest at a desired OCV and this sequence continues. *dQ*/*dV* profiles and impedance spectra (normalized by active mass) are compared for the three cells to understand which SOC leads to a more severe ageing.

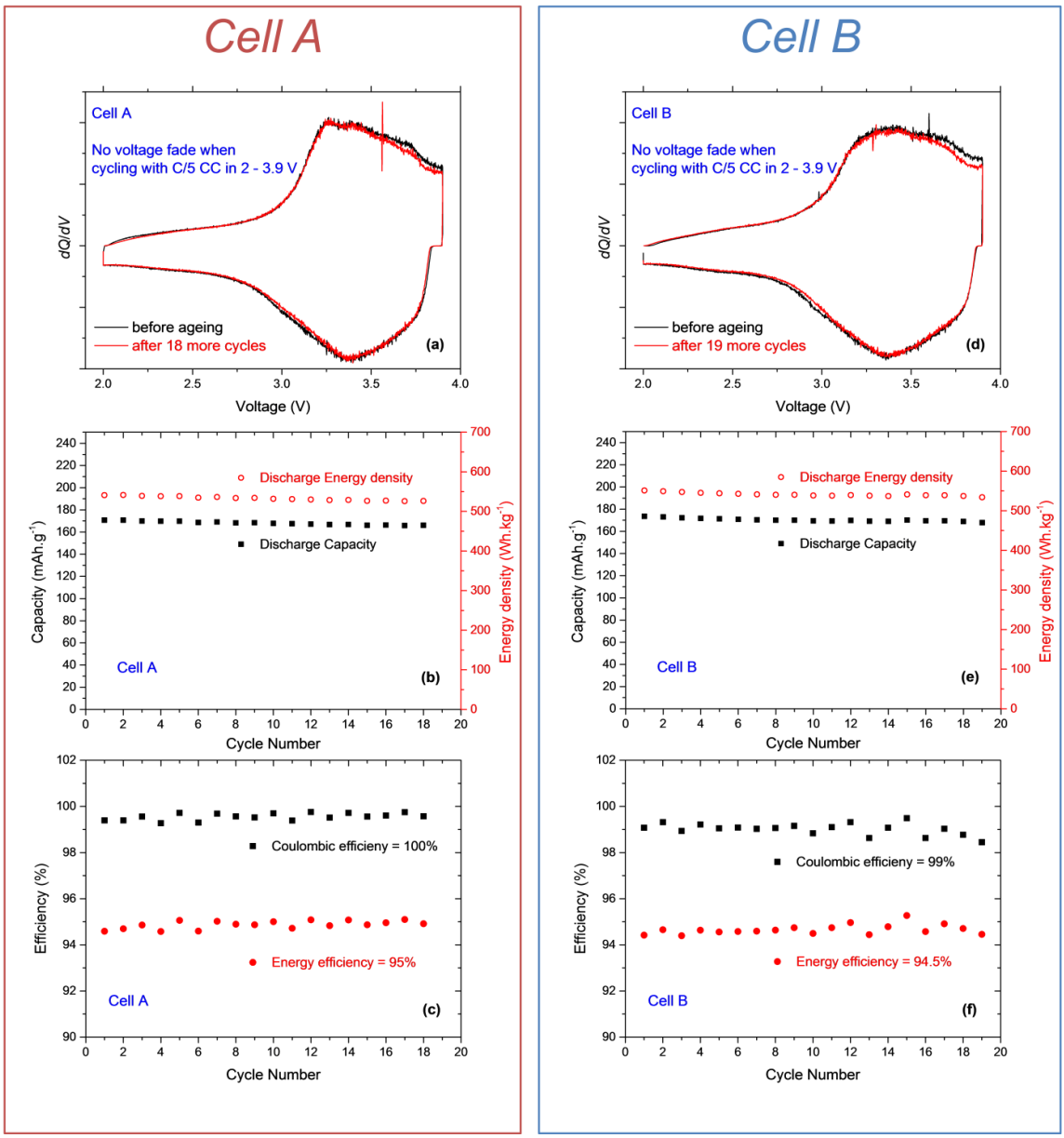


**Figure A1.14 |** Effect of cycling 'activated'-LRSO in a lower voltage range of 2 - 3.9 V at C/5 CC such that anionic redox is not activated deeply for two cells A (panels **a**, **b**, **c**) and B (panels **d**, **e**, **f**). *dQ*/*dV* profiles (**a**, **d**) neatly superimpose and do not show evidence of voltage fade. There is also more symmetry between charge and discharge indicating lower hysteresis. Energy density and capacity (**b**, **e**) over discharge are very stable with cycling. High coulombic efficiency ~100% with high energy efficiency ~95% (**c**, **f**) signifies good reversibility and much less hysteresis.

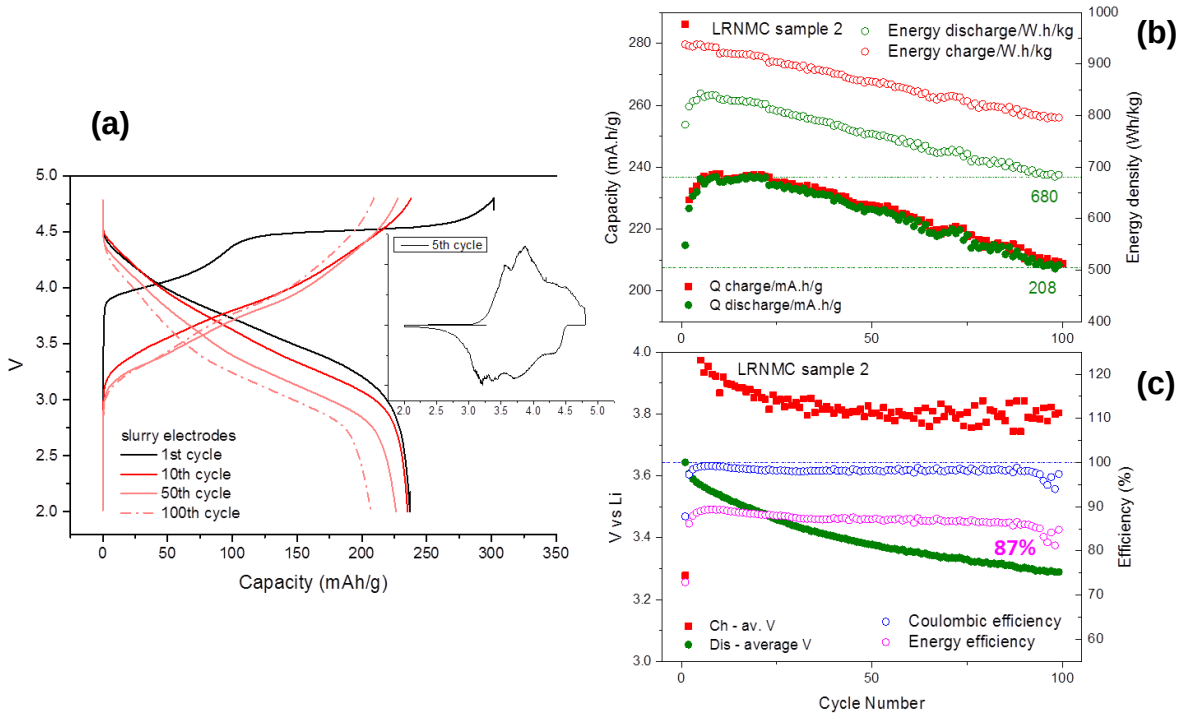


**Figure A1.15** | Li-rich NMC complementary data (at 40 mA $g^{-1}$ within 2 - 4.8 V). (**a**) Charge and discharge voltage profiles undergoing 'staircase' of 'S-shaped' transformation during 1$^{st}$ charge and further cycling shows gradual voltage fade. Asymmetric *dQ*/*dV* profiles between charge vs. discharge (inset) indicate hysteresis. The fading of capacity and energy density with increasing cycle number is shown in (**b**). A ~500mV gap persists between average charge vs. discharge voltages (**c**) and it is a direct consequence of hysteresis, which contributes to the decrease in energy efficiency to a value around 87% despite ~99% columbic efficiency.

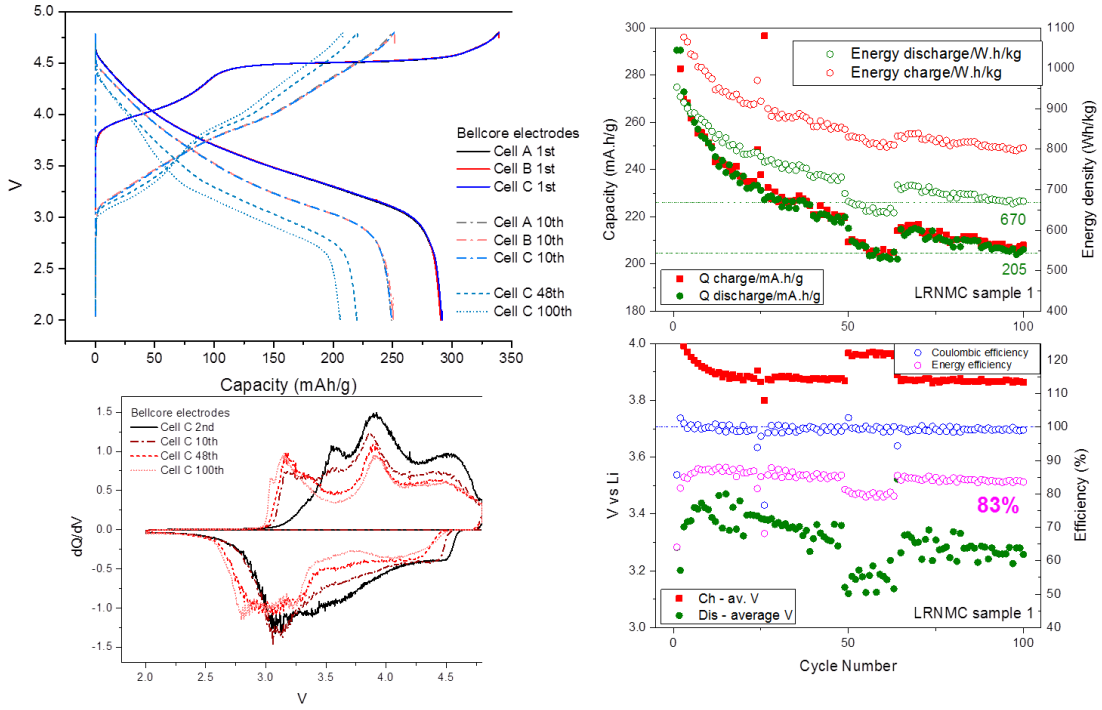


**Figure A1.16 |** Cycling properties of a different batch of Li-rich NMC having higher 1st cycle capacity.

# A2 – Supporting Information for Chapter III

## ○ Methods

**Material synthesis and electrode fabrication.** Similar to the Methods section of Appendix A1, the only difference being the electrode loading. To obtain a good signal to noise ratio at the Ru K-edge, the active material loading in the Bellcore-type electrodes was set to ~20 mg $cm^{-2}$. Circular discs of ~7 mm diameter were used in each cell.

**XAS sample preparation.** For *ex situ* sample preparation, Swagelok-type cells were assembled in an argon glovebox (moisture and oxygen < 1ppm) with Li metal foil at the negative electrode that was separated from the LRSO positive electrode by two layers of Whatman GF/D borosilicate glass-fiber sheets acting as the separator soaked with an electrolyte – LP100 (Merck) having 1 M $LiPF_6$ dissolved in ethylene carbonate : propylene carbonate : dimethyl carbonate in a 1 : 1 : 3 weight ratio. All cells were rested for 12 hours before cycling. After charging or discharging the cells to the desired state of charge (SoC), they were carefully (avoiding short-circuit) and immediately (to avoid self-discharge under open circuit) disassembled inside an argon glovebox to recover the positive electrode. The cycled electrodes were thoroughly rinsed three times with anhydrous dimethyl carbonate (DMC) to remove the remaining electrolyte and the soluble surface deposits. DMC was evaporated by leaving the samples under vacuum (using the glovebox antechamber) for at least 1 hour. Special care was taken to never expose the samples to air or moisture. For this, they were constantly maintained in dry argon atmosphere or in vacuum. For *ex situ* XAS measurements, each cycled electrode was placed between two layers of Kapton tape, which was then sealed inside the argon glovebox within two layers of air-tight transparent plastic pouches. The pouches were taken out of the glovebox just before the XAS measurements. For *operando* XAS measurements, an *in situ* electrochemical cell[210] (**Figure A2.1**), designed for transmission of the X-ray beam thanks to two Be windows (one on either side), was used for studying LRSO positive electrodes in a Li half-cell configuration. The cells were assembled in an argon glovebox with identical configuration as the above-mentioned Swagelok cells. The 1$^{st}$ cycle was studied by using a pristine electrode and the 5$^{th}$ cycle was studied by using an activated electrode that was previously

formatted by four CCCV cycles in a coin cell. The transfer for the activated electrode was done inside the glovebox immediately after disassembling the coin cell.

**Ru K-edge X-ray absorption spectroscopy (XAS).** *Ex situ* and *operando* XAS measurements at the Ru K-edge were performed in transmission mode (**Figure A2.2**) at the ROCK beamline[318] of synchrotron SOLEIL (France). Measurements performed in transmission mode provide bulk information averaged over many particles that are situated in the beam spot size of ~2 $mm^2$. A Si (220) channel-cut quick-XAS monochromator with an energy resolution of 2 eV at 22 keV was used. The intensity of the monochromatic X-ray beam was measured with three consecutive ionization detectors. The *ex situ* samples or the *operando* electrochemical cell were placed between the first and the second ionization chambers. For each measurement, successive spectra were collected at a rate of 2 Hz and averaged out over periods of 250 seconds (500 spectra) to enhance the signal to noise ratio. The time interval between two consecutive spectra in the *operando* experiments was higher (~20 minutes for the cell doing $1^{st}$ cycle and ~27 minutes for the cell doing $5^{th}$ cycle) since each time three different cells were simultaneously measured using a movable sample holder. Neither the current nor the acquisition was interrupted during cycling. The energy calibration was established with simultaneous absorption measurements on a $RuO_2$ reference placed between the second and the third ionization chambers. The data was treated using the Demeter package[319] for energy calibration and normalization. The normalized spectra were then globally analysed with Principal component analysis (PCA)[195] in order to find the number of orthogonal components needed to describe the whole evolution during cycling. The number of principal components was then used as basis for Multivariate curve resolution - alternating least squares (MCR-ALS)[196,197] analysis using the tool developed by Jaumot et al.[198] under the constraints of (*i*) non-negativity, and (*ii*) closure (sum of all concentrations equals 1.00). Finally, the reconstructed components were fitted using the Artemis software.[319] Fourier Transforms of EXAFS oscillations were carried out in the *k*-range from ~4.0 to ~16 $Å^{-1}$. Fitting was performed in the *R*-range from ~1.2 to ~3.2 Å using $k^3$ weight. EXAFS amplitudes and phase-shifts were calculated by FEFF7 with a starting model derived from $Li_2RuO_3$. Conventional least squares modelling was performed using the phase and amplitude factors calculated by FEFF7. Note that the FTs throughout Chapter III are not corrected for the phase shifts.

**Hard-X-ray photoelectron spectroscopy (HAXPES).** HAXPES measurements were performed on powders instead of slurry-electrodes. Li half-cells having LRSO powders ball milled with conductive Carbon Super P in a 91:09 ratio at the positive electrode (total weight kept ~40 mg for each cell to ensure repeatability) and Li metal foil at the negative electrode were assembled in Swagelok-type cells in an argon glovebox. After charging / discharging to desired SoCs, the cells were disassembled and the positive electrode powders were recovered, rinsed and dried as described above. Note that our *ex situ* electrode samples were recovered as loose powders that were thoroughly mixed. This averaged out any concentration gradients which can bias XPS results if slurry-electrodes were used instead. Great attention was paid to preserve samples from air exposure during transfer and handling. They were constantly maintained in dry argon atmosphere or in vacuum. For HAXPES, they were transferred from the argon glovebox to the beamline introduction chamber through a specially designed stainless steel transfer system (suitcase) preventing exposure to ambient. HAXPES measurements were carried out at the GALAXIES[320,321] beamline of SOLEIL synchrotron in France. The photon excitation energy h$\nu$ = 6.9 keV was obtained using the third order reflection of a Si(111) double-crystal monochromator. The photoelectrons were analysed by a SCIENTA EW4000 spectrometer, and the obtained energy resolution from the Au Fermi edge was 0.14 eV. No charge neutralizer was needed, and the pressure was kept around $10^{-8}$ mbar in the analysis chamber during the measurements. Experiments were carried out using the single-bunch mode (lowest synchrotron brilliance) to avoid degradation under the X-ray beam. The binding energy scale was calibrated from the C 1*s* core peak at 284.4 eV coming from Carbon Super P added to the positive electrode materials.

**O K-edge soft X-ray absorption spectroscopy (XAS).** O K-edge XAS spectra were recorded at the BACH beamline of the Elettra synchrotron facility in Trieste (Italy). The experiment was carried out in total fluorescence yield (TFY) mode with a monochromator resolution of 0.14 eV for entrance slits set at 20 microns. Incident energy was calibrated using Au 4*f* XPS peak. The $Li_{2-x}RuO_3$ *ex situ* samples were prepared as pellets without any carbon black or binder to avoid undesirable signals from surface components. Great attention was paid to preserve samples from air / moisture exposure during transfer and handling. They were constantly maintained in dry argon atmosphere and transferred from the argon glovebox to the beamline introduction chamber through a specially designed stainless steel transfer system (suitcase).

## ○ Supporting Figures

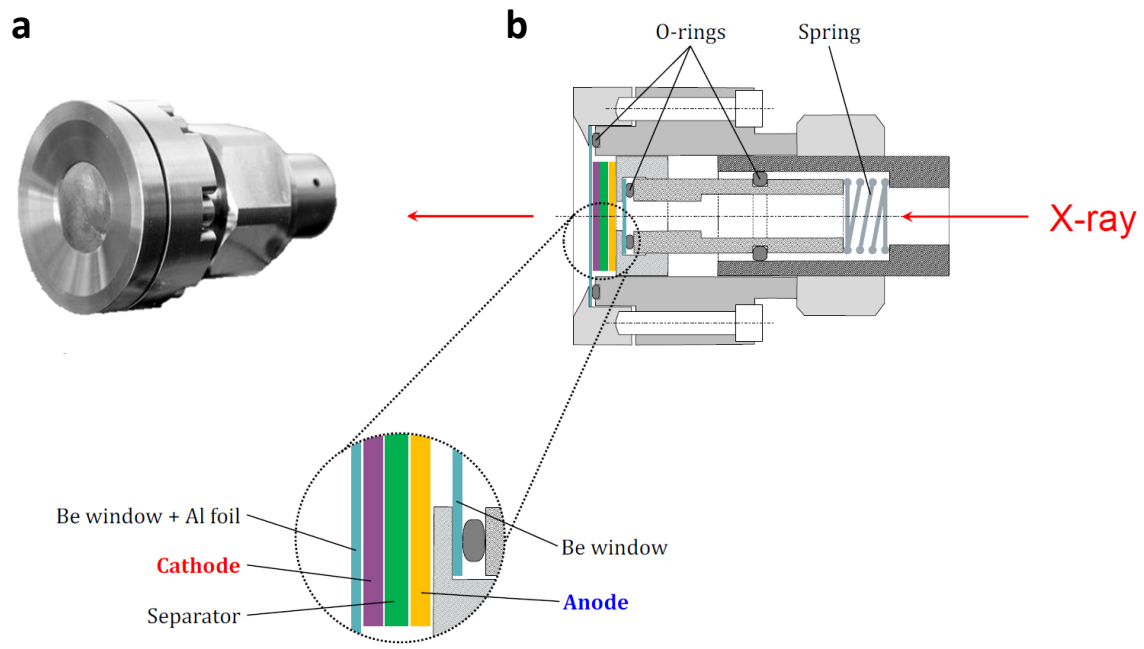


**Figure A2.1** | (**a**) A picture of the *in situ* cell[210] and (**b**) its schematic for XAS experiments in transmission mode, with a zoom of the electrochemical sandwich. Adapted from: *PhD thesis of Arnaud Perez, 2017.*

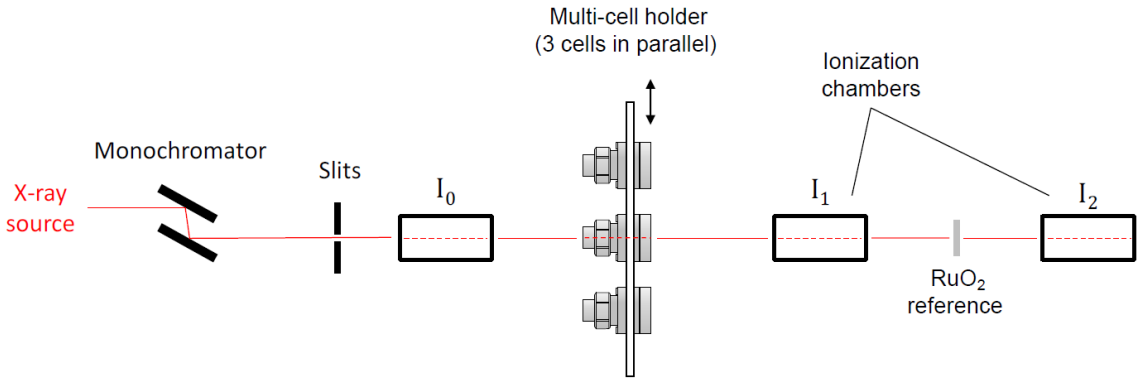


**Figure A2.2** | Schematic of the XAS experiment. Three *in situ* cells were cycled in parallel and were alternatively aligned with the beam to collect absorption spectra. Adapted from: *PhD thesis of Arnaud Perez, 2017.*

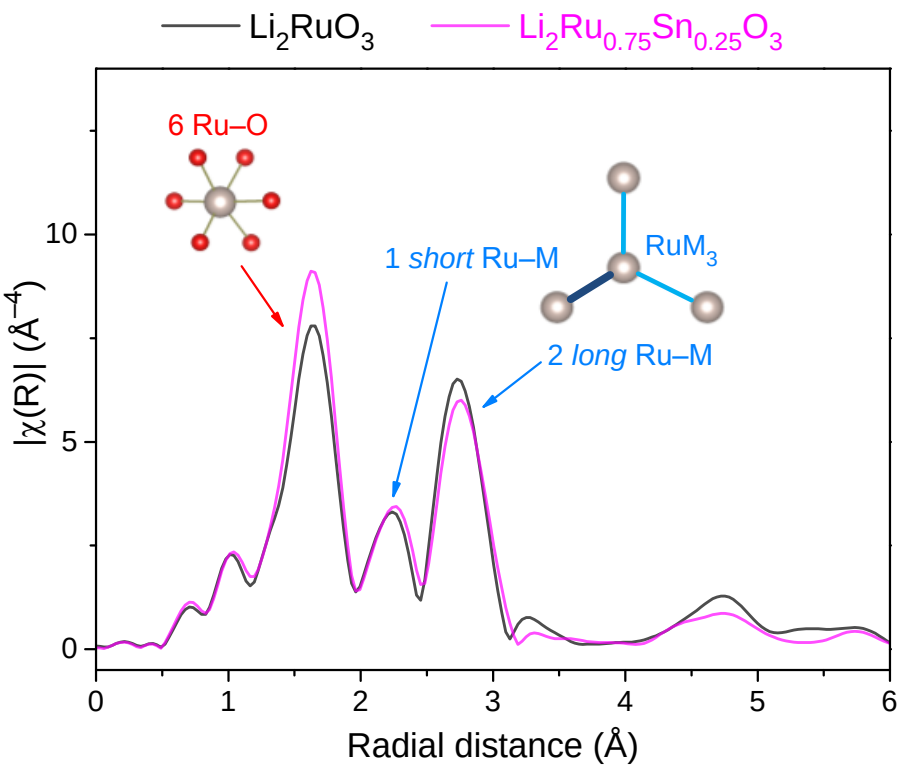


**Figure A2.3 |** Comparison of $Li_2RuO_3$ and LRSO. Magnitudes of Fourier transforms of $k^3$-weighted EXAFS oscillations are almost similar for the two compounds, i.e. with and without Sn substitution. The $|\chi(R)|$ plot is not corrected for phase shifts.

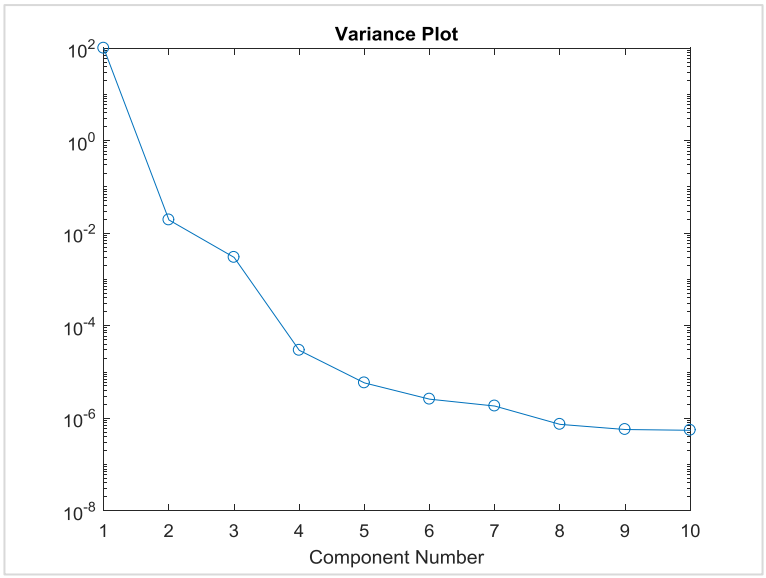


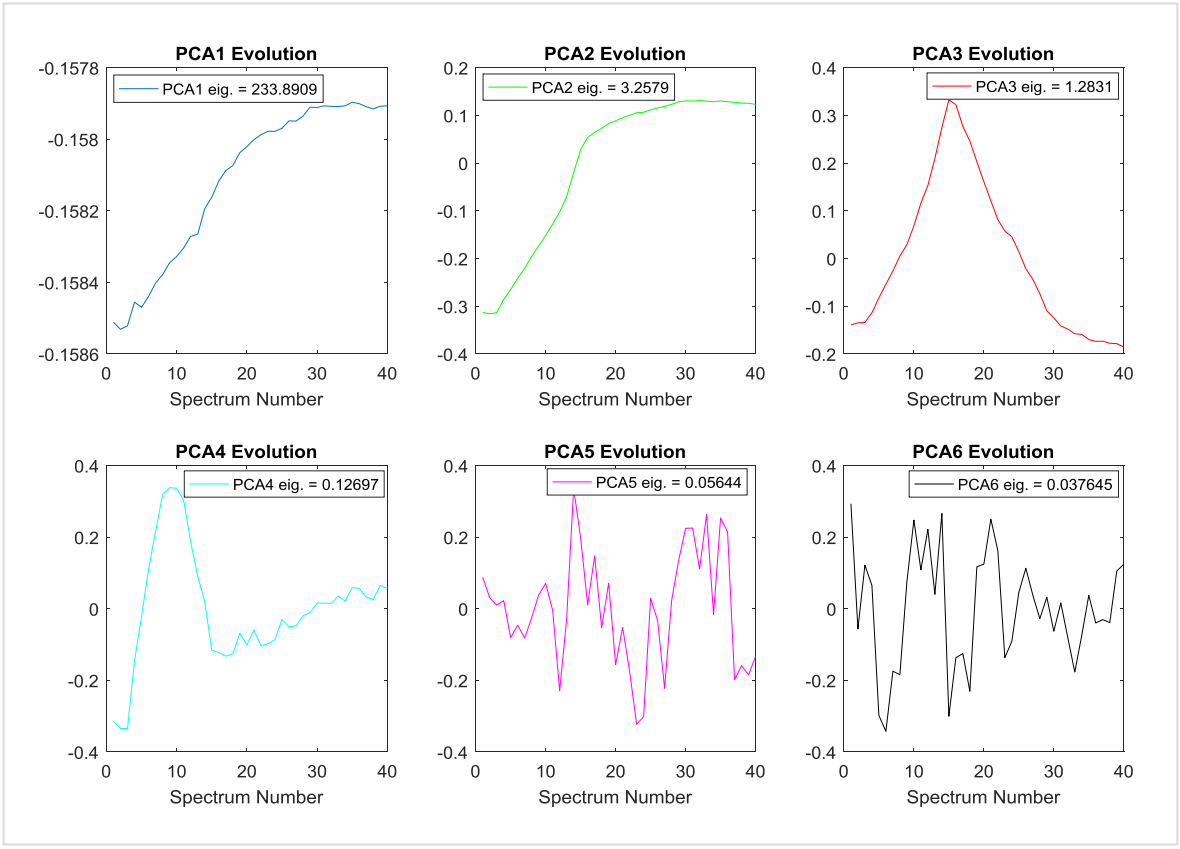


**Figure A2.4 |** Detailed PCA results for LRSO's 1st charge. The variance plot is shown at the top. The first four components capture nearly 100 % of the variance in the experimental data set. The evolution of scores for the six first components (bottom) suggests that the data can be explained by four principal components, since the scores of the first four components vary gradually, compared to the erratic variation of the last two components which therefore represent experimental noise.

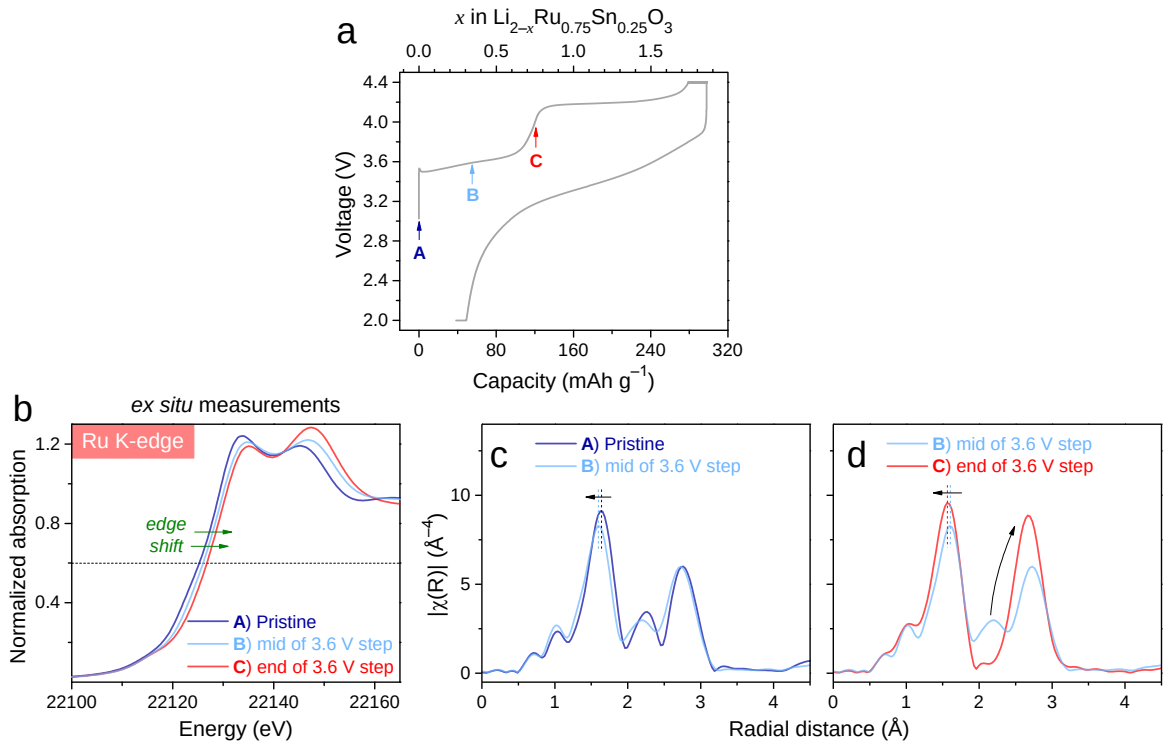


**Figure A2.5 |** *Ex situ* XAS results over the 3.6 V cationic redox step. (**a**) The 1st cycle voltage profile of LRSO showing the positions of samples. (**b**) XANES spectra of the three samples showing an edge shift as Li is removed which confirms $Ru^{4+/5+}$ oxidation. (**c**) Magnitudes of Fourier transforms of $k^3$-weighted EXAFS oscillations show that initial Li removal does not change the Ru–M network (both **A** and **B** being characterized by three peaks) but just leads to shirking of Ru–O distance (first shell). (**d**) Completion of the cationic oxidation (**B** to **C**) leads to the merging of unequal Ru–M distances into a single peak (indicated by curved arrow). Again the shift of Ru–O peak because of Ru oxidation can be visualized. The $|\chi(R)|$ plots are not corrected for phase shifts.

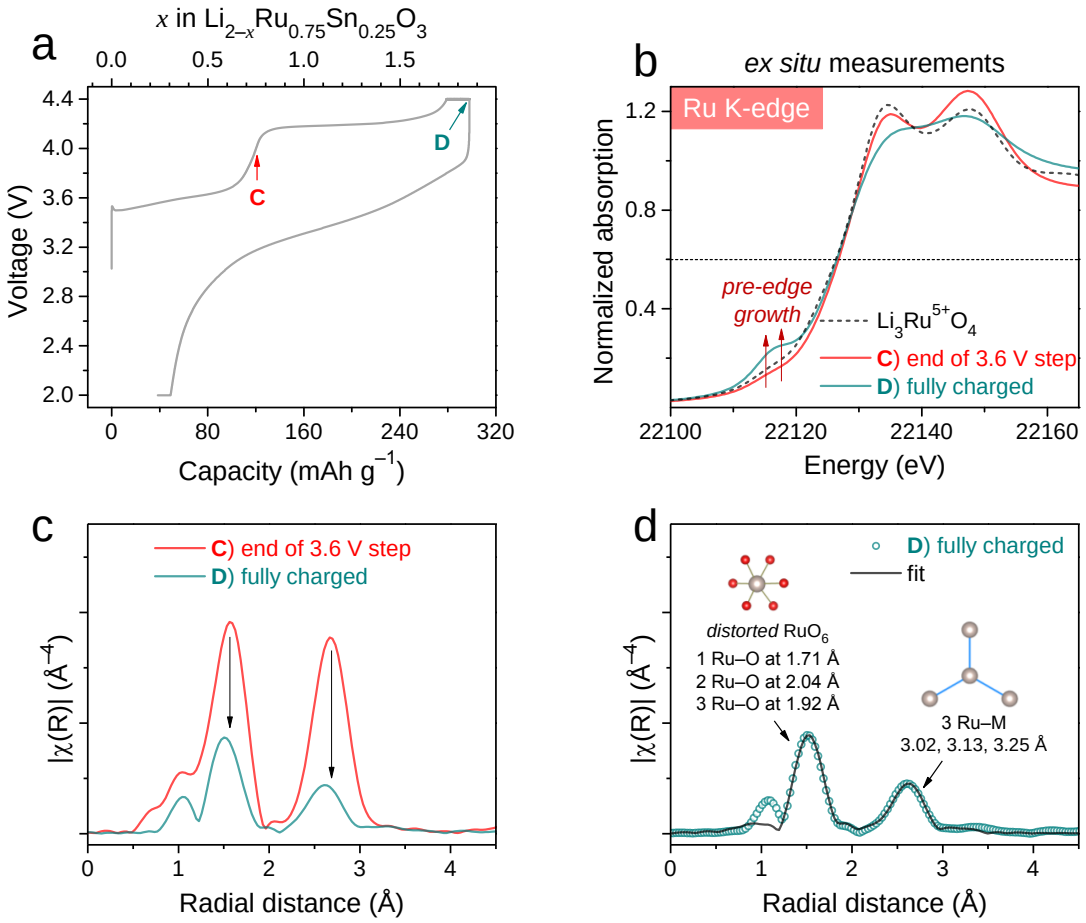


**Figure A2.6** | *Ex situ* XAS results over the 4.2 V anionic redox step. (**a**) The 1st cycle voltage profile of LRSO showing the positions of samples. (**b**) XANES spectra of the two samples showing a pre-edge peak growth as Li is removed, which confirms the distortion of $RuO_6$ octahedra. A comparison with $Li_3RuO_4$ (considering formal $Ru^{5+}$ state) confirms that Ru stays as $Ru^{5+}$ during the 4.2 V anionic redox plateau. Note also that $Li_3RuO_4$ does not show the pre-edge peak particular to the fully charged sample. (**c**) Magnitudes of Fourier transforms of $k^3$-weighted EXAFS oscillations show the peak intensity reduction (marked by vertical arrows) as a consequence of anionic oxidation, indicating disorder in the fully charged sample. (**d**) EXAFS fitting analysis of the fully charged sample is performed with the same structural model that is used for component **IV**. The $|\chi(R)|$ plots are not corrected for phase shifts.

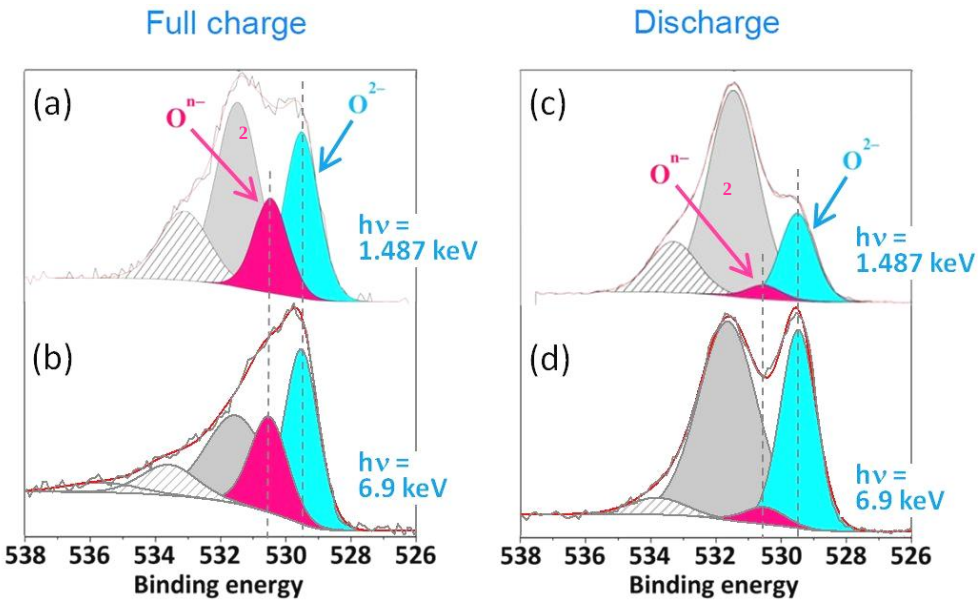


**Figure A2.7 |** Influence of photon energy on O 1*s* photoelectron spectra of LRSO. (**a**) and (**b**) after the first charge, (**c**) and (**d**) after the first discharge. HAXPES data recorded at photon energy of 6.9 keV are the same as presented in **Figure III.8**. In-house XPS data recorded at photon energy of 1.487 keV are taken from *Foix et al.*[105]. Gray peaks at higher binding energy come from electrolyte decomposition products in the surface layer (SEI layer).

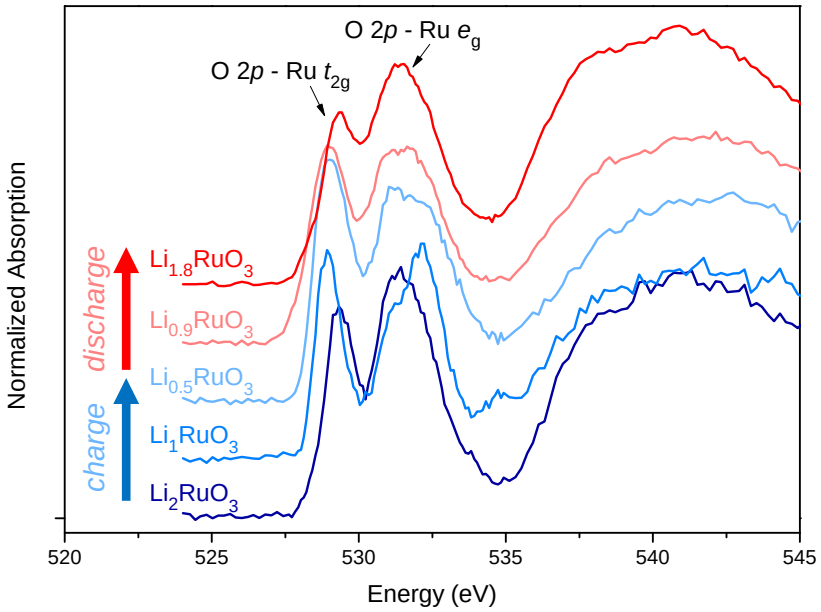


**Figure A2.8** | Normalized O K-edge XAS spectra for $Li_{2-x}RuO_3$ acquired in Total Fluorescence Yield (TFY) mode. The spectra are vertically shifted for the sake of clarity. In the O K-edge process, the 1*s* core electrons of O are promoted to the 2*p* empty states. Since the O 2*p* states close to the Fermi level are strongly hybridized with Ru 4*d* states, oxygen K-edge XAS can be used to monitor the hole created on the O 2*p*–Ru 4*d* orbitals during charge/discharge. The two main peaks correspond to the hybridized orbitals of O 2*p*–Ru $t_{2g}$ and O 2*p*–Ru $e_g$, respectively. A clear shift of the first peak and the increasing intensity are observed when charging from $Li_2RuO_3$ to $Li_1RuO_3$, i.e. when Ru oxidation state moves form 4+ to 5+. However, the peak position and its intensity are not affected by further delithiation from $Li_1RuO_3$ to $Li_{0.5}RuO_3$, while a clear broadening of the second peak is observed. Since the formation of $Ru^{6+}$ is excluded by using Ru K-edge XAS, this broadening could be ascribed to the formation of $(O_2)^{n-}$ species, as also proposed previously for $Na_{2-x}RuO_3$[122], but further theoretical work is needed to fully confirm this. The spectral changes are partially reversible on subsequent discharge.

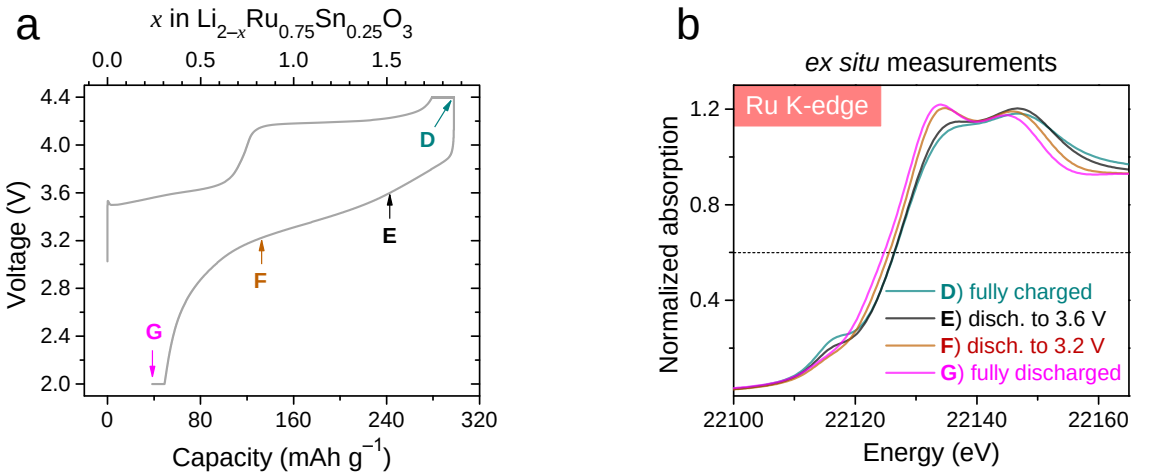


**Figure A2.9 |** *Ex situ* XAS results on 1st discharge. (**a**) The 1st cycle voltage profile showing the sample positions on 1st discharge. (**b**) Ru K-edge XANES spectra showing the disappearance of pre-edge peak on reduction at high potential (**D** to **E** to **F**, anionic redox) followed by an edge shift towards lower energy on reduction at low potential (**E** to **F** to **G**, cationic redox).

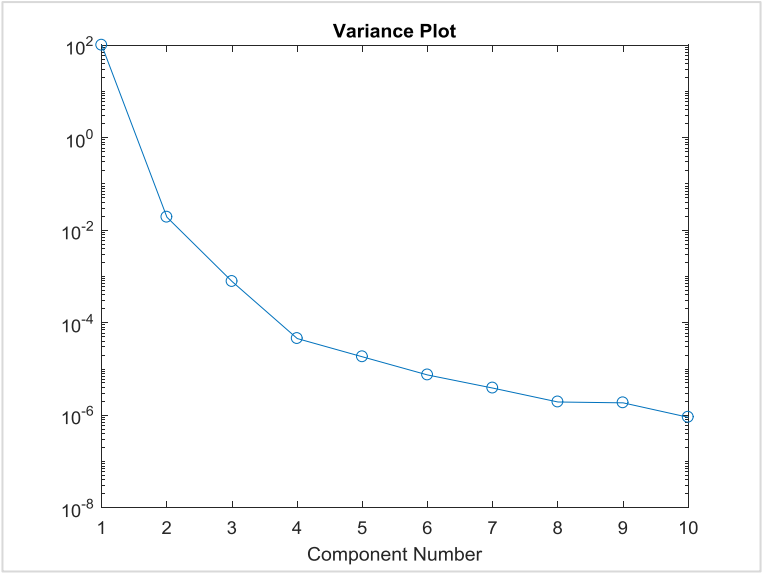


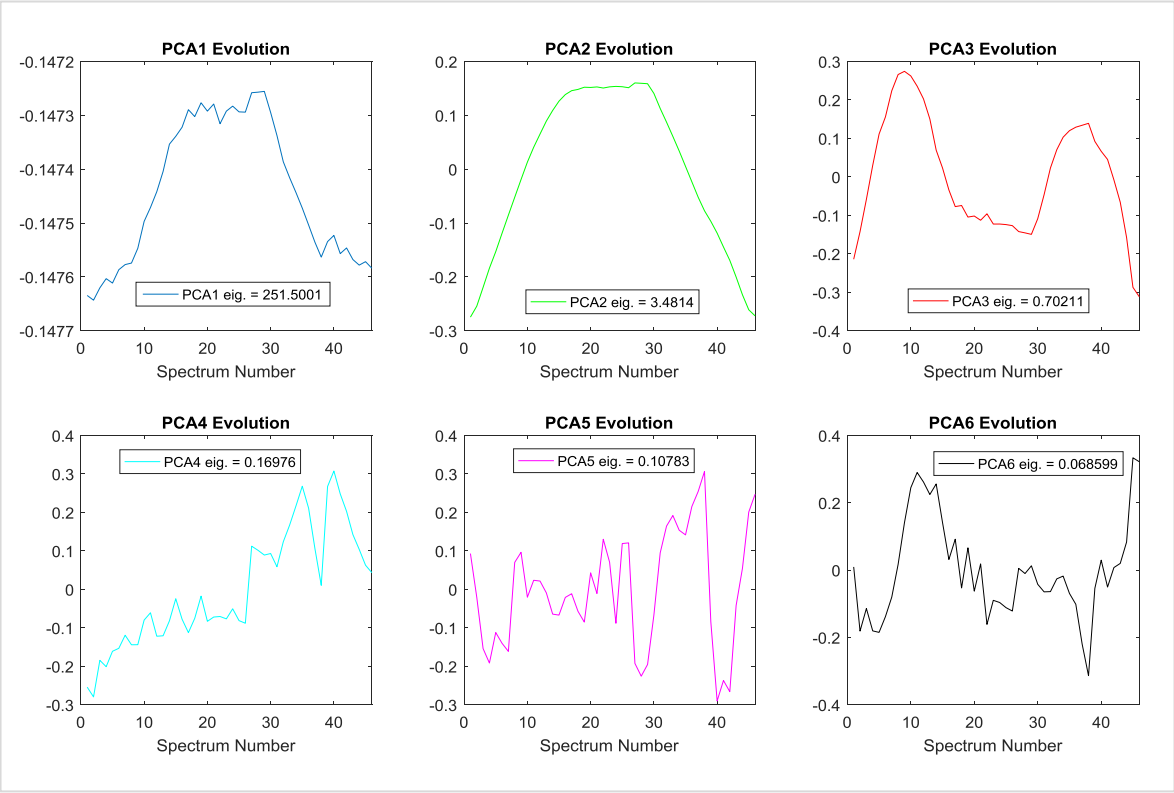


**Figure A2.10 |** Detailed PCA results for LRSO's 5th cycle. The variance plot is shown at the top. The first three components capture nearly 99.9999 % of the variance in the experimental data set. The evolution of scores for the first six components (bottom) suggests that the data can be explained by three principal components, since the scores of the first three components vary gradually, compared to the erratic variation of the last three components which therefore represent experimental noise.

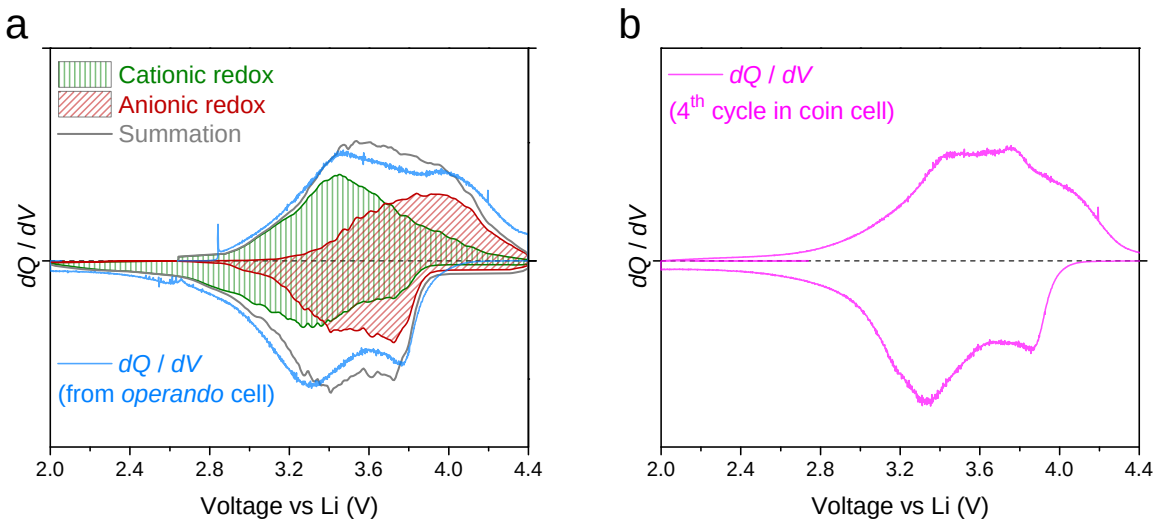


**Figure A2.11 |** Decoupling of cationic-anionic redox processes on the *dQ*/*dV* profiles. (**a**) Superimposition of the *dQ*/*dV* profile obtained in the *operando* cell with the summation of anionic and cationic contributions that were deconvoluted using PCA and MCR-ALS analyses (same as **Figure III.13** of main text). (**b**) The *dQ*/*dV* profile obtained in a coin cell which was used for activation of the electrode. All profiles display a similar overall shape, which demonstrates how powerful *operando* experiments can be if : (*i*) the electrochemistry in the *operando* cell matches that in regular cells, and (*ii*) the information obtained from the spectra represents the overall electrode.

**Note –** Satisfying these two above conditions is unfortunately not always possible, as we encountered later during the investigations of the $Li_2IrO_3$ phases using *operando* synchrotron-XRD and *operando* XAS (results not included in the thesis). In short, the overall electrochemical curves were correct but the electrode region that got exposed to the high energy X-ray beam (~5 % of the total electrode area) severely lagged behind (nearly "frozen") compared to the rest of the electrode. Besides the possible interaction of $Li_2IrO_3$ with high energy radiation, the slightly non-uniform pressure in the cell may have also contributed to such issues, therefore calling for improvements in cell design, especially since similar delays have already been reported with this cell.[199,210,322,323]

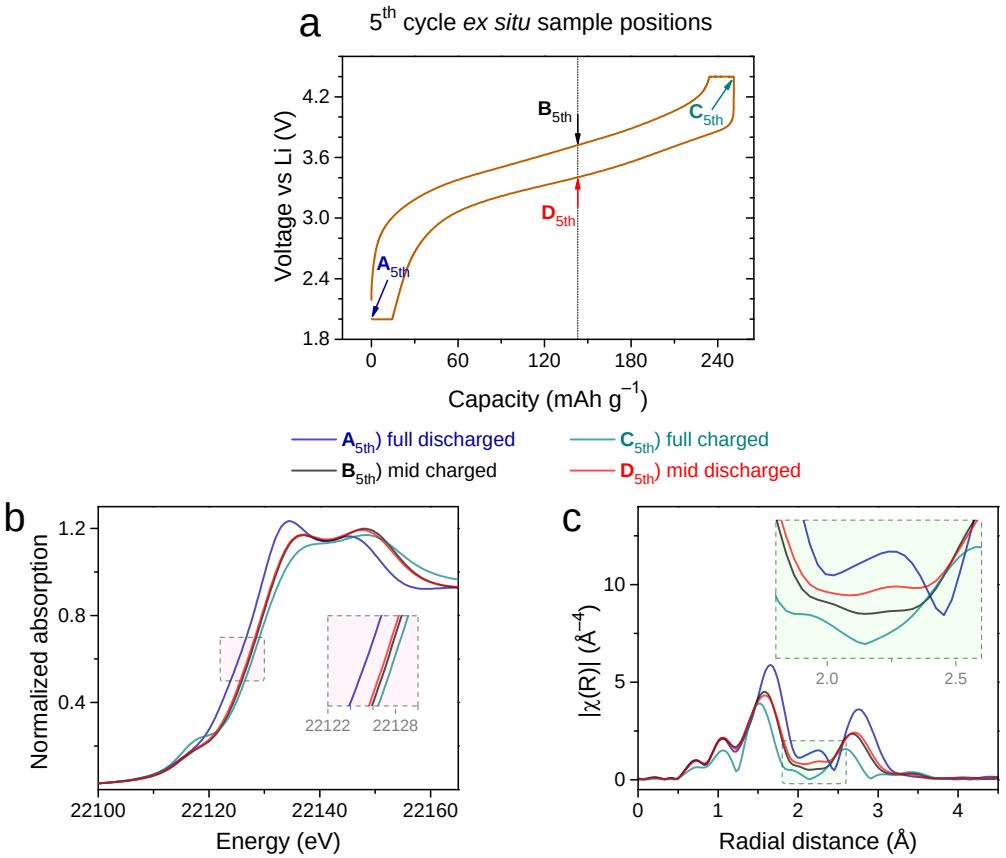


**Figure A2.12** | *Ex situ* Ru K-edge XAS results for LRSO's 5th cycle. (**a**) The voltage profile measured in Swagelok cells that were used to prepare the samples whose positions are marked. (**b**) XANES spectra of the four samples showing mainly an edge shift from $\mathbf{A}_{5th}$ to $\mathbf{B}_{5th}$ (cationic oxidation at low potential charge) followed by only a slight shift but a marked growth of pre-edge peak from $\mathbf{B}_{5th}$ to $\mathbf{C}_{5th}$ (mainly anionic oxidation at high potential on charge). On discharge, $\mathbf{C}_{5th}$ to $\mathbf{D}_{5th}$ involves disappearance of the pre-edge peak (anionic reduction on high potential discharge). A zoomed view of the edge positions (shown in inset) reveals a subtle difference between $\mathbf{B}_{5th}$ and $\mathbf{D}_{5th}$. The edge position of $\mathbf{D}_{5th}$ is at a slightly lower energy than that of $\mathbf{B}_{5th}$, which means different extents of Ru participation depending of electrochemical paths taken (charge vs. discharge) to arrive at the same overall SoC (or Li content). Conversely, for charge balancing, it can be concluded that oxygen is slightly more oxidized in $\mathbf{D}_{5th}$ than compared to $\mathbf{B}_{5th}$. (**c**) Magnitudes of Fourier transforms of $k^3$-weighted EXAFS oscillations for the four samples. The $|\chi(R)|$ plot is not corrected for phase shifts. The fully discharged and charged samples ($\mathbf{A}_{5th}$ and $\mathbf{C}_{5th}$) match with the *operando* results (components $\mathbf{I}_{5th}$ and $\mathbf{III}_{5th}$ respectively). There is a slight difference between the local structures of $\mathbf{B}_{5th}$ and $\mathbf{D}_{5th}$, as highlighted in a zoomed view around $R$ = 2.25 Å (see inset), where the peak associated with the short Ru–M distance is located. $\mathbf{D}_{5th}$ is closer to the fully discharged sample than $\mathbf{B}_{5th}$, as was also seen from the XANES spectra in panel (**b**). Overall, although the *ex situ* samples are relaxed over a few days, their results agree with the *operando* measurements and highlight a path dependence or voltage hysteresis.

# ○ Supporting Tables

**Table A2.1 |** Comparison of various models attempted to fit the EXAFS oscillations for Component **IV** (fully charged) during 1st charge. The fits were performed in the *R*-range from 1.10 to 2.05 (first peak only).†

| Model used to fit $RuO_6$ octahedra | *CN* | *R* (Å) | $\sigma^2$ (Å$^2$) | Graph | Comments |
|---|---|---|---|---|---|
| **6** (*one Ru–O shell*) | 6 | 1.951 (10) | 0.0085 (11) | 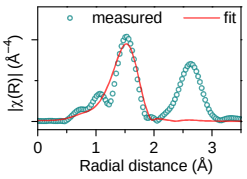  | Poor fit quality |
| | | | ***R-factor* = 0.1262** | | |
| **3+3** (*two Ru–O shells*) | 3 | 1.943 (10) | 0.0042 (11) | 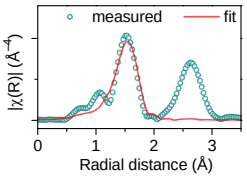  | Too large $\sigma^2$ |
| | 3 | 2.01 (26) | **0.036 (41)** | | |
| | | | *R-factor* = 0.0432 | | |
| **2+4** (*two Ru–O shells*) | 2 | 1.733 (84) | **0.018 (11)** | 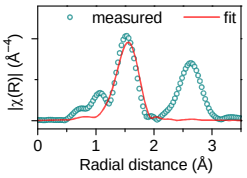  | Too large $\sigma^2$ |
| | 4 | 1.944 (9) | 0.0053 (8) | | |
| | | | *R-factor* = 0.0528 | | |
| **1+5** (*two Ru–O shells*) | 1 | 1.699 (24) | 0.0053 (22) | 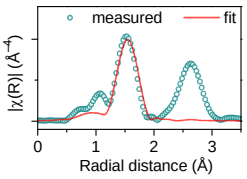  | Good, but can be improved |
| | 5 | 1.936 (8) | 0.0067 (8) | | |
| | | | ***R-factor* = 0.0364** | | |
| **1+1+4** (*three Ru–O shells*) | 1 | 1.741 (35) | 0.0056 (28) | 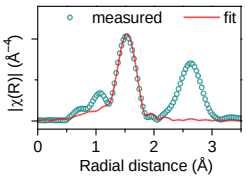  | Too small $\sigma^2$ |
| | 1 | 2.068 (24) | **0.0017 (21)** | | |
| | 4 | 1.930 (11) | 0.0034 (9) | | |
| | | | *R-factor* = 0.0088 | | |
| **1+2+3** (*three Ru–O shells*) | 1 | 1.746 (34) | 0.0054 (27) | 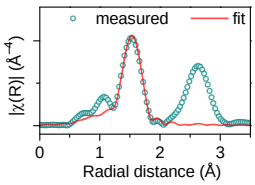  | Best fit |
| | 2 | 2.031 (19) | 0.0037 (24) | | |
| | 3 | 1.915 (12) | 0.0023 (12) | | |
| | | | ***R-factor* = 0.0075** | | |
| **2+2+2** (*three Ru–O shells*) | 2 | 1.810 (50) | **0.0131 (64)** | 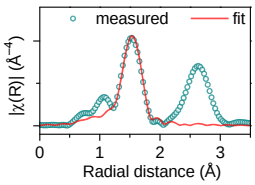  | $\sigma^2$ too small or too large |
| | 2 | 2.026 (19) | 0.0031 (25) | | |
| | 2 | 1.916 (11) | **0.0010 (12)** | | |
| | | | *R-factor* = 0.0098 | | |

† $E_0$ was determined from the energy value where jump is 0.6. The difference in threshold energy ($\Delta E_0$) and the amplitude reduction factor ($S_0^2$) were fixed at 0 and 1, respectively. The coordination numbers (*CN*) were kept constant and only the radial distances (*R*) and the Debye-Waller factors ($\sigma^2$) were allowed to vary.

**Table A2.2 |** Comparison of two models attempted to fit the EXAFS oscillations for Component **II**$_{5th}$ (*intermediate*) during 5$^{th}$ cycle. The fits were performed in the *R*-range from 1.24 to 2.05 (first peak only).[†]

| **Model used to fit $RuO_6$ octahedra** | ***C N*** | ***R* (Å)** | **$\sigma^2$ (Å$^2$)** | **Graph** | **Comments** |
|---|---|---|---|---|---|
| **6** (*one Ru–O shell*) | 6 | 1.977 (6) | 0.0070 (6) | 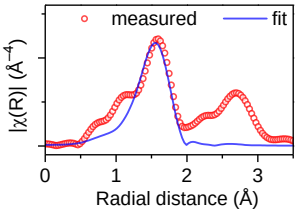 | Good, but can be improved |
| | | ***R-factor* = 0.0284** | | | |
| **1+5** (*two Ru–O shells*) | 1 | 1.862 (46) | 0.0044 (64) | 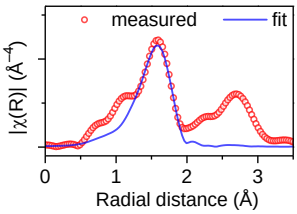 | **Best fit** |
| | 5 | 1.987 (11) | 0.0050 (17) | | |
| | | ***R-factor* = 0.0195** | | | |

[†] $E_0$ was determined from the energy value where jump is 0.6. The difference in threshold energy ($\Delta E_0$) and the amplitude reduction factor ($S_0^2$) were fixed at 0 and 1, respectively. The coordination numbers (*CN*) were kept constant and only the radial distances (*R*) and the Debye-Waller factors ($\sigma^2$) were allowed to vary.

# A3 – Supporting Information for Chapter IV

## ○ Methods for Part - IV*a* -

**Material synthesis and characterization.** $Li_{1.2}Ni_{0.13}Mn_{0.54}Co_{0.13}O_2$ (Li-rich NMC) powders were synthesized with a two-step process involving carbonate co-precipitation followed by heat treatment.[324] First, stoichiometric Ni-Mn-Co carbonate was co-precipitated from an aqueous solution of transition-metal sulphates by introducing in it an aqueous solution of sodium carbonate (2 M) and ammonia (0.2 M). This was carried out in a controlled manner (pH = 8, T = 55 °C, stirring speed = 1000 rpm) by using a continuously stirred tank reactor (Bioflow 320, Eppendorf) to regulate the morphology and homogeneity of particles. The resulting Ni-Mn-Co carbonate powders were heat treated with $Li_2CO_3$ at 850°C for 12 hours to obtain the Li-rich NMC powders with a primary particle size of ~100 nm as characterized by SEM (FEI Helios NanoLab 650). The crystal structure was confirmed with X-ray diffraction (BRUKER D8 Advance diffractometer with Cu Kα radiation) and the targeted elemental composition was verified with inductively coupled plasma – mass spectrometry.

***Ex situ* sample preparation.** Li half-cells having Li-rich NMC powders hand mixed (to preserve morphology) with conductive Carbon Super P in a 90:10 mass ratio at the positive electrode (total weight kept ~20 mg for each cell to ensure repeatability) and Li metal foil at the negative electrode were assembled in Swagelok-type cells in an Argon glovebox ($O_2$ < 0.1 ppm, $H_2O$ < 0.1 ppm). Note that Swagelok cells were preferred to coin-cells due to the possible risk of short-circuit during the coin-cell disassembly process that could lead to artificial reduction of the positive electrode. Positive and negative electrodes were separated with two layers of Whatman GF/D borosilicate glass-fibre sheets as the separator soaked with an electrolyte – LP100 (Merck) having 1 M $LiPF_6$ dissolved in ethylene carbonate : propylene carbonate : dimethyl carbonate in a 1 : 1 : 3 weight ratio. All cells are rested for 12 hours before testing. Once the desired SoC is achieved using a constant current density of ± 20 mA $g^{-1}$, the Swagelok cells were disassembled in the glovebox carefully (ensuring no short circuiting) and as soon as possible (to prevent self-discharge under open circuit). The positive electrode powders were rinsed thoroughly three times with anhydrous dimethyl carbonate (DMC) to get rid of the electrolyte and soluble

surface deposits. DMC was evaporated by leaving the samples in vacuum (using the glovebox antechamber) for at least 1 hour. Note that our *ex situ* electrode samples were recovered as loose powders that were thoroughly mixed. This averaged out any concentration gradients which can bias XPS results if slurry-electrodes are used instead.

**Sample handling and transfer.** Great attention was paid to preserve the samples from air and moisture exposure during transfer and handling. They were constantly maintained in dry argon atmosphere or in vacuum. For in-house XPS, they were transferred directly from the argon glovebox ($O_2$ < 0.1 ppm, $H_2O$ < 0.1 ppm) connected to the spectrometer. For HAXPES, they were transferred from the on-site argon glovebox to the beamline introduction chamber (that was kept under vacuum) via a specially-designed detachable stainless-steel transfer system ('suitcase'). The samples were first sealed in this 'suitcase' inside the glovebox and then transferred to the beamline within 15 minutes. All series of *ex situ* experiments (in-house XPS, HAXPES and XAS) were performed on the same samples by pasting the powders on carbon tape (**Figure A3.1a**).

**In-house XPS.** XPS measurements were performed with a Kratos Axis Ultra spectrometer, using a focused monochromatized Al Kα radiation ($h\upsilon$ = 1486.6 eV). The analysed area of the samples was 300 µm × 700 µm. Peaks were recorded with constant pass energy of 20 eV. For the Ag $3d_{5/2}$ line, the full width at half maximum (FWHM) was 0.58 eV under the recording conditions. No charge neutralization was required and the pressure was maintained around $10^{-8}$ mbar. The binding energy scale was calibrated from the C 1*s* core peak at 284.4 eV coming from Carbon Super P added to the positive electrode materials.

**Hard X-ray photoemission spectroscopy (HAXPES).** HAXPES measurements were carried out at the GALAXIES beamline[320,321] of SOLEIL synchrotron facility in France. Photon excitation energies of $h\upsilon$ = 3.0 and 6.9 keV were obtained from the first and the third order reflections of the Si(111) double-crystal monochromator, respectively. Photoelectrons were analysed by a SCIENTA EW4000 spectrometer, and the obtained energy resolution from the Au Fermi edge was 0.32 eV for 3.0 keV photon energy and 0.14 eV for 6.9 keV photon energy. No charge neutralizer was required, and the analysis chamber pressure was maintained around $10^{-8}$ mbar during the measurements. **Figure A3.1b** shows a photograph of the sample holders being loaded in the analysis chamber. Experiments were carried out using the single-bunch mode (lowest synchrotron brilliance)

to minimize degradation under the X-ray beam. The binding energy scale was calibrated to match the in-house XPS spectra on the same samples.

**Fitting procedure of O 1*s* photoelectron spectra.** The first rule was to use the minimum of components, i.e. an additional component was introduced only if it was not possible to fit the spectrum properly without it. The second rule was to constrain the positions and widths of the two O 1*s* components which are attributed to oxygenated species from the surface film. These components are well identified since the corresponding chemical species are also detected by other core peaks, namely C 1*s*, P 2*p*, F 1*s* (not shown in the thesis because of the great number of spectra, but systematically recorded and quantitatively analysed). Although the composition of the surface film changes as a function of the electrochemical steps, several oxygenated species arising from decomposition of the electrolyte (i.e. carbonate solvents and $LiPF_6$ salt) are always found in large quantities, e.g. $Li_2CO_3$, phosphates and fluorophosphates. This makes the O 1*s* signal shape of the surface film rather stable, and very similar to the numerous previous XPS studies on a wide variety of positive electrode materials for Li-ion batteries. Therefore these two components were constrained as follows: the first one was allowed to vary between 531.5 and 532.0 eV and the second one was allowed to vary between 533.0 and 533.5 eV. Their width was constrained to be equal, and allowed to vary between 1.5 and 2.0 eV for the photon energy 6.9 keV (this width depends on the monochromator resolution and it was broader for 3.0 keV). A shake-up satellite was observed in HAXPES spectra, depending on the state of charge. This additional peak is observed at a very high binding energy (535-536 eV) and has no impact on the fitting result of the other components. The two last O 1s components and the most important ones for the present study, i.e. the lattice $O^{2-}$ peak and the oxidized lattice oxygen $O^{n-}$ ($n < 2$) were fitted without any constraints. The results were very homogeneous in the whole series of samples in terms of line widths and relative position of the $O^{n-}$ peak with respect to the $O^{2-}$ peak.

**Soft-XAS measurements.** XAS spectra at Co $L_{II,III}$ edges were collected on the ANTARES beamline of SOLEIL synchrotron in France. The *ex situ* cathodes were transferred from an Ar-filled glove-box to the analysis chamber using the same procedure as for HAXPES measurements, in order to avoid air and moisture exposure. Acquisition using a Bruker detector was carried out in Total Fluorescence Yield (TFY) mode with about 100 nm probe depth. The radiation was monochromatized using a plane-grating

monochromator (PGM), which is characterized by a slit-less entrance and the use of two Varied Linear Spacing (VLS) gratings with a Variable Groove Depth (VGD) along the grating lines. All measurements were performed over the range of 765–805 eV with a step size of 0.1 eV. First a linear background was subtracted from the XAS spectra, and then they were normalized by the integrated area. Lorentzian curves were used to fit the peak positions of the normalized XAS spectra.

**Detailed electrochemical tests.** Bellcore-type free-standing positive electrodes were prepared as described previously in Appendix A1[194] having a composition of 73% (by weight) active material, 9% conductive Carbon Super P, and 18% binder - Poly(vinylidene fluoride-co-hexafluoropropylene). Note that ball milling was not performed for Li-rich NMC. Active material loading is ~6 mg $cm^{-2}$. The Bellcore-method leads to a low loading and high porosity, thereby ensuring that the cell's electrochemical response is dominated by the active material's properties. Circular electrodes of 0.95 $cm^2$ geometric area were punched out. All electrochemical tests were performed with BioLogic potentiostats in coin-type half-cells (except for three-electrode EIS which was performed in Swagelok-type cells) with Li metal foil at the negative electrode. Coin-type half-cells were assembled in an Argon glovebox with one layer of Whatman GF/D borosilicate glass-fiber sheet as the separator soaked with an electrolyte - LP100 (Merck). All cells are rested for 12 hours followed by five formation cycles in 2.0–4.8 V (the first cycle is carried out at 20 mA $g^{-1}$ and the next four at 40 mA $g^{-1}$), resulting in the activation of Li-rich NMC.

**Three-electrode impedance spectroscopy.** T-shaped Swagelok-type cells were prepared with Li metal foil as the counter electrode and a small piece of Li metal as the reference electrode that was fixed at the exposed tip of an otherwise enamelled thin copper wire (180 μm diameter). In order to avoid impedance distortions, the reference electrode was placed well within the electrode-sandwich formed by the positive and negative electrodes. Activated Li-rich NMC was used at the positive electrode after retrieving it from a coin-cell which had undergone five formation cycles as stated above. This was achieved by disassembling the coin-cell (in discharged state) in the glovebox and quickly transferring the electrode to the fresh three-electrode cell. Glass-fibre sheets soaked with LP100 (Merck) were used as separators. After a few hours of rest to allow wetting and a cycle to confirm the expected electrochemical response, EIS measurements were

performed at varying levels of SoC achieved using a GITT protocol. A 10 mV wave was applied with frequencies varying from 200 kHz to 1.4 mHz.

## ○ Supporting Figures for Part - IV*a* –

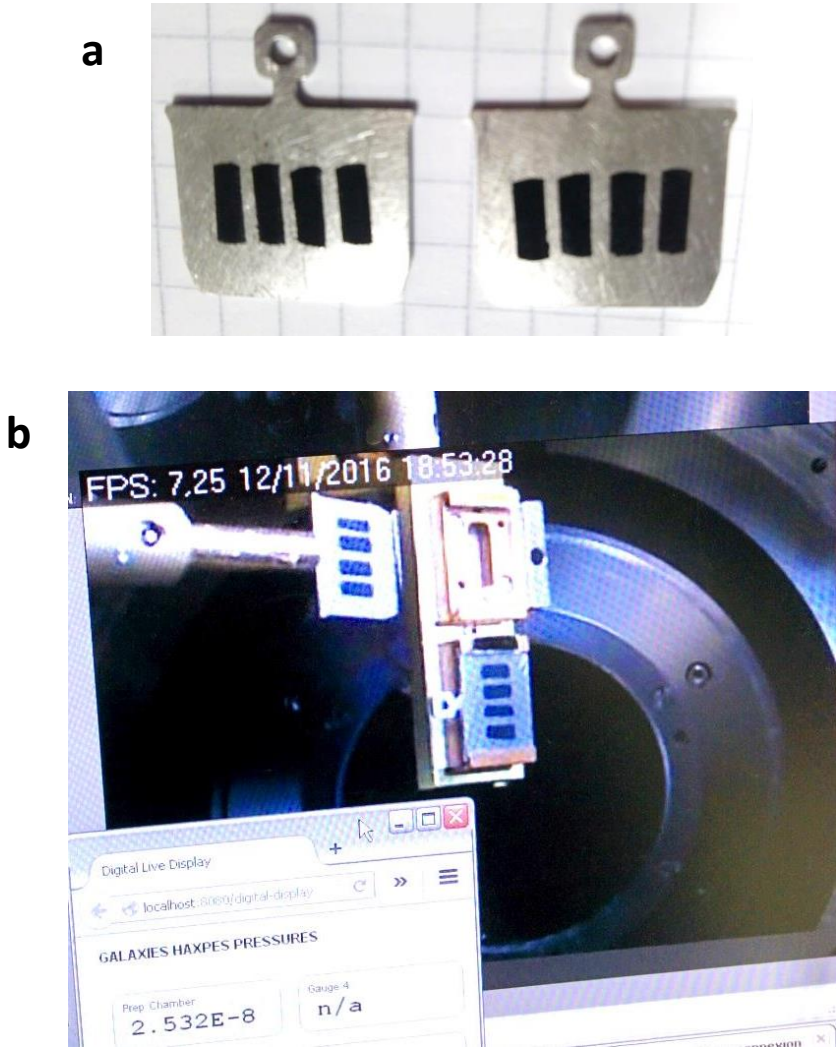


**Figure A3.1 |** Typical samples holders (**a**) used for the HAXPES experiments and a photograph (**b**) of them being loaded in the analysis chamber at the GALAXIES beamline.

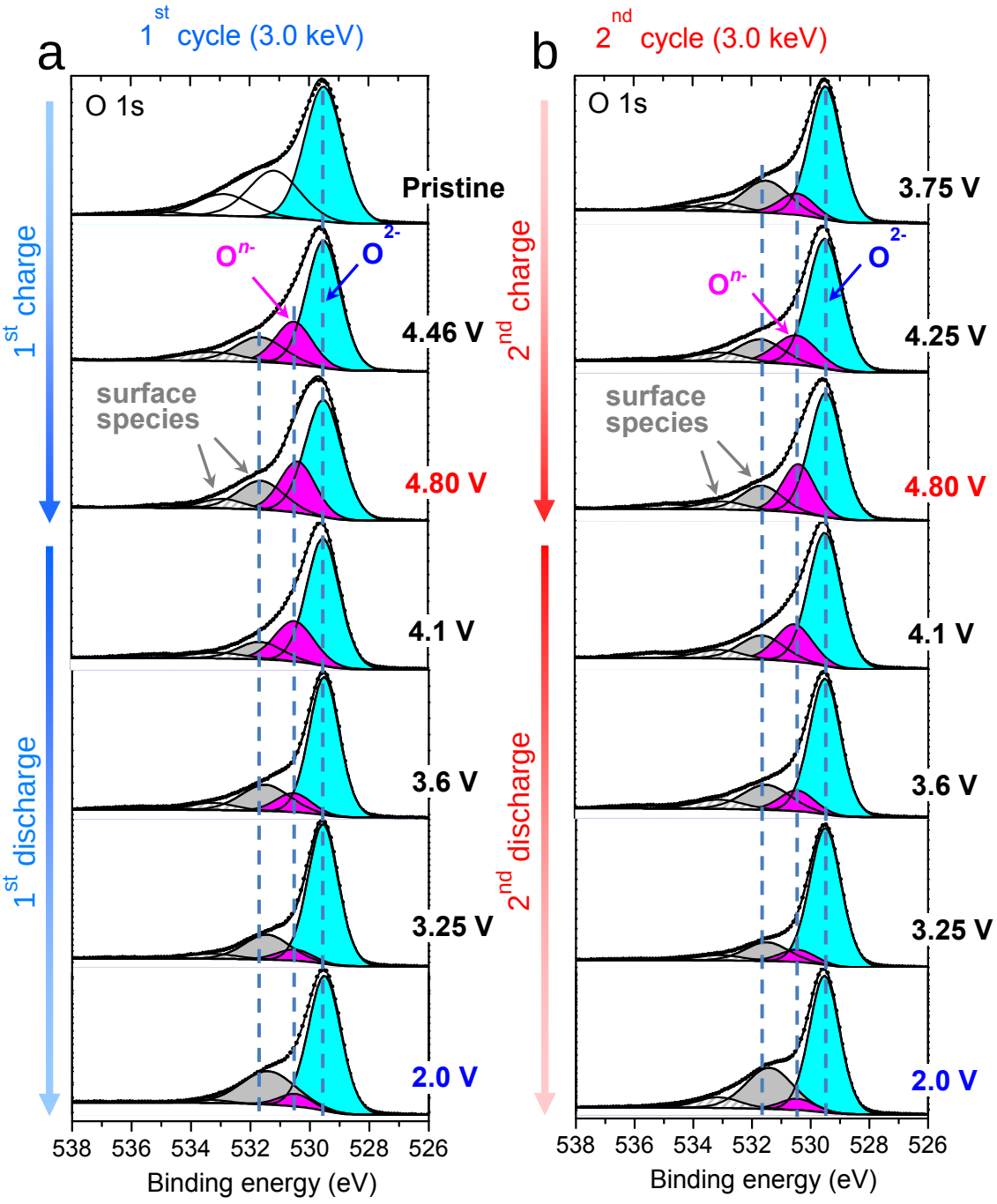


**Figure A3.2 |** O 1*s* photoelectron spectra of positive electrodes during the (**a**) 1st and (**b**) 2nd cycles recorded with HAXPES at 3.0 keV photon energy.

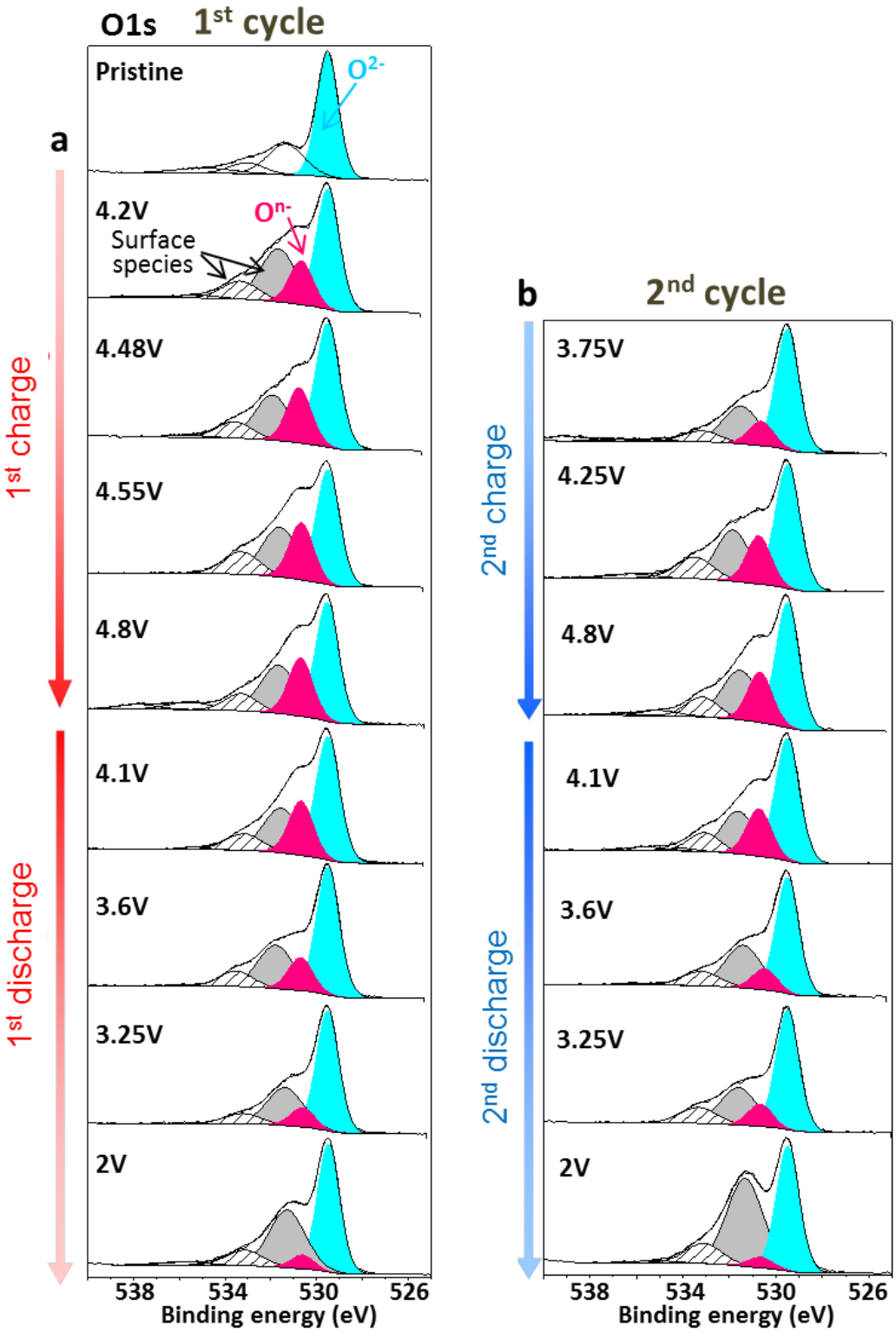


**Figure A3.3 |** O 1*s* photoelectron spectra of positive electrodes during the (**a**) 1st and (**b**) 2nd cycles at 1.487 keV photon energy (in-house XPS).

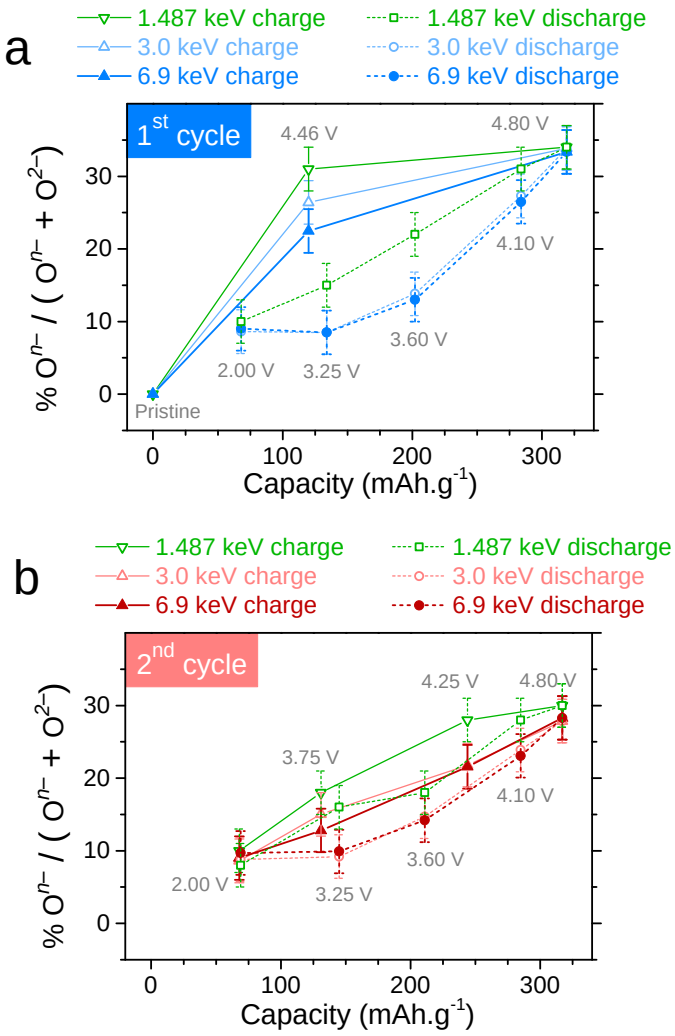


**Figure A3.4** | Comparing the effect of increasing photon energies on the estimated percentage of oxidized lattice oxygen in the active materials, defined as $O^{n-}$ / ($O^{n-}$ + $O^{2-}$), during the (**a**) 1st and (**b**) 2nd cycles plotted as a function of electrochemically observed capacity.

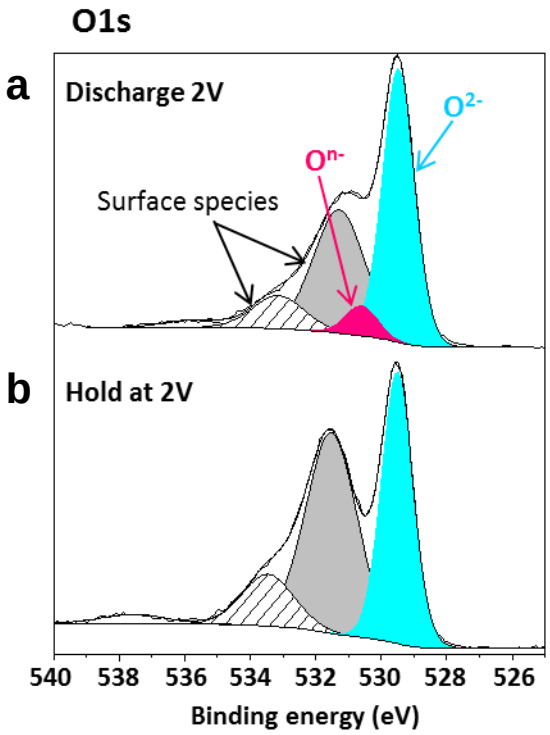


**Figure A3.5 |** (**a**) O 1*s* photoelectron spectrum of positive electrode after the 1st discharge to 2.0 V using a current density of 20 mA $g^{-1}$ compared to (**b**) the spectrum after the 1st discharge with similar protocol followed by an additional potentiostatic hold at 2.0 V (until the current decays to a small value of 1 mA $g^{-1}$). Photon energy is 1.487 keV.

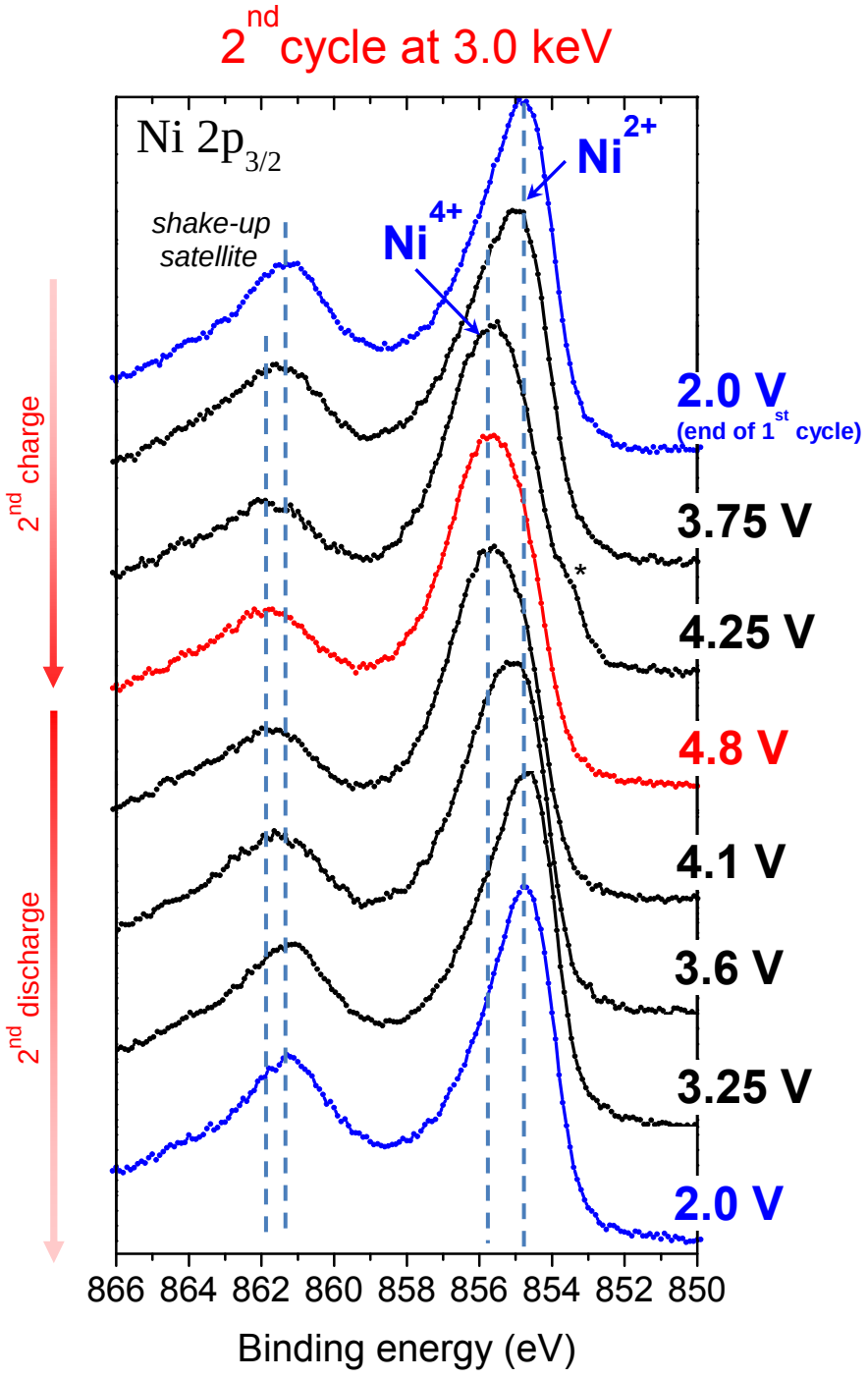


**Figure A3.6 |** Ni $2p_{3/2}$ photoelectron spectra of positive electrodes during the 2nd cycle recorded with HAXPES ($h\nu$ = 3.0 keV).

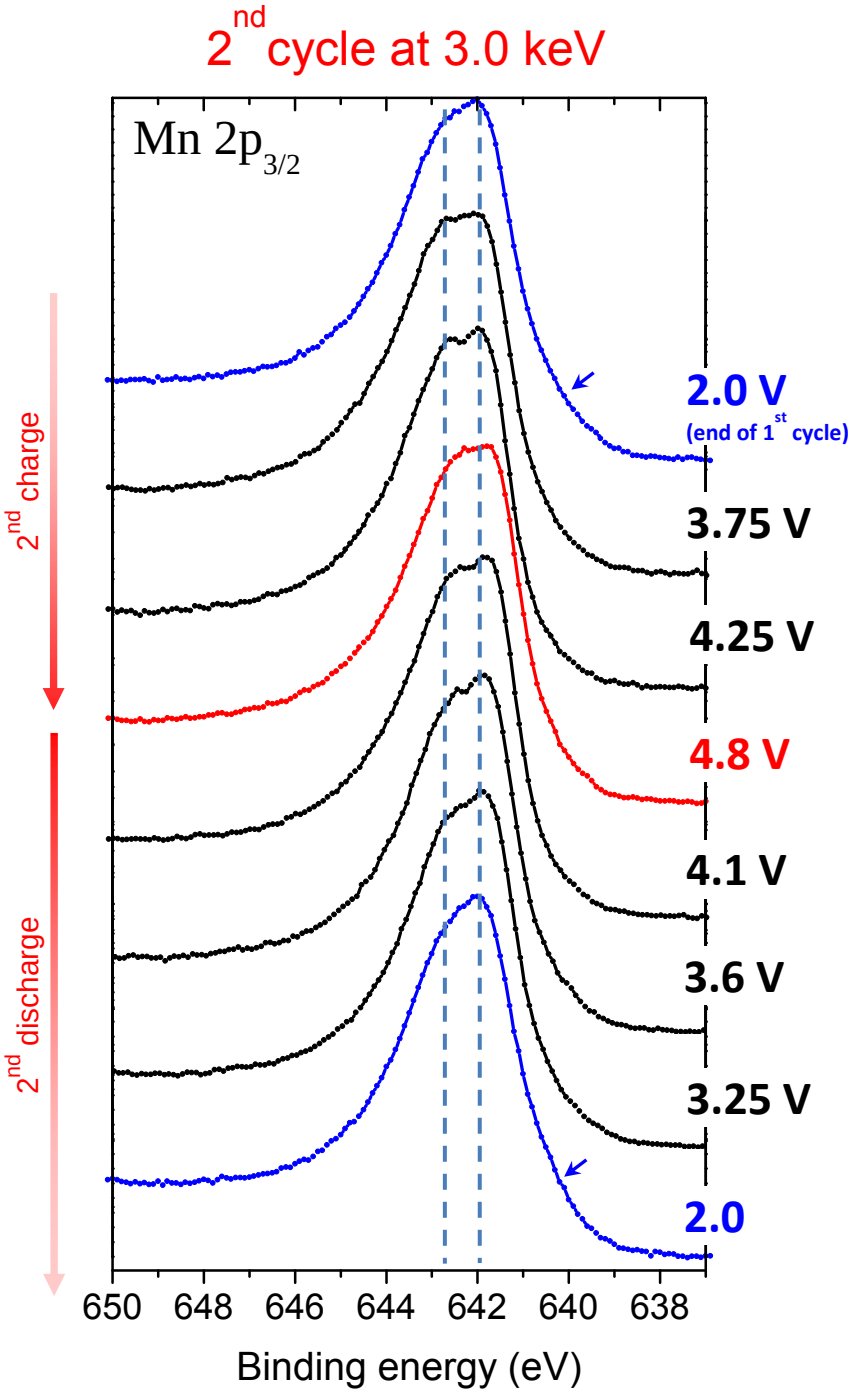


**Figure A3.7 |** Mn $2p_{3/2}$ photoelectron spectra of positive electrodes during the 2nd cycle recorded with HAXPES ($h\nu$ = 3.0 keV). Arrows point to the shoulder appearing in the fully discharged samples due to a partial reduction to $Mn^{3+}$.

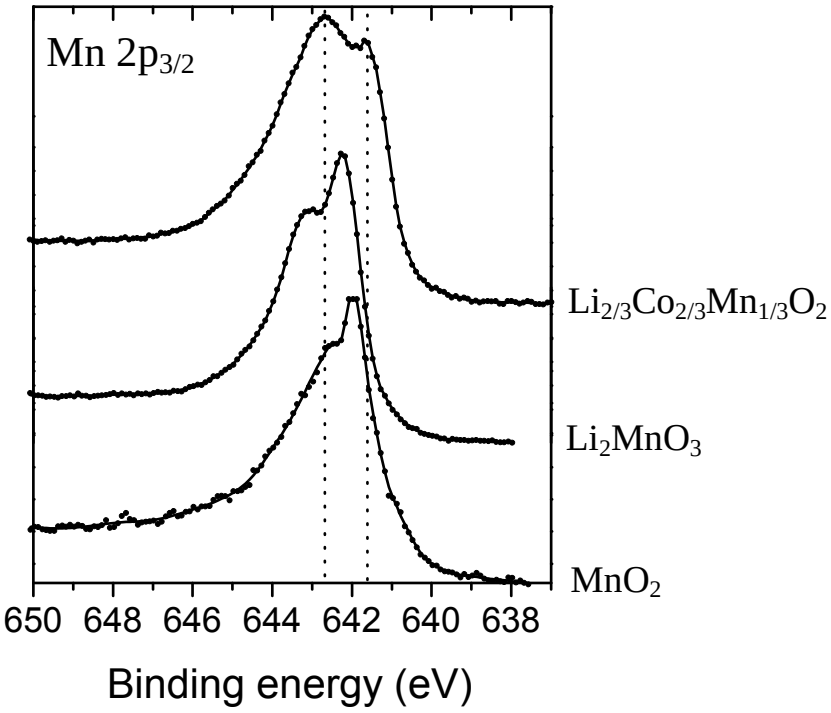


**Figure A3.8 |** Mn $2p_{3/2}$ photoelectron spectra of $Mn^{4+}$ compounds: $Li_2MnO_3$, $MnO_2$ and $Li_{2/3}Co_{2/3}Mn_{1/3}O_2$ showing the complex main peak fine structure that cannot be interpreted by two coexisting oxidation states, in the same way as for our Li-rich NMC samples. Spectra recorded at $h\nu$ = 1.487 keV.

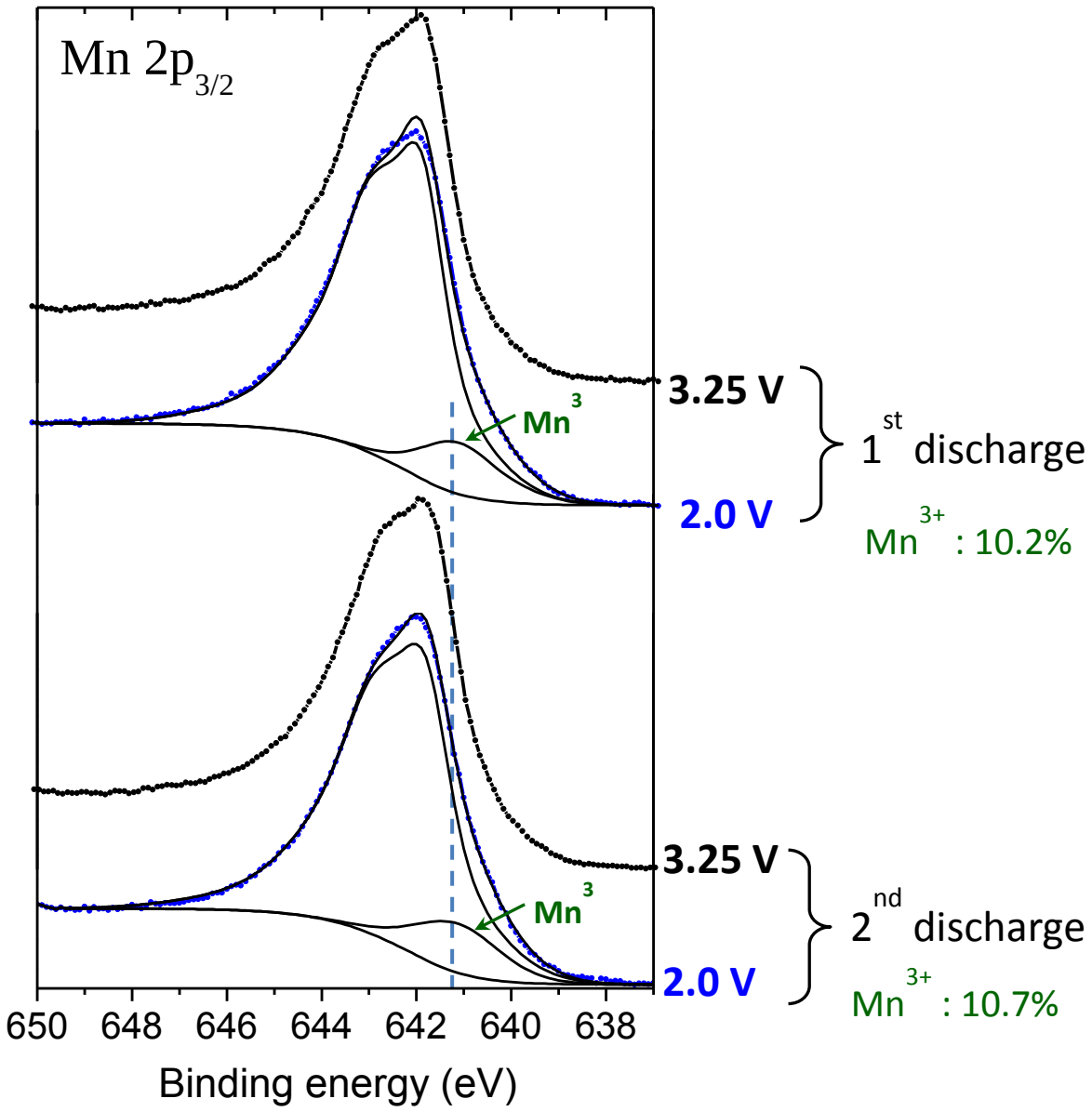


**Figure A3.9 |** Comparing the amount of $Mn^{3+}$ at the end of the 1st and the 2nd discharges, as estimated from HAXPES spectra ($h\nu$ = 3.0 keV). See main text for details of the fitting procedure.

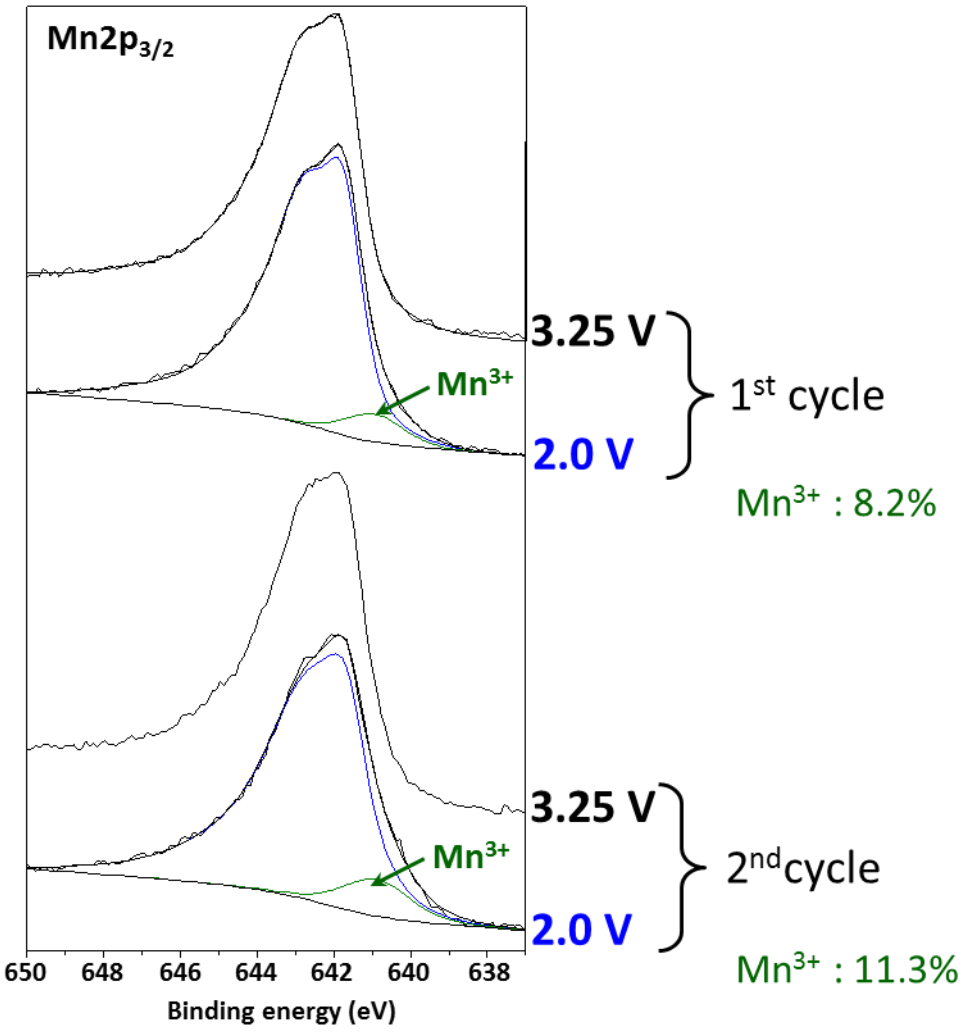


**Figure A3.10 |** Comparing the amount of $Mn^{3+}$ at the end of the 1st and the 2nd discharges estimated from in-house XPS spectra ($h\nu$ = 1.487 keV).

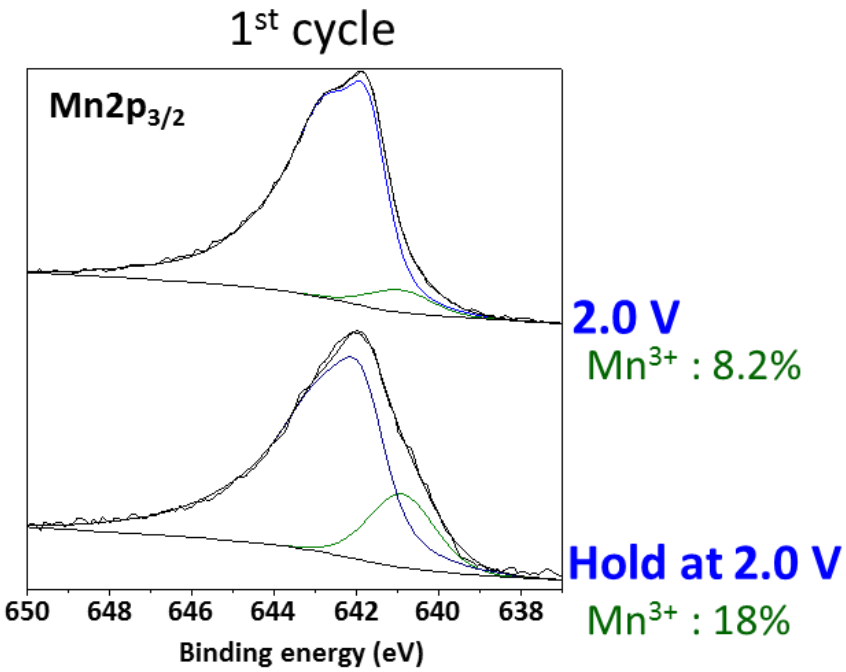


**Figure A3.11 |** Comparing the amount of $Mn^{3+}$ at the end of 1st discharge with and without a potentiostatic hold. In the top graph, the sample is prepared by discharging till 2.0 V at 20 $mA.g^{-1}$. In the bottom graph, discharge is continued after reaching 2.0 V by holding the potential till the current decays to a very small value of 1 $mA.g^{-1}$. The samples are the same as those in **Figure A3.5** that showed the O 1*s* spectra. Photon energy is 1.487 keV (in-house XPS).

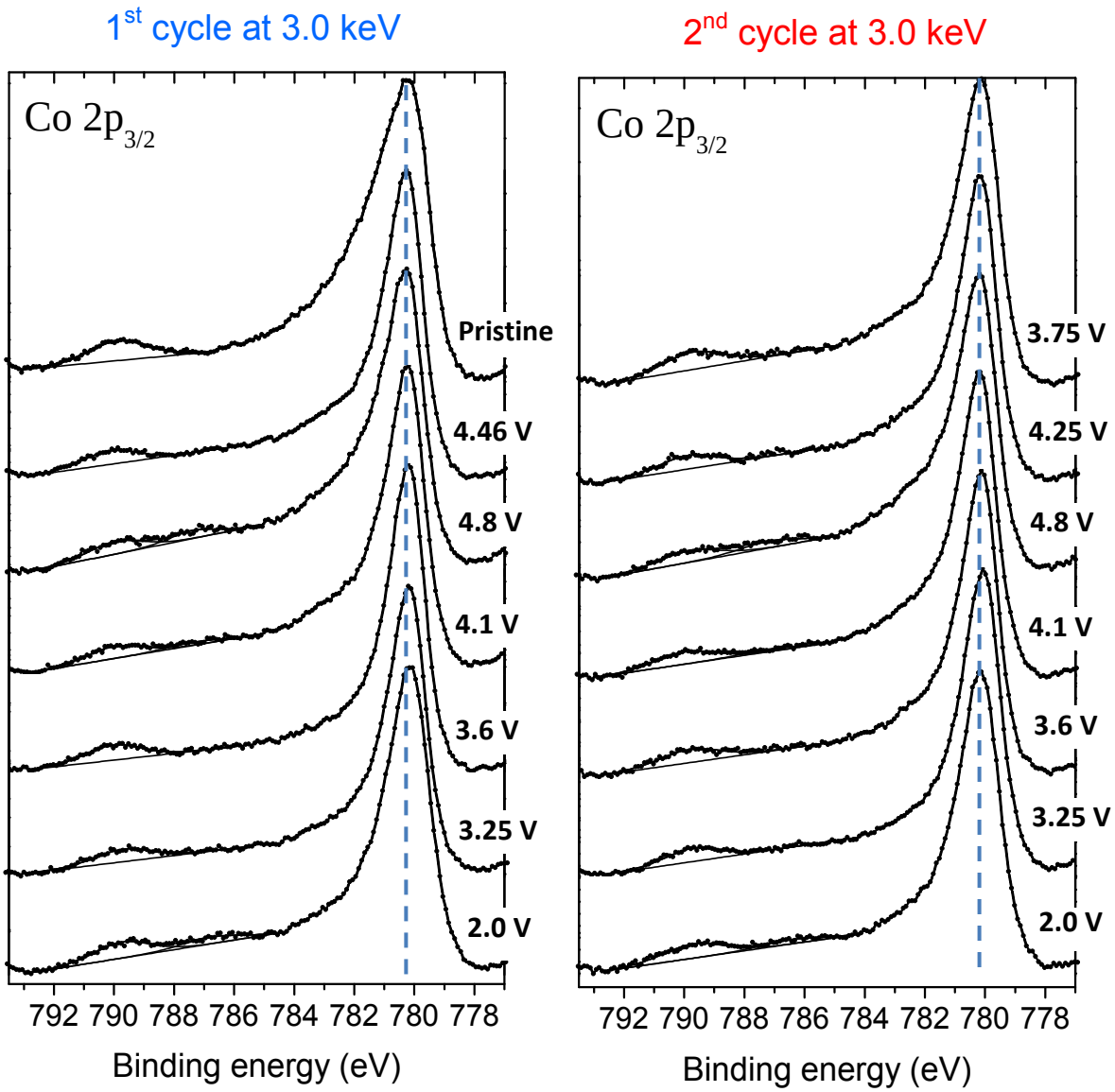


**Figure A3.12 |** Co $2p_{3/2}$ photoelectron spectra of positive electrodes during the 1st and 2nd cycles recorded with HAXPES ($h\nu$ = 3.0 keV). As expected, the main peak of Co $2p_{3/2}$ does not shift with redox but the area under its shake-up satellite can provide a signature of Co oxidation state change from 3+ to 4+ as previously shown for $Li_xCoO_2$.[86] In the beginning of 1st charge, Co oxidizes as evidenced by the loss of satellite intensity from pristine to 4.46 V. Afterwards, it is not possible to quantify clear trends as the satellite is quite small and is further affected by other unexplained satellites (only observed at high photon energy) that reproducibly evolve during the 1st and 2nd discharges.

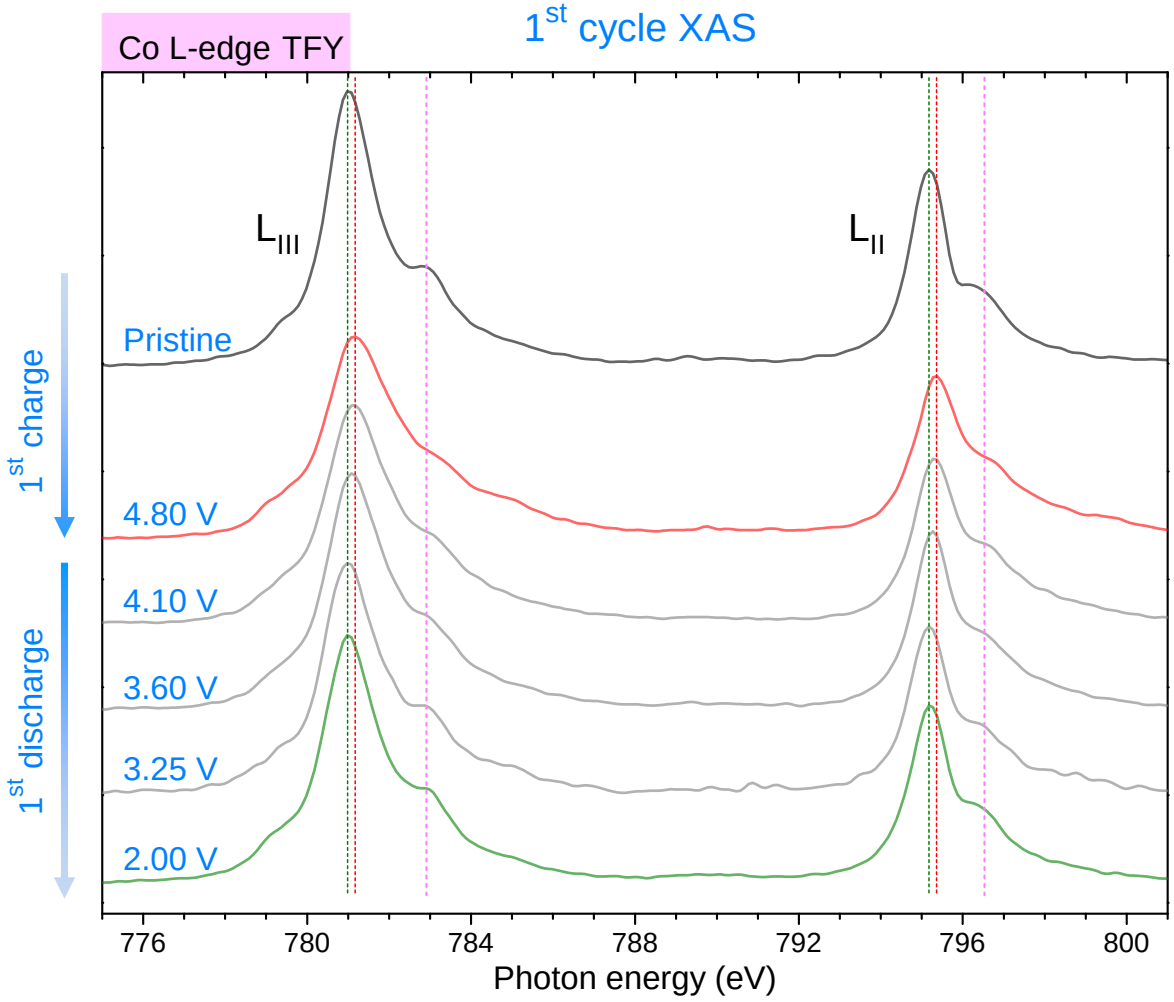


**Figure A3.13 |** Soft-XAS spectra for Co L-edges recorded in TFY mode during the 1st cycle. Both the $L_{II}$ and $L_{III}$ peaks slightly shift to higher photon energies on Co oxidation (charge) and lower energies on Co reduction (discharge). The peak shapes (shoulders at ~783 eV and ~796.5 eV) also reversibly evolve during charge and discharge.

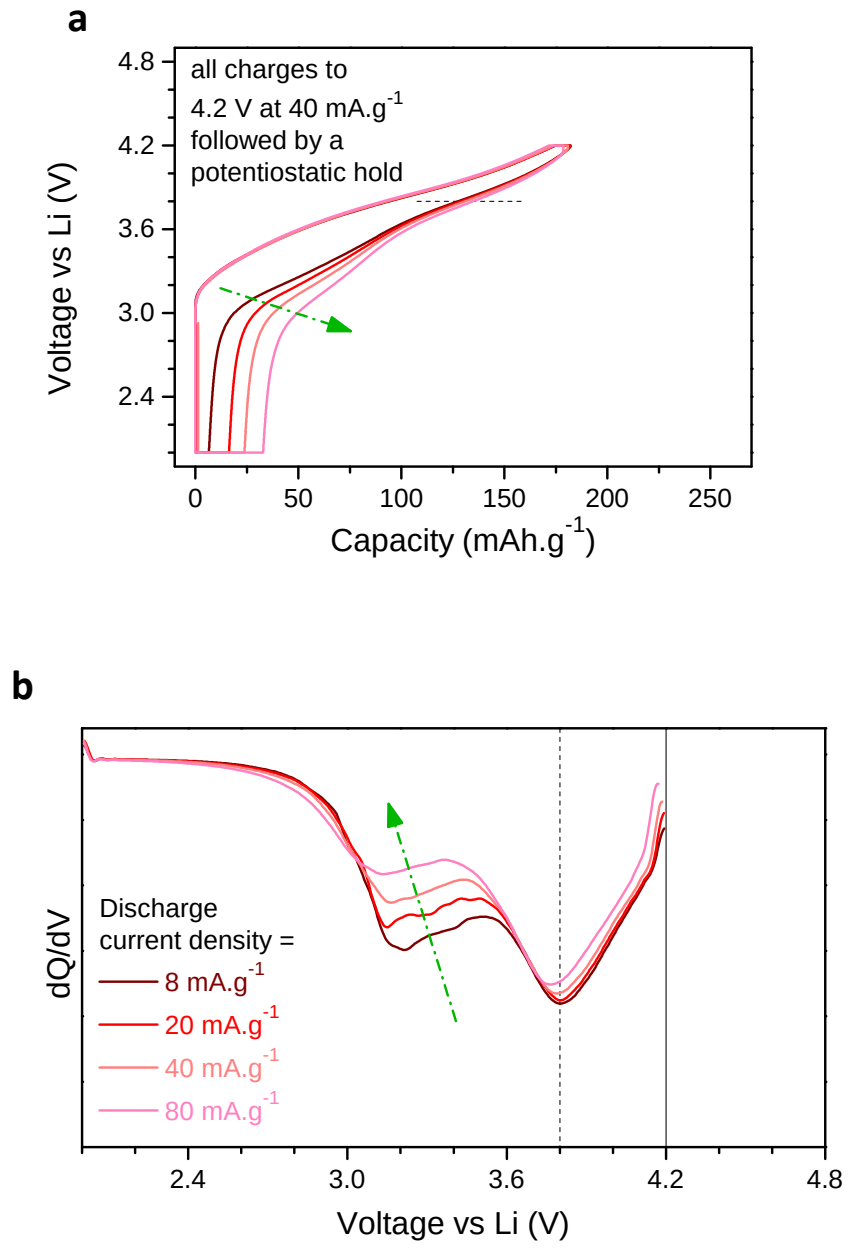


**Figure A3.14** | Effect of increasing discharge current densities on (**a**) half -cell voltage profiles and (**b**) corresponding *dQ*/*dV* curves. Li-rich NMC is first activated by a few formation cycles in 2.0 to 4.8 V. All charges are at 40 mA.g$^{-1}$ till 4.2 V and ending with a potentiostatic hold till current decays to 2 mA.g$^{-1}$ in order to ensure that identical Li stoichiometry is achieved at the beginning of each scan. For the same reason, discharges also end with a potentiostatic hold at 2.0 V, till the current decays to 2 mA.g$^{-1}$. The green arrow indicates the shift in profiles as current increases, thus highlighting resistive behaviour.

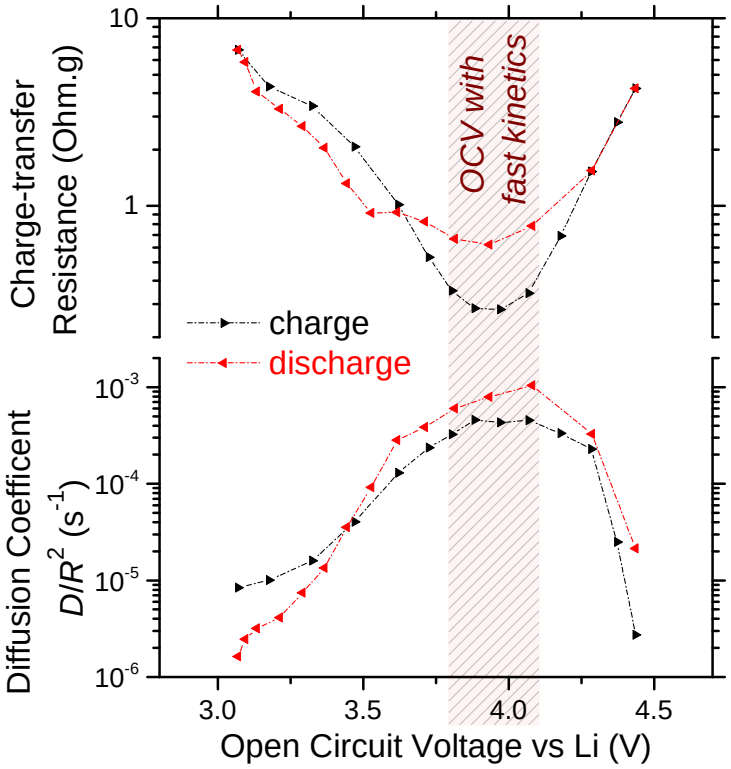


**Figure A3.15 |** Variation of kinetic parameters obtained from EIS plotted as a function of OCV.

## ○ Methods for Part - IV*b* -

**Material synthesis and characterization.** Same as Methods for Part - IV*a* -. The same batch of pristine material was used in both Parts.

***Ex situ* sample preparation.** Same as Methods for Part - IV*a* -, except the following differences. A lower loading was used (total weight kept ~12 mg for each cell) for long cycling. To prevent dendrite formation over long cycling, two extra layers of Cellguard separators were added in addition to two layers of Whatman GF/D borosilicate glass-fiber sheets. The first charge-discharge cycle was performed at a constant specific current of 20 mA $g^{-1}$. Then, long cycling was performed at 40 mA $g^{-1}$ (circa C/6). After achieving the desired number of cycles, the final sample preparation cycle was performed at a lower specific current of 20 mA $g^{-1}$ to reach either the full charged (4.8 V) or the full discharged (2.0 V) states.

**Sample handling and transfer.** Same as Methods for Part - IV*a* -.

**In-house XPS.** Same as Methods for Part - IV*a* -.

**Hard X-ray photoemission spectroscopy (HAXPES).** Same as Methods for Part - IV*a* -. Like for the 6.9 keV photons, the 10.0 keV photons were also obtained from the third order reflection of the Si(111) double-crystal monochromator.

**Estimation of relative capacity contributions.** The specific capacity of $Li_{1.20}Ni_{0.13}Mn_{0.54}Co_{0.13}O_2$ is 314 mAh $g^{-1}$ for the exchange of 1.0 $e^-$ per formula unit. In the second cycle, the HAXPES spectra reveal the completion of $Ni^{2+/3+/4+}$ redox process, 11 % activity of $Mn^{3+/4+}$, and we assume, for the sake of quantification, the completion of $Co^{3+/4+}$ redox. These cationic redox processes of $Ni^{2+/3+/4+}$ (2 $e^-$ × 0.13 ≡ 82 mAh $g^{-1}$), $Co^{3+/4+}$ (1 $e^-$ × 0.13 ≡ 41 mAh $g^{-1}$), and 11 % $Mn^{3+/4+}$ (11 % × 1 $e^-$ × 0.54 ≡ 18 mAh $g^{-1}$) account for 141 mAh $g^{-1}$, out of the total measured capacity of 264 mAh $g^{-1}$ in the second cycle. Reversible anionic redox therefore compensates for the remaining 123 mAh $g^{-1}$. The values of % $O^{n-}$ obtained from the quantification of O 1*s* HAXPES spectra on the second charge and discharge are respectively 28 % and 9 % . Therefore, a 19 % change in % $O^{n-}$ corresponds to 123 mAh $g^{-1}$ (i.e. ~6.4 mAh $g^{-1}$ for each % change). This conversion ratio was assumed constant for the quantification of later cycles. For example in the 72$^{nd}$ cycle,

the values of % $O^{n-}$ are 23 % and 9 % respectively on charge and discharge. Using the same conversion ratio as above, this 14 % change in % $O^{n-}$ corresponds to 90 mAh $g^{-1}$ of capacity from reversible anionic redox. Concerning Mn, HAXPES spectra reveal 22 % activity of $Mn^{3+/4+}$ redox (22 % × 1 $e^-$ × 0.54 ≡ 37 mAh $g^{-1}$). The remaining capacity of 112 mAh $g^{-1}$ (subtracting 90 mAh $g^{-1}$ and 37 mAh $g^{-1}$ from the total measured 239 mAh $g^{-1}$) is hence attributed to partially-incomplete $Ni^{2+/3+/4+}$ and $Co^{3+/4+}$ redox processes. Note that such calculations of nominal capacity should be interpreted within the uncertainty of HAXPES analysis and quantification.

## ○ Supporting Figures for Part - IV*b* -

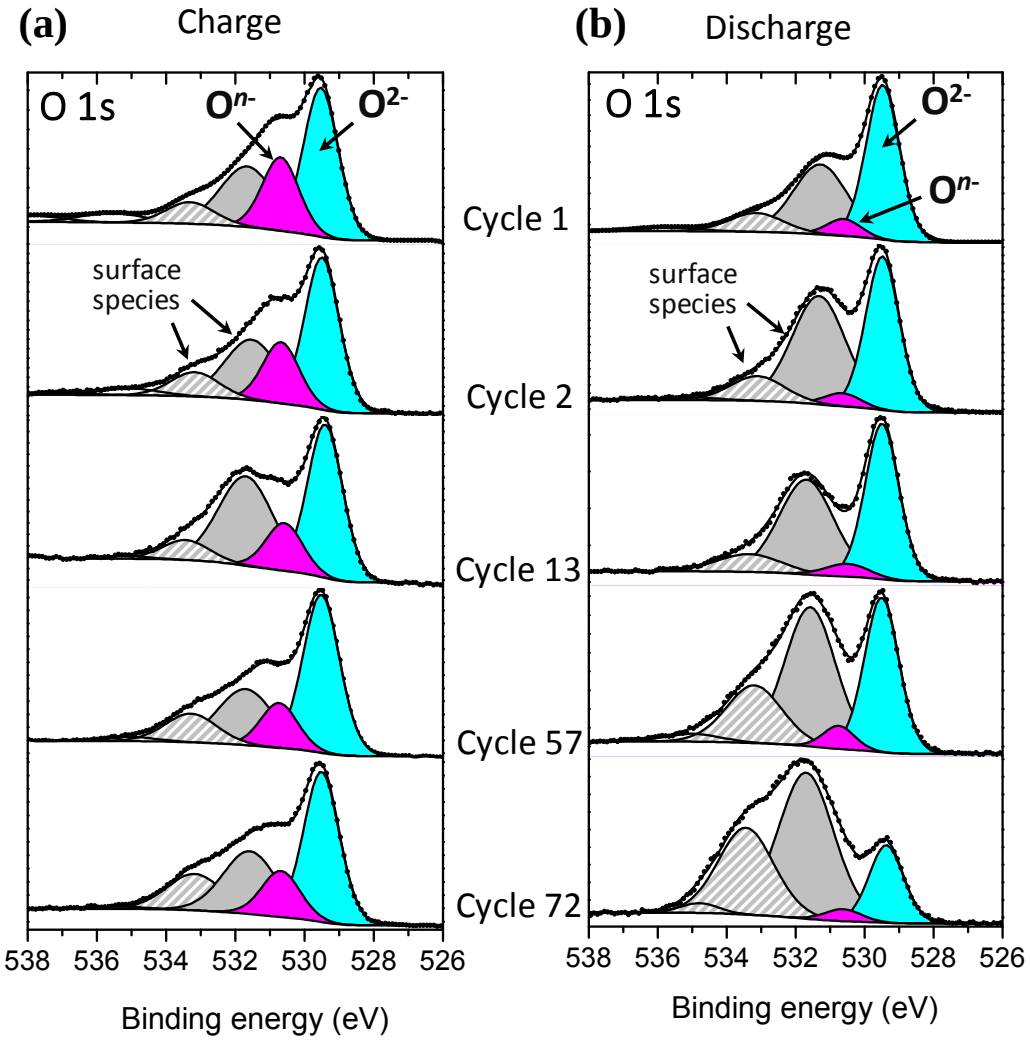


**Figure A3.16 |** Evolution of the anionic redox process over cycling. O 1*s* in-house XPS spectra recorded at 1.487 keV. (**a**) Samples charged to 4.8 V and (**b**) samples discharged to 2.0 V with gradually increasing cycle numbers.

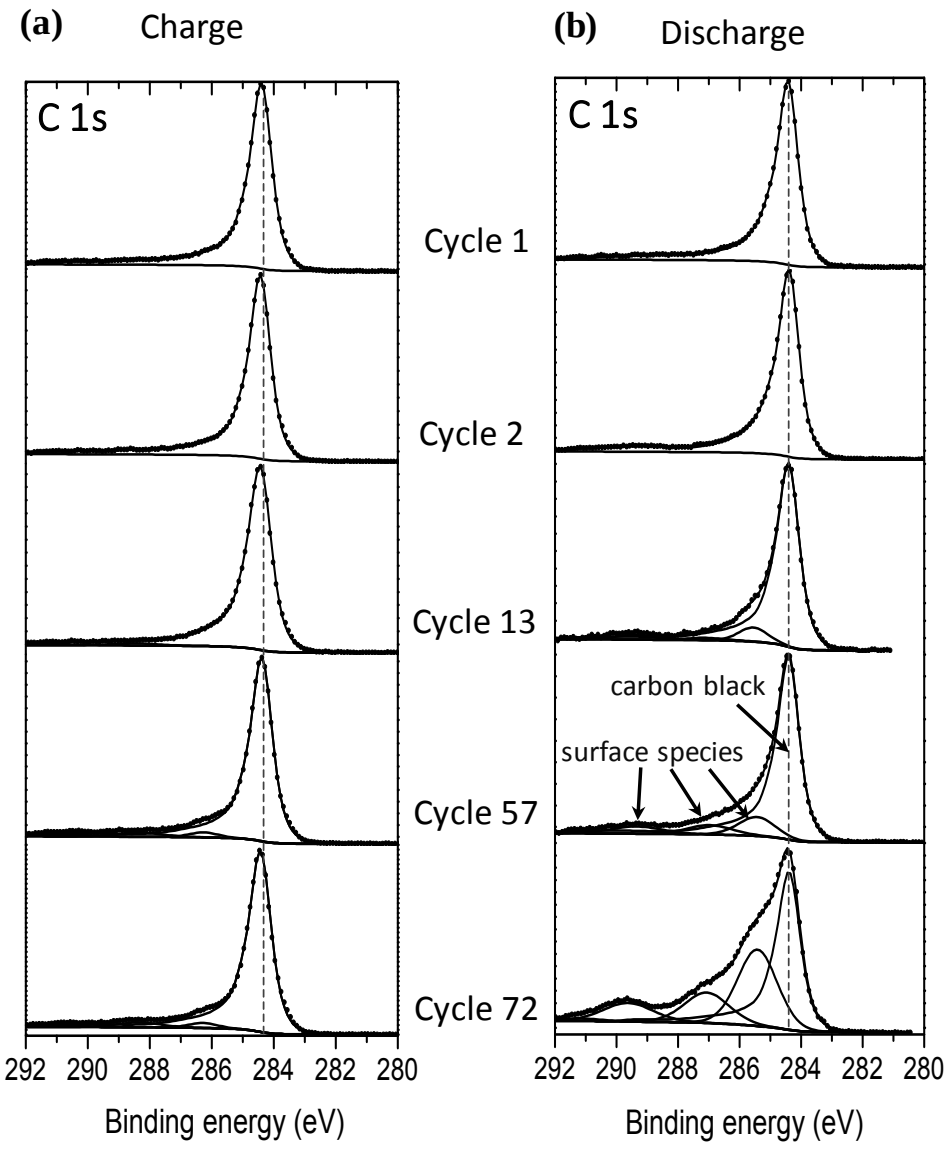


**Figure A3.17 |** C 1*s* in-house XPS spectra recorded at 1.487 keV. (**a**) Samples charged to 4.8 V and (**b**) samples discharged to 2.0 V with gradually increasing cycle numbers. The position of the carbon black peak at 284.4 eV was taken as reference for binding energy calibration.

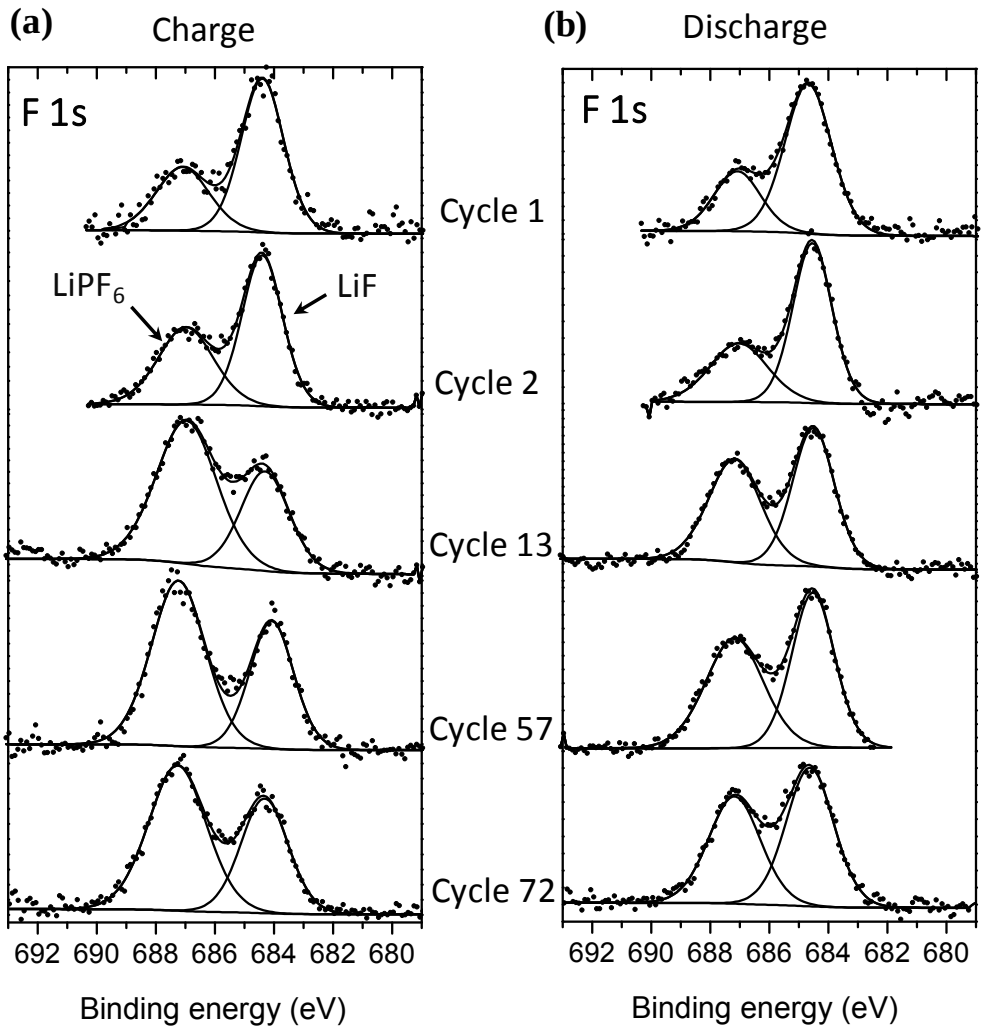


**Figure A3.18 |** F 1*s* in-house XPS spectra recorded at 1.487 keV. (**a**) Samples charged to 4.8 V and (**b**) samples discharged to 2.0 V with gradually increasing cycle numbers.

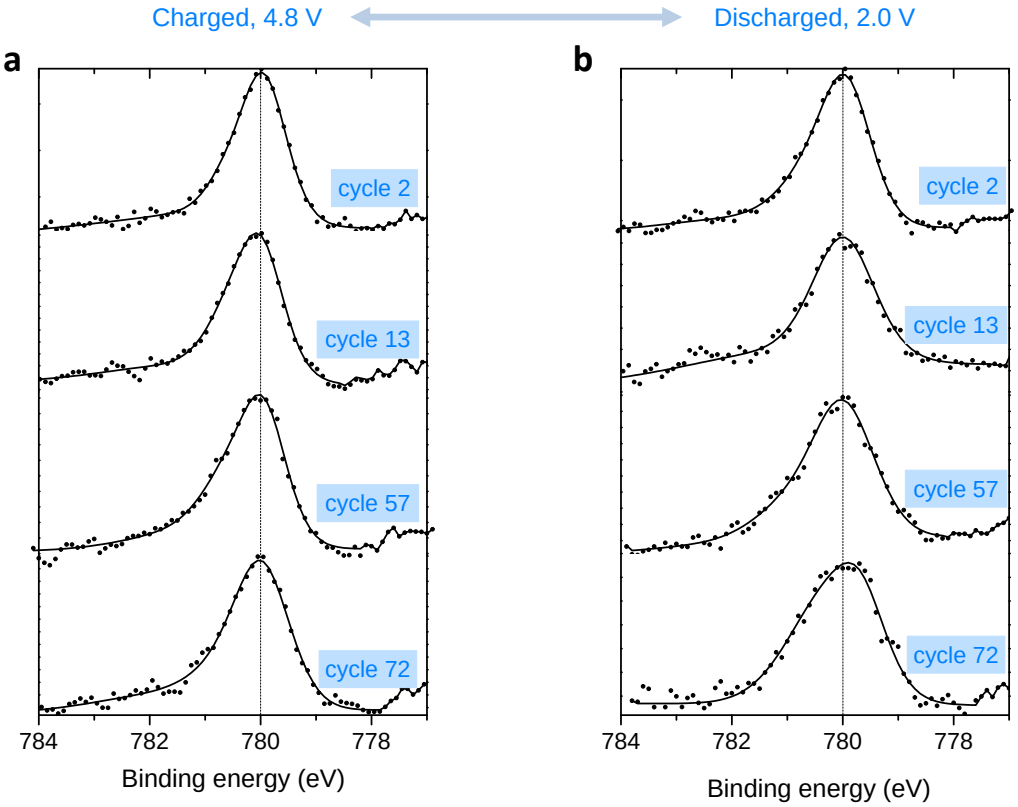


**Figure A3.19 |** Evolution of Co $2p_{3/2}$ over cycling. The main peak of Co $2p_{3/2}$ HAXPES spectra recorded at 6.9 keV for (**a**) the samples charged to 4.8 V and (**b**) the samples discharged to 2.0 V. There is no shift in the main peak's position between charge and discharge. However, this cannot be interpreted as an absence of participation of cobalt to the redox process, since the main peak binding energy is the same for $Co^{3+}$ and $Co^{4+}$, as shown previously for $Li_{1-x}CoO_2$.[86]

# A4 – Supporting Information for Chapter V

## ○ Methods

**Material synthesis, electrode fabrication, and coin-cell assembly.** Similar to the Methods section of Appendix A1, but with a higher electrode loading. The film was designed for an active material loading of ~20 mg $cm^{-2}$, ~200 µm film-thickness, and ~60% porosity. Such a relatively high loading was needed to generate reliable amounts of heat flow from the small coin cells. Using ~1 $cm^2$ circular discs of this electrode film, 2032 coin-type cells with Li metal foil as the negative electrode were assembled in an argon-filled glove-box with two layers of alumina-coated Celgard separators plus one layer of a Whatman GF/D borosilicate glass fibre separator. The electrolyte used was LP100 (Merck) having 1M $LiPF_6$ in ethylene carbonate : propylene carbonate : dimethyl carbonate in a 1 : 1 : 3 weight ratio. The C-rate in Chapter V is defined such that 1C corresponds to the removal of 1 Li per formula unit of LRSO in one hour (1C = 160.13 mA $g^{-1}$).

**Isothermal Calorimetry.** Depending on the experiment, the cells were pre-cycled at room temperature before being transferred into a TAM III Microcalorimeter (TA Instruments: stability ± $10^{-4}$ °C, accuracy ± 1 µW, precision ± 10 nW) for isothermal calorimetry measurements at 40 °C, as schematized in **Figure A4.1**. The baseline drift over the course of the experiments did not exceed ± 0.5 µW. All specifications and information regarding microcalorimetry calibration, cell connections, and operation procedures can be found in previous literature.[266–269] The electrochemical cycling was performed with a Maccor 4000 series cycler connected to the cells inside the calorimeter. Depending on the experiment, either a constant current (CC) or a constant current constant voltage (CCCV) protocol was used. The voltage hold of the CCCV step was terminated when current decayed to a low value of C/100. The observed heat flow, defined positive when heat is generated by the cell, mainly arises from the positive electrode. A constant "leakage heat" of +3.4 µW was required and this value was subtracted from the raw measured heat flow values.

## ○ Supporting Figures

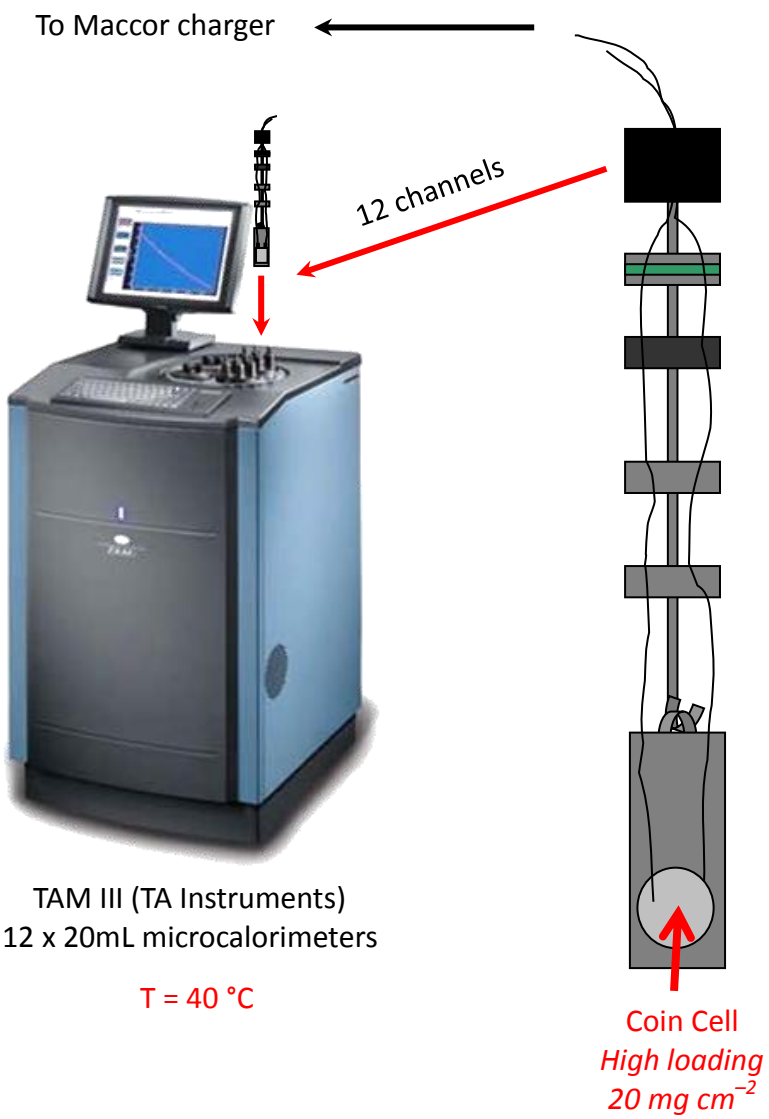


**Figure A4.1 |** Schematic illustration of the microcalorimetry experimental setup. Courtesy of *Stephen L. Glazier*.

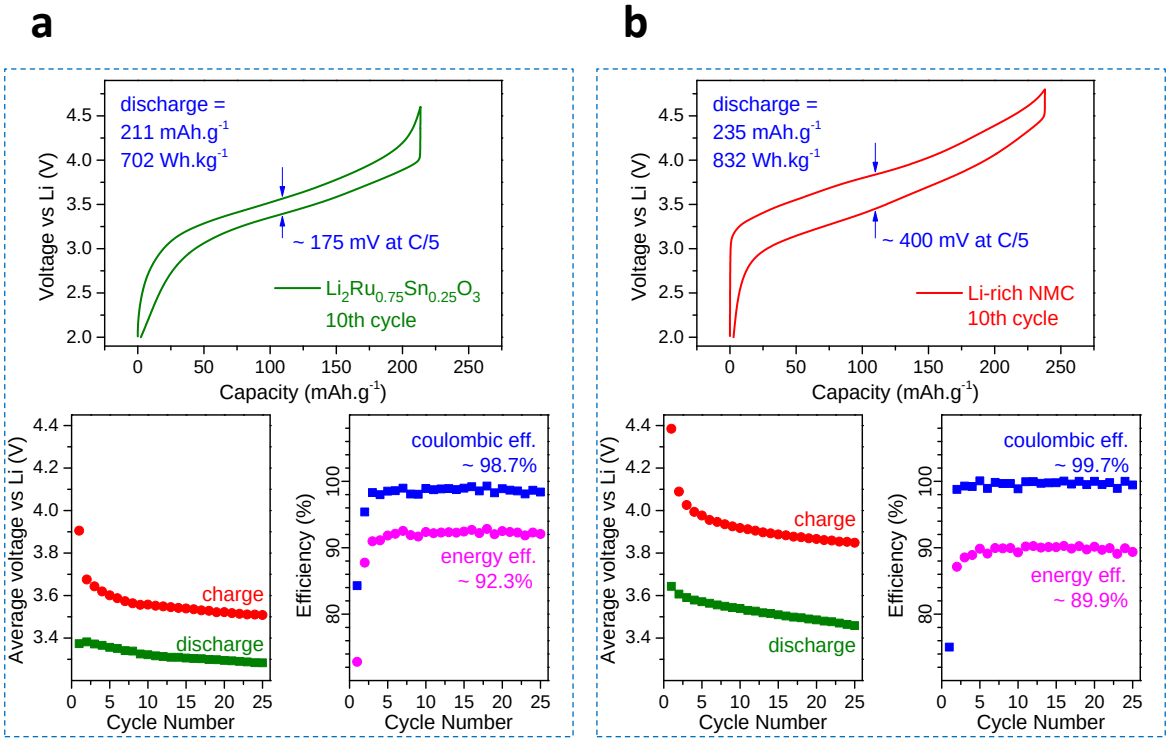


**Figure A4.2 |** A "head-to-head" comparison of (**a**) LRSO and (**b**) Li-rich NMC under similar cycling conditions in Li half-cells. The specific current is 32 mA $g^{-1}$ for LRSO and 40 mA $g^{-1}$ for Li-rich NMC, leading to approx. 6 hr charge or discharge for either of the two materials. Voltage hysteresis, present in both cathodes under such cycling conditions, is lower for LRSO, which therefore shows higher energy efficiency.

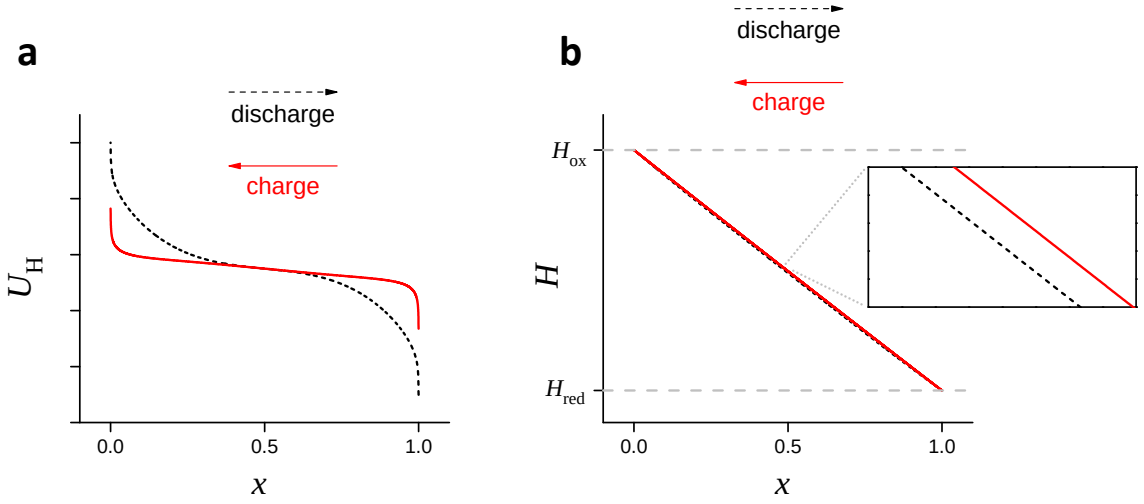


**Figure A4.3 |** Hypothetical variations of (**a**) $\boldsymbol{U_H}$ (enthalpy potential) and (**b**) $\boldsymbol{H}$ (enthalpy) for a cell that follows metastable paths under quasi-static operating conditions (i.e. at very small current values). The charge and discharge $\boldsymbol{U_H}$ profiles differ but do not form a hysteresis loop. Instead, they cross with each other in order to satisfy the following equation:

$$\oint_{cycle} U_H \, dx = 0$$

On the other hand, $\boldsymbol{H}$ that is obtained by integrating the same $\boldsymbol{U_H}$ profiles, forms a hysteresis loop, as shown by the magnification in the inset of (**b**). The enthalpy values on charge and discharge are slightly different for the same value of $x$, thus representing metastable states.

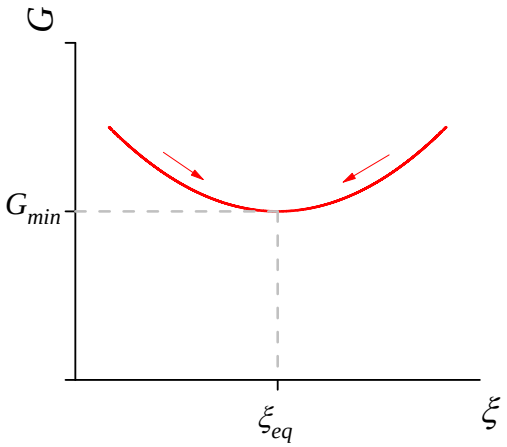


**Figure A4.4 |** Hypothetical variation of $\boldsymbol{G}$ (Gibbs free energy) with respect to $\boldsymbol{\xi}$ (reaction coordinate). $\boldsymbol{G}$ is minimum at the equilibrium and the arrows indicate the directions towards which the system moves in search for equilibrium. The affinity $\boldsymbol{A}$ is given by

$$A = -\frac{\partial G}{\partial \xi}\Big|_{T,P}$$

such that $\boldsymbol{A = 0}$ at the equilibrium.

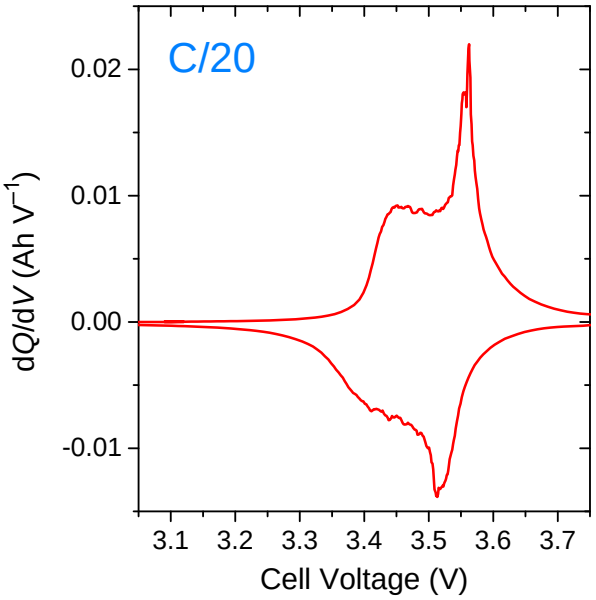


**Figure A4.5 |** The $\boldsymbol{dQ/dV}$ profile obtained at C/20 for the 3.5 V cationic redox step that is discussed in **Figure V.2**. The symmetric shape on charge vs. discharge indicates a fully reversible classical intercalation mechanism.

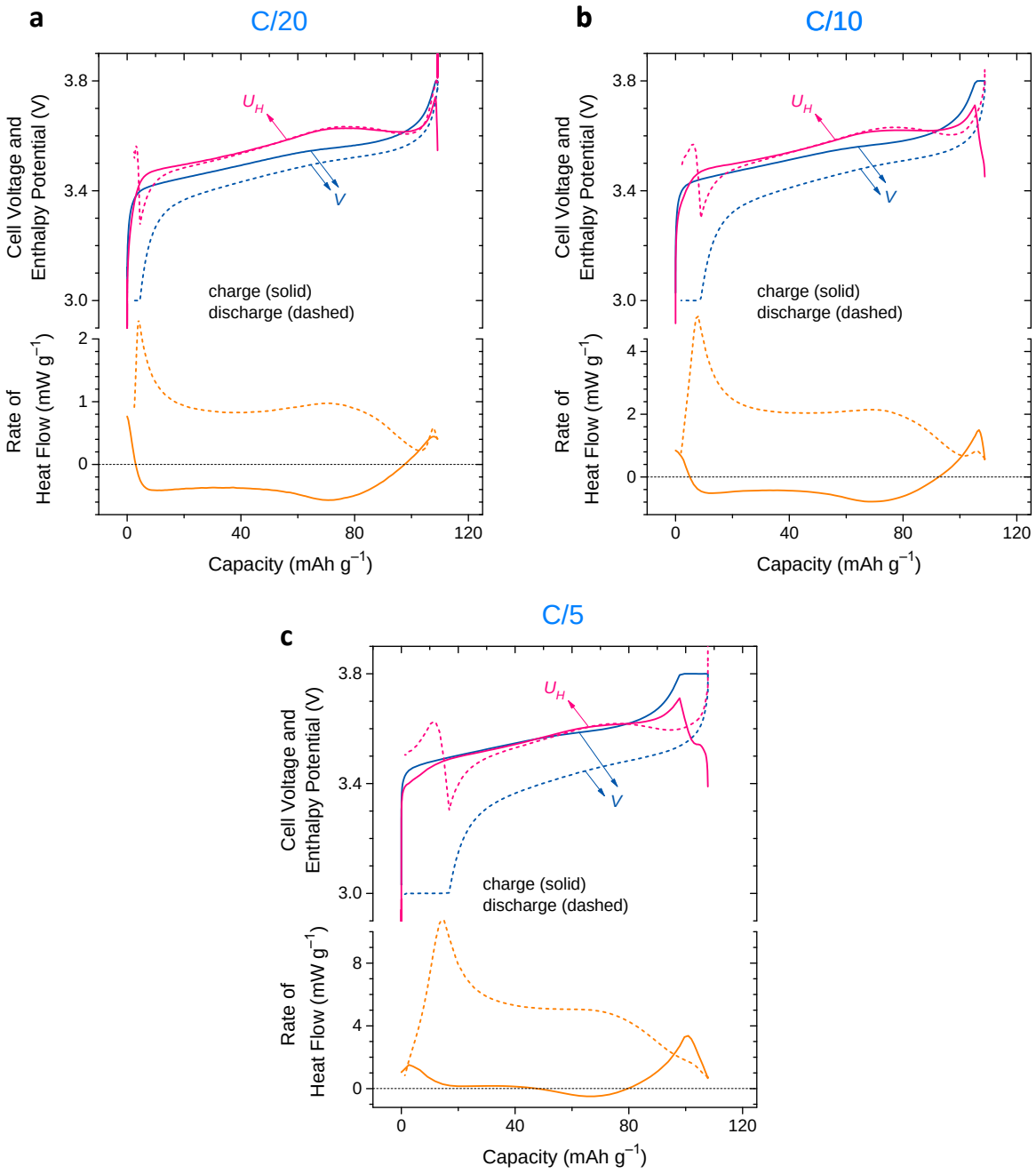


**Figure A4.6 |** The measured profiles for cell voltage (blue) and heat flow rate (orange) that were used to obtain the enthalpy potential profiles (pink) for the 3.5 V cationic redox step at (**a**) C/20, (**b**) C/10, and (**c**) C/5. This data complements **Figure V.2**.

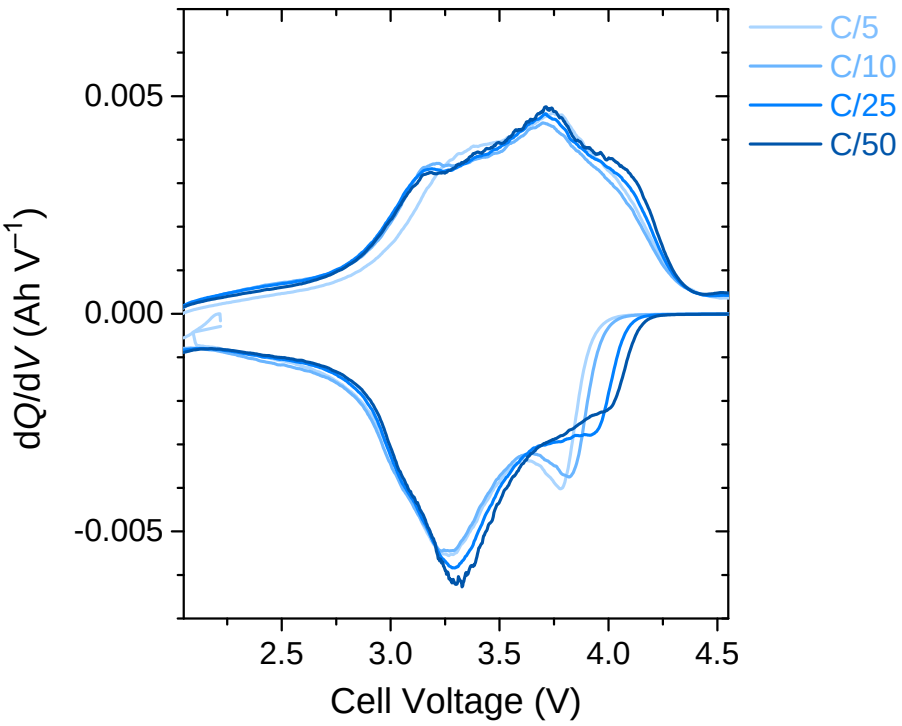


**Figure A4.7 | $dQ/dV$** curves for 'activated' LRSO cycled at different C-rates. These profiles correspond to the ones in **Figure V.4**. On discharge, the higher sensitivity of the anionic redox peak (around 3.8 V) can be seen in comparison to the fairly stable cationic redox peak (around 3.3 V), which is an identical observation to that in **Figure II.6**.

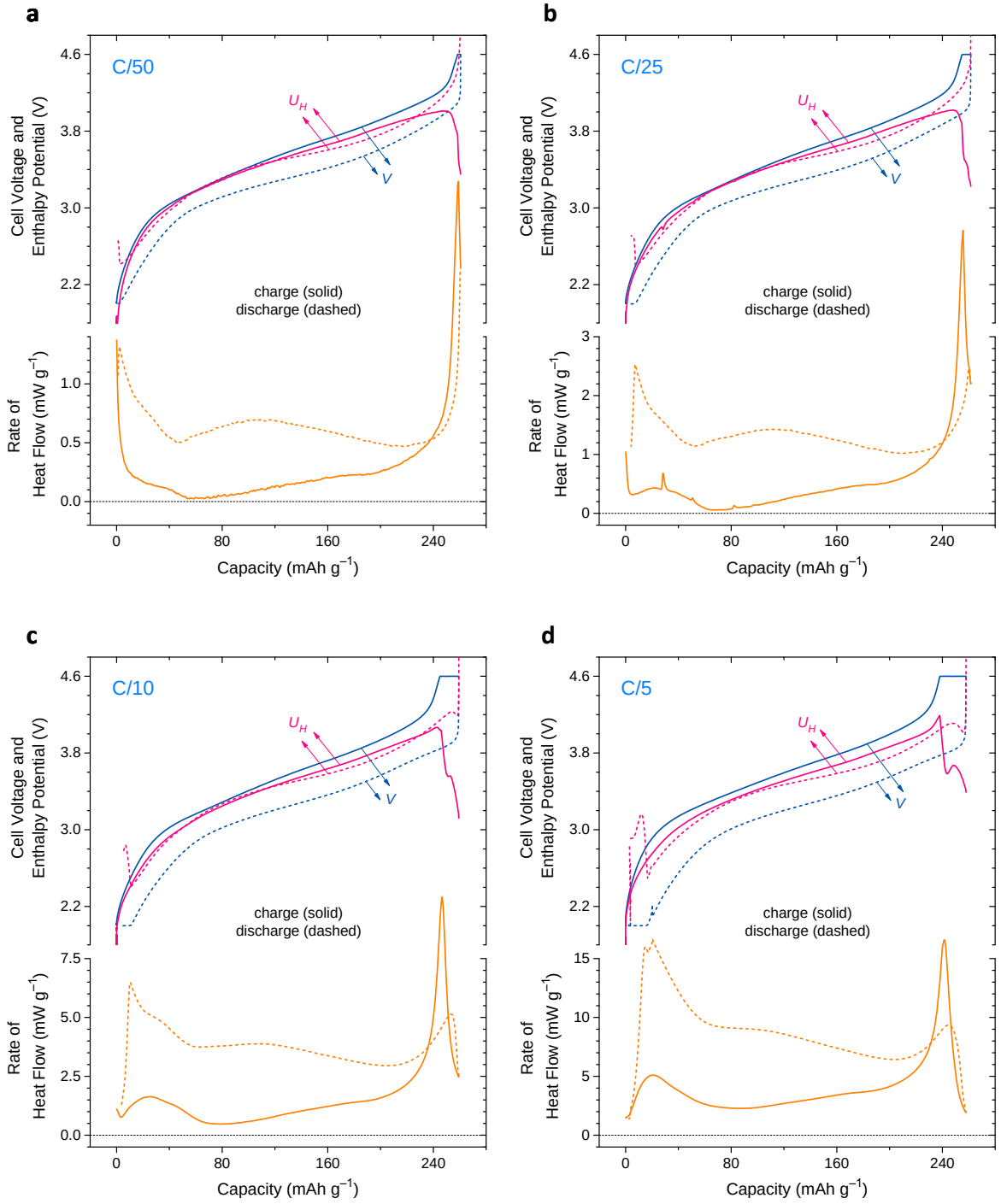


**Figure A4.8 |** The measured profiles for cell voltage (blue) and heat flow rate (orange) that were used to obtain the enthalpy potential profiles (pink) for 'activated' LRSO at (**a**) C/50, (**b**) C/25, (**c**) C/10, and (**d**) C/5. This data complements **Figure V.4**.

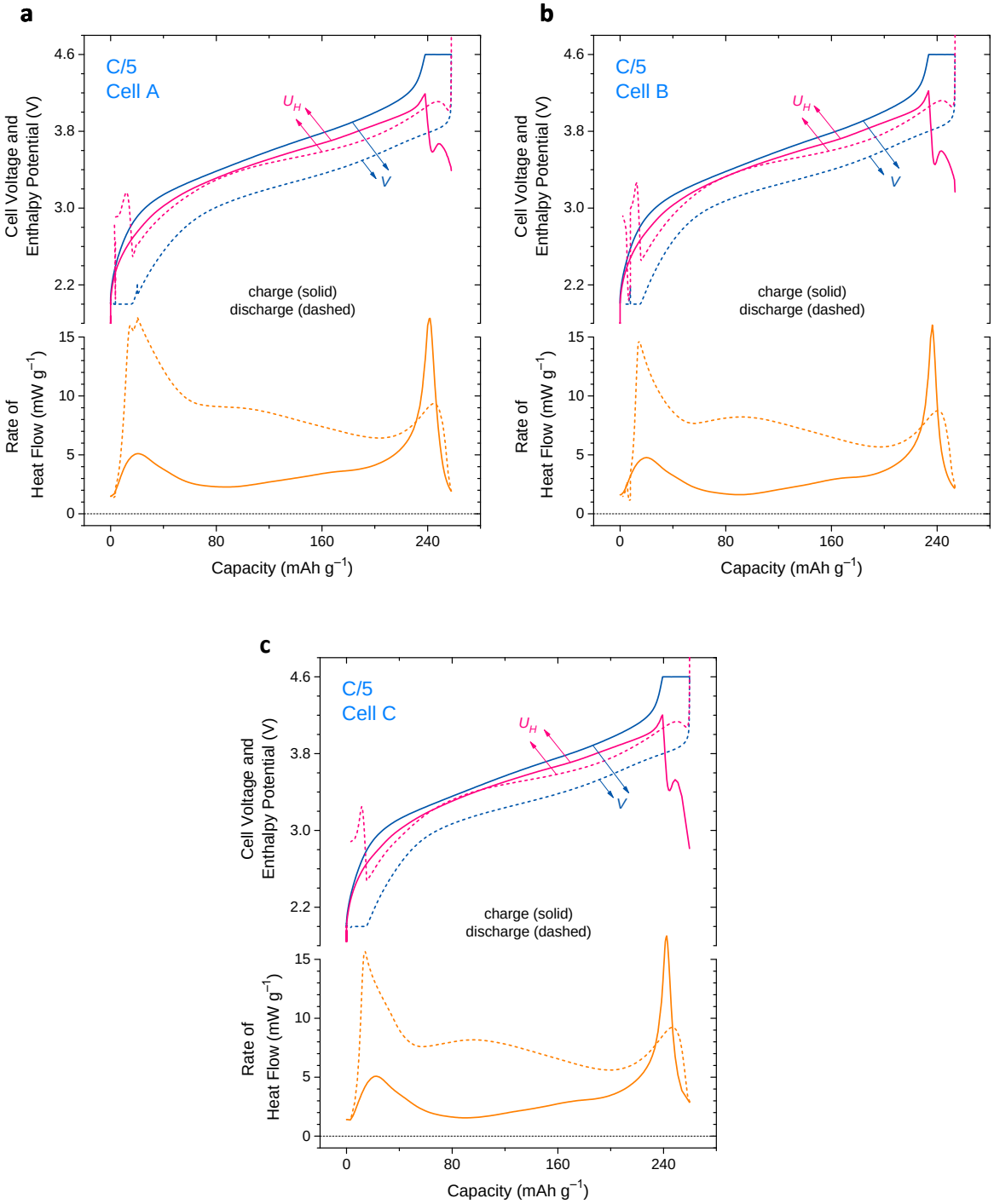


**Figure A4.9 |** The measured profiles for cell voltage (blue) and heat flow rate (orange) that were used to obtain the enthalpy potential profiles (pink) for 'activated' LRSO using three different cells (**a–c**). Note that the cell in panel (**a**) is same as the one in **Figure V.4** and it has a slightly higher internal resistance than the ones in (**b**) and (**c**) owing to the cell-to-cell variability. All three cells show slight path dependence in the enthalpy potential profiles.

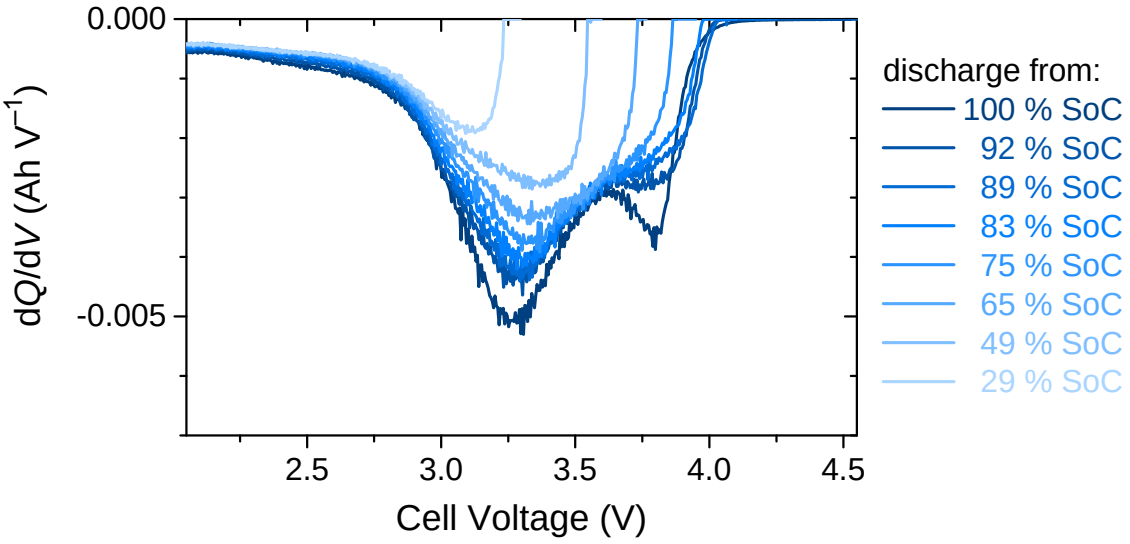


**Figure A4.10 |** $\boldsymbol{dQ/dV}$ curves for 'activated' LRSO discharged from different SoCs. These profiles correspond to the ones in **Figure V.5a**.

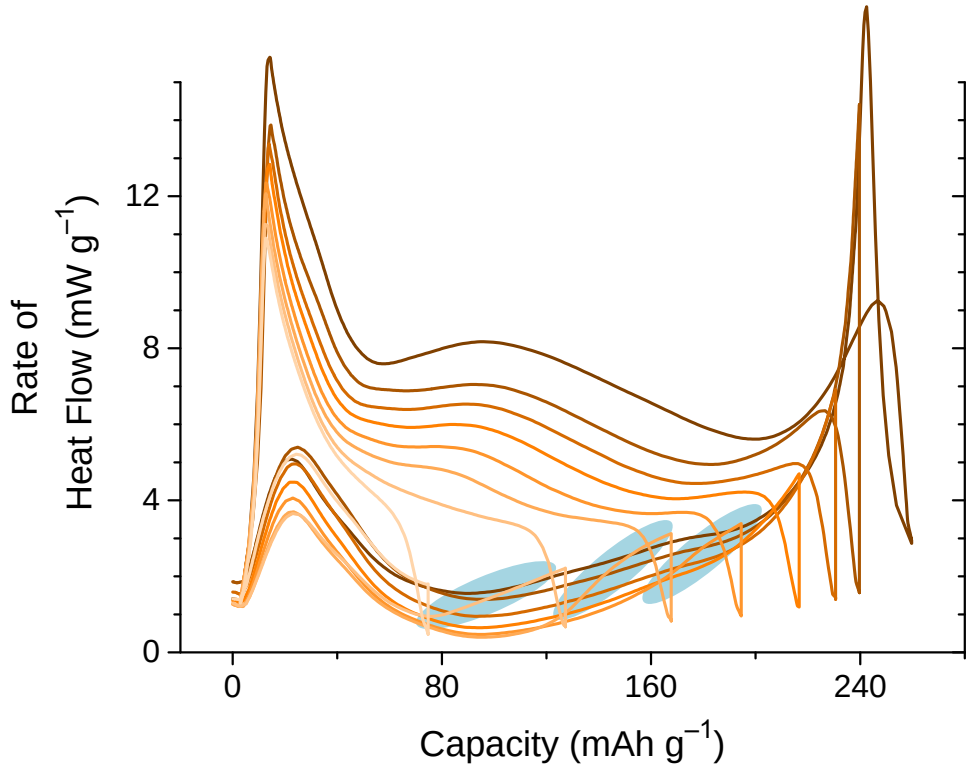


**Figure A4.11 |** Complete heat flow profiles for the voltage window opening experiment shown in **Figure V.5**. The slight differences in charge profiles cannot be explained at this stage. Moreover, a "memory effect" is also observed such that the charge heat flow rate slightly rises after crossing the previous SoC limit (as marked by the green highlighted zones). Again, no explanation can be provided for this at this stage.

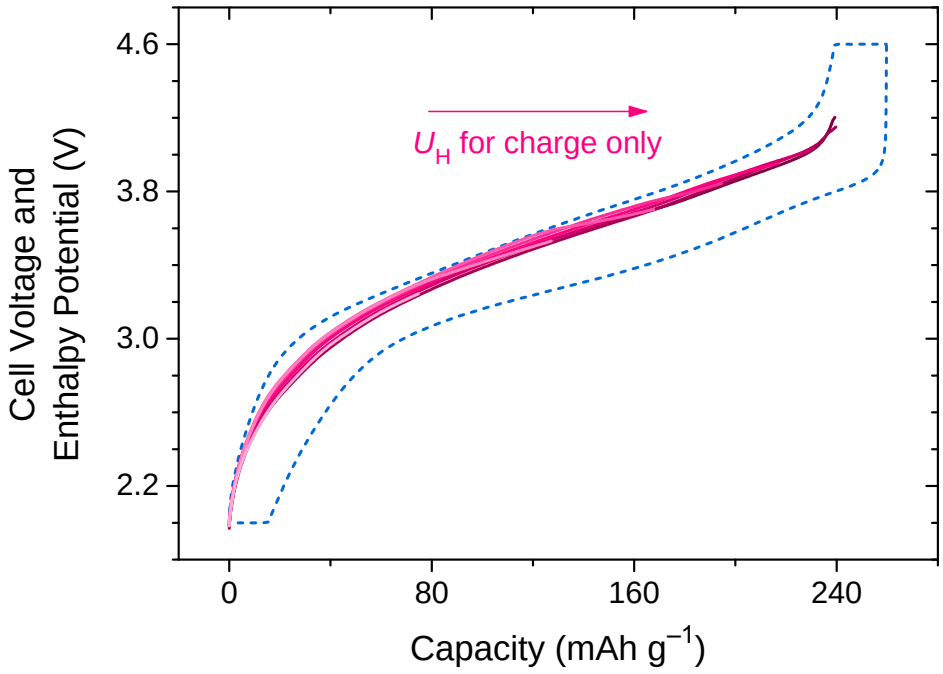


**Figure A4.12 |** The enthalpy potential profiles (on charge only) during the voltage window opening experiment carried out in **Figure V.5**.

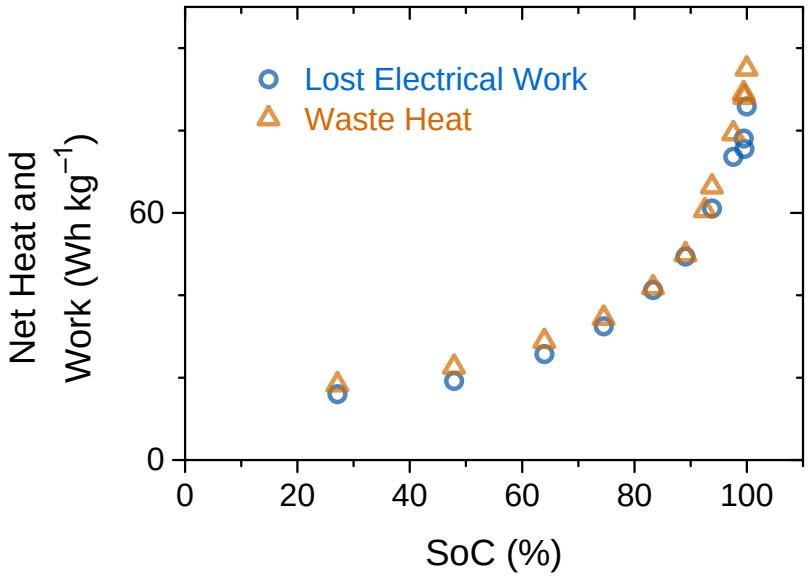


**Figure A4.13 |** As a function of SoC to which the cell is charged, a comparison of lost electrical work with waste heat over a complete charge–discharge cycle obtained by integrating respectively the cell voltage and the heat flow rate. A non-linear trend is again observed, thus indicating the worsening of voltage hysteresis with charging to higher SoCs. Note that there was no CCCV potentiostatic hold applied at 2.0 V to this cell, unlike the one in **Figure V.5**, leading to slightly lower values of net heat/work.

# A5 – Supporting Information for Chapter VI

## ○ Recommended protocols to evaluate the practicability

In light of the fundamental and practical results obtained on LRSO and Li-rich NMC electrodes in this thesis, it would be imperative to evaluate the practicability of emerging anionic redox based cathodes concerning real-world applications, where higher capacity is just one of the several stringent requirements. That is, besides showing higher capacity, a novel cathode must also outperform the existing ones in terms of rate capability, energy efficiency, and cycling stability, while staying competitive in cost and safety. Worth mentioning is the need for adopting some updated electrochemical testing protocols developed within this thesis, focusing specifically on the unique electrochemical properties that differentiate anionic redox compounds from classical cathodes. A list of recommended protocols, to facilitate consistent evaluation for the sake of correct comparison and practical evaluation, is given below.

- **Voltage hysteresis.** Voltage profiles should be measured at a low C-rate (slower than C/50) or with GITT/PITT to check for quasi-thermodynamic path-dependence. In that case, the *dQ*/*dV* profiles will not mirror between charge vs. discharge, and voltage window experiments (e.g. **Figure II.5** and **Figure IV.8**)[106,182] are recommended. Moreover, the lowered energy efficiency[156] should be reported.

- **Electrochemical kinetics.** To check whether sluggish kinetics accompanies anionic redox, the charge-transfer resistance and Li diffusion coefficient should be measured as a function of Li content via three-electrode impedance or other electroanalytical methods (e.g. **Figure II.7** and **Figure IV.10**).[106,194] In addition, recording *dQ*/*dV* profiles at different C-rates (e.g. **Figure II.6** and **Figure IV.9**) may provide a simple visual cue for sluggish kinetics of certain redox peaks.

- **Cyclability.** Capacity retention, a common metric for cyclability, can be remarkable for anionic redox cathodes such as optimized Li-rich NMCs, but it does not automatically imply voltage stabilization.[125,249,304,305] Therefore,

voltage fade should be reported by showing average charge / discharge voltages vs. cycle number (e.g. **Figure II.9** and **Figure IV.13**), as also recommended in previous literature.[165,179] Furthermore, while comparing different mitigation strategies, lets recall that some chemical / structural treatments unintentionally lead to capacity reduction (thereby lower extent of delithiation) and hence voltage fade 'appears' to ameliorate, but in reality it is just because the material is not being oxidized (utilized) fully.

## Anionic redox for high-energy batteries – Fundamental understanding, practical challenges, and future outlook


### Abstract :

Our increasing dependence on lithium-ion batteries for energy storage applications calls for continual performance improvements of their positive electrodes, which have so far relied solely on cationic redox of transition-metal ions for driving the electrochemical reactions. Great hope has recently been placed on the emergence of anionic redox – a transformational approach for designing Li-rich positive electrodes as it leads to a near-doubling of capacity – hence generating worldwide research interest. However, questions have been raised on the fundamental origins of anionic redox and whether its full potential can be realised in applications. This is exactly what this thesis aims to answer by using the knowledge from the fields of solid-state chemistry, electrochemistry, X-ray spectroscopy, and thermochemistry. We first provide a comprehensive historical account, a theoretical framework, some materials' design rules, and a survey of characterization techniques specific to anionic redox. Then, through comprehensive experimental studies that were performed in parallel on one 'model' (4*d* metal based) and one 'practical' (3*d* metal based) material, we highlight how the fundamental interplay between cationic and anionic redox processes governs the application-wise important properties of these promising battery materials (i.e. voltage hysteresis, rate performance, voltage decay, and heat generation,). Finally, using these results, we outline possible approaches for improving such materials and for designing novel ones. We also summarize their chances for market implementation in face of the competing nickel-based layered cathodes that are prevalent today.


Keywords : Lithium-ion batteries, Anionic redox, Solid-state electrochemistry, X-ray absorption spectroscopy, X-ray photoelectron spectroscopy, Isothermal calorimetry

---

## Redox anionique pour les batteries à haute énergie – Compréhension fondamentale, défis pratiques et perspectives d'avenir


### Résumé :

Notre dépendance croissante vis-à-vis des batteries lithium-ion pour le stockage d'énergie exige une amélioration de leurs électrodes positives, qui fonctionnent encore grâce au redox cationique des métaux de transition. L'émergence du redox anionique – une approche transformationnelle qui double la capacité des électrodes positives « Li-riches » – a récemment suscité de grands espoirs mondialement. Toutefois, des questions subsistent sur les origines fondamentales du redox anionique et sur son potentiel dans les applications pratiques. Cette thèse vise à répondre précisément à ces questions, en utilisant les connaissances de la chimie des solides, de l'électrochimie, de la spectroscopie des rayons X, et de la thermochimie. Pour ce faire, nous fournissons d'abord un compte rendu historique, un cadre théorique, les règles de conception de nouveaux matériaux, ainsi qu'un résumé des techniques de caractérisation propres au redox anionique. Ensuite, à travers des études expérimentales menées à la fois sur un matériau « modèle » (à base de métal 4*d*) et sur un matériau « pratique » (à base de métal 3*d*), nous montrons comment l'interaction fondamentale entre les processus de redox cationique et anionique régit les propriétés pratiques de ces matériaux (c'est-à-dire hystérésis de tension, performance de vitesse, chute de tension, et production de chaleur). Enfin, en utilisant ces résultats, nous décrivons les approches possibles pour améliorer ces matériaux et en concevoir de nouveaux. Nous résumons également leurs chances d'implantation sur le marché face aux cathodes lamellaires à base de nickel qui prévalent aujourd'hui.


Mots clés : Batteries lithium-ion, redox anionique, électrochimie, spectroscopie d'absorption des rayons X, spectroscopie de photoélectrons de rayons X, calorimétrie isothermique